THE UNIVERSITY
of EDINBURGH

The spatially resolved physical properties of high-redshift galaxies observed with KMOS

Owen James Turner

Doctor of Philosophy
The University of Edinburgh
August 2018

Lay Summary

Our knowledge of galaxies, specifically what they are made of and how they behave, has increased dramatically over the last 100 years. In the early 20th century, we believed that all objects were contained within the Milky Way, however it became clear, thanks to observational evidence collected with telescopes, that our Galaxy is one part in a tapestry containing hundreds of billions of unique 'island Universes'. As technology has developed, we've been able to see that there are different types of galaxies; for example those that actively form stars, and those which no longer do so. These galaxies are different in many other fundamental, and observable, *physical properties*. One of the most fascinating puzzles to those studying galaxies is to understand how different galaxies form and change over their lifetimes.

Light emitted by very distant galaxies takes a long time to reach us, due to finite speed of the light and the incredible size of our Universe. The most powerful telescopes can probe galaxies which are over 12 billion light-years away, thus providing a snapshot of the conditions of galaxies in the early Universe. As a result, we are now in a position to consider how, on average, the properties of different types of galaxies change over time. This thesis is concerned with studying in detail how *star-forming galaxies* behave in the early Universe, and understanding how they differ from local galaxies of the same type. This work lays the foundation for the next generation of facilities, which will allow us to see and understand even more.

Abstract

The formation and evolution of galaxies is governed by a set of complex non-linear physical processes. When we observe a galaxy at a particular epoch, we see a unique spatial distribution of stars, gas and dust, and can use the light emitted by these components to infer the chemical composition and dynamics of the galaxy. The spatial distribution of the different components, as well as the galaxy chemistry and dynamics, is shaped by the history of both the internal and external physical processes involving the galaxy until the time of observation. Although no two galaxies appear the same, the study of galaxy evolution is an attempt to understand generally the physical processes which lead to the observed distribution of galaxy properties at any stage across the history of the Universe. Many of these processes are still poorly understood, particularly in terms of the timescales over which they operate and their importance in the energetics of the galaxy. Much progress has been made in this area in both the local and distant Universe over recent years, thanks in particular to multi-object integral-field spectrographs, which have allowed for the spatial mapping of representative samples of the galaxy population.

This thesis presents studies of the spatially resolved dynamical and chemical properties of high-redshift star-forming galaxy samples, using integral-field spectroscopic observations with the K-band Multi-Object Spectrograph (KMOS). In Chapter 2 I describe the data reduction pipeline developed to process these observations. Specifically, I have added processing steps which extend this pipeline beyond the standard recipes and describe these in the chapter.

In Chapter 3, using a sample of 77 star-forming galaxies from the KMOS Deep Survey (KDS) at a median redshift of $z \simeq 3.5$, I demonstrate that the intrinsic, beam-smearing corrected velocity dispersions are ubiquitously high, with a sample median value of 70.8kms^{-1}. At this redshift, the KDS sample is the largest from which these observations have been made and the measurements indicate that the trend of increasing intrinsic velocity dispersions continues out to at least $z \simeq 3.5$.

In Chapter 4, by compiling 16 high-redshift comparison samples from the literature, I study the evolution of the stellar mass Tully-Fisher relation, demonstrating clearly that recent literature discrepancies can be explained by differing sample selection criteria. By also examining the rotation-velocity fields of the KDS galaxies, I discuss the possibility that a significant portion of gravitational support is provided by random motions, as evidenced by the redshift decline of the ratio of rotation velocity to velocity dispersion. This leads to the formulation of a 'total velocity' containing both velocity dispersion and rotation velocity terms. Combining the intrinsic velocity dispersion values with the rotation velocities of the galaxies is necessary to trace the galaxy potential wells at intermediate and high redshift. When this is done, the evolution of the normalisation of the total-velocity versus stellar-mass relation is consistent with a steady decline over cosmic time.

Finally, using multi-band KMOS observations from the KMOS LEnsed galaxies Velocity and Emission line Review (KLEVER) survey, I explore the spatial distribution of emission-line ratios across individual galaxies at $z \simeq 2.3$, finding significant variation in the dust content and gas excitation conditions between galaxy cores and outskirts. The majority of KLEVER galaxies are observed to have negative Balmer decrement gradients (centrally concentrated dust distributions), with more-negative gradients belonging to the galaxies with higher stellar mass, lower Hα velocity dispersions and lower Hα luminosities. Similarly, the dust-corrected ratio of the [O III]$\lambda\lambda$4960, 5007/[O II]$\lambda\lambda$3727, 3729 emission lines (which may be used as a proxy

for metallicity) for the majority of KLEVER galaxies has a radial profile with a positive gradient (i.e. higher metallicity cores), with more-positive gradients also correlating with higher stellar mass, lower Hα velocity dispersions and lower Hα luminosities. This work is still preliminary and requires further work to strengthen and build on the conclusions.

The fundamental objective of the work presented throughout this thesis is to understand the spatially-resolved dynamical and chemical structure of high-redshift star-forming galaxies and to draw conclusions regarding how they evolve into the star-forming galaxies we observe in the local Universe.

Declaration

I declare that this thesis was composed by myself, that the work contained herein is my own except where explicitly stated otherwise in the text, and that this work has not been submitted for any other degree or professional qualification except as specified.

Parts of the work that forms Chapters 3 and 4 of this thesis is either published, or has been submitted for publication in Turner et al. (2017, 2018).

(*Owen James Turner, August 2018*)

Acknowledgements

It is a difficult task to acknowledge the many people who've contributed in getting this thesis into a finished state. First I would like to thank the STFC for funding me throughout this PhD and for organising many great events that have enriched the experience. I would like to thank my supervisors Michele Cirasuolo, Ross McLure and Jim Dunlop for their tuition and guidance. Looking back over these 4 years I've developed a lot, both technically and as a person, and a large part of that is down to them. To my amazing colleagues at the Royal Observatory Edinburgh. We've been through the laughter and intense frustration together and their companionship has led to many wonderful memories. During my 6 month stay in Garching, whilst working at ESO, I made many great friends and received lots of amazing advice, so I would like to thank the ESO studentship programme for funding me whilst I was there and for the wonderful academic environment at Garching Forschungszentrum. I would like to say an enormous thank you to Chris Harrison for going above above-and-beyond to help me, both with the technical details of projects and also with paper writing and general guidance in life.

From a technical perspective, I've made continual use of the `TOPCAT` software and various `Astropy` packages, so a huge thanks to the developers who selflessly write and share this code which makes life much easier.

Of course, I owe so much to my mum and dad, not just during the PhD but also in the undergraduate years before. I'll fondly remember their visits to Edinburgh over the course of my 9 year university stint, patiently listening to whatever was troubling me at the time or celebrating the successes together. Finally, to Megan. You've looked after me over the years, put up with me disappearing for 6 months, encouraged me through the troughs and generally provided a great deal of inspiration and happiness. I love you, owe you many favours and am very much looking forward to post-PhD life together.

Contents

List of Figures

List of Tables

Chapter 1

Introduction

1.1 Overview

On the 26th April 1920, almost a century ago, Harlow Shapley and Heber Curtis met to publicly debate the physical nature of 'spiral nebulae'; specifically whether they are internal to the Milky Way Galaxy or separate 'island universes'. Thanks to observations made throughout the 1920s by Edwin Hubble, using the world's then most powerful telescope, the debate was settled conclusively in favour of Curtis's viewpoint, and spiral nebulae were recognised as external galaxies. Humanity started to grasp for the first time the distances between these aptly-named islands, the scale of the Universe and hence the extent of the unknown.

The 1920 'great debate' highlights three important facets of astronomical research. First that paradigm shifting discoveries, like those surrounding the nature of galaxies, were made relatively recently in our history, provoking a steep learning curve from the beginning of the 20th century onwards. Second that differences in the way researchers interpret data arise naturally and progress is made by the subsequent (sometimes theatrical) sharing of analysis methodologies. Third that our understanding of the Universe we inhabit has developed hand-in-hand with technology, which for a long

time in astronomy amounted literally to being able to see more clearly.

Our knowledge of the physical and temporal scale of the Universe, as well as the properties of the galaxy population at different locations across this space-time, has rapidly advanced in the intervening century. There are abundant and fast-accumulating data and literature describing the complexities of how galaxies form and evolve both secularly and through violent interactions with each other and their environments. Despite this progress, many open questions remain, relating particularly to the study of galaxy evolution, partly as a consequence of the technical and observational challenges of collecting data over large cosmological distances. The work presented throughout the main body of this thesis is my contribution to our understanding of galaxy properties and galaxy evolution.

The remainder of this chapter serves as a brief summary of conceptual and technological developments in astronomy, as a primer to the key concepts and issues involved in the study of galaxy evolution and as a discussion of research and open questions being currently tackled in these areas. Additional introductory material specific to the topic to be discussed is provided at the beginning of the subsequent chapters.

1.2 Historical summary of the study of galaxies

Humankind has been continually striving to grasp its position in the Universe for as long as records exist, with the dominant cosmological model being Ptolemaic (geocentric) until the latter stages of the Renaissance period, during which Heliocentrism began to take hold. Many household-name scientists, including Nicolaus Copernicus, Tycho Brahe, Galileo Galilei and Johannes Kepler are credited with being at the heart of this scientific revolution, which saw the development of the first telescopes and the flourishing of data-driven analysis. First edition copies of books published by those listed above are housed in the Royal Observatory Edinburgh's Crawford collection, some photographs of which are shown in Fig. 1.1.

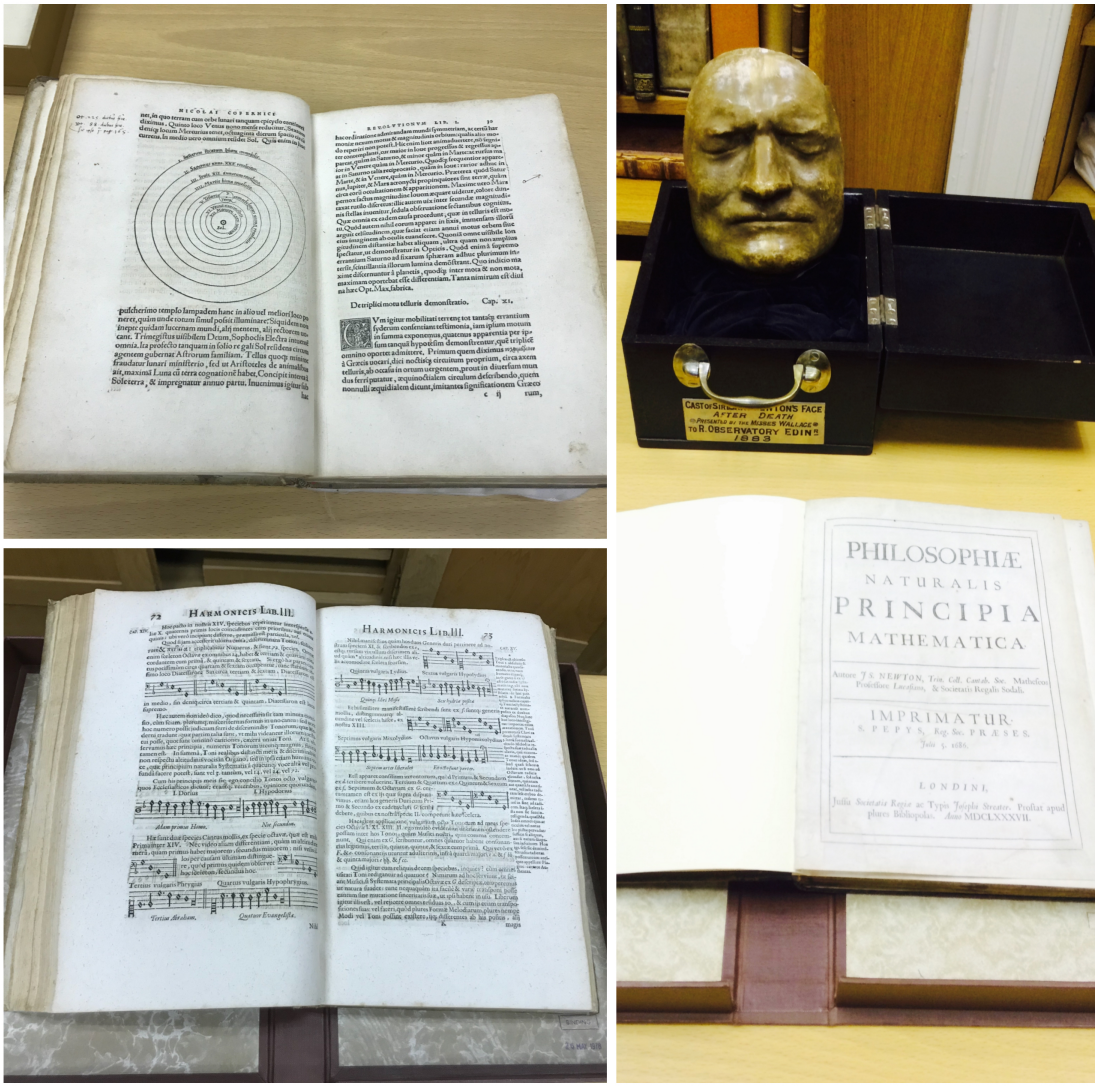

Figure 1.1: *Top Left:* Nicolaus Copernicus's 'De revolutionibus orbium coelestium' (Copernicus, 1543) open at the famous page describing his seminal Heliocentric model. *Bottom Left:* Johannes Kepler's 'Harmonices Mundi' (Kepler, 1619) open at the page detailing Kepler's representation of the motion of planets as a sequence of consonant musical notes. *Right:* Cast of Isaac Newton's face presented to the Royal Observatory Edinburgh in 1883, alongside Newton's Philosophiae Naturalis Principia Mathematica (Newton, 1687). The books are first edition copies and are part of the Crawford collection, this being a priceless library of old astronomical texts donated to the Royal Observatory Edinburgh in 1888 by James Ludovic Lindsay, 26th Earl of Crawford.

Thus began a cascade of theoretical and observational development, including Newton's theory of gravitation (Newton, 1687), Huygens' theory of light propagation (Huygens, 1690) later used by Young at the beginning of the 19th century to further understand

the interference and diffraction of light waves (Young, 1802), early quantitative measurements of the solar spectrum by Joseph Fraunhofer (e.g. Fraunhofer, 1817) and Gustav Kirchhoff, leading to Kirchhoff's thermodynamic laws (e.g. Kirchhoff, 1860), the cataloguing of nebulous celestial objects by Charles Messier (Messier, 1781), the Herschels (Herschel, 1802, 1864), James Dunlop in the southern hemisphere (Dunlop, 1828) and John Louis Emil Dreyer (Dreyer, 1888) and Einstein's theory of general relatively (Einstein, 1916). It is the objects in the catalogues of the nebulae which became the topic of the 'great debate' outlined above.

The debate was resolved when Edwin Hubble made use of the relationship between the period and luminosity of Cepheid variable stars discovered by Henrietta Leavitt (Leavitt, 1908; Leavitt & Pickering, 1912) to firmly establish the extragalactic nature of several nebulae (Hubble, 1925, 1926a, 1929b). Further work by Hubble explored and classified the diversity of galaxy morphologies (Hubble, 1926b), correctly deducing the existence of a bimodality in galaxy type. These are the spiral, or late-type, galaxies characterised by ordered rotation in a flattened disk and the elliptical, or early-type, galaxies characterised by smooth, featureless light distributions indicative of no preferred rotation axis (Hubble, 1926b). Hubble speculated on the connection between observed morphology and the combination of galaxy formation mechanism and evolutionary pathways. Building upon earlier work by Vesto Slipher (Slipher, 1917), Hubble also presented important evidence for an expanding Universe by comparing the recession velocities of galaxies with his estimates for their distances from the Earth.

Since these initial stages in the study of galaxies, monumental progress has been made. Astronomers have been systematically cataloguing galaxies in different patches of the sky with both imaging (see § 1.4.2) and spectroscopic (see § 1.4.3) campaigns out to ever-increasing redshifts, making use of spectacular advances in telescopes and their instrumentation. These observations constrain the range of physical processes within galaxies which lead to the emission of the radiation we detect, hence our knowledge of how galaxies behave and change has accumulated. Over the past century,

improvements in light-detection techniques (including improvements to the detectors themselves and our ability to send telescopes into space) have opened up new regions of the electromagnetic spectrum, revealing the full picture of multi-wavelength galaxy emission. A crucial step forward was the ability to digitise data following the invention of the Charge-Coupled Device (CCD; Boyle & Smith 1970), leading to more efficient observations and far easier storage, processing and sharing of data.

Of particular importance for the study of galaxies is Hubble's namesake, the *Hubble Space Telescope* (*HST*), which has demonstrated the existence of hundreds of billions of galaxies distributed throughout the observable universe using very deep observations of small patches of sky known as 'fields' (see § 1.4.2). *HST* has provided unprecedented data quality, enabling the observation/computation of correlations between the physical properties of large statistical samples of both the late-type and early-type galaxies. One key goal in galaxy evolution studies has been to track changes in so-called 'scaling relations' using populations of galaxies at different lookback times, this being a powerful probe of the ways in which average galaxy properties have changed over cosmic history.

This thesis focusses on using such methods to further understand the behaviour and evolution of late-type galaxies over a large fraction of the history of the Universe. The development of our current understanding of the physical properties of late-type galaxies, and how these properties have evolved over time, is reviewed throughout § 1.5. The following two sections offer a discussion of both the cosmological context in which galaxy evolution is taking place and the quantitative measurement of light using imaging, spectroscopy and integral-field spectroscopy.

1.3 Structure formation and evolution within ΛCDM

Overwhelming evidence now exists for the Big Bang model, which describes the birth and initial stages of our Universe. This evidence has accumulated principally

from increasingly-sophisticated analyses of temperature anisotropies in the Cosmic Microwave Background (CMB); a (nearly) isotropic blackbody radiation field encoded with information about the early and intervening Universe. Provided here are some fundamental details regarding the widely-accepted ΛCDM cosmological model which describes the matter/energy content and evolution of the Universe. For the sake of brevity, many important steps in the progress towards this paradigm are omitted. For more information, both Longair (2006) and Mo et al. (2010) provide excellent overviews of the historical details.

1.3.1 Inflation and structure formation

Armed with the knowledge that the Universe is expanding (Hubble, 1929a), one can reverse the arrow of time and consider the properties of the smaller, denser and hotter early Universe. George Gamow explored the possibility of primordial nucleosynthesis in this environment as the origin of the elements (e.g. Gamow, 1946, 1948) which had then been observed in the spectra of the sun and other stars (e.g. Fraunhofer, 1817; Kirchhoff, 1860). Gamow also predicted that the residual heat from such a Universe should be visible today as thermal radiation peaking in the microwave region of the spectrum. The subsequent detection of this 'cosmic microwave background radiation' provided compelling evidence to support a hot early Universe, as well as its subsequent cooling and expansion.

There is no single reference for the inception of the Big Bang model, rather it is the result of the complete reversal of the expansion to a gravitational singularity, named ironically after Fred Hoyle's 1949 description of a theory he passionately opposed. On its own, the model has many successes, for example as the mechanism to explain the above predictions of George Gamow and as a description of the thermal history of the Universe, but it also suffers from several conceptual issues. These include the **Flatness** and **Horizon** problems, which highlight respectively that the lack of any observed spacetime curvature and the isotropy of the CMB seem incredibly unlikely in

the context of the Big Bang model. The theory of inflation (Guth, 1981; Linde & D., 1982; Albrecht & Steinhardt, 1982) provides a resolution for these issues by postulating that immediately after the Big Bang, the Hubble radius of the Universe (i.e. the scale over which photons can propagate in the time elapsed since the Big Bang) expanded exponentially to become many orders-of-magnitude larger than the scale over which matter was in causal contact. This theory also offers a plausible origin for the formation of structures within the Universe.

Decades prior to the inflation theory it was calculated, by applying Jeans gravitational instability criterion (Jeans, 1902), that overdense regions of matter in an expanding Universe could detach from the universal expansion and collapse gravitationally to form bound 'structures' (e.g. Gamow & Teller, 1939; Lifshitz, 1946). This mechanism was put forward as an explanation for the origin of the galaxies (Gamow & Teller, 1939), which will be discussed further in the following subsection. For this reasoning to be successful however, there must have existed some initial spectrum of deviations from the mean density of matter in the Universe, referred to as density perturbations, the origin of which was unknown. The patches of high density would grow larger via aggregation of neighbouring material during early expansion, before subsequently collapsing when the Jeans criterion was satisfied. In the context of inflation, such density perturbations are seeded as quantum fluctuations in the pre-inflationary era and grow during the inflationary expansion. The origin of these quantum density perturbations is still not derivable from first principles and attempting to further understand these earliest epochs of our Universe is a very active area of research.

1.3.2 The formation of the first stars and galaxies

A galaxy is a gravitationally bound collection of stars, dust and gas which contains a central super-massive black hole. In order for a galaxy to form from the collapsing material, or gas, discussed above, the gas must be able to cool (i.e. to dissipate gravitational binding energy) effectively. This happens through a variety of radiative

processes at different temperatures, leading ultimately to a distribution of stars formed at a variety of times from dense gas clumps with different angular momenta. This 'monolithic collapse' scenario of galaxy formation (Eggen et al., 1962) explains the emergence of galaxies, starting from density perturbations in an expanding Universe, and was used to explain the present day distribution of disk and halo stars in the Milky Way.

The observed excess of virial to stellar mass in galaxy clusters (Zwicky, 1937) was the source of early speculation regarding the existence of dark matter. In the mid-to-late 1970s, evidence, based on the flat outer rotation curves (i.e. rotation-velocity versus radius) of spiral galaxies (e.g. Rubin et al., 1978, 1980) was mounting. Amidst speculation surrounding the nature of this additional observed mass component within galaxies, galaxy formation scenarios were adapted to include the gravitational collapse of a dark matter-baryon mixture, resulting in a dark matter halo and a cooling core of baryonic material (White & Rees, 1978). At the level of this introduction, the addition of dark matter doesn't change the conceptual framework of gravitational collapse, cooling and star formation to form a galaxy. However, the existence of a dark matter halo which is capable of transferring angular momentum to the central, collapsing baryons is hugely important in shaping the dynamics of the forming galaxy. This in turn is crucial for determining the distribution of stars and hence the observed morphological type at some later stage in the evolution of the galaxy. Dark matter also provides an explanation for the gravitational clustering of groups of galaxies, and so shapes the environments in which galaxies live.

The gravitational assembly and clustering of the dark matter density perturbations at a particular redshift slice form a pattern across the sky which is referred to as the cosmic web. The observed distribution of galaxies formed within this web is indeed highly structured, as revealed by large redshift surveys such as the Sloan Digital Sky Survey (SDSS; York et al. 2000; Abazajian et al. 2009), the 2 degree Field Galaxy Redshift Survey (2dFGRS;Colless et al. 2001) and the VIMOS Public Extragalactic Redshift Survey (VIPERS; Guzzo et al. 2014). Fig. 1.2 demonstrates this pattern by plotting

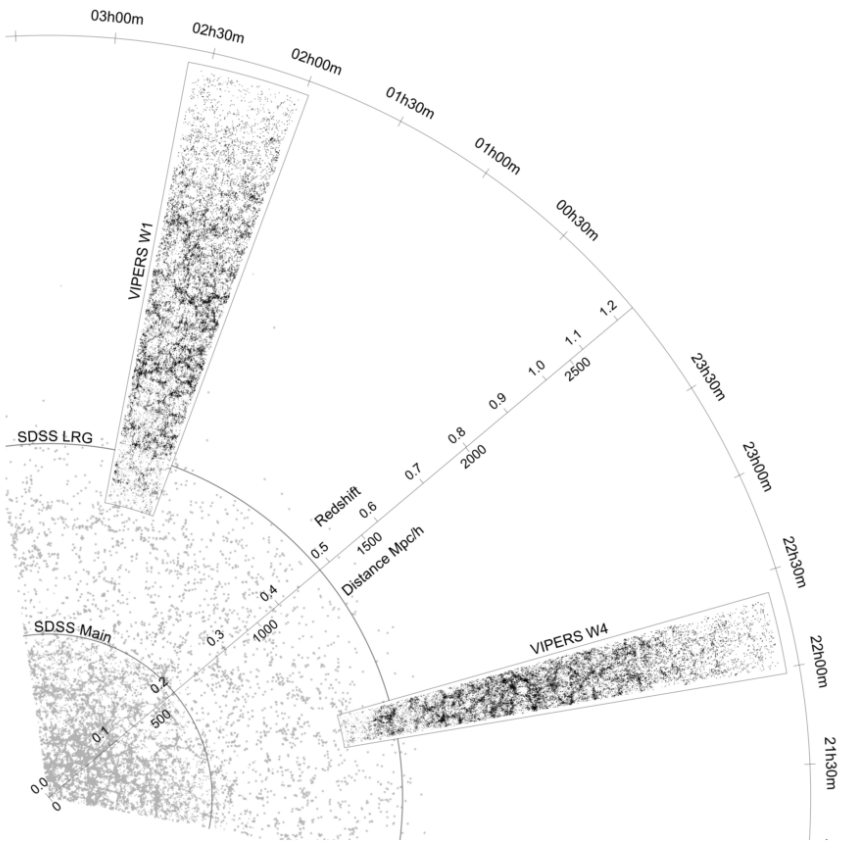

Figure 1.2: Redshift surveys such as the SDSS (York et al., 2000) and VIPERS (Guzzo et al., 2014) combine positional information with measured redshifts (distances) to unveil structure in the galaxy distribution. Each mark in this figure is an individual galaxy plotted in polar coordinates, with its right ascension as azimuthal and redshift as polar coordinate, extending to $z \sim 1.2$. The observed pattern is web-like, with overdense regions connected to one another by galaxy filaments. We believe this structure is shaped by the gravitational influence of dark matter, acting over timescales of billions of years. Thanks to modern multi-object spectrographs such as VIMOS, it is possible to investigate this pattern out to large cosmological distances. Taken from Fig. 15 of Guzzo et al. (2014).

Right Ascension (RA) against redshift in polar coordinates, using SDSS and VIPERS data which together cover the redshift range $0 < z < 1.2$. The individual galaxies follow an interconnected structure of overdensities, tracing the underlying dark matter skeleton of the Universe.

Fig. 1.3 depicts the concepts discussed above as a logical flow diagram, with different paths leading to the formation of different galaxy types (see § 1.3.4 for further discussion). Each process depicted in this chart is full of complexity, and it is a key

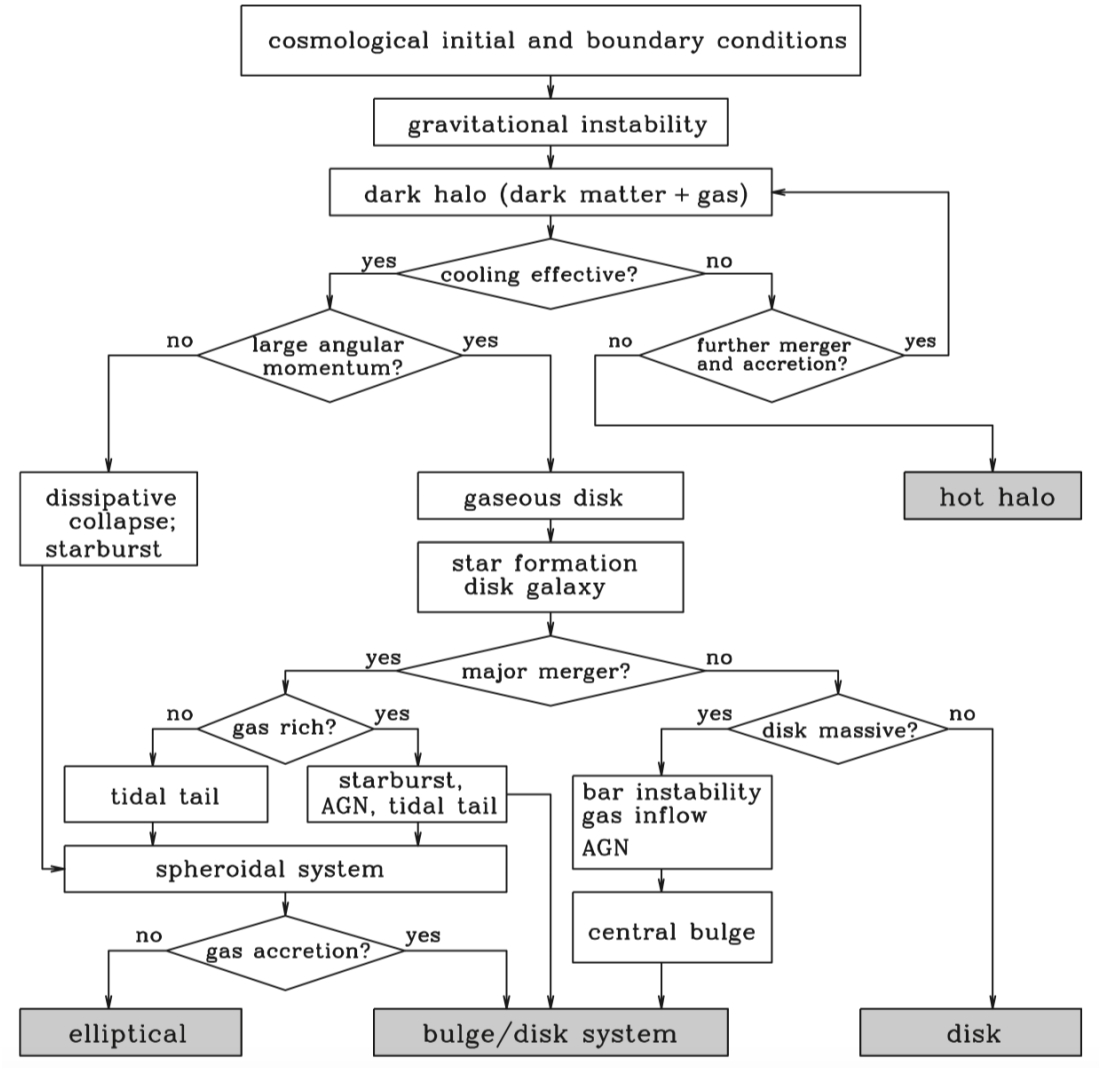

Figure 1.3: The fundamental processes dictating galaxy formation within the ΛCDM framework are shown here as a flowchart. Theoretically calculating the details of each of these processes, both in individual systems and within a cosmological context, and comparing with observations has shaped the current galaxy formation and evolution paradigms. Taken from Fig. 1.1. of Mo et al. (2010).

goal of galaxy formation researchers to investigate statistically and in a cosmological context how they proceed quantitatively.

1.3.3 The ΛCDM cosmological model

As mentioned above, the widespread acceptance of dark matter as the dominant matter component within our Universe is a relatively recent development. Even more recent

was the Nobel prize winning discovery that the expansion rate of the Universe is accelerating (Perlmutter et al., 1998; Riess et al., 1998), the accepted explanation of which is the existence of a uniform dark energy component (Λ) permeating all space, which dominates the mass-energy density of the Universe at late times. Along with cold dark matter (CDM), these two ill-understood components contribute over 95 per cent of the present day mass-energy density of the Universe.

ΛCDM is the 6-parameter cosmological model describing the inception, geometry, matter density and evolution of the Universe, assuming that general relativity is the correct theory of gravity operating on cosmological scales. In the context of this thesis, ΛCDM describes the environment in which the galaxy population forms and evolves. The most robust constraints on the parameters of this model come from precision measurements of brightness temperature anisotropies in the CMB radiation (e.g. Spergel et al., 2007; Planck Collaboration et al., 2015), which are imprints of the mass density distribution just 400,000 years after the Big Bang. However, competitive cosmological parameter constraints are now being derived from weak gravitational lensing studies (e.g. Heymans et al., 2013; DES Collaboration et al., 2017; Hildebrandt et al., 2017) and these are expected to become more precise with the next generation of wide-field telescope surveys (see § 1.4.2).

The remarkable agreement between theory and the power spectrum of CMB temperature fluctuations is one of the greatest triumphs in modern science. But that is not to say that ΛCDM is without flaws. Besides the unsettling truth that 95 per cent of the Universe exists in a 'dark' component, i.e. we fundamentally do not yet understand what dark energy and dark matter are, there are several potential issues with the theory, particularly on small scales. As outlined in a recent review by Bullock & Boylan-Kolchin (2017), these issues include missing satellites and puzzling satellite galaxy distributions, the core-cusp problem which describes a discrepancy between theoretical and observed halo dark matter density profiles and the Too-Big-to-Fail argument. ΛCDM provides a coherent theory for the formation and evolution of

galaxies and has withstood considerable theoretical and observational scrutiny, however as the above issues highlight, many details are still a matter of controversy and active research within the community.

1.3.4 Formation mechanisms of elliptical and spiral galaxies

The above discussion focusses generally on the formation of protogalaxies via the gravitational collapse of the expanding and non-uniform mixture of cold dark matter and baryons in the early Universe. It is from these systems that the stunning diversity of galaxies observed across cosmic time emerges, through a variety of secular (gradual rearrangement of energy and mass either internally or through interactions with the surrounding environment) and more violent physical processes. At each observed redshift regime, the galaxy population is observed to be bimodal, i.e. composed of both star-forming (spiral, late-type) and quiescent (elliptical, early-type) galaxies, although there is considerable diversity within each of these subpopulations. As outlined in the introduction of Dekel & Birnboim (2006) this bimodality is manifest in many observable physical properties such as dynamics, colour, morphology, star-formation rate and history, environment and both the stellar/halo mass. Moreover the relative number densities of the two subpopulations are changing with cosmic time, in the sense that the relative abundance of the 'red sequence' of quiescent galaxies is growing with increasing time since the Big Bang (e.g. Bell et al., 2004; Brammer et al., 2011; Muzzin et al., 2013). Naturally then, a further fundamental goal of galaxy formation studies is to understand and quantify the combination of fast and slow physical processes which lead to the formation and evolution of different galaxy types.

Tidal-torque theory (Hoyle, 1949), whereby rotational motions can be generated via tidal gravitational interactions with neighbouring systems, applied in the context of the gravitational instability and collapse picture (e.g. Peebles, 1969; Efstathiou & Jones, 1979; Barnes & Efstathiou, 1987), leads to the formation of rotating-disk systems concentrated at the centre of dark matter halos (provided that angular momentum is

conserved during collapse). Subsequent star formation proceeds predominantly in the disk to which the gas is confined, resulting in a population of halo stars formed in the initial collapse with no preferred orbital direction and the disk stars orbiting with the remaining gas in a flattened plane. Such systems may 'collide' with one another at some stage during their development in a process known as merging, and do so preferentially in the higher density regions of the cosmic web which contain most matter. Major mergers are defined as those where the progenitors have similar baryonic mass content (i.e. the baryonic mass ratio of the less massive galaxy to the more massive galaxy is > 0.25) and are capable of violently rearranging mass and energy within the interacting systems, inducing starburst events which may rapidly exhaust the gas reservoir of the merged galaxy.

Early, famous papers by Alar and Juri Toomre (Toomre & Toomre, 1972; Toomre, 1977) demonstrated that peculiar morphologies, and in particular 'elliptical remnants' could be left behind by such processes, suggesting that this is the dominant formation mechanism of elliptical galaxies. More recently, the paucity of massive quiescent galaxies at $z > 2.3$, as argued in van Dokkum et al. (2008), and their small sizes but high surface mass densities (e.g. Khochfar & Silk 2006; Toft et al. 2007; van Dokkum 2008) effectively rules out a monolithic collapse origin for the formation of elliptical galaxies. This is due to the scarcity of fully-assembled ellipticals at high redshift, and the very small effective radii of the observed high-redshift population, necessitating significant galaxy growth through the aggregation of additional material.

In the absence of the violence of major merger events, a second series of pathways by which elliptical galaxies may form are secular processes, which are both internal to individual galaxies and involve exchanges between a galaxy and its environment. These include star formation, chemical enrichment, energetic feedback from supernovae and Active Galactic Nuclei (AGN), bar formation, bulge growth and both inflows of cool molecular gas and outflows from the galaxy (e.g. Kormendy & Kennicutt 2004 and see Fig. 1.4). Ultimately it is the availability of gas which regulates the processes

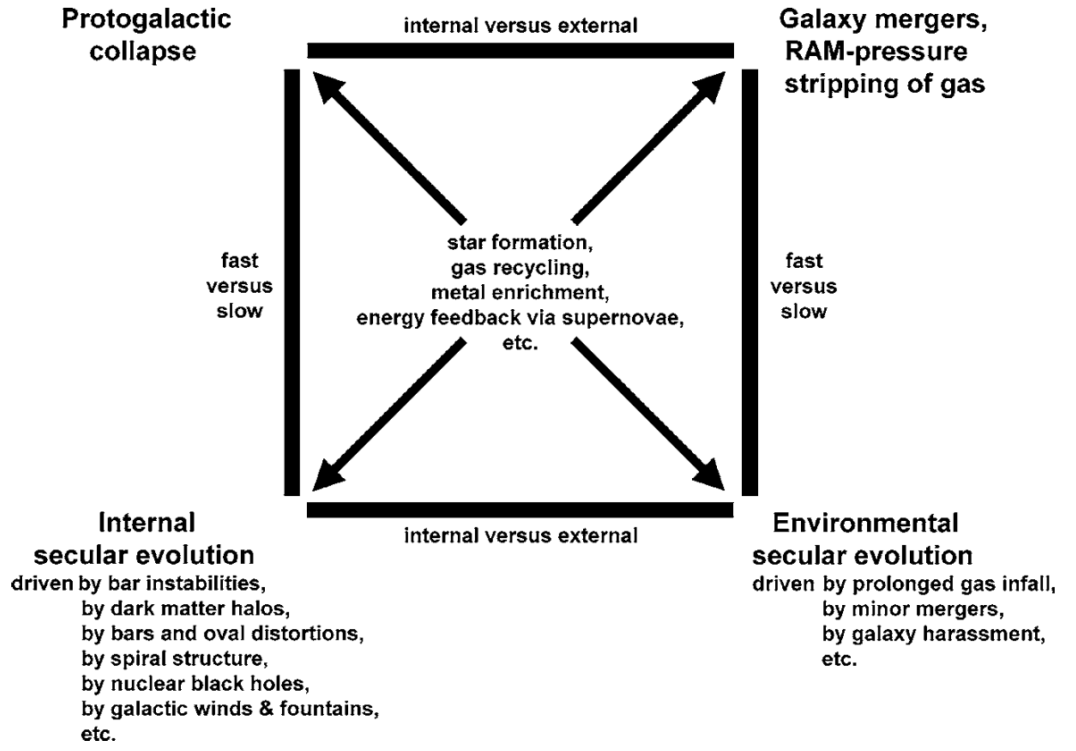

Figure 1.4: A combination of fast and slow internal and external processes, such as those listed here, are responsible for driving galaxy evolution and shaping the diverse morphologies of both elliptical and spiral galaxies. Taken from Fig. 1 of Kormendy & Kennicutt (2004).

driving galaxy evolution (e.g. Davé et al., 2011a,b; Saintonge et al., 2013; Lilly et al., 2013). Perhaps most important in the formation of elliptical galaxies are feedback processes. Since radiative cooling is a runaway process, it has long been predicted that, in the absence of additional energy input, all baryons would have collapsed into galaxies and formed stars by the present day (e.g. Larson, 1974; Cole, 1991; White & Frenk, 1991; Balogh et al., 2001; Bower et al., 2006). From observations of the *K*-band galaxy luminosity function it has been determined that only about 5 per cent of cosmic baryons have formed stars (e.g. Balogh et al., 2001), highlighting the importance of feedback mechanisms which heat and potentially expel the gas trapped within halos. The cessation of star formation as a consequence of the exhaustion or heating of halo gas is referred to as 'quenching', and may be induced by both internal and external processes (e.g. Peng et al. 2010; Peng et al. 2015). Quenching of star formation must be accompanied by morphological transformation to form an elliptical galaxy, with

this possibly occuring through 'harassment' by tidal fields in cluster environments (e.g. Moore et al., 1997) and via a combination of internal processes and minor mergers in less dense regions (e.g. Qu et al., 2017). There is currently a great deal of active research exploring the plethora of possible feedback-induced quenching and morphological transformation mechanisms.

In sum, within the ΛCDM structure formation framework, the oldest components of spiral galaxies form in monolithic collapse type events, whereas their younger disks, and irregular and elliptical systems are the result of both violent, starburst-inducing major mergers and secular processes which gradually rearrange mass and momentum. The quenching pathways and timescales are a strong function of environment, as evidenced by the highest-density peaks of the underlying dark matter distribution (galaxy clusters) preferentially containing red-and-dead galaxies (e.g. Peng et al. 2010). This also suggests that when the Universe was younger and denser, major merger events were a more common occurence and that in the distant future, as the Universe continues to expand and matter is distributed throughout a larger volume, secular processes will become dominant (e.g. Kormendy & Kennicutt, 2004). There does indeed appear to be evidence that the global major merger fraction is declining with increasing cosmic time (e.g. Khochfar & Burkert 2001; Conselice et al. 2003; Kormendy & Kennicutt 2004; Lotz et al. 2011 although see Stott et al. 2013a). The statistical power provided by modern spectroscopic surveys is helping to shed light on the processes responsible for building the elliptical population at the expense of the spiral population as a function of cosmic time and environment, as well as other parameters such as stellar and halo mass (e.g. Bluck et al., 2016).

The remainder of this thesis is concerned with understanding the evolving properties of the star-forming galaxy population across cosmic time, further details of which are provided in § 1.5. For a full description of galaxy evolution, it is crucial to keep in mind the connection between galaxy types and the inevitable global progress towards converting star-forming galaxies to elliptical galaxies in our ageing Universe.

1.3.5 Cosmological simulations

Computational power and theoretical understanding have progressed to a level where it is possible to simulate realistic incarnations of representative volumes of the galaxy distribution. These simulations follow the growth of dark matter structures in the very early Universe and the subsequent formation and evolution of the galaxy population up to the present day, incorporating prescriptions for the complicated baryonic processes which shape the different galaxy types. Initial conditions in the simulation are determined by the chosen cosmology, and the results provide a theoretical comparison for a host of observations, spanning almost all of the history of the Universe. Over the last 30 years, the two main approaches have been semi-analytic modelling (e.g. White & Frenk, 1991; Kauffmann, 2003; Cole et al., 2000; Khochfar & Silk, 2006) and full numerical hydrodynamical simulations (e.g. Springel et al., 2005; Vogelsberger et al., 2014; Schaye et al., 2015; Crain et al., 2015; Pillepich et al., 2018).

Semi-analytic, or phenomenological, models of galaxy formation add baryonic physics on top of pre-simulated dark matter histories using a set of analytic approximations. This has the advantage of being computationally cheap (in comparison to hydrodynamic simulations) to run large cosmological volumes, thus allowing for comparison of runs using different sets of physical prescriptions. The downfall is that, by definition, the analytic approximations do not capture the full complexity of the nonlinear processes inherent to galaxy formation, particularly on small scales, dictating the extent to which they may be compared with observations.

Full numerical hydrodynamic, or direct, models use a large number of particles, or grid points, to represent either dark matter only or the mixture of dark matter and baryons and explicitly solve the fundamental equations describing their interactions. Reflecting both our ignorance of the details of some physical processes (e.g. star formation, feedback) and the resolution limit of the simulations, some processes are dealt with using physical prescriptions akin to the semi-analytic method. For example, Fig. 1.5 shows outputs from the Millenium dark matter simulation (e.g. Springel et al., 2005), describing the

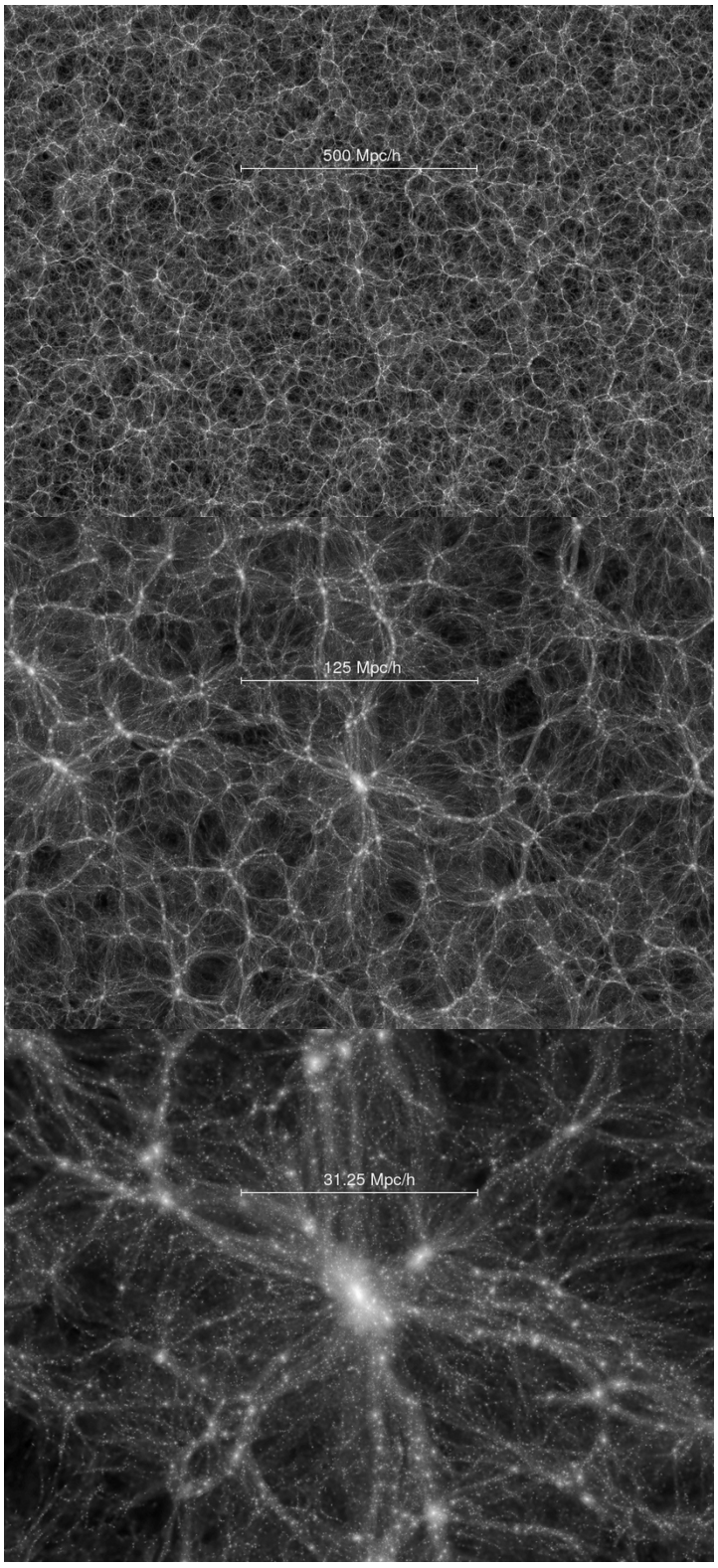

Figure 1.5: The top, middle and bottom panels show the predicted dark matter distribution at $z = 0$ on three different size scales from the Millenium simulation Springel et al. (2005). Lighter regions in the panels show where the density of dark matter is highest. This pattern (cf. Fig. 1.2) is shaped solely by the gravitational interaction of dark matter particles from the time of the Big Bang to the present day.

distribution of dark matter across a region of space at the present day. This simulation shows how gravity alone can shape the cosmic web of dark matter within which the galaxies are distributed as described in Fig. 1.2. The three panels in this figure show three different size scales, zooming in progressively towards a pronounced density peak. Stemming from this method are 'zoom' simulations (e.g. Springel et al., 2008; Hopkins et al., 2014, 2017) which allow for regions of interest (e.g. an individual dark matter halo) to be re-simulated with much higher resolution after calculating a lower resolution cosmic environment. Overall this approach is much more computationally expensive than semi-analytic models and can be performed over smaller volumes and with less freedom to experiment with simulation parameters. However, the simulations are rich in spatially-resolved structural and kinematic information for individual galaxies of different types over cosmic time.

There is now an encouraging agreement between the global properties of simulations using the two methods (e.g. Somerville & Davé, 2015), particularly for scales much larger than the resolution limit. The detail provided by modern, spatially-resolved observations, particularly from integral-field spectrographs (see § 1.4.4), necessitates comparison with hydrodynamical simulations such as Illustris (Vogelsberger et al., 2014) and the Evolution and Assembly of GaLaxies and their Environments (EAGLE) Schaye et al. (2015); Crain et al. (2015). The observations provide constraints for the simulation parameters, and so currently the use of both simulations and observations in tandem is driving forward our understanding of the details of galaxy formation. The algorithms and techniques, as well as the theoretical and computational challenges associated with running cosmological simulations are summarised in excellent recent review papers (e.g. Somerville & Davé, 2015; Naab & Ostriker, 2017).

1.4 Observing the galaxy population

Having focussed on the salient theoretical features of galaxy formation and evolution in section § 1.3, focus turns now to the observed properties of star-forming galaxies

across cosmic time. This section describes the primary techniques by which light is collected by telescopes and quantified by telescope instruments prior to being used to infer galaxy physical properties.

1.4.1 Very Large Telescopes and the troublesome atmosphere

The world's premier ground-based optical and near-infrared (NIR) research telescopes have several things in common: 1) they use reflective mirrors with large diameters; 2) they are situated at high altitudes; 3) the annual cloud coverage is very low; 4) the sites have exceptionally low relative humidity, so that the atmospheric water vapour content is minimal; 5) the atmospheric turbulence is low on average; 6) the sites are chosen to be in regions with very low light pollution. Large mirrors increase telescope sensitivity, as the number of photons collected per second is proportional to the collecting area, and mirror diameter dictates the diffraction-limited angular resolution of the instrument at a given wavelength. Points 2-5 above are steps towards minimising the possibility of scattering and absorption by atmospheric particles during the passage of photons through the Earth's atmosphere to the telescope. Of particular importance to the types of observations utilised throughout this thesis is distortion of incoming wavefronts caused by layers of atmospheric turbulence, which vary both spatially and temporally. This is quantified through the average Full-Width at Half-Maximum (FWHM) of the observed light distribution eminating from point sources, known as the 'seeing', which dictates the minimum size of spatially resolvable regions in the target objects. The combined response of the atmosphere and telescope instrument optics to light from point sources is described by a Point spread function (PSF). One of the main limitations of ground-based telescopes is that they operate at the mercy of the atmospheric turbulence ('seeing-limited' observations) which can increase the angular resolution to orders-of-magnitude above the intrinsic resolution set by the telescope mirror. This can have severe consequences for the quality of recorded data, especially when one seeks to trace spatial variations across the target objects.

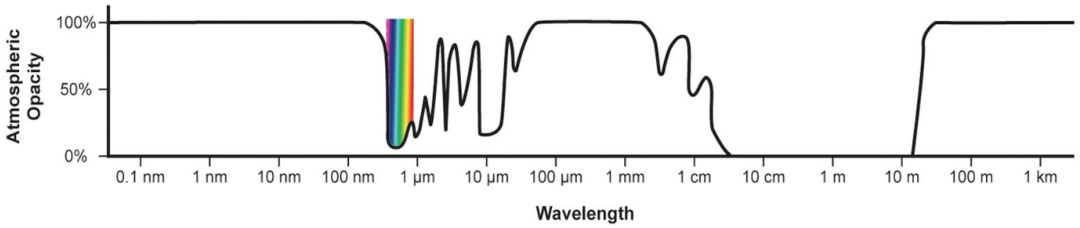

Figure 1.6: The atmosphere is either fully or partially opaque to the vast majority of the electromagnetic spectrum, necessitating space-based observations for all wavelengths bluewards of optical and also for much of the far-infrared. Observing the true flux of astronomical sources requires careful calibration using standard-star measurements.

As well as the optical and NIR, we now have telescopes collecting data across the full electromagnetic spectrum. Fig. 1.6 highlights that only the optical, NIR and part of the millimetre, sub-millimetre and radio regimes are accessible from the ground, with the atmosphere opaque to the remainder of the spectrum. These regions must be observed using space telescopes situated beyond the atmosphere. Collecting data which span a wide wavelength range for individual galaxies provides a more complete picture of the baryonic processes occuring at the time of emission, which radiate in vastly different wavelength regimes.

1.4.2 Photometry and multi-wavelength photometric surveys

Photometry refers to the quantification of the apparent brightness of objects in specific spectral windows, often using a set of filters to block photons with wavelengths outwith the chosen range. This is equivalent to photography, and produces images of the sky brightness averaged over the filter wavelengths with a field-of-view proportional to the ratio of the physical size of the CCD detector to the telescope focal length. By calibrating against standard stars with carefully measured observed brightnesses, the counts per second recorded by the CCD can be converted into a total energy per second per area, which is known as the flux. Typically the CCD pixel size is chosen to oversample the PSF of the observations, resulting in several flux measurements across each independent spatial resolution element.

The use of a specific filter set provides a coarse measure of the Spectral Energy

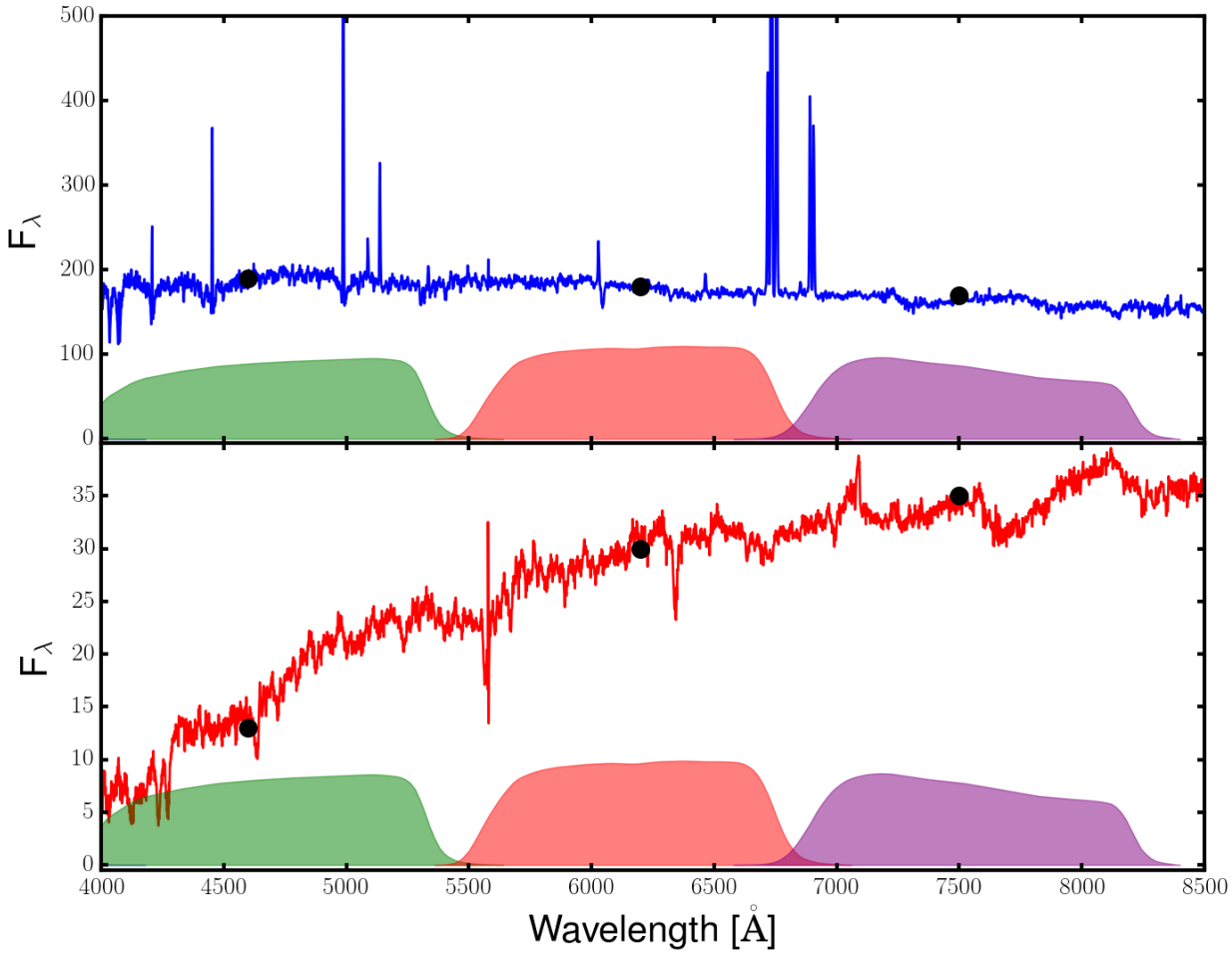

Figure 1.7: The top panel shows a set of typical photometry points collected using the overlaid filter set (black symbols) and a typical spectrum (blue line) for a local-Universe star-forming galaxy ($z = 0.026$), in arbitrary flux units. The shape of the SED is characterised by strong UV emission from young stars and strong emission lines from the ionised gas. The bottom panel shows the same for a local passive galaxy (red line, $z = 0.076$), characterised by emission from a redder, ageing stellar population and stellar absorption features.

Distribution (SED) of an object, as demonstrated in Fig. 1.7 by the black circles and overlaid filter curves for a star-forming (top panel) and passive (bottom panel) galaxy. Models can be constructed which describe the energy emitted by stars, gas and dust in a galaxy as a function of wavelength, using a technique called 'Stellar Population Synthesis' (SPS; e.g. Bruzual & Charlot 2003). The parameters in these models can describe, amongst other pysical properties, the stellar age, stellar and gas

metallicity, stellar mass, dust content, star-formation history and star-formation rate of the galaxy. The coloured curves in both panels show the best-fit SPS model, and clearly the more photometric data points collected, the better the constraints will be on the parameter values in the model. The data in Fig. 1.7 were collected using a combination of ground-based and space-based instruments spanning the optical and NIR wavelengths. Collecting data bluewards in the X-ray−UV as well as redwards in the submillimetre−radio regimes would provide further information to constrain the physical processes in the galaxy.

Over the last decade there have been a large number of photometric surveys, which range from large area/all sky to very deep, pencil-beam studies. To mention two important examples, the SDSS (York et al., 2000) and the Cosmic Assembly Near-infrared Deep Extragalactic Legacy Survey (CANDELS; Grogin et al. 2011; Guo et al. 2013) are designed to meet a diverse set of scientific objectives which require different observing strategies. The SDSS is a 'wide-field' survey, targetting large swathes of the northern hemisphere sky with relatively short integration times in multiple filters. Consequently, the objects detected are predominantly at low redshift ($z < 0.4$), with over 200 million galaxies covered to date. This offers very large number statistics for detailed, environmentally subdivided studies of the relationships between physical properties obtainable using photometry. Conversely, the CANDELS imaging with *HST* focusses on few, small and well-studied fields using very long exposure times to accumulate the signal-to-noise required to study faint galaxies in the early Universe. This limits the total number of objects and the cosmic volume surveyed, which is a necessary sacrifice when attempting to detect light that was emitted across very large cosmological distances. Multi-wavelength photometric data gathered during imaging surveys provide crucial morphological and spectral information across a wide wavelength range, and are often also used to support detailed, spectroscopic follow-up.

1.4.3 Spectroscopy and multi-wavelength spectroscopic surveys

Traditional spectroscopy uses either a fibre or a mask to collect light from a pre-determined, interesting region of the field-of-view across the chosen wavelength range. The light is then dispersed into a large number of spectral bins using either a prism or a grating. This process removes all spatial information and produces a one-dimensional spectrum of flux density versus wavelength. The ratio of the wavelength interval between adjacent spectral bins and the wavelength is called the spectral resolution, determined by the properties of the grating and the number of pixels arranged along the dispersion axis (i.e. the number of wavelengths at which the flux is measured). Spectrographs with high spectral resolution produce more detailed spectral energy distributions, at the expense of lower signal-to-noise in each of the spectral bins for a given integration time. The purpose of collecting spectra is to observe spectral 'features', such as the emission and absorption lines shown in the top and bottom panels of Fig. 1.7 respectively, which are rich in dynamical and chemical information. As well as feeding light into the dispersive element using a fibre or a mask, spatial information can be retained along a chosen axis with long-slit spectroscopy or full spatial information can be retained with integral-field spectroscopy (see § 1.4.4).

Analogous to the imaging campaigns, spectroscopic surveys are designed to answer specific questions relating to different periods throughout cosmic time, and commonly target the fields on the sky which are rich in ancillary photometric data. In recent years, several spectrographs which collect spectra for many objects simultaneously (multi-object spectrographs) have been commissioned, including SDSS, the Fibre Multi-Object spectrograph (FMOS; Kimura et al. 2010), the VIsible Multi-Object Spectrograph (VIMOS; Le Fevre et al. 2003) and the Multi-Object Spectrometer For Infra-Red Exploration (MOSFIRE; McLean et al. 2012), targeting different wavelength regimes in both the northern and southern hemisphere. These instruments have led to orders-of-magnitude increases in the number of objects with optical and NIR spectroscopy in both the local and distant Universe. This has been crucial in developing

our understanding of the complicated baryonic processes described throughout sections 1.3.4 and 1.3.5, again particularly with regards to the environmental dependence of feedback and the quenching of star formation. On top of these instruments, low-resolution grism spectroscopy with the *HST* Wide-Field Camera 3 (3D-*HST*; Momcheva et al. 2016), in which every object in the field of view is simultaneously dispersed, has provided further increases to the number of high-redshift galaxies with partial spatial information. In an ideal world, high-resolution spectroscopy spanning a long-wavelength baseline would be available for every galaxy. Our ability to collect this data is limited by the time and facilities required, however the current combination of photometric and spectroscopic data for growing sample sizes is allowing increasingly sophisticated analyses.

1.4.4 Integral-field spectroscopy and KMOS

As mentioned above, Integral-Field Spectroscopy (IFS) combines imaging and spectroscopy to produce three-dimensional data structures known as datacubes. These are comparable to $n \times m \times k$-dimensional Rubik's^{TM} cubes, where the first two axes describe the perpendicular x and y spatial dimensions and the third axis contains spectral information obtained from dispersing the light at each spatial location. The datacube thus contains a spectrum at the location of each *spatial pixel* (spaxel), as indicated in Fig. 1.8.

The purpose of this is to allow for analyses of the variation of the physical properties discernible using spectroscopy across the spatial extent of galaxies, rather than obtaining average properties for the whole galaxy. This information is crucial for understanding the detailed distributions of stars, gas and dust within individual galaxies and the physical processes which shaped these distributions. Integral-field spectroscopy is particularly useful for producing spatial maps of the dynamics (i.e. rotation velocity and velocity dispersion), ionisation state and chemical composition of galaxies using a tracer such as the ionised gas emission lines or stellar absorption features. Fig. 1.9, adapted from Maiolino et al. (2017) shows the continuum image alongside the flux,

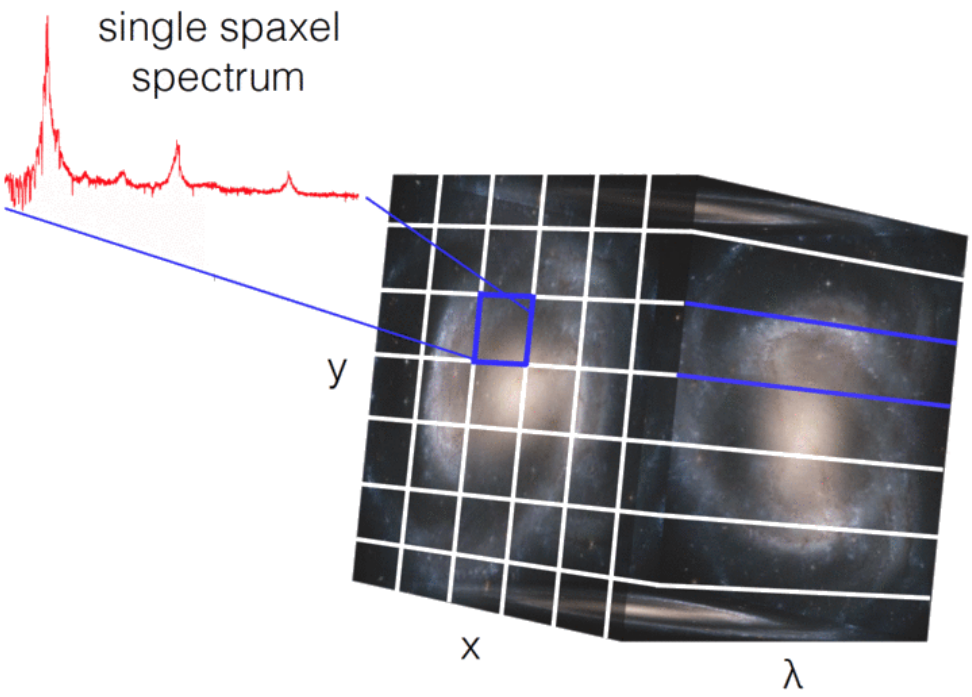

Figure 1.8: Integral-field spectroscopy involves the segmentation of a two-dimensional patch of sky into smaller regions, at each of which a spectrum is recorded. This produces a three-dimensional structure called a datacube which contains both spatial and spectral information. This is useful for studying the changing physical properties of galaxies across their spatial extent.

velocity and velocity dispersion profiles inferred from the Hα ionised gas emission line for the galaxy IRAS F23128-5919 at $z = 0.04$. The data were collected with the Multi-Unit Spectroscopic Explorer (MUSE) installed on Unit-Telescope 4 (UT4) of the European Southern Observatory's (ESO) Very Large Telescope (VLT) array, which is a panoramic integral-field spectrograph operating at optical wavelengths.

Three main techniques are used to segment and disperse the light from galaxies to produce a datacube, summarised in Fig. 1.10. The top row of this figure shows a *lenslet array* arranged across the focal plane. Each lenslet separately images light onto the spectrograph, which disperses the inputs at an angle to minimise overlap from the different spatial regions on the detector. The middle row depicts the use of a combination of lenslets on the focal plane to pickoff the light at different spatial

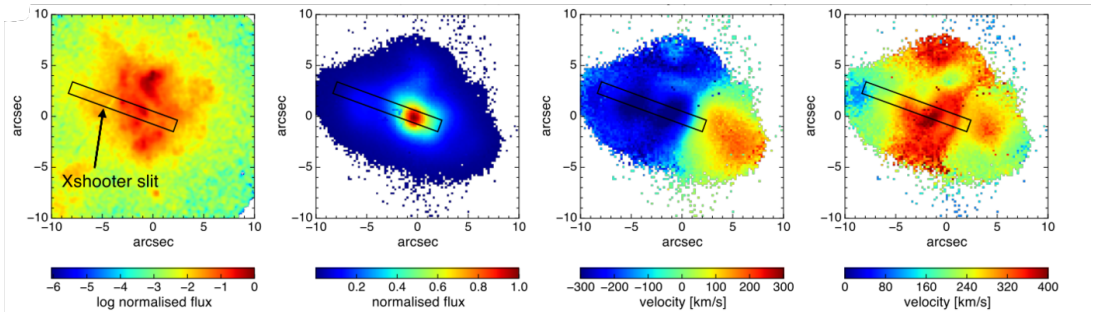

Figure 1.9: From left to right the four panels show 1) the continuum image 2) the Hα flux 3) the velocity inferred from the Hα emission line 4) the velocity dispersion inferred from the Hα emission line for the galaxy IRAS F23128-5919 at $z = 0.04$ (Maiolino et al., 2017). These data were collected with MUSE and demonstrate how integral-field spectroscopic measurements can be used to map out physical properties across the face of a galaxy.

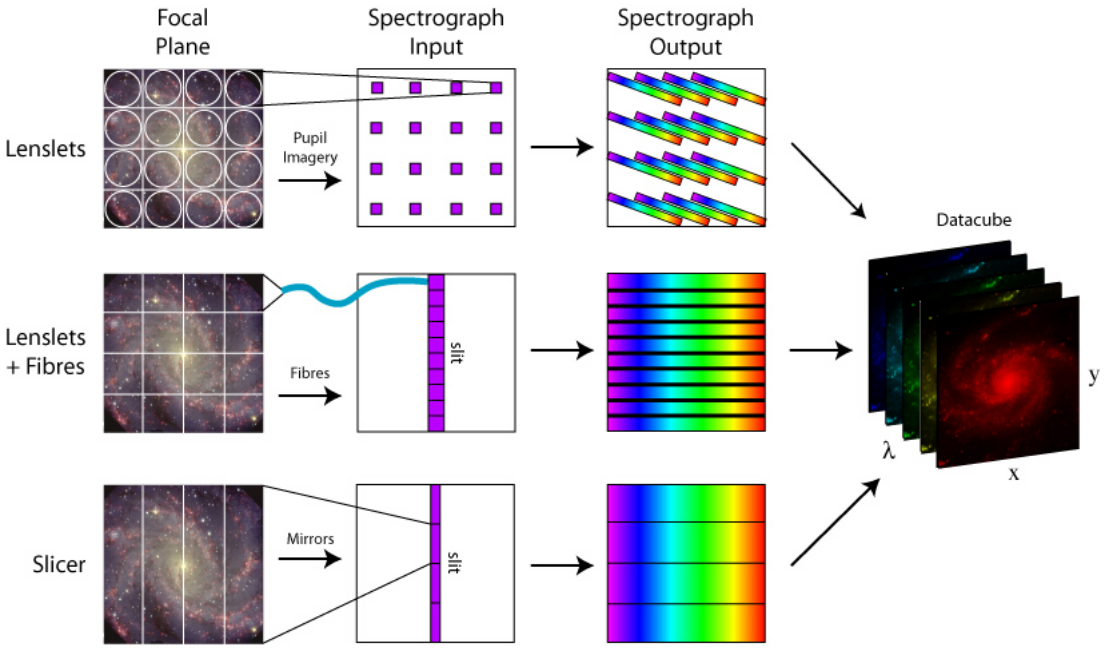

Figure 1.10: As described throughout the text, there are three popular methods for segmenting and dispersing the image, each of which leads to the production of a datacube (figure taken from Westmoquette et al. 2009).

locations and fibres which feed the light to the spectrograph. Again the light from the different locations is dispersed separately. The bottom row shows an arrangement of vertical image-slicing mirrors arranged at the focal plane to feed the spectrograph. Each image 'column' is composed of a series of pixels which are dispersed by the spectrograph onto the detector. Common to all three methods is a post-processing step, which takes the two-dimensional detector image and reconstructs a datacube using the pixels associated with spatial and spectral information.

This thesis makes extensive use of data collected using the K-band Multi-Object Spectrograph (KMOS; Sharples et al. 2005, 2013). This is a NIR integral-field spectrograph with 5 filters (*IZ,YJ,H,K,HK*;R=3200,3400,4000,4200,1800) covering the wavelength range $0.8 - 2.5\mu$m, installed at Nasmyth focus B of UT1 at the VLT array. The instrument uses image slicers, as per the bottom row of Fig. 1.10, to feed light to a grating spectrograph, where it is dispersed onto a 2k×2k Hawaii-2RG HgCdTe detector.

Unique to KMOS, as indicated in Fig. 1.11, are the 24 configurable Integral-Field Units (IFUs) which position pickoff mirrors across the field-of-view, allowing for up to 24 objects to be targetted simultaneously. The instrument uses 3 independent spectrograph/detector modules, feeding the light from 8 IFUs to each one of these modules separately. Each IFU has a projected spatial coverage of 2.8×2.8 arcseconds, large enough to encompass at least 2 effective radii on both sides of typical, edge-on galaxies at $z \gtrsim 1$. The IFUs may be positioned within a 7.2 arcminute diameter circular patrol field and use a default pixel scale of 0.2×0.2 arcseconds for oversampling of the seeing-limited PSF (although the observation dither pattern may be chosen so as to increase the spatial sampling, see Chapter 2). The VLT has established itself as the world's leading facility for integral-field spectroscopic research, also housing the pioneering instruments MUSE (mentioned above) and the Spectrograph for INtegral Field Observations in the Near Infrared (SINFONI; Eisenhauer et al. 2003).

The multiplexing capability of KMOS has allowed for orders-of-magnitude increases

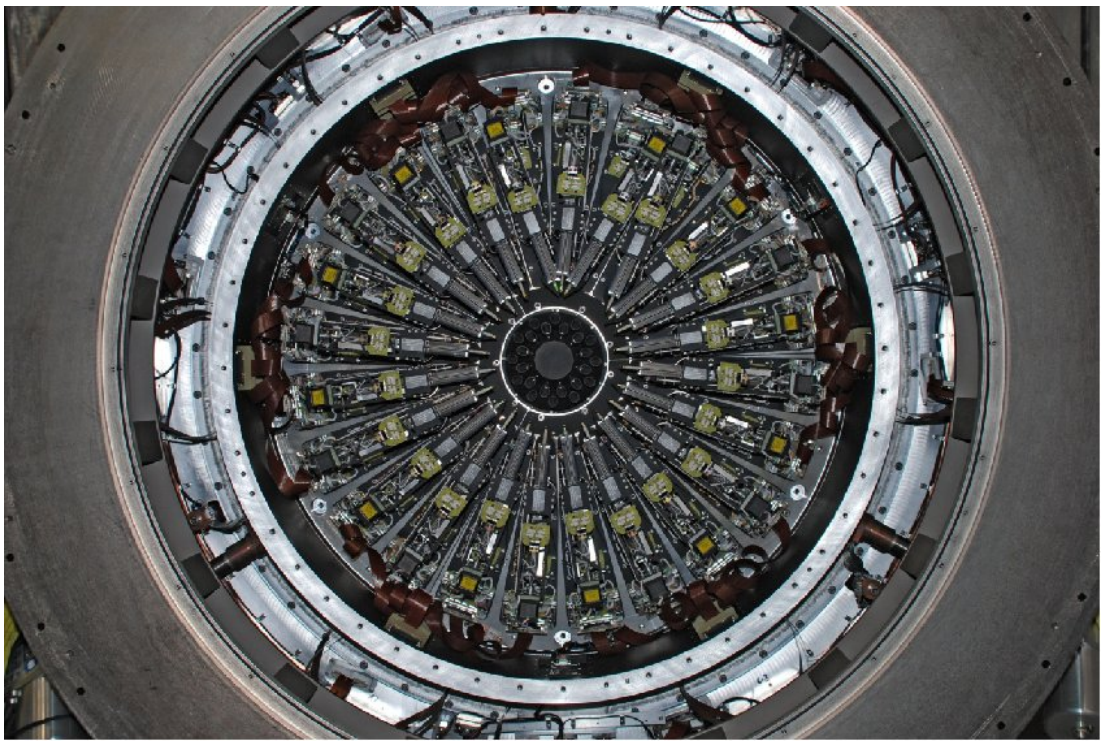

Figure 1.11: A view of the 24 KMOS arms with installed integral-field units (IFUs), used to select targets for simultaneous observing. This picture was taken in Edinburgh prior to dispatch of the instrument to paranal.

in the number of galaxies targetted with rest-optical integral-field spectroscopy in the intermediate and high-redshift Universe, as the integration times required to build large samples are greatly reduced. Of particular importance to this thesis are results established by large, NIR integral-field spectroscopic surveys of the intermediate and high-redshift Universe, such as the Spectroscopic Imaging survey in the Near-infrared with SINFONI (SINS; Förster Schreiber et al. 2009), KMOS^{3D} (Wisnioski et al., 2015) and the KMOS Redshift One Spectroscopic Survey (KROSS; Stott et al. 2016), which will be discussed further throughout § 1.5.

1.4.5 Observational challenges

Observers are faced with a plethora of practical challenges when using any of the techniques above to study galaxy evolution. Fundamentally, the timescales involved in galaxy evolution span billions of years and we of course cannot observe the progress of individual galaxies through their lifecycle, except with simulations. Most observational

studies therefore compare the average properties of the star-forming or passive populations at different epochs, assuming an evolutionary connection between the populations, although abundance-matching techniques exist to do this more realistically (e.g. Moster et al., 2013). These types of studies are prone to underestimating the true evolution of the passive population, as passive galaxies observed at low redshift may have transitioned from spiral galaxies or merging systems at higher redshift; an effect called progenitor bias (e.g. van Dokkum et al., 2001). Another challenge to observers are the large integration times required to build up large samples in spectroscopy, particularly at high redshift. The required integration times are usually calculated prior to requested telescope time using Exposure Time Calculators (ETCs), which take into account the instrument being used, atmospheric conditions, the wavelength range being observed and the intrinsic brightness of objects. Large integration times are predominantly a consequence of the cosmological surface brightness dimming factor of $(1 + z)^{-4}$ which affects all objects, necessitating integration times of at least several hours per object to achieve the required signal-to-noise on the targetted spectral features.

A common issue which affects NIR spectroscopy is emission from the OH molecule, residing in the Earth's upper atmosphere, with fluxes several orders-of-magnitude larger than emission from targetted galaxies. The OH emission varies both spatially and temporally on timescales of a few minutes, requiring dedicated exposures of blank sky regions which are located close to the object exposures both positionally and in time. These exposures are then processed in the same fashion and subtracted from the object spectra. However, even small differences in OH emission strength between frames leads to prohibitively large residuals at the level of the object flux. To combat this, various algorithms have been developed to scale the sky OH emission prior to subtraction (e.g. Davies, 2007) or to subtract models of the residual sky spectra (e.g. Soto et al., 2016), however results are never perfect (see Chapter 2). In addition, large telescope overhead times result from observing dedicated sky frames, motivating attempts to model the OH emission as a function of observing site and time (e.g. Skycorr; Noll et al. 2014).

A final point, mainly presenting a challenge to spatially-resolved observations, is the impact of the seeing on the signal-to-noise and spatial resolution of the data. Light passing through the atmosphere and telescope optics is convolved with the observational PSF, creating a weighted average of the galaxy physical properties across the seeing disk. This process is known as 'beam smearing', a common example of which is the flattening of rotation curves and broadening of velocity dispersions in observed dynamical measurements across the centre of rotating galaxies, where the velocity gradients are steep. An important step in the interpretation of observed integral-field spectroscopic data is thus to derive intrinsic galaxy properties by accounting for the impact of beam smearing, the severity of which is a function of galaxy size and the PSF (e.g. Bouché et al. 2015; Burkert et al. 2016; Johnson et al. 2018; see § 1.5.2 and Chapter 3). To reduce the impact of atmospheric convolution on the data, telescopes can be fitted with adaptive optics mirrors which move and distort to correct atmospheric wavefront distortions in real-time. These facilities are available for only a limited number of spectrographs and still require good seeing conditions for optimal performance, so at present the most common approach to tackling beam smearing is to account for its effects during analysis.

1.5 The physical properties of star-forming galaxies

It is evident that our Universe is constantly changing, and we have access to its historical records in the form of the physical properties of galaxies. The following sections describe some fundamental physical properties of star-forming galaxies which are evolving with time, inferred from photometric and spectroscopic observations spanning multiple epochs.

1.5.1 Cosmic star-formation rate density and the 'Main Sequence' of star formation

Since galaxy star-formation rates reflect both the availability of cold gas and the efficiency with which it is being converted into stars, the globally averaged *Star-Formation Rate Density* (SFRD) as a function of redshift traces both of these properties across the history of the Universe. The cosmic luminosity density at a given redshift and wavelength interval is measured by calculating the luminosity-weighted integral of the luminosity function at that redshift, constructed from observations over the relevant wavelength range. The cosmic SFRD is then found by multiplying the luminosity density by the appropriate conversion factor (e.g. Kennicutt, 1998).

In the recent review by Madau & Dickinson (2014) (and see also Behroozi et al. 2013; Bouwens et al. 2015), the cosmic SFRD was measured as a function of redshift over the redshift range $0 < z < 8$ using a large compilation of far-ultraviolet (FUV) and far-infrared (FIR) luminosity function parameterisations from the literature. Fig. 1.12 shows the combined (dust-corrected) FUV and FIR individual SFRD measurements and the best-fit parameterisation of the overall shape of the star-formation history of our Universe. This rises from $z \simeq 8$ to $z \simeq 2.5$, peaks somewhere in the redshift range $1 < z < 2.5$ before declining from the peak to the present day. There is still no first principles explanation for the shape of this curve, although naively a rising stage would be expected in the early Universe during the galaxy formation epoch as baryons collect in the centre of dark matter halos and a declining stage at later times when expansion has significantly increased the volume of the Universe, acting as a catalyst to galaxy quenching by preventing gas cooling (Madau & Dickinson, 2014) and lowering the cosmic accretion rate of gas onto galaxies (e.g. Dutton et al., 2010). The shape itself provides a fascinating insight into the changing activity of the Universe, telling us that typical star-forming galaxies at the peak of cosmic SFRD had instantaneous star-formation rates which were a factor of ~ 10 larger than typical star-forming galaxies at the present day.

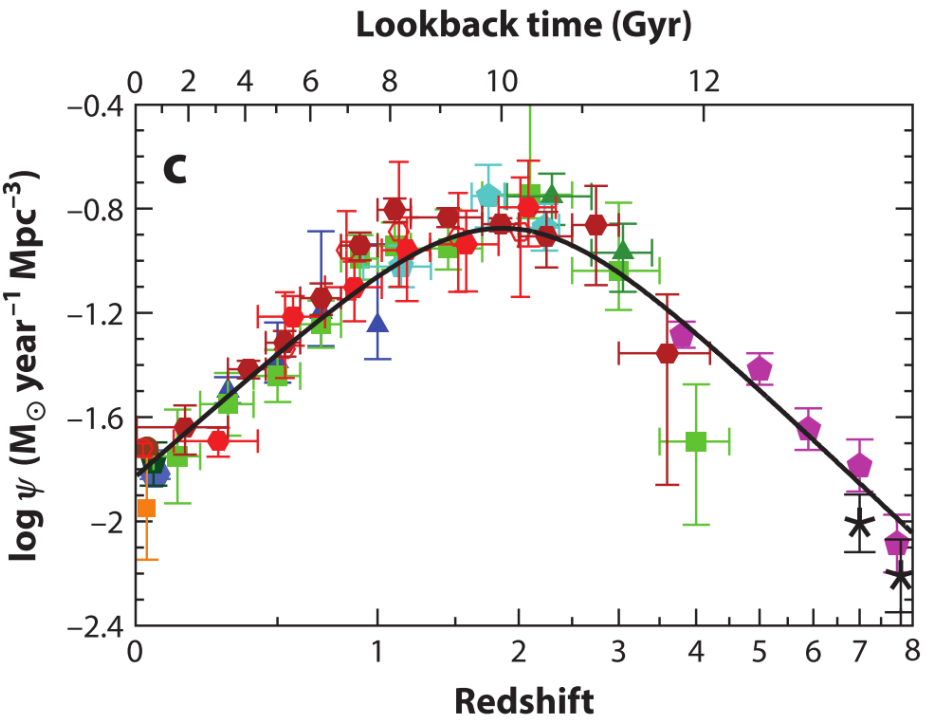

Figure 1.12: Throughout Madau & Dickinson (2014) many measurements of the UV and IR luminosity functions are discussed at various redshifts. By calculating the luminosity-weighted integral of these luminosity functions and converting to star-formation rates, the cosmic SFRD is obtained. The shape of the SFRD as a function of both lookback time and redshift is shown here (taken from Madau & Dickinson 2014), characterised by a peak somewhere in the redshift range $1 < z < 2.5$ and a decline on either side of this.

It was determined in the late 2000s in a series of papers (Elbaz et al., 2007; Noeske et al., 2007b; Daddi et al., 2007) that typical star-forming galaxies at a given redshift, out to at least $z \sim 6$ (e.g. Speagle et al., 2014), follow a tight, near-linear relationship between star-formation rate and stellar mass in the sense that more massive galaxies form stars at a greater rate. This relationship is deemed the 'Main Sequence' (Noeske et al., 2007b), highlighting that it is within galaxies following this correlation that the majority of stars in the Universe are formed. Consequently, other states of star formation within galaxies, such as starbursts induced by major merger events, do not contribute significantly to the cosmic SFRD due to the paucity of systems in this phase (e.g. Robaina et al., 2009; Rodighiero et al., 2011; Kaviraj et al., 2013; Lofthouse et al.,

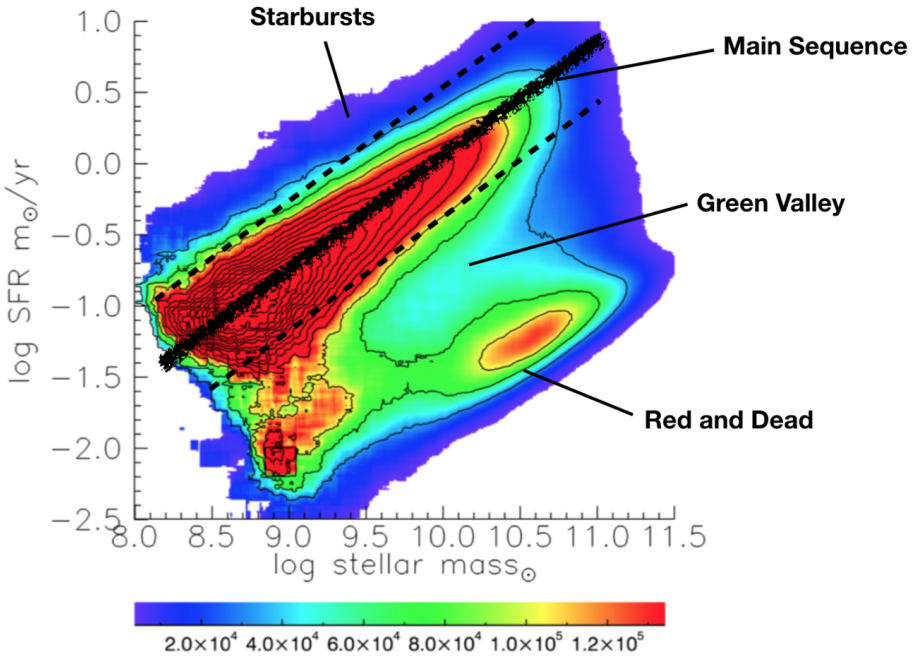

Figure 1.13: SDSS galaxies in the log star-formation rate log stellar-mass plane, adapted from Renzini & Peng (2015). Star-forming galaxies are predominantly defined by the main-sequence relation between star-formation rate and stellar mass, with a scatter of $\sim 0.2 - 0.35$ dex. Starburst, quenching and quenched galaxies are clearly visible as separate populations in this plane.

2017).

Fig. 1.13, adapted from Renzini & Peng (2015), shows the star-formation rate versus stellar-mass plane for local galaxies from the SDSS (see also Brinchmann et al. 2004 for a more detailed discussion of this relationship specifically for local galaxies). This figure contains both star-forming and 'red-and-dead' galaxies, as well as galaxies in the transition region between the two populations known as the 'green valley' (e.g. Wyder et al., 2007; Schiminovich et al., 2007; Martin et al., 2007; Fang et al., 2013; Abramson et al., 2016; Lin et al., 2017; Belfiore et al., 2018). Also shown are the starburst galaxies which lie significantly above the main sequence, currently experiencing a greatly enhanced episode of star formation triggered by some non-secular process, with number densities much lower than in the regions surrounding the main sequence.

The main sequence of star-forming galaxies is clearly visible, with intrinsic scatter of $\sim 0.2 - 0.35$ dex (e.g. Speagle et al., 2014) about the mean relation. The origin of this scatter reflects the physical processes which govern star formation and is a topic of current literature debate. Some authors claim that main-sequence scatter stems from differences in the accretion history, and consequently the gas fractions, of star-forming galaxies (e.g. Dutton et al., 2010; Tacconi et al., 2013) due to the correlation between specific star-formation rate and gas fraction, whilst others suggest that scatter is primarily driven by the inherent stochasticity of star-formation rates either on arbitrary timescales Kelson (2014) or in short, 'weather-like'[1] events. Finally the scatter has been suggested to reflect age gradients in the star-forming galaxies on the sequence, generated by Hubble-time scale differentiation between the galaxy star-formation histories (Noeske et al., 2007a; Speagle et al., 2014; Abramson et al., 2016).

The normalisation, slope and scatter of this relation are observed to evolve (e.g. Daddi et al., 2007; Rodighiero et al., 2010; Whitaker et al., 2012b, 2014; Rodighiero et al., 2014; Behroozi et al., 2013; Speagle et al., 2014), with high-redshift (up to some limit) galaxies having elevated star-formation rates at fixed stellar mass (see Fig. 1.12). Fig. 1.14, taken from Speagle et al. (2014), demonstrates this by plotting the best fitting linear main-sequence relations and scatter at different redshifts over the redshift range $0 < z < 4$ (the main-sequence is also commonly described with broken power-law and polynomial relations, e.g. Whitaker et al. 2014). Remarkably, the galaxies plotted on the star-formation rate versus stellar-mass plane in Fig. 1.13, spanning several orders-of-magnitude in star-formation activity, follow a common relationship between the total (atomic plus molecular) gas surface density and the surface density of star formation known as the Kennicutt-Schmidt law (e.g. Schmidt & Maarten, 1959; Kennicutt et al., 1998; Gao & Solomon, 2004), which appears to hold across a wide redshift range (e.g. Genzel et al., 2010). Equation 1.1 demonstrates the form of this relationship, with A

[1] this terminology has been taken from Abramson et al. (2016)

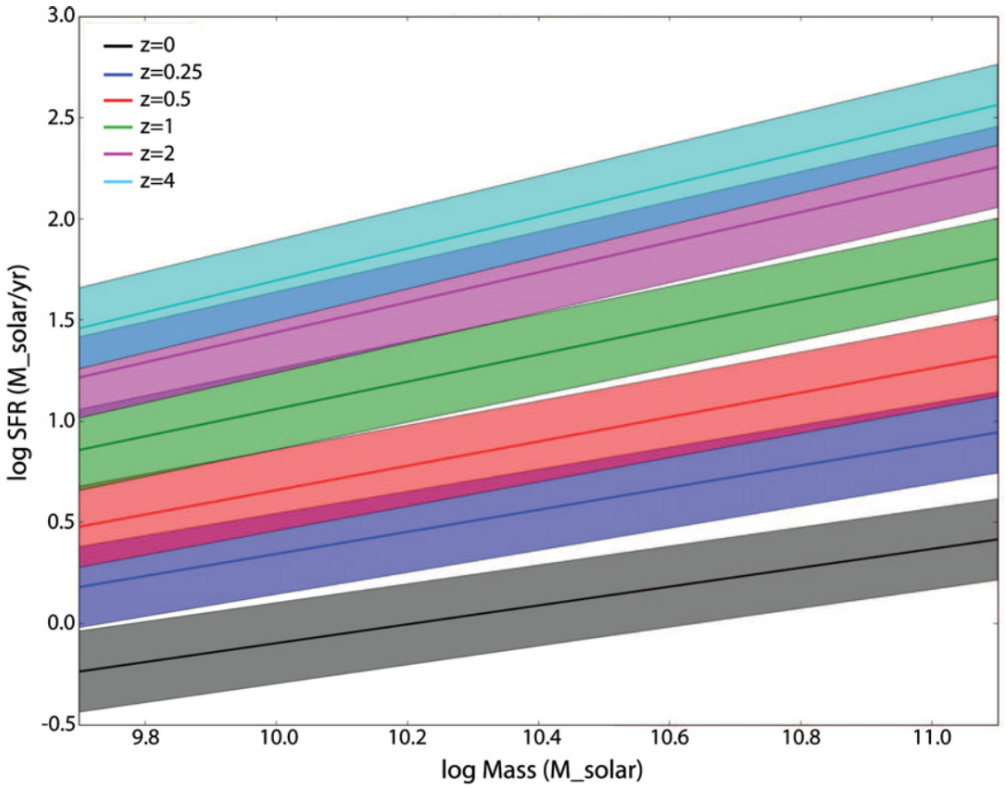

Figure 1.14: An analytic prescription for the evolution of the main sequence towards higher star-formation rates at fixed stellar mass is described in Speagle et al. (2014). The log-linear trends and scatter shown here demonstrate this evolution over the redshift range $0 < z < 4$.

equal to the absolute efficiency with which gas is converted into stars.

$$\sum\nolimits_{\mathrm{SFR}} = A \sum\nolimits_{\mathrm{gas}}^{N} \tag{1.1}$$

Along with the observation that typical star-forming galaxies were smaller at earlier times, and hence had higher gas surface densities (e.g. Toft et al., 2007; Trujillo et al., 2007; Buitrago et al., 2008; van der Wel et al., 2014), the correlation between gas and star-formation rate surface densities offers partial explanation for both the shape of the cosmic SFRD in Fig. 1.12 and the evolution of the main-sequence normalisation in Fig. 1.14.

As indicated in the left panel of Fig. 1.15, using a composite sample of normal-spiral and

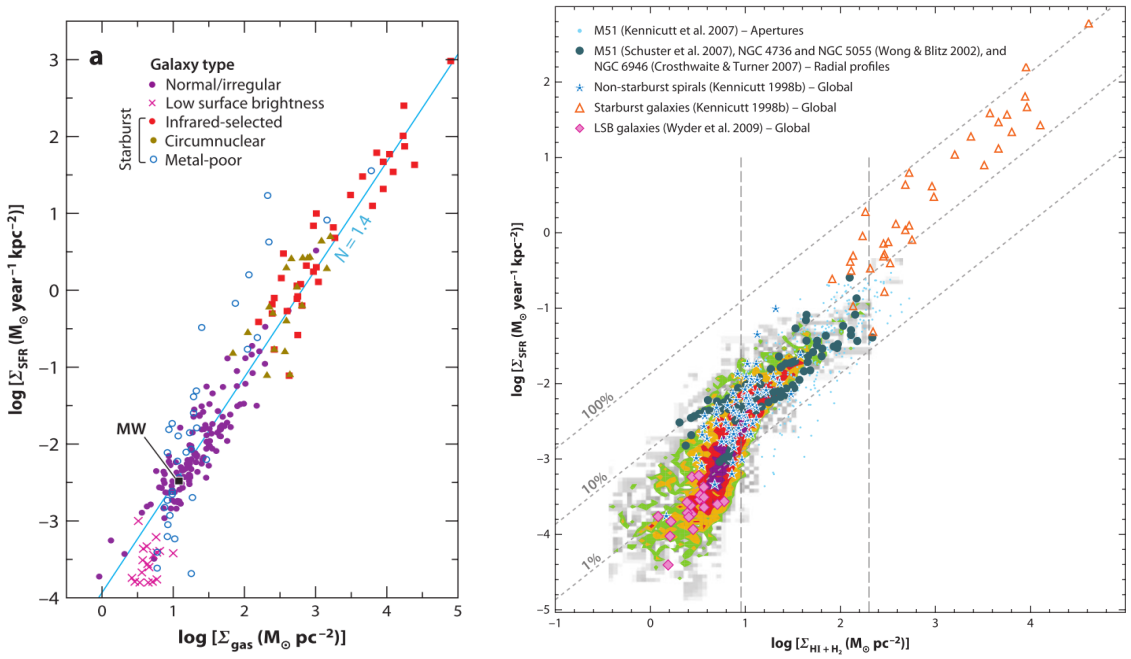

Figure 1.15: *Left:* Compilation of the global (i.e. galaxy averaged) correlation between the surface density of star formation and the total gas (atomic plus molecular) surface density, taken from Kennicutt & Evans (2012). *Right:* the star-formation law for subregions within individual galaxies from Bigiel et al. (2008) as reported in Kennicutt & Evans (2012)

starburst galaxies, Kennicutt et al. (1998) found that the global star-formation law can be described with an $N = 1.4$ power law and a single absolute star-formation efficiency across many orders-of-magnitude of gas surface density. This is an extremely useful parameterisation for star formation across a range of environments within numerical simulations. It should be stressed however that these quantities are gross averages over the spatial extent of the galaxies, and it is not realistic to expect star-formation efficiency to be constant across the range of gas surface densities being probed.

Instead, the situation can be viewed through a different lens on spatially resolved scales, as discussed in e.g. Kennicutt et al. (1998), in which different density regimes are traced within individual galaxies. Bigiel et al. (2008) clearly demonstrate this by studying the star-formation law on sub-kpc scales in a sample of local spiral galaxies. The diagonal dotted lines in the right panel of Fig. 1.15 show $N = 1.0$, linear star-formation laws with varying (labelled) star-formation efficiencies. The shaded pixels

show the combined resolved measurements within individual spirals, which are split by the vertical dotted lines into three density regimes. In the lowest density regime ($\sum_{\rm gas} < 9 M_{\odot} {\rm pc}^{-2}$), representative of the outskirts of galaxies where the gas is likely to be in the atomic phase, the efficiency of star formation varies dramatically and there is no strong correlation between gas surface density and star-formation rate. In the mid-density regime, dominated by molecular-phase hydrogen in the central regions of galaxies, stars are being formed at constant efficiency (between 2 – 10 per cent) and follow the linear relationship between gas and star-formation rate surface density.

In this framework, the global starburst measurements represent a more efficient phase of star formation resulting from a larger fraction of the molecular gas being in a dense, molecular-cloud-like state.

It is clear from Fig. 1.15 that (globally) star formation is an extremely inefficient process across the gas density regimes traced by typical star-forming galaxies, which fundamentally reflects the fact that only a small fraction of the molecular gas within galaxies is bound to star-forming molecular clouds. This itself is a consequence of the gas regulator model (e.g. Lilly et al., 2013) described briefly in § 1.3.4 in which the interplay between accretion, feedback and outflows regulates the growth and enrichment of galaxies via star formation. These processes, especially the efficiency with which stars form from molecular gas in different density regimes, are crucial ingredients to cosmological simulations of galaxy evolution, which is currently our only available method to study individual galaxies across cosmic time.

1.5.2 Dynamics and the dynamical evolution of star-forming galaxies

As described in § 1.3.4, it is generally assumed that the material within normal star-forming galaxies is arranged within a rotationally-supported disk, where deviations from perfectly circular orbits can be neglected (e.g. chapter 11 in Mo et al. 2010). The rotation curves of these objects are a reflection of the underlying distributions of both

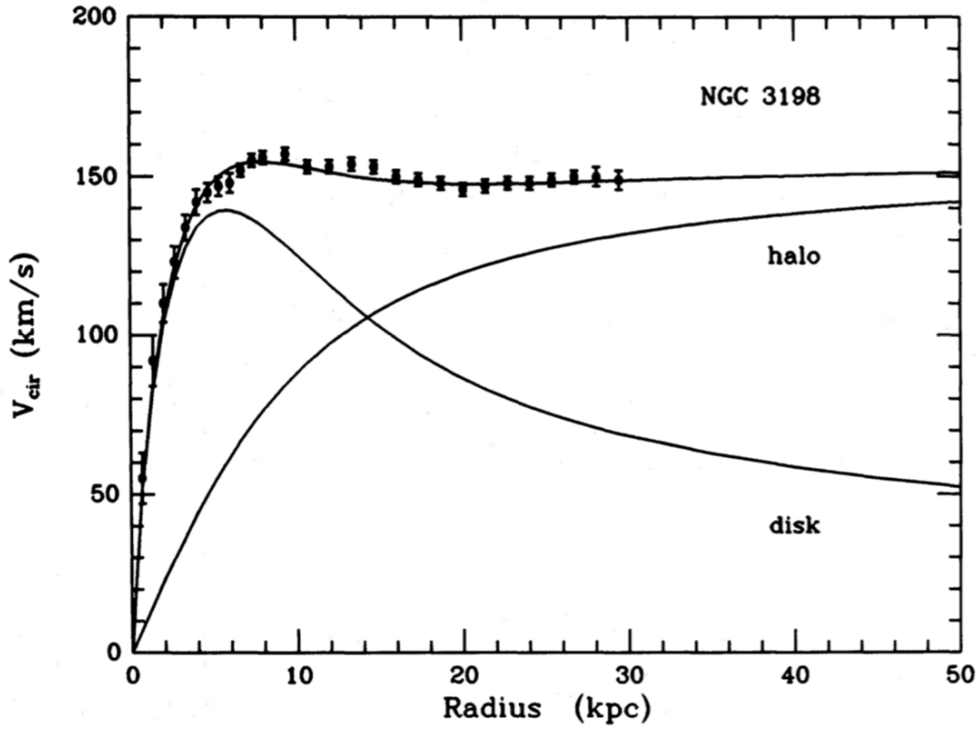

Figure 1.16: The observed (black points) and model rotation curves for NGC 3198 from van Albada et al. (1985), with the best fitting model given by the superposition of the disk and halo rotation curves. The rotation curve is characterised by a steep, rising phase in the centre, where the disk is dominated by baryons, followed by a flat outer rotation curve dominated by the dark matter halo. The velocity data, inferred from H I 21cm measurements, extend to 11 disk scale radii (i.e. well beyond the extent of the stars in the disk).

baryonic and dark matter, and hence the radial profile of the gravitational potential. Fig. 1.16, taken from van Albada et al. (1985), shows the observed rotation curve of NGC 3198, which is representative of the spiral galaxy rotation curves observed in both the local Universe (e.g. Lelli et al., 2016) and across intermediate and high redshifts (e.g. Swinbank et al., 2012a; Wisnioski et al., 2015; Stott et al., 2016; Harrison et al., 2017). These are characterised by a steep rise from the centre to a turnover radius, followed by constant rotation velocity over the scales traced by the observations.

As also indicated in Fig. 1.16, the flat section of the curve results from the superposition of the contributions from the disk of baryons (stars and gas) and the halo of dark material, so that the total enclosed mass continues to increase linearly beyond the visible extent of the galaxy.

Measuring rotation velocity and velocity dispersion from ioinised gas

One common method for obtaining the data used to constrain the shape of rotation curves is to collect spatially resolved spectroscopic observations of emission lines originating from ionised nebular gas (i.e. H II regions, see § 1.5.3). A suite of strong hydrogen, oxygen, neon, nitrogen, helium and sulphur emission lines can be observed in the rest-optical wavelength regime, accessible from the ground with 8-10m class telescopes in the redshift range $0 < z \lesssim 4$. The spectrum of a particular region of the galaxy, in the wavelength region surrounding the redshifted wavelength of the chosen emission line, describes the 'Line-of-Sight-Velocity-Distribution' (LOSVD; see Cappellari 2016 section 3.2 for a discussion) of the emitting particles. Given the tremendous number of particles in each targetted spatial region, the LOSVD is normal[2] about the mean rotation field value, with width determined by the random motions of the gas about the mean rotation velocity (e.g. Glazebrook, 2013). Thus, it is common to model emission lines with a gaussian function and to infer the kinematic properties from the gaussian parameters which best describe the data.

The fundamental dynamical properties obtained from spatially mapping one of these emission lines are the line-of-sight rotation velocity, $V_{\rm rot}$, inferred from the difference between the emission line and systemic-redshift shifted centroids, and the velocity dispersion, often denoted as σ, inferred from the emission line width, at each spatial location. $V_{\rm rot}$ and σ are the first and second-order moments of the LOSVD respectively. The combination of these two properties can be used to examine both the dynamical state of star-forming galaxies and the baryonic and dark matter mass distributions within them. Fig. 1.17, taken from Green et al. (2014), indicates the variation in the width and wavelength of Hα emission across the spaxels of an IFS measurement of a local disk galaxy. Three important details are evident: **1**) the Hα emission on the two sides of the rotating disk is redshifted or blueshifted with respect to the systemic velocity, made clear with the red−blue colour gradient and the overlaid 'spider-diagram' contours;

[2]assuming that there is no significant contribution from an irregular dynamical component such as accretion, an outflow, AGN broad-line regions or a merging foreground/background galaxy pair

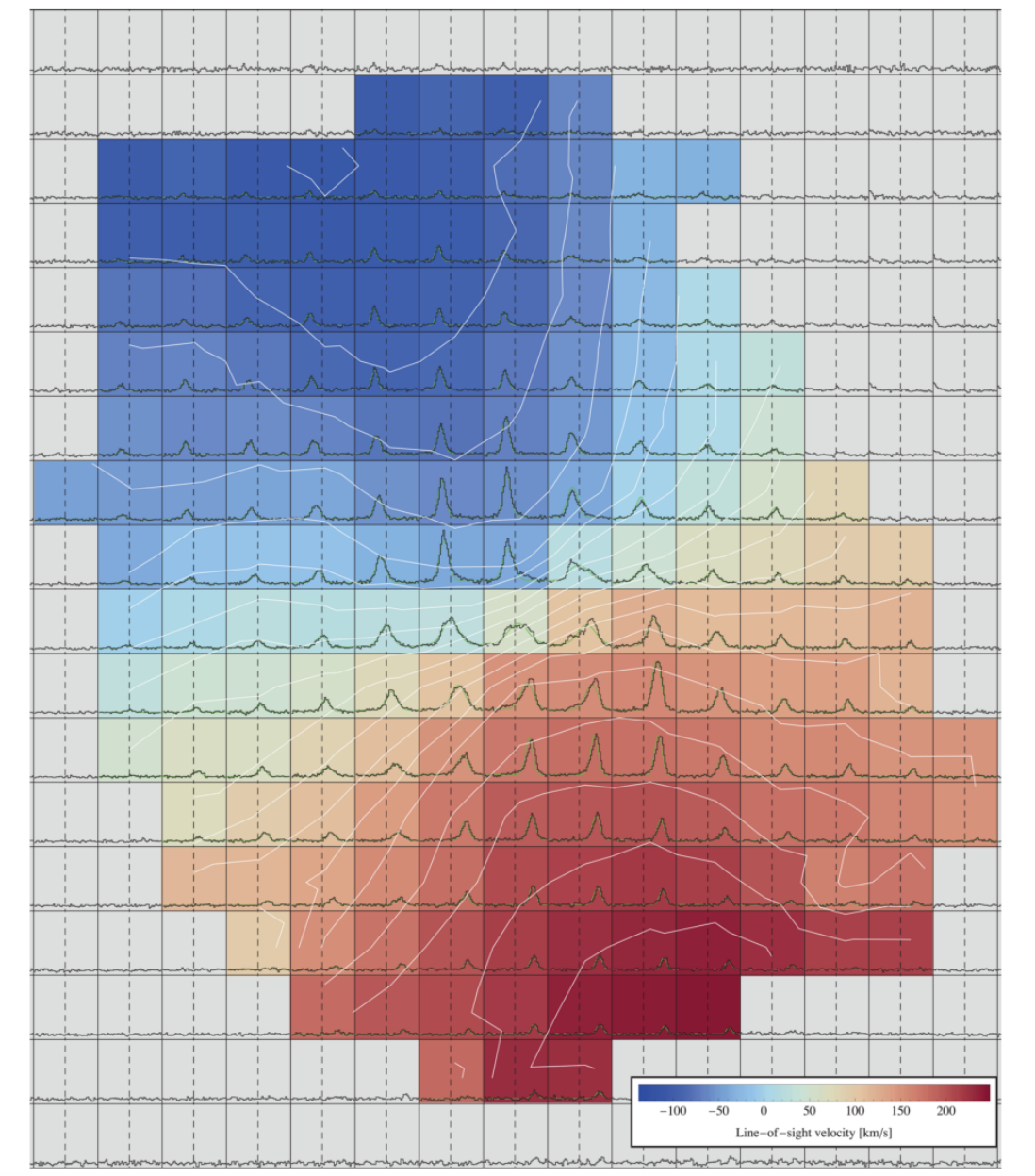

Figure 1.17: The spectral distribution of Hα emission is shown within each of the gridpoints, which cover different spatial locations across the galaxy. The line profile is redshifted towards the bottom right, blueshifted in the top left and smoothly transitions between these, indicating ordered disk rotation. The observed line profile is also broadened towards the galaxy centre as a consequence of line-profile convolution across the steep central velocity gradient (i.e. beam smearing). Taken from Green et al. (2014).

2) the emission lines are broader in the centre due to the beam-smearing effect (see below); **3**) The signal-to-noise of the emission line is weaker towards the outskirts of the galaxy as a result of the lower gas density.

As mentioned in § 1.4.5, one of the main challenges with dynamical studies of this nature is the conversion from observed to intrinsic rotation velocities and velocity dispersions. This is a consequence of the uncertainties and assumptions associated with inferring the inclinations of disk galaxies and the beam-smearing effect caused by the convolution of the data with the PSF of the observations. A common approach in the literature is to construct a simple model disk from a set of input parameters, which specify the disk emission line intensity in the spatial[3] and spectral directions (e.g. Forster Schreiber et al., 2006; Kassin et al., 2007; Genzel et al., 2008; Cresci et al., 2009; Gnerucci et al., 2011; Epinat et al., 2012; Swinbank et al., 2012a; Green et al., 2014; Bouché et al., 2015; Di Teodoro & Fraternali, 2015; Simons et al., 2016; Stott et al., 2016; Wuyts et al., 2016b; Burkert et al., 2016; Tiley et al., 2016; Pelliccia et al., 2017; Turner et al., 2017; Harrison et al., 2017; Johnson et al., 2018). Typically the disk model is constructed at much higher spatial and spectral resolution than the data, convolved with the empirically-determined PSF of the observations, resampled at the resolution of the observations, corrected for inclination and compared with the data to determine the model parameters.

To determine the intensity of the model in the spectral direction, the shape of the rotation curve must either be generated from the gravitational potential of the input mass distribution (e.g. Cresci et al. 2009 and see chapter 11 of Mo et al. 2010) or supplied in functional form. The first commonly used functional form is the physically motivated *Freeman Disk* (Freeman, 1970) rotation curve, generated from an exponential mass distribution:

$$V_{\rm rot}(r) = \frac{r}{R_D}\sqrt{\pi G \mu_0 R_D (I_0 K_0 - I_1 K_1)} \tag{1.2}$$

where R_D is the disk scalelength, μ_0 is the central surface mass density and the $I_n K_n$ are

[3]for longslit spectra this corresponds to a single dimension and specifying the flux at each pixel $[r_i]$ along the slit direction; for IFS measurements this corresponds to specifying the flux at each pixel $[x_i, y_i]$ in the two-dimensional intensity distribution.

the Bessel functions evaluated at $0.5r/R_D$. Other commonly-used functional forms are purely *phenomenological* in that they are analytic functions which match the shape of the rotation curves of local spiral galaxies, but aren't derived from any mass distribution. These include the *flat model*:

$$V_{\rm rot}(r) = \begin{cases} V_t \times \frac{r}{r_t} & \text{if} \quad r < r_t \\ V_t & \text{if} \quad r \geq r_t \end{cases} \tag{1.3}$$

and the *arctangent model*:

$$V_{\rm rot}(r) = V_t \frac{2}{\pi} \arctan\left(\frac{2r}{r_t}\right) \tag{1.4}$$

where V_t and r_t are the maximum velocity and turnover radius respectively (with r_t equal to the radius at which the rotation velocity is 70 per cent of V_t in the arctangent model). A comparison of these three models is provided in figure 3 of Pelliccia et al. (2017). Different groups take different approaches to fitting the disk model to the data. One approach is to first construct two-dimensional maps, or one-dimensional radial profiles (extracted in mock apertures along the kinematic position angle, $PA_{\rm kin}$) of the emission-line kinematic properties from the data. The same properties can then be extracted from the model, compared, and used to constrain the model parameters (e.g. Cresci et al., 2009; Stott et al., 2016; Harrison et al., 2017; Turner et al., 2017). This approach reduces the number of free parameters required in the model fitting. Alternatively, the disk models are compared directly with the three-dimensional (or two-dimensional in the case of longslit measurements) intensity distributions in the raw datacubes (e.g. Bouché et al., 2015; Di Teodoro & Fraternali, 2015). Common parameters varied in this fitting process include the galaxy centre ($[x_c, y_c]$), V_t, r_t, disk inclination angle, $PA_{\rm kin}$ and μ_0 and this is typically carried out using a Markov chain Monte Carlo (MCMC) method (e.g. Foreman-Mackey et al., 2013) or a genetic algorithm. Both fitting approaches described above benefit from the use of additional morphological information, typically from *HST*, which can be used to fix some of the

fit parameters; e.g. the inclination angle, $[x_c, y_c]$ and $PA_{\rm kin}$ if this is assumed to be equivalent to the morphological position angle, $PA_{\rm morph}$. Typically a constant intrinsic velocity dispersion is used in the disk model (see Fig. 1.18), as informed by the flat velocity dispersion profiles of both local and high-redshift galaxies (e.g. Epinat et al., 2008b; Wisnioski et al., 2015), and the model is used to examine the broadening of this intrinsic value caused by the beam smearing. The best-fit model can then be used to recover the intrinsic galaxy kinematic properties (i.e. to correct for the effects of beam-smearing), yielding rotation velocities systematically higher than observed and velocity dispersions systematically lower. The success of these techniques (our ability to recover intrinsic properties; e.g. Davies et al. 2011) depends upon the signal-to-noise of the data, particularly towards the galaxy outskirts where the rotation curve flattens, and the PSF of the observations (i.e. the number of independent resolution elements). This necessitates long integration times per galaxy (see figure 9 of Förster Schreiber et al. 2018) and observations are optimally carried out with the assistance of adaptive optics to minimise the width of the effective PSF (e.g. Swinbank et al., 2012a; Newman et al., 2013; Förster Schreiber et al., 2018).

Fitting the disk-model parameters can be computationally expensive, especially for IFS surveys studying hundreds of galaxies, and so an alternative, complimentary approach is to construct a set of *beam-smearing correction prescriptions* from a suite of disk-galaxy models. Fig. 1.18 shows a series of mock *KMOS* galaxies from Johnson et al. (2018) (see also Burkert et al. 2016), with galaxy mass increasing in successive rows.

The first three columns of this figure show the intrinsic velocity field, the velocity field after convolution with the PSF and the beam-smeared velocity dispersion. The one-dimensional red (intrinsic) and black (convolved) radial profiles in the final two columns clearly demonstrate that convolution with the PSF flattens the rotation curve and causes a prominent central peak in the observed velocity dispersion. The severity of these effects is a function of both the central velocity gradient and the ratio of galaxy to PSF size. The approach in both Johnson et al. (2018) and Burkert et al. (2016) is to provide lookup tables of rotation velocity and velocity dispersion correction factors

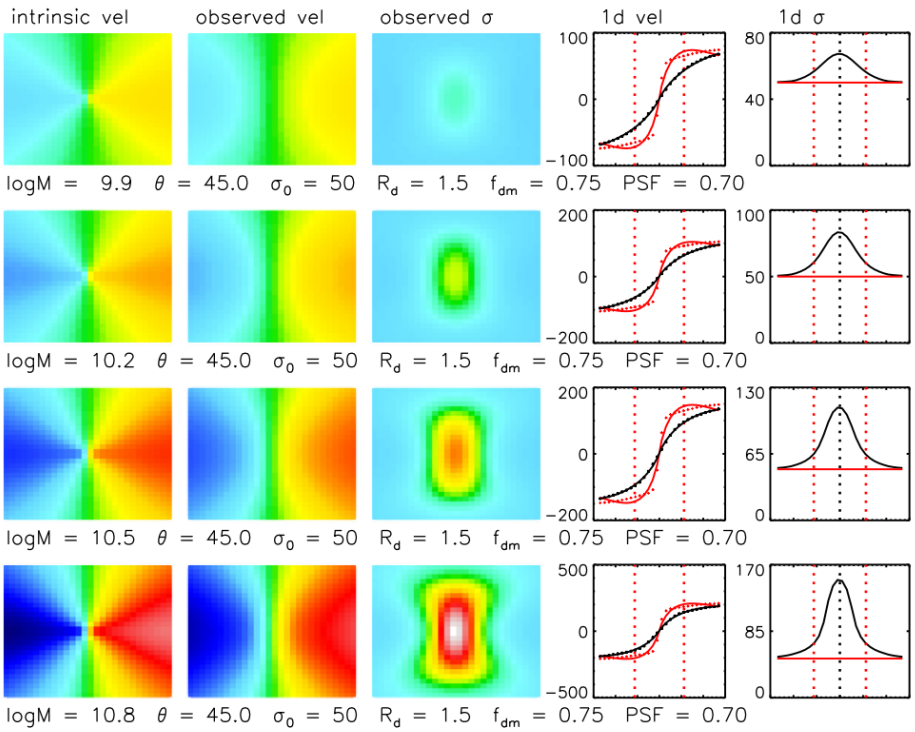

Figure 1.18: Systematic beam-smearing correction factors can be derived from mock observations, as described in Johnson et al. (2018). The columns above show the intrinsic galaxy velocity field, the convolved velocity field, the convolved velocity dispersion field and one-dimensional extractions of the intrinsic and convolved properties along $PA_{\rm kin}$. The magnitude of the impact of beam smearing on the observed kinematic properties depends on the PSF and the rotation velocity, and so correction factors are derived as a function of these parameters by constructing many mock galaxies observed in different conditions.

as a function of the above two properties, allowing for systematic correction of the observed kinematic values of large galaxy samples.

One method of increasing both the signal and angular resolution of the observations at no additional cost is to make use of *strong gravitational lensing*, whereby a foreground mass distribution acts as a magnifying lens for a background star-forming galaxy. Typically this occurs around very massive, foreground galaxy clusters[4] and, depending on the magnification factors, these lenses can allow for resolution at physical size scales of ~100 pc. There have been several studies of the kinematics of strongly lensed star-forming galaxies (e.g. Swinbank et al., 2007; Jones et al., 2010; Livermore et al.,

[4]see e.g. the 12 MAssive Cluster Survey (Ebeling et al., 2007)

2015; Leethochawalit et al., 2016; Mason et al., 2017; Toft et al., 2017; Girard et al., 2018; Patricio et al., 2018), although the analysis is challenging due to the physical distortion of the shape of the galaxies by the foreground lens. The results from these studies are generally consistent with the picture from unlensed surveys (see below), although complex kinematic features which would not be observed without lensing are often unveiled by the boosted angular resolution (e.g. Leethochawalit et al., 2016). The combination of adaptive-optics based IFS with strong gravitational lensing allows for the most detailed studies of the kinematics of star-forming galaxies, but can only be carried out for the small samples in which this phenomenon is observed.

To summarise this subsection, an important step in the analysis of kinematic data collected by longslit and integral-field spectrographs is the correction of beam-smearing effects via disk modelling or systematic parameter correction. Without this step, the galaxy kinematic properties would be systematically biased as a function of rotation velocity and size. Ultimately, one is left with the intrinsic kinematic properties of the galaxy sample which can then be used for the chosen scientific objective.

Gas versus stars

Kinematic measurements inferred from ionised gas emission lines trace the kinematics of the gas. These emission lines have much higher signal-to-noise than the stellar absorption features which must be used to trace the stellar kinematics, and so can be used as a tracer over a much wider redshift window. This gas moves in the same gravitational potential as the stars and so the naive assumption is that both components will exhibit similar rotation curves. In the local Universe, it is possible to infer kinematic parameters from both components in individual galaxies. Using data from the Sydney-Australian-Astronomical-Observatory Multi-object Integral-Field Spectrograph (SAMI) survey (Croom et al., 2012), Cortese et al. (2014) find that, on average, the rotation velocity of the gas, $V_{\rm rot}$(gas) is 0.14 dex higher than the rotation velocity of the stars, $V_{\rm rot}$(stars). This is a consequence of 'asymmetric drift' (e.g. Burkert et al., 2010), whereby a larger

portion of the stellar dynamical support is provided by random motions traced by the velocity dispersion, thus lowering the rotation velocity. The stellar velocity dispersion measurements, σ(stars), are on average 0.19 dex higher than σ(gas), although the relationship between $M_\star$ and σ(gas) is nonlinear, as galaxies with $\log(M_\star/M_\odot) < 10.0$ show roughly constant σ(gas). The physical explanation for this finding, complicated by the gas being collisional and stars being collisionless within galaxies, is possibly linked to gravitationally-maintained turbulence (e.g. Swinbank et al., 2012b; Krumholz et al., 2017; Johnson et al., 2018) but requires further study. As a consequence of the above, the stellar and gaseous root-mean-square velocities $V_{RMS} = \sqrt{V_{rot}^2 + \sigma^2}$ are roughly equal.

Comparisons of the stellar and gaseous kinematics have also been attempted at intermediate redshifts using very deep spectroscopic data. Guerou et al. (2017) studied a subsample of galaxies from the MUSE Hubble Ultra Deep Field (HUDF) survey (Bacon et al., 2017) over the redshift range $0.2 < z < 0.8$, finding no systematic differences in the rotation and dispersion properties of the stars and gas (although with large scatter) and roughly equivalent V_{RMS} values as per the local measurements. Also Bezanson et al. (2018) obtained measurements of the stellar kinematics of galaxies at $0.6 < z < 1.0$ from the Large Early Galaxy Astrophysics Census (LEGA-C) survey, finding large stellar velocity dispersion values which are constant across the galaxy disks. Upcoming work will compare these measurements with the kinematic properties of the gas (Straatman et al. *in prep.*). Both of these studies are very recent and represent the frontier of what is currently achievable with 8-10m class ground-based telescopes. Further, more detailed comparisons of gas and stellar kinematic measurements out to higher redshifts require the James Webb Space Telescope (JWST) or possibly even 30m class telescopes such as the Extremely Large Telescope (ELT).

Star-forming galaxy kinematics across cosmic time

As mentioned in § 1.4.4, the large IFS programmes of the last decade have driven forward our understanding of the dynamical state of star-forming galaxies across cosmic time. Early studies with the SINFONI spectrograph (Genzel et al., 2006; Forster Schreiber et al., 2006; Genzel et al., 2008; Förster Schreiber et al., 2009; Genzel et al., 2011; Förster Schreiber et al., 2011) revealed significant kinematic diversity amongst $z \sim 2$ *UV*-selected star-forming galaxies (e.g. figure 17 of Förster Schreiber et al. 2009). Kinematic classification of these galaxies is carried out through a combination of quantitative[5] and qualitative methods when the signal-to-noise of the data is low. These classifications revealed that about two thirds of the sample exhibit some degree of regular rotation in a disk (particularly the galaxies with the highest stellar mass); in itself an important result given the irregular, clumpy morphologies observed by *HST* at these redshifts (e.g. Elmegreen et al., 2004; Bournaud et al., 2007, 2008). These surveys also unveiled the existence of 'dispersion-dominated' galaxies with random motions of comparable magnitude to the rotational motions and also galaxies with 'merger-like' kinematics. The 'dynamically hot' dispersion-dominated galaxies, with high star-formation rates have no local analogue. Other IFS studies corroborated these results (e.g. Law et al., 2007, 2009; Gnerucci et al., 2011; Epinat et al., 2012), leading to a discussion of the physical origin of the large velocity dispersions, their energy source and their role in the dynamical mass budget of galaxies. The Toomre Q parameter Toomre (1964) expresses the susceptibility of regions within a galaxy to gravitational collapse:

$$Q_{\rm gas} = \frac{\kappa\sigma}{\pi G \sum_{\rm gas}} \tag{1.5}$$

with the epicyclic frequency $\kappa = aV_{\rm rot}/R$, where a is a dimensionless factor between

[5]see for example the kinemetry method of Krajnovic et al. (2006); Shapiro et al. (2008), which is a generalisation of surface photometry to the higher order moments of the LOSVD. In this approach, the observed velocity and velocity dispersion fields are first described by a series of concentric ellipses, and asymmetries in these fields are quantified using the coefficients of harmonic expansions along the ellipses.

$1 < a < 2$, dependent on the galaxy rotational structure, R provides some measure of the disk size and $\sum_{\rm gas}$ is the gas surface density (e.g. Glazebrook, 2013). For values $Q_{\rm gas} < 1$, the gas is unstable to gravitational collapse and indeed in Genzel et al. (2011) the authors construct maps of $Q_{\rm gas}$ where regions with $Q_{\rm gas} < 1$ appear to correlate with morphological clumps of star formation from rest-*UV HST* photometry. Also following Genzel et al. (2011), using $M_{\rm dyn} = V_{\rm rot}^2 R/G$ and $M_{\rm gas} = \pi R^2 \sum_{\rm gas}$, Equation 1.5 can be written:

$$Q_{\rm gas} = a \left(\frac{\sigma}{V_{\rm rot}} \right) \left(\frac{M_{\rm dyn}}{M_{\rm gas}} \right) \tag{1.6}$$

which for the values $Q_{\rm gas} \sim 1$ expected in unstable high-redshift disks becomes:

$$\frac{V_{\rm rot}}{\sigma} \approx \frac{1}{f_{\rm gas}} \tag{1.7}$$

with $f_{\rm gas}$ the gas fraction in that region. This offers an explanation for both the high observed velocity dispersions in high-redshift galaxies, as a consequence of high gas fractions (e.g. Tacconi et al., 2010, 2013), and also the existence of clumpy regions embedded in a rotating disk as $Q_{\rm gas} < 1$ gas regions which have collapsed due to gravitational instability.

Breakthrough work came after the advent of KMOS, since its multiplex enabled the collection of much larger samples of high-redshift galaxies targetted with deep IFS measurements. Wisnioski et al. (2015) describes initial measurements from the KMOS^{3D} survey[6] for $\sim$ 200 Hα detected star-forming galaxies at two redshift slices, centred at $z \sim 1$ and $z \sim 2.3$.

This work also studied the kinematic diversity and classification of the galaxies, finding a high fraction of rotationally-supported disks with large velocity dispersion values. Fig. 1.19 shows literature compilations of the intrinsic velocity dispersion ($\sigma_{\rm int}$) versus

[6]led by the Max Planck Institute for Extraterrestrial Physics group

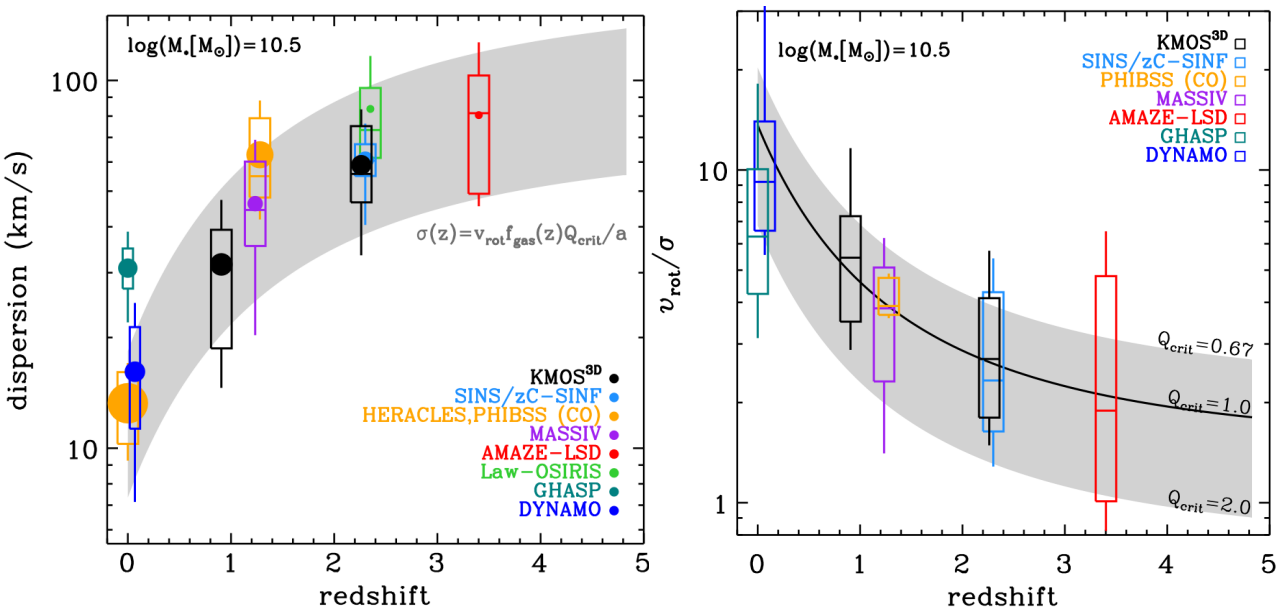

Figure 1.19: *Left:* Literature compilation of $\sigma_{\rm int}$ values from various spectroscopic studies spanning $0 < z < 3$. The increase in the mean $\sigma_{\rm int}$ values is clear and appears to follow the form dictated by Equation 1.7 as shown by the grey shaded region. *Right:* The resultant decline in the ratio $V_{\rm C}/\sigma_{\rm int}$ driven by the increased $\sigma_{\rm int}$ values. High-redshift disks are less dynamically stable than their local counterparts. Both panels are taken from Wisnioski et al. (2015).

redshift and $V_{\rm C}/\sigma_{\rm int}$[7] versus redshift relations presented in Wisnioski et al. (2015). This summarises the increase of $\sigma_{\rm int}$ and the corresponding decrease in $V_{\rm C}/\sigma_{\rm int}$ with increasing redshift over the range $0 < z < 3.5$. The redshift dependence of these relations is plotted with the grey shaded regions, formulated in terms of the observed $f_{\rm gas}$ versus redshift relation from Tacconi et al. (2013). These curves match the general trends of the data, substantiating the connection between $\sigma_{\rm int}$ and $f_{\rm gas}$. A possible reason for this connection could be the increased accretion rates, and hence star-formation rates, at high redshift (e.g. Dekel et al., 2009) driving disk turbulence (e.g. Krumholz et al., 2017; Johnson et al., 2018; Hung et al., 2018), however this issue requires further study. Chapter 3 presents an investigation of the kinematic properties of the largest sample of star-forming galaxies observed with IFS at $z \sim 3.5$. The observed trend between $\sigma_{\rm int}$ and redshift, as well as between $V_{\rm C}$ and redshift, is investigated and reasons for the observed values are discussed.

[7] $V_{\rm C}$ is used here to refer to a measure of the intrinsic rotation velocity.

This is an example of an area where simulations and observations will be used together to make progress. As mentioned above, it is not possible to trace the evolution of $\sigma_{\rm int}$ within individual systems. Therefore, determining the average redshift dependence of $\sigma_{\rm int}$ necessarily involves comparison of star-forming galaxy samples at different epochs, and the assumption of a progenitor−descendent relationship. A recent study, using galaxies from the FIRE zoom simulations, tracks changes in $\sigma_{\rm int}$[8], the gas infall rate, the star-formation rate, the gas fraction and stellar mass for individual galaxies between $0 < z < 4.5$. This is shown in Fig. 1.20, taken from Hung et al. (2018), for the three galaxies in the most massive simulated halos and demonstrates the stochasticity of and correlations between each of these properties on short timescales at $z \geq 0.5$. Within these simulations, increases in $\sigma_{\rm int}$ are related to periods of rapid accretion, which increase the gas fractions and the star-formation rates. Periods of low $\sigma_{\rm int}$ generally occur when there are few star-forming particles in the galaxies. The *average* trends across many simulation snapshots for 10 simulated FIRE galaxies match the trends seen in the data, in that velocity dispersions are low at low redshift when the accretion rate is no longer violent and stochastic.

The large observed velocity dispersions at high redshift have prompted consideration that $\sigma_{\rm gas}$ may be tracing pressure support against gravitational collapse, a feature which is not present in local disk galaxies. Several studies have explored the virtue of combining rotation velocity and velocity dispersion as a better tracer of the dynamical mass than rotation velocity alone (e.g. Weiner et al., 2006a; Kassin et al., 2007; Cresci et al., 2009; Kassin et al., 2012; Wuyts et al., 2016b; Simons et al., 2016; Übler et al., 2017; Turner et al., 2018). These studies unanimously report a tight relationship between stellar mass and the combined gas velocity dispersion and rotation velocity tracer. However, as mentioned above, the nature of the relationship between $\sigma_{\rm gas}$ and mass has yet to be demonstrated conclusively. The provision of pressure support against gravity, traced by velocity dispersions, is discussed for a collection of literature samples covering the redshift range $0 < z < 3.5$ in Chapter 4.

[8]the authors use a proxy for $\sigma_{\rm int}$, ($\sigma_{\rm 1D}$), derived from the simulation particles, although no clear distinction is made between stellar and gas particles. The authors verify this serves as an unbiased tracer.

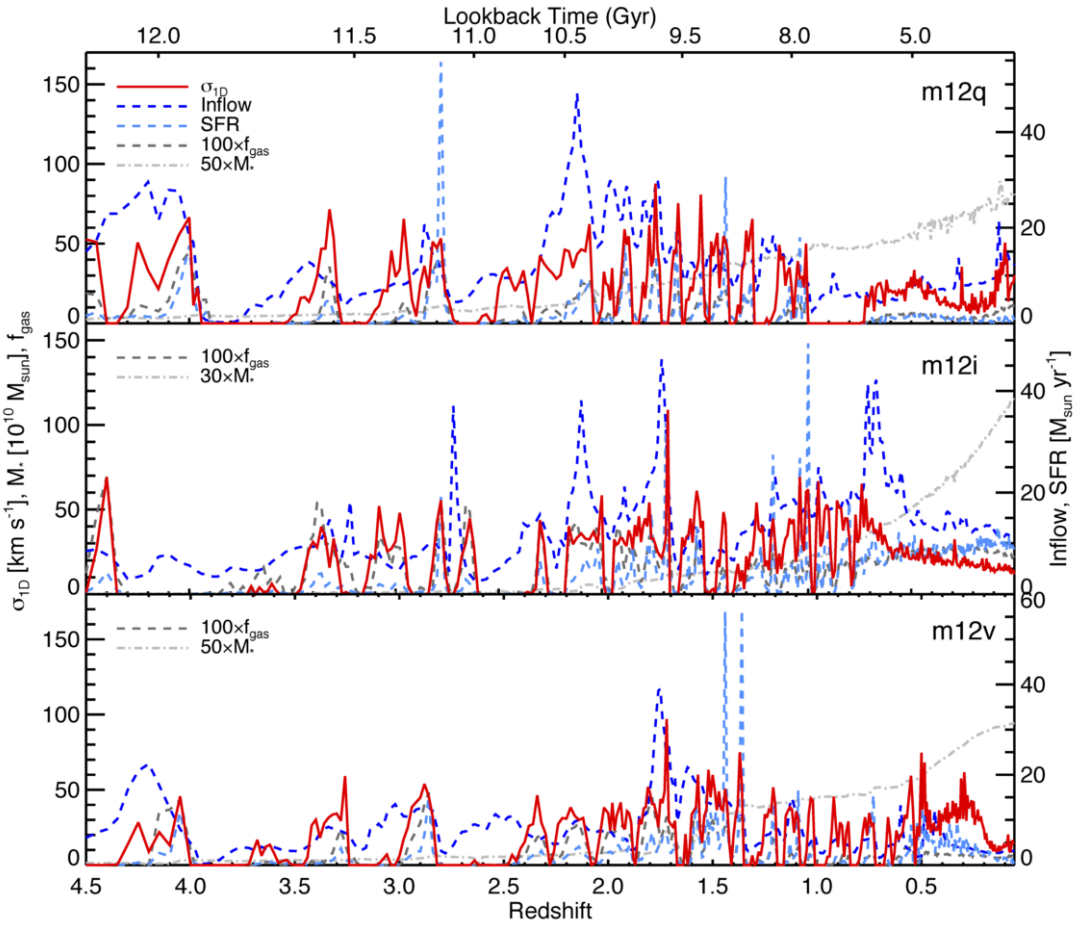

Figure 1.20: The evolution of several physical properties are shown for three individual galaxies inhabiting the most massive halo in three different FIRE simulation suites. The accretion rate, gas fraction, star-formation rate and intrinsic velocity dispersion all vary on short timescales at $z \geq 0.5$ within individual galaxies. Additionally, the variations are temporally correlated indicating that the increased observed average velocity dispersions at high redshift are a reflection primarily of more violent accretion and star formation. Taken from Hung et al. (2018).

The KMOS Redshift One Spectroscopic Survey[9] (KROSS; Stott et al. 2016) has detected Hα emission in $\sim$ 600 star-forming galaxies at $z \sim 1$, corresponding to a lookback time of 8 Gyr. This is an order-of-magnitude larger than previous IFS surveys at this redshift, allowing for a robust inspection of the dynamical properties of galaxies in this period of the Universe, spanning a wide range of global galaxy properties. Dramatic plots such as that shown in Fig. 1.21 can be made with such surveys, which is taken from Harrison et al. (2017) and displays the distribution of galaxy velocity fields across the main sequence.

[9]led by the University of Durham astronomy department

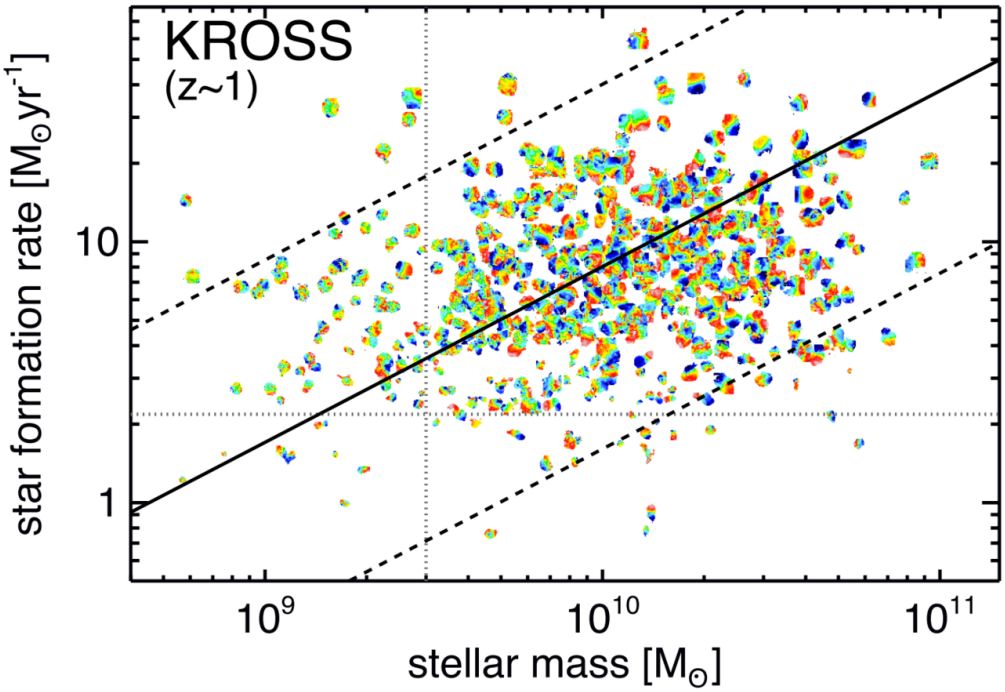

Figure 1.21: The distribution of rotation-velocity fields from KROSS star-forming galaxies on the star-formation rate versus stellar mass main sequence, taken from Harrison et al. (2017). Overwhelmingly the galaxies display some degree of ordered rotation, with physically smaller systems located at lower stellar mass values.

Stott et al. (2016) demonstrate using the KROSS sample and other literature data that there is a decline in the Rotation-Dominated Fraction (RDF) of star-forming galaxies between $0 < z < 3$, consistent with the results of Wisnioski et al. (2015). Harrison et al. (2017) study the specific angular momentum versus stellar-mass relation with KROSS at $z \sim 1$, finding a clear paucity of angular momentum at fixed stellar mass in comparison with local galaxies and a clear connection between angular momentum content and morphology at fixed stellar mass.

Using galaxies from the KROSS sample, both Tiley et al. (2016) and Harrison et al. (2017) study the rotation-velocity versus stellar-mass relation (i.e. the Stellar-Mass Tully-Fisher relation, SMTFR, Tully & Fisher 1977) which traces the relationship between dynamical and stellar mass. Evolution of this relationship across cosmic time thus traces changes in the dark-to-luminous mass ratio and also the redistribution of mass between stellar and gaseous components. This evolution is investigated by

comparing the slope and normalisation of the SMTFR fitted to galaxy samples at $z > 0$ with those of well-understood reference samples at $z = 0$ (e.g. Bell & de Jong, 2001; Pizagno et al., 2007; Reyes et al., 2011). It is common in the literature, due to the difficulty of accurately constraining the slope of the high-redshift SMTFR with small samples of limited dynamic range, to fix the slope to a local reference value and focus on changes to the normalisation. The above KROSS studies, utilising the statistical power of several hundred galaxy IFS measurements, demonstrate that the observed evolution of the normalisation of the SMTFR is a strong function of the ratio of the intrinsic rotation velocity to the velocity dispersion, $V_C/\sigma_{\rm int}$. There have been many other studies of the evolution of this relation using samples of varying size and median redshift (e.g. Flores et al., 2006; Kassin et al., 2007; Puech et al., 2008; Cresci et al., 2009; Miller et al., 2011; Gnerucci et al., 2011; Miller et al., 2012; Swinbank et al., 2012a; Green et al., 2014; Simons et al., 2016; Übler et al., 2017; Swinbank et al., 2017; Pelliccia et al., 2017; Straatman et al., 2017). Generally the results of these studies are not in agreement and are challenging to interpret due to different galaxy sample selection criteria and analysis methodologies. Theoretically, the following simplistic relation was derived in Mo et al. (1998) to describe the redshift evolution of the relationship between disk mass and circular velocity:

$$M_d = \frac{m_d V_C^3}{10GH(z)} \tag{1.8}$$

with M_d the disk mass, m_d the fraction of the halo mass corresponding to the disk and $H(z)$ the Hubble expansion parameter. This predicts that, at earlier times, disks should have larger rotation velocities at fixed stellar mass, due to the lower fraction of the halo mass in stars and the larger values of $H(z)$. In reality, this relationship relies upon a number of assumptions relating to the conversion from halo to disk properties and the dependence on these conversion factors with redshift. Übler et al. (2017) equation 5 describes a toy model for the evolution of the SMTFR with more realistic and redshift dependent conversion factors. Using the KMOS^{3D} dataset at $z \sim 1$ and $z \sim 2.3$, this study concludes that to explain the observed evolution, which is flat between these redshift slices, high-redshift disks must be strongly baryon dominated (also provided

as the explanation for observed falling outer rotation curves in individual KMOS^{3D} galaxies; Genzel et al. 2017). A further important conclusion from Übler et al. (2017) is that velocity dispersions must be accounted for in the derivation of the true circular velocities of the galaxies. Semi-analytic and hydrodynamical simulations can also be used to probe the evolution of the SMTFR, including a range of complex baryonic processes throughout the modelling (e.g. Dutton et al., 2011; Schaye et al., 2015). These models generically predict higher rotation velocities at fixed stellar mass in the early Universe (to varying degrees; see e.g. Tiley et al. 2016; Straatman et al. 2017), however simulations represent an idealised scenario where dynamical support is purely rotational. Simulation predictions for the evolution of the SMTFR at present should thus be seen as an upper limit for the evolution, observed departures from which may provide additional evidence for pressure support in the dynamical mass budget. Chapter 4 (and see Turner et al. 2018) provides a careful study and literature comparison of the impact of sample selection criteria on the inferred evolution of the SMTFR, both with and without the inclusion of pressure support traced by intrinsic velocity dispersions.

Overall the emergent picture from IFS and longslit surveys is one in which turbulent and clumpy star-forming disks gradually settle over time, evolving towards lower velocity dispersions, higher Toomre Q parameters and increased rotation support. Crucial questions which remain to be answered include:

- What is the nature of dispersion-dominated galaxies at high redshift?
- What drives and maintains gas-phase turbulence in high-redshift disk galaxies?
- Will the large observed gaseous velocity dispersions be reflected in large stellar velocity dispersions at high redshift?
- What is the dynamical state of disk galaxies, as traced by multi-phase gas observations at $z > 3$? (see Chapter 3)
- To what extent do the large observed gaseous velocities at high redshift reflect pressure support against gravitational collapse? (see Chapter 4)

- To what extent do scaling relations such as those between rotation velocity and stellar mass, and between angular momentum and stellar mass evolve with redshift, reflecting changes in the mass distribution between different components and the evolution of galaxy sizes? (see Chapter 4)

1.5.3 The chemical and interstellar medium evolution of star-forming galaxies

One of the byproducts of star formation and stellar evolution is a yield of elements with atomic numbers > 2 (referred to generically as 'metals'), fused in the interiors of stars, into the interstellar medium (ISM) of galaxies via supernovae and stellar winds. The presence of these elements is imprinted into both the stellar and nebular spectra of galaxies as absorption and emission features respectively. The prevalence of heavy elements in a galaxy is generally quantified throughout the literature as the relative abundance of oxygen to hydrogen particles, expressed in units of $12+\log(\mathrm{O/H})$, with O the number density of oxygen particles and H the number density of hydrogen particles, and referred to as the galaxy 'metallicity'. As per the dynamical studies described above, the chemical properties of increasingly-large samples of star-forming galaxies are being systematically catalogued at low and high redshifts using a combination of spectroscopic and IFS measurements. These measurements provide valuable constraints for both analytic models and full cosmological hydrodynamical simulations seeking to describe the enrichment history of galaxies.

The measurement of a galaxy (or galaxy region) metallicity requires conversion between the observed strength of spectral features and the abundance of the corresponding elemental species responsible for the emission. In the case of star-forming galaxies, the features used to do this are emission lines originating from H II regions, which are ionised gaseous nebulae surrounding hot, young stars. It is the ultraviolet radiation emitted by these stars, responsible for the photoionisation, which powers the emission from the gas. The energies of photoelectrons in H II regions have recently been found to

follow κ-distributions, which depart slightly from the equilibrium Maxwell-Boltzmann distribution, typically with *electron temperatures*, T_e, in the range 5000K < T_e < 20000K. It is these electrons which participate in the atomic processes responsible for the production of emission-line spectra. The 'direct' method of abundance determination requires measurement of the ratio of intensities of two lines with different excitation energies, emitted by a single ionic species (e.g. [O III]$\lambda\lambda$4959,5007 to [O III]λ4363; Osterbrock 1989; Stasińska 2002a,b). This method also requires knowledge of the *electron density*, n_e, which can be found using the ratio of emission lines from levels of similar energies within a single ion (e.g. [O III]$\lambda\lambda$3727,3729 or [S II]$\lambda\lambda$6717,6731). It is only feasible to measure abundances this way for individual galaxies in the local Universe, as the [O III]λ4363 emission line is very weak and often undetected, particularly in low-metallicity environments.

Consequently, statistical calibration methods which use the ratios of 'strong' emission lines to determine abundance have been formulated (e.g. Pagel et al., 1979; Pilyugin, 2001; Pettini & Pagel, 2004; Pilyugin & Thuan, 2005; Nagao et al., 2006; Pilyugin et al., 2010, 2012; Brown et al., 2016; Cowie et al., 2016; Curti et al., 2017). These rely upon empirical relationships between the strong-line ratios and abundances determined for local galaxies using the direct method. It is unlikely to be appropriate to apply these calibrations to the strong-line ratios of high-redshift galaxies, within which it has been conclusively shown that the nebular conditions are significantly more extreme (e.g. Kewley et al. 2013b; Steidel et al. 2014; Masters et al. 2014; Shapley et al. 2015; Sanders et al. 2016; Masters et al. 2016; Kashino et al. 2016; Cullen et al. 2016; Strom et al. 2017; and see below). Therefore, determining the absolute abundances in high redshift galaxies is notoriously challenging. A second branch of strong-line methods have also been inspired by the observational challenges described above, these being theoretical calibrations based on the combination of SPS and photoionisation models (e.g. Sutherland & Dopita, 1993; Ferland et al., 2013), which provide predictions for the metallicity-sensitive strong lines for a given set of input parameters, including metallicity (e.g. McGaugh, 1991; Kewley & Dopita, 2002; Tremonti & Heckman,

2004; Dopita et al., 2016). Application of different theoretical and empirical strong-line methods can result in $12+\log(O/H)$ offsets of up to 0.7 dex, rendering it extremely dangerous to apply different methods at different redshifts when studying metallicity evolution (e.g. Kewley & Ellison, 2008; Cullen et al., 2014), however attempts have been made to place the different metallicity calibrations on the same baseline (e.g. Kewley & Ellison, 2008).

Galaxies in the local Universe are observed to fall on a tight sequence ($\pm$0.1 dex) in the metallicity versus stellar-mass plane, known as the Mass-Metallicity Relationship (MZR; e.g. Tremonti & Heckman 2004), with additional dependency on galaxy star-formation rate (i.e. the Fundamental Metallicity Relation; Mannucci et al. 2010). This relation is observed out to at least $z \simeq 3$ (e.g. Erb et al., 2006; Maiolino et al., 2008; Mannucci et al., 2010; Zahid et al., 2011; Yabe et al., 2012; Stott et al., 2013b; Steidel et al., 2014; Salim et al., 2015; Sanders et al., 2015) and paints a clear picture whereby galaxies with larger stellar mass have produced more heavy elements as a direct consequence of the larger time-integrated star formation.

The normalisation and slope of this relation is observed to evolve with redshift, as demonstrated in Fig. 1.22 taken from Zahid et al. (2013). At all stellar masses, the star-forming galaxy population is less enriched when observed towards increasingly-high redshifts. The shape of the MZR is commonly fitted with the following functional form (e.g. Moustakas et al., 2011; Zahid et al., 2013):

$$12 + \log(O/H) = Z_0 - \log\left[1 + \left(\frac{M_\star}{M_0}\right)\right] \tag{1.9}$$

where the physical interpretation of Z_0 is the asymptotic metallicity towards which the relation approaches and M_0 is the stellar mass at which the relation flattens. In the context of an inflow model of chemical evolution, where star formation is fueled by the accretion of pristine gas, Zahid et al. (2013) further describe Z_0 as the saturation metallicity equivalent to the nucleosynthetic yield of oxygen into the ISM. The flattening of the slope of the MZR towards lower redshift can be interpreted either as a 'chemical

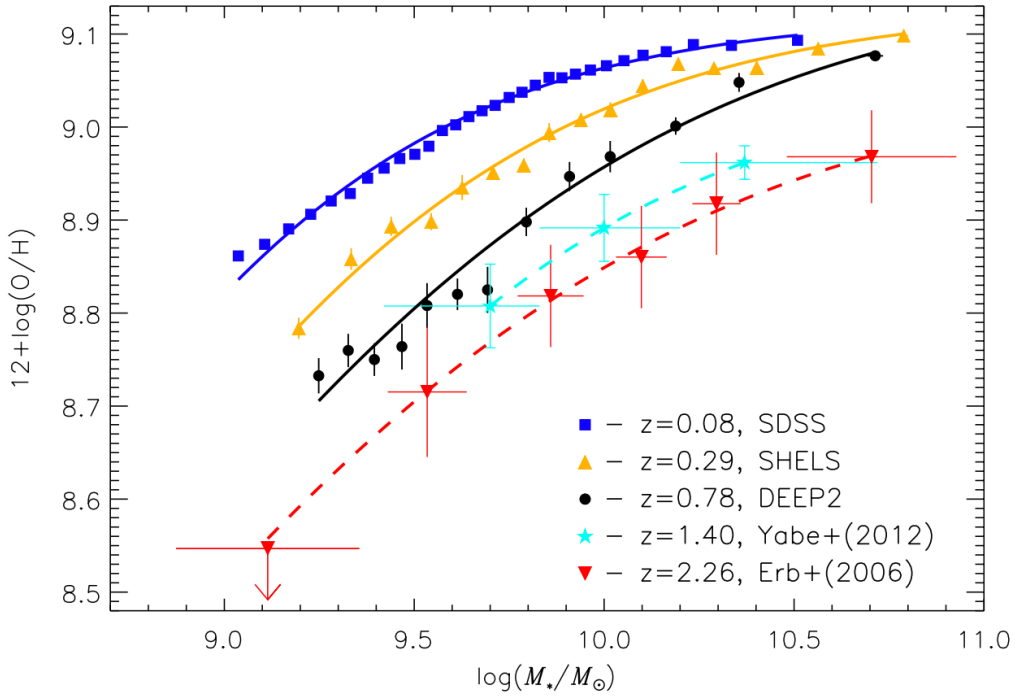

Figure 1.22: The MZR and its evolution over the redshift range $0 < z < 2.3$ from Zahid et al. (2013). The functional form of the fits is given in Equation 1.9 and the physical interpretation of this relation is discussed in the text.

downsizing' effect, whereby massive galaxies formed and enriched earlier and more rapidly (e.g. Cowie et al., 1996) or as a redshift evolution of the mass M_0 at which the metallicity of star-forming galaxies begins to saturate (due to the lower accretion rates and smaller gas reservoirs at late times). For star-forming galaxies which are free to exchange materials with their environments, the evolution of gas-phase metallicity can be described analytically by writing down a set of equations describing the yield of metals into the ISM, the mass-loaded outflows and inflows of pristine gas into the systems (e.g. Lilly et al., 2013; Zahid et al., 2014). These are described in detail throughout Lilly et al. (2013) and summarised schematically in terms of the galaxy system in Fig. 1.23.

As mentioned above, it is the photoionisation of hydrogen by the ultraviolet radiation emitted by hot, young stars which leads to the production of nebular emission-line spectra. This photoionisation can also occur through other means, notably by the much harder radiation field emitted by AGN, leading to dramatic differences in the

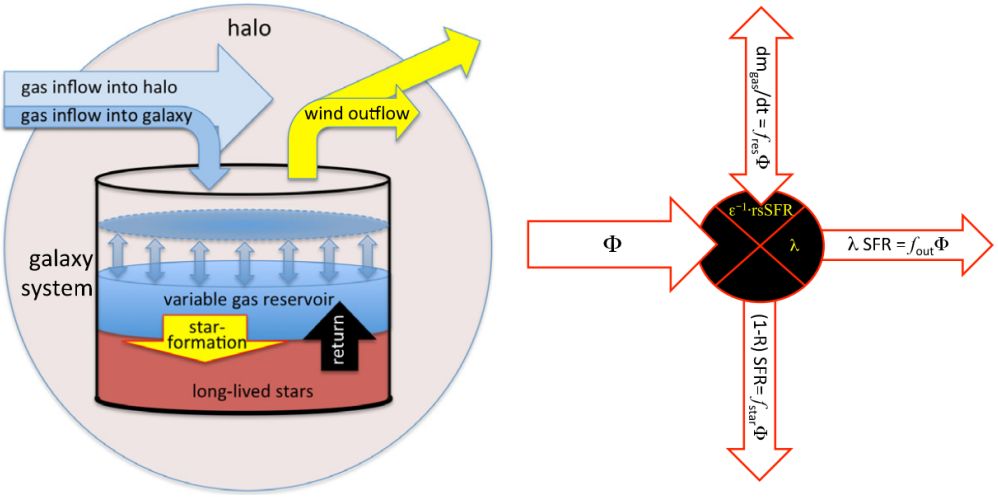

Figure 1.23: The regulator model from Lilly et al. (2013) describes the interplay between accretion, galaxy gas reservoirs, star formation and metal yield into the ISM and outflows.

observed ratios of strong nebular lines[10]. It is therefore crucial to separate AGN powered nebulae, to which the application of strong-line abundance methods are not appropriate, from those powered by young stars in H II regions. One method of doing so is to make use of emission line ratio Baldwin-Phillips-Terlevich (BPT; Baldwin et al. 1981) diagrams, within which star-forming galaxies are confined to a tight sequence governed by: **(1)** the spread of abundance throughout the population; **(2)** the hardness of the ionising stellar radiation field; **(3)** the galaxy ISM conditions (e.g. Kewley et al., 2013a). The x and y-axes of these diagrams should involve ratios of emission lines produced by ionised species to Balmer lines, be intrinsically bright so that they can be detected out to high redshift and be located close in wavelength to minimise the impact of dust extinction. The most commonly used diagram satisfying these criteria utilises [O III]/Hβ versus [N II]/Hα, for which the positions of local galaxies are well-understood both theoretically and observationally (e.g. Kewley & Dopita, 2001; Tremonti & Heckman, 2004).

Fig. 1.24, from Kewley et al. (2013a), shows the location of both star-forming galaxies

[10]see also the increasing body of work describing the contamination of H II region spectra by Diffuse Ionised Gas (DIG) and Low-Ionisation Nuclear Emission line Regions (LINERs) possibly photoionised by evolved stellar populations, or 'leaky' H II regions (e.g. Kewley et al., 2013a; Belfiore et al., 2015; Zhang et al., 2017; Sanders et al., 2017).

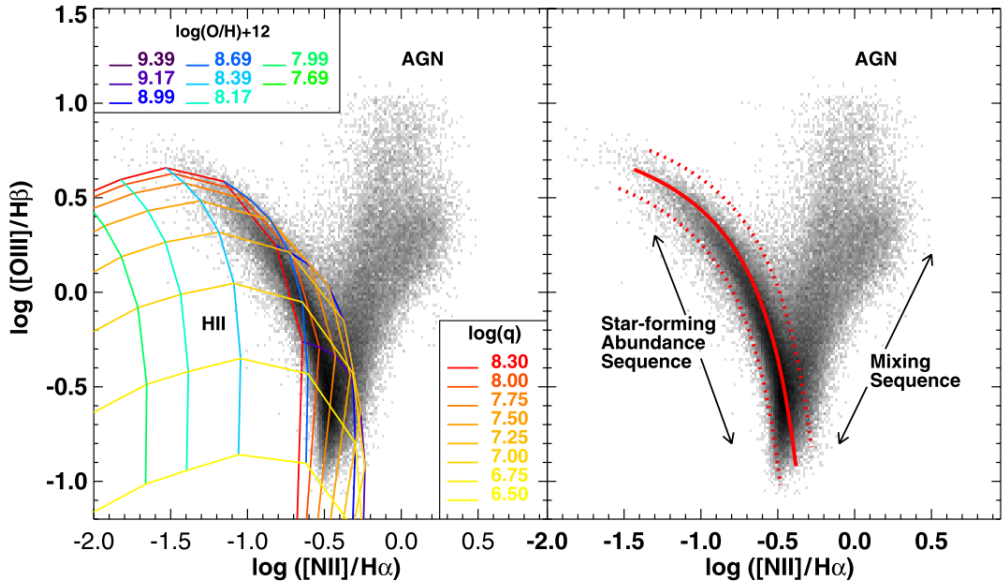

Figure 1.24: The location of local galaxies (grey points) and photoionisation model predictions governed by the input metallicity and ionisation parameter are shown in the [O III]/Hβ versus [N II]/Hα BPT diagram. Star-forming galaxies form a tight sequence which is separate from the AGN locus and dictated by the galaxy ISM conditions. Taken from Kewley et al. (2013a).

and AGN from SDSS in this plane, clearly separated by a 'mixing sequence' of ionising sources, with an overlaid grid of photoionisation predictions goverened by input metallicity and ionisation parameter, $q_{\rm ion}$. This parameter is defined as the product of the speed of light, c, and the ratio of the number density of hydrogen-ionising photons, $n_{\rm ion}$, to the number density of hydrogen particles, roughly equivalent to the electron density, n_e:

$$q_{\rm ion} = c \times \frac{n_{\rm ion}}{n_e} \tag{1.10}$$

and dictates the relative number of particles in upper and lower ionisation states (e.g. Sanders et al., 2016). Comparison of these model grids with the data offers one route to constraining such parameters, which show, for example, that local-Universe galaxies in the upper-left envelope with large [O III]/Hβ and small [N II]/Hα line ratios are characterised by low metallicities and high ionisation parameters.

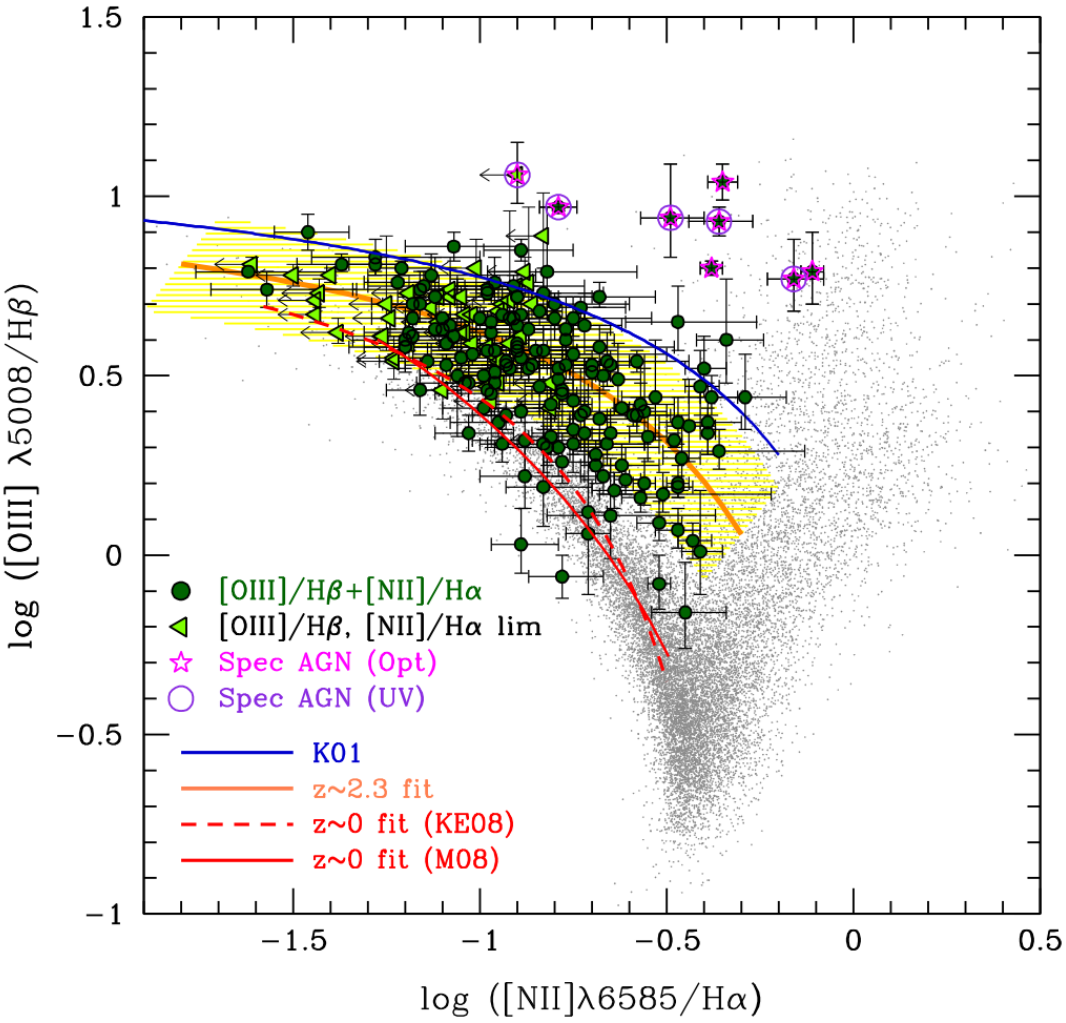

Figure 1.25: The high-redshift view of the [O III]/Hβ versus [N II]/Hα diagram, showing that the locus of $z \sim 2.3$ star-forming galaxies from the KBSS-MOSFIRE campaign is systematically offset with respect to the SDSS galaxies. This is usually interpreted as evidence that high-redshift galaxies have more extreme ISM conditions that their local counterparts. Taken from Steidel et al. (2014).

The sequence of high-redshift star-forming galaxies is observed either to be offset from, or to fall exclusively at the extreme end of the local distribution in such line-ratio diagrams. This is manifest in the [O III]/Hβ versus [N II]/Hα plane for the $z \sim 2.3$ Keck Baryonic Structure Survey (KBSS)-MOSFIRE sample Steidel et al. (2014), as shown in Fig. 1.25. The $z \sim 2.3$ galaxies are consistent with either higher values of [O III]/Hβ or [N II]/Hα with the other ratio held fixed, or else a combination of increases in both ratios. Many other examples of systematic line-ratio differences between local and high-redshift galaxies are presented in papers from KBSS-MOSFIRE (e.g. Steidel et al., 2016; Strom et al., 2017), the MOSFIRE Deep Evolution Field (MOSDEF;

e.g. Shapley et al. 2015; Sanders et al. 2016) and the FMOS-COSMOS survey (e.g. Kashino et al., 2016). There is still no unanimously agreed explanation for the line-ratio offsets, although it appears plausible that a combination of higher ionisation parameters, electron densities and harder ionising spectra are ubiquitous throughout the high-redshift samples[11] (e.g. Cullen et al., 2016). The location of high-redshift galaxies in line-ratio diagrams has recently motivated recalibration of empirical strong-line abundance indicators using stacks of extreme 'local analogue' galaxies from SDSS (e.g. Curti et al., 2017; Bian et al., 2018) which may be more applicable to high-redshift sources. Theoretical strong-line methods can also be adjusted to operate with more extreme ISM conditions (e.g. Dopita et al., 2016), however since the exact ISM changes responsible for the observed offsets aren't fully understood, there are degeneracies between the sets of input parameters which can describe the data (e.g. Bian et al., 2018).

In recent years there has been increased focus on using IFS measurements to study possible metallicity gradients within star-forming galaxies. Such gradients are linked to the history of enrichment and the physical processes which rearrange materials within the galaxies. Some of the earliest work in this field, described by Searle (1971), established that spiral galaxies in the local Universe exhibit *negative*[12] metallicity gradients. This is supported by the measured iron abundance gradient in the Milky Way of -0.06 dex kpc^{-1} (e.g. Friel et al., 2002; Cheng et al., 2012), and suggests an 'inside-out' formation picture whereby gas collected at the galaxy centre, formed stars and became enriched much quicker than in the outskirts. Following this picture, it is expected that star-forming galaxies should have steeper metallicity gradients at higher redshift which flatten over time (e.g. Maciel et al., 2003; Marcon-Uchida et al., 2010).

As summarised in Fig. 1.26, taken from Wuyts et al. (2016a), this is not at all the unanimously observed picture in high-redshift studies of metallicity gradients. The

[11] the possibility of a variation of the N/O ratio at fixed metallicity has also been proposed as a partial explanation for the line-ratio offsets (e.g. Masters et al., 2014; Shapley et al., 2015; Sanders et al., 2016; Masters et al., 2016).

[12] i.e. the central regions of the galaxy are more metal rich than the outskirts

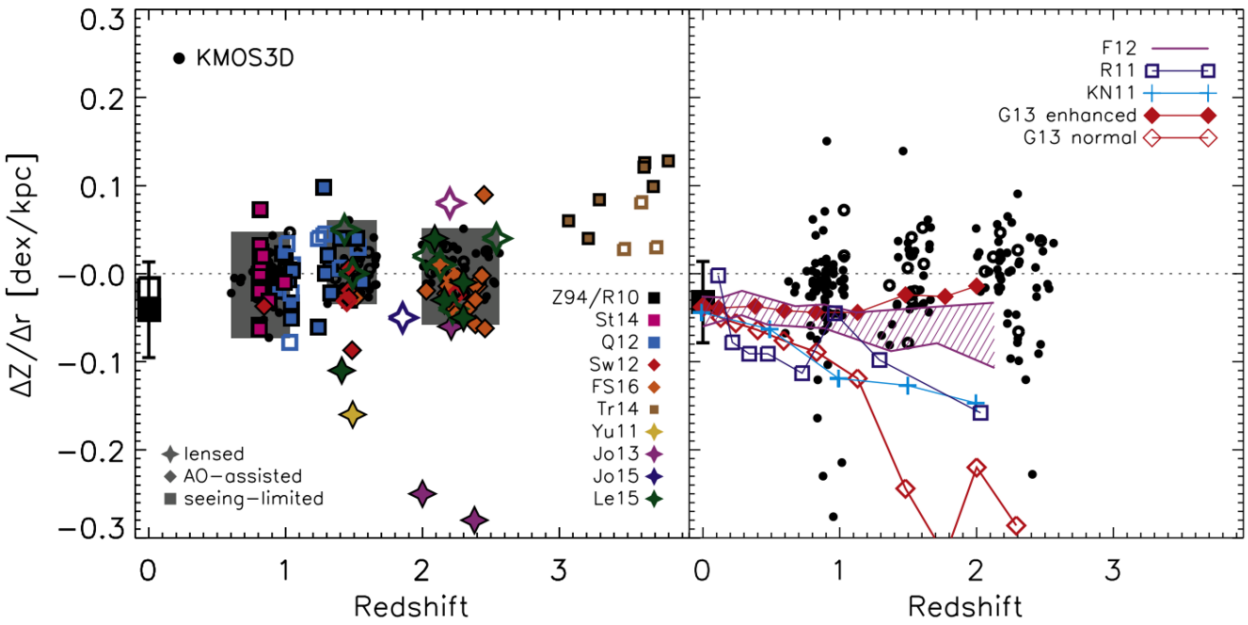

Figure 1.26: *Left:* A compilation of metallicity gradients observed in the literature, from a combination of strongly lensed and unlensed, AO-assisted and seeing-limited observations from Wuyts et al. (2016a). No general high-redshift trend emerges, with flat, positive and negative gradients observed across the range of angular resolutions at $z > 1$. *Right:* Metallicity gradients from numerical simulations, generically predicting more-negative gradients at higher redshift, which are flattened by the effects of feedback.

left panel of this figure shows a compilation of observed metallicity gradients (e.g. Cresci et al., 2010; Yuan et al., 2011; Swinbank et al., 2012a; Queyrel et al., 2012; Jones et al., 2013; Stott et al., 2014; Troncoso et al., 2014; Sanchez et al., 2014; Leethochawalit et al., 2016; Wuyts et al., 2016a), including both gravitationally lensed (e.g. Yuan et al., 2011; Jones et al., 2013; Leethochawalit et al., 2016) and AO-assisted measurements (e.g. Swinbank et al., 2012a). No clear picture emerges from these observations, as, at $z > 1$, flat, positive and negative gradients are observed across the range of angular resolutions. It is worth noting that these measurements are still extremely challenging, as they require detection of several of the rest-optical emission lines, which can be intrinsically faint, and are subject to the degrading effects of beam smearing discussed throughout § 1.5.2. Determining abundance gradients also requires strong-line calibration methods, which, as discussed above, are far from bulletproof. Conversely, the simulation results reported in the right panel of Fig. 1.26 all predict negative gradients which steepen with increasing redshift in the absence of feedback (e.g. Gibson et al., 2013). The impact of feedback is to redistribute energy and material

from the galaxy centres, thus flattening the observed abundance gradients. Another method by which gradients can be flattened are major and minor galaxy interactions (e.g. Rupke et al., 2010b,a), which violently rearrange material and are more prevalent towards earlier times (e.g. Lotz et al., 2008).

The current picture painted by the literature with regards to spatially-resolved emission-line ratios and abundance gradients at high redshift is far from definitive. In Chapter 5 we present first results from the KLEVER survey, which is an ESO large programme aiming to obtain spatially-resolved rest-optical emission-line measurements across multiple wavebands with KMOS. Along with other ongoing campaigns, this survey aims to answer open questions such as:

- What determines the systematic offsets or extremity of observed line ratios at high redshift?
- Are local empirical and theoretical abundance calibrations applicable at high redshift, even if they are calculated using 'local analogue' galaxies?
- What determines the observed diversity, and predominant flatness, of observed high-redshift metallicity gradients?
- To what extent do other line ratios, such as [O III]/[O II] vary across the spatial extent of high-redshift galaxies?

1.6 Thesis overview

The goal of this thesis is to use integral-field spectroscopy to place observational constraints on the dynamics and dynamical evolution, as well as the spatially resolved ISM conditions and chemical evolution of high-redshift star-forming galaxies. This is achieved by analysing data collected with the K-band Multi-Object Spectrograph, processed using a custom data-reduction pipeline which builds upon the standard reduction recipes supplied by ESO. A crucial component of the work is the extraction

of information from low signal-to-noise ionised gas emission lines, and so the analysis techniques adopted in this thesis focus on automating this task to run on samples of reduced datacubes. A summary of the contents of each chapter is provided below.

- **Chapter 2:** The custom KMOS data reduction pipeline is described, focussing on important additions to the standard ESO recipes which include readout channel bias correction, PSF star monitoring and sky-subtraction improvements

- **Chapter 3:** The dynamical analysis of the largest sample of $z \sim 3.5$ star-forming galaxies observed with integral-field spectroscopy, (The KMOS Deep Survey), is described. From an initial sample of 63 star-forming galaxies detected in [O III]λ5007 emission, an isolated and resolved sample of 33 galaxies is defined and analysed using a combined morpho-kinematic approach. In particular, we construct and fit galaxy disk models to kinematic maps determined from the data, in order to extract measures of the intrinsic rotation velocities, V_C and velocity dispersions, σ_{int} of the galaxies. This work approximately doubles the number of galaxies in this redshift regime with measured V_C and σ_{int} and explores the trends in these kinematic properties with cosmic time.

- **Chapter 4:** Building from the $z \sim 3.5$ kinematic measurements of the previous chapter, a detailed investigation of the evolution of the stellar mass Tully-Fisher relation is carried out. This project was motivated by the plethora of inconsistent literature results regarding this evolution. It is shown explicitly, using a sample of 20 literature comparison samples spanning $0 < z < 3.5$, that the inferred normalisation of the stellar mass Tully-Fisher relation is goverened by sample selection criteria, as traced by V_C/σ_{int}. This reconciles discrepant literature results and highlights the importance of accounting for the sample kinematic properties when intercomparing results. The increasing importance of σ_{int} in the dynamical mass budget of high-redshift galaxies is also discussed.

- **Chapter 5:** The KMOS LEnsed galaxies Velocity and Emission line Review (KLEVER) survey is a new ESO large programme which will collect resolved measurements of a complete set of strong, rest-optical emission lines for large

samples of both lensed and unlensed galaxies at $z \simeq 1.5$ and $z \simeq 2.3$. Equipped with this data, it will be possible to study the spatially-resolved dust properties, ISM conditions and metallicity gradients of high-redshift star-forming galaxies spanning a wide range in physical properties. Preliminary analysis of 4 KMOS pointings targetting unlensed galaxies is described, and evidence for negative Balmer decrement gradients and negative metallicity gradients across the majority of the sample is presented.

Chapter 2

KMOS Data reduction

Abstract

When carrying out spectroscopy, the photons from distant galaxies which reach our telescopes are dispersed and recorded as counts on the pixels of the detector. In order to make use of this data for scientific analysis, a series of calibration steps must first be applied to recover a measure of the object flux on each detector pixel as a function of wavelength. This process is referred to as 'data reduction', and the series of automated steps leading between the raw and reduced data as the 'data reduction pipeline'. This chapter describes the steps applied to convert KMOS detector data into science-ready datacubes, focussing on additional processing steps beyond the standard ESO data reduction recipes, implemented to improve the quality of the final products. Specifically, these additional steps deal with detector readout channel bias, the shifting and stacking of individual exposures with the aid of PSF stars and improved skyline subtraction with principal component analysis.

2.1 General spectroscopic data reduction

There is a common set of reduction processes which must be applied to raw spectroscopic detector data in preparation for scientific analysis. The following subsections describe these general steps, before focussing on the specific example of KMOS spectroscopic data reduction in § 2.2. The purpose of these steps is to reduce noise in the science exposures and to both wavelength and flux calibrate the data. This requires that dedicated calibration exposures are collected, as overheads to the science exposures, and processed as part of the reduction pipeline.

2.1.1 Dark subtraction

One of the sets of calibration exposures required are *dark frames*, which are exposures of the optics of the system when it is not illuminated by any source of light. The purpose of these exposures is twofold: 1) To identify and mask 'hot' detector pixels with unphysically large count values; 2) to subtract thermal electrons produced in the instrument (i.e. counts which are not of astrophysical origin). In the case of spectroscopic data, the magnitude of the thermal electron signature is a strong function of wavelength, particularly when working in the *K*-band.

2.1.2 Flatfielding

The process of flatfielding accounts for differences in pixel sensitivity across the detector. Again, this requires dedicated calibration exposures, in this case of a uniform light source. These exposures are used to produce a map of the normalised brightness across the detector, which can in turn be used to correct the science exposures so that the esponse is uniform at all locations.

2.1.3 Wavelength Calibration

The raw data on the detector are initially arranged in pixel coordinates. In order to convert these into wavelength units, it is necessary to use observations of a reference source which has emission features at precisely known wavelength values. The passage of the light through the optics of the system places these features on specific pixels, and by associating these pixels with the known wavelength values, a wavelength solution for the entire detector is obtained. This process is known as wavelength calibration. The reference observations are stored in static-calibration files and applied automatically using wavelength calibration software specific to the spectrograph being used.

2.1.4 Flux Calibration

The photons which arrive at the detector generate free electrons. These create a charge, which is recorded when the device is read-out, providing a digital record of the light arriving at the device. However, what we are interested in is a measure of the incident *flux*, rather than a digital record of the electron counts on each of the CCD pixels. Analogous to the wavelength calibration step, we need reference observations of stars with precisely known magnitudes to inform us how to convert between counts on the detector and flux units. These are referred to as standard-star observations. An additional complication here is that we can observe astronomical objects at different airmasses, with objects closer to the zenith suffering less attenuation than those at higher airmass, approaching the horizon. Consequently, the standard stars must be observed at a similar time and airmass to the object observations, so that the conversion between counts and flux is accurate. A *telluric spectrum* is also produced, which records the response of the detector to light of different wavelengths, allowing for one to correct for the drop in sensitivity towards the edges of the filter and for any prominent atmospheric absorption features across the chosen waveband.

2.2 The KMOS specific data-reduction pipeline

The sequence of steps mentioned in the previous section are necessary components when preparing the raw data collected by any spectrograph for scientific analysis. The following subsections describe the specific set of procedures followed to reduce the data collected by KMOS.

2.2.1 Constructing datacubes from individual exposures

As mentioned in § 1.4.4, KMOS is comprised of 3 independent spectrograph/detector modules. The light from 8 IFUs is dispersed onto each 2k×2k Hawaii-2RG HgCdTe detector, as shown for a single detector in Fig. 2.1. This figure shows a raw detector image from a 300 second KMOS exposure, indicating the width of a single IFU channel on the detector and with two blank columns due to inactive IFUs. The exposure is dominated by sky emission, which is several orders of magnitude brighter than the emission from the faint galaxies targetted in the center of the IFUs. It is also clear from this image that lines of constant wavelength are curved, an effect which is caused by the reflection angles and path-length differences travelled by photons of constant wavelength approaching different regions of the detector. This curvature is corrected throughout the reduction. The following sections briefly describe the processes by which individual exposures, such as those in Fig. 2.1, are calibrated, converted into three-dimensional datacubes and stacked together to produce the final datacubes used during the analysis. These processes require calibration exposures which are taken both during the night-time observations (i.e. standard-star frames) and in the day following the observations (i.e. the static-calibration files). As indicated in the sections below, the backbone of the reduction pipeline used in this thesis is comprised of recipes created for the ESO Common Pipeline Library, accessed and executed using the ESO Recipe Execution Tool (EsoRex).

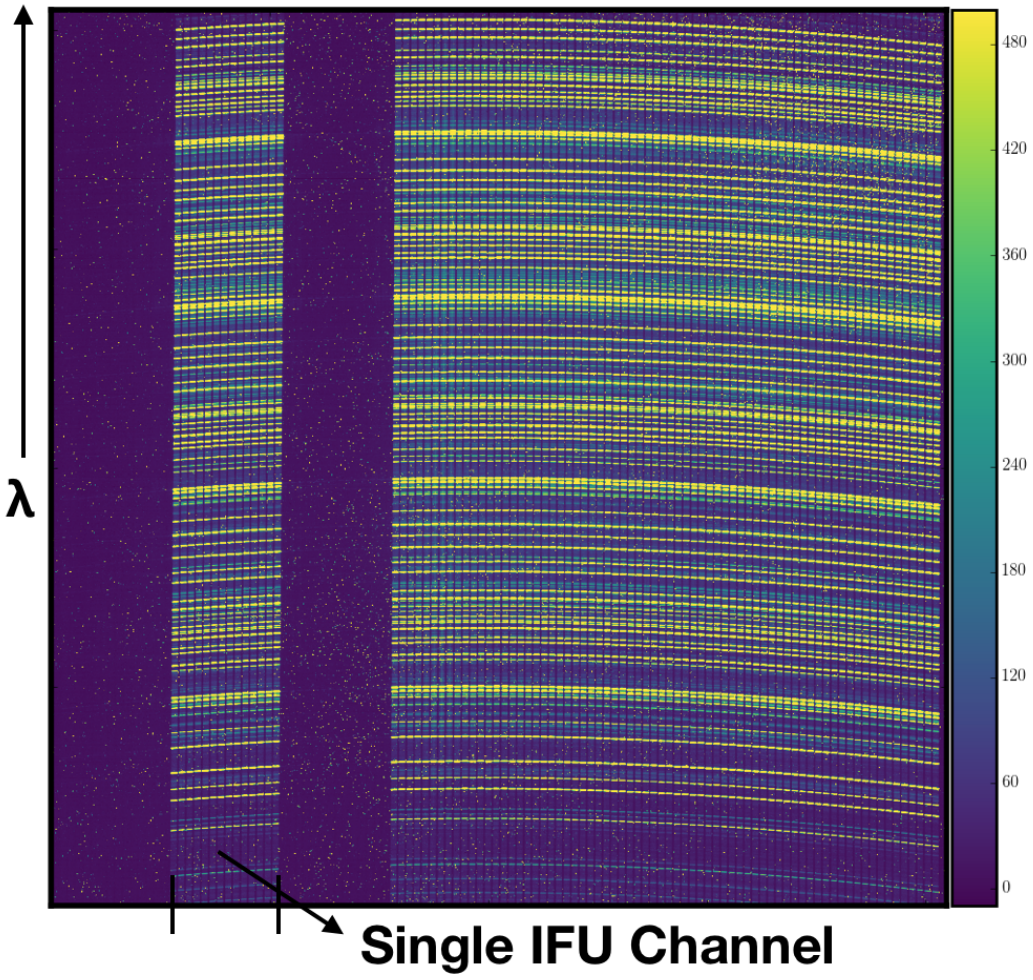

Figure 2.1: An example of raw detector data from an exposure using the KMOS *H*-band filter and grating. The instrumental setup comprises 3 such detectors, with the light from 8 IFUs dispersed into horizontal channels on each detector as shown. It is apparent from the OH skylines (which dominate the raw detector images) that slices of constant wavelength are curved (see text for discussion). The first and third IFUs were inactive during this exposure, causing the blank columns which are punctuated by bright 'hot' pixels (see Fig. 2.2).

Dark frames and bad pixel map growth

As mentioned in the previous section, the dual function of the dark exposures is to identify fixed-pattern noise across each of the three detectors and to subtract the counts generated by thermal electrons in the KMOS instrument. The fixed-pattern noise is usually in the form of 'hot' pixels which record unphysically large counts due to electrical charges leaking into the pixels (i.e. the count values are not associated with any astrophysical source). If these are not dealt with properly by masking, these counts

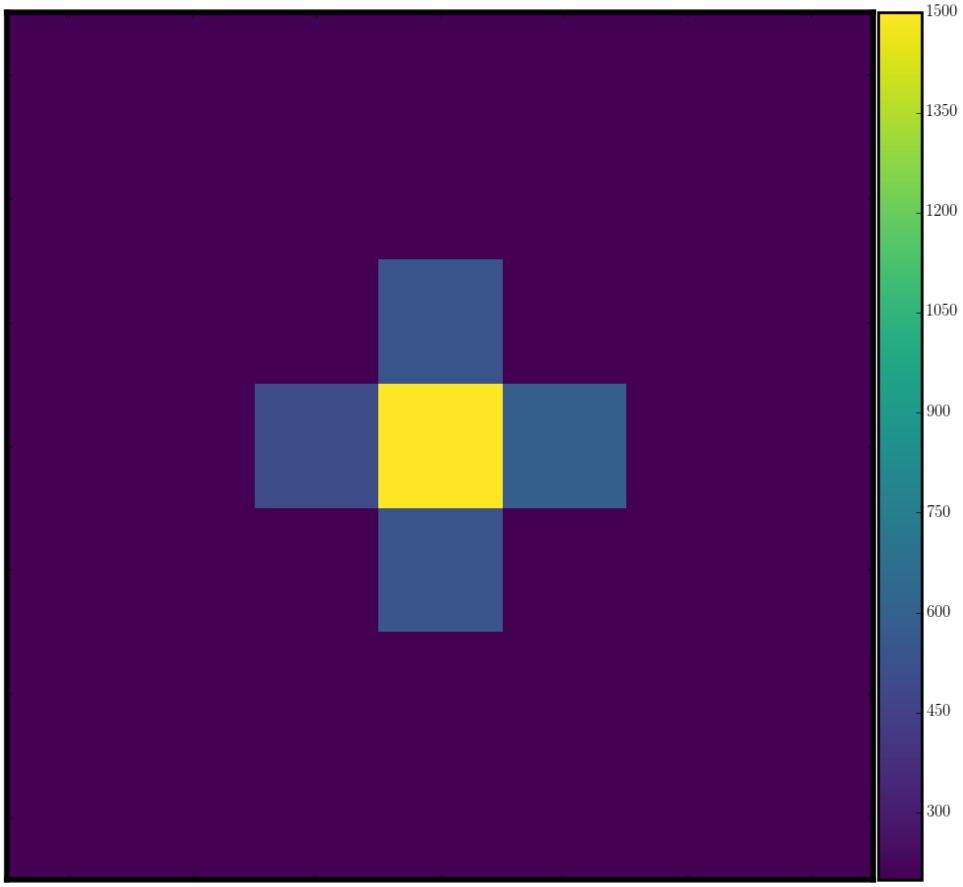

Figure 2.2: The prominent central hot pixel has a count value of $\sim 2 \times 10^5$. The fluxes in the neighbouring pixels scale with this value and are several orders of magnitude lower, but still much higher than the background level. Given that this shape is often not identified by the `kmos_dark` recipe, we grow the bad pixel map using a cross-shaped pattern, as described in the text.

will be propagated through into the final datacubes. The EsoRex `kmos_dark` recipe combines the dark frames into a master exposure, from which offending pixels are identified and recorded in the output files as a bad pixel map.

Upon inspection of the raw data, we find that the prominent hot pixels 'leak' counts into their neighbours to leave behind the cross-shaped pattern shown in Fig. 2.2. This shape is often not reflected in the mask output from the `kmos_dark` recipe, and so we 'grow' the bad pixel map by adding a cross-shaped region around each identified hot pixel. The resultant bad pixel map is propagated through each subsequent recipe.

Flatfielding and illumination correction

Flatfield exposures of a light source are taken the day after each set of observations in the correct waveband and these are processed using the EsoRex `kmos_flat` recipe. The output of this is the master flatfield frame, containing the sensitivity correction factor for each pixel and for each detector (and at 6 different rotator angles[1]). This flatfield frame is applied during the science reduction. The `kmos_flat` recipe also outputs the x and y positions of each illuminated pixel from the centre of each IFU in milliarcseconds. This information is required to reconstruct the spatial components of the datacubes. It is recommended to also apply an illumination correction on top of the sensitivity correction, to account for the fact that the detector is not equally illuminated by the lightsource during the flatfield exposures. This illumination correction is produced using dedicated flatfield exposures of the sky, processed using the EsoRex `kmos_illumination` recipe.

Wavelength calibration

The raw detector image contains a measure of the flux value at each pixel number in the y-direction. The process of converting these numbers into wavelengths is called wavelength calibration. Exposures of arclamps, usually filled with an inert gas (neon and argon in this case), exhibit strong emission at wavelength values known to high precision. These are collected the day following a sequence of observations, and the positions of the known emission lines on the detectors can then be used for wavelength calibration of the observations. This is carried out in practice with the `kmos_wave_cal` routine and produces an output file containing the wavelength in microns for every illuminated pixel across the 3 detectors at 6 different rotator angles.

[1]Both the telescope and the KMOS instrument are rotated to track the target field of view over the course of each night. The instrument rotator angle dictates the precise mapping between both spatial and spectral pixels on the detector and the path of light through the optics of the instrument. Consequently, it is necessary to record calibration exposures at 6 different rotator angles (i.e. at 60 degree intervals between 0 and 300 degrees) and choose the calibration closest to actual rotation angle to process the observations.

Flux calibration

Standard stars of known magnitude are observed at roughly the same time and position as the target observations. This is to ensure that the standard star, and hence the telluric spectrum of atmospheric contamination which varies both temporally and spatially, is observed through similar airmass as the targets. The standard-star observations are used to calibrate the conversion between detector counts and the common flux density units $\mathrm{ergs}^{-1}\mathrm{cm}^{-2}\mu\mathrm{m}^{-1}$. The recipe `kmos_std_star` returns the telluric spectrum[2] and a measure of the magnitude zeropoint for each IFU. The datacube spectra are then calibrated using the standard formula

$$F_\lambda = \mathrm{ctss}^{-1} \times F_0 \times 10^{-0.4 \times ZP} \tag{2.1}$$

where ctss^{-1} are the counts per second recorded by the detector and ZP is the zeropoint returned from `kmos_std_star`. This flux calibration step can either be carried out automatically by the pipeline during the execution of the recipe, or performed in post-processing of the reduced datacubes using the zeropoint parameters.

Correcting for differential readout channel bias

Counts are assigned to the pixels on the KMOS detectors by reading out the charge values in columns which are 64 pixels wide, called the readout channels. Each readout channel has an independent amplifier, and so the way in which charge is converted to counts can vary between channels. This leads to differences in the median count value as a function of channel number across the detector. This can be seen in object-minus-sky exposures as the appearance of vertical stripes, corresponding to different count baselines, in adjacent readout channels. This is shown in the left panel of Fig. 2.3 and if left uncorrected will lead to flux bandings across the reduced datacubes. Also apparent at the base (short wavelength) end of the detector in the left panel is a brighter region

[2]This is a measure of the shape of the atmospheric absorption profile, recorded as a one-dimensional spectrum. The final spectra must be divided by this to recover the object flux.

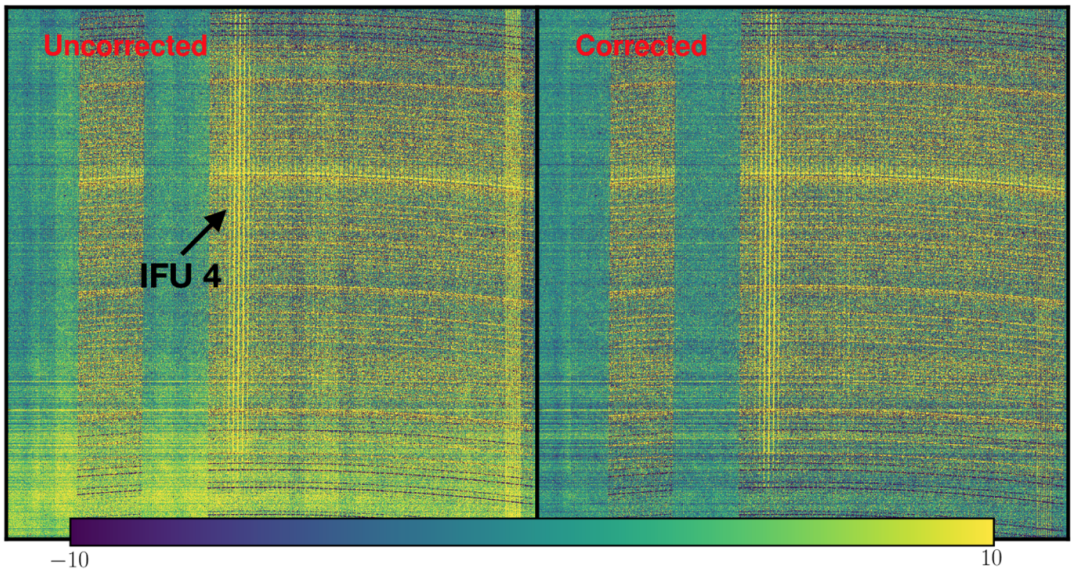

Figure 2.3: *Left:* The uncorrected object-minus-sky detector image is shown, with both the control star in IFU 4 and skyline-subtraction residuals clearly visible. The darker vertical stripes correspond to the 64 pixel-wide readout channels. The readout process determines the median count value in each column, the value of which varies across the detector. The long wavelength end of the detector sits at a higher flux baseline due to wavelength-dependent differences in the throughput of the object and sky exposures. These effects must both be corrected in order to remove flux bandings across the spatial extent and 'wave' like patterns across the spectral extent of the reconstructed datacubes. *Right:* The same exposure, corrected following the procedure described in the text. The uniform baseline is close to zero, as demonstrated in Fig. 2.4.

at a different flux baseline. This is caused by wavelength-dependent differences in the throughput of the object and sky exposures, and appears in the final spectra as 'wave' like patterns in the flux baseline.

To correct for both these effects, the non-illuminated pixels in both the object and sky exposures on each detector are identified using the wavelength calibration frame and used as the flux-baseline reference. Specifically, each detector is divided into vertical channels of 64 pixel width and horizontal channels of 128 pixel width. Within each of these segments, the median difference between the sky and object fluxes in the reference pixels is computed. This value is added to the object exposures, so that the median difference between the sky and object exposures (caused by systematic differences in readout and throughout) in each segment is close to 0. The updated object detector values are then stored in a separate file and used throughout the remainder of the reduction, providing a consistent flux baseline across the datacube.

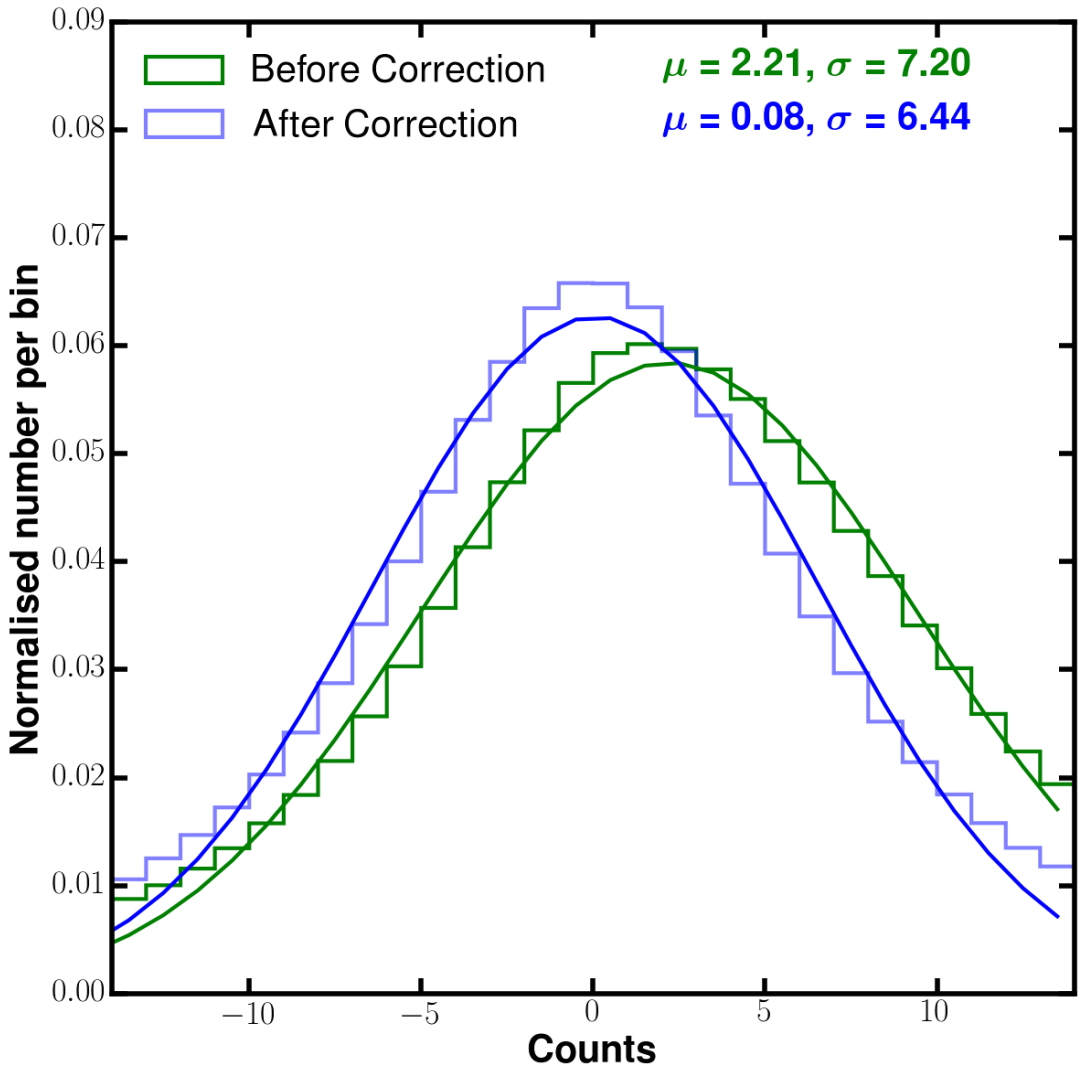

Figure 2.4: Flux histograms across the full detector image before (green) and after (blue) correction using the reference pixel method described in the text. The correction shifts the mean value close to zero and narrows the distribution about the mean.

The impact of this correction is further highlighted in Fig. 2.4, which shows the histograms of flux values across the full detector in the object-minus-sky frame generated from an example pair of exposures (representative of the typical case). The green histogram shows the flux values before correction, which are not centred around zero. The application of the correction shifts the mean value close to zero and narrows the distribution, resulting in a constant flux baseline in the sky-subtracted object exposure. A variant of this procedure is available in the EsoRex recipe `kmos_sci_red`, referred to as an 'overscan correction'. However, this method only tackles the readout column issue and does not account for a varying flux baseline across the detector.

Following regular communication with the KMOS pipeline expert at ESO, a procedure based upon that described in this subsection will be implemented in the pipeline in a future release.

Sky subtraction and cube reconstruction

Sky subtraction has already been mentioned in the previous section, and is a necessary step to remove all signals not related to the target objects. The Observing Blocks (OBs) typically contain exposures of blank patches of sky which are nodded to periodically and observed for the same length of time as the object exposures. A standard observation pattern is 'O-S-O', where the central sky frame is used to correct both the preceding and following object frames. The positions of the individual KMOS arms whilst in the 'O' and 'S' configurations are set using ESO's KMOS Arm Allocator (KARMA) tool, which also deals with selection of the telescope guide star and the initial acquisition of object positions across the field of view. Of particular importance during the sky-subtraction process is the removal of the OH skylines discussed throughout § 1.4.5. Because of the temporal and spatial variability of these features, it is necessary to pair together sky and object frames which are both close on the sky and in time. This also limits the exposure time for individual frames if reasonable OH subtraction is to be achieved; throughout this work we make use of a default exposure time of 300 seconds.

An additional complication comes in the form of 'spectral flexure'. As the telescope tracks the object across the sky, the rotator angle changes, shifting the position of the heavy KMOS instrument over the course of an OB. This results in small shifts of features in both the spatial and spectral direction on the detector. As a result, the OH emission lines can become spectrally misaligned in object-sky pair detector images, leaving large P-Cygni shaped residuals following sky subtraction. An example of this effect is shown in Fig. 2.5, where the dark and light stripes across the sky-subtracted image at constant wavelength indicate a transition between over and under-subtraction of the OH features. It is clear that the severity of this effect increases as the object position moves close to zenith, forcing the telescope to rotate faster to track.

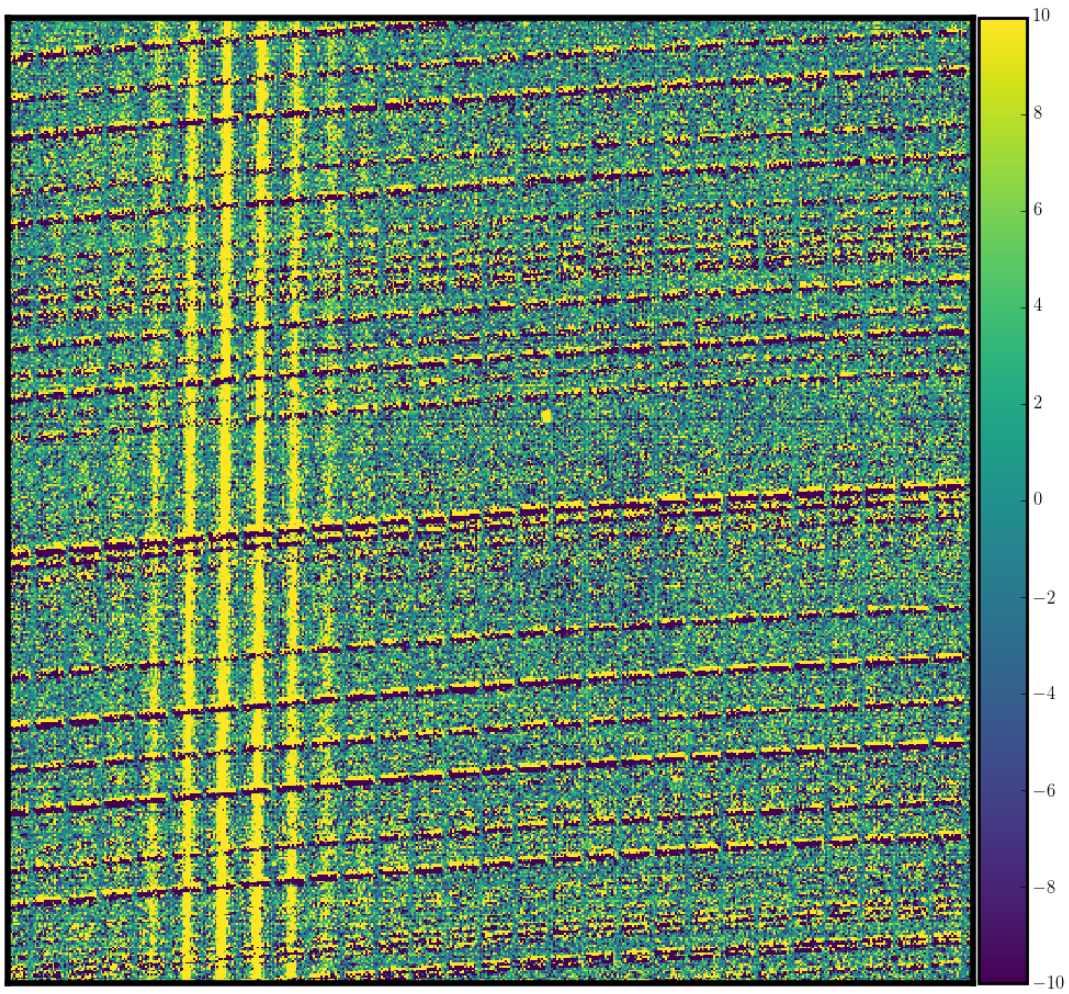

Figure 2.5: Spectral flexure causes slight misalignment in the physical positioning of fixed-wavelength OH features on the detector. Consequently, a direct object-minus-sky frame can exhibit P-Cygni shaped profiles due to the over and under-subtraction of misaligned OH emission. This is apparent in this object-minus-sky detector image as the vertically adjacent bright and dark stripes across the slitlets located at the wavelengths of OH features. To the left of the image, the emission from one of the control stars tracked in the observation is visible.

Sky subtraction is performed automatically during the `kmos_sci_red` recipe, which also reconstructs a datacube for each IFU from the information produced during the recipes described previously, with the option to interpolate to a finer pixel scale (see § 2.2.2). The 'skytweak' (Davies, 2007) option included in this recipe is used to

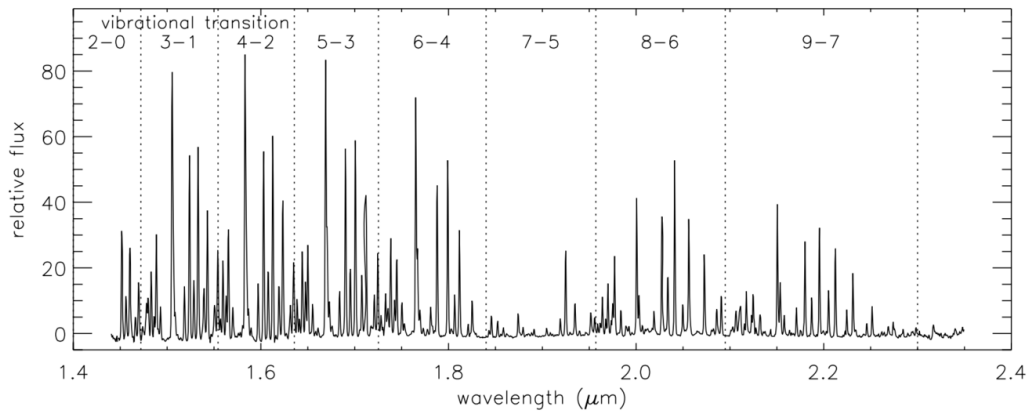

Figure 2.6: The spectrum of emission lines from the OH molecule across the *H* and *K*-bands is shown. Fortuitously, 'families' of emission lines, which tend to scale in amplitude together due to each family arising from transitions between specific vibrational energy levels, fall within well-defined wavelength intervals. This is one of the key principles of the skytweak method from Davies (2007), described in the text. The figure is taken from Davies (2007).

enhance the sky-subtraction performance as follows. The spectrum in each spaxel of the reconstructed sky frame of an object-sky pair is divided into segments which contain 'families' of OH emission lines resulting from a particular vibrational energy transition (see Fig. 2.6). A different constant scaling factor is applied to each vibrational energy transition family in order to recover an amplitude which best matches the object frame OH emission lines. To account for the spectral flexure described in this subsection, shifts are applied to the wavelengths of the OH emission lines in the sky frames, which can optionally include stretching of the wavelength solution.

Overall this procedure of shifting and scaling dramatically improves the sky-subtraction residuals over a crude sky subtraction. However, there are some cases where the residuals are still unacceptably large, particularly for observations which have required telescope tracking close to the zenith. An additional layer of sky-subtraction residual processing is carried out to tackle this issue. This makes use of the Zurich Atmosphere Purge (ZAP) software described in Soto et al. (2016), to perform principal component analysis on the post-skytweak residual spectra within the datacubes. The purpose of this software is to construct a set of eigenspectra which describe the skyline residual features, but do not contain contributions from the target objects. The first step is to filter the data

by either masking wavelength regions which contain emission from the target object or by subtracting a weighted spectrum which preserves the narrow sky residual lines but removes object signals. After this filtering step, the algorithm segments the spectra in each spaxel into wavelength regions corresponding to the OH vibrational transition families, due to the coherence of residual features in these regions reducing the number of eigenspectra required to adequately describe the residual patterns. Singular value decomposition is then performed on the $n \times m$[3] matrix from each wavelength segment to identify the eigenspectra which fully describe the input cube.

For every spaxel, the number of eigenspectra required to describe the residual pattern is optimised and the subsequent residual spectra are subtracted from the datacube. Fig. 2.7 demonstrates the application of this procedure for a region of the *H*-band, using a stacked cube with initially poor skytweak subtraction within the individual frames. The panels show the summed spectrum from spaxels falling with a 0.6 arcsecond diameter aperture of a $z \sim 3.5$ galaxy, so that the [O II]λ3727,λ3729 doublet is shifted into the *H*-band. The top panel has not had the ZAP algorithm applied and shows strong sky-subtraction residuals, which would be problematic when attempting to automatically fit the [O II]λ3727,λ3729 doublet. The bottom panel shows the output after applying ZAP to the individual frames in the stack, markedly improving the residual features with no impact to the emission line. The results presented in Fig. 2.7 make use of a KMOS specific version of the ZAP software, kindly provided by Trevor Mendel[4] (*private communication*).

In summary, the set of reduction steps described in this section result in flux calibrated and sky-subtracted datacubes for every frame and for every KMOS IFU. The pipeline to this stage is automated and runs on a set file structure containing the OB raw data and the associated calibration files. So far, results making use of parts of this pipeline have been published in Patrick et al. (2017); Turner et al. (2018, 2017); Girard et al.

[3] n here corresponds to the number of spatial pixels across the face of the datacube, and m to the number of pixels in the wavelength segment

[4] Dr. J. Trevor Mendel, trevor.mendel@anu.edu.au, ASTRO-3D Research Fellow, ANU College of Science

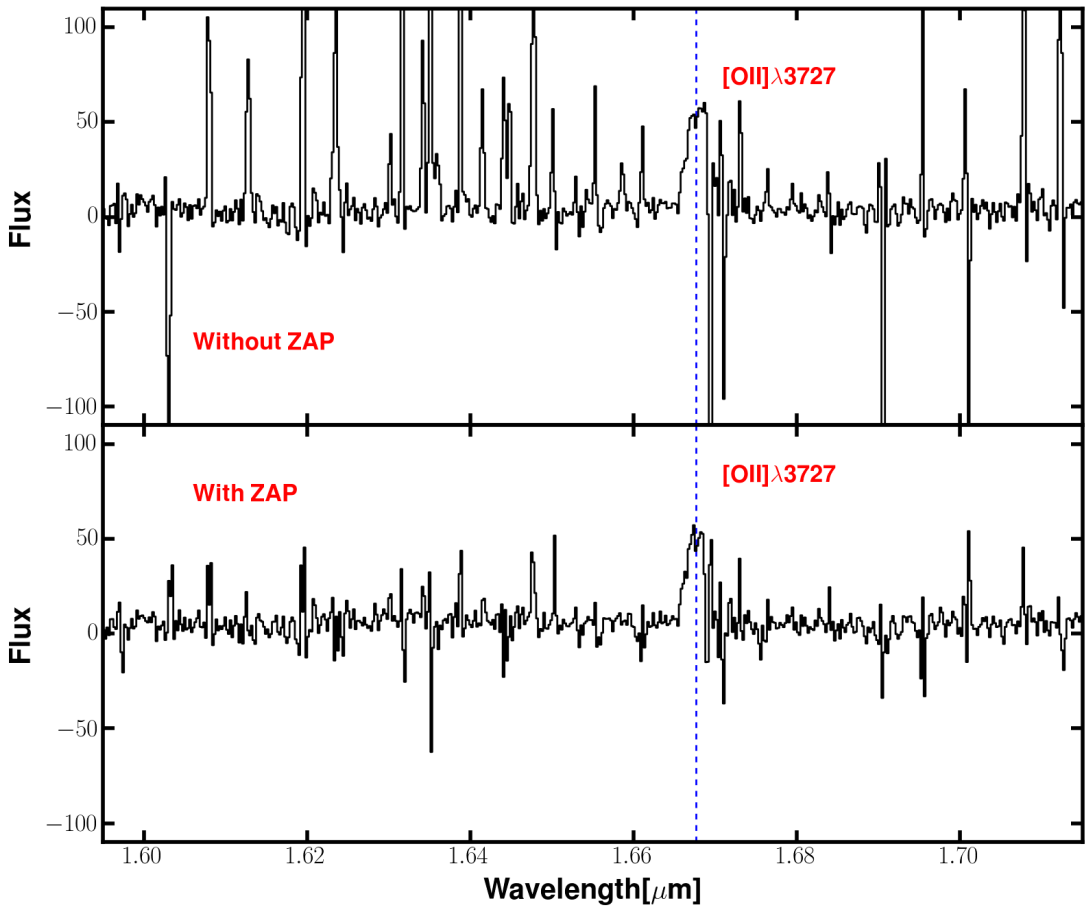

Figure 2.7: *Top:* The summed *H*-band spectrum across a 0.6 arcsecond diameter aperture for a $z \sim 3.5$ galaxy, with the [O II]λ3727,λ3729 doublet visible. In this panel, skytweak has been applied but the ZAP procedure has not, and several strong residual features, including those immediately longwards of the [O II]λ3727,λ3729 doublet are apparent. *Bottom:* The same galaxy as the top panel, with ZAP applied after skytweak. This is a clear improvement in the residual features and the object signal has been preserved.

(2018) and two further submitted papers, as well as the results presented in Chapter 5 of this thesis. The following subsection describes the process by which these cubes are stacked to produce the final cubes for each target galaxy.

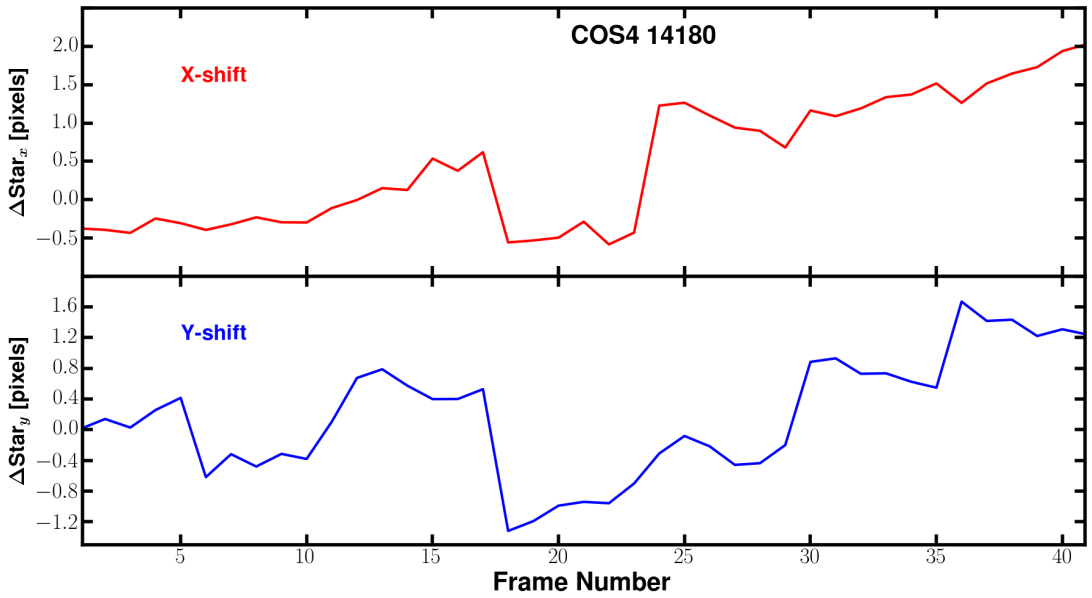

Figure 2.8: The evolution of the drift of the telescope away from the prescribed dither pattern in both the x and y directions is shown. The units of the y-axes are in pixels, with 1 pixel equal to a shift of 0.1″. The drifts are caused by flexure of the instrument as the telescope moves, shifting the objects increasingly far away from where they are supposed to be within the IFUs.

2.2.2 Stacking datacubes

Monitoring sky-subtraction and PSF evolution

As part of the preparation of OBs, a dither pattern is specified so that each object is moved around the field of view within the IFUs. This avoids the same spatial and spectral regions always falling on hot pixels of the detector and increases the spatial sampling of the PSF if the dither pattern includes shifts which are smaller than the default 0.2×0.2 arcsecond spaxel size. Therefore, to stack individual exposures together, the frames must be shifted using the dither pattern stored in the header of the files. However, a second consequence of the flexure issue described in the previous section is the tendency of the telescope to drift in both spatial directions away from the prescribed dither pattern over time. To account for this, the spatial positions of 3 control stars (one for each detector) are monitored over the course of every OB.

The issue is summarised in Fig. 2.8, which shows the difference between the $[x, y]$

centre position of one of the control stars and the prescribed dither pattern in the file header (i.e. the drift of the telescope caused by flexure). This figure shows that the drift values typically evolve over the course of an OB, ranging between 0−0.2 arcseconds in both directions, however for certain OBs the discrepancy can become as large as 1 arcsecond, suggesting that monitoring the spatial shifts of individual frames with control stars is extremely beneficial for the final signal-to-noise. The 3 control stars are used to generate a series of shift values which must be applied to the individual frames. This generally requires subpixel interpolation of the flux values onto a common grid, which is performed using the EsoRex `kmos_shift` recipe. Overall, the individual cubes are stacked together with the EsoRex `kmos_combine` recipe using a 3-sigma clipping routine and median stacking to generate the final datacubes.

As part of the control star tracking, the evolution of the PSF over the course of an OB is also monitored, an example of which is shown for good seeing conditions in Fig. 2.9. It is important for a given science objective to know the PSF, as this determines the size of spatial regions which can be considered independent. The PSF information is used to automatically reject frames which exceed a chosen seeing threshold (typically 0.8 arcseconds) and also to inform the convolution scale throughout the dynamical modelling (see § 3.3.2).

Finally, as part of the stacking procedure, the sky-subtraction quality is monitored as a function of frame and IFU. This is done in each IFU by first identifying the wavelength pixels dominated by OH emission using the corresponding reconstructed cube in the dithered sky position. The median of the absolute value[5] of these pixels, in a median-stacked spectrum extracted from the central 1 arcsecond of the datacube, is taken as an indicator of the sky-subtraction performance. Thus, higher values of this metric indicate poorer performance. Fig. 2.10 demonstrates this performance value, in data which has not yet been flux calibrated, as a function of IFU, where the different coloured lines correspond to the frames of the OB. Part of the variation is due to the telescope field of view passing close to the zenith, but there are strong spikes of poor performance

[5]The absolute value is used to account for possible P-Cygni profiles in the spectra

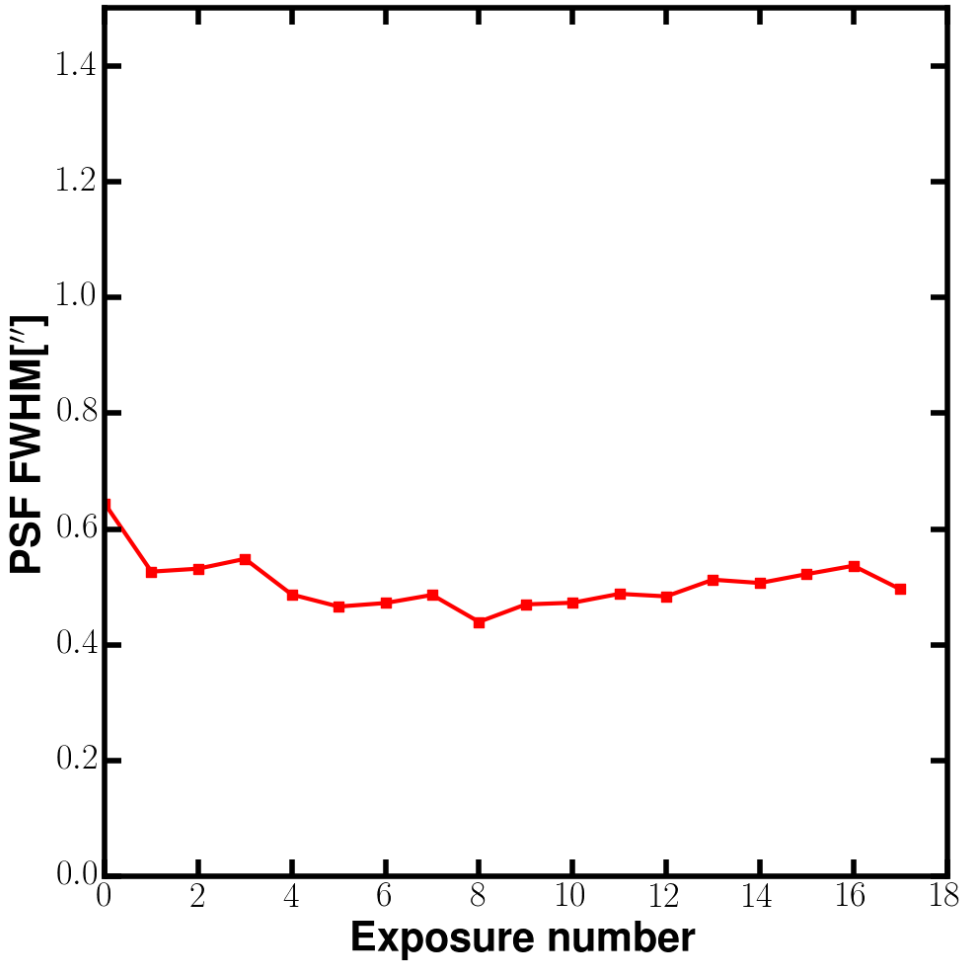

Figure 2.9: The PSF can change substantially over the course of an OB. Frames exceeding a given threshold, nominally 0.8 arcseconds, are automatically rejected from the stacking as they harm the effective spatial resolution of the final cube. In this example the seeing remains at a constant value of approximately 0.5 arcseconds over the OB.

as a function of IFU which are not yet understood. Fig. 2.11 provides another view of the sky-subtraction performance in each IFU as a function of frame, where the top row corresponds to IFUs 1−8, the middle to 9−16 and the bottom to 17−24. By examining the typical sky-subtraction performance values, a threshold can be placed in each IFU to omit particularly poor frames from the final stack.

The shifting of the individual datacubes, as well as PSF and sky-subtraction evaluation, is carried out in a separate script which operates using the output from the initial reduction steps described in § 2.2.1. In this way, there is complete user control over

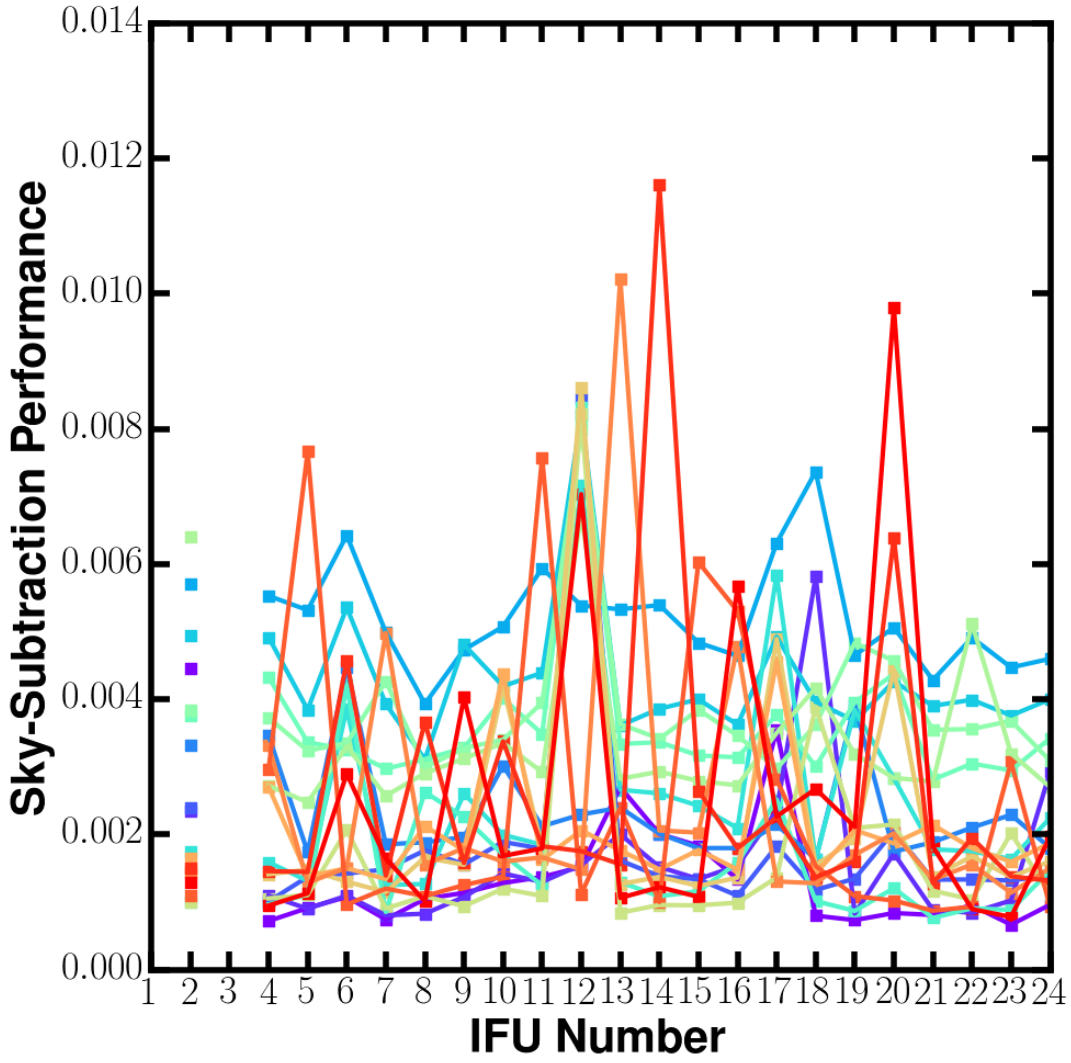

Figure 2.10: The sky-subtraction performance, as described in the text, is shown as a function of IFU number, with the different coloured lines corresponding to the frames in the OB. High values in the y-axis correspond to poorer subtraction of the OH emission lines. There is a clear temporal and IFU-dependent variance in the sky-subtraction quality which is not fully understood.

which frames constitute the final stack for each object. Typical exposure times have ranged between 8−10 hours per object for the data described in Chapter 3, which for 300 second exposures corresponds to about 90−110 individual science frames to be processed and stacked. These integration times are necessary to spatially resolve faint emission lines in distant star-forming galaxies.

Fig. 2.12 presents a schematic overview of the different components of this KMOS data

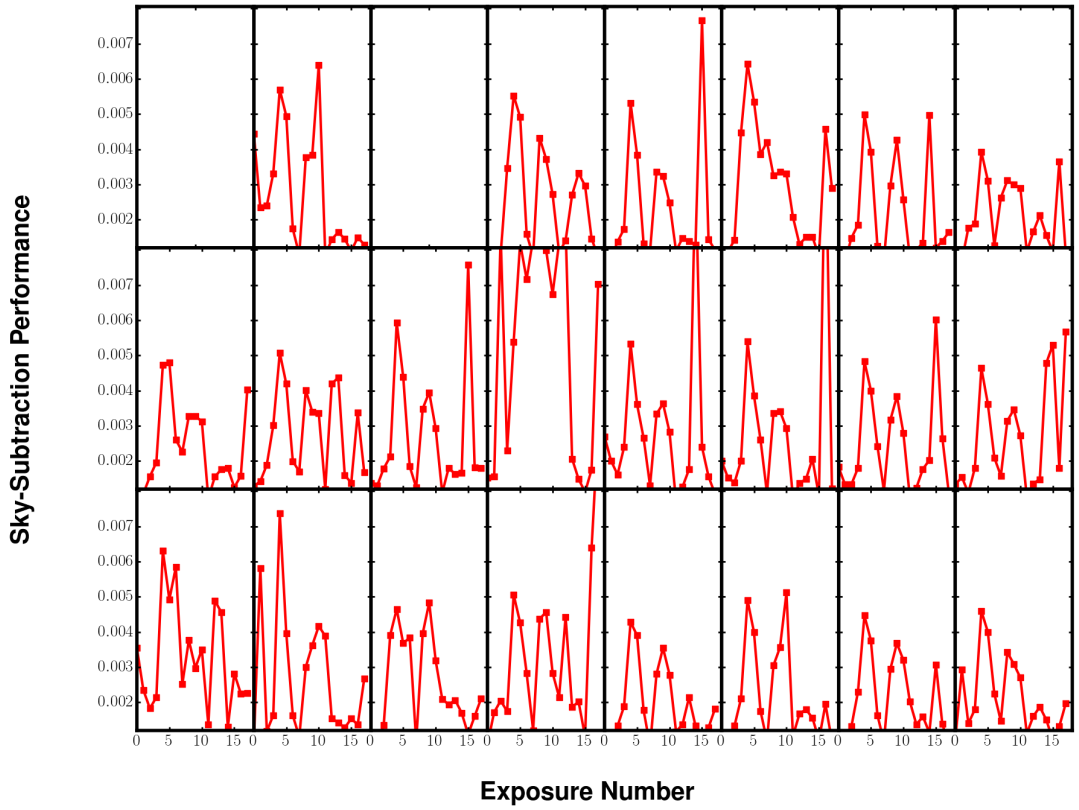

Figure 2.11: The sky-subtraction quality is plotted in each IFU as a function of frame, where the first row corresponds to IFUs 1−8 etc. By examining the typical sky-subtraction quality, a threshold can be placed on the sky-subtraction performance to remove particularly poor frames from the final stack for each object.

reduction pipeline, including the EsoRex recipes in black rectangles and the additional processing steps in red hexagons. The remainder of this thesis involves analysis of datacubes which have been constructed following these procedures.

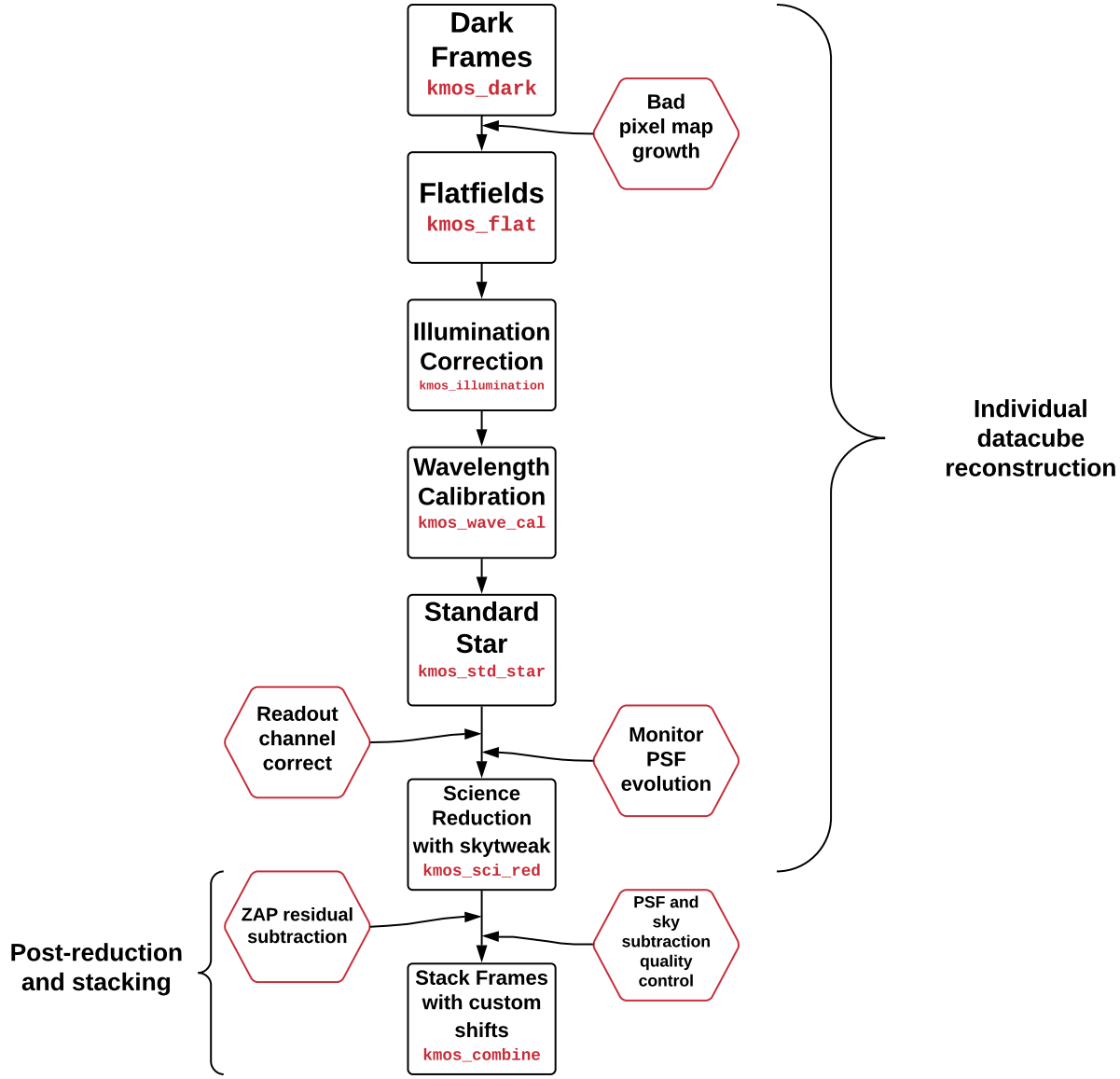

Figure 2.12: The steps of the KMOS reduction pipeline used throughout this thesis are outlined in the chart. The rectangular boxes show the standard reduction stages, with the ESOREX recipes names shown in red. The red hexagonal boxes show the non-standard pipeline additions described in the text, indicating the stage throughout the flow process they are included.

Chapter 3

The KMOS Deep Survey (KDS) I: dynamical measurements of typical star-forming galaxies at $z \simeq 3.5$

Abstract

In this chapter we present dynamical measurements from the KMOS (*K*-band Multi-Object Spectrograph) Deep Survey (KDS), which is comprised of 77 typical star-forming galaxies at $z \simeq 3.5$ in the mass range $9.0 < \log(M_\star/M_\odot) < 10.5$. These measurements constrain the internal dynamics, the intrinsic velocity dispersions ($\sigma_{\rm int}$) and rotation velocities (V_C) of galaxies in the high-redshift Universe. The mean velocity dispersion of the galaxies in our sample is $\sigma_{\rm int} = 70.8^{+3.3}_{-3.1}{\rm km\,s^{-1}}$, revealing that the increasing average $\sigma_{\rm int}$ with increasing redshift, reported for $z \lesssim 2$, continues out to $z \simeq 3.5$. Only $36 \pm 8\%$ of our galaxies are rotation-dominated ($V_C/\sigma_{\rm int} > 1$), with the sample average $V_C/\sigma_{\rm int}$ value much smaller than at lower redshift. After carefully selecting comparable star-forming samples at multiple epochs, we find that the rotation-dominated fraction (RDF) evolves with redshift following the relation RDF $= -0.2\,z + 1$. The rotation-dominated KDS galaxies show no clear offset from the local

rotation velocity-stellar mass (i.e. $V_C - M_\star$) relation, although a smaller fraction of the galaxies are on the relation due to the increase in the dispersion-dominated fraction. These observations are consistent with a simple equilibrium model picture, in which random motions are boosted in high-redshift galaxies by a combination of the increasing gas fractions, accretion efficiency, specific star-formation rate and stellar feedback and which may provide significant pressure support against gravity on the galactic disk scale.

3.1 Introduction

The galaxy population at all redshifts appears to be bimodal in many physical properties (e.g. as described in Dekel & Birnboim, 2006), with a preference for the most massive galaxies to lie on the red sequence, characterised by red optical colours, low star-formation rates (SFRs) and spherical morphologies, and less massive galaxies in the blue sequence, characterised by blue colours, high star-formation rates and disky morphologies. For these blue, star-forming galaxies (SFGs) there is a roughly linear correlation between SFR and stellar mass ($M_\star$) (e.g. Daddi et al., 2007; Noeske et al., 2007b; Elbaz et al., 2007), in the sense that galaxies which have already accumulated a larger stellar population tend to have higher SFRs. This correlation, or 'main-sequence', underpins the 'equilibrium model', in which the SFR of galaxies is regulated by the availability of gas, with outflows and accretion events sustaining the galaxy gas reservoirs in a rough equilibrium as the galaxy evolves (e.g. Davé et al., 2012; Lilly et al., 2013; Saintonge et al., 2013). The main-sequence has been studied comprehensively, using multi-wavelength SFR tracers, between $0 < z < 3$ (e.g. Rodighiero et al., 2011; Karim et al., 2011; Whitaker et al., 2012b; Behroozi et al., 2013; Whitaker et al., 2014; Rodighiero et al., 2014; Speagle et al., 2014; Pannella et al., 2014; Sobral et al., 2014; Sparre et al., 2015; Lee et al., 2015; Schreiber et al., 2015; Renzini & Peng, 2015; Nelson et al., 2016), showing evolution of the relation towards higher SFRs at fixed $M_\star$ with increasing redshift, reflecting the increase of the cosmic Star-Formation Rate Density (SFRD) in this redshift range (e.g. Madau & Dickinson, 2014; Khostovan

et al., 2015). At each redshift slice it has been suggested that galaxies on the main-sequence evolve secularly, regulated by their gas reservoirs, meaning that selecting such populations offers the chance to explore the evolution of the physical properties of typical SFGs across cosmic time. This assumes that high-redshift, main-sequence galaxies are the progenitors of their lower redshift counterparts, which may not be the case (e.g. Gladders et al., 2013; Kelson, 2014; Abramson et al., 2016) and also assumes that we can learn about galaxy evolution (i.e. how individual galaxies develop in physical properties over time) by studying the mean properties of populations at different epochs.

The picture is complicated by the addition of major and minor galaxy mergers which can rapidly change the physical properties of galaxies (e.g. Toomre, 1977; Lotz et al., 2008; Conselice et al., 2011; Conselice, 2014) and the relative importance of in-situ, secular stellar mass growth vs. stellar mass aggregation via mergers is the subject of much work involving both observations and simulations (e.g. Robaina et al., 2009; Kaviraj et al., 2013; Stott et al., 2013a; Lofthouse et al., 2017; Qu et al., 2017). To account for the growing number density of quiescent galaxies from $z \simeq 2.5$ to the present day (e.g. Bell et al., 2004; Faber et al., 2007; Brown et al., 2007; Ilbert et al., 2010; Brammer et al., 2011; Muzzin et al., 2013; Buitrago et al., 2013) there must also be processes which shut-off star-formation within main-sequence galaxies (i.e. quenching) which, to explain observations, must be a function of both mass and environment (Peng et al. 2010; Darvish et al. 2016).

Recent cosmological volume simulations provide subgrid recipes for the complex interplay of baryonic processes which are at work as galaxies evolve, and can track the development of individual galaxies from early stages, to maturity and through quenching (Dubois et al., 2014; Vogelsberger et al., 2014; Schaye et al., 2015). Observations can aid the predictive power of such simulations by providing constraints on the evolving physical properties of galaxy populations. The observed dynamical properties of galaxies contain information about the transfer of angular momentum between their dark matter halos and baryons, and the subsequent dissipation of this angular momentum (through gravitational collapse, mergers and outflows e.g. Fall 1983; Romanowsky &

Fall 2012; Fall & Romanowsky 2013), constituting an important set of quantities for simulations to reproduce. Developments in both Integral-Field Spectroscopy (IFS) instrumentation and data analysis tools over the last decade have led to the observation of two-dimensional velocity and velocity dispersion fields for large samples of galaxies of different morphological types, spanning a wide redshift range (e.g. Sarzi et al., 2006; Flores et al., 2006; Epinat et al., 2008b; Förster Schreiber et al., 2009; Cappellari et al., 2011; Gnerucci et al., 2011; Epinat et al., 2012; Croom et al., 2012; Swinbank et al., 2012a,b; Bundy et al., 2015; Wisnioski et al., 2015; Stott et al., 2016; Harrison et al., 2017; Swinbank et al., 2017). When interpreted in tandem with high-resolution imaging data from the *Hubble Space Telescope (HST)*, these data provide information about the range of physical processes which are driving galaxy evolution. In particular, in recent years the multiplexing capabilities of KMOS (Sharples et al., 2013) have allowed for IFS kinematic observations for large galaxy samples to be assembled rapidly (Sobral et al., 2013b; Wisnioski et al., 2015; Stott et al., 2016; Mason et al., 2017; Harrison et al., 2017) providing an order-of-magnitude boost in statistical power over previous high-redshift campaigns.

Random motions within the interstellar medium of SFGs appear to increase with increasing redshift between $0 < z < 3$, as traced by their observed velocity dispersions, $\sigma_{\rm obs}$ (Genzel et al., 2008; Förster Schreiber et al., 2009; Law et al., 2009; Cresci et al., 2009; Gnerucci et al., 2011; Epinat et al., 2012; Kassin et al., 2012; Green et al., 2014; Wisnioski et al., 2015; Stott et al., 2016). This has been explained in terms of increased 'activity' in galaxies during and before the global peak in cosmic SFRD (Madau & Dickinson, 2014), in the form of higher specific star-formation rates (sSFRs) (Wisnioski et al., 2015), larger gas reservoirs (Law et al., 2009; Förster Schreiber et al., 2009; Wisnioski et al., 2015; Stott et al., 2016), more efficient accretion (Law et al., 2009), increased stellar feedback from supernovae (Kassin et al., 2012) and turbulent disk instabilities (Law et al., 2009; Bournaud et al., 2007; Bournaud & Frédéric, 2016), all of which combine to increase $\sigma_{\rm obs}$ and complicate its interpretation.

There is also an increasing body of work measuring the relationship between the observed maximum rotation velocity of a galaxy, a tracer for the total dynamical mass,

and its stellar mass, known as the stellar mass Tully-Fisher Relation (smTFR) (Tully & Fisher, 1977), with surveys reporting disparate results for the evolution of this relation with redshift (e.g. Puech et al., 2008; Miller et al., 2011; Gnerucci et al., 2011; Swinbank et al., 2012a; Simons et al., 2016; Tiley et al., 2016; Harrison et al., 2017; Straatman et al., 2017; Übler et al., 2017). Systematic differences in measurement and modelling techniques at high-redshift, especially with regards to beam-smearing corrections, combine with our poor understanding of progenitors and descendants to blur the evolutionary picture which these surveys paint. Additionally, there has been increasing focus in recent years on whether the measured velocity dispersions track random motions which provide partial gravitational support for high-redshift galaxy disks (e.g. Burkert et al., 2010; Wuyts et al., 2016b; Übler et al., 2017; Genzel et al., 2017; Lang et al., 2017). These random motions may become an increasingly significant component of the dynamical mass budget with increasing redshift (Wuyts et al., 2016b) and pressure gradients across the disk could result in a decrease in the observed rotation velocities (Burkert et al., 2010). Different interpretations of the gaseous velocity dispersions and their role in providing pressure support against gravity also complicate the evolutionary picture.

In this chapter we present new results from the KMOS Deep Survey (KDS), which is a guaranteed time programme focusing on the spatially-resolved properties of main-sequence SFGs at $z \simeq 3.5$, a time when the Universe was building to peak activity. With this survey, we aim to complement existent studies by providing deep IFS data for the largest number of galaxies at this redshift. By making use of KMOS (with integration times of 7.5-9 hours), we have been able to study [O III]λ5007 emission in 77 galaxies spanning the mass range $9.0 < \log(M_\star/M_\odot) < 10.5$, roughly doubling the number of galaxies observed via IFS at $z > 3$. In order to interpret the evolution of the physical properties of typical star-forming galaxies we have carefully constructed a set of comparison samples spanning $0 < z < 3$. These samples use integral-field spectroscopy to track the ionised gas emission in star-forming galaxies and follow consistent kinematic parameter extraction methods. By doing this we seek to minimise

the impact of systematic differences introduced by differing approaches to defining and extracting kinematic parameters.

There are still many open questions which we can begin to answer by studying the emission from regions of ionised gas within individual galaxies at these redshifts:

(i) What are the dynamical properties of main-sequence galaxies at this early stage in their lifetimes?

(ii) What are the radial gradients in metal enrichment within these galaxies and what can this tell us about the physical mechanisms responsible for redistributing metals?

(iii) What is the connection between the gas-phase metallicity and kinematics, particularly in terms of inflows and outflows of material?

This Chapter focuses on (i) by deriving and interpreting the spatially-resolved kinematics of the KDS galaxies, particularly the rotation velocities and velocity dispersions, using the [O III]λ5007 emission line, discussing what we can learn about the nature of galaxy formation at $z \simeq 3.5$ and forming evolutionary links with lower redshift work.

The structure of the chapter is as follows. In § 3.2 we present the survey description, sample selection, observation strategy and data reduction, leading to stacked datacubes for each of the KDS galaxies. In § 3.3 we describe the derivation of morphological and kinematic properties for our galaxies, explaining the kinematic modelling approach and the beam-smearing corrections which lead to intrinsic measurements of the rotation velocities, V_C, and velocity dispersions $\sigma_{\rm int}$ for each of the galaxies classified as morphologically isolated and spatially-resolved in the [O III]λ5007 emission line. § 3.4 presents an analysis of these derived kinematic parameters, comparing with lower redshift work where possible and drawing conclusions about the evolutionary trends and possible underlying physical mechanisms. We discuss these results in § 3.5 and

present our conclusions in § 3.6. Throughout this work we assume a flat ΛCDM cosmology with (h, Ω_m, Ω_Λ) = (0.7, 0.3, 0.7).

3.2 Survey description, sample selection and observations

3.2.1 The KDS survey description and sample selection

The KDS is a KMOS study of the gas kinematics and metallicity in 77 SFGs with a median redshift of $z \simeq 3.5$, probing a representative section of the galaxy main-sequence. The addition of these data approximately doubles the number of galaxies observed via IFS at this redshift (Cresci et al., 2010; Lemoine-Busserolle et al., 2010; Gnerucci et al., 2011; Troncoso et al., 2014), and will allow for a statistically-significant investigation of the dynamics and metal content of SFGs during a crucial period of galaxy evolution. The key science goals of the KDS are to investigate the resolved kinematic properties of high-redshift galaxies in the peak epoch of galaxy formation (particularly the fraction of rotating disks and the degree of disk turbulence) and also to study the spatial distribution of metals within these galaxies in the context of their observed dynamics. We seek to probe both a 'field' environment in which the density of galaxies is typical for this redshift and a 'cluster' environment containing a known galaxy over-density, in order to gauge the role of environment in determining the kinematics and metallicities of SFGs during this early stage in their formation history. To achieve this we require very deep exposure times in excess of 7 hours on source to reach the signal-to-noise required to detect line emission in the outskirts of the galaxies where the rotation curves begin to flatten, and to achieve adequate signal-to-noise across several ionised emission lines within individual spatial pixels (spaxels). Consequently, the KDS is one of the deepest spectroscopic datasets available at this redshift.

Sample selection

Target selection for the KDS sample is designed to pick out SFGs at $z \simeq 3.5$, supported by deep, multi-wavelength ancillary data. Within this redshift range the [O III]$\lambda\lambda$4959,5007 and Hβ emission lines are visible in the *K*-band and the [O II]$\lambda\lambda$3727,3729 doublet is visible in the *H*-band, both of which are observable with KMOS. From these lines, [O III]λ5007 generally has the highest signal-to-noise and so is well suited to dynamical studies, whereas [O III]λ4959, Hβ and the [O II]$\lambda\lambda$3727,3729 doublet complement [O III]λ5007 as tracers of the galaxy metallicities. To ensure a high detection rate of the ionised gas emission lines in the KDS we select galaxies in well-studied fields that have a wealth of imaging and spectroscopic data. Most of the galaxies for the KMOS observations had a confirmed spectroscopic redshift (see below). A subset of the selected cluster galaxies in the SSA22 field were blindly-detected in Lyα emission during a narrow-band imaging study of a known overdensity of Lyman Break Galaxies (LBGs) at $z \simeq 3.09$ (Steidel et al., 2000). In each pointing, few sources had no spectroscopic redshift and were selected on the basis of their photometric redshift. We make no further cuts to the sample on the basis of mass and SFR, in order to probe a more representative region of the star-forming main-sequence at this redshift (see Fig. 3.1).

GOODS-S

Two of the three field environment pointings are selected within the GOODS-S region (Guo et al., 2013); accessible from the VLT and with excellent multi-wavelength coverage, including deep *HST WFC3 F160W* imaging with a 0.06″ pixel scale and $\simeq$ 0.2″ PSF, which is well suited for constraining galaxy morphology (Grogin et al., 2011; Koekemoer et al., 2011). We selected targets from the various spectroscopic campaigns which have targetted GOODS-S, including measurements from VIMOS (Balestra et al., 2010; Cassata et al., 2015), FORS2 (Vanzella et al., 2005, 2006, 2008) and both LRIS and FORS2 as outlined in Wuyts et al. (2009). These targets must be within the redshift range $3 < z < 3.8$, have high spectral quality (as quantified by

Table 3.1: This table summarises the KDS pointing statistics for the full observed sample of 77 galaxies. The columns list the pointing name and galaxy environment probed, the central pointing coordinates, the number of observed, detected, resolved and merging objects as described in § 3.2.2, the waveband observed with KMOS, the exposure time and the PSF measured in the *K*-band.

Pointing	RA	DEC	N_{obs}	N_{Det}	% Det.	N_{Res}	% Res	N_{Merg}	% Merg*	Band[a]	Exp (ks)	PSF (″)[b]
GOODS-S-P1(field)	03:32:25.910	−27:51:58.710	20	17	85	14	70	2	17	*K*	32.4	0.50
GOODS-S-P2(field)	03:32:32.217	−27:43:08.000	17	14	82	13	76	2	18	*K*	31.8	0.52
SSA22-P1(cluster)	22:17:11.867	+00:15:44.700	21	15	71	9	46	8	89	*HK*	38.1	0.62
SSA22-P2(field)	22:17:35.120	+00:09:30.500	19	17	89	12	63	2	18	*HK*	27.8	0.57

[a] We also observed the two GOODS-S pointings in the *H*-band to cover the [O II]λ3727,3729 emission lines and a description of these observations will be given in a future work.

[b] The PSF values correspond to measurements in the *K*-band.

* Note that the Merger percentage is computed with respect to the number of resolved galaxies; the other percentages are computed with respect to the total number of galaxies observed in that pointing.

the VIMOS redshift flag equal '3' or '4', and the FORS2 quality flag equal 'A') and we carefully excluded those targets for which the [O III]λ5007 or Hβ emission lines, observable in the *K*-band at these redshifts, would be shifted into a spectral region plagued by strong OH emission. The galaxies which remain after imposing these criteria are distributed across the GOODS-S field, and we selected two regions where $\simeq$ 20 targets could be allocated to the KMOS IFUs (noting that the IFUs can patrol a 7.2′ diameter patch of sky during a single pointing). We name these GOODS-S-P1 and GOODS-S-P2, which which we observe 20 and 17 galaxies respectively (see Table 3.1).[1]

SSA22

A single cluster environment pointing was selected from the SSA22 field, (Steidel et al., 1998, 2000, 2003; Shapley et al., 2003), which, as mentioned above, is an overdensity of LBG candidates at $z \simeq 3.09$. Hundreds of spectroscopic redshifts have been confirmed for these LBGs with follow-up observations using LRIS (Shapley et al., 2003; Nestor et al., 2013). A combination of deep *B,V,R* band imaging with the Subaru Suprime-Cam (Matsuda et al., 2004), deep narrow-band imaging at 3640Å (Matsuda et al., 2004) and at 4977Å (Nestor et al., 2011; Yamada et al., 2012) and archival *HST ACS* and *WFC3* imaging provides ancillary data in excellent support of integral field spectroscopy, albeit over a shorter wavelength baseline and with shallower exposures than in the GOODS-S field. Fortunately at $z \simeq 3.09$ the [O III]λ5007 line is shifted into a region of the *K*-band which is free from OH features and so for the cluster environment pointing we filled the KMOS IFUs with galaxies located towards the centre of the SSA22 protocluster (SSA22-P1).

We also added a further field environment pointing to the south of the main SSA22 spatial overdensity where the density of galaxies is typical of the field environment (SSA22-P2). In SSA22-P1 and SSA22-P2 we observe 19 and 21 galaxies respectively. In summary, we have chosen three field environment pointings and a single cluster

[1]We note that the number of observed galaxies quoted for GOODS-S-P2 does not include two observed targets which were later found to have $z < 0.5$.

environment pointing across GOODS-S and SSA22, comprising a total of 77 galaxies, as described in Table 3.1. [2]

3.2.2 Observations and data reduction

Our data for the 77 KDS targets were observed using KMOS (Sharples et al., 2013), which is a second generation IFS mounted at the Nasmyth focus of UT1 at the VLT. The instrument has 24 moveable pickoff arms, each with an integrated IFU, which patrol a region 7.2′ in diameter on the sky, providing considerable flexibility when selecting sources for a single pointing. The light from a set of 8 IFUs is dispersed by a single spectrograph and recorded on a 2k×2k Hawaii-2RG HgCdTe near-IR detector, so that the instrument is comprised of three effectively independent modules. Each IFU has 14×14 spatial pixels which are 0.2″ in size, and the central wavelength of the *K*-band grating has a spectral resolution of $R \simeq 4200$ (*H*-band $R \simeq 4000$, *HK*-band $R \simeq 2000$).

Observations

To achieve the science goals of the KDS, the target galaxies at $3 < z < 3.8$ were observed in both the *K*-band, into which the [O III]λ5007 and Hβ lines are redshifted, and the *H*-band, into which the [O II]$\lambda\lambda$3727,3729 doublet is redshifted, allowing both dynamical and chemical abundance measurements. The GOODS-S pointings were observed in the *H* and *K*-bands separately, however, due to loss of observing time the SSA22 galaxies were observed with the KMOS *HK* filter, which has the disadvantage of effectively halving the spectral resolution, but allows for coverage of the *H*-band and *K*-band regions simultaneously.

We prepared each pointing using the KARMA tool (Wegner & Muschielok, 2008), taking care to allocate at least one IFU to observations of a 'control' star closeby

[2]Additional pointings in the COSMOS and UDS fields were originally scheduled as part of the GTO project, however 50% of the observing time was lost to bad weather during these visitor mode observations.

on the sky to allow for precise monitoring of the evolution of seeing conditions and the shift of the telescope away from the prescribed dither pattern (see § 3.2.2). For the four pointings described above and summarised in Table 3.1, we adopted the standard object-sky-object (OSO) nod-to-sky observation pattern, with 300s exposures and alternating 0.2″/0.1″ dither pattern for increased spatial sampling around each of the target galaxies. This procedure allowed for datacube reconstruction with 0.1″ size spaxels as described in § 3.2.2.

The observations were carried out during ESO observing periods P92-P96 using Guaranteed Time Observations (Programme IDs: 092.A-0399(A), 093.A-0122(A,B), 094.A-0214(A,B),095.A-0680(A,B),096.A-0315(A,B,C)) with excellent seeing conditions. In GOODS-S-P1 and GOODS-S-P2 the median K-band seeing was $\simeq 0.5''$ and for the SSA22-cluster and SSA22-field pointings the K-band seeing ranged between $\simeq 0.55 - 0.65''$. We observed 17-21 $z \simeq 3.5$ targets in each field (see Table 3.1), with these numbers less than the available 24 arms for each pointing due to the combination of three broken pickoff arms during the P92/93 observing semesters and our requirement to observe at least one control star throughout an Observing Block (OB).

This Chapter is concerned with the spatially-resolved kinematics of the KDS galaxies. Consequently, we now focus exclusively on the spatially-resolved [O III]λ5007 measurements in the K-band spectral window. The details of the H-band data reduction and corresponding metallicity analyses will be described in a future study.

Data reduction

The details of the data reduction are described in Chapter 2. Here we briefly recall the main points. The data reduction process primarly made use of the Software Package for Astronomical Reduction with KMOS, (SPARK; Davies et al. 2013), implemented using the ESO Recipe Execution Tool (ESOREX) (Freudling et al., 2013). In addition to the SPARK recipes, custom Python scripts were run at different stages of the pipeline

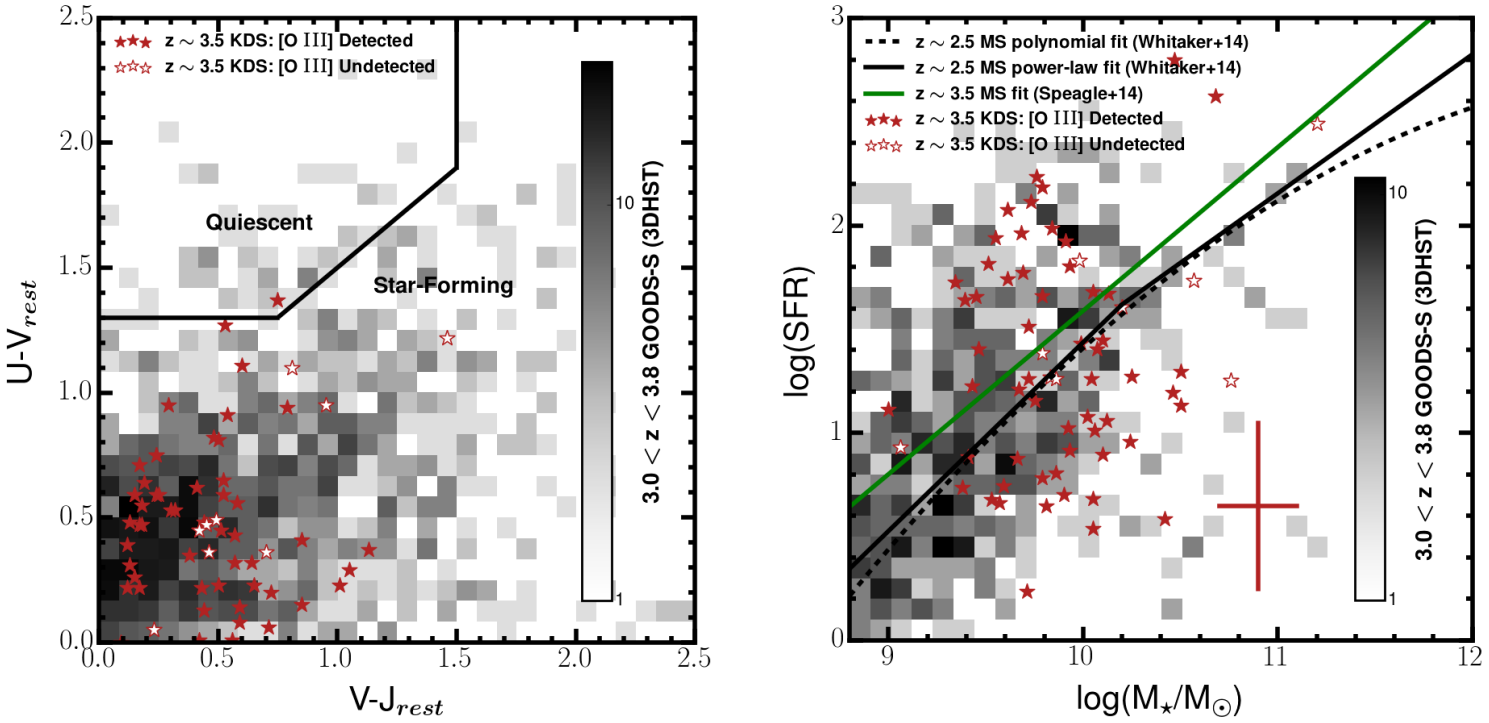

Figure 3.1: *Left:* The distribution of all 77 KDS galaxies in rest-frame UVJ colour space is plotted, with filled symbols showing galaxies detected in [O III]λ5007 and open symbols showing those which were not detected. Also plotted in this plane are $\simeq$ 4000 galaxies in GOODS-S with $3.0 < z < 3.8$ (mirroring the KDS redshift range) from the 3D-*HST* survey (Brammer et al., 2012; Momcheva et al., 2016), with the filled squares denoting the density of galaxies in that region. We use the galaxy selection criteria defined in Whitaker et al. (2012a) to highlight star-forming and quiescent regions (motivated by the age sequence of quiescent galaxies), finding that all but one of the KDS galaxies are clearly in the star-forming region and overlap with the highest density of 3D-*HST* targets. *Right:* We plot the location of the KDS galaxies in the SFR versus M$_\star$ plane, using the same symbol convention. The same GOODS-S galaxies from the 3D-*HST* survey as in the left panel are plotted with the filled squares, as a reference for the typical relationship between SFR and M$_\star$. The black solid line and the dashed line show the $z \simeq 2.5$ broken power-law and quadratic fit to the main-sequence respectively, described in Whitaker et al. (2014). We include the MS relation evaluated at $z = 3.5$ (the median redshift of the KDS sample) described in Speagle et al. (2014) and given in Equation 3.1 as the green line, with the discrepancy between the two relations representating the expected main-sequence evolution between these redshifts. Within the typical uncertainties (see error bars) the KDS sample is representative of $z \simeq 3.5$ SFGs.

and are described throughout this section.

The SPARK recipes were used to create dark frames and to flatfield, illumination correct and wavelength calibrate the raw data. An additional step, which is not part of the standard reduction process, was carried out at this stage, to address readout channel bias. Differences in the readout process within each 64-pixel wide channel on the detector image lead to varying flux baselines across each of the individual exposures. We corrected back to a uniform flux baseline across the detector image for each object exposure by identifying pixels which are not illuminated in every readout channel and subtracting their median value from the rest of the pixels in the channel. This is a separate issue to non-uniform illumination across the detectors, which is corrected by applying the illumination correction frame to the stacked datacubes.

Standard star observations were carried out on the same night as the science observations and were processed in an identical manner to the science data. Following this pre-processing, each of the object exposures was reconstructed independently, using the closest sky exposure for subtraction, to give more control over the construction of the final stacks for each target galaxy. Each 300s exposure was reconstructed into a datacube with interpolated $0.1 \times 0.1''$ spaxel size, facilitated by the subpixel dither pattern discussed in § 3.2.2 which boosts the effective pixel scale of the observations.

Sky subtraction was enhanced using the SKYTWEAK option within SPARK (Davies, 2007), which counters the varying amplitude of OH lines between exposures by scaling 'families' of OH lines independently to match the data. Wavelength miscalibration between exposures due to spectral flexure of the instrument is also accounted for by applying spectral shifts to the OH families during the procedure, and in general the use of the SKYTWEAK option in the *K*-band greatly reduces the sky-line residuals. We monitored the evolution of the atmospheric PSF and the position of the control stars over the OBs, to allow us to reject raw frames where the averaged *K*-band seeing rose above $0.8''$ and to measure the spatial shifts required for the final stack more precisely. The PSF was determined by fitting the collapsed *K*-band image of the stacked control

stars in each pointing with an elliptical gaussian, with the values reported in Table 3.1. The telescope tends to drift from its acquired position over the course of an OB and the difference between the dither pattern shifts and the measured position of the control stars provides the value by which each exposure must be shifted to create the stack.

We stacked all 300s exposures for each galaxy which pass the seeing criteria using 3-sigma clipping, leaving us with a flux and wavelength-calibrated datacube for every object in the KDS sample. We have found that the thermal background is often under-subtracted across the spatial extent of the cube following a first pass through the pipeline, leading to excess flux towards the long wavelength end of the *K*-band. To account for this, a polynomial function is fit, using the python package LMFIT (Newville et al., 2014), which makes use of the Levenberg-Marquardt algorithm for non-linear curve fitting, to the median stacked spectrum from spaxels in the datacube which contain no object flux and then subtracted from each spaxel in turn.

The central coordinates of each pointing, the number of target galaxies observed, N_{obs}, the number of galaxies with [O III]λ5007 detected as measured by attempting to fit the redshifted line in the integrated galaxy spectrum using the known redshift value, $N_{Det} = 63/77$ (82%), the number with spatially-resolved [O III]λ5007 emission, N_{Res} (see § 3.3.2), the on source exposure time and the averaged seeing conditions are listed in Table 3.1.

3.2.3 Stellar masses and SFRs

The wealth of ancillary data in both fields allows for a consistent treatment of the SED modelling, providing physical properties which are directly comparable between the cluster and field environments. These derived properties are considered in the context of the galaxy main-sequence, to verify that the KDS sample contains typical SFGs at $z \simeq 3.5$.

SED fitting and main-sequence

In order to constrain their SFRs and stellar masses, the available photometry for the KDS targets was analysed using the SED fitting software described in McLure et al. (2011) and McLeod et al. (2015). The photometry for each target was fit with the same set of solar metallicity BC03 (Bruzual & Charlot, 2003) templates adopted by the 3D-HST team Momcheva et al. (2016), and derived stellar masses and SFRs were based on a Chabrier IMF. In addition, the SED fitting software accounts for the presence of strong nebular emission lines according to the line ratios determined by Cullen et al. (2014). During the SED fitting process, dust attenuation was accounted for using the Calzetti et al. (2000) reddening law, with dust attenuation allowed to vary freely within the range $0.0 < A_V < 4.0$. Based on the adopted template set, the median stellar mass for the full observed sample is $\log(M_\star/M_\odot) = 9.8$. Fitting the photometry of the KDS targets with 0.2 $Z\odot$ templates, rather than solar metallicity templates, typically reduces the derived stellar masses by $\simeq 0.1$ dex, but this change does not affect the conclusions of this work. In GOODS-S, we have compared our derived stellar masses to those in Santini et al. (2015) (which presents an average result from 10 different sets of analyses), finding a median difference between the two sets of values of $\Delta\log(M_\star/M_\odot) = 0.009$. We also note that using the star-forming galaxy templates described in Wuyts et al. (2011b) typically leads to stellar masses which are 0.2 dex higher.

In the left panel of Fig. 3.1 we plot the KDS galaxies in the rest-frame *U-V* vs. *V-J* colour space. This is a commonly used diagnostic plane for selecting star-forming and quiescent galaxies (e.g. Williams et al., 2009b; Brammer et al., 2011; Whitaker et al., 2012a) with the age gradients of the stars within quiescent galaxies placing them in a different region of the plane to those which are actively forming stars. The selection criteria defined in Whitaker et al. (2012a) (which evolve only gently with redshift), separate quiescent and star-forming regions, which are indicated by the black wedge. We also make use of the rest-frame colours of $\simeq 4000$ primarily star-forming galaxies located in GOODS-S between $3.0 < z < 3.8$ (based upon the 'z_best classification flag') from the 3D-*HST* survey (Brammer et al., 2012; Momcheva et al., 2016). The filled squares indicate the density of 3D-*HST* targets in colour space and we observe

that the peak density location is consistent with the location of the KDS targets, all but one of which are in the star-forming region.

In the right panel of Fig. 3.1 we plot the $M_\star$ and SFR 'main-sequence' for the KDS galaxies with SFR measurements, in combination with the derived physical properties of the same GOODS-S galaxies as in the left panel. We also plot both the linear-break and quadratic $z \simeq 2.5$ main-sequence fits to the 3D-*HST* data described in Whitaker et al. (2014) with the solid and dashed black lines as well as the main-sequence relation described in Speagle et al. (2014) given in Equation 3.1, evaluated at $z \simeq 3.5$ (where the age of the Universe is 1.77 Gyr) with the green line.

$$\mathrm{logSFR}(M_\star, t) = (0.84 - 0.026 \times t)\log(M_\star/M_\odot) - (6.51 - 0.11 \times t) \tag{3.1}$$

The difference in position of these relations highlights the main-sequence evolution towards higher SFRs at fixed $M_\star$ between $z \simeq 2.5 - 3.5$. The KDS galaxies scatter, within the errors, consistently above and below the $z \simeq 3$ main-sequence.

When taken together, both panels indicate that the KDS sample is representatitve of typical star-forming galaxies at $z > 3$.

3.3 Analysis

3.3.1 Morphological Measurements

For a robust interpretation of the observed velocity fields, it was necessary to separately determine the morphological properties of the galaxies from high-resolution images. This imaging was used primarily to determine morphological parameters which characterise the size (quantified here through the half-light radius, $R_{1/2}$), morphological position angle, PA_{morph}, and axis ratio, b/a, of the galaxies. In the following sections we describe the approach chosen to recover these parameters, also describing comparisons with matched galaxies in the morphological parameter catalogue of van der Wel et al.

(2012). At $3 < z < 4$ and $0.1 < z < 1$ we made use of secure spectroscopic redshifts obtained for SFGs during the ESO public surveys zCOSMOS (Lilly et al., 2007), VUDS (Tasca et al., 2016), GOODS_FORS2 (Vanzella et al., 2005, 2006, 2008) and GOODS_VIMOS (Balestra et al., 2010) to cross-match with van der Wel et al. (2012). This allowed us to investigate the morphological properties of typical star-forming galaxy populations at two redshift slices in comparison with those determined for the KDS sample. The imaging also helped to distinguish multiple 'merging' components with small angular separations from objects which are morphologically isolated, which we discuss in § 3.3.2 and § 3.3.3 where we refine our sample for dynamical analysis.

Applying GALFIT to the imaging data

We used GALFIT (Peng et al. 2010) to fit 2D analytic functions, convolved with the PSF, to the observed *HST* images of the KDS field galaxies across GOODS-S and SSA22 in a consistent way. The GOODS-S imaging data used is the latest release of the total field in *WFC3 F160W* band, which traces the rest-frame near-UV at $z \simeq 3.5$, available via the CANDELS (Grogin et al., 2011; Koekemoer et al., 2011) data access portal[3]. For SSA22 we made use of archival *HST* imaging[4] data in the *WFC3 F160W* band (P.I. Lehmer: PID 13844; P.I. Mannucci: PID 11735) and the *ACS F814W* band, tracing $\simeq$ 2500Å light at $z \simeq 3.1$ (P.I. Chapman: PID 10405; P.I. Abraham: PID 9760; P.I. Siana: PID 12527). The *HST* coverage is shallower in SSA22 (exposure times of $\simeq$ 5 ks) and the *F160W* coverage is concentrated on the SSA22-cluster and so we resorted to the bluer *ACS F814W* data to derive morphological parameters in SSA22-P2 (also in SSA22-P2, 4 galaxies do not have any *HST* coverage as indicated in Table 3.2).

We first ran SExtractor (Bertin & Arnouts, 1996) on the relevant images to recover initial input parameters and segmentation maps for running GALFIT, and then extracted postage stamp regions around the galaxies in the KDS sample. At this redshift, the galaxies are more compact and generally we could not resolve more complicated morphological

[3] http://candels.ucolick.org/data_access/Latest_Release.html
[4] https://archive.stsci.edu/hst/search.php

features such as spiral arms and bars and so we followed the simple method of fitting Sérsic profiles, with the Sérsic index fixed to the exponential disk value of $n = 1$. In the *F160W* band, the adopted PSF was a hybrid between the Tiny Tim *H*-band model (Krist et al., 2011) in the PSF centre and an empirical stack of stars observed in the *H*-band for the wings (van der Wel et al., 2012) and in the *F814W* band we used the pure Tiny Tim *ACS* high-resolution PSF model. During the fitting process all other morphological parameters, including $R_{1/2}$, the central x and y coordinates, $PA_{\rm morph}$ and inclination, were free to vary.

This method was justified by the recovery of similar mean χ^2 values when fitting floating Sérsic index models and bulge/disk models with both an $n = 1$ and $n = 4$ component (following the procedure described in Bruce et al. 2012) to those recovered from the fixed exponential disk fit. Additionally, 24 GOODS-S objects were also detected in the van der Wel et al. (2012) catalogue, for which the median Sérsic index value is $n = 1.2$. Of these 24 galaxies, 2 are found to have $n > 2.5$ (lbg_32 and lbg_109, see supplementary material § 3.10), although both show disk-like kinematics with a monotonic velocity gradient. The galaxy lbg_32 can be fit with an $n = 1$ Sérsic profile with small residuals, however lbg_109 has a centrally concentrated light distribution which is not well captured by the $n = 1$ profile. This demonstrates that fitting exponential flux distributions is a valid approach for the sample at large. The use of exponential profiles also facilitates comparison with recent large surveys such as KMOS^{3D} (Wisnioski et al., 2015) and KROSS (Harrison et al., 2017) in which beam-smearing correction factors were applied to the derived kinematic parameters as a function of exponential disk scale length, $R_{\rm d}$, defined as $R_{1/2} \simeq 1.68 R_{\rm d}$ (see § 3.7.5).

This analysis provided us with three crucial morphological parameters required to support the kinematic analysis of § 3.3.2, namely the axis ratio b/a, half-light radius $R_{1/2}$ and the morphological position angle $PA_{\rm morph}$. Example *HST* images and GALFIT outputs are given in Fig. 3.3 for selected galaxies, and maps for the full isolated field sample (see § 3.3.2) are plotted throughout supplementary material § 3.10.

The errorbars produced by GALFIT are purely statistical and are determined from the

covariance matrix used in the fitting, resulting in unrealistically small uncertainties on the derived galaxy parameters (Häußler et al., 2007; Bruce et al., 2012). Throughout the following subsections we discuss the more reasonable adopted errors on each of the relevant morphological parameters in turn. In each of the following sections we also discuss the approach followed to recover the morphological parameters for the galaxies without *HST* coverage. The interpretation of the sample as a whole is not affected by the small number of galaxies without *HST* imaging.

Inclination angles

We used the derived b/a values to determine galaxy inclination angles. As suggested in Holmberg (1958), by modelling the disk galaxies as an oblate spheroid, the inclination angle can be recovered from the observed axis ratio as shown in Equation 3.2, where $\frac{b}{a}$ is the ratio of minor to major axis of an ellipse fit to the galaxy profile on the sky, i is the inclination angle and q_0 is the axis ratio of an edge-on system.

$$cos^2 i = \frac{\left(\frac{b}{a}\right)^2 - q_0^2}{1 - q_0^2} \tag{3.2}$$

To derive the inclination, we selected a value for q_0, and following the discussion in (Law et al., 2012a) we chose a value appropriate for thick disks, $q_0 = 0.2$ (e.g. Epinat et al., 2012; Harrison et al., 2017). However, as discussed in Harrison et al. (2017), varying the q_0 value by a factor of 2 makes only a small change to the final inclination corrected velocity values, with the difference $< 10\%$ in the case of the KDS galaxies in the isolated field sample (see § 3.3.3).

The inclination angle calculated for each galaxy is used to correct the observed velocity field, which is the line of sight component of the intrinsic velocity field, with the correction factor increasing with increasing b/a. The median difference between the derived b/a values and those presented in van der Wel et al. (2012) for the 22 matched GOODS-S galaxies is $\Delta b/a = 0.0002$. The b/a distribution shown in Fig. 3.2 (plotted for the 28 galaxies in the isolated field sample with *HST* imaging, § 3.3.3) is

Table 3.2: Physical properties of the resolved and morphologically isolated KDS field galaxies as measured from SED fitting and from applying GALFIT (Peng et al. 2010).

ID	RA	Dec	z	K^a_{AB}	$\log(M_\star/M_\odot)^b$	b/a	$i^{\circ\,c}$	PA°_{morph}	$R_{1/2}$(kpc)^d
b012141_012208	03:32:23.290	−27:51:57.348	3.471	24.12	9.8	0.36	72	9	1.57
b15573	03:32:27.638	−27:50:59.676	3.583	23.60	9.8	0.28	78	146	0.52
bs006516	03:32:14.791	−27:50:46.500	3.215	23.94	9.8	0.50	61	146	1.91
bs006541	03:32:14.820	−27:52:04.620	3.475	23.44	10.1	0.44	66	168	1.83
bs008543	03:32:17.890	−27:50:50.136	3.474	22.73	10.5	0.50	61	67	1.59
bs009818	03:32:19.810	−27:53:00.852	3.706	24.18	9.7	0.80	37	148	1.24
bs014828	03:32:26.760	−27:52:25.896	3.562	23.58	9.7	0.31	76	63	1.61
bs016759	03:32:29.141	−27:48:52.596	3.602	23.85	9.9	0.65	50	49	0.87
lbg_20	03:32:41.244	−27:52:20.676	3.225	24.97	9.5	0.64	52	1	1.28
lbg_24	03:32:39.754	−27:39:56.628	3.279	24.67	9.6	0.53	60	34	1.27
lbg_25	03:32:29.189	−27:40:22.476	3.322	24.95	9.4	0.30	76	78	1.18
lbg_30	03:32:42.854	−27:42:06.300	3.419	23.85	10.0	0.79	38	66	0.95
lbg_32	03:32:34.399	−27:41:24.324	3.417	23.84	9.9	0.60	54	40	1.88
lbg_38	03:32:22.474	−27:44:38.436	3.488	24.58	9.9	0.58	56	137	0.92
lbg_91	03:32:27.202	−27:41:51.756	3.170	24.65	9.8	0.58	56	79	0.89

Table 3.2: Continued.

ID	RA	Dec	z	K_{AB}^{a}	$\log(M_\star/M_\odot)^{b}$	b/a	i°^{c}	PA°_{morph}	$R_{1/2}$(kpc)^{d}
lbg_94	03:32:28.949	−27:44:11.688	3.367	24.54	9.9	0.22	84	81	1.16
lbg_105	03:32:24.005	−27:52:16.140	3.092	23.79	9.3	0.56	57	128	1.72
lbg_109	03:32:20.935	−27:43:46.344	3.600	24.63	9.7	0.60	54	119	1.98
lbg_111	03:32:42.497	−27:45:51.696	3.609	24.01	9.7	0.74	42	80	0.64
lbg_112	03:32:17.134	−27:42:17.784	3.617	25.16	9.6	0.79	38	43	0.46
lbg_113	03:32:35.957	−27:41:49.956	3.622	24.01	9.6	0.52	60	15	0.87
lbg_121	03:32:19.606	−27:48:40.032	3.708	25.36	9.1	0.65	50	106	0.42
lbg_124	03:32:33.324	−27:50:07.332	3.794	24.96	9.0	0.56	57	50	0.78
*n3_006	22:17:24.859	+00:11:17.620	3.069	22.98	10.5	0.57	57	156	2.52
n3_009	22:17:28.330	+00:12:11.600	3.069	-	8.7	0.75	42	84	1.06
n_c3	22:17:32.585	+00:10:57.180	3.096	24.96	9.8	0.71	46	94	0.56
lab18	22:17:28.850	+00:07:51.800	3.101	-	8.2	0.85	32	27	0.46
*lab25	22:17:22.603	+00:15:51.330	3.067	-	8.4	0.57	57	87	2.18
s_sa22a-d3	22:17:32.453	+00:11:32.920	3.069	23.46	9.7	0.39	70	125	1.78
s_sa22b-c20	22:17:48.845	+00:10:13.840	3.196	23.91	9.5	0.57	57	76	1.59
*s_sa22b-d5	22:17:35.808	+00:06:10.340	3.175	23.72	10.2	0.57	57	60	3.30
s_sa22b-d9	22:17:22.303	+00:08:04.130	3.084	24.25	10.1	0.65	50	60	0.50
*s_sa22b-md25	22:17:41.690	+00:06:20.460	3.304	24.62	8.6	0.57	57	9	1.39

[a] K-band magnitude errors are typically ±0.05 magnitudes.
[b] Representative error of 0.2 dex from SED modelling used throughout this study (see § 3.2.3).
[c] Fixed 10 percent inclination error assumed (i.e. $\delta i = i/10$, see § 3.3.1)
[d] Fixed 10 percent $R_{1/2}$ error assumed (see § 3.3.1).
* No *HST* coverage: $PA_{\rm morph}$ set to $PA_{\rm kin}$ value; b/a and $R_{1/2}$ estimated as explained throughout the text.

consistent with being uniform between $0.3 < b/a < 0.9$, with a median value of 0.58, corresponding to i = 57.0° using the conversion given in Equation 3.2, with $q_0 = 0.2$. This compares well with the theoretical mean value of 57.3° computed for a population of galaxies with randomly drawn viewing angles (see e.g. the appendix in Law et al. 2009), which reassured us that we were not biased towards deriving either particularly low or particularly high inclination angles.

As mentioned in § 3.3.1, the error reported by GALFIT on the model b/a value is unrealistically small. Guided by the results of the Monte Carlo approach described in Epinat et al. (2012) we adopted a conservative nominal inclination angle uncertainty of 10%, i.e. $\delta i = i/10$. For the galaxies without *HST* coverage, the inclination angle was set to the KDS sample median of 57.0° and we used the standard deviation of the KDS inclinations, 13.2°, for the inclination uncertainty. This added an additional factor of $\simeq 1.3$ to the uncertainty in the derived velocities for these galaxies.

Position angles

The second GALFIT parameter was $PA_{\rm morph}$, which is the direction of the photometric major axis of the galaxy on the sky. We visually inspected each of the GALFIT maps to check that the derived $PA_{\rm morph}$ follows the galaxy light distribution (with $PA_{\rm morph}$ indicated by the orange dashed line in Fig. 3.3) and when this was not the case it was usually an indication of multiple distinct components or tidal streams (see § 3.3.3 where we remove multiple-component objects from the final sample). We note that discrepancy between $PA_{\rm morph}$ and the kinematic position angle, $PA_{\rm kin}$, is an indicator of sub-structure in the morphology (e.g. Queyrel et al., 2012; Wisnioski et al., 2015; Rodrigues et al., 2017), and deviations can indicate clumps or mergers which may influence the underlying kinematics or bias the derived $PA_{\rm morph}$ towards a particular direction. We discuss this topic further in § 3.3.2. For the galaxies without *HST* coverage we fixed $PA_{\rm morph}$ equal to $PA_{\rm kin}$, for the analysis described in § 3.3.2.

Half-light radii

The half-light radius, $R_{1/2}$, provides an indication of the disk sizes, and hence gave us a common fiducial distance from the centre of the galaxy at which to extract rotation velocities. As discussed throughout the introduction and in supplementary material § 3.7.1, methods used to derive the intrinsic rotation velocity, V_C, vary widely between studies, and so to compare with previous work it is necessary to extract kinematic parameters consistently from the derived rotation curves. Knowledge of $R_{1/2}$ gives a well defined and consistent point across the extent of the galaxy at which to extract velocities, which is important when making comparisons to previous IFU studies (see supplementary material § 3.7.1 and e.g. Förster Schreiber et al. 2009; Epinat et al. 2012; Wisnioski et al. 2015; Stott et al. 2016; Harrison et al. 2017; Swinbank et al. 2017). Throughout our dynamical modelling, and to derive a beam-smearing correction to the rotation velocities and velocity dispersions (see § 3.3.2), we also required the $R_{1/2}$ value for each galaxy. The median difference between the derived $R_{1/2}$ values and those presented in van der Wel et al. (2012) for the 22 matched GOODS-S galaxies is $\Delta R_{1/2} = 0.0054''$ (corresponding to 0.04kpc at $z \simeq 3.5$).

Bruce et al. (2012) present a detailed error analysis of the morphological parameters of $1 < z < 3$ galaxies in the CANDELS fields (which includes *HST* data covering the GOODS-S field which we exploited during this work), reporting that the magnitude of the error on $R_{1/2}$ is typically at the 10% level. We adopted a nominal error of 10% for our recovered $R_{1/2}$ values and note that the errors on V_C and $\sigma_{\rm int}$ are dominated by measurement errors and uncertainties connected with assumptions about the inclination angle correction and the velocity dispersion distribution in high-redshift galaxies (see § 3.9).

To measure $R_{1/2}$ for the 4 galaxies without *HST* coverage, we fit the [O III]λ5007 narrow-band images, which are extracted from the KMOS datacubes by median stacking the 20 wavelength slices closest to the [O III]λ5007 line (10 on either side of the central wavelength pixel), with an exponential profile, and subtracted the appropriate PSF from

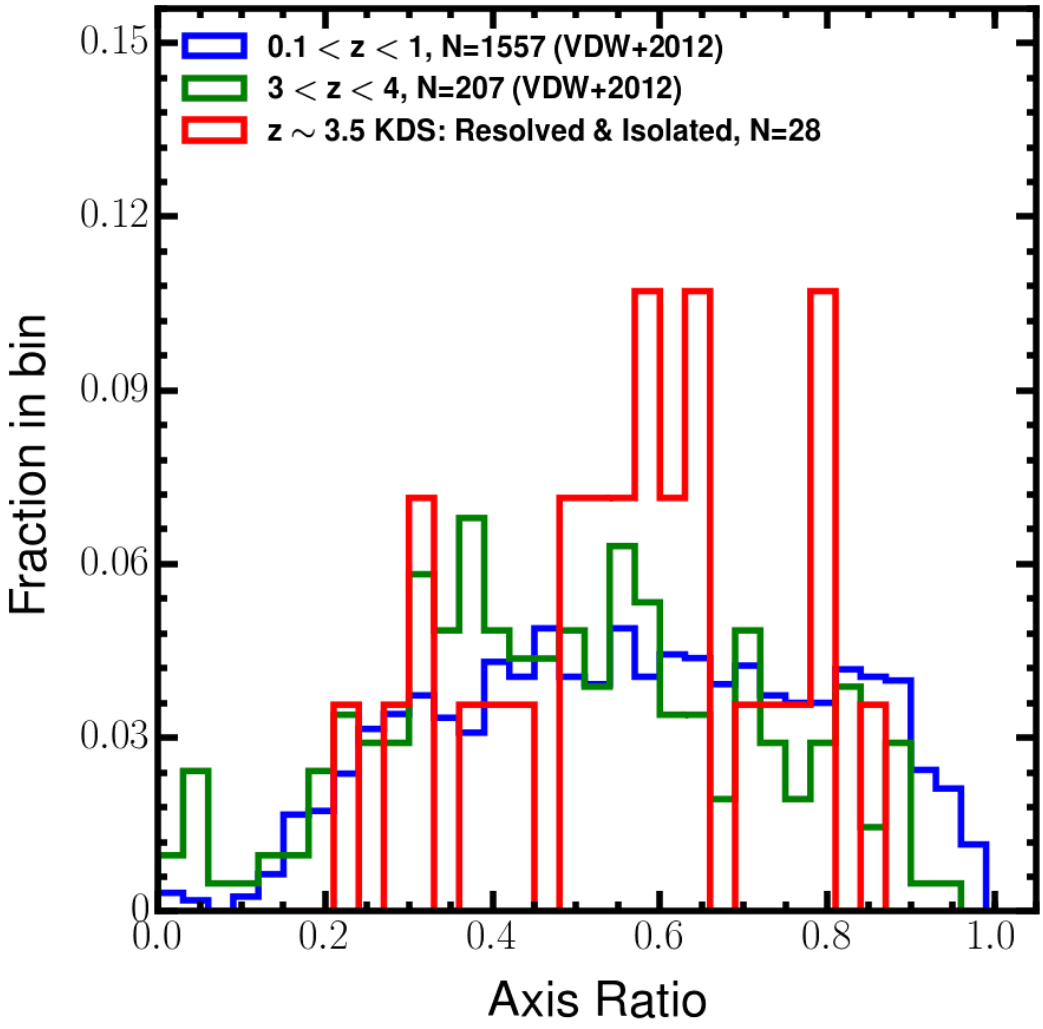

Figure 3.2: The normalised counts of KDS galaxies in bins of axis ratio is plotted, along with the normalised counts from the morphological catalogue presented in van der Wel et al. (2012) in two redshift ranges. The axis ratio distribution appears to be constant with time as traced by the reference samples, and the KDS values are in good agreement with a relatively uniform distribution spanning $0.3 < b/a < 0.9$. This suggests that we are not biased towards deriving a particular value for the axis ratio.

the recovered $R_{1/2}$ value. We note that the extracted rotation velocities are not sensitive to the precise $R_{1/2}$ values, since we measure these at $2R_{1/2}$ (see § 3.3.2) where the intrinsic model rotation curves have already reached flattening.

3.3.2 Kinematic Measurements

We proceeded to extract 2D kinematic measurements from the 63 KDS datacubes detected in integrated [O III]λ5007 emission by fitting the [O III]λ5007 emission line profiles within individual spaxels. The sample was then refined to galaxies which are spatially-resolved in the [O III]λ5007 emission line in order to make dynamical measurements. We also describe our dynamical modelling and the approach we have followed to extract V_C and σ_{int}, using the models to derive beam-smearing corrections for each galaxy. We made use of the imaging data described in the previous sections to reduce the number of free parameters in the model, an approach which is necessary when working in this signal-to-noise regime.

Spaxel Fitting

We aimed to extract two-dimensional maps of the [O III]λ5007 flux, velocity and velocity dispersion from each of the 63 stacked and calibrated KDS datacubes with an [O III]λ5007 detection. These properties are extracted via modelling emission line profiles within each spaxel, with a set of acceptance criteria imposed to determine whether the fit quality is high enough to allow the inferred properties to pass into the final 2D maps of the flux and kinematics. We concentrated solely on the [O III]λ5007 emission line which always had signal-to-noise higher than both [O III]λ4959 and Hβ and was detected over a larger area of each IFU.

Each 0.1″ spaxel across a datacube was considered in turn. The redshift value determined from fitting the [O III]λ5007 line in the integrated galaxy spectrum, z_{sys}, was used to determine the central wavelength of the redshifted [O III]λ5007 line, $\lambda_{obs_{5007}}$. We searched a narrow region around $\lambda_{obs_{5007}}$ for the peak flux, assumed to correspond to the ionised gas emission, and extracted a 5Å region (corresponding to 20 spectral elements) centred on this peak. This truncated spectrum was then used in the fitting procedure for each spaxel. The width of the extraction region was large enough to

encompass unphysically large velocity shifts, but not so large as to compromise the fitting by potentially encompassing regions of the spectrum plagued by strong sky-line residuals. A single gaussian model was fit to the extraction region, again using LMFIT (Newville et al., 2014), returning the values of the best-fitting flux, F_g, central wavelength, λ_g, and dispersion, σ_g. These parameters, along with the estimate of the noise in the datacube, were used to assess whether the fitting of the [O III]λ5007 line is acceptable or not.

The noise was estimated by masking all datacube spaxels containing object flux and computing the standard deviation of the flux values in the spectral extraction region for all remaining spaxels inwards of 0.3″ from the cube boundary (over the same spectral region as considered to find the peak object flux). This boundary constraint was chosen to mitigate edge effects, where the noise increased sharply due to fewer individual exposures constituting the final stack in these regions. The final noise value was then taken as the standard deviation of the results from each unmasked spaxel, as shown in Equation 3.3, where $F_{i,background}$ are the flux values across the spatial regions containing no object flux in the spectral extraction region, and N_m denotes the noise estimated from masking the datacube.

$$N_m = STD\left(\sum_i F^2_{i,background}\right) \tag{3.3}$$

The signal in each spaxel was taken as the sum of the flux values across the spectral extraction region, $F_{i,object}$, as shown in Equation 3.4, where S denotes the signal.

$$S = \sum_i F_{i,object} \tag{3.4}$$

The criteria for accepting the fit within a given spaxel are as follows:

(i) The uncertainties on any of the parameters of the gaussian-fit as returned by LMFIT must not exceed 30%

(ii) $\frac{S}{N_m} > 3$

We imposed a further criterion to help remove fits to spectral features unrelated to the galaxy (e.g. fits to skyline residuals), which was important for 'cleaning up' accepted spaxels in the 2D maps which were clearly unrelated to the galaxy. For this test we subtracted the galaxy continuum and imposed that $0.7 < F_g/S < 1.3$, where F_g is the flux from the gaussian-fit to the [O III]λ5007 line and S is the signal in the extraction region from Equation 3.4. If all three criteria were satisfied, the spaxel was accepted.

From the gaussian-fit, we recovered the centre, λ_g, the width, σ_g, and the area, F_g. The velocity was computed from λ_g using Equation 3.5 and the velocity dispersion was computed from σ_g using Equation 3.6, where V_{obs} and σ_{obs} are the observed rotation velocity and velocity dispersion respectively, c is the speed of light, z_{sys} is the redshift determined from the integrated galaxy spectrum, $\lambda_{5007} = 0.500824\mu$m is the rest wavelength of [O III]λ5007 in vacuum and σ_{inst} is a measure of the KMOS instrumental resolution value averaged across gaussian-fits to several skylines (equal to 31.1 km s^{-1} in the *K*-band and 55.4 km s^{-1} in the *HK*-band).

$$V_{obs} = \frac{\lambda_g - (1 + z_{sys})\lambda_{5007}}{(1 + z_{sys})\lambda_{5007}} \times c \tag{3.5}$$

$$\sigma_{obs} = \sqrt{\left(\frac{\sigma_g}{(1 + z_{sys})\lambda_{5007}} \times c\right)^2 - \sigma_{inst}^2} \tag{3.6}$$

To estimate the errors on the observed quantities, the gaussian-fit was repeated 1000 times, with each flux value in the extraction region perturbed by the noise value, N_m. For each of these 1000 fits the gaussian parameters were used to compute the observed properties. The resultant distributions of observed quantities were gaussian and we measured the median as the final value for V_{obs}, σ_{obs} and F_g within that spaxel, and the

standard deviation of the distribution as the observational uncertainty. A map of each of these observed parameters was constructed by applying this procedure to each spaxel.

If a spaxel did not meet the criteria, we follow the procedure described in Stott et al. (2016) and binned with neighbouring spaxels to create a box of area $0.3\times0.3''$. This was carried out by median stacking the extraction region spectra in each of the neighbouring spaxels. The criteria were then re-examined, and if satisfied, the Monte-Carlo procedure was carried out. If the binned spaxels fail the criteria, one final iteration was carried out to bin to a box of area $0.5 \times 0.5''$, roughly equivalent to the size of the seeing disk (see Table 3.1). If after the widest binning the criteria were not satisfied, no value was assigned to that spaxel in the extracted maps.

The process was automated and applied to each of the 63/77 KDS galaxies with an [O III]λ5007 detection. Following the fitting procedure, the galaxies were clasified as spatially-resolved in [O III]λ5007 emission or not if the spatial extent of the accepted spaxels in the [O III]λ5007 flux map was equivalent to or greater than the seeing disk. For each pointing, the number of resolved galaxies, N_{Res}, was added to Table 3.1. We find that 48/63 (76%) of the detected KDS galaxies across both the field (39/48) and cluster (9/48) environments were spatially-resolved and showed clear velocity structure. The 15/63 (24%) galaxies which were not spatially-resolved were dropped at this stage due to the uncertainties associated with deriving kinematic properties and classifications from a single resolution element. The physical properties of all spatially-resolved galaxies in both GOODS-S and SSA22 are listed in Table 3.2.

The morphological information of § 3.3.1 was combined with this spatially-resolved condition to define two galaxy subsamples. 6/39 (15%) of the resolved galaxies across the 3 field environment pointings and almost all (8/9) of the cluster environment galaxies in SSA22-P1 have multiple photometric components (i.e. there is more than a single peak in the *HST* photometry), which complicates the interpretation of the observed dynamics for these targets. We removed the cluster environment pointing

from the full dynamical analysis, although we show examples of the *HST* imaging, flux, dispersion and velocity maps of the cluster target galaxies in Fig. 3.12. The remaining 6/39 merging candidates in the field environment are referred to as the 'merger field sample' throughout the remainder of the chapter. The 33/39 morphologically isolated field galaxies which are spatially-resolved are referred to as the 'isolated field sample' throughout the remainder of the chapter.

3D modelling and beam-smearing corrections

As mentioned in the introduction, there is no universal standard for defining V_C and σ_{int}, particularly when a dynamical model is used to provide beam-smearing corrections for σ_{int} and to extrapolate beyond the data in order to measure V_C. Physically motivated models take into account the potential-well of the galaxy through knowledge of the mass distribution (e.g. Genzel et al., 2008; Förster Schreiber et al., 2009; Gnerucci et al., 2011; Wisnioski et al., 2015; Swinbank et al., 2017). Phenomenological models assume a fixed function known to reproduce observed galactic rotation curves which flatten at large radii (e.g. Epinat et al., 2010, 2012; Swinbank et al., 2012a; Stott et al., 2016; Harrison et al., 2017). Both of the above examples fit to 1D or 2D fields extracted from the datacubes using line-fitting software. Recently, algorithms such as Galpak^{3D} (Bouché et al., 2015) and 3D-Barolo (Di Teodoro & Fraternali, 2015) have emerged, fitting directly to the flux in the datacube in order to constrain the kinematic properties.

There are three reasons to construct model velocity fields for the isolated field sample galaxies; the first is to interpolate between data points; the second is to extrapolate the observations smoothly to some fiducial radius from which V_C can be extracted; the third is to estimate the effect of beam-smearing on both the velocity and velocity dispersion fields so that we recover the set of intrinsic galaxy parameters which best describe the observations. As a brief overview, we used a Markov chain Monte Carlo (MCMC) procedure to construct a series of intrinsic model datacubes for each galaxy, convolved these with the atmospheric PSF and then fit to the data. The beam-smearing corrected kinematic parameters were then extracted from the intrinsic galaxy models

as described in more detail below. In this analysis, we minimised the number of free parameters by making use of information from *HST* imaging and by assuming a fixed function to describe the rotation curves as described in the following subsection. This is particularly important when dealing with galaxies at $z > 3$, since often there is not enough signal-to-noise away from the centre of the galaxy to observe the flattening of the rotation curve, consequently requiring extrapolation to determine $V_{\rm C}$. The following section describes our 3D modelling procedure, and the validation of our results through comparison with the techniques used to determine the dynamical properties presented in Harrison et al. (2017).

Constructing model datacubes

For each galaxy with spatially-resolved [O III]λ5007 emission we constructed a series of model datacubes with the same spatial dimensions as the observed datacube and populated each spaxel with an [O III]λ5007 emission line that has central wavelength determined using $z_{\rm sys}$. This central wavelength was then shifted using the velocity derived at each spaxel from the velocity field model described below. Following the procedure adopted by numerous authors (e.g. Epinat et al., 2010, 2012; Swinbank et al., 2012a; Stott et al., 2016; Mason et al., 2017) the velocity field of the gas was modelled as a thin disk with the discrete velocity points along $PA_{\rm kin}$ determined by Equation 3.7, which has been found to reproduce the rotation curves of galaxies in the local Universe (e.g. Courteau, 1997):

$$v_r = \frac{2}{\pi} v_{\rm asym} \arctan\left(\frac{r}{r_{\rm t}}\right) \tag{3.7}$$

with 'r' measured as the distance from the centre of rotation. This model was then projected onto the cube using the inclination angle determined in § 3.3.1 and sampled with 4 times finer pixel scale than the KMOS raw data before binning back to the previous resolution. The pixel scale refinement was necessary to capture the steep velocity gradients across the central regions.

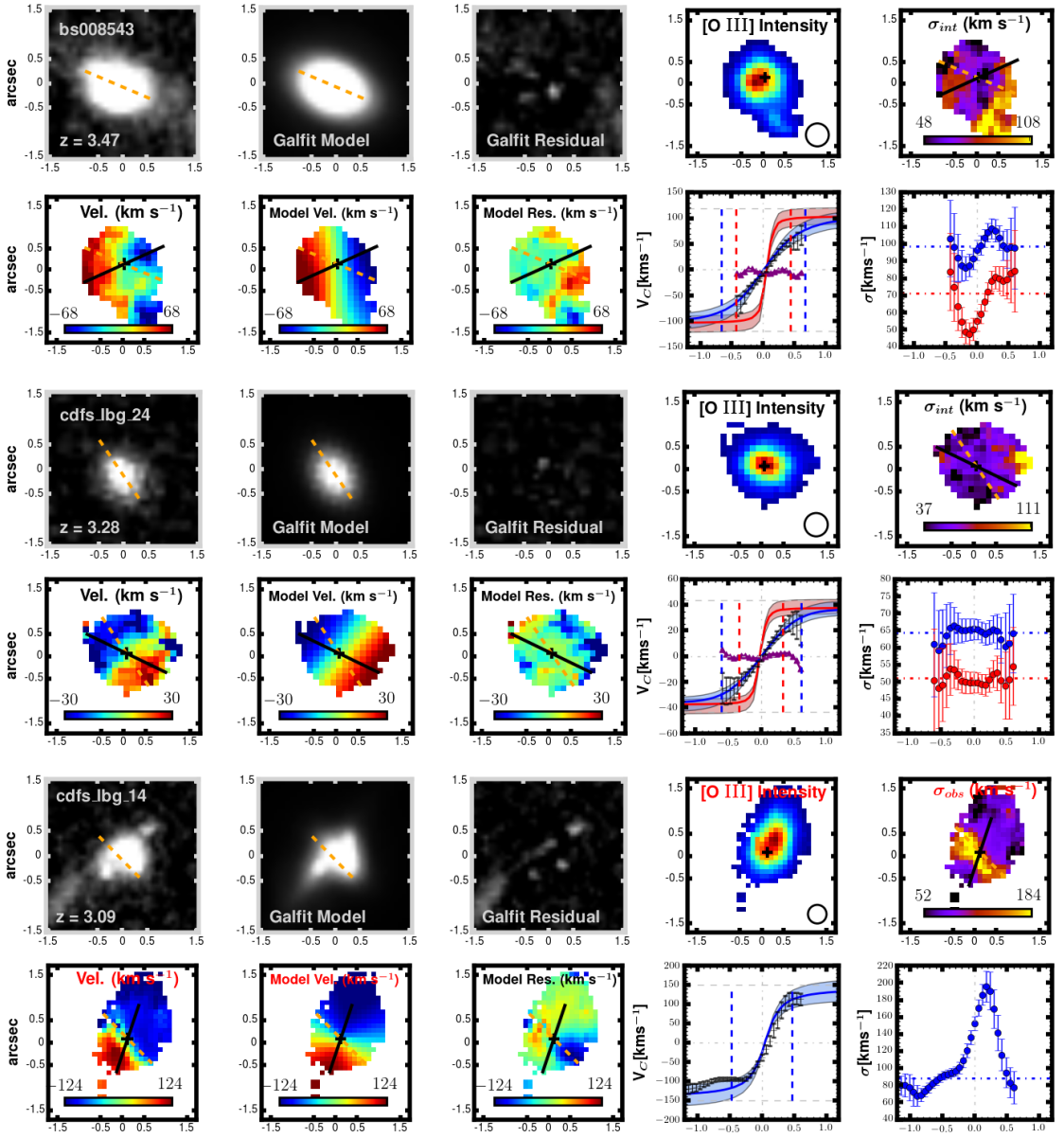

Figure 3.3: We plot the kinematic grids for one rotation-dominated galaxy (top grid), one dispersion-dominated galaxy (middle grid) and one merger candidate (bottom grid) (see § 3.3.3) from the KDS. For each galaxy we plot on the top row the *HST* image, GALFIT model and GALFIT residuals, along with the observed [O III]λ5007 intensity map and velocity dispersion map. On the bottom row we plot the observed velocity map, the beam-smeared model velocity and data-model velocity residuals with colour bar limits tuned to the velocity model. The solid black line and dashed orange line plotted in various panels show $PA_{\rm kin}$ and $PA_{\rm morph}$ respectively. Also on the bottom row, we plot extractions along $PA_{\rm kin}$ for both the velocity and velocity dispersion. The grey points with errorbars on the velocity extraction plot are from the observed velocity map, the blue line and blue shaded regions represent the beam-smeared model fit to the data and errors respectively, whereas the red line and shaded regions are the intrinsic model from which $V_{\rm C}$ is extracted. Further details regarding the symbols used in each of the panels are provided in Figure 3.10.

The velocity decreases with a factor of $\cos(\phi)$ from the kinematic position axis, where ϕ is the angle measured clockwise from the axis, which points to the direction of the positive side of the velocity field. The 6 free parameters of the model; $(x_{\rm cen}, y_{\rm cen}), i, PA_{\rm kin}, {\rm r_t}, v_{\rm asym}$, were first reduced to 5 by using the inclination from the *HST* axis ratio. We also fixed the $(x_{\rm cen}, y_{\rm cen})$ parameters to the location of the stellar continuum peak within the collapsed cubes, a proxy for the centre of the gravitational potential-well, to leave only 3 free parameters to vary in the MCMC sampling. Due to the faintness of the continuum, there are several galaxies for which we could not reliably estimate the rotation centre using this method and instead set $(x_{\rm cen}, y_{\rm cen})$ to coincide with the peak [O III]λ5007 flux location (approach described in Harrison et al. 2017). Using the continuum to fix the rotation centre was generally more successful for the SSA22 galaxies, since the use of the *HK* filter increases the signal-to-noise of the continuum by collapsing over twice the wavelength range.

The intrinsic flux profile of these simulated [O III]λ5007 lines in the spatial direction was determined using the GALFIT model derived in § 3.3.1 (which assumes that the [O III]λ5007 emission profile follows the stellar profile) and the intrinsic velocity dispersion of the line was set to follow a uniform distribution with a default width of 50 km s^{-1}. This default line width was selected following examination of figure 10 of Wisnioski et al. (2015), which places observational constraints on the velocity dispersions of typical star-forming galaxies at $z \simeq 3.0$, and we discuss the impact of this assumption in § 3.9.1 by using sensible alternative values. The reported errors on $\sigma_{\rm int}$ take this assumption into account.

The simulated, intrinsic [O III]λ5007 cube was then convolved slice by slice using fast Fourier transform libraries with the *K*-band atmospheric seeing profile (Table 3.1). The velocity and velocity dispersion values were then re-measured in each spaxel to produce 'beam-smeared' 2D maps of the kinematic parameters. We fit the beam-smeared velocity field to the observed velocity field, using MCMC sampling with the python package 'emcee' (Foreman-Mackey et al., 2013) to vary the intrinsic model parameters,

seeking the combination of parameters which maximises the log-Likelihood function given by Equation 3.8, which fully accounts for the errors on the observed velocity field:

$$\ln\mathcal{L} = \frac{-0.5\sum_{i=1}^{N}(d_i - M_i)^2}{\delta_{v_i}^2} - \ln\left(\frac{1}{\delta_{v_i}^2}\right) \tag{3.8}$$

where δ_{v_i} are the observed velocity errors, d_i are the data points and M_i are the convolved model velocity values.

The MCMC sampling provided a distribution of parameter values around those which give the maximum-likelihood. We confirmed also by examining the individual parameter chains that the MCMC run has been properly 'burned-in' and that the parameter estimates converged around the 50th percentile values. The 16th and 84th percentiles of these distributions were used to assess the model uncertainties as described in § 3.9.1.

Following the construction of a convolved model cube and the measurement of the beam-smeared maps, we extract beam-smearing corrected values for $V_{\rm C}$ and $\sigma_{\rm int}$, as described throughout the following subsections. There have been several different methods used to extract $V_{\rm C}$ and $\sigma_{\rm int}$ in previous surveys at different redshifts. We select a set of comparison samples with similar galaxy selection criteria and kinematic parameter extraction methods to those described above in order to make comparisons with the KDS across different redshift slices (see § 3.4). We have re-evaluated the means and medians of the kinematic properties in these samples in order to make fair and reliable comparisons. An overview of the comparison samples is provided in supplementary material § 3.7.1, which also describes the approach used to compute average parameter values.

Beam-smearing corrected rotation velocities

The intrinsic velocity, $V_{\rm C}$, was found by reading off from the best-fitting intrinsic 2D model grid at the intrinsic $2R_{1/2}$ value ($\simeq 3.4R_{\rm d}$, where $R_{\rm d}$ is the scale length for an

exponential disk). This extraction radius is shown with the vertical red dashed line in the panels of Fig. 3.3 showing the 1D velocity extraction. The V_C value extracted at $2R_{1/2}$ is a commonly used measure of the 'peak' of the rotation curve (e.g. Miller et al., 2011; Stott et al., 2016; Pelliccia et al., 2017; Harrison et al., 2017; Swinbank et al., 2017) and extracting the velocity at $\geqslant 2R_{1/2}$ can be crucial for measuring the majority of the total angular momentum (e.g. Obreschkow et al., 2016; Harrison et al., 2017; Swinbank et al., 2017). This is similar to the measurement of the velocity at the radius enclosing 80% of the total light, V_{80} ($\simeq 3R_d$), (Tiley et al., 2016).

The mean and median V_C values for the isolated field sample are $76.7^{+4.9}_{-4.5}$km s^{-1} and $57.0^{+6.6}_{-6.3}$km s^{-1} respectively, which are less than observed for lower redshift typical star-forming galaxies (see § 3.4.1 for a discussion). In order to determine the beam-smearing correction factor, we also extracted the velocity from the beam-smeared model at the convolved $2R_{1/2}$ radius, represented by the vertical blue dashed line in Fig. 3.3, to recover the beam-smeared velocity, V_{BS}. The magnitude of the beam-smearing correction, (V_C/V_{BS}), has a mean and median value of 1.29 and 1.21 for the isolated field sample and we discuss the observational and model uncertainties which combine to give the V_C errors in § 3.9.1.

In 14/39 of the isolated field sample galaxies, the intrinsic $2R_{1/2}$ fiducial radius used to extract V_C from the model was greater than the last observed radius, however only 2 galaxies required extrapolation > 0.4″ (i.e. 2 KMOS pixels) with a mean extrapolation of 0.17″. The extent of the extrapolation for each galaxy is made clear throughout the kinematics plots in supplementary material § 3.10, with the intrinsic and convolved $2R_{1/2}$ extraction radii marked on each velocity thumbnail.

Beam-smearing corrected intrinsic dispersions

Convolution of the model velocity field with the seeing profile produces a peak in the beam-smeared velocity dispersion map at the centre of rotation. The model therefore provides a beam-smearing correction for the velocity dispersion in every spaxel. This

is dependent primarily on the magnitude of the velocity gradient across the parameter maps, where larger velocity gradients result in larger central velocity dispersions.

By comparing the best-fitting simulated datacube with the assumption for the isotropic velocity dispersion, we recovered the beam-smearing correction for each galaxy. The 2D beam-smearing correction map, $\sigma_{\rm BS}$, was computed on a spaxel-by-spaxel basis as the difference between the beam-smeared dispersion produced by the model and the assumed intrinsic velocity dispersion of 50 km s^{-1} i.e. $\sigma_{\rm BS,i} = \sigma_{\rm simulated,i} - \sigma_{\rm assumed,i}$ (where $\sigma_{\rm assumed,i}$ was fixed at 50 km s^{-1} as described in § 3.3.2 and $\sigma_{\rm simulated,i}$ is the simulated velocity dispersion recovered under this assumption). The impact of the value of $\sigma_{\rm assumed}$ on the magnitude of the $\sigma_{\rm BS,i}$ correction is discussed further in § 3.9.1 and the $\sigma_{\rm int}$ errors take this into account. We note also that not all of the observed $\sigma_{\rm int}$ profiles peak in the centre, and since we did not attempt to fit the velocity dispersions, this is a feature the model could not reproduce.

To measure the $\sigma_{\rm int}$ value for each galaxy in our sample, we applied Equation 3.9 in each spaxel to derive an intrinsic sigma map, where $\sigma_{\rm g,i}$ is the value in the ith spaxel recovered from the gaussian-fit to the [O III]λ5007 emission line.

$$\sigma_{\rm cor,i} = \sqrt{\left(\sigma_{\rm g,i} - \sigma_{\rm BS,i}\right)^2 - \sigma^2_{\rm inst,i}} \tag{3.9}$$

In Equation 3.9 we have subtracted the beam-smearing correction linearly following the analysis presented in Appendix A of Stott et al. (2016), which shows that linear subtraction recovers input velocity dispersion values more accurately than subtraction in quadrature. However, we note that if quadrature subtraction is applied the sample mean velocity dispersion increases by $\simeq$ 5%, which does not affect the results of this chapter. The median of the $\sigma_{\rm cor,i}$ map is taken as the $\sigma_{\rm int}$ value for each galaxy and the median of the observed map is the $\sigma_{\rm obs}$ value (see Table 3.3). The mean and median $\sigma_{\rm int}$ values in the isolated field sample are $70.8^{+3.3}_{-3.1}$km s^{-1} and $71.0^{+5.0}_{-4.8}$km s^{-1} respectively, higher than for typical star-forming galaxies at lower redshift as has been extensively reported (e.g. Genzel et al., 2006, 2008; Förster Schreiber et al., 2009; Law et al., 2009; Gnerucci et al., 2011; Epinat et al., 2012; Wisnioski et al., 2015). The

magnitude of the beam-smearing correction, ($\sigma_{\rm int}/\sigma_{\rm obs}$), has a mean and median value of 0.81 and 0.79 respectively for the isolated field sample.

To test the robustness of our beam-smearing correction approach, we also computed $V_{\rm C}$ and $\sigma_{\rm int}$ values using the independently derived correction factors, which are a function of the velocity gradient and the ratio $R_{1/2}/R_{\rm psf}$, detailed in Johnson et al. (2018) and used to evaluate the final kinematic parameters in Harrison et al. (2017). These correction factors were applied to $V_{\rm BS}$ and $\sigma_{\rm obs}$ in order to compute $V_{\rm C}$ and $\sigma_{\rm int}$. When following this approach, for the isolated field sample, the derived $V_{\rm C}$ values agree with our own corrections to within $\simeq$ 10%, and the $\sigma_{\rm int}$ values to within $\simeq$ 5%, which is within the errors on these quantities. This confirmed that the choice of modelling and kinematic parameter extraction described above is consistent with the $z \simeq 0.9$ KROSS methods (Harrison et al., 2017). We also observed that the shape and width of the observed and intrinsic kinematic parameter distributions are equivalent, suggesting that the corrections do not over-extrapolate from the raw numbers.

We present the observed and model determined kinematic parameters in Table 3.3 for the isolated field sample.

Kinematic and photometric axes

The dynamical model parameter $PA_{\rm Kin}$ was compared with $PA_{\rm morph}$ computed by GALFIT in § 3.3.1 to indicate the degree of misalignment between the gaseous and stellar components of the galaxies. This follows the analysis described in e.g. Epinat et al. 2008b, 2012; Barrera-Ballesteros et al. 2014, 2015; Wisnioski et al. 2015; Harrison et al. 2017; Swinbank et al. 2017, where rotating galaxies generally have $\Delta PA \equiv |PA_{\rm kin} - PA_{\rm morph}| < 30^{\circ}$, with the discrepancy increasing as a function of axis ratio due to $PA_{\rm morph}$ becoming more difficult to measure as the galaxy becomes more 'face-on'. Significant misalignment between the two axes can be a signature of galaxy interaction.

The resolved KDS galaxies at $z \simeq 3.5$ generally have larger ΔPA values than those

at lower redshift (median $\Delta PA = 37°$) and this observation has several potential explanations. For the majority of galaxies we are not in a regime where prominent morphological features are resolved in the *HST* imaging, so that $PA_{\rm morph}$ is biased by single Sérsic fits as described in Rodrigues et al. (2017). Another factor which could be partially driving increased misalignment in the KDS is the use of the full observed 2D velocity field to determine the kinematic position angle. This generally does not give the same answer as simply connecting the velocity extrema, as we verified by rotating $PA_{\rm Kin}$ in 1° increments and choosing the value which maximises the velocity gradient, calling this $PA_{\rm rot}$. If the direction of the 'zero-velocity strip' across the centre of the velocity maps is not perpendicular to the line connecting the velocity extrema, the $PA_{\rm Kin}$ determined from MCMC will be different to the $PA_{\rm rot}$ determined from rotation (e.g. GOODS-S galaxy bs006541 in fig. 3.11). As a test, we have verified that extracting $V_{\rm C}$ values along $PA_{\rm rot}$ (which differs from $PA_{\rm Kin}$ typically by only a few degrees) makes only a small difference to the final $V_{\rm C}$ values, with the errors dominated by measurement uncertainties and model assumptions. Further, the increased prevalence of random motions at $z \simeq 3.5$ (see § 3.4.2), in comparison to at intermediate redshift, could partially explain misalignment of the stellar and gaseous components.

3.3.3 Morpho-Kinematic classification

We proceeded to further divide the isolated field sample galaxies into two subsamples on the basis of the ratio $V_{\rm C}/\sigma_{\rm int}$. This is a simple empirical diagnostic for whether a galaxy is 'rotation-dominated' with $V_{\rm C}/\sigma_{\rm int} > 1$, or 'dispersion-dominated' with $V_{\rm C}/\sigma_{\rm int} < 1$ (i.e. a method to measure the prevalence of rotational and random motions; Epinat et al., 2012; Wisnioski et al., 2015; Stott et al., 2016; Harrison et al., 2017). Previous studies have used various classification schemes of varying complexity to identify rotation-dominated galaxies which also appear to be 'disk-like' and we briefly mention some of these in § 3.3.3. We describe our simple classification criteria for the isolated field sample based on a joint consideration of the high-resolution photometry and derived kinematic parameters in § 3.3.3 and mention the KDS merger candidates in more detail in the following section.

Table 3.3: The dynamical properties for the KDS isolated field sample galaxies. The observed properties are measured directly from the extracted two-dimensional maps (with $\sigma_{\rm obs}$ corrected for the KMOS instrumental resolution), whereas $V_{\rm C}$ and $\sigma_{\rm int}$ have been corrected for the effects of beam-smearing as described throughout the text. Each galaxy is classified as rotation-dominated or dispersion-dominated if the ratio $V_{\rm C}/\sigma_{\rm int}$ is greater than or less than 1 respectively, as highlighted in the 'Class' column.

ID	$V_{\rm obs}$(km s^{-1})	$V_{\rm C}$(km s^{-1})	$\sigma_{\rm obs}$(km s^{-1})	$\sigma_{\rm int}$(km s^{-1})	$V_{\rm C}/\sigma_{\rm int}$	PA$^{\circ}_{kin}$	Class[a]
b012141_012208	32±13	93^{+48}_{-40}	90±18	63^{+28}_{-30}	$1.47^{+1.04}_{-0.92}$	122^{+9}_{-9}	RD
b15573	61±21	81^{+30}_{-33}	107±23	84^{+28}_{-26}	$0.97^{+0.47}_{-0.52}$	118^{+10}_{18}	DD
bs006516	49±4	61^{+10}_{-9}	58±8	45^{+10}_{-9}	$1.35^{+0.37}_{-0.38}$	144^{+4}_{-4}	RD
bs006541	33±8	65^{+24}_{-20}	92±7	83^{+9}_{-16}	$0.78^{+0.34}_{-0.26}$	23^{+3}_{-4}	DD
bs008543	68±13	111^{+20}_{-16}	94±7	71^{+13}_{-10}	$1.56^{+0.37}_{-0.38}$	114^{+1}_{-1}	RD
bs009818	39±16	84^{+39}_{-23}	92±19	79^{+21}_{-31}	$1.06^{+0.65}_{-0.41}$	72^{+13}_{-15}	RD
bs014828	31±15	46^{+23}_{-23}	93±15	88^{+15}_{-17}	$0.53^{+0.28}_{-0.28}$	44^{+15}_{-11}	DD
bs016759	55±9	110^{+30}_{-21}	77±11	57^{+17}_{-22}	$1.93^{+0.93}_{-0.7}$	75^{+6}_{-6}	RD
lbg_20	20±6	56^{+30}_{-19}	47±6	40^{+7}_{-21}	$1.39^{+1.04}_{-0.53}$	41^{+9}_{-10}	RD
lbg_24	26±6	42^{+9}_{-7}	57±5	51^{+5}_{-6}	$0.82^{+0.21}_{-0.17}$	64^{+3}_{-4}	DD
lbg_25	14±5	33^{+13}_{-13}	47±6	41^{+6}_{-8}	$0.8^{+0.37}_{-0.34}$	87^{+7}_{-12}	DD
lbg_30	20±6	66^{+19}_{-17}	89±11	77^{+14}_{-17}	$0.86^{+0.32}_{-0.27}$	46^{+6}_{-42}	DD
lbg_32	65±5	121^{+13}_{-12}	100±13	76^{+16}_{-15}	$1.58^{+0.36}_{-0.37}$	11^{+2}_{-1}	RD
lbg_38	26±7	97^{+72}_{-34}	71±10	53^{+16}_{-53}	$1.82^{+2.3}_{-0.86}$	47^{+2}_{-3}	RD
lbg_91	48±10	91^{+15}_{-18}	94±8	71^{+16}_{-14}	$1.28^{+0.33}_{-0.39}$	40^{+5}_{-3}	RD
lbg_94	18±8	34^{+19}_{-15}	60±6	55^{+7}_{-8}	$0.62^{+0.36}_{-0.29}$	41^{+18}_{-9}	DD

Table 3.3: Continued.

ID	$V_{\rm obs}$(km s^{-1})	$V_{\rm C}$(km s^{-1})	$\sigma_{\rm obs}$(km s^{-1})	$\sigma_{\rm int}$(km s^{-1})	$V_{\rm C}/\sigma_{\rm int}$	PA$^{\circ}_{kin}$	Class[a]
lbg_105	11±8	32^{+17}_{-16}	61±18	59^{+18}_{-18}	$0.54^{+0.34}_{-0.32}$	170^{+4}_{-7}	DD
lbg_109	26±8	53^{+21}_{-15}	96±16	91^{+16}_{-18}	$0.58^{+0.26}_{-0.2}$	157^{+11}_{-11}	DD
lbg_111	36±12	58^{+24}_{-17}	85±14	81^{+14}_{-16}	$0.71^{+0.33}_{-0.25}$	168^{+4}_{-5}	DD
lbg_112	27±3	63^{+19}_{-11}	88±5	78^{+8}_{-11}	$0.81^{+0.28}_{-0.17}$	4^{+34}_{-12}	DD
lbg_113	50±20	41^{+41}_{-29}	113±22	108^{+23}_{-25}	$0.39^{+0.39}_{-0.29}$	1^{+34}_{-26}	DD
lbg_121	33±9	54^{+33}_{-24}	67±18	50^{+21}_{-27}	$1.06^{+0.87}_{-0.65}$	55^{+34}_{-26}	RD
lbg_124	9±8	32^{+27}_{-18}	52±19	46^{+19}_{-23}	$0.71^{+0.69}_{-0.5}$	39^{+20}_{-14}	DD
*n3_006	36±23	81^{+47}_{-29}	133±26	125^{+27}_{-31}	$0.65^{+0.41}_{-0.27}$	156^{+13}_{-12}	DD
n3_009	21±9	49^{+26}_{-16}	56±13	48^{+14}_{-45}	$1.01^{+1.1}_{-0.45}$	20^{+28}_{-25}	RD
n_c3	26±8	51^{+17}_{-18}	84±11	72^{+12}_{-13}	$0.72^{+0.28}_{-0.29}$	137^{+4}_{-15}	DD
lab18	23±11	41^{+17}_{-14}	69±6	62^{+7}_{-15}	$0.67^{+0.32}_{-0.24}$	54^{+18}_{-26}	DD
*lab25	37±11	48^{+22}_{-16}	58±8	49^{+10}_{-19}	$0.98^{+0.59}_{-0.4}$	72^{+14}_{-13}	DD
s_sa22a-d3	53±17	109^{+52}_{-32}	115±13	93^{+20}_{-36}	$1.16^{+0.72}_{-0.43}$	30^{+2}_{-2}	RD
s_sa22b-c20	66±18	139^{+33}_{-30}	97±17	48^{+34}_{-51}	$2.87^{+3.12}_{-2.14}$	37^{+26}_{-11}	RD
*s_sa22b-d5	27±10	57^{+26}_{-23}	38±20	23^{+23}_{-18}	$2.45^{+3.44}_{-2.41}$	60^{+19}_{-19}	RD
s_sa22b-d9	32±14	46^{+22}_{-15}	83±8	73^{+10}_{-17}	$0.63^{+0.33}_{-0.23}$	12^{+23}_{-7}	DD
*s_sa22b-md25	44±15	57^{+34}_{-24}	87±19	75^{+21}_{-30}	$0.76^{+0.56}_{-0.39}$	9^{+12}_{-7}	DD

[a] RD = Rotation-Dominated; DD = Dispersion-Dominated

* No *HST* coverage; see Table 3.2

KDS merger candidates

We considered both the HST imaging and information from the [O III]λ5007 line within the datacubes when classifying galaxies as mergers, using the following three criteria: i) Multiple components were detected in the high-resolution, HST imaging, which cannot be fit with a single GALFIT component; ii) The [O III]λ5007 flux maps examined in QFitsView (Ott & Thomas, 2012) had more than one peak across the spatial extent of the cube; iii) The object spectrum showed peaks at multiple wavelengths, rather than a smoothly varying line profile. When fit using the procedure described in § 3.3.2, this manifests as extreme rotation velocities and velocity dispersion values in the velocity and velocity dispersion maps.

Galaxies which met all three of these criteria were classed as mergers. One benefit of studying the *HST* photometry in tandem with the kinematics was to uncover 'rotation doppelgängers', which mimic disk rotation from a purely kinematic perspective (i.e. can be fit with the arctangent model (see § 3.3.2) with small residuals), but are likely two or more potentially interacting components at slightly different redshifts (e.g. the bottom grid in Fig. 3.3).

This has been discussed in Hung et al. (2015), where redshifted local interacting galaxies are misclassified as single rotating disks on the basis of their kinematics. In short, the galaxies with multiple photometric components do not always have disordered kinematics and so the kinematics alone are not sufficient for classification. It was difficult to distinguish in some cases between two *HST* components rotating together in a single disk (i.e. clumpy disk galaxies e.g. Elmegreen et al. 2004; Bournaud et al. 2007; Förster Schreiber et al. 2009) with a receding and approaching side and two [O III]λ5007 emitting blobs which are offset along the line of sight. We chose to omit these galaxies from the analysis described in § 3.4, to minimise the risk of contaminating the kinematics of the sample with mergers.

In 6/39 of the resolved KDS field galaxies (one count per merger) the merging classification criteria were met, which translates into a merger rate of 15%. In 8/9

resolved KDS cluster galaxies the criteria were met, translating into a merger rate of 89% (see Table 3.1). The higher merger rate observed for the cluster galaxies is perhaps unsurprising since they were drawn from a higher density environment, and these interactions will inevitably have major consequences for the consumption and stripping of gas, as well as the morphological and dynamical evolution within these galaxies. The observation of frequent mergers, which cause major kinematic disturbances, is also in support of the evidence that galaxies living at the peak of the cosmic density field at lower redshift tend to be redder, less active and morphologically early-type, having presumably rapidly exhausted their gas supply throughout these violent interactions at high-redshifts (e.g. Steidel et al., 1998; White et al., 2007; Kodama et al., 2007; Zheng et al., 2009). As mentioned above, we omit galaxies in the cluster pointing (SSA22-P1) from the results presented in § 3.4 due to the complexity added by galaxy interactions to the interpretation of cluster galaxy velocity fields. We keep the KDS galaxies without *HST* coverage on the basis that we do not identify double components in the [O III]λ5007 maps. In the kinematic grids throughout 3.12 (as well as the bottom grid in 3.3) we present the *HST* imaging, kinematic maps and one-dimensional kinematic extractions for the KDS merger candidates in both the field and cluster environments.

Isolated field sample classification

As mentioned above, various methods have been used throughout the literature to quantify the kinematic structure of star-forming galaxies at different redshifts. These include the kinemetry approach which quantifies aysmmetries in the 2D moment maps described in Shapiro et al. (2008) and applied throughout in Förster Schreiber et al. (2009) and Cresci et al. (2009). In Wisnioski et al. (2015) a set of 5 criteria (see their section 4) identify rotation-dominated and disky galaxies by assessing the smoothness of the velocity gradient, the degree of rotational support through the ratio of the velocity to velocity dispersion, V_{rot}/σ, the ΔPA misalignment and the position of the kinematic centre in relation to both the peak in the velocity dispersion map and the centroid of the continuum centre (also see Rodrigues et al. 2017 for a re-analysis of KMOS^{3D} data at $z \simeq 1$ using the same criteria). In Epinat et al. (2012), a detailed description of a

morpho-kinematic classification is outlined in their section 4, based on the proximity of counterparts in the imaging, ΔPA and V_C/σ_{int}. In Gnerucci et al. (2011) an inclined plane is fit to the velocity map and the χ^2 of this fit is evaluated in order to test for the presence of smooth velocity gradients, which they find for the 11/33 galaxies described in § 3.7.10.

We used a simple approach (dictated by the signal-to-noise of the isolated field sample) and calculated rotation and dispersion-dominated percentages on the basis of V_C/σ_{int} alone with repsect to the total number of resolved galaxies in the field environment (39, see Table 3.1). The morphologically isolated KDS field galaxies were classified as rotation-dominated if $V_C/\sigma_{int} > 1$, 14/39 or 36% of the sample, and dispersion-dominated if $V_C/\sigma_{int} < 1$, 19/39 or 49% of the sample, as indicated in the final column of Table 3.3. We plot the best-fitting smeared and intrinsic models for the isolated field galaxies in supplementary material § 3.10, where the galaxies have been divided into rotation and dispersion-dominated categories in Figures 3.10 and 3.11 respectively.

Summary of the final sample for further analyses

In summary, we analysed 77 typical $z \simeq 3.5$ SFGs spanning both cluster and field environments, finding 63 with integrated [O III]λ5007 emission (§ 3.2.2). This sample was refined to 48 galaxies (62%) with spatially-resolved [O III]λ5007 emission (§ 3.3.2). Due to the unusually high merger-candidate rate of 89% in the cluster environment (identified by searching the high-resolution *HST* imaging for photometric counterparts), we omitted the 9 spatially-resolved galaxies in SSA22-P1 from further consideration. In the remaining sample of 39 field environment galaxies we identified 6 merger candidates, giving a field galaxy merger rate of 15%, which constitute the 'merger field sample'. The remaining 33 galaxies constitute the 'isolated field sample', for which we measured morphological parameters using GALFIT to fit exponential disks to the *HST* imaging (see § 3.3.1 and Table 3.2) and derived beam-smearing corrected measurements of the rotation velocities extracted at $2R_{1/2}$ and the intrinsic velocity dispersions (see § 3.3.2 and Table 3.3).

The isolated field sample was further divided into 14/39 rotation-dominated galaxies (36% with respect to full field sample) and 19/39 dispersion-dominated galaxies (49%) on the basis of the ratio V_C/σ_{int} (see § 3.3.3), with the remaining 6/39 (15%) classified as mergers.

Throughout the remainder of the chapter we discuss the derived kinematic properties of the isolated field sample in further detail.

3.4 Results

In the previous sections we presented our morphological and kinematic analyses for the 77 galaxies covering both cluster and field environments in the KDS survey. These galaxies are representative of typical star-forming galaxies at $z \simeq 3.5$, as verified by comparing with fits to the galaxy main-sequence at this redshift. Through a combined morpho-kinematic classification described in § 3.3.3, we first reduced the sample to 39 spatially-resolved field environment galaxies and then to 33 isolated field sample galaxies which have spatially-resolved [O III]λ5007 emission and are morphologically isolated (i.e. not merger candidates), which is the largest sample of galaxies observed with integral-field spectroscopy at this redshift. For these galaxies we measured morphological properties as listed in Table 3.2 and extracted intrinsic, beam-smearing corrected measurements of the rotation velocities, V_C, and velocity dispersions, σ_{int}, as listed in Table 3.3, which we used to classify the galaxies as either rotation or dispersion-dominated. The morphological and kinematic grids for these 33/39 isolated field sample galaxies and the 6/39 merger candidates are plotted in supplementary material § 3.10.

Throughout the following sections we analyse the derived kinematic parameters of the isolated field sample, placing the galaxies in the context of galaxy evolution using the comparison samples spanning a wide redshift baseline described in supplementary material § 3.7.1. In supplementary material § 3.7.1 we describe our careful assessment

of lower redshift samples from the literature, using tabulated data where possible to re-compute mean and median V_C and σ_{int} values. These fair comparisons help to disentangle true evolution in the kinematic properties of typical star-forming galaxies from systematic effects originating in disparate measurement techniques or galaxy selection criteria. During the following sections we will make statements about dynamical evolution by connecting the dots of these different surveys, assuming that they trace the average properties of typical star-forming galaxies at their respective mean redshifts.

We proceed first to investigate the relationship between rotation velocity and stellar mass for both the rotation and dispersion-dominated isolated field galaxies.

3.4.1 Rotation velocity and stellar mass

In the ΛCDM paradigm, galaxies form when baryons accumulate and cool in the centres of dark matter halos, subsequently forming a rotating disk of stars and gas. The relationship between stellar mass and rotation velocity describes the connection between the luminous mass and the total dynamical mass in a system. The connection has been studied extensively at low redshift (e.g. Bell & de Jong, 2001; Rhee et al., 2003; Reyes et al., 2011) with fits to late-type, rotating galaxies in the $V_C - M_\star$ plane having a well-defined slope and normalisation. Observing this 'stellar mass Tully-Fisher relation' at different epochs thus offers constraints for galaxy formation and evolution models seeking to explain simultaneously the properties of dark matter halos and the dynamical properties of disk galaxies (e.g. Dubois et al., 2014; Vogelsberger et al., 2014; Schaye et al., 2015). In principle, studying whether the stellar mass Tully-Fisher relation evolves with redshift gives us information about when galaxies accumulate their stellar mass and rotation velocities. Any offset from the local relation towards lower $M_\star$ values at fixed rotation velocity suggests that the dynamical mass is in place, but the stellar mass is yet to be formed (e.g. Puech et al., 2008; Cresci et al., 2009; Puech et al., 2010; Gnerucci et al., 2011; Swinbank et al., 2012a; Straatman et al., 2017; Übler et al., 2017). As has been discussed recently, information about the

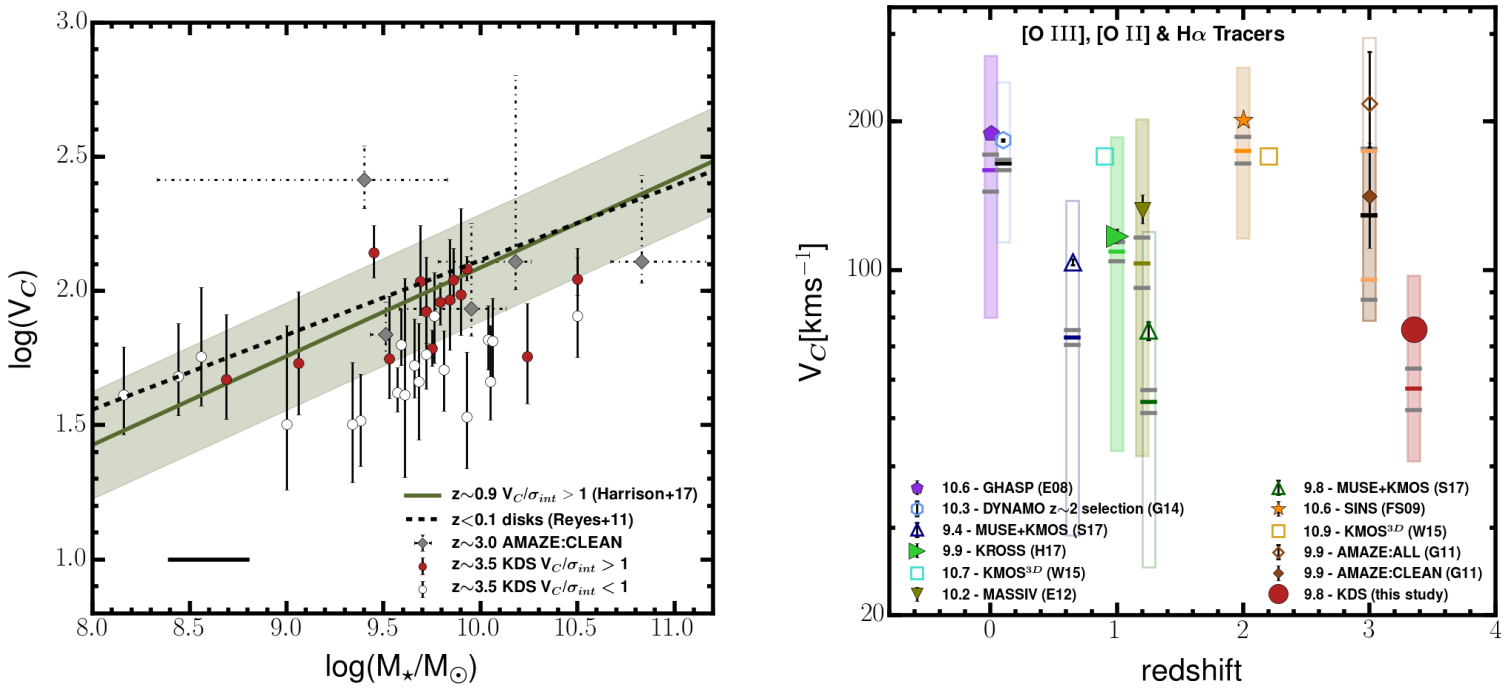

Figure 3.4: *Left:* We plot $\log(V_C)$ vs. $\log(M_\star/M_\odot)$ for the isolated field sample, with the rotation-dominated galaxies in red and dispersion-dominated galaxies with the hollow symbols. We also plot with the solid green line the $z \simeq 0.9$ relation recovered from a fit to $\simeq 400$ rotation-dominated galaxies from the KROSS survey Harrison et al. (2017), with the shaded region showing the associated $\simeq$0.2 dex scatter on the fit. This $z \simeq 0.9$ relation shows no signifcant evolution from the fit to a local sample of spiral galaxies with $z < 0.1$, presented in Reyes et al. (2011). The rotation-dominated KDS galaxies, and galaxies classed as reliable from the AMAZE survey (Gnerucci et al., 2011), also show no evolution from this relation within the scatter, with the dispersion-dominated galaxies scattering below the relation. This highlights the need for careful sample selection when constructing this relation. *Right:* The mean, median and distributions of the comparison sample V_C measurements are plotted against redshift. The symbol positions with black errorbars (some not visible), show the mean values and the horizontal filled and grey bars show the median values and associated errors. Note that the median errors for the AMAZE Clean sample are shaded orange to avoid confusion with the full sample. The filled symbols and shaded regions denote surveys deemed directly comparable (as explained in supplementary material § 3.7.1), and the mean mass of each survey (in units of $\log(M_\star/M_\odot)$) is listed beside the survey name. The V_C distributions in each of the individual studies are wide, reflecting the galaxy diversity within each sample. The low mean value of V_C in the KDS isolated field sample is driven mainly by averaging over a sample which contains a higher fraction of dispersion-dominated galaxies with lower rotation velocities.

redshift evolution of gas fractions, $f_g = M_{\rm gas}/{\rm M_{bar}}$ where $\rm M_{bar}$ is the baryonic mass, disk mass fractions, $\rm m_d = M_{bar}/M_H$ where $\rm M_H$ is the halo mass, dark matter fractions, $f_{\rm DM}(R_{1/2}) = V^2_{\rm DM}(R_{1/2})/V^2_C(R_{1/2})$ where $V_{\rm DM}$ is the dark matter circular velocity, may also be encoded in measured offsets from the local stellar mass Tully-Fisher relation (Wuyts et al., 2016b; Übler et al., 2017; Genzel et al., 2017).

We plot the relationship between rotation velocity and stellar mass for the isolated field sample in the left panel of Fig. 3.4. We compare to the relationship from Harrison et al. (2017), in which the inverse stellar mass Tully-Fisher relation is fit to $\simeq$ 400 star-forming galaxies with $9.5 < \log({\rm M_\star/M_\odot}) < 10.5$ at $z \simeq 0.9$, measured to be rotation-dominated with $V_{\rm C}/\sigma_{\rm int} > 1$. This is the closest matched sample in terms of analysis and selection criteria, therefore providing a robust comparison. The data are used to constrain parameters 'a' and 'b' in the equation $logV_{\rm C} = b + a[logM_\star - 10.10]$ (see their section 4.2) finding $a_{z=0.9} = 0.33 \pm 0.11$ and $b_{z=0.9} = 2.12 \pm 0.04$. We plot this best fit relation with the solid green line, with the green shaded region giving the typical scatter of 0.2 dex along the velocity axis.

The rotation-dominated KDS isolated field sample galaxies are broadly consistent within the scatter with the $z \simeq 0.9$ relation, but with a tendency to lie below the relation. When considered alone, the mean velocity of the rotation-dominated isolated field sample galaxies ($V_{\rm C} = 96.7^{+7.3}_{-7.2}{\rm km\,s^{-1}}$) at their mean mass of $\log({\rm M_\star/M_\odot}) = 9.8$ is $\simeq 0.05$ dex beneath the KROSS relation at the same mass. The dispersion-dominated KDS galaxies sit clearly separated and below the $z \simeq 0.9$ relation, bringing significant scatter to lower $V_{\rm C}$ values at fixed $\rm M_\star$ as is also observed in $z \simeq 0.9$ dispersion-dominated galaxies and for early-type galaxies in the local Universe (e.g. Romanowsky & Fall, 2012). We plot also the five galaxies from the AMAZE Clean ($z \simeq 3$) sample, which are consistent within the scatter with the relation for typical star-forming galaxies at $z \simeq 0.9$. The $z \simeq 0.9$ fit parameters are consistent with those measured in the local Universe, $a_{z=0} = 0.278 \pm 0.010$ and $b_{z=0} = 2.142 \pm 0.004$, for a sample of $z < 0.1$ disks from Reyes et al. (2011), which are in a similar mass range to the KROSS galaxies in Harrison et al. (2017) and traced with Hα emission. In Reyes et al. (2011), $V_{\rm C}$ has been extracted at the same radius and we plot this $z \simeq 0.1$ local relation as the dashed

black line in the left panel of Fig. 3.4. The agreement between the parameters derived at $z \simeq 0$ and $z \simeq 0.9$ suggests that there is no evolution of the slope/normalisation of the stellar mass Tully-Fisher relation for rotation-dominated star-forming galaxies between these redshifts.

Studies of the redshift evolution of the stellar mass Tully-Fisher relation do not explain how individual, unperturbed galaxies move around the rotation velocity stellar mass plane with redshift. High-redshift galaxy surveys typically do not trace the progenitors of those at lower redshift, as evidenced by the larger observed stellar and baryonic masses (e.g. Cresci et al., 2009; Reyes et al., 2011; Wisnioski et al., 2015; Übler et al., 2017). Rather, these studies trace the evolution of the relation itself, the position of which is dictated by the mean properties of typical star-forming galaxies at each redshift slice. Some authors have reported that as redshift increases, the relation shifts towards lower masses at fixed rotation velocity (e.g. Puech et al., 2008; Cresci et al., 2009; Puech et al., 2010; Straatman et al., 2017; Übler et al., 2017). However most find that when selecting rotation-dominated galaxies between $0.5 < z < 2$ (e.g. Flores et al., 2006; Miller et al., 2011; Kassin et al., 2012; Miller et al., 2012; Vergani et al., 2012; Miller et al., 2014; Contini et al., 2016; Di Teodoro et al., 2016; Pelliccia et al., 2017; Molina et al., 2017; Harrison et al., 2017) the results are consistent with zero evolution of the slope and zero-point of the relation. At $z \simeq 3$ observations are limited and in Gnerucci et al. (2011) an offset of -1.29 dex towards lower mass at fixed rotation velocity is claimed, although there is large degree of scatter between the individual galaxies, and the AMAZE Clean sample from Gnerucci et al. (2011) defined in § 3.7.10 is consistent with the $z \simeq 0$ relation.

Conclusions on the evolution of the stellar mass Tully-Fisher relation are a strong function of sample selection; in Tiley et al. (2016) where a stricter $V_C/\sigma_{int} > 3$ cut is applied, evolution to lower masses at fixed rotation velocity is observed at $z \simeq 0.9$, which is not the case when using the $V_C/\sigma_{int} > 1$ cut. Similarly in Cresci et al. (2009) evolution of the normalisation of the stellar mass Tully-Fisher relation is observed at

$z \simeq 2$ using only robust rotators from the SINS sample with mean $V_C/\sigma_{int} = 5$. In both cases the observed evolution is mainly the result of omitting rotation-dominated galaxies with lower V_C values. Conversely, fitting the stellar mass Tully-Fisher relation through a full sample including dispersion-dominated galaxies would shift the zero-point in the opposite sense. This new, robust analyses of typical $z \simeq 3.5$ star-forming galaxies is consistent with the majority of work that shows no evolution for rotation-dominated galaxies across all epochs.

In summary, with the KDS, we have added the largest sample of galaxies observed with integral-field spectroscopy at $z > 3$, and with our simple $V_C/\sigma_{int} > 1$ cut we conclude that the stellar mass Tully-Fisher relation defined for rotation-dominated star-forming galaxies appears to show no evolution between $z \simeq 0.1$ and $z \simeq 3.5$. However, as we will show in § 3.4.3, the $V_C/\sigma_{int} > 1$ subsamples become increasingly less representative of typical star-forming galaxies with increasing redshift. We also explore this in the context of the mean rotation velocities of the comparison samples throughout the following subsection.

The evolution of maximum circular velocity

In the right panel of Fig. 3.4 we plot the fractional error weighted mean, median and distributions of V_C values reported in the comparison (see supplementary material § 3.7.1) and KDS isolated field samples to highlight two observations:

- At each redshift slice the V_C distributions are extremely broad, with mean values sensitive to the average stellar mass of each survey.
- The mean isolated field sample V_C value is less than reported in the lower redshift comparison samples with similar mean $M_\star$ values. This is a result of averaging over a sample containing a higher fraction of dispersion-dominated galaxies.

The right panel of Fig. 3.4 indicates that the V_C distributions for the comparison and KDS isolated field samples are wide, reflecting the mass range and the mixture of rotation/dispersion-dominated galaxies which constitute the samples. The mass

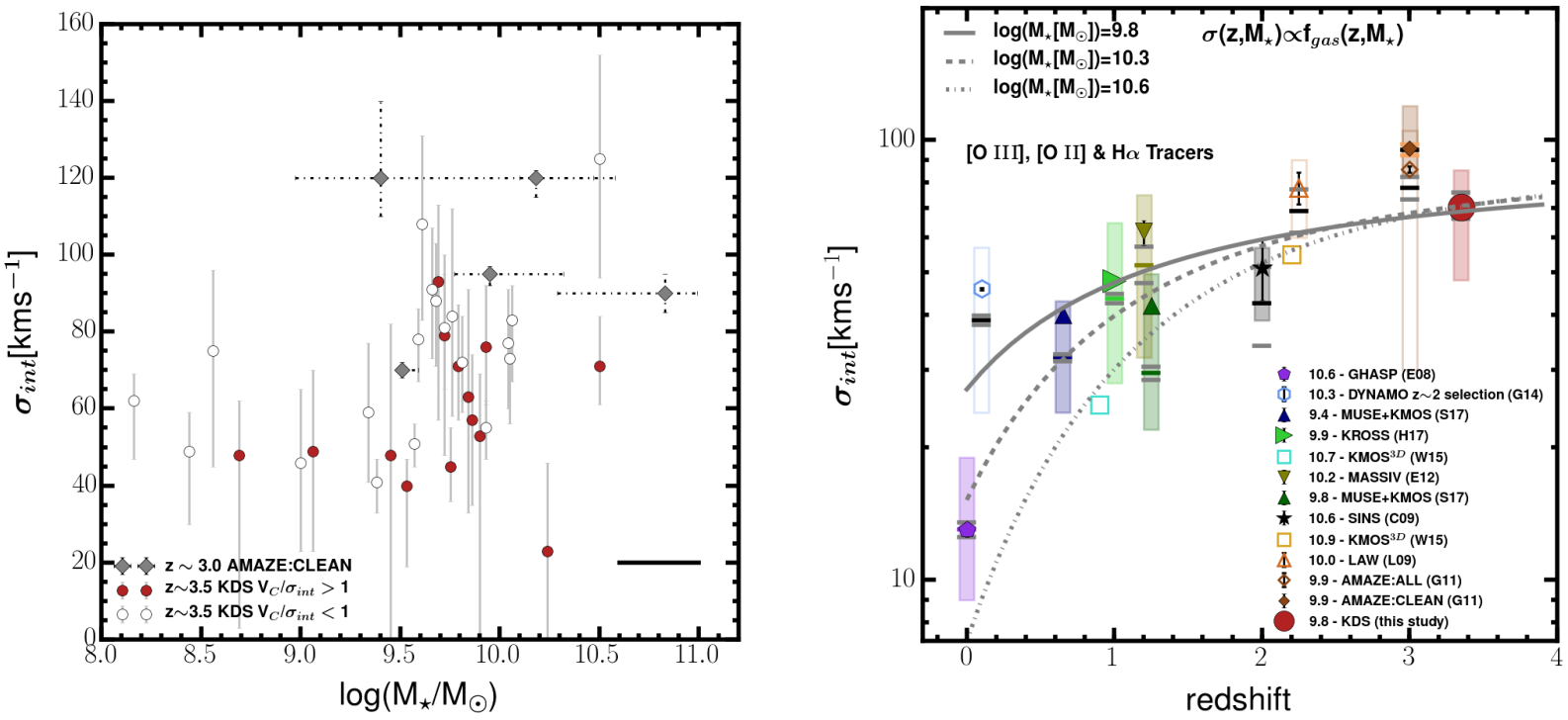

Figure 3.5: *Left:* We plot the intrinsic velocity dispersion against stellar mass for the rotation and dispersion-dominated isolated field sample galaxies, along with the AMAZE Clean ($z \simeq 3$) sample. The $\sigma_{\rm int}$ values are typically distributed between $40 - 90 {\rm km\,s^{-1}}$ and show no clear correlation with stellar mass, highlighting the complicated relationship between these two quantities. *Right:* We present a compilation of literature $\sigma_{\rm int}$ values plotted against redshift for surveys spanning $0 < z < 4$. The mean $\sigma_{\rm int}$ values increase from $\simeq 15 {\rm km\,s^{-1}}$ in the local Universe to $> 70 {\rm km\,s^{-1}}$ at $z > 3$. The symbol convention is the same as in the right panel of Figure 3.4. The $\sigma_{\rm int}(z, M_\star) \propto f_{\rm gas}(z, M_\star)$ scaling relation from Wisnioski et al. (2015), the form of which is discussed in § 3.5.1, is plotted for three different $M_\star$ values. These tracks indicate the way in which $\sigma_{\rm int}$ evolves for samples of star-forming galaxies with different mean $M_\star$ values, which is a proxy for the dynamical maturity of the galaxies. The KDS data point appears to be consistent with the scenario proposed in previous work, whereby the mean $\sigma_{\rm int}$ increases over cosmic time, with large scatter between individual galaxies, as a result of increased gas fractions (Wisnioski et al., 2015) and the more efficient accretion of cold gas driving disk instabilities (e.g. Law et al., 2009; Genzel et al., 2011).

distribution within each sample drives the location of the mean rotation velocity, with samples that have larger mean stellar mass values showing larger mean rotation velocities. The isolated field sample mean and median V_C values are $76.7^{+4.9}_{-4.5}$km s^{-1} and $57.0^{+6.6}_{-6.3}$km s^{-1}. However, the mean and median rotation velocity of the rotation dominated galaxies are $V_C = 96.7^{+7.3}_{-7.2}$km s^{-1} and $V_C = 93.0^{+8.1}_{-7.7}$km s^{-1} respectively, suggesting that averaging over a sample containing a large number of dispersion dominated galaxies brings the averages down.

It is difficult to assess whether the V_C values reported in the comparison samples (the modelling and extraction techniques differ as described in supplementary material § 3.7.1) are directly comparable. The GHASP, MASSIV, KROSS and KDS samples should in principle yield comparable V_C values which rely on extracting from the data at a fiducial radius or using a velocity shear value, but the comparison to the dynamical models of SINS and AMAZE is not so clear. Further caveats when making comparisons between the velocity distributions of different samples are variations in disk half-light radii and the spatial resolution of the observations. In Newman et al. (2013) it is shown that it is often not possible to resolve rotational structure in seeing-limited conditions, with this effect more severe for compact galaxies. Consequently, the non-uniform disk-sizes and spatial resolution across the comparison samples may result in additional variations between the inferred rotation velocities. As a result, mainly of the differences in mass distribution between the samples, we do not attempt to interpret any evolutionary trends from the right panel of Fig. 3.4. However, Simons et al. (2017) have demonstrated with a consistently selected and processed sample of star-forming galaxies between $0 < z < 2.5$, that there is a mild drop in rotation velocities with increasing redshift over this interval in both low and high-mass bins.

In a rotationally supported system, the circular velocity is set by the requirement to support the total mass in the system, i.e. the combination of gas mass, stellar mass and dark matter mass, against gravitational collapse. V_C increases with increasing total mass and so we would expect the systems with larger average stellar mass, assuming that these are indicative of systems with greater total mass, to have larger V_C, which appears generally to be the case in the right panel of Fig. 3.4 where the KMOS^{3D}, GHASP

and SINS galaxies have the largest inferred V_C values. Using the average stellar mass values and velocity extraction radii in the isolated field sample, $\log(M_\star/M_\odot) = 9.8$ and $2R_{1/2} = 3.2kpc$ respectively, and assuming simple, circular Keplerian orbits where the rotational motions alone support the mass of the system, we can calculate a rough lower limit of $\langle V_C \rangle > 95 \mathrm{km\,s^{-1}}$ for the baryonic material in the galaxies (since the inclusion of the gas mass and dark matter mass would raise this estimate). This value is greater than the mean and median values of the isolated field sample, but comparable to the mean and median of the rotation dominated galaxies, suggesting that rotation in these systems could support, at most, the stellar mass of the galaxy.

As mentioned above, the observation of a low mean V_C value in the full isolated field sample is primarily explainable through averaging over a sample with a higher fraction of dispersion-dominated galaxies with lower rotation velocities. This is seen in the left panel of Fig. 3.4 where the dispersion-dominated galaxies sit clearly below and separated from the stellar mass Tully-Fisher relation. However, it has also been discussed that pressure support, provided by turbulence and measured through the galaxy velocity dispersions, may partially compensate the gravitational force within galaxy disks and contribute to lowering the rotation velocities through an 'asymmetric drift' correction (e.g. Burkert et al., 2010; Newman et al., 2013; Genzel et al., 2017). This topic is discussed further throughout § 3.5.

We proceed to consider the cause of the high number of dispersion-dominated galaxies in our sample and the obvious candidate is the increase of velocity dispersion with redshift (e.g. Genzel et al., 2006, 2008; Förster Schreiber et al., 2009; Law et al., 2009; Gnerucci et al., 2011; Epinat et al., 2012; Wisnioski et al., 2015). There are also some galaxies in our sample where the observed velocity field has clear rotational structure and reaches flattening (e.g. see Fig. 3.11 lbg_24 with $\log(M_\star/M_\odot) = 9.75$), with inferred V_C smaller than σ_{int}. This suggests again that the increase in random motions could influence the rotation velocities and that the accumulation of a massive stellar population is necessary to stabilise a galaxy (e.g. Law et al., 2009, 2012c,b; Newman et al., 2013; Wisnioski et al., 2015). These ideas are explored in the following sections.

3.4.2 Velocity dispersions

In the left panel of Fig. 3.5 we plot the isolated field galaxies, split into dispersion and rotation-dominated classes, along with the AMAZE Clean ($z \simeq 3$) sample, in the $\sigma_{\rm int}$ vs. $M_\star$ plane. This is an interesting relationship to explore as it has been suggested that rotation velocity alone may not be a good tracer of total dynamical mass at high-redshift and that random motions traced by $\sigma_{\rm int}$ may contribute to supporting some fraction of this total dynamical mass (e.g. Kassin et al., 2007; Burkert et al., 2010; Kassin et al., 2012; Law et al., 2012c,b; Übler et al., 2017; Genzel et al., 2017). However, the extent to which the gaseous $\sigma_{\rm int}$ values reported here trace stellar mass is unclear, with physical processes such as disk turbulence, gas accretion and subsequent disk instabilities contributing to the magnitude of the velocity dispersion. All of these processes are also more prevalent at high-redshift (Genzel et al., 2006; Förster Schreiber et al., 2009; Law et al., 2009; Genzel et al., 2011; Wisnioski et al., 2015; Wuyts et al., 2016b), leaving $\sigma_{\rm int}$ as a challenging property to interpret.

We observe no clear correlation between the gaseous velocity dispersion and stellar mass in any of the sub-samples, highlighting the complicated relationship between these quantities at high-redshift. The beam-smearing corrected $\sigma_{\rm int}$ values, with distribution median, 16th percentile and 84th percentile equal to $71.0 {\rm km\,s^{-1}}$, $48.0 {\rm km\,s^{-1}}$ and $85.4 {\rm km\,s^{-1}}$ respectively, are larger than in the local Universe where typically $\sigma_{\rm int} = 10 - 20 {\rm km\,s^{-1}}$ (Epinat et al., 2008a) (see § 3.4.2 and § 3.5 for a discussion). Generally, the dispersion-dominated galaxies have higher $\sigma_{\rm int}$ values in the left panel of Fig. 3.5, however the rotation-dominated galaxies also span the full distribution width.

The evolution of velocity dispersion

In the right panel of Fig. 3.5 we plot the fractional error weighted mean, median and distributions of $\sigma_{\rm int}$ from the comparison and KDS isolated field samples. The values increase sharply from $\sigma_{\rm int} \simeq 10 - 20 {\rm km\,s^{-1}}$ as traced by $z \simeq 0$ measurements of typical

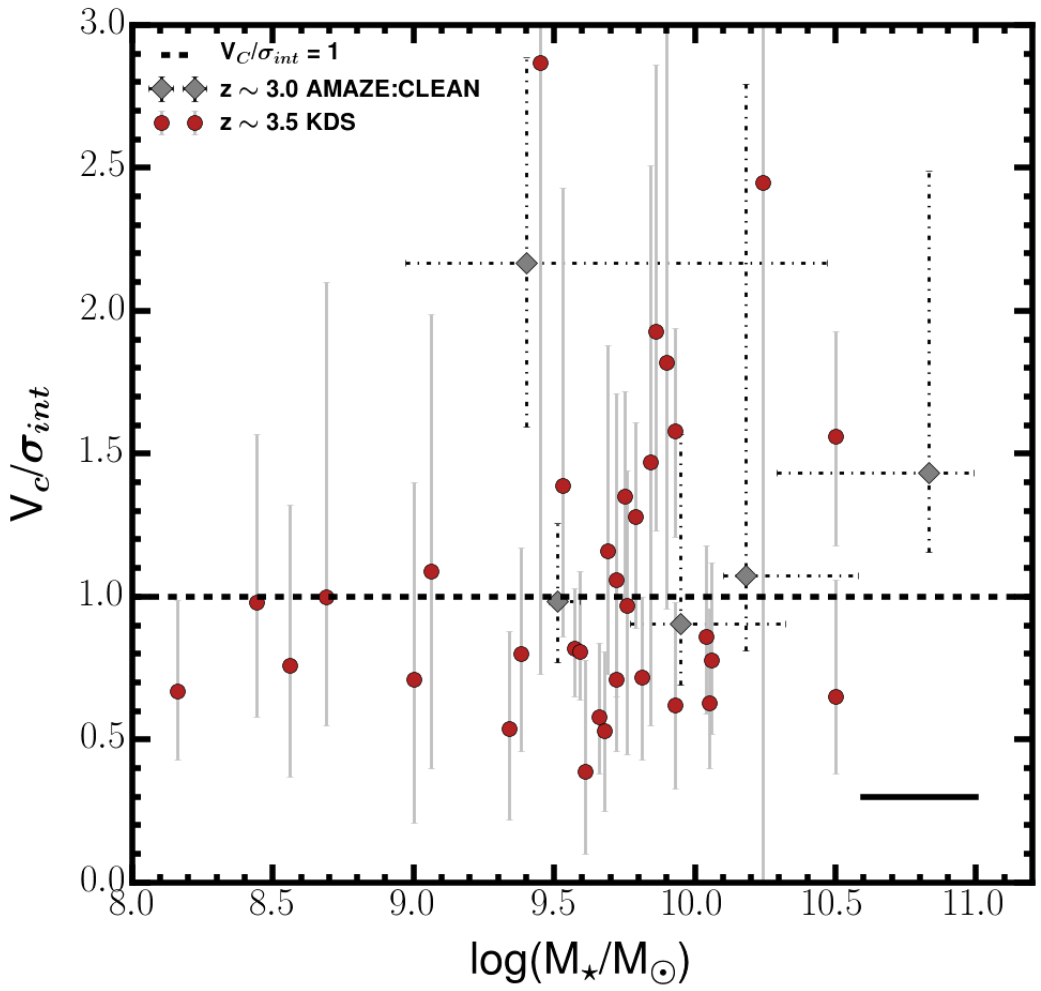

Figure 3.6: The distribution of galaxies in the $V_C/\sigma_{\rm int}$ vs. $M_\star$ plane is shown for the isolated field sample, along with the galaxies in the AMAZE Clean ($z \simeq 3$) sample. We mark the $V_C/\sigma_{\rm int} = 1$ line dividing rotation and dispersion-dominated galaxies in this panel, finding that more massive galaxies (e.g. $\log(M_\star/M_\odot) > 9.5$) are more likely to be rotation-dominated, with dispersion-dominated galaxies spread across the stellar mass range.

SFGs to $\sigma_{\rm int} \simeq 30-60 {\rm km\,s^{-1}}$ at $z \simeq 1$ to $\sigma_{\rm int} \simeq 40-90 {\rm km\,s^{-1}}$ at $z \simeq 3$, but with a wide range of values observed at each redshift. There appears to be a trend for the surveys with lower average stellar mass (MASSIV, DYNAMO, LAW 2009, KROSS, AMAZE) to have higher velocity dispersions than the surveys with larger average stellar mass (GHASP, KMOS^{3D}, SINS).

In agreement with the evolution of gas fractions described in § 3.5.1 (and see the tracks in the right panel of Fig. 3.5), we find that the mean velocity dispersion measurements

from samples of typical star-forming galaxies are decreasing with redshift, with a dependence on mass such that samples with higher stellar mass have lower velocity dispersions at each epoch. The redshift and mass dependence of these tracks is discussed in Wisnioski et al. (2015) and discussed in more detail throughout § 3.5.1, where we also discuss possible physical explanations for the increase in velocity dispersions with redshift.

These new data from the KDS sustain the observation that velocity dispersion is increasing with redshift and provide strong constraints on the internal dynamics of typical star-forming galaxies between $z = 3 - 3.8$. When considered in conjunction with data from the literature in the right panel of Fig. 3.5, it appears that the stellar mass of galaxies may play a role in mediating the velocity dispersion values (see § 3.5.1).

We proceed now to consider both the rotation velocities and velocity dispersions in tandem by considering V_C/σ_{int} and the rotation-dominated fraction of galaxies in the isolated field sample.

3.4.3 V_C/σ_{int} and the rotation-dominated fraction

In Fig. 3.6 we plot the ratio of V_C/σ_{int} against $M_\star$ for the isolated field sample, also including galaxies from the AMAZE Clean ($z \simeq 3$) sample for reference. In the local Universe, disky, SFGs are observed to have V_C/σ_{int} values in excess of 10 (i.e. the disks are 'well settled'), due to the decline of velocity dispersion across cosmic time, as gas fractions and disk turbulence decrease (e.g. Epinat et al., 2008a,b). Clearly the isolated field sample galaxies are in a different physical regime, with mean and median V_C/σ_{int} values of $1.08^{+0.18}_{-0.15}$ and $0.97^{+0.14}_{-0.11}$ respectively. This is despite many of the dispersion-dominated galaxies showing clear velocity gradients across the observed velocity maps (supplementary material § 3.10), with the arctangent model providing a good fit to the rotation curves. This suggests that although rotational motions are present within the disks, they are small or comparable with the elevated σ_{int} values observed throughout the $z \simeq 3.5$ sample.

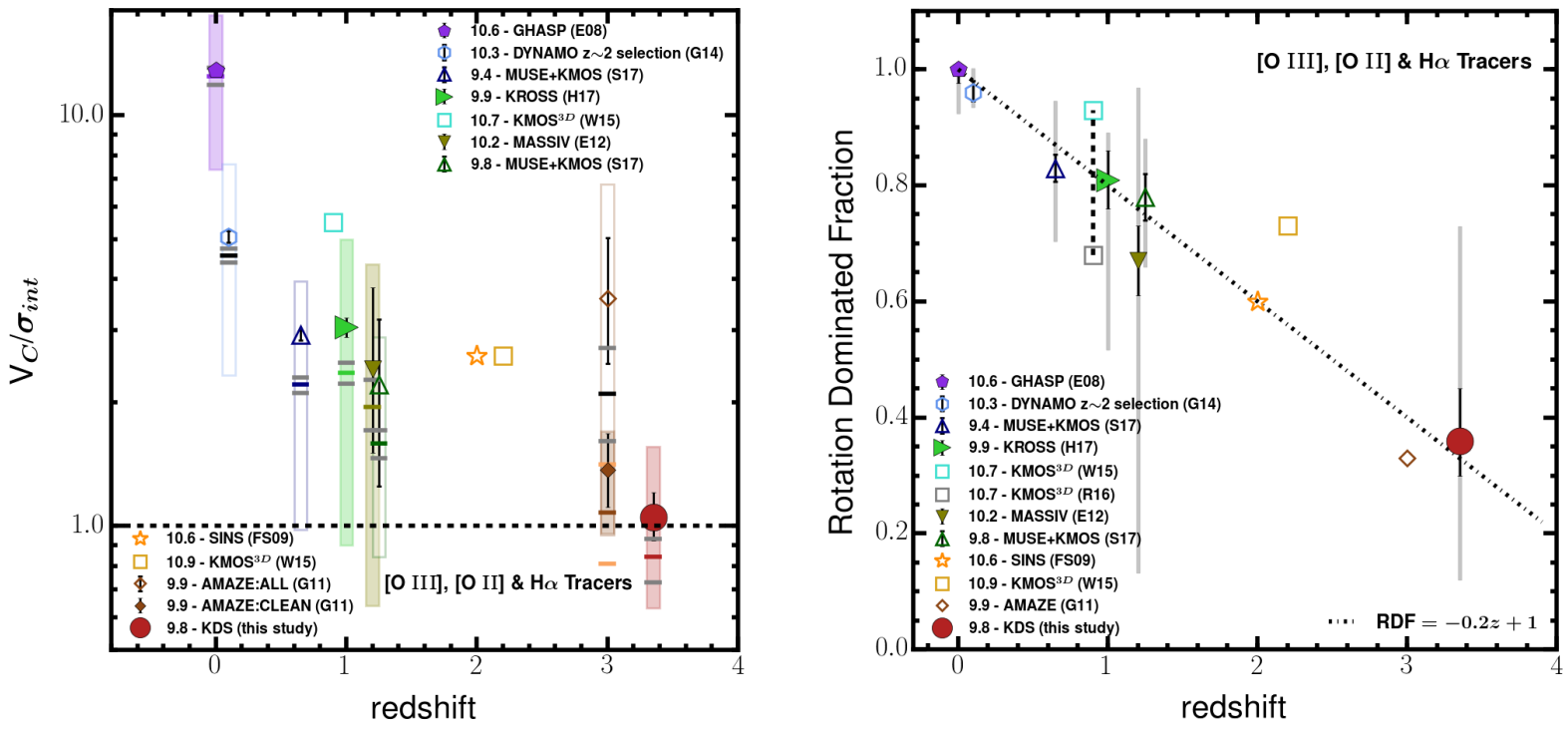

Figure 3.7: *Left:* $V_C/\sigma_{\rm int}$ is plotted against redshift for the comparison samples spanning $0 < z < 4$. We see a clear decline in the mean $V_C/\sigma_{\rm int}$ values with redshift, but with wide ranges in the individual measurements. There is a connection between $V_C/\sigma_{\rm int}$ and the stellar mass of the surveys, with larger mean $M_\star$ surveys reporting higher mean $V_C/\sigma_{\rm int}$. *Right:* We plot the associated rotation-dominated fraction, defined as the fraction of galaxies in each sample with $V_C/\sigma_{\rm int} > 1$. The narrow shaded regions represent the maximum and miminum RDF, computed as described in supplementary material § 3.7.1. It appears that the rotation-dominated fraction drops from $\simeq$ 100% in the local Universe to 60% at intermediate redshifts and then to $\simeq$ 35% at $z \simeq 3.5$, again with the trend for high $V_C/\sigma_{\rm int}$ values in the larger $M_\star$ surveys reflected by higher rotation-dominated fractions. The dot-dash line is the empirically defined RDF $= -0.2\,z + 1$, which appears to roughly follow the cosmic decline of the rotation dominated fraction. In both panels, the symbol convention is the same as in the right panel of Figure 3.4.

The $V_C/\sigma_{int} = 1$ line dividing rotation and dispersion-dominated galaxies is marked on Fig. 3.6, separating the dispersion and rotation-dominated galaxies by definition. There is a spread of rotation and dispersion-dominated galaxies across the stellar mass range, with rotation-dominated galaxies more likely to be found above $\log(M_\star/M_\odot) > 9.5$. The Rotation-Dominated Fraction (RDF), calculated with respect to the full field sample of 39 galaxies, is 0.36±0.08, which is substantially lower than in the local and intermediate redshift Universe (e.g. Epinat et al., 2008a,b; Green et al., 2014). We interpret these results in the context of the cosmic evolution of the rotation dominated fraction using the comparison samples in § 3.4.3.

The evolution of the rotation-dominated fraction

In the left and right panels of Fig. 3.7 we plot V_C/σ_{int} and the closely connected rotation-dominated fraction respectively, as a function of redshift, for the KDS isolated field sample and the comparison samples described in supplementary material § 3.7.1. In each sample, the rotation dominated fraction is computed as the fraction of galaxies with $V_C/\sigma_{int} > 1$, which, given the varying data quality across the comparison samples, is a simple and fair way to study the redshift evolution of this quantity. The filled and hollow symbols with black errorbars in the left panel of Fig. 3.7 represent the mean and error on the mean, and the horizontal lines show the median and error on the median. The shaded regions give the 16th and 84th percentiles of the distribution of individual V_C/σ_{int} measurements, plotted here to indicate the range of measurements at each redshift slice. In the right panel of Fig. 3.7, we have also computed the maximum and minimum RDF for these surveys by adding and subtracting the V_C/σ_{int} error values respectively and recomputing the rotation-dominated fraction. These are shown with the thin grey shaded regions and are intended to give an indication of the limits of the RDF at different redshift slices given the size of the errors on the individual points.

The rotation-dominated fraction, traced simply by the V_C/σ_{int} ratio inferred from ionised gas emission lines, drops from $\simeq$ 100% of galaxies in the local Universe to $\simeq 2/3$ of galaxies in the $z \simeq 1-2$ Universe and to $\simeq 1/3$ above $z \simeq 3$, albeit with individual surveys reporting wide V_C/σ_{int} distributions at each redshift slice. This is highlighted in the right panel of Fig. 3.7 by overplotting the RDF $= -0.2\,z + 1$ line which appears to roughly follow the decline of the rotation-dominated with redshift as described in Stott et al. (2016). The width of the V_C/σ_{int} distributions indicate the galaxy diversity at each redshift slice, driven by the collection of galaxy masses, sSFRs, gas fractions, morphologies and evolutionary states which comprise each sample. Scatter above and below the RDF $= -0.2\,z + 1$ evolution line may be attributed in part to the different mean stellar masses of the surveys, with those that have larger stellar masses tending to scatter above this line. This draws again from the idea that higher stellar mass values suggest that the galaxies are more evolved, with more gas having been converted into stars for the bulk of the sample, which provides stability for a rotating disk and pushes the rotation-dominated fraction higher (see § 3.5). This is shown explicitly in Simons et al. (2017), where galaxies in higher stellar mass bins have larger V_C/σ_{int} at every epoch. It is important to note that the results in the right panel of Fig. 3.7 are subject to the same half-light radius and spatial resolution caveats discussed in section § 3.4.1, which may lead to an increase in velocity dispersions and a decrease in rotation velocities when galaxies are compact and the spatial resolution of the observations is poorer. Specifically for the KDS sample, the disk sizes are smaller than at intermediate redshift, and so it may be more challenging to fully resolve the rotational structure of the galaxies (e.g. Newman et al., 2013).

In summary, the rotation-dominated galaxies in the isolated field sample appear to conform with a redshift invariant V_C - $M_\star$ relation. Due to increased velocity dispersions, these rotation-dominated galaxies account for only 36% of the field sample and so are less representative of typical star-forming galaxies at $z \simeq 3.5$ than at intermediate and low redshifts. Explanations for the increase of σ_{int} with redshift (and hence the decline of V_C/σ_{int}) with cosmic time as well as the nature of dispersion-

dominated galaxies have been discussed at length throughout other studies (e.g Förster Schreiber et al., 2009; Law et al., 2009; Burkert et al., 2010; Newman et al., 2013; Wisnioski et al., 2015) and we revisit these in the following discussion.

3.5 Discussion

Throughout § 3.4 we have investigated the derived kinematic parameters of the isolated field sample, showing first that, within the scatter, the rotation-dominated galaxies sit on a rotation velocity - stellar mass relationship consistent with what is observed in the local Universe. The mean rotation velocity of the isolated field sample is low as a result of averaging over a sample containing a large number of dispersion-dominated galaxies (66% of the sample) and probable pressure support from turbulent motions (e.g. Burkert et al., 2010). This increased number of dispersion-dominated galaxies in comparison to low and intermediate redshifts appears to be driven by high velocity dispersions at $z \simeq 3.5$. In this section we discuss possible physical origins for the elevated random motions traced by $\sigma_{\rm int}$ and their impact on the galactic dynamics.

3.5.1 The origin and impact of increased velocity dispersions at high-redshift

Previous studies have claimed that the elevated velocity dispersions observed at high-redshift are a consequence of both internal and external processes. Law et al. (2009) observe galaxies with elevated velocity dispersions at $z \simeq 2.2$ (see Fig. 3.5) and attribute this to gravitational instabilities following efficient accretion, which can occur when the cold gas becomes dynamically dominant.

Genzel et al. (2011) show that for dispersion-dominated galaxies, the scales susceptible to gravitational collapse are of the order of the galactic half-light radius. Systems such as these form highly unstable and roughly spherical stellar distributions with large internal motions at early times, before more gradual accretion from the galactic halo

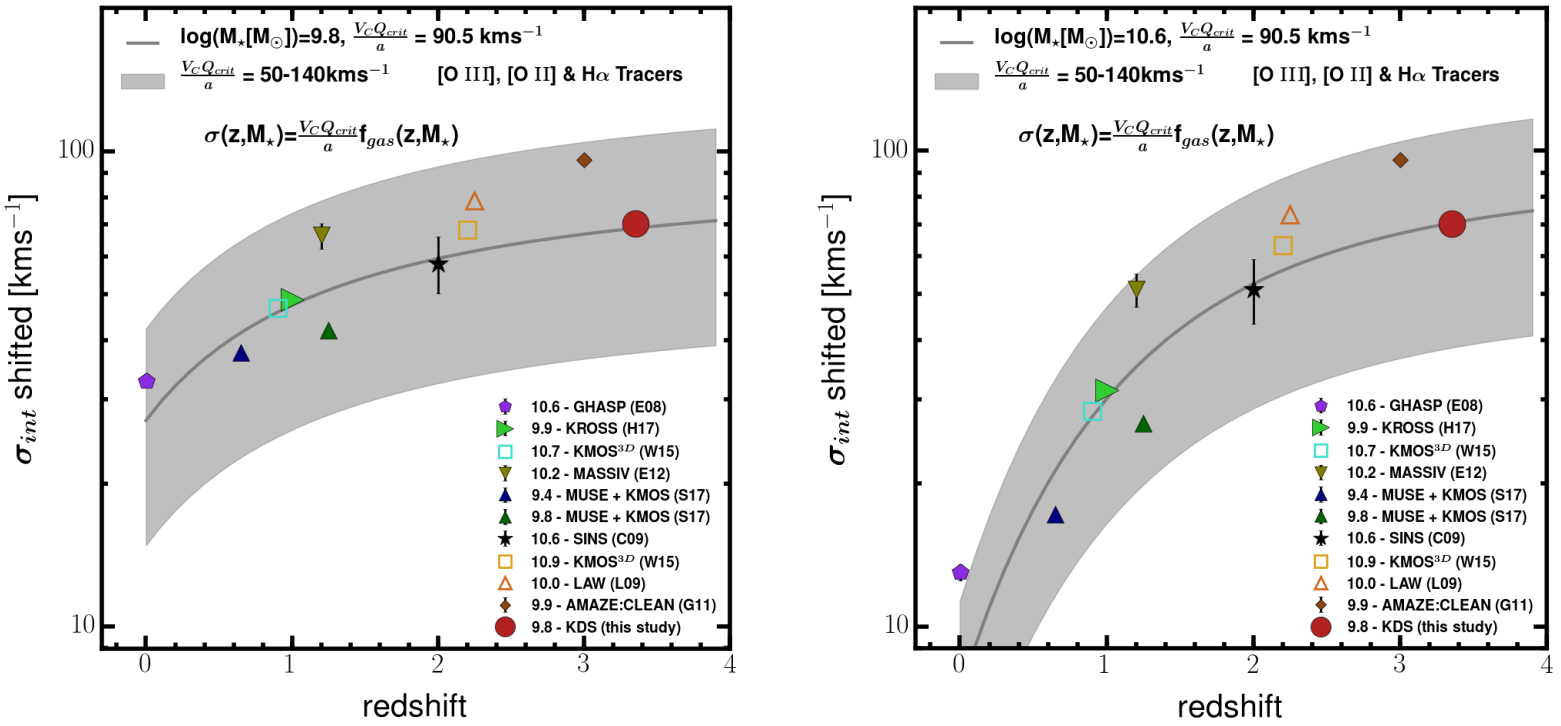

Figure 3.8: *Left:* We plot the $\sigma_{\rm int}$ values for the comparison samples as well as the isolated field sample, shifted as described in the text to a reference mass of $\log(M_\star/M_\odot) = 9.8$ (the median mass of the isolated field sample). The grey line shows the model prediction with $V_C Q_{\rm crit}/a = 90.5 {\rm km\,s^{-1}}$, as dictated by our data. The grey shaded region encompasses the model predictions with lower and upper bounds using $V_C Q_{\rm crit}/a = 50 - 140 {\rm km\,s^{-1}}$ respectively (corresponding roughly to the velocity range $V_C = 70 - 200 {\rm km\,s^{-1}}$, spanned by galaxies in the comparison samples, under the assumption that $Q_{\rm crit} = 1.0$ and $a = \sqrt{2}$ as discussed in the text). The shifted points are in line with the scenario whereby the sample averaged velocity dispersions increase with redshift as a result of increasing average gas fractions. *Right:* The same as in the left panel for a reference mass of $\log(M_\star/M_\odot) = 10.6$. The steeper slope beyond $z \simeq 2$ highlights the model decrease in gas fraction, and hence velocity dispersion, for galaxies which have accumulated a larger stellar population.

forms an extended, stable, gaseous disk which instigates kinematic order (Law et al., 2009; Genzel et al., 2011). The physical mechanisms responsible for the increase in $\sigma_{\rm int}$ may also result in a reduction in the observed rotation velocities by partially compensating the gravitational force throughout the galactic disk (e.g. Burkert et al., 2010; Wuyts et al., 2016b; Übler et al., 2017; Genzel et al., 2017; Lang et al., 2017). Following this, $\sigma_{\rm int}$ decreases over time as ordered rotation begins to dominate and pressure support becomes increasingly insignificant (e.g. Burkert et al., 2010; Übler et al., 2017; Genzel et al., 2017; Lang et al., 2017). This is in line with the evolution of gas fractions observed at intermediate and high-redshifts (e.g. Saintonge et al., 2013; Tacconi et al., 2013, 2018), with the gas reservoirs of galaxies fed by the accretion of cold gas.

Burkert et al. (2010) show, starting from the hydrostatic equation, that negative pressure gradients sourced by the disk turbulence generated through gravitational instabilities result in a decrease in observed rotation velocities. This has prompted others (e.g. Wuyts et al., 2016b; Übler et al., 2017; Lang et al., 2017) to encorporate a velocity dispersion term in the derivation of maximum circular velocities, which contributes to (but is not entirely responsible for) the observed shift in the zero-point of the stellar mass Tully-Fisher relation between $z \simeq 0 - 0.9$. Übler et al. (2017) also claim that without the inclusion of this term incorrect conclusions surrounding the evolution of the Tully-Fisher relation will be drawn. We have not encorporated such a term when deriving the rotation velocities of the isolated field sample, but note that as a consequence of our galaxies showing some of the most extreme intrinsic dispersions observed, this would undoubtedly lead to a different distribution in the $V_{\rm C} - {\rm M}_\star$ plane. The contribution of pressure to rotation velocity for the KDS sample will be explored in more detail in a future work.

In Wisnioski et al. (2015) the authors present a scaling relation describing the increase of $\sigma_{\rm int}$ with redshift in terms of the key observable properties: gas fraction, $f_{\rm gas}$, gas depletion timescale, t_{dep}, and specific star-formation rate, sSFR. Here we explore how well this model describes the evolution in velocity dispersion, incorporating our new

measurement at $z \simeq 3.5$ from the KDS. The function describing the evolution of the velocity dispersion with redshift is shown below in Equation 3.10, where $Q_{\rm crit}$ is the critical Toomre parameter for stability against gravitational collapse (Toomre, 1964), and a is a dimensionless parameter which depends on the assumed distribution of gas and gravitational potential Forster Schreiber et al. (2006).

$$\sigma(z, M_\star) = \frac{V_{\rm C} Q_{\rm crit}}{a} f_{\rm gas}(z, M_\star) \tag{3.10}$$

The gas fraction is a function of gas depletion timescale, with an assumed redshift dependence, and specific star-formation rate, with an assumed mass and redshift dependence (see Wisnioski et al. 2015 Equations 3-6, summarised below by Equations 3.11 and 3.12).

$$\begin{aligned} f_{\rm gas} &= \frac{1}{1 + \left(\mathrm{t_{dep}sSFR}\right)^{-1}} \\ &= \frac{1}{1 + \left(1.5 \times 10^{\mathrm{a(M_\star)}} (1+z)^{\mathrm{b(M_\star)}+\alpha}\right)^{-1}} \end{aligned} \tag{3.11}$$

$$\begin{aligned} \mathrm{a(M_\star)} &= -10.73 + \frac{1.26}{1 + e^{\left(10.49 - \log(\mathrm{M_\star/M_\odot})\right)/(-0.25)}} \\ \mathrm{b(M_\star)} &= 1.85 + \frac{1.57}{1 + e^{\left(10.35 - \log(\mathrm{M_\star/M_\odot})\right)/(0.19)}} \end{aligned} \tag{3.12}$$

This relation is an expression of the belief that high-redshift galaxies experience more intense and efficient gas inflow, with the accumulation of a more massive stellar population providing stability against perturbations. In this equilibrium model framework (e.g. Davé et al., 2012; Lilly et al., 2013; Saintonge et al., 2013), populations of disk galaxies with higher average stellar mass have lower average velocity dispersions due to this stability condition.

In the right panel of Fig. 3.5 we plot Equation 3.10 for three different input mass values ($\log(\mathrm{M_\star/M_\odot}) = 9.8, 10.3, 10.6$, roughly spanning the mass range of the comparison samples), using the updated depletion time scaling relation from Tacconi et al. (2018)

(i.e. $t_{dep} \propto (1+z)^{-0.57}$, meaning $\alpha = 0.57$ in Equation 3.11). The Equation $\sigma(z, M_\star) \propto f_{gas}(z, M_\star)$ is scaled so that the lowest mass track conincides with the KDS data point, finding a proportionality constant $V_C Q_{crit}/a = 90.5 km\,s^{-1}$, which we assume when plotting all three tracks in Fig. 3.5.

In this model, the velocity dispersions increase more steeply with increasing stellar mass, as shown by the solid and dashed lines in Fig. 3.5. At higher redshift, these lines converge, suggesting that the predictions for the gas fraction become independent of stellar mass in this regime. In general, the surveys with higher stellar mass have lower velocity dispersions, in support of the model hypothesis.

Since stellar mass appears to be a crucial factor in regulating the velocity dispersions within galaxies, and the comparison samples have disparate stellar mass ranges, we use the model to shift the σ_{int} values according to their stellar mass to a reference mass value as per Wisnioski et al. (2015). This is done by computing the difference between the model predicted σ_{int} value at the stellar mass of each comparison survey, and at the reference mass for the appropriate redshift, and shifting the reported σ_{int} by this value. We do this for two reference mass values; $\log(M_\star/M_\odot) = 9.8$ (the median mass of the isolated field sample, left panel of Fig. 3.8) and $\log(M_\star/M_\odot) = 10.6$ (right panel of Fig. 3.8).

In both panels, the solid grey line denotes the model prediction using the parameter combination determined above; $V_C Q_{crit}/a = 90.5 km\,s^{-1}$. The grey shaded regions encompass model predictions with lower and upper bounds defined by $V_C Q_{crit}/a = 50 - 140 km\,s^{-1}$ respectively. Assuming that $Q_{crit} = 1.0$ (as for a quasi-stable thin disk e.g. Forster Schreiber et al. 2006; Burkert et al. 2010) and $a = \sqrt{2}$ (as for a disk with constant rotation velocity Wisnioski et al. 2015), this range corresponds to $V_C = 70 - 200 km\,s^{-1}$, which is roughly the velocity range spanned by our comparison samples, and the solid grey line corresponds to $V_C = 128 km\,s^{-1}$. Whilst the KDS mean rotation velocity sits at the bottom of this range, possible explanations are: **(1)** The rotation velocities of the KDS galaxies are underestimated as a result of the velocity dispersion contribution discussed above; **(2)** $Q_{crit} \neq 1$ or $a \neq \sqrt{2}$ as a consequence of

changing physical conditions at high-redshift.

Although the details of the coefficients of Equation 3.10 are unclear (i.e. V_C is not fixed at one value for the comparison samples and is itself linked to stellar mass, and both Q_{crit} and a could vary with redshift), the shape of the velocity dispersion evolution appears to follow that of the gas fraction, as suggested by the model. The difference between the slopes in the left and right panels highlights the role of stellar mass in the kinematic settling of galaxies between $z \simeq 3$ and the local Universe. The isolated field sample data, in combination with comparison sample results spanning $z = 0 - 3$, thus suggest that the time evolution of the velocity dispersion measured from ionised gas emission lines is intimately linked to the consumption of gas and the accumulation of stars in a stable disk (e.g. Law et al., 2009, 2012c,b; Wisnioski et al., 2015). Rotation-dominated galaxies become less representative of the typical star-forming population at these redshifts as a result of the increased velocity dispersions (shown in Fig. 3.7), constituting only $\simeq 1/3$ of the isolated field sample at $z \simeq 3.5$. This suggests that we are probing more chaotic and unstable systems, subject to gravitational instabilities and collapse on the disk scale length (Burkert et al., 2010; Genzel et al., 2011), residing in a much more active period of the Universe in terms of both accretion and star-formation. Recent results indicate that these systems may become strongly baryon-dominated on the galaxy disk scale at high-redshift (Übler et al., 2017; Lang et al., 2017; Genzel et al., 2017), which could imply that the increasing contribution of dark matter to galaxy disks with decreasing redshift plays a role in the evolution of velocity dispersions.

The precise interpretation of the velocity dispersion remains unclear, although there is mounting evidence that random motions have an increasingly significant contribution to the mass budget of high-redshift galaxies (e.g. Kassin et al., 2007; Law et al., 2009; Burkert et al., 2010; Kassin et al., 2012; Wuyts et al., 2016b; Lang et al., 2017; Übler et al., 2017; Genzel et al., 2017). The nature of dispersion-dominated galaxies at high-redshift has been discussed in Newman et al. (2013) using Adaptive-Optics (AO) and seeing limited observations of the same galaxies. The AO observations show that, in some cases, galaxies which are clasified as dispersion-dominated with seeing

limited observations reveal much larger velocity gradients at higher spatial resolution. This highlights that beam-smearing effects can wash-out observed rotational motions, particularly for small galaxies. We have attempted to account for beam-smearing using half-light radius and velocity gradient dependent dynamical modelling, but we acknowledge that these observations are challenging and cannot rule out the presence of unresolved velocity gradients in our seeing-limited dataset. Smaller galaxies do have intrinsically smaller rotation velocities, whilst there is no observed dependence of velocity dispersion on galaxy size (e.g. Newman et al., 2013). Dispersion-dominated galaxies are therefore likely to be at an earlier evolutionary stage and unstable to gravitational instabilities which generate turbulence which is then maintained by the potential energy of the gas in the disk (Burkert et al., 2010; Newman et al., 2013).

Bringing the above points together, turbulent motions consume an increasingly significant fraction of the energy budget at high-redshift when typical star-forming galaxies are at earlier evolutionary stages. The KDS isolated field sample presents an extension of these trends to higher redshift, where galaxies are even more likely to be dispersion-dominated, and pressure support may be more significant than explored at $z \simeq 2.3$ (Wuyts et al., 2016b; Übler et al., 2017; Genzel et al., 2017; Lang et al., 2017). However, the precise interpretation of $\sigma_{\rm int}$ measured from ionised gas emission lines remains unclear, and future observations of both stellar and gaseous velocity dispersions in tandem with *JWST* will allow for unambigous investigations into the nature of gaseous velocity dispersions at high-redshift.

In summary, the isolated field sample galaxies are diverse and kinematically immature, with $\simeq 2/3$ of the sample being dominated by random motions which may contribute to supporting a portion of the dynamical mass (e.g. Kassin et al., 2007; Burkert et al., 2010; Kassin et al., 2012; Newman et al., 2013; Straatman et al., 2017; Übler et al., 2017; Lang et al., 2017). In the context of the equilibrium model explored here, these galaxies will evolve gradually with redshift along the velocity-mass relationship into stable disk galaxies which have converted their gas reservoirs into stellar mass (e.g. Lilly et al., 2013; Tacconi et al., 2013; Wisnioski et al., 2015; Tacconi et al., 2018).

Future work at higher resolution and redshift will trace the extent to which gas-derived velocity dispersions trace the stellar dispersions and will investigate even earlier and more chaotic stages in the lifetimes of late-type galaxies.

3.6 Conclusions

We have presented new dynamical measurements of 33 typical star-forming galaxies spanning both cluster and field environments at $z \simeq 3.5$ as part of the KMOS Deep Survey, based on IFU data observed with KMOS. These measurements push back the frontier of IFU observations in the early Universe and provide more robust constraints on the internal and rotational dynamics of $9.0 < \log(M_\star/M_\odot) < 10.5$ typical star-forming galaxies at these redshifts. By using a combined morpho-kinematic classification based on broad-band *HST* imaging and our IFU data, we have separated interacting galaxies from the sample, finding merger rates consistent between the field pointings ($\simeq 15\%$) and a very high merger rate in the cluster pointing ($\simeq 89\%$). We have made beam-smearing corrected measurements of V_C and σ_{int} for the remaining isolated field galaxies, and we interpret these in the context of previous dynamical studies using IFU data (supplementary material § 3.7.1 and Table 3.4). The main conclusions of this work are summarised as follows:

- We use a fractional error weighted mean to derive the mean kinematic parameters of the KDS isolated field sample of $V_C = 76.7^{+4.9}_{-4.5}$km s^{-1} and $\sigma_{int} = 70.8^{+3.3}_{-3.1}$km s^{-1} (right panels of Figures 3.4 and 3.5 respectively). Rotation (dispersion) dominated galaxies are defined as those with $V_C/\sigma_{int} > (<)1$.

- We plot the mean V_C values of the comparison samples and the KDS isolated field sample, finding significant diversity in V_C measurements in each survey (right panel of Fig. 3.4). The spread in measurements is a result of the samples containing a mixture of rotation and dispersion-dominated galaxies with varying $M_\star$ values, and the low mean KDS value is primarily the result of averaging over a sample with a high fraction of dispersion-dominated galaxies and indicating

the impact pressure support may have on reducing rotation velocities. At higher $M_\star$, the accumulation of a stellar population provides stability, leading to an interplay between $\sigma_{\rm int}$ and V_C mediated across redshift by the cosmic decline of gas fractions, sSFRs and accretion (e.g. Law et al., 2012c; Wisnioski et al., 2015).

- When the V_C values are viewed as a function of mass in the inverse stellar mass Tully-Fisher Relation, the rotation-dominated galaxies are correlated with mass and lie within the errors on the same relation as derived for rotation-dominated galaxies with $9.0 < \log(M_\star/M_\odot) < 11.0$ at $z \simeq 0.9$ in the KROSS survey (Fig. 3.4). This relation is consistent with star-forming galaxies at $z = 0$ and so we report no significant evolution in the slope or zero-point of the smTFR between $z = 0 - 3.5$. Consistency of sample selection and measurement techniques are crucial factors when determining evolution in the V_C vs. $M_\star$ plane by comparing samples at different redshifts. The dispersion-dominated galaxies in the isolated field sample scatter below the trend.

- When considering the rotation-dominated galaxies alone, the mean and median rotation velocities are $V_C = 96.7^{+7.3}_{-7.2}\mathrm{km\,s^{-1}}$ and $V_C = 93.0^{+12.0}_{-12.5}\mathrm{km\,s^{-1}}$ respectively, which are roughly equivalent to a simple lower limit virial theorem calculation using the mean mass and half-light radius of the sample. This suggests that pressure forces, which are more significant at high-redshift, may play a role in supporting the total mass in all of the galaxies in the isolated field sample (e.g. Burkert et al., 2010).

- 14/33 isolated field sample galaxies are rotation-dominated and 19/33 are dispersion-dominated, with a tendency for galaxies with higher $M_\star$ to have larger values of $V_C/\sigma_{\rm int}$ (Fig. 3.6). This gives a rotation-dominated fraction of $36 \pm 8\%$ in the isolated field sample, substantially less than surveys at lower redshift, although there is significant diversity amongst the individual $V_C/\sigma_{\rm int}$ measurements at each redshift slice (left and right panels of Fig. 3.7). When viewed as a function of redshift, the rotation dominated fraction appears to follow the scaling relation $\mathrm{RDF} = -0.2\,z + 1$.

- We plot mean $\sigma_{\rm int}$ values computed in a consistent way for SFG samples spanning a wide redshift baseline (the comparison samples described in supplementary material § 3.7.1), finding a sharp increase in $\sigma_{\rm int}$ values between $z = 0 - 1$ and a fairly shallow increase thereafter, mediated by the mean $M_\star$ of the galaxy samples (right panel of Fig. 3.5). This is in line with a simple equilibrium model prescription in which the gas fractions and the impact of several physical mechanisms such as accretion of gas from the IGM, stellar feedback and turbulence increase with redshift and combine to increase random motions within high-redshift galaxies.

3.7 Chapter 3 supplementary material

3.7.1 Comparison samples

In § 3.4 we compare the isolated field sample results with the results of surveys tracing dynamics with ionised gas emission across a wide redshift baseline, to determine the evolving physical state of SFGs as the age of the Universe increases. The galaxy selection criteria in these surveys, with the exception of DYNAMO (Green et al., 2014) as discussed below, consistently picks out representative star-forming galaxies at each epoch and the dynamical properties are traced by observing either the [O III]λ5007, [O II]λ3727,3729 or Hα ionised gas emission lines.

Given the range of modelling and kinematic parameter extraction methods it is important to verify the extent to which the results from these surveys can be directly compared and treated as forming an evolutionary sequence, which we test in the following subsections by considering each survey in turn.

We make use of tabulated data from the surveys, where available, to compute sample averages using the following method. The fractional error weighted mean of $V_{\rm C}/\sigma_{\rm int}$, $\sigma_{\rm int}$ and $V_{\rm C}$ in each of the samples is computed (i.e. we do not want the derived values with extremely large errors to dominate the averages). The errors on these mean

Table 3.4: The mean and median kinematic properties used throughout Figures 3.4, 3.5 and 3.7 for the different surveys. The errors on the mean and median represent the statistical errors from bootstrap resampling. For each of the comparison samples, the cross or tick after each of the mean kinematic properties indicates whether we have defined this as a fair value to compare against, with further details provided throughout supplementary material § 3.7.2 - § 3.7.10.

Survey	$\langle z \rangle$	$\left\langle \log\left(\frac{M_\star}{M_\odot}\right)\right\rangle$	$\langle V_C \rangle$	med(V_C)	$\langle \sigma_{int} \rangle$	med(σ_{int})	$\left\langle \frac{V_C}{\sigma_{int}} \right\rangle$	med$\left(\frac{V_C}{\sigma_{int}}\right)$	RDF
GHASP	0.001	10.6	$189.0^{+3.5}_{-3.0}$ ✓	$159.4^{+12.0}_{-15.0}$	$13.0^{+0.5}_{-0.5}$ ✓	$13.0^{+0.5}_{-0.5}$	$12.9^{+0.5}_{-0.4}$ ✓	$12.5^{+0.6}_{-0.6}$	$1.00^{+0.00}_{-0.02}$ ✓
DYNAMO	0.1	10.3	$183.0^{+1.0}_{-1.0}$ ✗	$164.0^{+3.0}_{-5.0}$	$45.9^{+0.3}_{-0.3}$ ✗	$39.0^{+0.9}_{-1.0}$	$5.1^{+0.2}_{-0.2}$ ✗	$4.6^{+0.2}_{-0.2}$	$0.96^{+0.02}_{-0.02}$ ✗
MUSE+KMOS	0.65	9.4	$103.8^{+1.5}_{-1.6}$ ✗	$73.0^{+2.5}_{-2.5}$	$40.0^{+0.3}_{-0.3}$ ✓	$32.0^{+0.6}_{-0.5}$	$2.9^{+0.1}_{-0.1}$ ✗	$2.21^{+0.1}_{-0.1}$	$0.83^{+0.02}_{-0.02}$ ✗
KROSS	0.9	9.9	$117.0^{+4.0}_{-4.0}$ ✓	$109.0^{+5.0}_{-5.0}$	$45.0^{+0.6}_{-0.5}$ ✓	$43.2^{+0.8}_{-0.8}$	$3.1^{+0.2}_{-0.2}$ ✓	$2.4^{+0.1}_{-0.1}$	$0.81^{+0.05}_{-0.05}$ ✓
KMOS^{3D}	1.0	10.7	170.0	-	25.0 ✗	-	5.5 ✗	-	0.93 ✗
MASSIV	1.2	10.2	$132.1^{+10.4}_{-8.2}$ ✓	$103.0^{+13.4}_{-11.0}$	$61.8^{+3.8}_{-4.2}$ ✓	$52.0^{+5.2}_{-4.7}$	$2.4^{+1.4}_{-0.9}$ ✓	$2.0^{+0.3}_{-0.2}$	$0.67^{+0.06}_{-0.06}$ ✓
MUSE+KMOS	1.25	9.8	$75.5^{+3.0}_{-3.3}$ ✗	$54.0^{+3.0}_{-2.8}$	$42.0^{+0.5}_{-0.5}$ ✓	$29.5^{+1.0}_{-1.0}$	$2.2^{+1.0}_{-1.0}$ ✗	$1.59^{+0.1}_{-0.1}$	$0.78^{+0.04}_{-0.04}$ ✗
SINS(C09)	2.0	10.6	$232.0^{+12.8}_{-12.7}$✓	$240.0^{+18.0}_{-17.2}$	$51.2^{+8.0}_{-7.9}$ ✓	$42.5^{+9.1}_{-8.5}$	$5.0^{+0.9}_{-1.0}$ ✗	$4.7^{+1.0}_{-1.0}$	1.0 ✓
SINS(F09)	2.0	10.6	$201.3^{+4.3}_{-4.0}$ ✓	$174.0^{+12.1}_{-10.3}$	- ✗	-	2.6 ✗	-	0.60 ✗
KMOS^{3D}	2.2	10.9	170.0 ✗	-	55.0 ✗	-	2.6 ✗	-	0.73 ✗
LAW 09	2.3	10.0	- ✗	-	$78.0^{+6.5}_{-6.5}$ ✗	$69.0^{+8.3}_{-7.5}$	- ✗	-	0.73 ✗
AMAZE (Full)	3.0	10.0	$217.0^{+59.1}_{-40.2}$✗	$129.0^{+47.5}_{-42.8}$	$85.9^{+1.5}_{-1.4}$ ✗	$78.0^{+4.5}_{-4.8}$	$3.6^{+1.5}_{-1.1}$ ✗	$2.1^{+0.6}_{-0.5}$	0.33 ✗
AMAZE (Clean)	3.0	10.0	$140.8^{+40.1}_{-30.2}$✓	$129.0^{+45.0}_{-33.4}$	$95.7^{+2.0}_{-2.0}$ ✓	$95.0^{+2.6}_{-2.6}$	$1.4^{+0.3}_{-0.3}$ ✓	$1.1^{+0.3}_{-0.3}$	- ✗
KDS	3.5	9.8	$75.7^{+4.4}_{-4.4}$ ✓	$57.5^{+5.5}_{-5.5}$	$70.3^{+3.3}_{-3.1}$ ✓	$71.0^{+5.0}_{-4.8}$	$1.1^{+0.2}_{-0.1}$ ✓	$0.84^{+0.1}_{-0.1}$	$0.36^{+0.08}_{-0.08}$ ✓

values are computed in a statistical sense, by generating bootstrapped samples, with replacement, with size equivalent to the original survey sample size and with values perturbed by a random number drawn from a gaussian distribution with width given by the error on the original point. The same process is applied to compute the errors on the sample medians and we report the 16th and 84th percentiles of the distributions of each of the above quantities as an indicator of the distribution width, and hence galaxy diversity, at each redshift slice. These results are listed in Table 3.4 and discussed in detail throughout § 3.4, where we will make statements about dynamical evolution by connecting the dots of these different surveys, assuming that on average they are tracing a population of SFGs which evolve across cosmic time. Throughout the plots in § 3.4 we highlight which values can be directly compared, due to consistency of sample selection and measurement methods, using filled and hollow symbols. This is also highlighted with the ticks and crosses beside the mean values in Table 3.4.

3.7.2 GHASP ($z \simeq 0$)

The GHASP survey (Epinat et al., 2008a,b, E08) makes use of Fabry-Perot observations of 203 spiral and irregular galaxies with median $\log(M_\star/M_\odot) = 10.6$ in the local Universe ($z \simeq 0$) to produce 3D Hα datacubes. The data extend out to several half-light radii and in each case tilted ring models are fit to determine V_C at large radii where the rotation curves have flattened, with $\sigma_{\rm int}$ given as the dispersion in the rotation velocity across the whole field. In this survey, the mean and median kinematic properties computed from the tabulated literature values are directly comparable to the KDS and we used filled symbols in the plots throughout § 3.4 to highlight this.

3.7.3 DYNAMO ($z \simeq 0.1$, but selected with physical properties resembling $z \simeq 2$)

In the DYNAMO survey (Green et al., 2014, G14), Hα IFU data of 67 galaxies with median $\log(M_\star/M_\odot) = 10.3$ at $z \simeq 0.1$ are presented. The selection criteria is such

that half of the sample have high sSFRs representative of SFGs at $z \simeq 2$, and are also found to have higher $f_{\rm gas}$ values than locally, mimicking the physical conditions of $z \simeq 2$ SFGs. $V_{\rm C}$ values are extracted at a fixed radius from an arctangent model fit to the velocity fields ($1.6R_{1/2}$ as measured in the r-band) and $\sigma_{\rm int}$ is taken as the luminosity weighted average of the beam-smearing corrected dispersion field. We make use of tabulated data from this survey, but use hollow symbols throughout the plots in § 3.4 to highlight the difference in selection critera.

3.7.4 MUSE and KMOS ($z \simeq 0.65$ and $z \simeq 1.25$)

In Swinbank et al. (2017) a collection of $\simeq$ 400 star-forming galaxies observed in [O II]λ3727,3729 with MUSE and Hα emission with KMOS is described. Of this parent sample, inclination corrected velocities and intrinsic velocity dispersions are derived for 179 galaxies, to which we make comparisons. The observations span the redshift range $0.2 < z < 1.6$ and we split the data into two subsets with $z < 1.0$ (129 galaxies with mean redshift of $z = 0.65$, mean stellar mass of $\log(\mathrm{M}_\star/\mathrm{M}_\odot) = 9.80$) and $z > 1.0$ (50 galaxies with mean redshift of $z = 1.25$, mean stellar mass $\log(\mathrm{M}_\star/\mathrm{M}_\odot) = 9.80$). The reported velocities are extracted at $3R_{\rm d}$, comparable to the extraction radius for the KDS sample, but these have not been beam-smearing corrected. The intrinsic velocity dispersions have been corrected for beam-smearing effects. For this reason, the velocity dispersions are deemed directly comparable to the KDS, reflected by the filled symbols throughout the plots in § 3.4, but the points involving velocity measurements are represented by hollow symbols due to the lack of a beam-smearing correction.

3.7.5 KROSS ($z \simeq 0.9$)

We make comparisons to the most recent KROSS results (Harrison et al., 2017, H17), which presents KMOS Hα observations of $\simeq$ 600 SFGs with median $\log(\mathrm{M}_\star/\mathrm{M}_\odot) = 9.9$ and $z \simeq 0.9$. $V_{\rm C}$ values are extracted from exponential disk fits to the data at $2R_{1/2}$ (differing from arctangent fits by a median of 0.5%) with the $\sigma_{\rm int}$ values also extracted

at $2R_{1/2}$ when the data extend to this radius and when they do not $\sigma_{\rm int}$ is taken to be the median of the $\sigma_{\rm obs}$ map. These quantities are then beam-smearing corrected as described in H17 section 3.3.3. Due to the consistency of modelling and measurement techniques, the $z \simeq 0.9$ galaxies in this sample are directly comparable to the KDS and are plotted throughout § 3.4 with filled symbols.

3.7.6 KMOS^{3D} ($z \simeq 1.0$ and $z \simeq 2.3$)

The KMOS^{3D} results described in (Wisnioski et al., 2015, W15) describe KMOS Hα observations of $\simeq 191$ massive SFGs across two redshift slices. At $z \simeq 1.0$ the galaxies have $\log(\mathrm{M}_\star/\mathrm{M}_\odot) = 10.7$ and at $z \simeq 2.3$ the median is $\log(\mathrm{M}_\star/\mathrm{M}_\odot) = 10.9$, over an order-of-magnitude above the KDS median of $\log(\mathrm{M}_\star/\mathrm{M}_\odot) = 9.8$. The rotation velocity is taken as $V_{\rm C} = \frac{1}{2\sin(i)}(v_{\rm obs_{max}} - v_{\rm obs_{min}})$ and $\sigma_{\rm int}$ is extracted from the $\sigma_{\rm obs}$ map far from the kinematic centre, where the effects of beam-smearing are negligible. No tabulated values are provided for this survey, and so we cannot re-compute the mean and median values. We make use of values quoted in W15 at both redshift intervals throughout § 3.4, plotting these with hollow symbols due to the inconsistency of measurement method.

3.7.7 MASSIV ($z \simeq 1.2$)

The MASSIV sample (Epinat et al., 2012, E12) uses SINFONI Hα observations of 50 SFGs with median $\log(\mathrm{M}_\star/\mathrm{M}_\odot) = 10.2$ at $z \simeq 1.2$. An arctangent function is fit to the data and $V_{\rm C}$ is extracted at $\simeq 1.7R_{1/2}$ and the $\sigma_{\rm int}$ value is derived from the $\sigma_{\rm obs}$ map by subtracting in quadrature the beam-smearing correction value as per § 3.3.2. We make use of tabulated values presented in this survey to compute the mean and median kinematic properties, plotted with filled symbols throughout § 3.4.

3.7.8 SINS ($z \simeq 2.0$)

The SINS survey (Förster Schreiber et al., 2009, FS09) presents SINFONI Hα observations of 80 massive galaxies with median $\log(M_\star/M_\odot) = 10.6$ at $z \simeq 2.0$. Galaxies in this sample are classified as rotation or dispersion-dominated following FS09 section 9.5.1 which classifies rotation-dominated galaxies using the observed velocity and integrated velocity dispersion criteria $V_{\rm obs}/(2\sigma_{\rm tot}) > 0.4$.

V_C values for rotation-dominated galaxies are computed using a combined velocity gradient + width approach (Forster Schreiber et al., 2006) and for dispersion-dominated galaxies using the velocity width. Only integrated velocity dispersions are presented for the full sample. In addition, (Cresci et al., 2009, C09) model robust rotators in the SINS sample using the IDL code DYSMAL, which derives rotation curves given an input radial mass distribution. In this approach, the V_C value comes from the best-fitting model parameter and $\sigma_{\rm int}$ is calculated using Equation 3.13, with the best-fitting σ_{01} used (reflecting thin and thick disks; see their text for more detail) and with σ_{02}, an additional component of isotropic velocity dispersion throughout the disk, left as a free parameter in the fitting.

$$\sigma_{01} = \sqrt{\frac{v^2(R)h_z}{R}} \quad OR \quad \sigma_{01} = \frac{v(R)h_z}{R} \qquad \sigma_{\rm int} = \sqrt{\sigma_{01}^2 + \sigma_{02}^2} \tag{3.13}$$

It is unclear whether the V_C values for the full sample from FS09 are directly comparable, but we make use of the tabulated values for completeness and plot these with filled symbols throughout § 3.4. The velocity dispersion values, $V_C/\sigma_{\rm int}$ and the rotation dominated fraction from FS09 are plotted with hollow symbols throughout § 3.4 (using the results listed in W15 for the point locations) due to the difference in measurement method for the velocity dispersion values.

The V_C and σ_{int} values in C09 are likely biased towards rotation-dominated galaxies with a well-settled disk. Nonetheless, we plot these values with filled symbols in § 3.4 as a directly comparable dataset, omitting the V_C/σ_{int} values and the rotation dominated fraction, which are listed for the full FS09 sample.

3.7.9 LAW 09 ($z \simeq 2.3$)

In (Law et al., 2009, L09) OSIRIS [O III]λ5007 and Hα observations are collected for 13 galaxies with median $\log(M_\star/M_\odot) = 10.0$ at $z \simeq 2.3$. The 'velocity shear' is computed as $v_{shear} = \frac{1}{2}(v_{max} - v_{min})$ without inclination correction and σ_{int} is the flux-weighted mean of σ_{obs}. We note that the σ_{mean} values and errors tabulated in the Law et al. (2009) paper are the flux-weighted mean and standard deviation of the measurements in individual spaxels in each galaxy, not corrected for beam-smearing in any way. These measurements are expected to be larger than the σ_{int} measurements at similar redshift which have been beam-smearing corrected, or extracted at the galaxy outskirts where the effects of beam-smearing are much smaller. We use tabulated data σ_{int} data in L09 to compare this distribution with other results, but plot with a hollow symbol due to the lack of a beam-smearing correction.

3.7.10 AMAZE ($z \simeq 3.0$)

The AMAZE sample (Gnerucci et al., 2011, G11) presents SINFONI [O III]λ5007 measurements for 33 galaxies with median $\log(M_\star/M_\odot) = 9.9$ at $z \simeq 3$, closest in redshift to the KDS galaxies. In this study, rotation curves and intrinsic velocity dispersions are derived from a modelled exponential mass distribution, with the extracted V_C value taken as the large radius limit of the rotation curve and the σ_{int} as the maximum of the difference in quadrature between the σ_{obs} map and the σ_{model} map (which also takes into account instrumental resolution and beam-smearing; see their Equation 8). A caveat when comparing with the G11 values is that dynamical properties are computed for 11 rotation-dominated galaxies in their sample, with the

remaining 22 galaxies not analysed.

Also, for 5 galaxies in G11, V_C is not well constrained and no errorbar is given; for these objects we take the fractional error on V_C equal to 1 when computing the sample averages. The σ_{int} errors for individual galaxies are generally very small, and for 3 galaxies the σ_{int} value is consistent with 0 km s^{-1}. For the mean value computation for the full sample we set these equal to the SINFONI resolution limit of 30 km s^{-1}. A total of 6/11 galaxies either have no errors on V_C or have σ_{int} values consistent with 0 km s^{-1}, which we refer to as the AMAZE 'Unconstrained' sample and represent these with hollow symbols throughout the plots in § 3.4.

This Unconstrained sample also contains the galaxy s_sa22a-M38, common between the KDS and G11, classified here as a merger due to double *HST* components and twin peaks in the object spectrum, but classified in G11 as a rotating galaxy with $V_C = 346$km s^{-1} (although the authors discuss the possibility that the galaxy could be either a close pair or two clumps embedded within a rotating disk). We use tabulated values from the full analysed sample of 11 galaxies, plotting these with hollow symbols throughout § 3.4 as a consequence of the caveats listed above. The 5/11 galaxies which are not in the Unconstrained sample are referred to as the AMAZE 'Clean sample' and are directly comparable to the KDS. These are plotted with filled symbols throughout § 3.4. We plot the quoted rotation-dominated fraction of 33% as a hollow symbol, noting that this could be higher if any of the 22/33 galaxies not analysed are rotation-dominated.

This comparison sample summary shows that there are many different approaches for computing the same intrinsic kinematic parameters, dictated by data quality and model preference, however, despite this diversity, over the past decade the studies appear to be converging on 'modelling out' the effects of beam-smearing using similar approaches (e.g. as described in Davies et al. 2011, where removing the effects of beam-smearing with spectrally and spatially convolved models is also the least biased approach). This trend towards consistency is encouraging, and, as described in § 3.3.2, we have also

shaped our approach towards extracting intrinsic kinematic parameters after correcting for beam-smearing effects quantified in the modelling. We stress that, keeping in mind sample selection, mass ranges and kinematic parameter extraction methods are crucial when comparing results between different surveys.

3.8 Intrinsic parameter distributions

In Fig. 3.9 we plot the distribution of the isolated field sample in the $\sigma_{\rm int}$ vs. $\log(V_{\rm C})$ plane. The $V_{\rm C} = \sigma_{\rm int}$ line roughly bisects the KDS sample, and separates the dispersion-dominated and rotation-dominated galaxies by definition. The isolated field sample galaxies are clustered around a relatively tight region in both $V_{\rm C}$ and $\sigma_{\rm int}$ and there is good agreement between the KDS and AMAZE Clean ($z \simeq 3$) samples. The galaxies in the AMAZE Unconstrained sample generally have much larger $V_{\rm C}$ values despite occupying a similar stellar mass range to our isolated field sample, with this being a consequence of large model extrapolations beyond the observed data. We follow the bootstrapping procedure described in supplementary material § 3.7.1 to compute error weighted averages and statistical errors.

3.9 Kinematic parameters error estimates

3.9.1 3D modelling kinematic parameter error estimates

As mentioned in § 3.3.2, the MCMC sampling provides distributions for each of the model parameters, from which we can extract the 84th and 16th percentile values as the +/- 1-σ errors. During the following procedure, $\rm PA_{kin}$ is fixed to the maximum-likelihood value for all model evaluations. We proceed to reconstruct the beam-smeared and intrinsic dynamical models for each of the isolated field galaxies using the 16th and 84th percentile parameters, with the lower velocity 16th percentile model constructed using the upper limit on the inclination, and the 84th percentile model using the lower

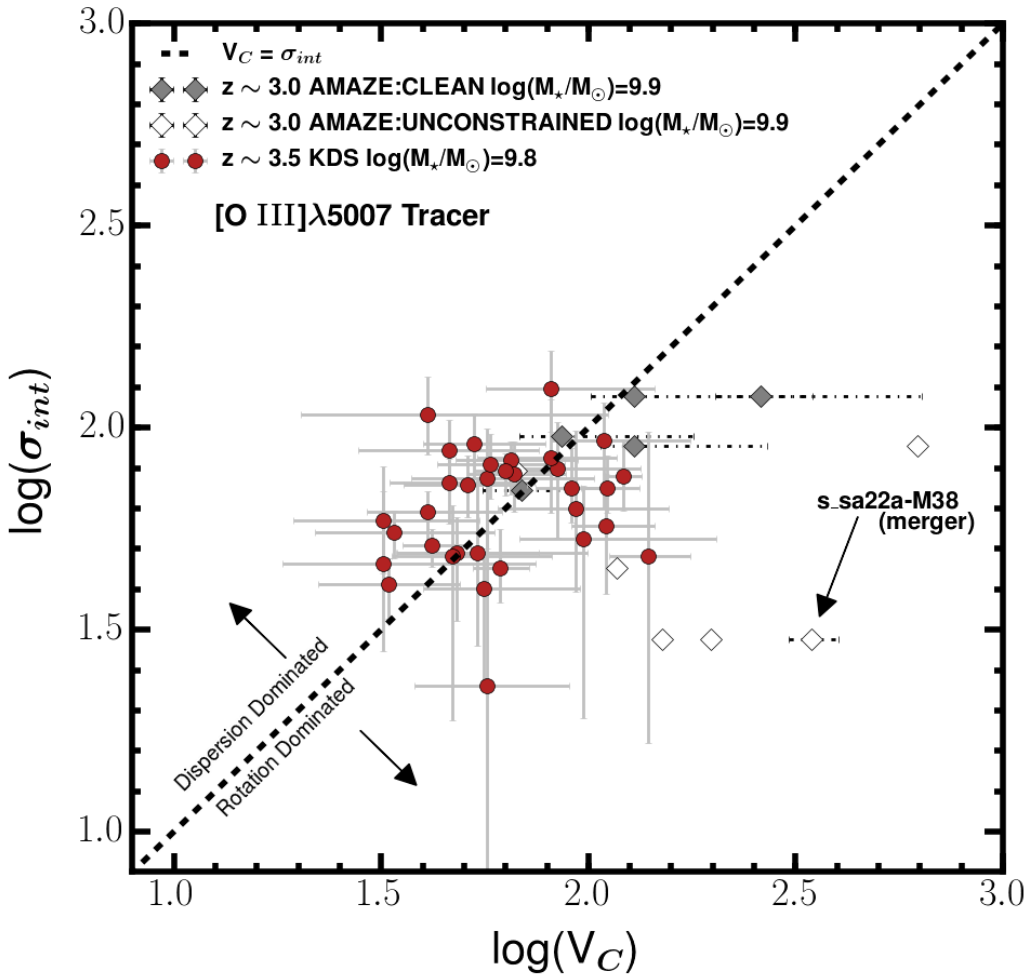

Figure 3.9: The distribution of the isolated field sample in the $\sigma_{\rm int}$ vs. $V_{\rm C}$ plane is plotted with the red symbols. The AMAZE Clean ($z \simeq 3$) sample galaxies (see § 3.7.10) are plotted with grey symbols and the AMAZE Unconstrained sample with hollow symbols. There is no strong correlation between the two parameters in either of these surveys and we note that the KDS and AMAZE Clean galaxies are generally in agreement. The $V_{\rm C}/\sigma_{\rm int} = 1$ line divides the galaxies classified as rotation-dominated and dispersion-dominated. The galaxy s_sa22a-M38, classified here as a merger but classified in Gnerucci et al. (2011) as a rotating galaxy with $V_{\rm C} = 346 {\rm km\,s^{-1}}$ is marked on the plot.

limit. To clearly distinguish the 1-σ error regions for both the beam-smeared and intrinsic models, the region between the 16th and 84th percentile evaluations is shaded blue and red respectively in the velocity extaction panels throughout Figures 3.10 and 3.11. The +/- 1-σ error values for both $V_{\rm C}$ are then calculated using the equations below, which also take into account the measurement errors, with $\bar{\sigma}_{v_{\rm obs}}$ equal to the

average observational uncertainty extracted along PA_{kin}. The subscripts '16th' and '84th' denote the parameters used to construct the model from which the velocity has been extracted.

$$\delta V_{\rm C}+ = \sqrt{(V_{\rm C-84} - V_{\rm C})^2 + \left(\bar{\delta} V_{\rm obs}\right)^2} \tag{3.14}$$

$$\delta V_{\rm C}- = \sqrt{(V_{\rm C} - V_{\rm C-16})^2 + \left(\bar{\delta} V_{\rm obs}\right)^2} \tag{3.15}$$

The upper and lower errors on the $\sigma_{\rm int}$ are calculated using a similar approach. To encorporate the uncertainty introduced in the modelling by assuming a fixed value of $\sigma_{\rm int} = 50{\rm km\,s^{-1}}$, we make two further model evaluations using both the 16th and 84th percentile parameters with $\sigma_{\rm int} = 40{\rm km\,s^{-1}}$ and $\sigma_{\rm int} = 80{\rm km\,s^{-1}}$, with these limits roughly encompassing the range of observed and predicted velocity dispersion values at $z \simeq 3.5$ as shown in Wisnioski et al. (2015) figure 10. When assuming the broader $\sigma_{\rm int} = 80{\rm km\,s^{-1}}$ value in each spaxel the beam-smearing correction decreases, as the impact of convolution with spectral lines in adjacent spaxels with shifted velocity centres is less severe. Conversely, assuming $\sigma_{\rm int} = 40{\rm km\,s^{-1}}$ increases the beam-smearing. We calculate the minimum and maxmimum intrinsic velocity dispersion, $\sigma_{\rm int-84-40}$ and $\sigma_{\rm int-16-80}$, using equations 3.16 and 3.17 respectively:

$$\sigma_{\rm int-84-40} = \sqrt{(\sigma_{\rm obs} - \sigma_{\rm bs-84-40})^2 - \sigma_{\rm sky}^2} \tag{3.16}$$

$$\sigma_{\rm int-16-80} = \sqrt{(\sigma_{\rm obs} - \sigma_{\rm bs-16-80})^2 - \sigma_{\rm sky}^2} \tag{3.17}$$

where $\sigma_{\rm bs-84-40} = \sigma_{model-84-40} - 40$ and $\sigma_{\rm bs-16-80} = \sigma_{model16-80} - 80$ are the beam-smeared maps. The lower and upper errors on $\sigma_{\rm int}$ are then given by the following:

$$\delta\sigma_{\rm int}+ = \sqrt{(\sigma_{\rm int} - \sigma_{\rm int-84-40})^2 + (\bar{\sigma}_{\sigma_{\rm obs}})^2} \tag{3.18}$$

$$\delta\sigma_{\rm int}- = \sqrt{(\sigma_{\rm int-16-80} - \sigma_{\rm int})^2 + (\bar{\sigma}_{\sigma_{\rm obs}})^2} \tag{3.19}$$

with $\bar{\sigma}_{\sigma_{\rm obs}}$ equal to the average of the velocity dispersion measurement errors. Once these quantities have been measured, the upper and lower errors on the ratio $V_{\rm C}/\sigma_{\rm int}$ can be computed using equations 3.20 and 3.21.

$$\delta\frac{V_{\rm C}}{\sigma_{\rm int}}+ = \frac{V_{\rm C}}{\sigma_{\rm int}}\sqrt{\left(\frac{\delta V_{\rm C}+}{V_{\rm C}}\right)^2 + \left(\frac{\delta\sigma_{\rm int}+}{\sigma_{\rm int}}\right)^2} \tag{3.20}$$

$$\delta\frac{V_{\rm C}}{\sigma_{\rm int}}- = \frac{V_{\rm C}}{\sigma_{\rm int}}\sqrt{\left(\frac{\delta V_{\rm C}-}{V_{\rm C}}\right)^2 + \left(\frac{\delta\sigma_{\rm int}+-}{\sigma_{\rm int}}\right)^2} \tag{3.21}$$

3.10 Kinematics Plots

In Figures 3.10, 3.11 and 3.12 we plot the kinematic grids for the KDS galaxies classified as rotation-dominated, dispersion-dominated and merger candidates respectively. The figure captions provide more information on each of the panels of these grids.

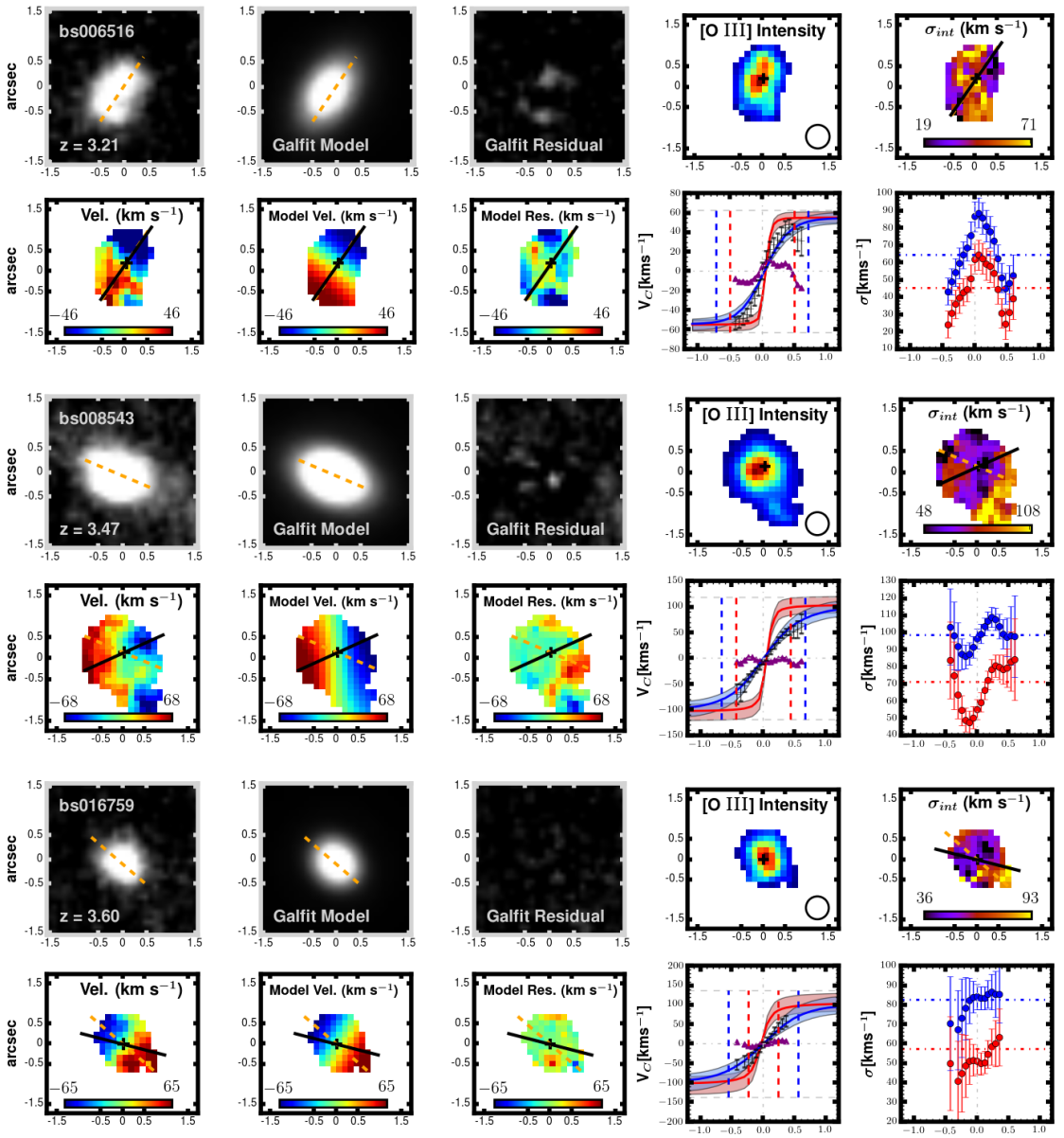

Figure 3.10: We plot the kinematic grids for the 14/33 isolated field sample galaxies classified as rotation-dominated. For each galaxy we plot the *HST* image, GALFIT model and GALFIT residuals, along with the observed [O III]λ5007 intensity map, dispersion map and velocity map extracted from the datacubes with gaussian-fits to the individual spaxels as described in § 3.3.2. The solid black line and dashed orange line plotted in various panels show $\mathrm{PA_{kin}}$ and PA_{morph} respectively. On the bottom row we plot the beam-smeared model velocity and data-model velocity residuals with colour bar limits tuned to the velocity model. Also on the bottom row, we plot extractions along $\mathrm{PA_{kin}}$ for both the velocity and velocity dispersion. The grey points with errorbars on the velocity extraction plot are from the observed velocity map, the blue line and blue shaded regions represent the beam-smeared model fit to the data and errors respectively, whereas the red line and shaded regions are the intrinsic model from which V_{C} is extracted. The purple symbols represent the extraction along $\mathrm{PA_{kin}}$ from the residual map, and the two vertical dashed lines denote the intrinsic (inner) and convolved (outer) $2R_{1/2}$ values, with V_{C} extracted at the intrinsic value and V_{BS} extracted at the convolved value of the intrinsic and observed profiles respectively. The intrinsic models flatten at small radii, and so small changes in $R_{1/2}$ have negligible impact on the final, extracted V_{C} values. The blue points on the velocity dispersion extraction plot show the values extracted from the observed dispersion map and the red are from the beam-smearing corrected map as per Equation 3.6, and the vertical dashed lines have the same meaning as for the velocity extraction plot. Also plotted with the blue and red dot-dash horizontal lines are the median values of the observed and intrinsic (i.e. σ_{int}) dispersion maps respectively.

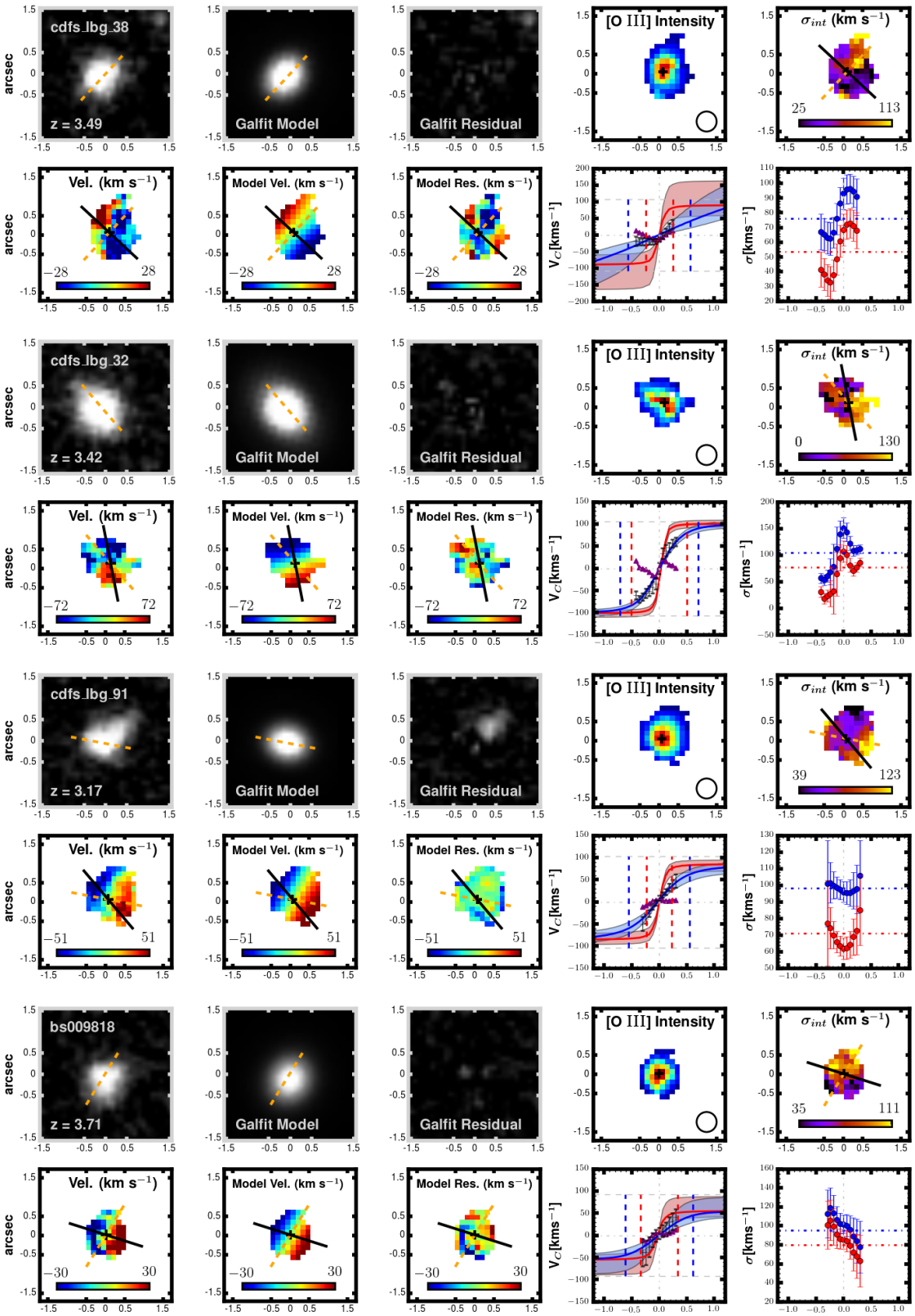

Figure 3.10: **Continued.**

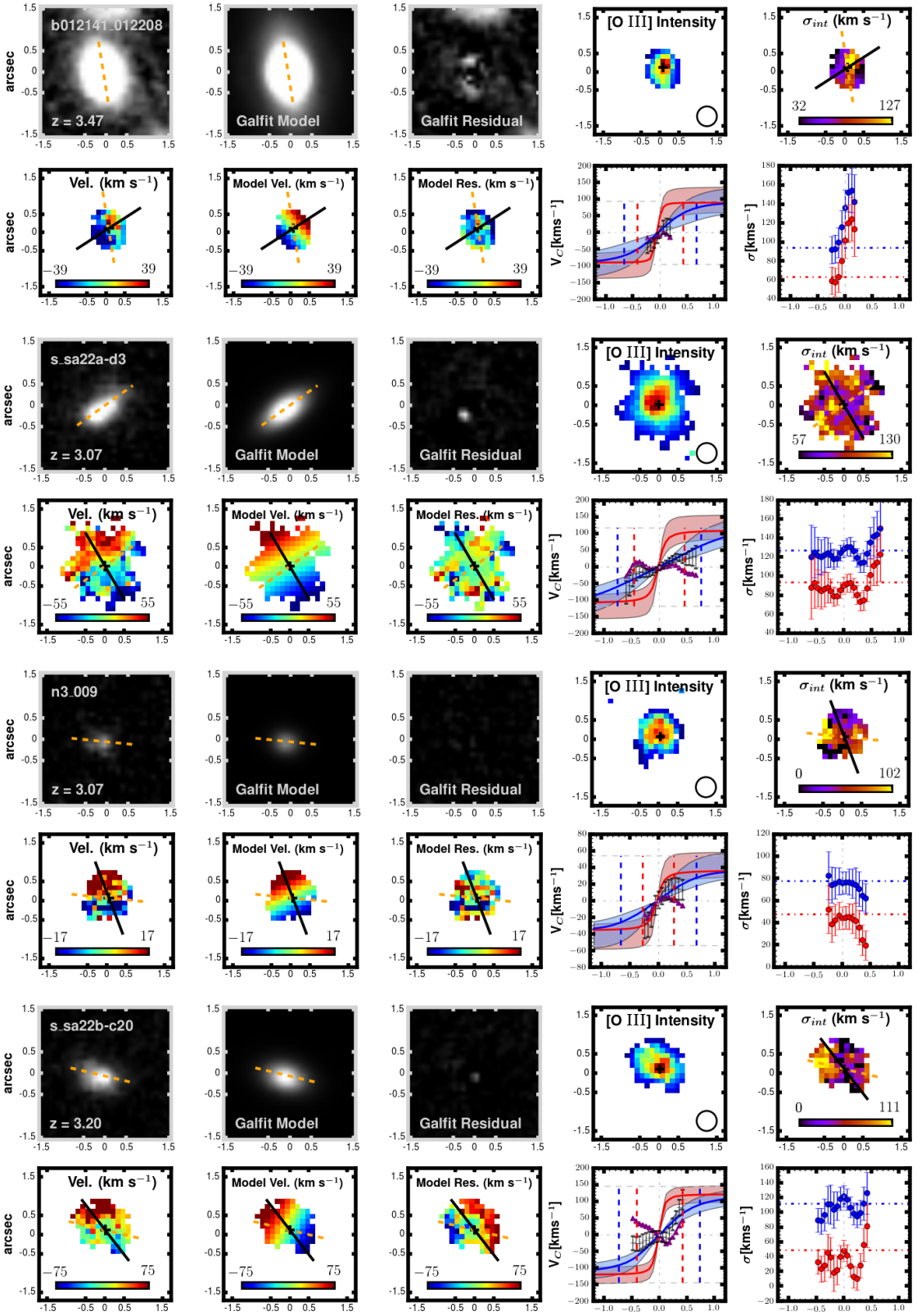

Figure 3.10: **Continued.**

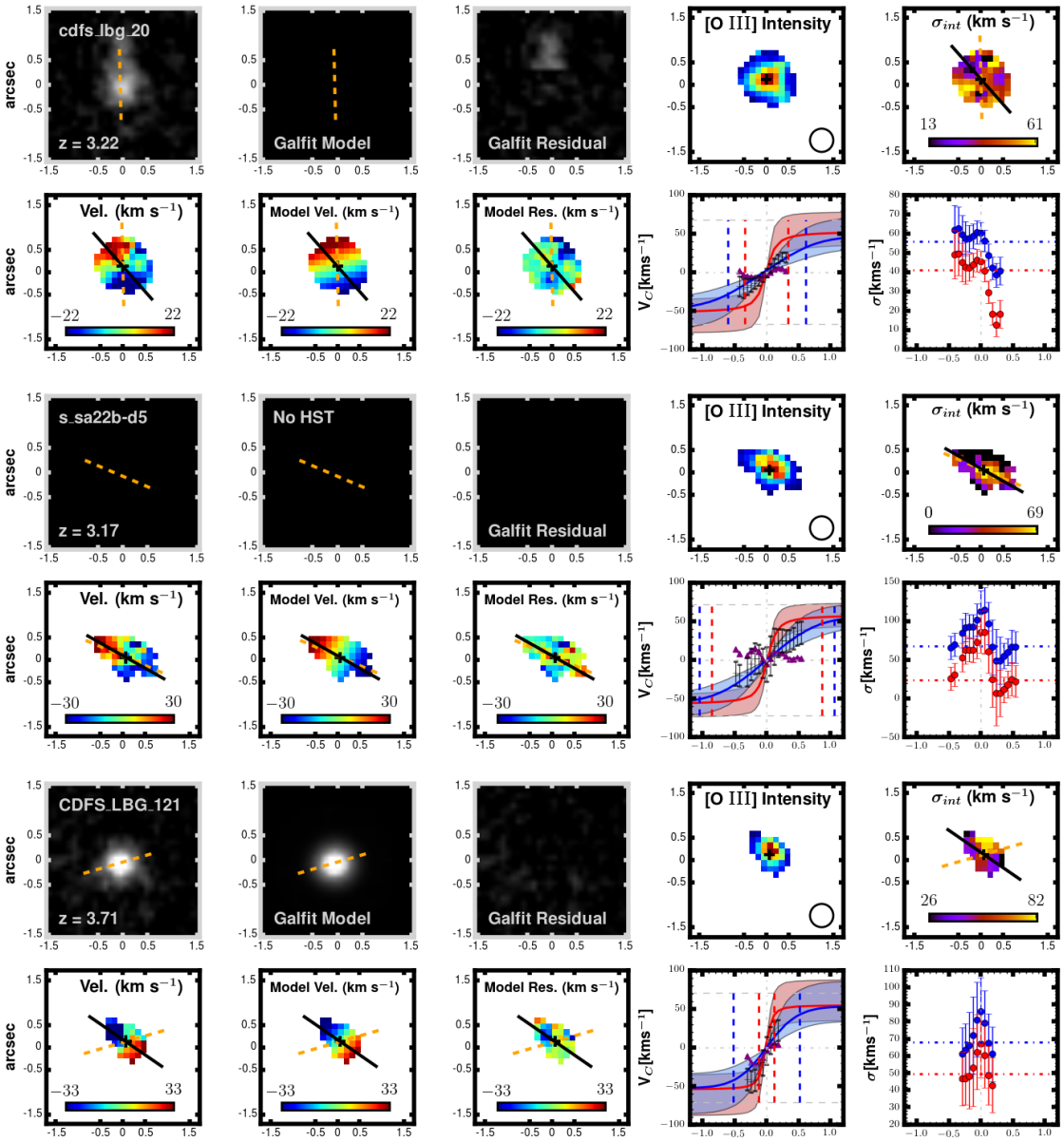

Figure 3.10: **Continued.**

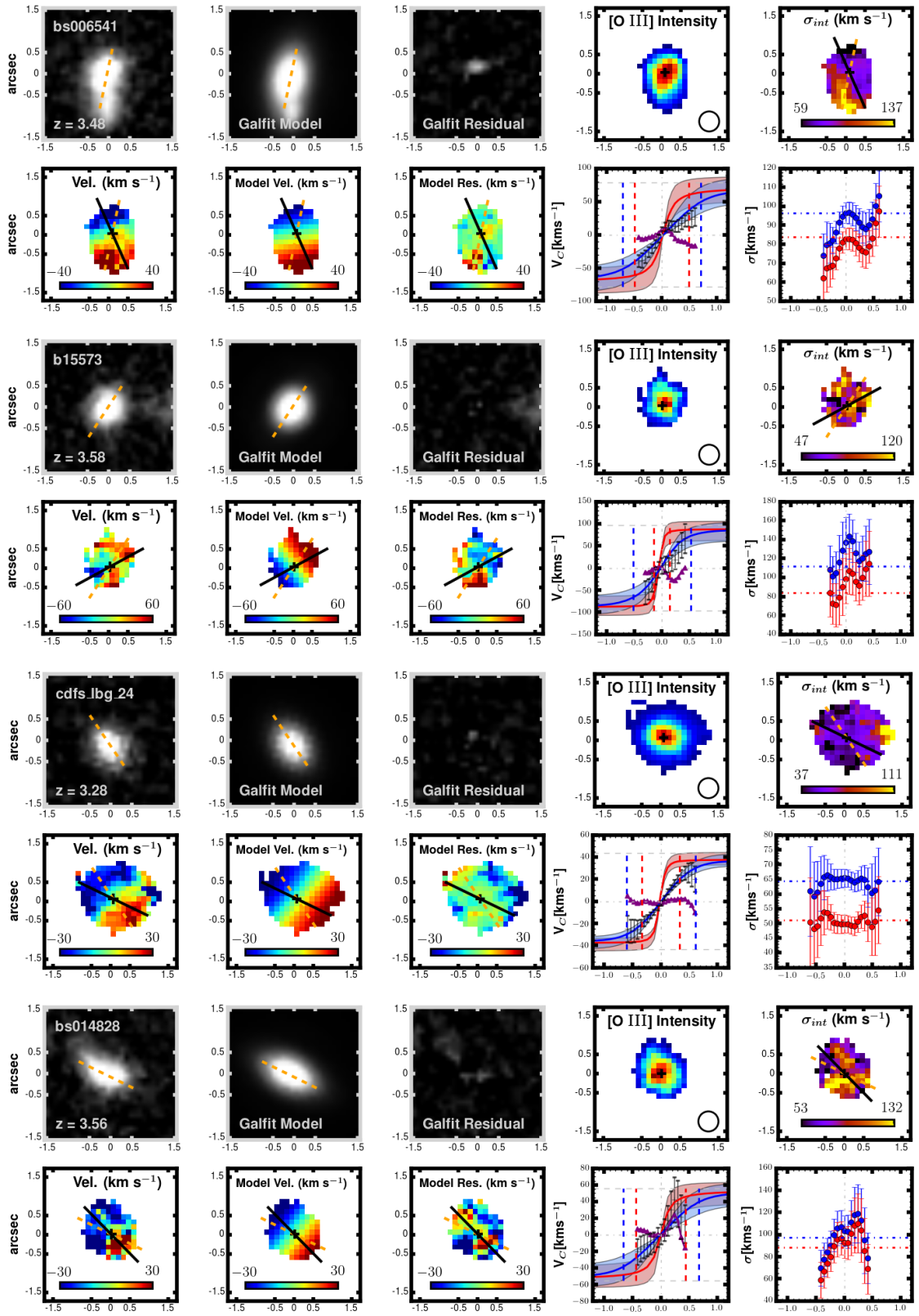

Figure 3.11: The same as in figure 3.10 but for the dispersion-dominated galaxies.

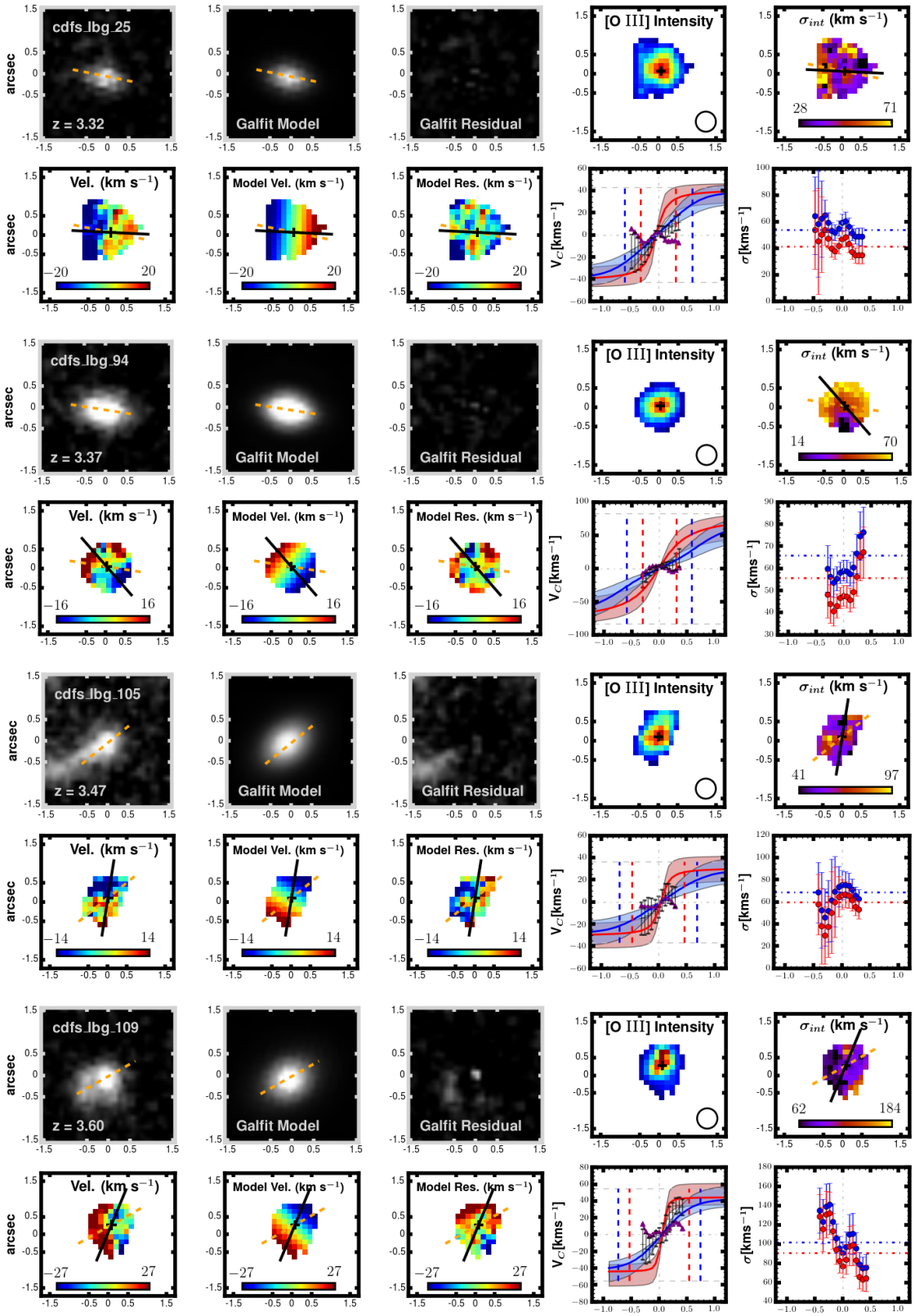

Figure 3.11: **Continued.**

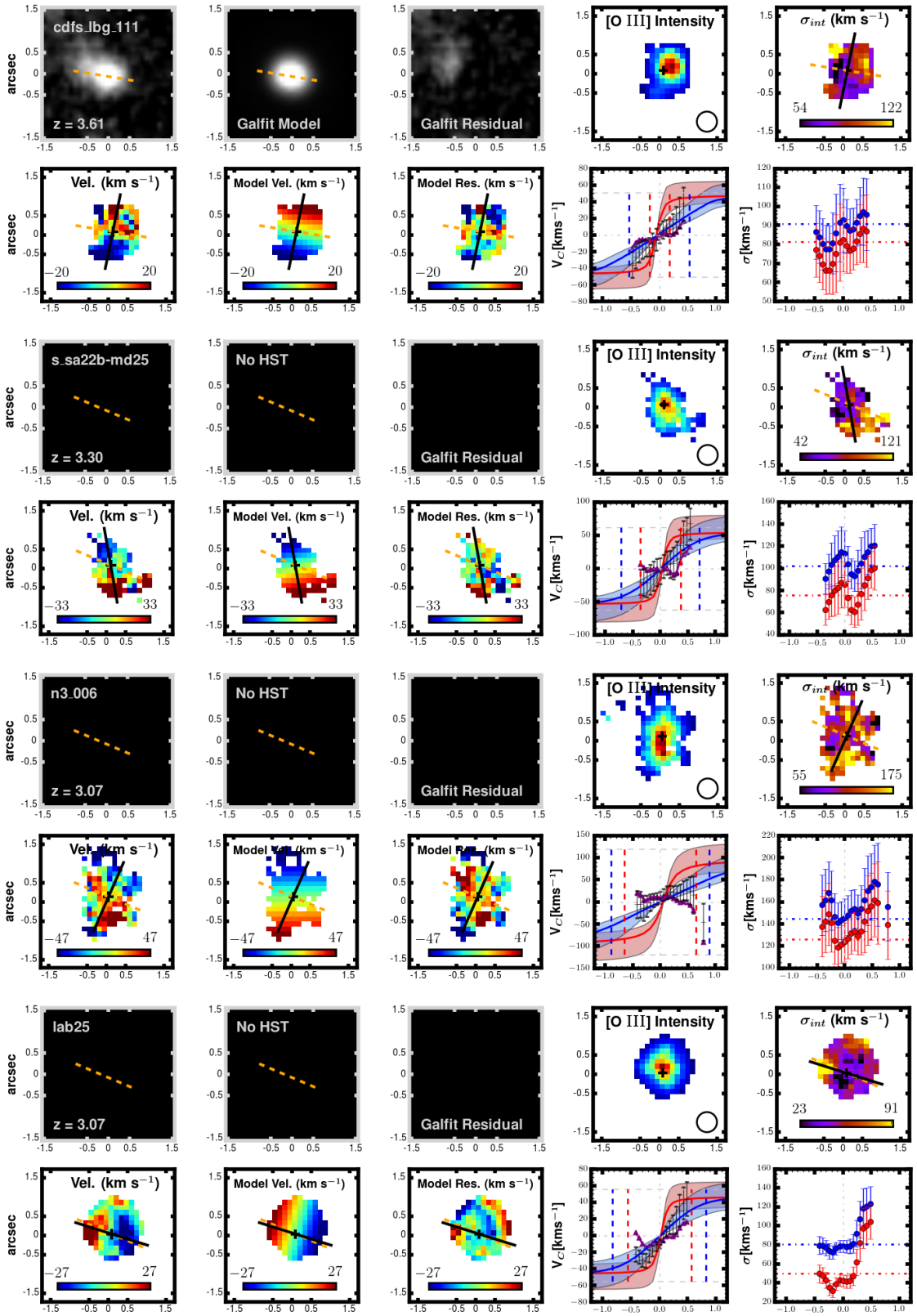

Figure 3.11: **Continued.**

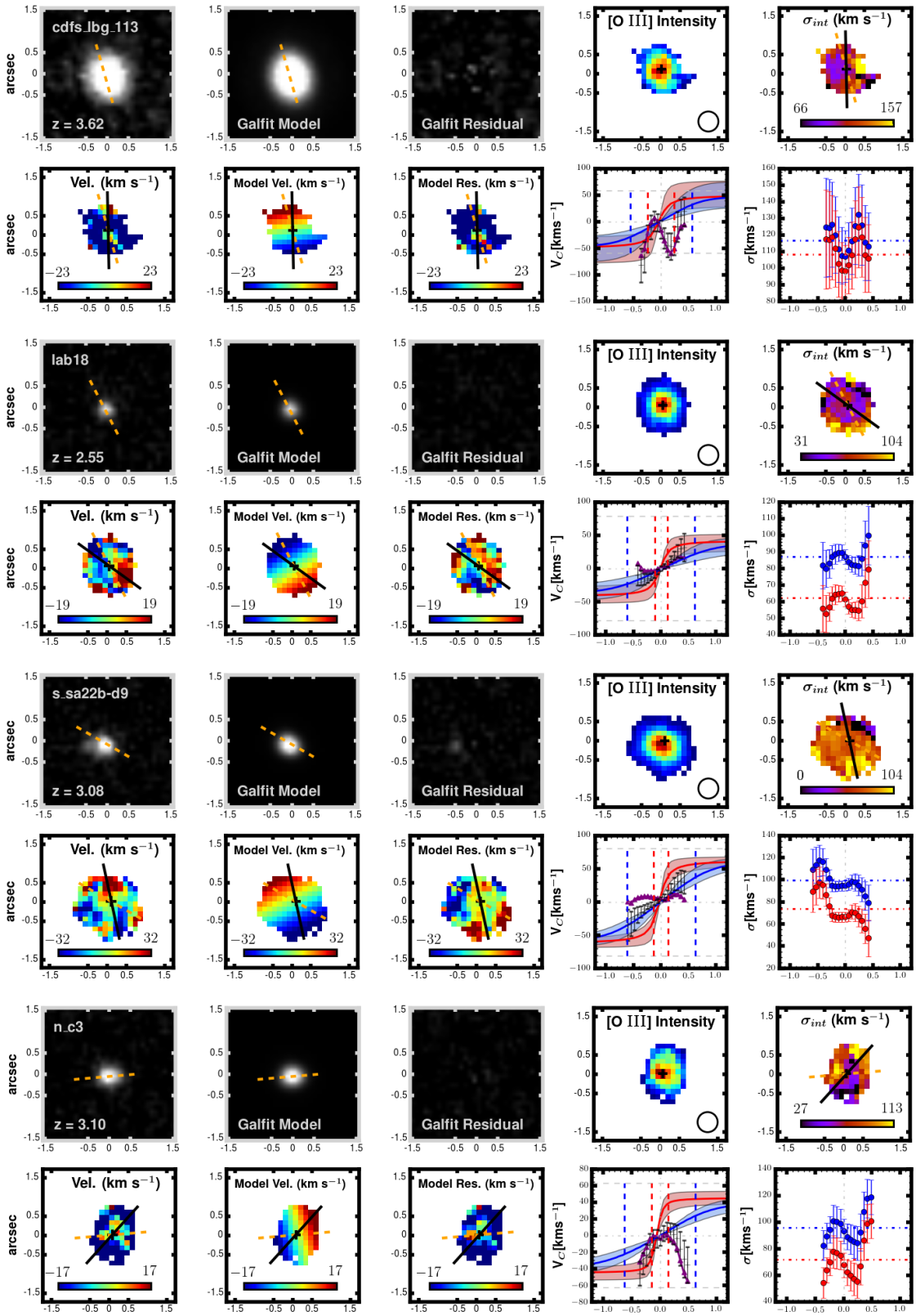

Figure 3.11: **Continued.**

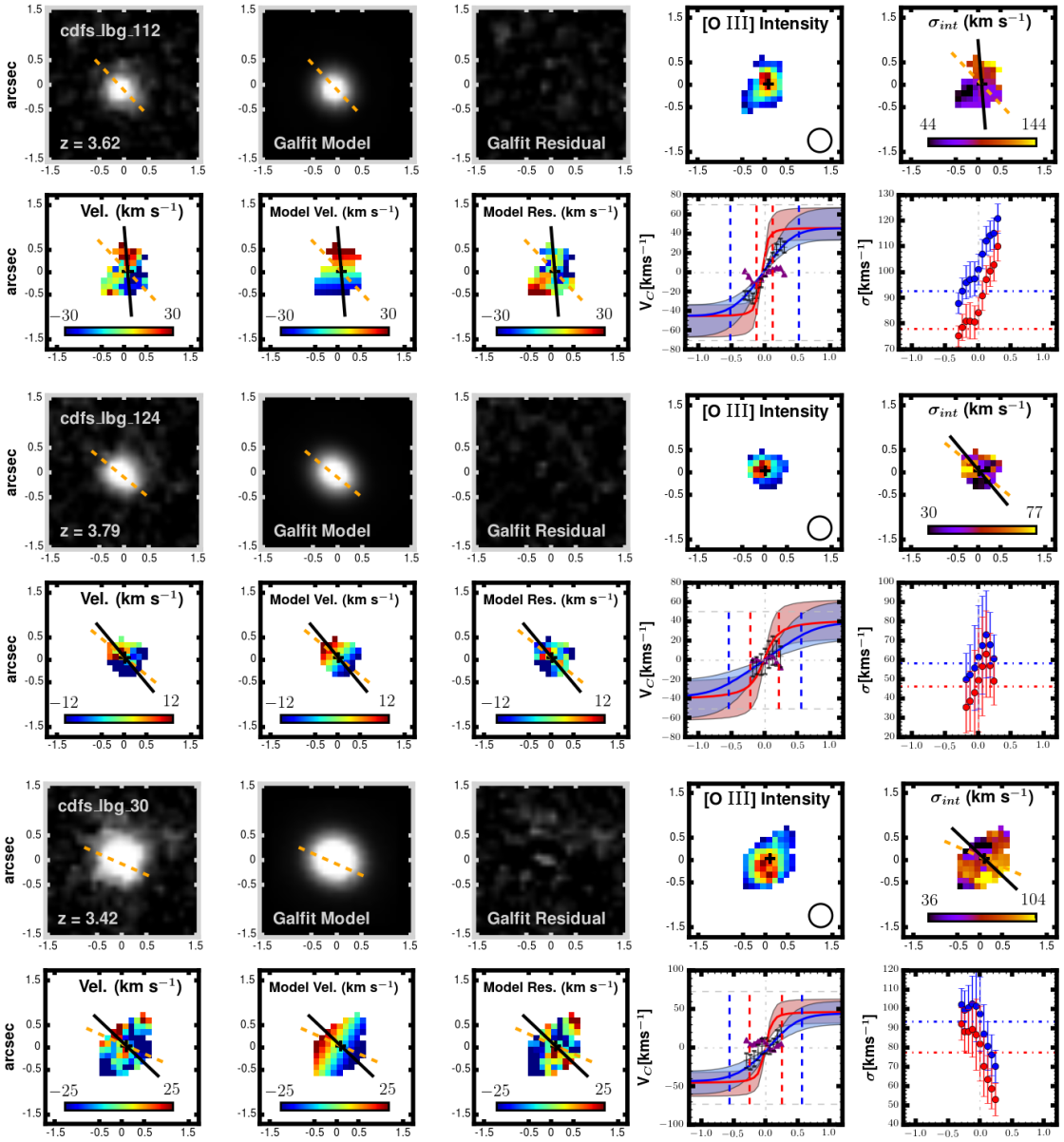

Figure 3.11: **Continued.**

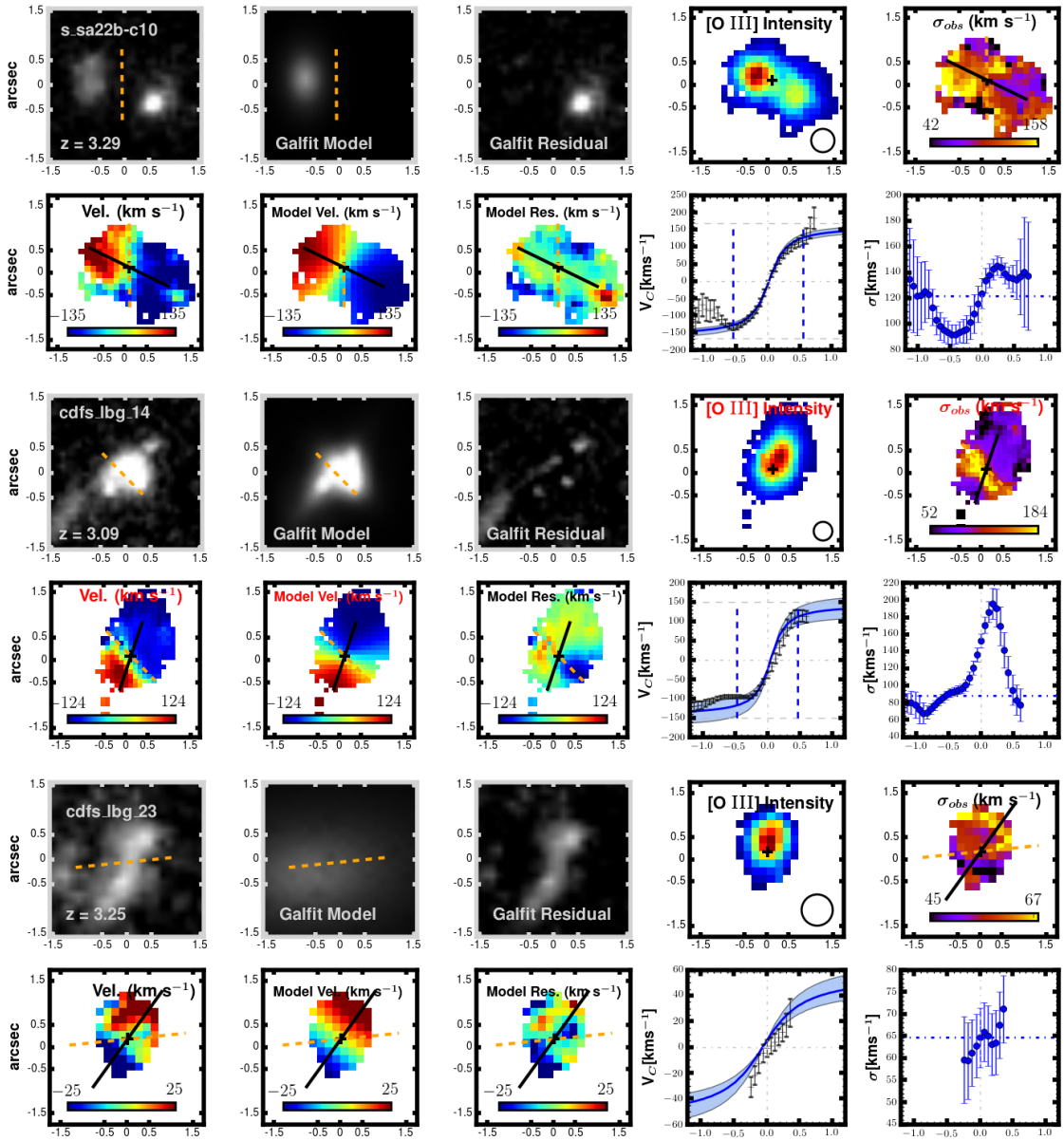

Figure 3.12: The same as for figure 3.10 but for the merger candidates. In this case we plot only fits to the data in the velocity extraction plot with the blue line, rather than attempting the full beam-smearing analysis. Several of the galaxies here mimic rotation from a purely kinematic perspective, but have two or more *HST* components and an accompanying double peak in the object spectrum at the object centre, leading to large velocity dispersions when single gaussian-fits are attempted.

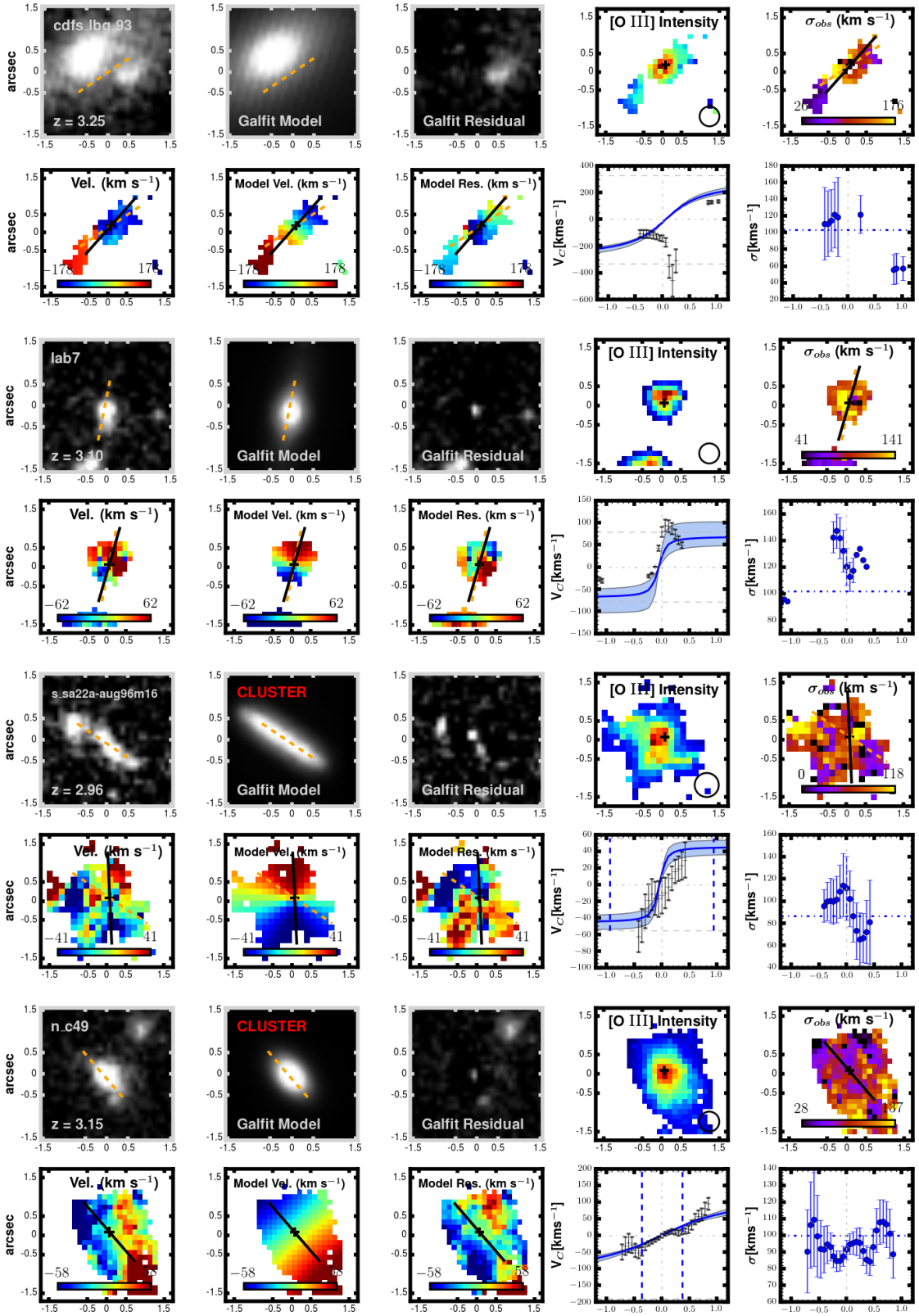

Figure 3.12: **Continued.**

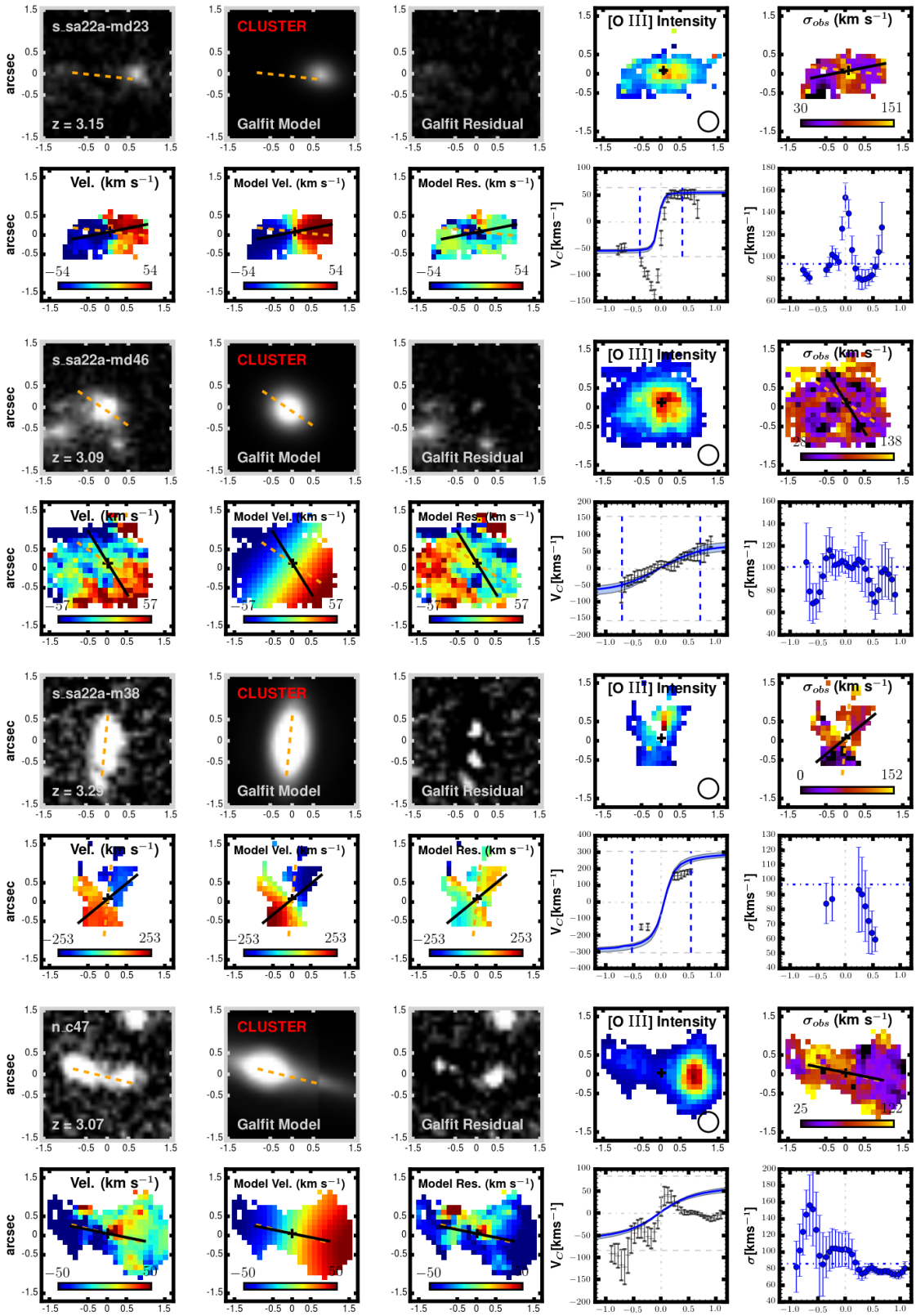

Figure 3.12: **Continued.**

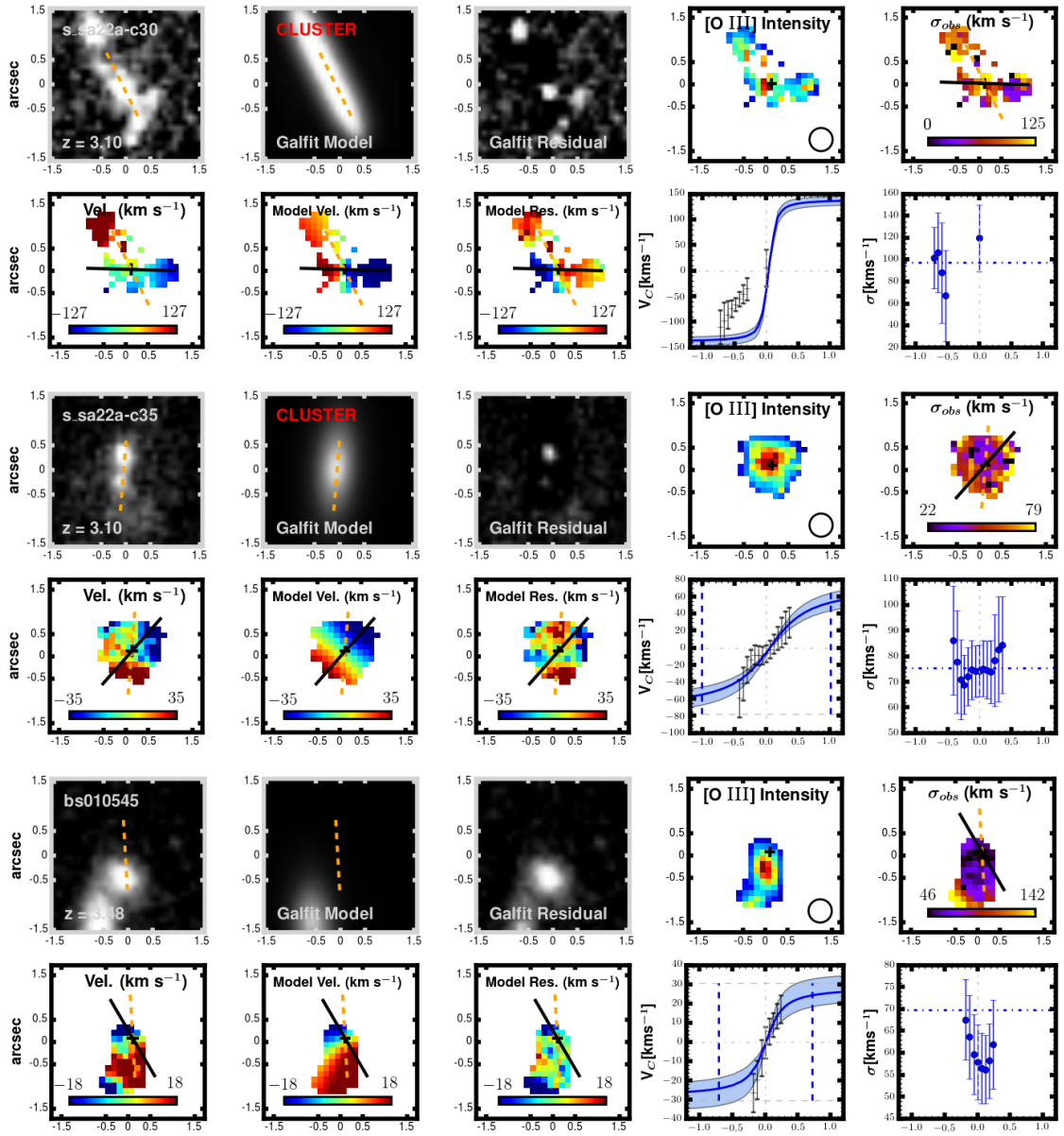

Figure 3.12: **Continued.**

Chapter 4

The KMOS Deep Survey (KDS) II: The evolution of the stellar-mass Tully-Fisher relation since $z \simeq 3.5$

Abstract

We use a sample of 29 $z \simeq 3.4 - 3.8$ galaxies from the KMOS Deep Survey (KDS), combined with ~ 1200 lower redshift galaxies from 16 literature comparison samples, to investigate the evolution of the stellar-mass Tully-Fisher relationship over $0 < z < 3.5$. We first establish the slope and normalisation of the local rotation-velocity – stellar-mass ($V_C - M_\star$) relationship using a reference sample of nearby spiral galaxies; thereafter we fix the slope, and focus on the evolution of the velocity normalisation with redshift. The rotation-dominated KDS galaxies at $z \simeq 3.5$ have rotation velocities $\simeq -0.1$ dex lower than local reference galaxies at fixed stellar mass. Using KDS galaxies in combination with the comparison samples, we demonstrate that such derived TFR offsets are strongly driven by the median ratio of rotation velocity to velocity dispersion ($\sigma_{\rm int}$) of the galaxy sample used. The apparently discrepant results in the literature can be reconciled when this is accounted for. Confining attention to samples of galaxies that are especially

'disky' (i.e., high V_C/σ_{int}), for which V_C is likely a good tracer of dynamical mass, we measure rotation velocities at fixed stellar mass which are consistently ~ 0.1 dex higher than in the local universe. However, these subsamples become increasingly less representative of the star-forming galaxy population at $z \geq 1$. If instead a pressure support term is included to create a 'total' effective velocity, $V_{tot} = (V_C^2 + 4.0\sigma_{int}^2)^{0.5}$, then all KDS galaxies and those in the comparison samples (irrespective of their 'diskiness') appear to lie on the same locus in the total-velocity versus stellar-mass plane. The trend between total-velocity zero-point and redshift is consistent with a steady evolution of $M_\star/M_{dyn}$ with cosmic time over 12 Gyr.

4.1 Introduction

Typical star-forming galaxies are usually defined as those that lie on the relatively tight relationship between star-formation rate (SFR) and stellar mass ($M_\star$) that is observed over a wide redshift range (e.g. Daddi et al., 2007; Noeske et al., 2007b; Elbaz et al., 2007). As well as the arrival and departure of galaxies from this sequence, due to the combination of processes which replenish and quench star formation (e.g. Peng et al. 2010; Tacchella et al. 2015), the mean physical properties of typical star-forming galaxies evolve over time. This is manifest in the evolution of: the main-sequence normalisation (e.g. Whitaker et al., 2012b, 2014); the mass-metallicity relationship normalisation (e.g. Erb et al., 2006; Maiolino et al., 2008; Cullen et al., 2014); disk sizes (e.g. Trujillo et al., 2007; van der Wel et al., 2014) and dynamical properties (e.g. Cresci et al., 2009; Wisnioski et al., 2015; Tiley et al., 2016; Harrison et al., 2017; Swinbank et al., 2017).

Much of the observational progress over the last decade can be attributed to the advent of integral-field spectroscopy, a technique in which an array of spectra can be collected across a given spatial region, allowing for spatially-resolved measurements of the dynamical and chemical properties of both star-forming and quiescent galaxies to be made (e.g. Epinat et al., 2008a; Förster Schreiber et al., 2009; Gnerucci et al., 2011;

Epinat et al., 2012; Troncoso et al., 2014; Wisnioski et al., 2015; Stott et al., 2016; Di Teodoro et al., 2016; Swinbank et al., 2017; Turner et al., 2017). In tandem with this, the internal gas properties (e.g. kinematics, metallicity gradients) can now be predicted by high-resolution cosmological simulations for 100s-1000s of galaxies (e.g. Schaye et al., 2015; Genel et al., 2015; Lagos et al., 2017; Swinbank et al., 2017). However, these models require several 'sub-grid' assumptions to describe the many processes which govern how galaxies evolve, such as nonlinear feedback from star formation and active galactic nuclei (e.g. Schaye et al., 2015). These assumptions must be refined or refuted by comparison to observations, ideally using large samples of galaxies across cosmic time with integral-field spectroscopic data.

Galaxy samples have now been observed using integral-field spectroscopy, spanning the redshift range $0 < z < 4$, thanks in particular to the Spectrograph for INtegral-Field Observations in the Near Infrared (SINFONI; Eisenhauer et al. 2003) and the multiplexing capabilities of the *K*-band Multi-Object Spectrograph (KMOS; Sharples et al. 2013). The number of observations is continually growing, and as a result we are better placed than ever to study the evolving star-forming population over this redshift interval, corresponding to 12 Gyr of cosmic time (i.e. most of the history of the Universe). A picture of the dynamical evolution of star-forming galaxies has emerged, in which initially turbulent systems with large intrinsic velocity dispersions ($\sigma_{\rm int}$) 'settle' over time (e.g. Law et al., 2009; Simons et al., 2016), leading to lower observed $\sigma_{\rm int}$ values and therefore higher ratios of rotation velocity to velocity dispersion ($V_{\rm C}/\sigma_{\rm int}$) with decreasing redshift (e.g. Wisnioski et al. 2015; Simons et al. 2017; Turner et al. 2017; Johnson et al. 2018 and Chapter 3, although see Di Teodoro et al. 2016 for a discussion of how $\sigma_{\rm int}$ could be overstimated at intermediate redshifts).

The evolution of dynamical scaling relations in star-forming galaxies provides information about the partition of the total mass between dark matter, stars and gas, as well as shedding light on the stability of the galaxy disks. One important example is the stellar mass 'Tully-Fisher' relation (Tully & Fisher, 1977; Bell & de Jong, 2001)

which connects the stellar mass within a galaxy to the rotation velocity, a tracer of the total dynamical mass. A change in the slope of the relationship with increasing redshift indicates a stellar-mass dependent change to the connection between velocity and total galaxy mass. A change in the normalisation indicates a redistribution of the total mass in the galaxy between visible and dark components on the scales traced by the observations. It is mostly accepted that the number of galaxies observed and the data quality are too low to accurately constrain the slope of the relationship at $z > 1$, and so evolution is assessed by fixing the slope to a reference value measured in the local Universe and monitoring shifts in the normalisation (e.g. Puech et al., 2008; Cresci et al., 2009; Miller et al., 2011, 2012; Tiley et al., 2016; Harrison et al., 2017; Straatman et al., 2017; Pelliccia et al., 2017; Übler et al., 2017). However, there is no consensus throughout these studies on how the normalisation of the relationship changes over cosmic time. Systematic differences introduced by the choice of analysis method can lead to diverging conclusions, such as the choice of local reference relationship and the sample-selection criteria (e.g. Tiley et al., 2016; Harrison et al., 2017). In this chapter we investigate the evolution of the stellar mass Tully-Fisher relation from $z \sim 3.5$ to $z = 0$, and reconcile discrepant literature results over this range.

Furthermore, it has recently emerged that the rotation velocity may be an inadequate tracer of the total dynamical mass, especially at high redshift, due to the contribution of pressure support to the dynamical mass budget. For example Kassin et al. (2007) show that the $S_{0.5} = \sqrt{0.5V_C^2 + \sigma_g^2}$ parameter correlates more tightly with mass than the rotation velocities alone for galaxies over the redshift range $0 < z < 1.2$, where σ_g is the beam-smearing-corrected velocity dispersion of the galaxies. Burkert et al. (2010) also show that the addition of a pressure term to the equation of hydrostatic equilibrium can reduce the observed rotation velocities of star-forming galaxies, prompting others to adopt a corrected rotation velocity which accounts for the contribution from pressure (e.g. Newman et al., 2013; Übler et al., 2017). In Übler et al. (2017), a pressure-corrected velocity is explored in the context of the evolution of the stellar-mass Tully-Fisher relation out to $z \sim 2.3$, concluding that it is necessary to account for pressure support to truly trace the evolution of dynamical mass with redshift. These works have

sparked a new debate on how best to explore the connection between dynamical and stellar mass over cosmic time. In this study we expand such investigations out to $z \sim 3.5$.

The KMOS-Deep Survey (KDS; see Chapter 3 and Turner et al. 2017), is a programme which aims to study the dynamical and chemical properties of 77 star-forming galaxies at $z \simeq 3.5$. As described in Chapter 3, a detailed study of the dynamical properties of a sample of isolated KDS galaxies revealed that only one third are dominated by ordered rotation, as a result of low rotation velocities and high velocity dispersions. This is significantly lower than the $\sim 80-100$ per cent of star-forming galaxies at $z \leq 1$ observed to be rotation-dominated. We concluded that, for the majority of $z = 3.5$ star-forming galaxies, random motions are prevalent throughout the galaxy disk and, as suggested above, it may be important to account for these when attempting to trace the total dynamical mass of the galaxies. In this chapter we discuss the stellar-mass Tully-Fisher relation for the KDS galaxies and use a compilation of comparison samples in the literature spanning $0 < z < 3.5$ to assess the evolution of the relation. We also consider the impact of pressure support, traced by velocity dispersions, to the dynamical properties of the KDS and comparison sample galaxies.

The structure of the chapter is as follows. In § 4.2 we give a brief overview of the selection criteria, data reduction and extraction of physical properties for the KDS sample. In § 4.3 we present our study of the stellar-mass Tully-Fisher relation for the KDS galaxies, and using our compilation of comparison samples we discuss the dependence of the observed evolution of the relationship on sample-selection criteria. In § 4.4 we explore the impact of accounting for pressure support, traced by the velocity dispersions, in the dynamical mass budget of the galaxies, and formulate an effective 'total velocity'. Using the comparison samples, we then study the evolutionary trends of the total-velocity versus stellar-mass relation. In § 4.5 we present our conclusions. Throughout this work we assume a flat ΛCDM cosmology with (h, Ω_m, Ω_Λ) = (0.7, 0.3, 0.7).

4.2 Survey description, sample selection and observations

The KDS is a survey of the gas kinematics and chemical compositions of 77 star-forming, $z \simeq 3.5$ galaxies observed with KMOS. Full details of the survey, sample selection, data reduction, dynamical modelling and kinematic parameter extraction can be found in Chapter 3. However, below we present a brief overview of the survey, and of the KDS sample used throughout § 4.3 and § 4.4.

4.2.1 The KDS & sample selection

The KMOS Deep Survey (KDS) is a guaranteed time programme focusing on the spatially-resolved properties of typical star-forming galaxies at $z \simeq 3.5$. These data have been collected to guide our understanding of early disk formation in terms of both the observed kinematics and the chemistry, as inferred through observations of the ionised gas emission lines.

The 77 KDS target galaxies have previous spectroscopic redshift measurement and were selected to fall in the redshift range $3.0 < z < 3.8$. We include regions of both low and high galaxy density, spanning GOODS-S (e.g. Koekemoer et al., 2011; Grogin et al., 2011; Guo et al., 2013) and SSA22 (e.g. Steidel et al., 1998). These fields are covered by rest-frame ultraviolet to far-infrared high-resolution ancillary photometry, allowing us to infer galactic physical properties with SED fitting and to recover the morphological properties of the galaxies. The measurement of stellar masses is described in detail in Chapter 3. Briefly, we make use of the available multi-wavelength photometry to fit the galaxy SEDs following the procedure described in McLure et al. (2011). We use solar metallicity BC03 (Bruzual & Charlot, 2003) templates with a Chabrier (2003) Initial Mass Function (IMF), account for dust attenuation using the Calzetti reddening law (Calzetti et al., 2000) with dust attenuation allowed to vary freely over the range $0.0 < A_V < 4.0$, and include the effects of strong nebular emission lines according

to the line ratios determined by Cullen et al. (2014). We focus on the stellar mass range $9.0 < \log(M_\star/M_\odot) < 10.5$, (i.e. the range covered by local reference data, see Fig. 4.9), which leads to 4 KDS galaxies with $\log(M_\star/M_\odot) < 9.0$ being omitted from the subsequent analysis. The median stellar mass of the galaxies in this range is $\log(M_\star/M_\odot) = 9.8$. We have also verified using both the rest-frame UVJ colour space diagnostic and the star-formation rate versus stellar mass 'main-sequence' plot that the KDS target galaxies fall in the loci defined by typical star-forming galaxies at these redshifts.

4.2.2 KMOS observations and data reduction

KMOS is a second-generation Integral-Field Spectrograph (IFS) mounted at the Nasmyth focal plane of Unit Telescope 1 (UT1) at the European Southern Observatory's Very Large Telescope (ESO/VLT). The instrument has 24 moveable pickoff arms, each with an integrated IFU, which patrol a region 7.2′ in diameter on the sky, providing considerable flexibility when selecting sources for a single pointing. The light from each set of 8 IFUs is dispersed by a single spectrograph and recorded on a 2k×2k Hawaii-2RG HgCdTe near-infrared detector, so that the instrument is comprised of three effectively independent modules.

The target galaxies were observed with KMOS in the H and K-bands during ESO observing periods P92-P96 using Guaranteed Time Observations (Programme IDs: 092.A-0399(A), 093.A-0122(A,B), 094.A-0214(A,B), 095.A-0680(A,B), 096.A-0315(A,B,C)) with excellent K-band seeing conditions ranging between $0.5 - 0.7''$. At these redshifts, the Hβ, [O III]λ4959 and [O III]λ5007 emission lines are shifted into the K-band and the [O II]λ3727,3729 doublet is shifted into the H-band. When used together, these features are rich in both kinematic and chemical information. The on-source exposure times were in the range 7-10 hours, accumulated using a standard object-sky-object (OSO) nod-to-sky observation pattern, with 300s exposures and alternating $0.2''/0.1''$ dither pattern for increased spatial sampling around each of the target galaxies. We also observed standard stars to allow for flux calibration of

the data products, and the spatial locations of control stars were monitored throughout the observations to determine the shifts which must be applied to each exposure when creating the final object stacks (see Chapter 2).

Data reduction was carried out using the Software Package for Astronomical Reduction with KMOS, (SPARK; Davies et al. 2013), implemented using the ESO Recipe Execution Tool (ESOREX) (Freudling et al., 2013), with additional python scripts for non-standard methods (see Chapter 2). Following the reduction of each object-sky pair, all exposures were stacked together to create a final datacube for each object, which was flux calibrated using the standard star observations. We attempted to make an integrated measurement of the [O III]λ5007 emission line in each cube (the highest S/N line), detecting emission in 62 (81 per cent) of the galaxies in the sample.

4.2.3 Morphological and kinematic measurements

Full details of the measurement of morphological and kinematic parameters for the KDS galaxies are provided in Chapter 3, and we briefly recap those here. To accurately constrain the kinematics of the KDS sample, it was important to measure the galaxy sizes and inclination angles, which allowed us to extract rotation velocities at a known fiducial radius and correct the line-of-sight velocity component. We used GALFIT (Peng et al. 2010) to constrain the half-light radii ($R_{1/2}$) and axis-ratios of the KDS galaxies by fitting exponential light profiles to the *Hubble Space Telescope* (*HST*) *WFC3 F160W* imaging. In each of the stacked datacubes where an integrated [O III]λ5007 measurement was made, we extracted two-dimensional flux, velocity and velocity dispersion maps by fitting gaussian profiles to the individual spatial-pixels (spaxels) of the cube. We classified 47/62 galaxies with an integrated [O III]λ5007 measurement as spatially-resolved, with this being defined as those galaxies where the extent of the [O III]λ5007 flux map is more extended than the Point Spread Function (PSF) of the observations.

For the dynamical modelling, a series of mock datacubes were populated with

[O III]λ5007 emission lines in an exponential spatial flux distribution and with a two-dimensional velocity field which followed the arctangent function. These intrinsic models were convolved with the atmospheric PSF, measured from the observations, and fitted to the observed velocity field, which generated both observed and intrinsic model velocity fields and a map of the beam-smearing corrections to the observed velocity dispersions. The rotation velocities were extracted from the best-fit intrinsic model at a fiducial radius of $2R_{1/2}$ (corresponding to $\simeq 3.4R_{\rm d}$, where $R_{\rm d}$ is the exponential disk scale radius). The velocity dispersion value for each galaxy was taken as the median of the intrinsic velocity dispersion maps, i.e. the observed map with the beam-smearing correction map subtracted linearly and the intrumental resolution map subtracted in quadrature. In summary, the outcome of the dynamical modelling procedure was a measure of the intrinsic rotation velocity, $V_{\rm C}$, and the intrinsic velocity dispersion, $\sigma_{\rm int}$, for each galaxy in the spatially-resolved sample.

The high-resolution *HST* imaging allowed us to identify galaxies involved in probable late-stage merger events, for which the interpretation of velocity and velocity dispersion fields is complicated. Galaxies with multiple morphological components within 1 arcsecond, most of the time found to have irregular kinematics, were removed from the sample. After identifying KDS targets which are spatially-resolved and removing the merger candidates, we are left with 29 galaxies in the specified mass range (see § 4.2.1), which we refer to as the 'isolated-field sample' throughout the remainder of this chapter, and which constitute the KDS sample for the analysis described in the following sections. The isolated-field sample is further subdivided into 'rotation-dominated' with $V_{\rm C}/\sigma_{\rm int} > 1$ (13/29) and 'dispersion-dominated' with $V_{\rm C}/\sigma_{\rm int} < 1$ (16/29) galaxies, as a simple method to distinguish between whether ordered rotation or random motions dominate the gas dynamics of the system. The morphological and kinematic properties of the isolated-field sample are listed in Chapter 3.

4.2.4 Comparison samples

Throughout this work we make use of 5 'local' ($z = 0$) and 16 'distant' ($z \sim 0.1 - 3$) comparison samples to establish the impact of sample selection effects on the evolution of the stellar mass Tully-Fisher relation. In § 4.3.2 and § 4.3.2 we demonstrate that, irrespective of the complexities of the individual sample selection criteria, the typical 'diskiness' of the samples, traced by the median V_C/σ_{int}, governs the inferred stellar mass Tully-Fisher relations. A detailed description of each of these samples is provided in § 4.6, to which we refer the reader for more information. Throughout § 4.3.2 we apply the same fitting methodology to each of the comparison samples in order to provide consistent results over the wide redshift range traced by the measurements.

Briefly, we obtained the published rotation velocities, velocity dispersions and stellar masses of these star-forming galaxy samples spanning $0 < z < 3$, correcting the stellar masses to a Chabrier (2003) IMF where required, and monitoring the methods used to measure rotation velocities and intrinsic velocity dispersions. Systematic errors can be introduced to the results if different prescriptions have been followed to compute the galaxy physical properties, in particular the rotation velocities and stellar masses. Typically, the approach taken throughout the comparison samples is to extract galaxy rotation velocities at some fixed, fiducial radius. The radius used is not consistent throughout the samples, which can impact the measured rotation velocity, however as described further throughout § 4.6 this has a maximum impact of ~ 0.04 dex on the measured zero-points of the inferred Tully-Fisher relations. We use 'anchor' samples at $z = 0$ (Reyes et al. 2011; see section 4.6.1), $z \sim 1.0$ (the KROSS sample Harrison et al. 2017; see section 4.6.2) and $z \sim 3.5$ (the KDS sample described in the previous subsections) with consistent kinematic measurements, in order to establish evolutionary trends in the stellar mass Tully-Fisher relation free from the above caveat.

Additionally, despite stellar mass being the most robust parameter recovered from SED fitting, systematic differences in measured values may arise if the data quality and fitting

methodology is not uniform across the comparison samples (e.g. Pforr et al., 2012). To explore two extreme measurement cases we made use of two different stellar mass measurements in our KROSS anchor sample, computed using: (1) a fixed mass-to-light ratio across the sample (Harrison et al., 2017) and (2) a full SED fitting procedure (Tiley et al., 2019). The Tully-Fisher relation fit results described in § 4.3.2 are identical in both cases, as a combined result of the slope of the fitted relation being fixed and the process of fitting the normalisation effectively averaging over the individual stellar mass values. The nature of this fitting strategy mitigates the possible impact of the different stellar mass measurement prescriptions used throughout the comparison samples. We note that excellent ancillary photometric data spanning the *UV-NIR* wavelength range was utilised in the comparison sample studies to measure stellar masses, reducing the measurement uncertainties (e.g. Pforr et al., 2012).

To summarise, the samples were carefully-selected to contain typical star-forming galaxies with dynamics and stellar masses computed using comparable methodologies (see § 4.6 for more details). In some cases, we do not consider the measured kinematic properties to be directly comparable to the other samples; we highlight these results using grey hollow symbols in the plots throughout § 4.3 & § 4.4. We list the fit results in Table 4.1, and plot the data used for these fits in Figs 4.13 and 4.14.

4.3 The evolution of the stellar-mass Tully-Fisher relation

The stellar-mass Tully-Fisher relation (e.g. Bell & de Jong, 2001) connects the stellar mass within a galaxy to the rotation velocity, and hence, in the case of a disk galaxy, the total dynamical mass. It is thus a powerful tracer of the stellar assembly history of galaxies. There is currently a debate in the literature surrounding both the extent of the evolution of this scaling relation and the interpretation of an observed evolution. In comparison with the stellar-mass Tully-Fisher relation zero-point derived using

local spiral galaxies, some surveys report a varying degree of evolution over the range $0 < z < 2$ (e.g. Puech et al., 2008; Cresci et al., 2009; Straatman et al., 2017; Übler et al., 2017) for massive, disky galaxies. Others report very little evolution using samples of star-forming galaxies covering a wide range in stellar mass and showing significant kinematic and morphological diversity (e.g. Miller et al., 2011, 2012; Harrison et al., 2017). In the following sections we fit the stellar-mass Tully-Fisher relation to KDS isolated-field sample galaxies and study the evolution of the relationship out to $z \sim 4$. We do this using the compilation of comparison samples described in § 4.2.4, carefully exploring the impact of differing sample-selection criteria on the inferred evolution. All of the galaxy samples are fitted in the rotation-velocity versus stellar-mass plane and so offsets from the local stellar-mass Tully-Fisher relation are quoted in terms of the velocity zero-point, which differs from the mass zero-points often quoted throughout the literature by a factor of $-1/\alpha$, where α is the slope of the relation defined in the following section.

4.3.1 The stellar-mass Tully-Fisher relation for the KDS galaxies

In Fig. 4.1 we plot intrinsic rotation velocity against stellar mass for the rotation-dominated and dispersion-dominated KDS subsamples. For comparison, we plot the density of $z \simeq 1$ rotation-dominated and dispersion-dominated KROSS galaxies (see § 4.6.2 for a description of the KROSS sample) in this plane using the blue and red contours respectively. In order to place the KDS galaxies in context in the rotation-velocity versus stellar-mass plane, it is important to choose a reliable $z \simeq 0$ comparison sample. We define the local stellar-mass Tully-Fisher relation by fitting the spiral galaxy sample from Reyes et al. (2011), which contains 189 galaxies covering a wide range in stellar mass.

To fit this sample we use the python package LMFIT (Newville et al., 2014) which makes use of the Levenberg-Marquardt algorithm. The relation $\log(V_C) = \beta + \alpha[\log(M_\star) - 10.1]$ (as per e.g. Reyes et al. 2011; Harrison et al. 2017) is fitted to the Reyes et al. (2011) galaxies, with both the slope and intercept allowed to vary. When performing

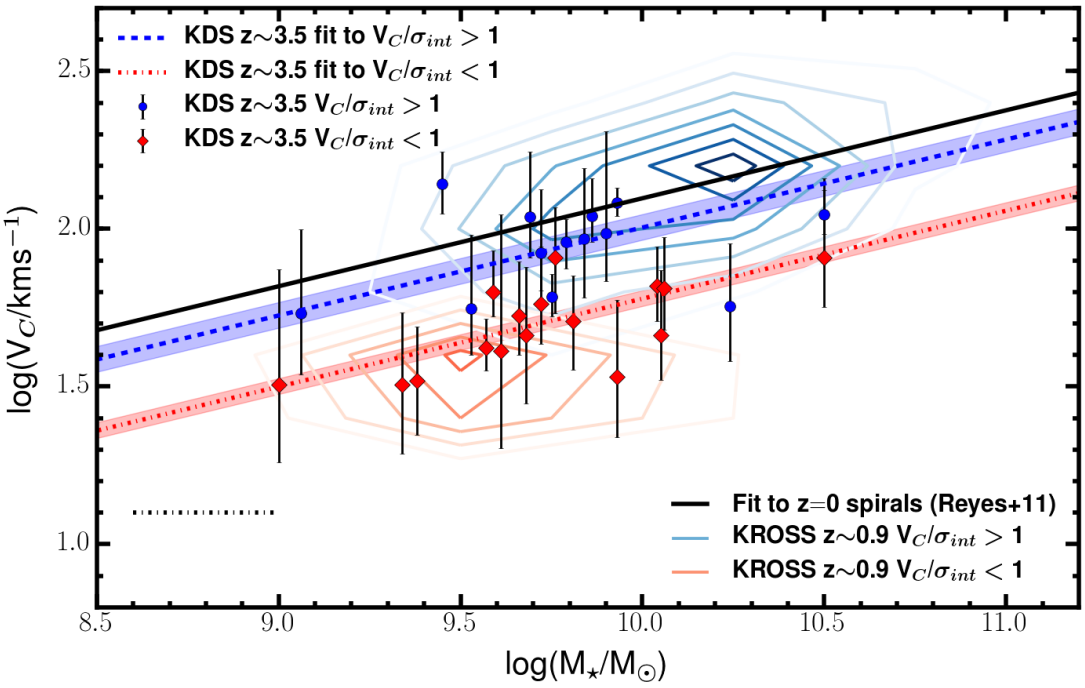

Figure 4.1: Rotation velocity versus stellar-mass for the rotation-dominated (blue-circular) and dispersion-dominated (red-diamond) KDS isolated-field sample galaxies. The black dot-dashed line in the lower left indicates the ±0.2 dex error on the KDS stellar masses. The solid black line shows the fit to local spiral galaxies from Reyes et al. (2011) using the fitting the relation $\log(V_C) = \beta + \alpha[\log(M_\star) - 10.1]$, which constitutes our local reference relation (see § 4.6.1). The blue-dashed and red-dot-dashed lines show the fits to the rotation-dominated and dispersion-dominated KDS galaxies respectively, using the fixed slope $\alpha = 0.279$ recovered from the fit to the Reyes et al. (2011) spirals. The shaded regions around these lines represent the $1-\sigma$ uncertainty on the fit. The blue and red contours show the density of rotation-dominated and dispersion-dominated galaxies from KROSS (Harrison et al., 2017), both starting at 10 and increasing in increments of 10 and 3 respectively. The velocity zero-point offset for the rotation-dominated KDS galaxies is $\simeq -0.10$ dex below the local relation, with the dispersion-dominated galaxies $\simeq -0.35$ dex below.

linear regression to model the relationship between these two derived, galactic physical properties, it is important to include a term which accounts for intrinsic scatter. This intrinsic scatter may be a result of variation in galaxy physical properties not monitored in the data being fitted (e.g. Weiner et al., 2006b; Bradford et al., 2016) (i.e. the relationship between rotation velocity and stellar mass is linear but not narrow). The data measurement errors may also be underestimated due to sytematic uncertainties in the conversion from flux measurements to physical properties, and so the intrinsic scatter parameter is best thought of as a measure of the scatter not accounted for by the measurement errors (Tiley et al., 2016). We therefore seek to minimise

$$\chi^2 = \sum_i \frac{\{\log(V_{\rm C,i}) - (\beta + \alpha[\log(M_{\star,i}) - 10.1])\}^2}{\sigma_i^2} \tag{4.1}$$

where $V_{\rm C,i}$ and $M_{\star,i}$ are the individual rotation velocity and stellar mass measurements, β and α are the intercept and slope of the linear model which are free to vary in the fit and, as derived in the appendix of Weiner et al. (2006b), assuming gaussian intrinsic scatter, $\sigma_{\rm scatter}$, that the stellar mass and velocity errors are independent, we can write

$$\sigma_i^2 = \delta {V_{\rm C,i}}^2 + \alpha^2 \delta {M_{\star,i}}^2 + \sigma_{\rm scatter}^2 \tag{4.2}$$

where σ_i is the total uncertainty on each datapoint and $\delta V_{\rm C,i}$ and $\delta M_{\star,i}$ are the velocity and stellar mass measurement errors. In practice we use a fixed stellar mass measurement error of 0.2 dex[1] and vary $\sigma_{\rm scatter}$ in the fit to achieve a reduced chi-squared value which is equal to 1. We find best-fit values of $\beta_{z=0} = 2.125 \pm 0.004$ and $\alpha_{z=0} = 0.279 \pm 0.009$ for the Reyes et al. (2011) sample, which we use as our reference local relation for all subsequent comparisons. The normalisation and slope quoted in Reyes et al. (2011) are $\beta_{\rm Reyes} = 2.142 \pm 0.004$ and $\alpha_{\rm Reyes} = 0.278 \pm 0.010$ respectively. The slope we measure when re-fitting the data is consistent within the errors and the small difference between normalisations is the result of converting between the Kroupa IMF (Kroupa, 2002) adopted in Reyes et al. (2011) and the Chabrier IMF used

[1]0.2 dex is the typical uncertainty on the stellar masses recovered from SED fitting in the KDS isolated-field sample, although varying this fixed error between 0.0-0.3 dex does not alter the fit results

throughout this work (more details in § 4.6.1)[2].

Other surveys (Tiley et al. 2016; Straatman et al. 2017; Harrison et al. 2017; Übler et al. 2017) have also made use of the Reyes et al. (2011) sample as a local reference, using the fit parameters quoted in Reyes et al. (2011) in order to study the evolution of the stellar-mass Tully-Fisher relation. Several local samples exist, leading to several possible reference relations which differ from one another in terms of slope and normalisation. As discussed in § 4.6.1, the commonly adopted reference samples span $\simeq 0.05$ dex in velocity normalisation, and so the choice of which to use has an impact on the conclusions drawn for the evolution of the stellar-mass Tully-Fisher relation (e.g. Straatman et al., 2017). For example, when defining the local relation using a fit to spiral galaxies from Romanowsky & Fall (2012), the reference velocity zero-point is $\simeq 0.05$ dex higher. For some samples, this uncertainty could account for a significant fraction of the observed evolution of the stellar-mass Tully-Fisher relation to high redshift (see Figs 4.9, 4.10 and 4.11), which we discuss further in § 4.4.2.

The rotation-dominated and dispersion-dominated galaxies in the KDS isolated-field sample are fitted following the same procedure as above, but with the slope held fixed to the local value of $\alpha_{z=0} = 0.279$. Fixing the slope allows us to focus on the evolution of the normalisation of the relation by applying a consistent functional form at each redshift. We find $\beta_{\mathrm{rot},z=3.5} = 2.032 \pm 0.041$ and $\beta_{\mathrm{disp},z=3.5} = 1.807 \pm 0.041$ which are offset from the local relation by $\simeq -0.10$ dex and $\simeq -0.35$ dex in velocity zero-point respectively. As mentioned above, it is common to quote stellar-mass zero-point offsets in units of $\log(M_\star/M_\odot)$, which differ from the velocity zero-point offsets by a factor of $-1/\alpha$. The KDS velocity zero-point offsets correspond to +0.33 dex and +1.22 dex offsets in stellar mass for the rotation-dominated and dispersion-dominated galaxies respectively.

[2]We have verified our fit results by finding an almost-identical solution of $\beta_{z=0} = 2.126 \pm 0.004$ and $\alpha_{z=0} = 0.281 \pm 0.009$ using the HYPER-FIT package (Robotham & Obreschkow, 2015) online interface (`http://hyperfit.icrar.org`), which recovers the unique best fitting linear relationship between two variables including intrinsic scatter.

We also fit the fixed slope relation to the rotation-dominated and dispersion-dominated KROSS (Harrison et al., 2017) galaxies to find $\beta_{\mathrm{rot},z=1} = 2.113 \pm 0.010$, $\beta_{\mathrm{disp},z=1} = 1.558 \pm 0.027$. In Harrison et al. (2017), the rotation-dominated KROSS galaxies, defined as those with $V_{\mathrm{C}}/\sigma_{\mathrm{int}} > 1$, are fitted in the velocity versus stellar-mass plane with the slope allowed to vary, reporting fit parameter values $\alpha_{\mathrm{Harrison}} = 0.33 \pm 0.11$ and $\beta_{\mathrm{Harrison}} = 2.12 \pm 0.04$. The fixed slope we use and the normalisation we recover are both consistent within the errors with the results from Harrison et al. (2017).

Fig. 4.1 shows that the rotation-dominated KDS galaxies have lower rotation velocities at fixed stellar mass than the local reference and intermediate redshift KROSS star-forming galaxies. The KDS rotation-dominated velocity zero-point is offset in the opposite sense to other intermediate redshift studies of the stellar-mass Tully-Fisher relation, which either show no evolution (e.g. Miller et al., 2011, 2012; Epinat et al., 2012; Pelliccia et al., 2017; Harrison et al., 2017) or evolution of up to +0.12 dex in velocity zero-point (e.g. Cresci et al., 2009; Straatman et al., 2017; Übler et al., 2017). The shifts towards higher velocities are usually interpreted as an increase in the ratio of dynamical to stellar mass with increasing redshift, as galaxies have yet to convert their gas mass into stars. We show in § 4.4 that the KDS offset is likely a consequence of the increasing significance of pressure support at high redshift (e.g. Kassin et al., 2012; Simons et al., 2017; Übler et al., 2017), leading observationally to an increase in velocity dispersions at the expense of rotation velocity (e.g. Burkert et al., 2010; Simons et al., 2017).

To study the inferred evolution of the stellar-mass Tully-Fisher relation, we apply the same fitting analysis to our compilation of 16 distant star-forming galaxy comparison samples with median redshifts in the range $0 < z < 3.5$. We also explore the link between sample-selection criteria and the inferred evolution of the stellar-mass Tully-Fisher relation in the following subsections.

4.3.2 Evolution of the stellar-mass Tully-Fisher relation out to $z \sim 3.5$

The fitting analysis described above is applied to the 5 local and 16 distant star-forming galaxy comparison samples described throughout § 4.6 (and see § 4.2.4). For each of these comparison samples we make use of tabulated velocities, velocity dispersions (when available) and stellar masses and have converted all stellar mass measurements to a common Chabrier (2003) IMF. Using this information, we create rotation-dominated ($V_C/\sigma_{int} > 1$) and dispersion-dominated ($V_C/\sigma_{int} < 1$) subsamples in each of the comparison samples where this is possible (some of the samples by design contain only rotation-dominated galaxies). The $V_C/\sigma_{int} > 1$ criteria is one way to pick out 'disk' galaxies, i.e. those where the rotational motions exceed the random motions. We explore how defining disk galaxies in different ways, e.g. with a stricter V_C/σ_{int} cut, is connected to the observed stellar-mass Tully-Fisher evolution in § 4.3.2. We fit the stellar-mass Tully-Fisher relation following the procedure described throughout § 4.3, with slope fixed to the local reference value of $\alpha_{z=0} = 0.279$, to:

(i) The full samples (RD & DD: All)

(ii) The rotation-dominated galaxies only (RD: $V_C/\sigma_{int} > 1$)

(iii) The dispersion-dominated galaxies only (DD: $V_C/\sigma_{int} < 1$)

The corresponding fits to the data are shown in § 4.7. In Fig. 4.2 we compare the velocity zero-points recovered from these fits with the local velocity zero-point. In the three panels of Fig. 4.2 the y-axis shows the difference between the fitted velocity zero-point at the redshift of the comparison sample and the local zero-point. Hollow, grey symbols indicate the samples for which direct comparisons to the other results are complicated due to differences in the measurement of kinematic properties (e.g. no beam-smearing corrections applied) as explained throughout supplementary material § 4.6.2. Positive values indicate that the galaxies have higher velocities at fixed stellar mass relative to the local sample, which could be interpreted as a higher ratio of dynamical to stellar

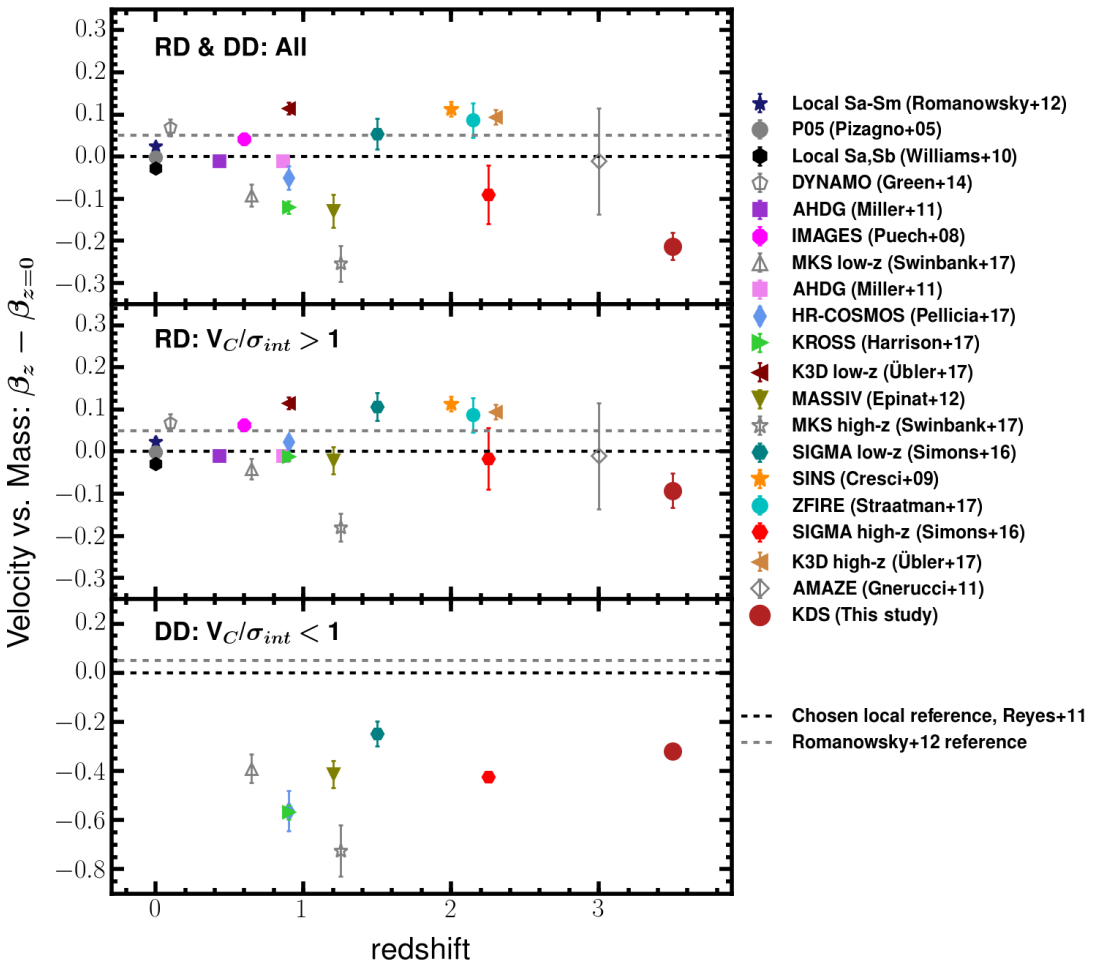

Figure 4.2: The velocity-normalisation offsets, $\Delta\beta$, from the local stellar-mass Tully-Fisher relation against redshift. In each panel the dashed-black horizontal line shows the Reyes et al. (2011) reference velocity zero-point, and the dashed grey horizontal line shows the approximate +0.05 dex zero-point shift found when adopting a local reference relation recovered from fitting galaxies from Romanowsky & Fall (2012) (see the text and § 4.6.1). The studies from which the comparison sample data have been taken are shown in the legend. Generally the median stellar mass of subsamples from the same parent sample vary between the three panels, with dispersion-dominated galaxies having somewhat lower values. We list these values, as well as the Tully-Fisher offsets, in Table 4.1. *Top:* The fits to the full galaxy samples (including rotation-dominated and dispersion-dominated galaxies; see § 4.7). *Middle:* The same as the top panel but with only the rotation-dominated galaxies. The majority of points fall between −0.10 dex to +0.10 dex in velocity zero-point offset from the local relation (i.e. between $\simeq \pm 0.35$ dex offset in stellar-mass zero-point). The KDS galaxies are offset to lower velocities at fixed stellar mass, suggesting that rotation velocity alone is not a good tracer of dynamical mass at $z \sim 3.5$ (see § 4.4). *Bottom:* The same as the top and middle panels, but with only the dispersion-dominated galaxies. In each survey where dispersion-dominated galaxies are available, the measured zero-points from the fits are significantly lower than the local zero-point.

mass. Negative values indicate the opposite, however we will discuss the limitations of directly comparing dynamical mass, inferred using observed rotation velocities alone, and stellar mass in § 4.4.

The top panel of Fig. 4.2 shows the fits to the full samples. By virtue of these samples containing both rotation-dominated and dispersion-dominated galaxies, which sit in discrepant locations in the velocity versus stellar-mass plane (see Figs 4.1 & 4.13), the velocity zero-points recovered from these fits are biased low and have large uncertainties. The middle panel of Fig. 4.2 shows the results of fitting the rotation-dominated galaxies in the comparison samples. Note that some of the samples only contain rotation-dominated galaxies and so the point locations are unchanged between the top and middle panels. The 13 'reliable' (filled, colour symbols in Fig. 4.2) distant comparison samples have offsets bounded by shifts of roughly −0.10 dex to +0.10 dex in velocity zero-point from the local relation (i.e. between ±0.35 dex offset in stellar-mass zero-points). The middle panel of Fig. 4.2 does not contain any information about sample-selection effects, e.g. the correlation between the median V_C/σ_{int} of each of the rotation-dominated comparison samples and the observed Tully-Fisher offset (e.g. Tiley et al., 2016), or the median stellar mass of the samples. When viewed in isolation, plots such as these provide limited insight into the evolution of scaling relations, since sample selection is a dominant caveat. We show this explicitly in § 4.3.2 and § 4.3.2.

The bottom panel of Fig. 4.2 shows the offsets from the local stellar-mass Tully-Fisher relation for the dispersion-dominated subsamples, which are substantially below the local reference relation with velocity zero-point offsets spanning −0.4 to −0.8 dex. The correlation between rotation velocity and stellar mass is less apparent in these subsamples, leading to large uncertainties in the recovered velocity zero-points. It is not physically motivated to look at dispersion-dominated galaxies in the context of the stellar-mass Tully-Fisher relation, however we include the top and bottom panels here for comparison to the corresponding panels in Fig. 4.7, which explores the evolution of the 'total-velocity' (including a contribution from velocity dispersion in supporting the

total mass of the systems, see § 4.4.2) versus stellar-mass relation. Furthermore, the difference in offsets between the rotation-dominated and dispersion-dominated systems highlights that the galaxy sample used (in terms of the V_C/σ_{int} values) is critical in determining the inferred evolution of the stellar-mass Tully-Fisher relation. We explore this in detail in the following subsection.

The importance of sample selection in the observed evolution of the stellar-mass Tully-Fisher relation

The aim of this subsection is predominantly to shed light on the discrepant literature results describing the evolution of the stellar-mass Tully-Fisher relation beyond the local Universe. The carefully-selected and consistently-treated comparison samples used in this work allow the evolution to be studied across both a wide redshift range, corresponding to 12 Gyr of cosmic time, and a wide range of galaxy properties (see supplementary material § 4.6.2). Samples are often constructed for Tully-Fisher analysis by imposing selection criteria which aim to identify star-forming galaxies that are most 'disky', i.e. most kinematically evolved, and hence most representative of the spiral galaxies used to construct the local Tully-Fisher samples (e.g. Cresci et al., 2009; Übler et al., 2017). However, at high redshift these sample-selection cuts may exclude the majority of the parent sample due to, for example, the decline in the ratio of V_C/σ_{int} with increasing redshift (e.g. Wisnioski et al., 2015; Turner et al., 2017; Johnson et al., 2018) as explored in Chapter 3. Consequently, samples resulting from strict selection criteria may not be representative of the population of typical evolving-disk galaxies at the corresponding redshift. The key point is that the analysis of star-forming samples that are selected to be increasingly disky will lead to different conclusions than the analysis of parent population representative samples, due to differences in the kinematic properties of the two sample types at fixed stellar mass.

In the following subsections we show the effect of sample selection by exploring the dependence of the rotation-dominated ($V_C/\sigma_{int} > 1$ samples) stellar-mass Tully-

Fisher offsets presented in the middle panel of Fig. 4.2 on two diagnostics of sample-selection criteria: (1) The fraction of the parent samples used in the Tully-Fisher analysis with respect to the empirically-determined rotation-dominated fraction (§ 4.3.2); (2) The median V_C/σ_{int} of the comparison samples with respect to an equilibrium model prediction for this quantity (§ 4.3.2). We define values for these diagnostics for the typical evolving-disk population and study the link between comparison sample Tully-Fisher offsets and the departure from these values.

Parent sample fraction and Tully-Fisher offsets

In the following, we define the parent sample of each of the comparison samples as the number of galaxies which have been observed spectroscopically and in which the target emission line has been detected. The parent samples are discussed explicitly in supplementary material § 4.6.2. The parent fraction is defined for each of the comparison samples as the ratio of the number of galaxies used for the stellar-mass Tully-Fisher analysis in § 4.3.1 (i.e. middle panel of Fig. 4.2) to the number of galaxies in the parent sample, as defined above. As a result of the decline in rotation-dominated galaxies with redshift (e.g. Stott et al., 2016; Turner et al., 2017), a smaller fraction of the parent samples are considered for fitting in the rotation-velocity versus stellar-mass plane at higher redshift. To account for this we normalise each parent fraction using an empirically defined relation between the observed rotation-dominated fractions and redshift. This relation is defined as RDF = $-0.2\,z + 1$, and is plotted in the left panel of Fig. 4.3 (adapted from Chapter 3), which also shows the rotation-dominated fraction of the parent samples against redshift. The normalised parent fraction is defined as the ratio of the parent fraction to the empirical rotation-dominated fraction, measured at the median redshift of the samples. We define the evolving-disk population at each redshift as all galaxies with $V_C/\sigma_{int} > 1$, so that the fraction of galaxies that would be used in a rotation-dominated Tully-Fisher analysis is equal to the rotation-dominated fraction, following the above empirical relation. Within this framework, the normalised parent sample is small when the Tully-Fisher analysis is being applied to rarer objects which constitute only a small fraction of the full sample, and hence are not representative

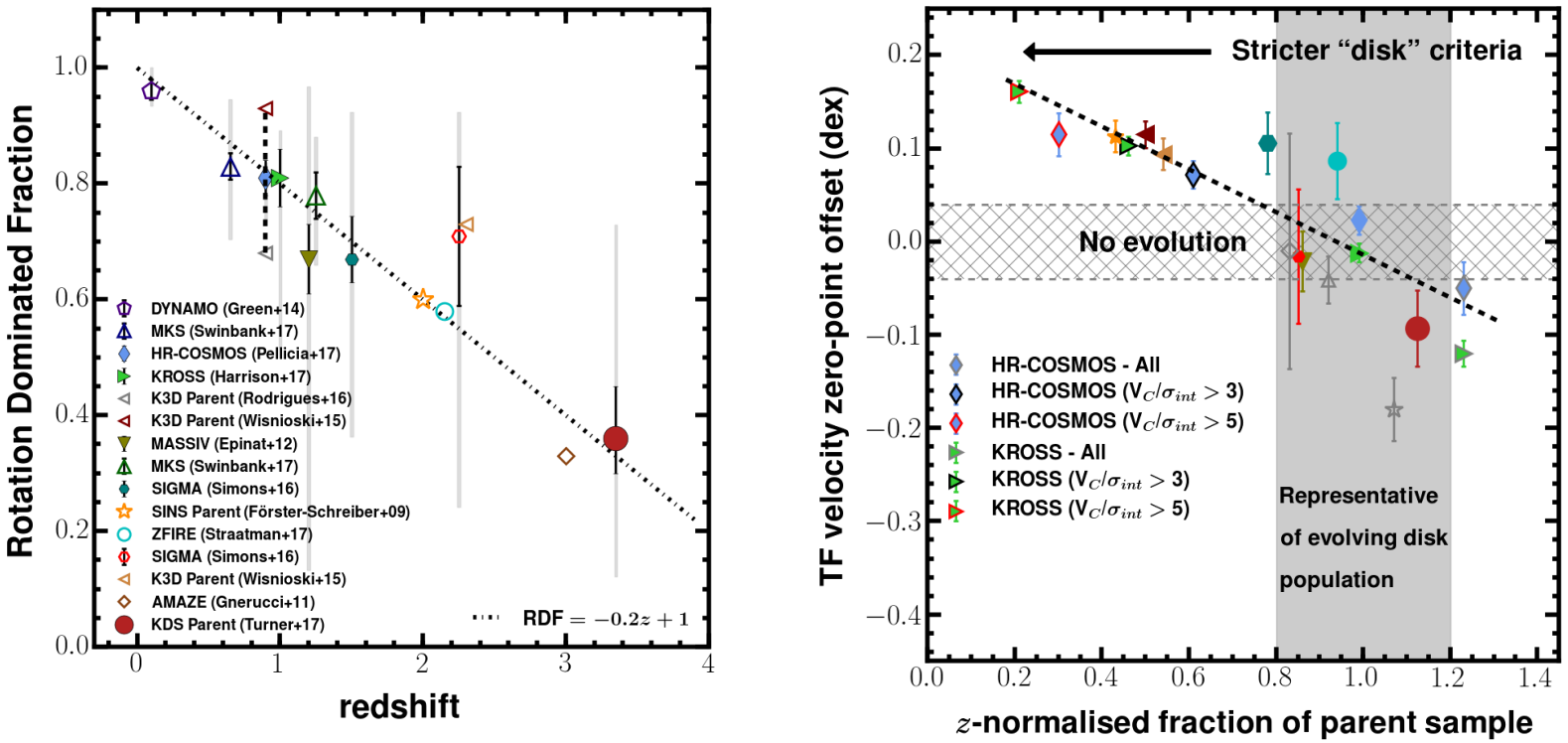

Figure 4.3: *Left:* The rotation-dominated fraction of star-forming galaxy samples is plotted as a function of redshift (adapted from Chapter 3), which evolves following the empirical relation RDF = $-0.2\,z + 1$ (dot-dashed track). *Right:* The velocity zero-point offsets from the local Tully-Fisher relation, from fitting the rotation-dominated sources (Fig. 4.2, middle), against the fraction of the parent sample used to fit the relation. This fraction is redshift-normalised by dividing it by the representative rotation-dominated fraction at that redshift (dot-dashed track in the left panel). The studies from which the data have been collected are shown in the legend of Fig. 4.2, and the symbols corresponding to the new subsamples created by varying the $V_C/\sigma_{\rm int}$ cuts (see text) are indicated in the legend of this figure. Samples in which the fraction of the parent sample used in the Tully-Fisher analysis is within ~ 20 per cent of the representative rotation-dominated fraction are defined as 'representative of evolving-disk population' (grey shaded region and see § 4.3.2). The black dashed line shows a linear, error-weighted fit to the data points with parameters $y = -0.23x + 0.22$. A clear trend emerges: when the fraction of the parent sample used to fit the Tully-Fisher relation is close to the representative rotation-dominated fraction at that redshift - no offsets are typically found. In contrast, when a small fraction of the parent population is used, due to increasingly-strict 'disk' criteria, large, positive offsets are found.

of the typical evolving-disk population at that epoch (i.e. moving towards smaller fractions reflects the application of increasingly-strict disk criteria).

In the right panel of Fig. 4.3 we plot the offsets from the local Tully-Fisher relation for each comparison sample, only containing rotation-dominated ($V_C/\sigma_{int} > 1$) sources, against normalised parent fraction. Using the KROSS data and the HR-COSMOS data we perform an additional sample cut of $V_C/\sigma_{int} > 3$ and $V_C/\sigma_{int} > 5$ and also include the full samples (including dispersion-dominated galaxies, for which the normalised parent fraction can exceed 1) to further explore the impact of selection criteria.

Using these subsamples we re-fit the stellar-mass Tully-Fisher relation, determining the new offsets from the local relation and the new normalised parent fractions. The symbols representing the $V_C/\sigma_{int} > 3$ and $V_C/\sigma_{int} > 5$ cuts are given black and red outlines respectively.

We highlight on Fig. 4.3, using a vertical shaded region, the location of samples which are representative of the evolving-disk population (based on the above definition). The grey regions are lower and upper bounds (corresponding to roughly ±0.1 dex, or ∼ 20 per cent tolerance) on whether the normalised parent fraction is in agreement with the expected location of the evolving-disk population. We also suggest a region of no stellar-mass Tully-Fisher evolution with the horizontal hatching between ±0.04 dex[3] in velocity zero-point offset (roughly equivalent to the KDS rotation-dominated offset error). The black arrow indicates the direction of increasingly-strict disk criteria, applied to isolate 'disky' galaxies that are the closest match kinematically to the star-forming systems observed locally.

Clearly the samples with selection criteria designed to pick out the most disky galaxies, i.e. those with small normalised parent fractions, are those which show evolution towards higher rotation velocities at fixed stellar mass. The most extreme example of

[3]Corresponding to ±0.15 dex in stellar-mass zero-point

this is for the KROSS sample with a cut of $V_C/\sigma_{int} > 5$, showing significant evolution towards higher rotation velocities at fixed stellar mass in comparison to the local stellar-mass Tully-Fisher relation. Conversely, the representative samples tend not to show evolution in the Tully-Fisher relation and the high-redshift KDS galaxies appear to show evolution towards lower rotation velocities at fixed stellar mass, as a result of the decline in rotation velocities and the increased contribution of velocity dispersions to the dynamics of these systems (see § 4.4). The KROSS ALL and HR-COSMOS ALL samples have normalised parent fractions greater than 1.2, which is a consequence of the samples containing both rotation-dominated and dispersion-dominated galaxies.

We highlight the correlation between Tully-Fisher velocity offset and parent fraction by fitting a linear, error-weighted function to the datapoints in the right panel of Fig. 4.3 (black dashed line) recovering the relation $y = -0.23x + 0.22$. In § 4.3.2 we interpret this correlation further. However, despite this correlation, it is important to note a potential pitfall of this framework is that galaxies are often omitted from Tully-Fisher samples due to the lack of sufficient kinematic data, rather than specific sample selection criteria, even when $V_C/\sigma_{int} > 1$. If deeper data were acquired for these galaxies, this could lead to an increase in the normalised parent fraction with no corresponding change to the zero point of the best-fitting Tully-Fisher relation. This has motivated us to explore the impact of sample selection criteria using a second method in the following subsection, that being the median V_C/σ_{int} of the Tully-Fisher samples.

Median V_C/σ_{int} and Tully-Fisher offsets

The median V_C/σ_{int} values of the samples offers a second way to probe the effect of sample-selection criteria. It is necessary to account for the cosmic decline and mass dependence of V_C/σ_{int} (e.g. Wisnioski et al., 2015; Simons et al., 2017; Turner et al., 2017) in order to make direct comparisons between the median V_C/σ_{int} values of samples at different redshifts. One way to do this is to use the simple equilibrium model proposed in Wisnioski et al. (2015), which provides a prediction for V_C/σ_{int} as

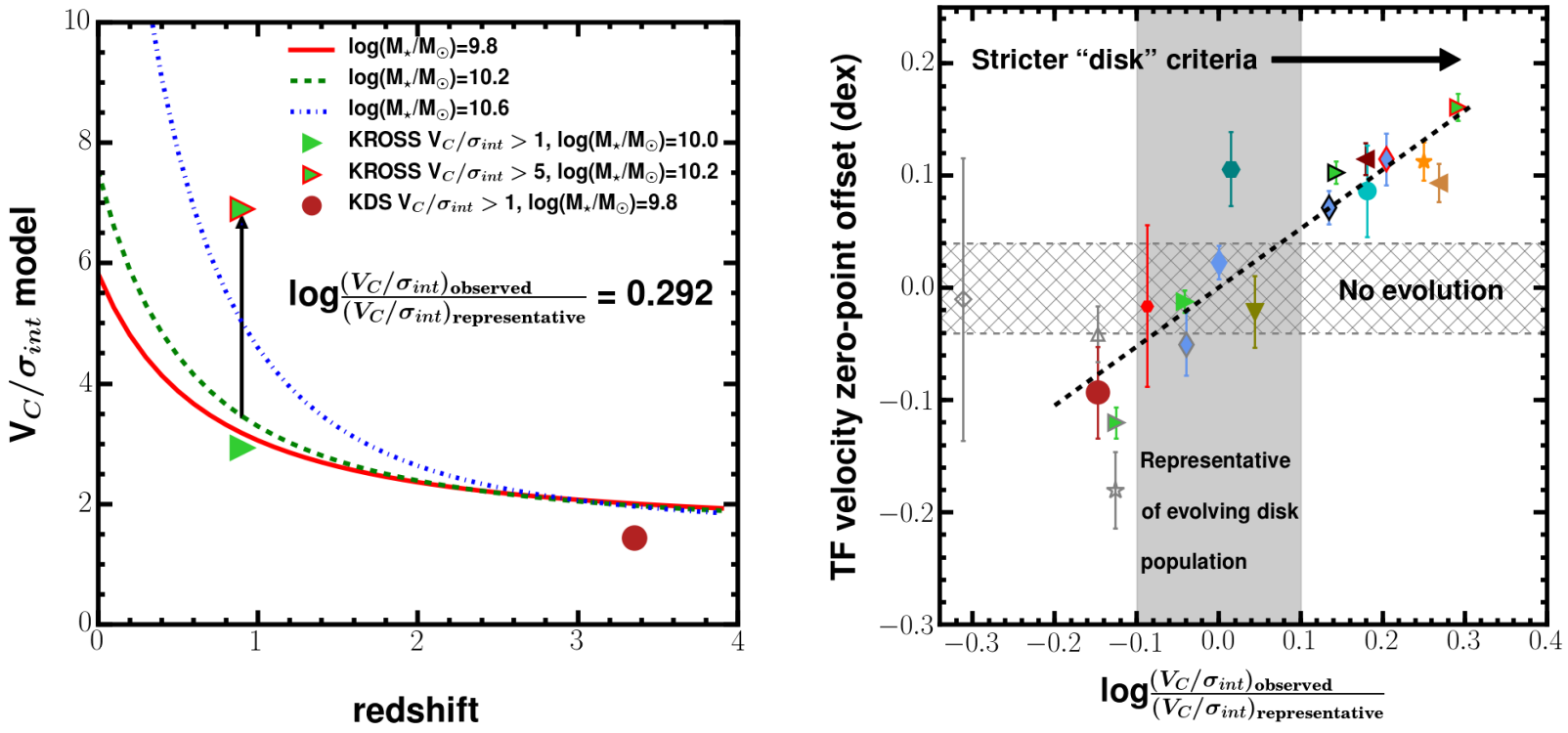

Figure 4.4: *Left:* $V_C/\sigma_{\rm int}$ predictions computed using Equation 4.3, which is a function of the median stellar mass and redshift of a sample of galaxies. Three example curves which show the dependence of the predicted $V_C/\sigma_{\rm int}$ values on mass and redshift are shown. For each comparison sample we compute a $\Delta\log(V_C/\sigma_{\rm int})$ value (Equation 4.4) by comparing the median observed $V_C/\sigma_{\rm int}$ value with the prediction from the model. We plot the KDS $V_C/\sigma_{\rm int} > 1$, the KROSS $V_C/\sigma_{\rm int} > 1$ and the KROSS $V_C/\sigma_{\rm int} > 5$ datapoints to indicate the position of the samples relative to the model curves. *Right:* The velocity zero-point Tully-Fisher offsets from fitting the rotation-dominated sources (Fig. 4.2, middle) versus $\Delta\log(V_C/\sigma_{\rm int})$. The studies from which the data have been collected are shown in the legend of Fig. 4.2 and the symbols with colour outlines have the same definition as the legend of Fig. 4.3. The black-dashed line shows the linear, error-weighted fit to the data, which has equation $y = 0.53x + 0.0$. The application of increasingly-strict disk criteria produces samples with median $V_C/\sigma_{\rm int}$ values larger than the model predictions, and leads to increasingly-large positive velocity zero-point offsets from the local Tully-Fisher relation.

a function of both mass and redshift, summarised by Equation 4.3:

$$\frac{V_{\rm C}}{\sigma_{\rm int}}(z, M_\star) = \frac{a}{Q_{\rm crit} f_{\rm gas}(z, M_\star)} \tag{4.3}$$

where $a = \sqrt{2}$ and $Q_{\rm crit} = 1.0$ for a marginally stable gas disk. The redshift and mass dependencies are encoded in the gas fraction, the functional form of which is provided in Wisnioski et al. (2015) Equations 3-6. Empirically, the model curves match the observed $V_{\rm C}/\sigma_{\rm int}$ values in the parent samples (see Fig. 11 of Wisnioski et al. 2015). Therefore, irrespective of the assumptions in the model, it provides a useful description of the evolving typical $V_{\rm C}/\sigma_{\rm int}$ value for star-forming galaxies as a function of redshift. Using the model curves we can compute a fiducial $V_{\rm C}/\sigma_{\rm int}$ for the comparison samples of known median stellar mass and redshift, representative of a population of typical star-forming galaxies with those properties, and determine the difference between this and the observed $V_{\rm C}/\sigma_{\rm int}$ for the same sample. We use the model to define the evolving-disk population, by specifying that the median $V_{\rm C}/\sigma_{\rm int}$ of this population, at a given mass and redshift, is given by the model curves.

The left panel of Fig. 4.4 demonstrates the redshift evolution of $V_{\rm C}/\sigma_{\rm int}$ for three different median stellar masses. As an example, we show the location of the KDS $V_{\rm C}/\sigma_{\rm int} > 1$, the KROSS $V_{\rm C}/\sigma_{\rm int} > 1$ and the KROSS $V_{\rm C}/\sigma_{\rm int} > 5$ samples. We define the departure of the observed median $V_{\rm C}/\sigma_{\rm int}$ from the model prediction using the following log ratio:

$$\Delta\log(V_{\rm C}/\sigma_{\rm int}) = \log\frac{(V_{\rm C}/\sigma_{\rm int})_{\rm observed}}{(V_{\rm C}/\sigma_{\rm int})_{\rm representative}} \tag{4.4}$$

where $(V_{\rm C}/\sigma_{\rm int})_{\rm observed}$ is the median observed ratio and $(V_{\rm C}/\sigma_{\rm int})_{\rm representative}$ is the model prediction at the median stellar mass and redshift of the sample. The black arrow in the left panel of Fig. 4.4 shows the magnitude of this ratio for the KROSS $V_{\rm C}/\sigma_{\rm int} > 5$ sample. In the right panel of Fig. 4.4 we plot the stellar-mass Tully-Fisher offsets for

each comparison sample against their associated $\Delta\log(V_C/\sigma_{int})$ from Equation 4.4. The grey-shaded region is again an indication of whether the comparison samples are in agreement with the expectation for the evolving-disk population, with a tolerance of ± 0.1 dex. Both the KDS and KROSS ALL samples have median V_C/σ_{int} values lower than the representative region. This is due to a combination of high velocity dispersions and low rotation velocities, which may no longer serve as a sufficient probe of the true dynamical mass (see § 4.4). We plot the same hatched, no-evolution region as in the right panel of Fig. 4.3 and show the direction of increasingly-strict sample-selection criteria with the black arrow.

There is a clear relationship, which appears to hold throughout the comparison samples, between the stellar-mass Tully-Fisher offsets and $\Delta\log(V_C/\sigma_{int})$, again with the most extreme example being the KROSS sample with a cut of $V_C/\sigma_{int} > 5$. Larger Tully-Fisher velocity zero-point offsets are observed for samples where the observed median V_C/σ_{int} becomes increasingly larger than the corresponding model prediction, which we highlight using a linear, error-weighted fit to the datapoints in the right panel of Fig. 4.4 (black dashed line), which has the best-fit relation $y = 0.53x + 0.0$. The representative samples cluster around zero Tully-Fisher offset, suggesting that the model V_C/σ_{int} curves define a reference, non-evolving Tully-Fisher relation. If an observed sample of star-forming galaxies at a particular median redshift has median V_C/σ_{int} consistent with the model prediction, the standard Tully-Fisher relation fitted to those data will be in agreement with the local relation. However it is possible to apply stricter kinematic criteria, such as the rotation-dominated galaxies being characterised by a higher V_C/σ_{int} cut, which brings the median V_C/σ_{int} of the new rotation-dominated sample higher at fixed stellar mass. The response in the velocity versus stellar-mass plane is an evolution of the zero-point of the stellar-mass Tully-Fisher relation towards higher rotation velocities at fixed stellar mass in comparison to the local relation. This is most clearly seen for the KROSS and HR-COSMOS subsamples in the right panel of Fig. 4.4, to which several different V_C/σ_{int} cuts have been applied (and see also Tiley et al. 2016).

The $V_C/\sigma_{int} > 1.0$ cut used to distinguish between rotation-dominated and dispersion-dominated galaxies is arbitrary and it is crucial to bear in mind that the evolution of the Tully-Fisher relation is dependent on where this boundary is placed. Also in Tiley et al. (2019) the authors show that the combination of lower data quality at intermediate and high redshift, and attempts to apply corrections in order to recover intrinsic properties, results in sources scattering in and out of the $V_C/\sigma_{int} > 1$ bin. This suggests that, at high redshift, the dynamical state of sources above and below this threshold can be ambiguous, due to the difficulties associated with accurately extracting kinematic properties. The interpretation of the relationship between $\Delta\log(V_C/\sigma_{int})$ and Tully-Fisher offset is discussed further in the following subsection.

Interpretation

Figs 4.3 and 4.4, and the associated discussions above, describe the increased kinematic diversity of the evolving galaxy disks at high redshift. At a particular stellar mass there exists a range of V_C/σ_{int} values, which we interpret here as being an indicator of the kinematic maturity of the galaxy disks. The different comparison sample selection criteria have resulted in samples characterised by a range of median V_C/σ_{int} values, and we have shown that fitting the stellar-mass Tully-Fisher relation to the highest V_C/σ_{int} samples leads to the largest inferred evolution from the local relation. Assuming that these galaxies do not have velocities which are biased high by large inclination corrections, fits to these subsamples answer the question: 'what happens in the rotation-velocity versus stellar-mass plane to star-forming galaxies that are most like those disks we observe locally?'. Furthermore, the high V_C/σ_{int} samples have the advantage that rotation velocity is a better tracer of the dynamical mass. However, with increasing redshift, these sources become increasingly rare and progressively less representative of the underlying evolving-disk population.

The results of this chapter indicate that for high V_C/σ_{int} samples we find Tully-Fisher

velocity zero-point evolution of +0.08 to +0.12 dex (i.e. stellar-mass zero-point evolution of −0.30 to −0.45 dex) at $z \geq 1$, in agreement with previous work studying galaxies in this regime. This evolution is consistent with a picture in which star-forming galaxies at high redshift have similar dynamical mass, but with higher gas fractions, and have simply not yet converted this gas into stars (e.g. Puech et al., 2008; Übler et al., 2017). Variation in the offsets is determined by sample-selection criteria, which alter the magnitude of the inferred Tully-Fisher evolution in a prescribed way as explored above. Other factors which alter the inferred evolution are the choice of local reference relation (see Figs 4.9, 4.10 and 4.11 in § 4.6) and the methods followed to extract kinematic parameters (which we do not attempt to correct for in this work).

The inferred evolution from the highest V_C/σ_{int} star-forming galaxies also appears to be consistent with the predicted evolution of the velocity versus stellar-mass relation from cosmological simulations (e.g. Dutton et al., 2011). However, the model predictions for the evolution of the Tully-Fisher relation with redshift from (e.g. Dutton et al., 2011) or the EAGLE simulation, (Schaye et al., 2015) as presented in Tiley et al. (2019), represent an idealised scenario where all of the dynamical mass is supported by ordered rotation. In reality this does not appear to be the case (e.g. Burkert et al., 2010; Übler et al., 2017; Turner et al., 2017) and the contribution of random motions to supporting dynamical mass becomes increasingly significant with increasing redshift. The agreement between model predictions for the evolution of the stellar-mass Tully-Fisher relation and the fits to high V_C/σ_{int} samples again suggests that these galaxies are closest to being supported purely by ordered rotation.

One can instead focus on larger samples which are more representative of the typical evolving-disk population at a particular epoch, are more kinematically diverse and may have a larger contribution from random motions to supporting the dynamical mass of the systems (e.g. Harrison et al., 2017). In this case, the velocity zero-point of the stellar-mass Tully-Fisher relation does not evolve strongly and may even evolve in the opposite sense at $z > 3$, where pressure support is most significant, as suggested in Chapter 3. In between these extremes, the offsets from the local stellar-mass Tully-Fisher relation

are mediated by both the median V_C/σ_{int} of the sample and the fraction of galaxies used in the Tully-Fisher analysis relative to the parent sample as demonstrated in Figs 4.3 and 4.4. However, it is not easy to physically interpret this evolution in relation to a dynamical-mass to stellar-mass ratio evolution.

As has been explored recently, it is necessary to account for the contribution of random motions to the dynamics of the system, especially at high redshift where star-forming galaxies appear to be highly pressurised (e.g. Kassin et al., 2012; Übler et al., 2017). Doing so provides an opportunity to trace the true dynamical mass and to unify samples consisting of both rotation-dominated and dispersion-dominated galaxies, thus mitigating the effects of sample selection. We explore the extent to which the rotation velocities may underestimate dynamical mass for the KDS galaxies in § 4.4.1 and consequently derive the possible form of a 'total velocity', that includes a contribution from the velocity dispersion. Analogous to § 4.3.2, we then proceed to study the evolution of the total-velocity versus stellar-mass relation, using our compilation of comparison samples, throughout the following sections.

4.4 Velocity dispersion contribution in tracing dynamical mass

4.4.1 The virial mass content of the KDS galaxies

In this subsection we discuss the concept of 'total velocity' for the KDS galaxies, that includes a velocity-dispersion contribution ($\eta\sigma_{int}$), where η can be constrained by the comparison between stellar and virial mass. This closely follows the results of a number of studies over the last decade, starting with Weiner et al. (2006a,b), demonstrating that there is a tighter relationship between pressure-corrected velocity and stellar mass than there is between velocity and stellar mass alone. The formulation of this expression involves making an assumption for the value of the ratio of dynamical to stellar mass for

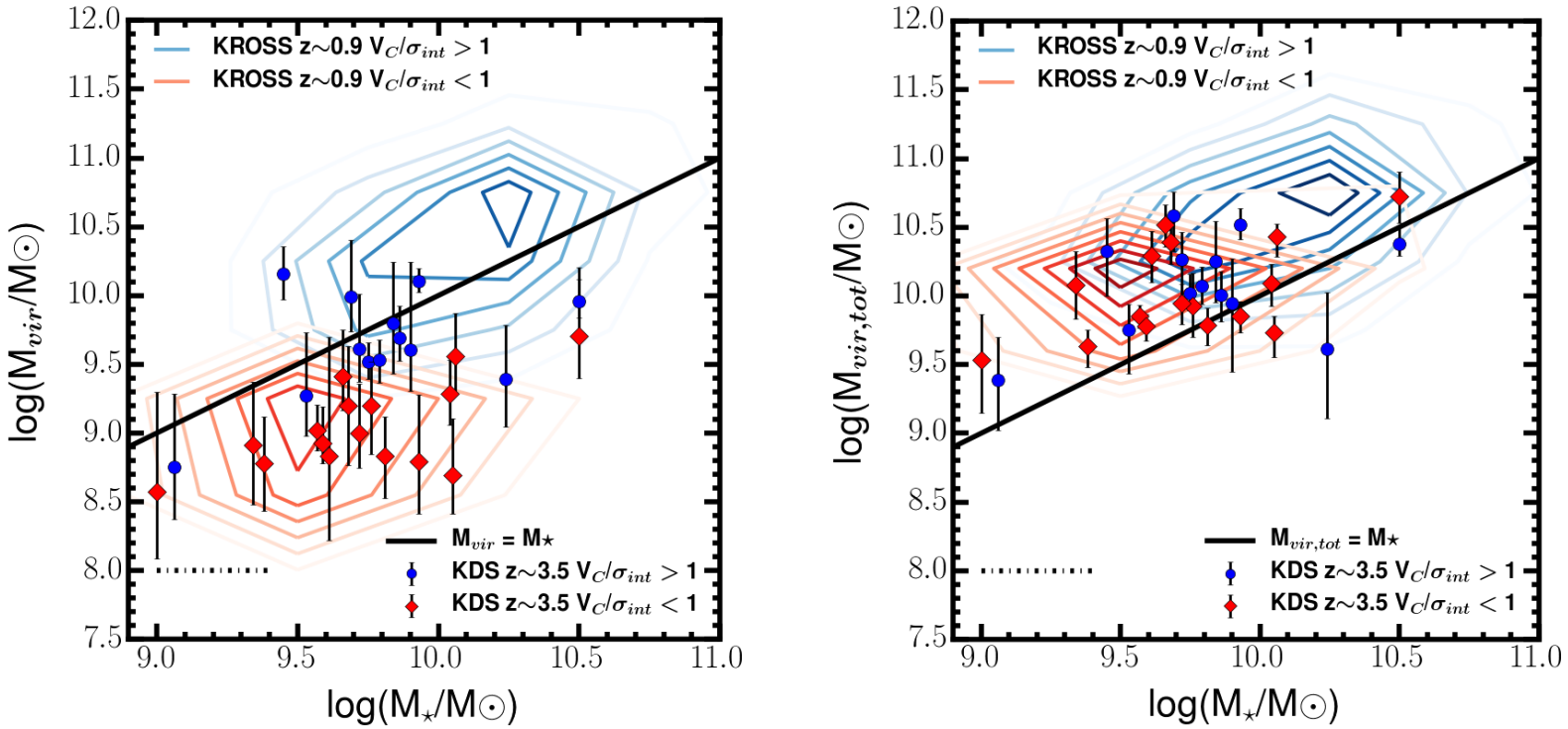

Figure 4.5: *Left:* Virial mass computed using only rotation velocities (Equation 4.6) versus stellar mass for the KDS isolated-field sample, with the black line indicating equality between virial mass and stellar mass. The black dot-dashed line in the lower left indicates the ±0.2 dex error on the KDS stellar masses (this is also the case in the right panel). The blue-circular symbols show the KDS galaxies with $V_C/\sigma_{int} > 1$ and the red-diamond symbols show the KDS galaxies with $V_C/\sigma_{int} < 1$, occupying a region with lower M_{vir} values than the rotation-dominated galaxies. The majority of the points lie in the unphysical $M_{vir} < M_\star$ region, indicating that rotation velocity alone is not sufficient to provide gravitational support for the stellar mass in the systems. The blue and red contours show the density of rotation-dominated and dispersion-dominated galaxies from KROSS (Harrison et al., 2017), both starting at 10 and increasing in increments of 10 and 3 respectively. *Right:* Total virial mass, $M_{vir,tot}$, computed with an additional component traced by the velocity dispersion, versus stellar mass, with the black line indicating equality between these quantities. The addition of this component shifts most galaxies into the $M_{vir,tot} > M_\star$ region and highlights the potential for a combination of random motions and ordered rotation to play a role in supporting the total virial mass.

the KDS galaxies at $z \simeq 3.5$, which is inherently uncertain. However, this assumption can be informed by considering the observed gas fractions in high-redshift galaxies (e.g. Tacconi et al., 2013, 2018) and explored by adopting different values for the ratio in § 4.4.2.

The observed dynamics of a galaxy can be used to infer the total mass enclosed at different radii, which can then be compared with the stellar mass from SED fitting. In this way the partitioning of the total mass between baryonic components can be studied and compared with predictions. Assuming that a galaxy is supported against gravitational collapse by ordered rotation, the rotation velocity can be used to trace the mass enclosed within radius R as follows:

$$M\,(<R) = \frac{RV_{\rm C}(R)^2}{G} \tag{4.5}$$

For the KDS isolated-field sample galaxies the rotation velocities are extracted at a radius of $2R_{1/2}$ from the intrinsic models and so the mass enclosed within this radius is given by:

$$M_{\rm vir} = \frac{2R_{1/2}V_{\rm C}^2}{G} \tag{4.6}$$

which we refer to hereafter as the virial mass, $M_{\rm vir}$. In the left panel of Fig. 4.5, we plot virial mass, computed using this simple equation, against stellar mass for the KDS isolated-field sample galaxies. The majority of galaxies in the isolated-field sample show $M_{\rm vir} < M_\star$ (with median value $M_{\rm vir}/M_\star = 0.32 \pm 0.23$), including those in the rotation-dominated subsample (for which the median value of $M_{\rm vir}/M_\star = 0.59 \pm 0.43$). This is surprising because at a radius of $2R_{1/2}$ for the KDS galaxies we are tracing the bulk of the stellar mass distribution[4], and so in principle the virial mass should exceed the stellar mass if it is a measure of the total mass enclosed within $2R_{1/2}$. Indeed at

[4]We have verified in Chapter 3 that 23/24 KDS isolated-field sample galaxies also detected in van der Wel et al. (2012) follow Sérsic light profiles with $n \sim 1$. For this (exponential) distribution, a radius of $2R_{1/2}$ encloses $\sim$ 85 per cent of the stellar light, from which the stellar mass is inferred through SED fitting.

the KDS median redshift of $z \simeq 3.5$, the gas fractions can be ≥ 50 per cent for typical star-forming galaxies (Tacconi et al., 2013, 2018), and dark matter is also present within the galactic disk. If these components are gravitationally supported by rotation alone, the virial mass computed using Equation 4.6 should be substantially larger than the stellar mass of the galaxies.

To place the KDS galaxies in the context of lower redshift results, we again use galaxies from the KROSS sample. The red and blue contours in the left panel of Fig. 4.5 indicate the density of the dispersion-dominated and rotation-dominated KROSS sample galaxies respectively in the virial mass versus stellar mass plane. The majority of the KROSS rotation-dominated galaxies show $M_{\rm vir} > M_{\star}$ and almost all KROSS dispersion-dominated galaxies show $M_{\rm vir} < M_{\star}$.

As shown in § 4.3.1, the rotation-dominated KDS galaxies are $\simeq -0.10$ dex in velocity zero-point beneath the local stellar-mass Tully-Fisher relation from Reyes et al. (2011). The KDS galaxies also have half-light radii which are a factor of $\simeq 3-4$ smaller than these local galaxies. In order for the total mass in the more compact KDS galaxies to be supported by rotation alone, we would expect that they 'spin up' to higher rotation velocities at fixed stellar mass. Observationally this does not appear to be the case (see e.g. Simons et al. 2017) suggesting that rotational motions alone are not sufficient to provide gravitational support for the total mass in the KDS galaxies, which also appears to be the case for many of the intermediate redshift KROSS galaxies. A possible solution to the virial to stellar mass discrepancy is that random motions in the systems, as traced by the velocity dispersions, provide partial gravitational support for the total disk mass as has been previously suggested (e.g. Kassin et al., 2007; Burkert et al., 2010; Kassin et al., 2012; Newman et al., 2013; Übler et al., 2017). This contribution becomes increasingly significant with increasing redshift as the ratio of rotation velocity to velocity dispersion decreases. This is referred to as an 'asymmetric drift' correction (e.g. Burkert et al., 2010), where turbulent pressure support generated by gravitational instabilities renders the observed rotation velocity a poor tracer of the total virial mass in the galaxy. A revised description of the total virial mass, $M_{\rm vir,tot}$, is

given by

$$M_{\rm vir,tot} = \frac{2R_{1/2}\left(V_{\rm C}^2 + \eta\sigma_{\rm int}^2\right)}{G} \tag{4.7}$$

which includes a contribution from the velocity dispersion of the galaxies. Here we do not seek to derive a precise value for η, rather to show that a significant contribution to the dynamical mass from random motions appears necessary in order to provide gravitational support for the expected baryonic material within $2R_{1/2}$. We use the value $\eta = 4.0$, for which the median ratio of total virial mass to stellar mass in the KDS isolated-field sample is equal to 2 (i.e. median $M_{\rm vir,tot}/M_\star = 2$[5]). This implies that, on average across the KDS sample and on the scales traced by the observations, the dynamical mass should be twice as large as the stellar mass. This is reasonable given the large observed gas fractions at high redshift (e.g. Tacconi et al., 2013, 2018), and assuming that much of the gas is concentrated within $2R_{1/2}$. The value $\eta = 4.0$ is comparable to the value found for an exponential mass distribution ($\eta = 3.4$, e.g. Burkert et al. 2010; Newman et al. 2013).

The adopted value of η is somewhat arbitrary, and so the impact on the fitting results when varying this parameter between a minimum of $\eta = 2.0$ (corresponding to median $M_{\rm vir,tot}/M_\star \sim 1.1$) and a maximum of $\eta = 6.0$ (corresponding to median $M_{\rm vir,tot}/M_\star \sim 2.7$) is explored throughout § 4.4.2.

In the right panel of Fig. 4.5 we plot total virial mass, computed using Equation 4.7, versus stellar mass for the KDS galaxies. By design, with this additional virial mass component sourced by the velocity dispersions, most of the isolated-field sample galaxies shift to the $M_{\rm vir,tot} > M_\star$ region and the discrepancy between dispersion-dominated and rotation-dominated galaxies no longer remains. We again plot the rotation-dominated and dispersion-dominated KROSS sample galaxies with the blue and red contours respectively in this plane, with $M_{\rm vir,tot}$ computed using the same

[5]The η values required for individual galaxies to have $M_{\rm vir,tot}/M_\star = 2$ vary widely, with $\eta_{\rm min} = 0.25$ and $\eta_{\rm max} = 37$.

equation. The dispersion-dominated galaxies from the KROSS sample also shift into the $M_{\rm vir} > M_{\star}$ region, showing similar values to the galaxies from the KDS sample.

From Equation 4.7, we can also define a 'total velocity', which is given by

$$V_{\rm tot} = \sqrt{V_{\rm C}^2 + \eta\sigma_{\rm int}^2} \tag{4.8}$$

with $\eta = 4.0$ as explained above. This is similar to the $S_{0.5} = \sqrt{0.5V_{\rm C}^2 + \sigma_{\rm int}^2}$ relation (e.g. Weiner et al. 2006a,b; Kassin et al. 2007; Covington et al. 2010; Simons et al. 2017; i.e. $V_{\rm tot}$ is equivalent to $\sqrt{2}S_{0.5}$ when $\eta = 2.0$) in which beam smearing corrected rotation velocity and velocity dispersion are combined to give a better tracer of dynamical mass (and cf. also the circular velocity given by equation 1 of Übler et al. 2017 and equation 1 of Förster Schreiber et al. 2018). We proceed to explore the derived total velocities in the context of the total-velocity versus stellar-mass relation throughout the following sections.

4.4.2 The total-velocity versus stellar-mass relation for the KDS galaxies

Given the sample-selection caveats discussed in § 4.3.2, it would be extremely useful to measure the evolution of the connection between dynamical and stellar mass following a method which is insensitive to sample-selection effects. By extension, this would allow fits to full galaxy samples (i.e. both rotation-dominated, defined in whatever way, and dispersion-dominated) regardless of the observed kinematic properties of the individual galaxies. Motivated by the use of the $S_{0.5}$ parameter to study full galaxy samples in Kassin et al. (2007, 2012) (and recently to study galaxy kinematics measured using a consistent methodology over a long redshift baseline in Simons et al. 2017), we include pressure support (following Equation 4.8) to the rotation velocities of the KDS galaxies and plot the total-velocity versus stellar-mass relation in the right panel of Fig. 4.6. We assume that the contribution of pressure to the rotation velocities of local galaxies is negligible, due to the large $V_{\rm C}/\sigma_{\rm int}$ ratios, and continue to compare higher redshift fits

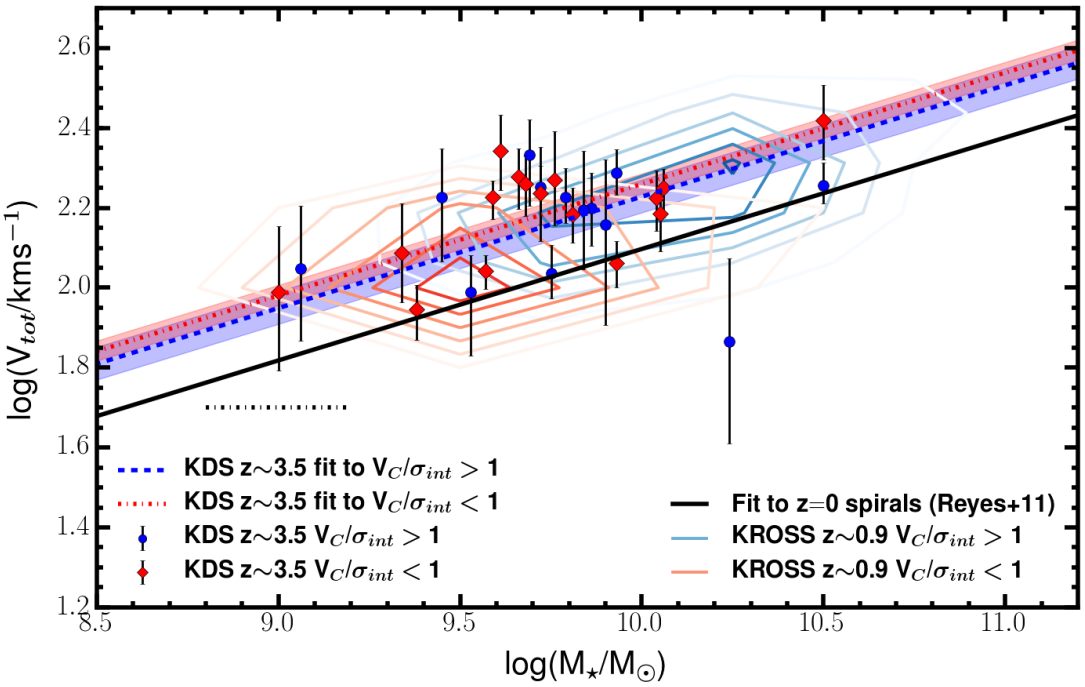

Figure 4.6: Total-velocity versus stellar-mass for both the KDS and KROSS galaxies, with the same symbol convention, fit-lines and local reference relation as Fig. 4.1. As discussed in the text, the total velocity is likely a better tracer of the true dynamical mass than the rotation velocity alone. In contrast to Fig. 4.1, the rotation-dominated and dispersion-dominated galaxies from both KDS and KROSS fall on the same sequence when using the total velocity rather than the rotation velocity. This suggests that sample-selection effects, which aim to distinguish between these subsamples, are less important when studying the total-velocity versus stellar-mass relation. The relation $\log(V_{\rm tot}) = \beta + \alpha[\log(M_\star) - 10.1]$ is fitted to the combined samples of rotation-dominated and dispersion-dominated galaxies in KDS and KROSS, returning zero-point offsets which are in agreement, and roughly +0.1 dex in total-velocity zero-point above the local zero-point.

with the fiducial relation recovered from the fit to the Reyes et al. (2011) galaxies. This approach is verified by adding a constant velocity dispersion of 20kms^{-1}, appropriate for local spiral galaxies (e.g. Epinat et al., 2008a), and calculating the total velocity of the Reyes et al. (2011) galaxies using Equation 4.8. The normalisation difference between the total-velocity versus stellar-mass and velocity versus stellar-mass relations is +0.02 dex, which is small in comparison to other systematics such as the choice of η parameter and local reference relation.

In the total-velocity versus stellar-mass plane, the discrepancy between rotation-

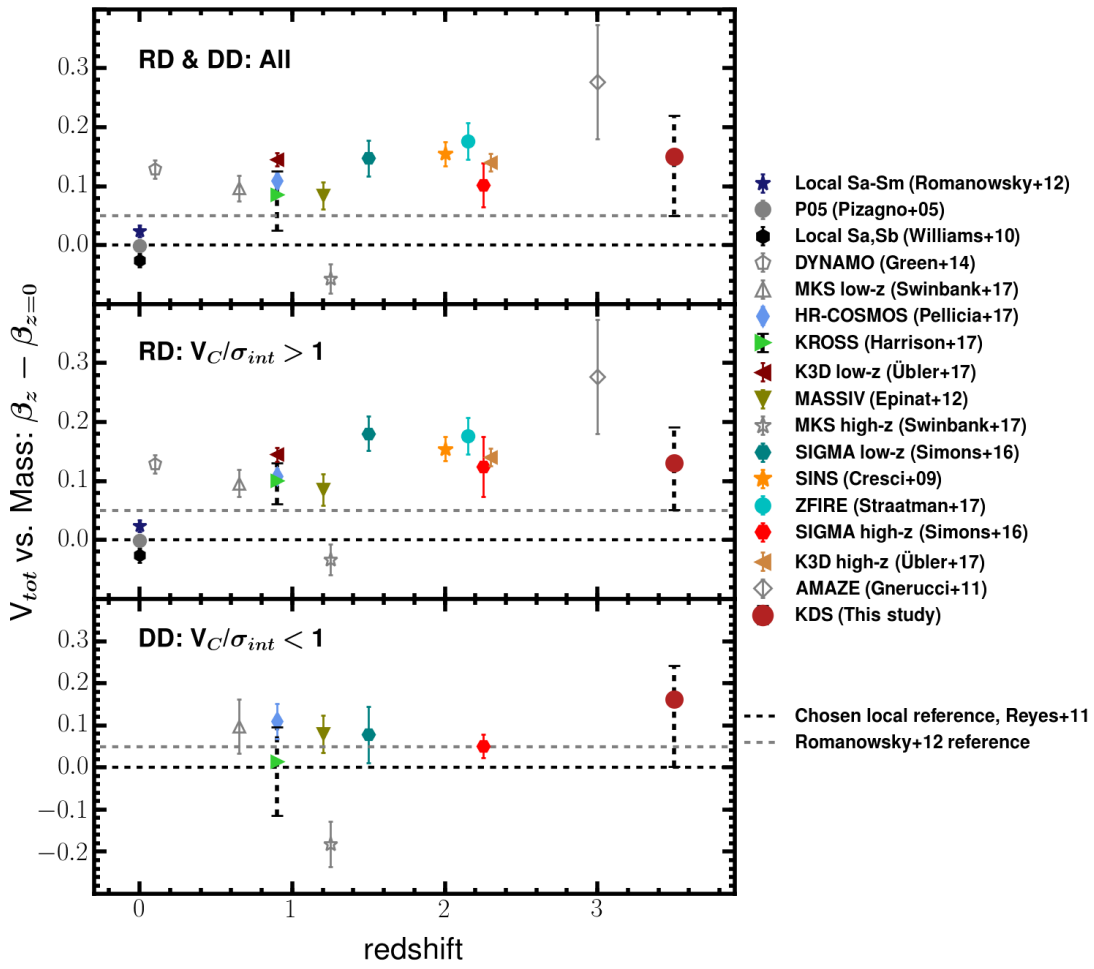

Figure 4.7: Total velocity offsets from the local stellar-mass Tully-Fisher relation for each of the comparison samples, plotted against redshift. Each panel is the same as in Fig. 4.2 but with the Tully-Fisher offsets computed using the total velocity from Equation 4.8. As per Fig. 4.2 we indicate the zero-point shift of +0.05 dex found when using the Romanowsky & Fall (2012) reference relation with the grey-dashed line. Also indicated with the black-dashed error bar on the KDS and KROSS datapoints is the error associated with varying the total velocity using $2.0 < \eta < 6.0$ (see text). The dispersion-dominated galaxies sit on almost the same relationship as the rotation-dominated galaxies, so that the fits to the full galaxy samples no longer average over two subsamples in different regions of the plane. The fits to the full samples and the rotation-dominated galaxies with added pressure support suggest a fairly constant shift in total-velocity zero-point of between +0.08 to +0.15 dex (−0.30 to −0.55 dex in stellar-mass zero-point) at $z \geq 1$.

dominated and dispersion-dominated galaxies disappears for the KDS sample and is greatly reduced in the KROSS sample. The same fitting procedure as described above is applied in turn to the full KDS sample, the rotation-dominated subsample and the dispersion-dominated subsample, returning the values $\beta_{\mathrm{tot,all},z=3.5} = 2.275 \pm 0.023$,

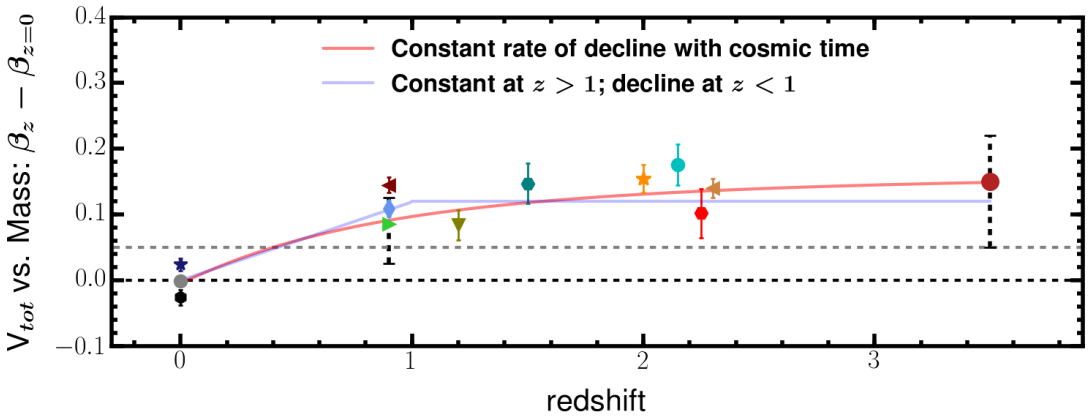

Figure 4.8: We replicate the top panel of Fig. 4.7, plotting the full-sample total-velocity offsets against redshift, with the grey-hollow symbols omitted. The red solid line shows an offset which is declining constantly with time, starting at an offset of +0.15 dex (see text). This reflects a constant decline in the ratio of dynamical to stellar mass throughout star-forming galaxy samples as the age of the Universe increases. The blue solid line shows a constant offset of +0.12 dex at $z > 1$, followed by a constant decline at $z < 1$. On the basis of these data, we cannot distinguish between these two scenarios.

$\beta_{\mathrm{tot,rot},z=3.5} = 2.256 \pm 0.041$ and $\beta_{\mathrm{tot,disp},z=3.5} = 2.288 \pm 0.025$. Fitting the same subsamples of KROSS galaxies returns the values values $\beta_{\mathrm{tot,all},z=1} = 2.211 \pm 0.008$, $\beta_{\mathrm{tot,rot},z=1} = 2.226 \pm 0.008$ and $\beta_{\mathrm{tot,disp},z=1} = 2.140 \pm 0.019$. The fits to the full KDS and KROSS samples suggest total-velocity zero-point offsets of $\simeq +0.14$ dex and $\simeq +0.08$ dex towards higher total velocities at fixed stellar mass respectively from the local relation. Crucially, because of the high velocity dispersions observed throughout the KDS sample in Chapter 3, the zero-point offsets shift substantially to move above the local relation, bringing the rotation-dominated and dispersion-dominated subsamples into agreement. This balance between the increased random motions and decreased rotational motions in the KDS galaxies suggests that V_{tot} is a better tracer of the dynamical mass.

For this analysis we chose $\eta = 4.0$ in Equation 4.8, corresponding to the value required for the KDS sample median $M_{\mathrm{vir,tot}}/M_{\star} = 2$. In Epinat et al. (2009) the value $\eta = 1.35$ is adopted and in Newman et al. (2013) $\eta = 3.4$ is quoted for an exponential mass distribution. In Covington et al. (2010) the authors consider the quantity S_{observed}, equivalent to using $\eta = 2.0$ in Equation 4.8, computed using the observed kinematics.

The authors find that using $S_{\rm observed}$ leads to underestimation of the total mass enclosed within a given radius, consistent with our findings that for $\eta = 2.0$ a significant fraction of the full KDS sample falls below the $M_{\rm vir,tot} = M_{\star}$ line (36 percent, decreasing to 17 percent when $\eta = 4.0$).

If we adopt $\eta = 2.0$ and fit the full sample of KDS galaxies in the total-velocity versus stellar-mass plane using the above relation, we recover the normalisation $\beta_{\rm tot,all,\eta=2.0} = 2.162 \pm 0.021$ and with $\eta = 6.0$ we find $\beta_{\rm tot,all,\eta=6.0} = 2.337 \pm 0.021$. Taking these values as encompassing the range of possible total-velocity zero-points leads to large errors on the quoted zero-point above, so that it reads $\beta_{\rm tot,all,z=3.5} = 2.275^{+0.07}_{-0.10}$ (i.e. a zero-point offset from the local relation of $+0.15^{+0.07}_{-0.10}$ dex). However at the lower end of the $2.0 < \eta < 6.0$ range, the discrepancy between the expected virial and stellar mass (see § 4.4.1) is still present and towards the upper end the relationship between virial mass and stellar mass flattens, suggesting that the velocity dispersion term is too large. The precise choice of η has a significant impact on the extent to which the KDS total-velocity versus stellar-mass relationship is observed to evolve. However, for the reasons above we believe $\eta = 4.0$ is a reasonable choice. In the following subsection we study the evolution of the total-velocity versus stellar-mass relation using the distant comparison samples and assuming $\eta = 4.0$ at each redshift. In reality, η could be a more complicated function of galaxy size, and hence redshift, however due to the additional uncertainty of ensuring parity amongst the comparison sample size measurements we do not explore this possibility here.

Evolution of the total-velocity versus stellar-mass relation out to $z \sim 3.5$

To explore these ideas over a wider redshift baseline, we calculate the total velocities of the comparison sample galaxies, where possible, and apply the same fitting method as described in § 4.3.1. We again use a fixed slope of $\alpha_{z=0} = 0.279$, in order to measure the total-velocity zero-point offsets from the local relation. This allows us to compare with the offsets measured from fitting the standard stellar-mass Tully-Fisher

relation throughout § 4.3.2. In Fig. 4.7 we plot the total-velocity versus stellar-mass offsets against redshift for each of the comparison samples in which velocity dispersion measurements were available. The most dramatic difference between Figs 4.2 and 4.7 is the velocity zero-point shift in the bottom panel, for the dispersion-dominated galaxies, which move up to almost the same position in the total-velocity versus stellar-mass plane as the rotation-dominated galaxies (see Fig. 4.14 also).

The offsets computed from fits to the full samples and to the rotation-dominated subsamples are now almost indistinguishable, with the comparison samples at $z \geq 1$ showing offsets in the range +0.08 to +0.15 dex in total-velocity zero-point (−0.30 to −0.55 dex in stellar-mass zero-point) above the local relation. These results are subject to several systematics. For example setting $\eta = 2.0$ and $\eta = 6.0$ in Equation 4.8 as described above leads to large errors on the recovered KDS total-velocity offsets. We show these errors, associated with the uncertainty in the value of η, with the black-dashed error bars in each of the panels of Fig. 4.7. We stress that this error is not so severe for the lower redshift comparison samples in which the velocity dispersions are smaller and highlight this by plotting the equivalent error bars on the KROSS datapoints at $z \simeq 1$. Adopting a different local reference relation can change the KDS offset by −0.05 dex (see Figs 4.10 and 4.11), represented in Fig. 4.7 by the grey-dashed zero-point lines. The impact of these effects adds uncertainty to the extent of the inferred evolution of the total-velocity versus stellar-mass relation. However, the total-velocity offsets are consistently positive amongst the star-forming galaxy comparison samples at $z \geq 1$. This suggests an evolving ratio of dynamical to stellar mass and a transition between the magnitude of the dynamical support provided by ordered and random motions, due to the steady rise in the intrinsic velocity dispersions of star-forming galaxies with increasing redshift (e.g. Wisnioski et al., 2015; Turner et al., 2017). We focus on the interpretation of this result in the following section.

4.4.3 The addition of velocity dispersion is required to trace the galaxy potential wells

As was discussed in § 4.4.2 and in Fig. 4.7, a more complete way to study the evolution of the relationship between dynamical and stellar mass is to attempt to account for the effects of pressure support in the galaxies. This reduces the kinematic diversity observed in high-redshift galaxies by including the 'missing' dynamical component traced by velocity dispersions, bringing rotation-dominated and dispersion-dominated galaxies into better agreement in the velocity versus stellar-mass plane (see the fits in Fig. 4.14) and allowing us to fit the Tully-Fisher relation to the full samples of galaxies. This avoids the problematic issue of choosing criteria to define a Tully-Fisher sample, which, as we have shown throughout § 4.3.2, entirely determine the extent to which the relation is observed to evolve.

The fits suggest that the pressure corrected samples all have positive total-velocity versus stellar-mass relation offsets, with a mean value of roughly +0.12 dex in total-velocity zero-point (−0.45 dex in stellar-mass zero-point) from the local stellar-mass Tully-Fisher relation. This is similar in magnitude to the offsets of −0.44 dex at $z \simeq 0.9$ and −0.42 dex at $z \simeq 2.3$ in stellar-mass zero-point quoted in Übler et al. (2017), in which the effects of pressure support have been included. This is interpreted as a decrease in stellar mass relative to gas mass, as well as an increasing baryonic to dark matter fraction with redshift on the scales traced by the ionised gas emission. The combined impact of these effects would maintain a relatively constant ratio of dynamical to stellar mass on the disk scale above $z \simeq 1.0$, which is traced by the stellar-mass Tully-Fisher relation. In Fig. 4.8 we plot the total-velocity offsets measured from fitting the combined rotation-dominated and dispersion-dominated galaxies throughout the comparison samples, (i.e. a reproduction of the top panel of Fig. 4.7). The blue line shows an offset that is at a constant level of +0.12 dex at $z > 1$ and declines to the local relation at a constant rate (relative to redshift) at $z < 1$.

An alternative scenario is that populations of star-forming galaxies have been gradually drifting onto the local Tully-Fisher relation by maintaining constant total velocity and growing in stellar mass at a rate which is roughly constant with time. To demonstrate this, we plot an offset of +0.15 dex at $z = 3.5$ (corresponding to 12 Gyr in the past) which declines constantly with time onto the local relationship at $z = 0$, with the red line in Fig. 4.8. Both scenarios imply an important period of stellar mass assembly within star-forming galaxy populations at $z < 1$ which starts to bring them onto the local stellar-mass Tully-Fisher relation. The blue and red lines, representing the increased influence of dark matter on disk scales (e.g. Übler et al., 2017; Lang et al., 2017; Genzel et al., 2017) and a constant decline in the ratio of dynamical to stellar mass with time respectively, both appear to provide an adequate description of the data. However the data do not allow us to further distinguish between these two scenarios.

What is clear is that the trend to observe positive velocity zero-point offsets across all the comparison samples is not seen unless a velocity dispersion term is taken into account, as a direct consequence of sample-selection effects and the incomplete dynamical evolution of star-forming galaxies at intermediate and high redshift. This is especially true for the KDS sample, in which the large observed velocity dispersions suggest that accounting for pressure support of this type is especially important at $z \simeq 3.5$, where the interstellar medium is increasingly turbulent and gas rich. It will be intriguing to follow up these observations in the future with increased senstitivity and higher spatial resolution, i.e. in the *JWST* era, in order to compare stellar and gaseous velocity dispersions and to further test the role of motions traced by the gaseous velocity dispersion in supporting mass in the systems against gravitational collapse.

4.5 Conclusions

We have used rotation velocity, V_C, and velocity dispersion, $\sigma_{\rm int}$ measurements for 29 galaxies from the KMOS Deep Survey described in Chapter 3, along with kinematic measurements of $\simeq$ 1200 galaxies from several carefully-selected comparison samples

spanning $0 < z < 3$ (see § 4.6), to investigate the evolution of the stellar-mass Tully-Fisher relation. To explain discrepant literature results, we have explored the connection between sample-selection effects and Tully-Fisher evolution, finding a strong correlation between two tracers of sample-selection criteria and velocity zero-point offsets from the local reference relation. We have also studied the impact of adding pressure support in the derivation of rotation velocities as a way to both trace the true dynamical mass and to mitigate the effects of sample-selection criteria. In doing so, we have added valuable datapoints at $z \simeq 3.5$ which constrain the evolution of both the rotation-velocity and pressure-corrected velocity versus stellar mass relationships. The main conclusions of this work are summarised as follows:

- We fit the stellar-mass Tully-Fisher relation, $\log(V_C) = \beta + \alpha[\log(M_\star) - 10.1]$, to rotation-dominated galaxies ($V_C/\sigma_{\rm int} > 1$) from the KMOS Deep Survey using a fixed slope of $\alpha = 0.279$, determined from fitting the same relation to local reference data from Reyes et al. (2011). The recovered velocity zero-point, $\beta_{{\rm rot},z=3.5} = 2.02 \pm 0.04$, is offset by -0.10 dex ($+0.37$ dex in stellar-mass zero-point) from the $z = 0$ reference relation velocity zero-point, suggesting lower rotation velocities at fixed stellar mass in the KDS galaxies (see Fig. 4.1).

- We fit the same fixed-slope relation to rotation-dominated and dispersion-dominated subsamples from 16 distant comparison samples culled from the literature spanning $0 < z < 3.5$, and originally constructed with a range of sample selection criteria (see Fig. 4.2). The impact of the different selection criteria is to bias the median kinematic properties of the different comparison samples. There is no clear relationship between the inferred zero-points of the stellar-mass Tully-Fisher relation and redshift for the rotation-dominated subsamples, however we find a striking correlation between the Tully-Fisher offsets and the median $V_C/\sigma_{\rm int}$ of the samples, redshift normalised using a simple equilibrium model prediction (Fig. 4.4). Increasingly-strict 'disky' sample-selection criteria result in larger inferred velocity offsets at fixed stellar mass with respect to the local Tully-Fisher relation. The strong connection between sample-selection criteria and Tully-

Fisher offsets highlights the kinematic diversity of high-redshift galaxies and demonstrates that previous, discrepant results in the literature for the evolution of the stellar-mass Tully-Fisher relation can be explained by taking sample-selection criteria into account.

- We show using a comparison of the KDS virial mass and stellar mass that a contribution from velocity dispersion is likely required to trace dynamical mass and consequently define a 'total velocity' of the form $V_{\rm tot} = \sqrt{V_{\rm C}^2 + 4.0\sigma_{\rm int}^2}$ (Fig. 4.5). Using this relation, rotation-dominated and dispersion-dominated galaxies lie on the same sequence in the total-velocity versus stellar-mass plane (Fig. 4.6), in contrast to in the rotation-velocity versus stellar-mass plane. This allows us to fit the full KDS sample (both rotation-dominated and dispersion-dominated) consistently in the total-velocity versus stellar-mass plane without imposing any sample-selection criteria, finding an offset of +0.14 dex in total-velocity zero-point from the local relation.

- Using the total velocity also unifies the rotation-dominated and dispersion-dominated galaxies throughout the comparison samples, removing the need to define an arbitrary $V_{\rm C}/\sigma_{\rm int}$ boundary to distinguish between rotation-dominated and dispersion-dominated galaxies. We explore the evolution of the total-velocity versus stellar-mass relation, which is independent of selection criteria, finding a mean total-velocity zero-point offset from the local relation of $\sim +0.12$ dex (-0.45 dex in stellar-mass zero-point) at $z \geq 1$ (see Fig. 4.7). The evolutionary trend throughout the total-velocity offsets suggests a constant decline in the ratio of dynamical to stellar mass with cosmic time at $z < 4$, reflecting the accumulation of stellar mass and the kinematic evolution of star-forming galaxies. However, the data do not allow us to distinguish this scenario from one in which the ratio of dynamical to stellar mass stays constant in the range $1 < z < 4$ and declines steadily thereafter (Fig. 4.8).

It is crucial to consider the dynamical maturity of galaxies when determining whether

the stellar-mass Tully-Fisher relation evolves with redshift. Physically interpreting Tully-Fisher evolution as tracing evolution of the ratio of dynamical to stellar mass requires that rotation velocity is a good tracer of dynamical mass. This is most likely to be true for high V_C/σ_{int} samples, within which the total mass of the galaxies is closest to being supported entirely by ordered rotation, however these samples become less representative of the evolving-disk population at high redshift. The galaxies in samples with lower median V_C/σ_{int} have made less progress towards forming a stable, rotating disk and have lower velocities at fixed stellar mass, with the magnitude of the velocity dispersion tracing the 'missing' dynamical mass component. Adding in a pressure support term to the velocities resolves the discrepancy in the rotation-velocity versus stellar-mass plane between star-forming galaxies at a particular epoch which span a wide range in V_C/σ_{int}, and allows a single relation to be fitted to full samples without imposing sample cuts which potentially bias the results. The evolutionary trend in the pressure-corrected stellar-mass Tully-Fisher relation with redshift suggests a scenario in which gas rich galaxies at high redshift have yet to form the bulk of their stars and may have a smaller baryon to dark matter fraction on the disk scale.

4.6 Chapter 4 supplementary material

When attempting to assess the evolution of scaling relations by comparing the results from different surveys across cosmic time, it is essential to monitor sample-selection criteria and the differing methods used to compute the physical properties of the galaxies. We carefully chose several local and distant comparison samples which have studied the dynamical properties of star-forming galaxies of varying median stellar mass, and paid close attention to the measurement of stellar mass (correcting to a Chabrier 2003 IMF where appropriate), intrinsic rotation velocities and velocity dispersions. We list the details of these measurements for each of the local and distant comparison samples in the following subsections. We chose the spiral galaxies presented in Reyes et al. (2011) as our local reference sample to assess evolution in the rotation-velocity and total-velocity versus stellar-mass planes. The choice of local reference relation can impact the extent to which the stellar-mass Tully-Fisher relation is observed to evolve. We verify using a different local reference sample from Romanowsky & Fall (2012) (details in section 4.6.1 and see Figs 4.9, 4.10 and 4.11) that the recovered evolutionary trends are unchanged when the fit to the Romanowsky & Fall (2012) galaxies is adopted. As described in the main-text, we fitted the stellar-mass Tully-Fisher relation to this sample to recover the local slope and velocity zero-point. By fitting fixed-slope relations to the local and distant comparison samples, and comparing with the reference sample zero-point, we found the data points used in the evolution plots throughout § 4.3 (i.e. Figs 4.2 and 4.7). We also list 4 alternative measurements of the local stellar-mass Tully-Fisher relation (details in § 4.6.1 - § 4.6.1) and plot these in Fig. 4.9, noting that the Reyes et al. (2011) relation is intermediate in slope and zero point between these relations.

Throughout the comparison samples there are two main measures of rotation velocity; those which have been extracted from the rotation curve at $2.2R_{\rm d}$ and those which have been extracted at $3.4R_{\rm d}$. Amongst the KROSS galaxies, for which we have access to both of these measures, the median of the ratio $V3.4R_{\rm d}/V2.2R_{\rm d}$ is equal to 1.08 for the full sample and 1.09 for the rotation-dominated galaxies. Similarly for the KDS sample

the median ratio is equal to 1.08 for the full sample and 1.07 for the rotation-dominated galaxies. In Figs 4.2-4.4 we plot the zero-point offsets recovered from fitting the $V3.4R_{\rm d}$ vs. $M_\star$ relation for the KROSS and KDS galaxies at $z \simeq 1$ and $z \simeq 3.5$ respectively, since this measure of rotation velocity is closer to the V_{80} measurement used in the Reyes et al. (2011) reference sample and is more appropriately used in conjunction with the total stellar mass. If we instead fit the $V2.2R_{\rm d}$ vs. $M_\star$ relations, the recovered offsets are $\simeq -0.04$ dex lower, corresponding to the factor of 1.08 difference in median velocities between the two measures. This is a small, but not insignificant, shift in the context of Figs 4.2-4.4, which does not disrupt the inferred evolutionary trends and which we believe to be representative of the maximum zero-point shift which can be caused by differences in rotation velocity measurements. The $z \simeq 0$ reference, $z \simeq 1$ KROSS and $z \simeq 3.5$ KDS rotation velocity measures are consistent with one another. We do not attempt to systematically correct the rotation velocities of the other comparison samples distributed across this redshift range and so, depending on the rotation velocity measure used as stated in each following subsections, the inferred Tully-Fisher zero-point offsets are subject to shifts of up to $\simeq -0.04$ dex.

4.6.1 Local comparison samples

Reyes et al. 2011 spiral galaxies ($z \simeq 0$)

Reyes et al. (2011) presented a detailed study of the stellar-mass Tully-Fisher relation using a representative sample of 189 disk galaxies from the Sloan Digital Sky Survey (SDSS). Rotation velocities, V_{80}, were extracted by fitting an arctangent function to the Hα position-velocity profiles and reading off at the radius containing 80 per cent of the i-band light (i.e. roughly $3R_{\rm d}$). Stellar masses were computed using the method of Bell et al. (2003), which uses colour-dependent mass-to-light ratios, and we converted from the Kroupa (2002) IMF adopted in Reyes et al. (2011) to a Chabrier IMF (i.e. we apply a $\simeq 0.06$ dex shift towards higher stellar mass). The median stellar mass is $\log(M_\star/M_\odot) = 10.2$. We fitted the stellar-mass Tully-Fisher relation to the galaxies in this survey using the relation $\log(V_{\rm C}) = \beta + \alpha[\log(M_\star) - 10.10]$, with both slope and

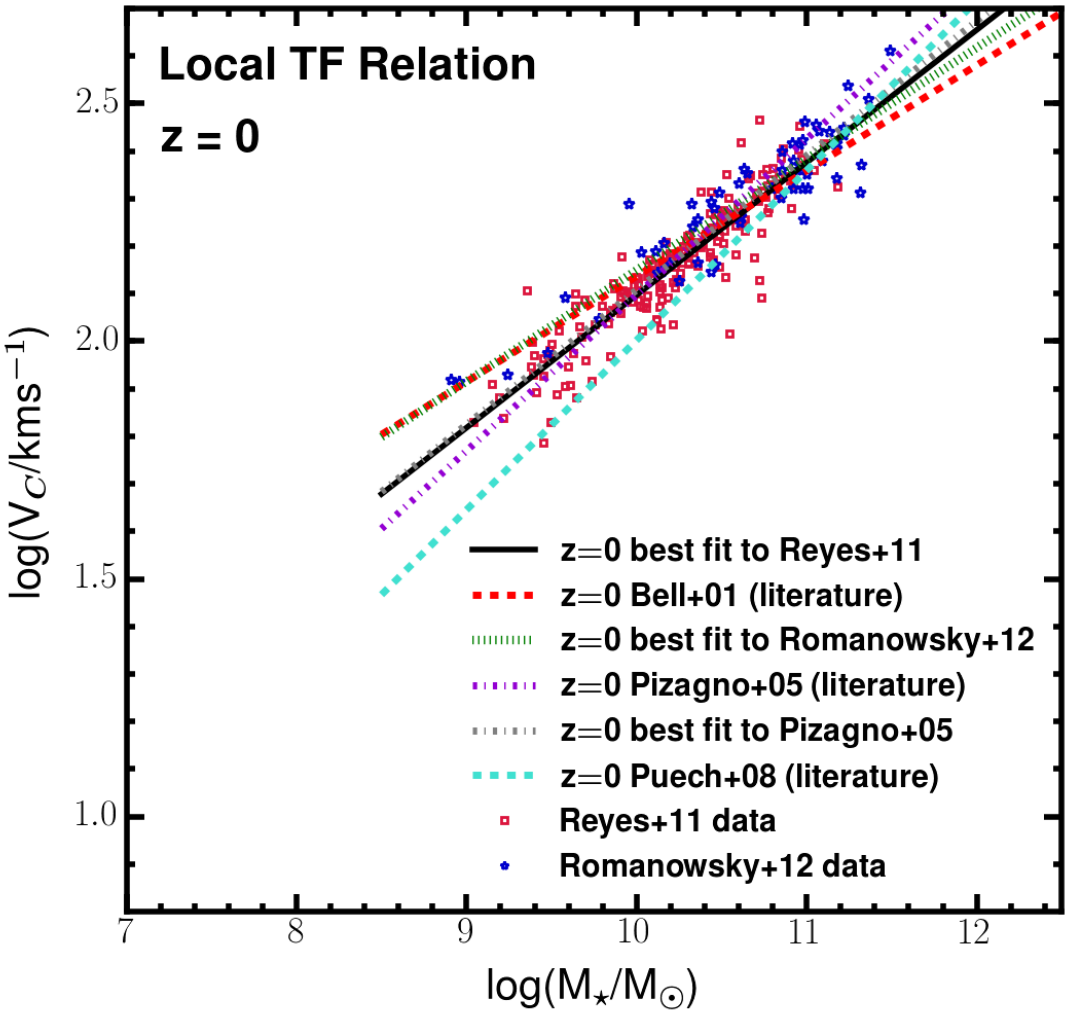

Figure 4.9: 189 spiral galaxies from Reyes et al. (2011) are plotted with the red squares and 57 Sa-Sm type spiral galaxies from Romanowsky & Fall (2012) are plotted with the blue stars in the rotation-velocity versus stellar-mass plane. The relation $\log(V_C) = \beta + \alpha[\log(M_\star) - 10.1]$ was fitted to both samples, finding best fit parameters $\beta_{z=0} = 2.173$ and $\alpha_{z=0} = 0.234$ for the Romanowsky & Fall (2012) sample (green-dashed line) and $\beta_{z=0} = 2.125$ and $\alpha_{z=0} = 0.279$ for the Reyes et al. (2011) sample (black-solid line). To put these fits in context we also plot the most commonly-used local stellar-mass Tully-Fisher relations taken directly from the literature (i.e. without re-fitting the data points) and our best-fit to the Pizagno et al. (2005) galaxies. We used the Reyes et al. (2011) relation as our local reference, as this has been used commonly in other studies of the stellar-mass Tully-Fisher relation, has been recovered from a fit to a large number of galaxies and is intermediate in slope between the relations plotted in this figure. As described in the main text (§ 4.3.2), when adopting the Romanowsky & Fall (2012) relation as a reference, the velocity zero-point offsets inferred for the comparison samples shift by −0.05 dex, however the evolutionary trends remain the same. Further information on these local comparison samples is given throughout § 4.6.1.

intercept free to vary, finding $\beta_{z=0} = 2.125 \pm 0.004$ and $\alpha_{z=0} = 0.279 \pm 0.009$, in good agreement with the values $\beta_{z=0} = 2.142 \pm 0.004$ and $\alpha_{z=0} = 0.278 \pm 0.010$ quoted in Reyes et al. (2011), with the small normalisation discrepancy a result of the change in IMF. Subsequently, we study the evolution of the stellar-mass Tully-Fisher relation (§ 4.3.2) and the total-velocity versus stellar-mass relation (§ 4.4.2) by holding the slope fixed to this local value and determining the velocity zero-points of the distant samples (see supplementary material § 4.6.2). This has been verified in § 4.4.2 by re-fitting the total velocities of the Reyes et al. (2011) galaxies, assuming velocity dispersion values typical for the local Universe (e.g. Epinat et al., 2008b), finding negligible difference in the zero-point and slope recovered from the velocity versus stellar-mass fit.

Romanowsky & Fall 2012 spiral galaxies ($z \simeq 0$)

Romanowsky & Fall (2012) carried out a detailed analysis of the kinematic properties of 64 spiral galaxies and 40 early-type galaxies in a study of the specific angular momentum of galaxies in the local Universe. In Romanowsky & Fall (2012), these spiral galaxies were taken from the compilation of Kent (1986, 1987, 1988), which covers a wide range of morphological types from Sa-Sm and with gas rotation curve measurements from optical emission lines (Rubin et al., 1980, 1982, 1985) and H I measurements (various literature sources). The rotation velocity was extracted from these rotation curves, which extend to several effective radii, at the point of flattening. No velocity dispersion measurements were presented for the spiral galaxies in this sample and so we assumed that the galaxies are rotation-dominated. We corrected the stellar masses presented in Romanowsky & Fall (2012), computed by assuming a fixed mass-to-light ratio for all spiral galaxies, using Equation 1 of Fall & Romanowsky (2013), which asserts that the mass-to-light ratio is a function of extinction corrected $(B-V)_0$ colour. The $(B-V)_0$ colours were taken from the HYPERLEDA catalogue (Paturel et al., 2003), in which 7 of the 64 spiral galaxies do not have a measurement, leaving a reference sample size of 57 galaxies. The median stellar mass for this reference sample is $\log(M_\star/M_\odot) = 10.8$.

The stellar-mass Tully-Fisher relation was not studied in Romanowsky & Fall (2012).

We fitted the same relation as described in the section above to this sample, recovering the parameters $\beta_{z=0} = 2.173 \pm 0.008$ and $\alpha_{z=0} = 0.234 \pm 0.015$. This provided an alernative local relation with which to make comparisons, and is explored in detail throughout Figs 4.9, 4.10 and 4.11.

Williams et al. 2009 early-type spirals ($z \simeq 0$)

Williams et al. (2009a, 2010) described kinematic measurements of 14 local early-type spiral galaxies (Sa,Sb) and 14 S0 type galaxies. We focus solely on the early-type spirals as a comparison sample throughout this work. We adopted the gas velocity, available for 10/14 galaxies, derived from fitting the flat region of the [N II] position-velocity diagram and giving values which are $\simeq -0.10$ dex lower on average than the stellar velocities, leaving 10 early-type spiral galaxies for analysis. Velocity dispersion measurements were not presented for these galaxies and so we do not compute or plot $V_{\rm tot}$ and assumed the galaxies that form this comparison sample are dominated by ordered rotation. The *Ks*-band mass-to-light ratio was computed for each galaxy by leaving it as a free parameter in the dynamical modelling, and was then used to find the stellar mass of the galaxies. The mean mass-to-light ratio adopted in Williams et al. (2009a) is a factor of 1.71 higher than for the early-type spirals in Romanowsky & Fall (2012). We applied this mean correction factor to the stellar masses presented in Williams et al. (2010) for consistency with Romanowsky & Fall (2012), and hence the other comparison samples. After applying this correction the median stellar mass for this sample is $\log(M_\star/M_\odot) = 11.0$.

Bell and de Jong 2001 spiral galaxies ($z \simeq 0$)

Bell & de Jong (2001) used a sample of local spiral galaxies to examine the stellar-mass Tully-Fisher relation, with stellar masses computed using colour-dependent mass-to-light ratios and a 'diet Salpeter' IMF. This resulted in stellar masses $\simeq 0.08$ dex larger than the Chabrier IMF (Cresci et al., 2009). The velocities were taken from Verheijen & W. (1997), which used the flat part of the H I rotation curve for galaxies in the

Ursa Major Cluster. The stellar-mass Tully-Fisher relation presented in Bell & de Jong (2001): $\log(V_C) = (2.159 \pm 0.009) + (0.222 \pm 0.013)[\log(M_\star) - 10.1]$ (having converted to the formalism used in this study and added +0.024 dex to the velocity zero-point in the conversion from diet Salpeter to Chabrier IMF), has been used frequently as a local comparison relation throughout the literature. This is in good agreement with our fit to the Romanowsky & Fall (2012) spirals and we make use of this relation in Fig. 4.9, which presents our comparison of local reference relations.

Pizagno et al. 2005 SDSS spirals ($z \simeq 0$)

Another popular local reference sample is Pizagno et al. (2005), in which the stellar-mass Tully-Fisher relation was fitted to a collection of 81 spiral galaxies from the Sloan Digital Sky Survey (SDSS), with stellar masses measured using colour dependent mass-to-light ratios following Bell et al. (2003), assuming a diet Salpeter IMF. The rotation velocities were extracted from the velocity profiles at $2.2R_d$. We converted their fit result to our formalism, using the Chabrier IMF, giving $\log(V_C) = (2.130 \pm 0.033) + (0.328 \pm 0.013)[\log(M_\star) - 10.1]$, which has slope marginally steeper than our fit to the Reyes et al. (2011) spirals. We have used the tabulated data in Pizagno et al. (2005), with stellar masses corrected to a Chabrier IMF, to refit the stellar-mass Tully-Fisher relation with slope and zero-point free to vary, and found the best fit $\log(V_C) = (2.136 \pm 0.007) + (0.283 \pm 0.011)[\log(M_\star) - 10.1]$. This is in slight tension with the original fit, which has a steeper slope, and in better agreement with the Reyes et al. (2011) reference relation (of which the data in Pizagno et al. (2005) is a subset).

Hammer et al. 2007, Puech et al. 2008 ($z \simeq 0$)

In Hammer et al. (2007), the K-band Tully-Fisher relation was constructed for a compilation of galaxies from 3 different studies (Courteau, 1997; Verheijen & W., 2001; Pizagno et al., 2007) containing spiral galaxies with Hubble types Sa-

Sm. This was converted to the stellar-mass Tully-Fisher in Puech et al. (2008) by applying colour dependent mass-to-light ratios as per Bell et al. (2003), with a diet Salpeter IMF. The best-fit relation, after correcting to a Chabrier IMF, is $\log(V_C) = 2.038 + 0.357[\log(M_\star) - 10.1]$ which again has a significantly steeper slope than in Bell & de Jong (2001). Whilst carrying out this fit, the authors restricted themselves to the high-mass end of the Tully-Fisher relations by only considering galaxies with $\log(V_C) > 2.2$. It is possible that this resulted in a steeper slope in the velocity versus stellar-mass plane, since a narrow mass range provides little constraint on the slope of the fit.

Summary of local comparison samples

In Fig. 4.9 we plot the stellar-mass Tully-Fisher relations recovered from fitting the data in Pizagno et al. (2005); Reyes et al. (2011); Romanowsky & Fall (2012), as well as the literature relations from Bell & de Jong (2001); Pizagno et al. (2005); Puech et al. (2008) in an attempt to understand any discrepancy between these. We plot also the data from Romanowsky & Fall (2012) with the blue stars and the data from Reyes et al. (2011) with the red squares. Generally these are in good agreement over the range $10.0 < \log(M_\star/M_\odot) < 11.0$, where the density of the reference galaxies is highest, but diverge when extrapolated to lower stellar masses as a result of differences in the slope of the relations. The chosen local reference relation will therefore impact the inferred evolution of the stellar-mass Tully-Fisher relation when carrying out the fixed-slope fitting procedure described in § 4.3.2. Throughout this work we used the fit to the Reyes et al. (2011) data as our local reference relation, which has slope intermediate between the two extremes explored in Fig. 4.9. We also carried out the analysis of § 4.3.2 using the fit to the Romanowsky & Fall (2012) data as our local comparison sample (which is almost equivalent to the Bell & de Jong (2001) relation), and found the same evolutionary trends but with the velocity zero-points shifted by roughly -0.05 dex towards lower values due to a combination of the shallower slope and higher velocity normalisation in the Romanowsky & Fall (2012) galaxies. In Figs 4.10 and 4.11 we

Table 4.1: We list the zero-points, β, recovered from fitting the function $\log(V) = \beta + \alpha[\log(M_\star) - 10.1]$ to the velocity versus stellar-mass and total-velocity versus stellar-mass relations for the local and distant comparison samples listed in § 4.6.1 and § 4.6.2 respectively. The slope, α, is held fixed throughout the fitting to the value 0.279 recovered from fitting the local galaxy sample presented in Reyes et al. (2011). For reference, the slopes and zero-points of popular local comparison samples from the literature are presented in § 4.6.1. The grey cells show the zero-point parameters which are not deemed directly comparable to the others, as explained throughout supplementary material § 4.6.2, and are correspondingly plotted with grey hollow symbols in Figs 4.2, 4.3, 4.4, 4.7 and 4.10.

Survey	z	$M_\star$			Number			β values from fits to the data					
								V_C vs. $M_\star$, $\alpha = 0.279$			V_{tot} vs. $M_\star$, $\alpha = 0.279$		
		All	RD	DD	All	RD	DD	All	RD	DD	All	RD	DD
Local Samples													
Reyes+11 (REFERENCE)	0.0	10.2	10.2	-	16	16	0	2.125 ± 0.004	2.125 ± 0.004	-	-	-	-
Romanowsky+12	0.0	10.8	10.8	-	16	16	0	2.149 ± 0.010	2.149 ± 0.010	-	-	-	-
Pizagno+05	0.0	10.3	10.3	-	81	81	0	2.124 ± 0.008	2.124 ± 0.008	-	-	-	-
Williams+10	0.0	11.2	11.2	-	10	10	0	2.097 ± 0.012	2.097 ± 0.012	-	-	-	-
Distant Samples													
DYNAMO	0.1	10.3	10.3	-	51	51	0	2.194 ± 0.020	2.194 ± 0.020	-	2.254 ± 0.015	2.254 ± 0.015	-
AHDG (low-z)	0.4	10.0	10.0	-	67	67	0	2.115 ± 0.011	2.115 ± 0.011	-	-	-	-
*IMAGES	0.6	10.3	10.3	-	28	14	0	2.167 ± 0.013	2.188 ± 0.014	-	-	-	-
MKS (low-z)	0.7	9.3	9.4	8.8	106	86	20	2.033 ± 0.026	2.084 ± 0.025	1.735 ± 0.045	2.222 ± 0.022	2.221 ± 0.023	2.223 ± 0.064
AHDG (high-z)	0.8	10.3	10.3	-	62	62	0	2.116 ± 0.012	2.116 ± 0.012	-	-	-	-
HR-COSMOS	0.9	10.1	10.2	9.7	80	65	15	2.075 ± 0.028	2.148 ± 0.015	1.563 ± 0.083	2.234 ± 0.013	2.234 ± 0.012	2.235 ± 0.041
KROSS	0.9	10.0	10.1	9.7	475	328	93	2.005 ± 0.014	2.113 ± 0.010	1.558 ± 0.027	2.211 ± 0.008	2.226 ± 0.008	2.140 ± 0.019
KMOS^{3D} (low-z)	0.9	10.5	10.5	-	65	65	0	2.240 ± 0.013	2.240 ± 0.013	-	2.270 ± 0.012	2.273 ± 0.011	-
MASSIV	1.2	9.9	10.1	9.8	46	30	16	1.996 ± 0.039	2.104 ± 0.033	1.713 ± 0.056	2.209 ± 0.023	2.210 ± 0.027	2.205 ± 0.044
MKS (high-z)	1.3	9.9	10.0	9.3	43	35	8	1.871 ± 0.043	1.945 ± 0.034	1.401 ± 0.103	2.067 ± 0.025	2.092 ± 0.026	1.943 ± 0.053
SIGMA (low-z)	1.5	10.1	10.2	9.5	27	18	9	2.179 ± 0.037	2.231 ± 0.033	1.878 ± 0.050	2.272 ± 0.031	2.306 ± 0.029	2.203 ± 0.067
SINS	2.0	10.6	10.6	-	16	16	0	2.238 ± 0.017	2.238 ± 0.017	-	2.280 ± 0.021	2.283 ± 0.016	-
ZFIRE	2.2	10.2	10.2	-	21	21	0	2.212 ± 0.041	2.212 ± 0.041	-	2.301 ± 0.031	2.301 ± 0.031	-
SIGMA (high-z)	2.3	10.0	10.2	10.0	17	12	5	2.035 ± 0.069	2.109 ± 0.073	1.702 ± 0.014	2.227 ± 0.037	2.250 ± 0.051	2.176 ± 0.028
KMOS^{3D} (high-z)	2.3	10.5	10.5	-	46	46	0	2.219 ± 0.017	2.219 ± 0.017	-	2.265 ± 0.015	2.265 ± 0.015	-
AMAZE	3.0	10.0	10.0	-	5	5	0	2.114 ± 0.126	2.114 ± 0.126	-	2.402 ± 0.097	2.402 ± 0.097	-
KDS	3.5	9.8	9.8	9.7	29	13	16	1.913 ± 0.032	2.032 ± 0.041	1.807 ± 0.025	2.275 ± 0.022	2.256 ± 0.041	2.288 ± 0.025

* The categories 'All' and 'RD' in this case correspond to the combination of the perturbed rotators and rotation-dominated galaxies and the rotation-dominated galaxies on their own respectively (see § 4.6.2). None of the galaxies in these categories are classified as dispersion-dominated.

plot the velocity and total-velocity offsets against redshift (analogous to Figs 4.2 and 4.7) recovered from adopting the Romanowsky & Fall (2012) stellar-mass Tully-Fisher relation as a local reference. This −0.05 dex shift is a significant fraction of the evolution of the stellar-mass Tully-Fisher relation inferred for the 'diskiest' galaxies in § 4.3.2 (+0.12 dex) and if the Romanowsky & Fall (2012) relation was adopted we would infer that there had been less evolution out to $z \sim 3.5$. We stress however that the same evolutionary trends are recovered in our test of the two different reference relations.

4.6.2 Distant comparison samples

We now list the details of the distant comparison samples, noting the methods used to extract the kinematic parameters and the number of galaxies in each parent sample. We discuss the properties which are deemed not comparable to the other samples (grey hollow symbols throughout § 4.3 and § 4.4 and grey cells in Table 4.1). In some of the studies from which the data have been drawn, the authors make specific reference to the evolution of the stellar-mass Tully-Fisher relation. We compare the conclusions presented in the original studies with those that we find here using the same data.

DYNAMO ($z \simeq 0.1$)

Green et al. (2014) described Hα IFU measurements of 67 star-forming galaxies, with half the sample selected as $z \simeq 2$ analogues on the basis of high specific star-formation rates and gas fractions. For this reason, the sample does not represent 'typical' star-forming galaxies at $z \simeq 0.1$ and we use hollow symbols for the DYNAMO data points throughout the figures in § 4.3 and § 4.4. The velocity values were extracted at a fixed radius from an arctangent model fitted to the velocity fields ($2.7R_{\rm d}$, where $R_{\rm d}$ is the exponential scale radius, here measured in the r-band) and the velocity dispersion was taken as the luminosity-weighted average of the beam-smearing corrected dispersion field. The galaxies were classified using the scheme described in Flores et al. (2006). We removed galaxies flagged to have 'complex kinematics' and those with $V_{\rm C}/\sigma_{\rm int} < 1$,

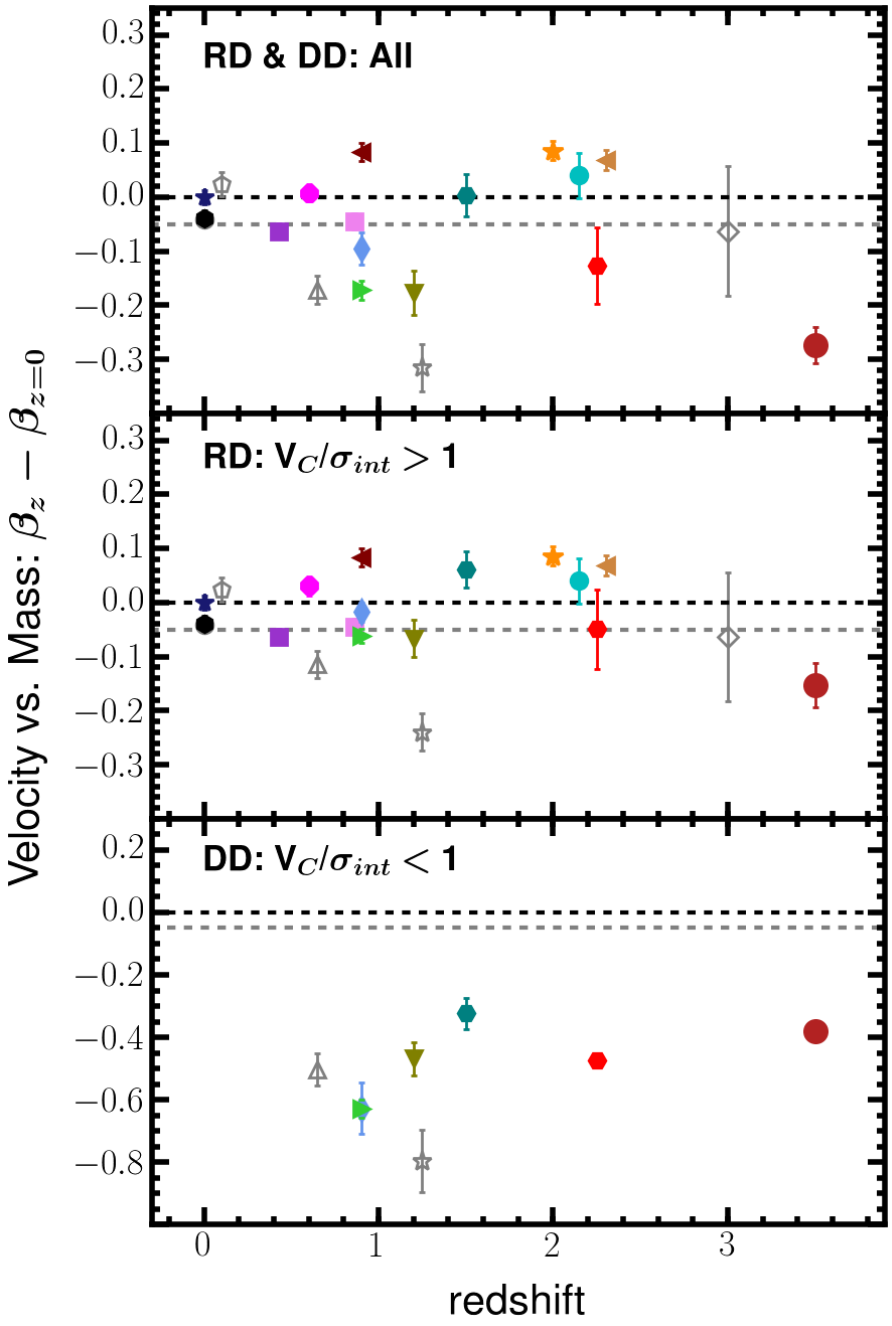

Figure 4.10: The stellar-mass Tully-Fisher offsets against redshift, as per Fig. 4.2, using a local stellar-mass Tully-Fisher relation defined from fitting the Romanowsky & Fall (2012) galaxies. This has both a shallower slope and a higher velocity zero-point than the Reyes et al. (2011) relation and has almost the same functional form as the commonly adopted Bell & de Jong (2001) relation. The result when adopting this relation is a shift towards lower velocity zero-point offsets throughout the comparison samples by $\simeq -0.05$ dex, although the trends remain unchanged. We show the approximate position of the Reyes et al. (2011) zero-point with the grey-dashed horizontal line in each of the three panels.

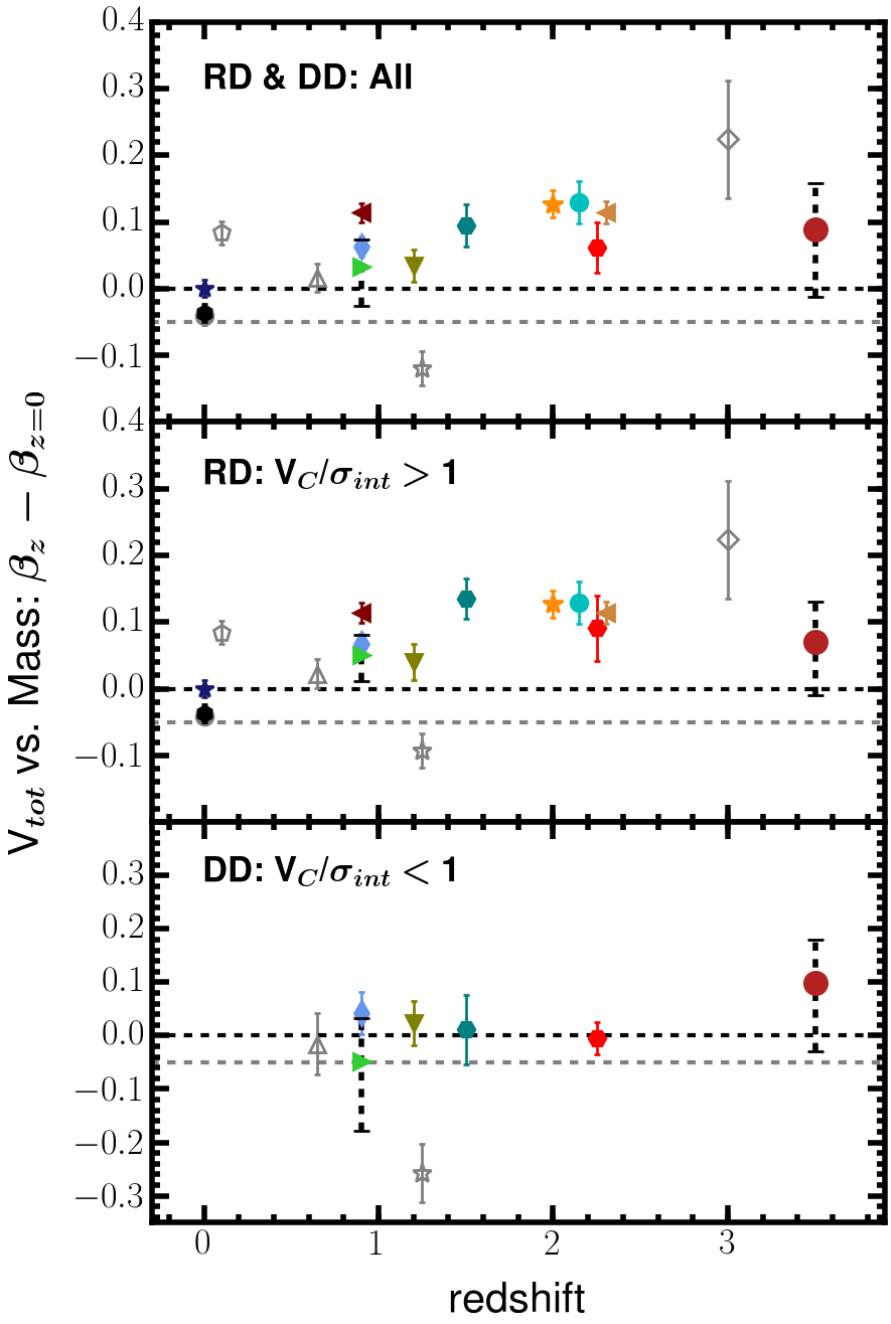

Figure 4.11: The total-velocity versus stellar-mass offsets against redshift, as per Fig. 4.7, using the local relation from fitting the Romanowsky & Fall (2012) galaxies. Using this local relation shifts the total-velocity zero-points downwards by approximately $\simeq -0.05$ dex, although the trend for all comparison samples to be offset to higher total velocities at fixed stellar mass is still observed. The position of the Reyes et al. (2011) zero-point is again shown with the grey-dashed horizontal line and the black-dashed error bars on the KDS and KROSS datapoints indicate the range of total-velocity zero-point offset differences found when varying the η parameter over the range $2.0 < \eta < 6.0$ as per Fig. 4.7.

to leave only the rotation-dominated subsample of 51 galaxies. The stellar masses were computed in Kauffmann (2003), using model mass-to-light ratios and dust corrected z-band luminosities, with the sample having median stellar mass of $\log(M_\star/M_\odot) = 10.3$. Throughout Green et al. (2014) the stellar-mass Tully-Fisher relation was explored, finding an evolution of $\simeq +0.09$ dex (no error) in velocity zero-point towards higher velocities at fixed stellar mass in comparison to the local relation of Bell & de Jong (2001). This is slightly larger than the offset of $+0.07 \pm 0.01$ dex in velocity zero-point we find in comparison to the Reyes et al. (2011) reference relation and significantly larger than the evolution inferred in comparison to the Romanowsky & Fall (2012) relation (which is close to the Bell & de Jong 2001 relation, see Fig. 4.9). This suggests some tension between the fit results for the DYNAMO sample presented in Green et al. (2014) and the results inferred from the same data throughout this study. However, in both the original results and from the fitting analysis in this chapter, there appears to be evolution of the stellar-mass Tully-Fisher relation in the DYNAMO galaxies at $z \simeq 0.1$ (roughly 1 Gyr in the past). This is possibly a consequence of the sample selection, in which many of the galaxies in the sample have unusually high gas content, and hence a large ratio of dynamical to stellar mass, for this redshift.

AHDG ($z \simeq 0.4$ and $z \simeq 0.8$)

In this study, Miller et al. (2011) described photometric and kinematic measurements of 129 disk-like galaxies with a broad morphological selection criteria that included irregular systems, systems which displayed signs of interactions and bulge-dominated disks. The broad selection criteria was chosen to reduce potential bias towards selecting only symmetric spirals, which represent the end point of isolated evolution. In this work we split the full sample into a low redshift subsample with $0.2 < z < 0.6$, with median $z = 0.4$ and containing 67 galaxies and a high-redshift subsample with $0.6 < z < 1.3$, with median $z = 0.8$ and containing 62 galaxies. Velocity measurements were computed from Keck II DEIMOS spectra, using an arctangent fit to the position-velocity diagrams of various optical emission lines and extracting at a fiducial radius of $2.2R_\mathrm{d}$. No velocity dispersion measurements were made and so again we do not

measure $V_{\rm tot}$ and assumed, given the disk-like selection criteria, that all galaxies in both redshift ranges are dominated by ordered rotation. Stellar masses were computed from SED fitting using a Chabrier IMF, with the authors then using the mass enclosed within $2.2R_{\rm d}$. The remainder of the comparison samples used the total stellar mass whilst fitting the stellar-mass Tully-Fisher relation, and so we added +0.187 dex (as stated in Miller et al. 2012) to the quoted stellar masses to account for this. Following this correction, the median stellar mass values are $\log(M_\star/M_\odot) = 10.0$ and $\log(M_\star/M_\odot) = 10.3$ for the low and high-redshift subsamples respectively.

Throughout Miller et al. (2011, 2012) the stellar-mass Tully-Fisher relation was explored in comparison to local relations presented in Bell & de Jong (2001) and Pizagno et al. (2005), finding no evidence for evolution in the zero-point of the fit to the data. This is consistent with the lack of evolution found in our analysis for the same data. In Miller et al. (2011, 2012) the authors did not attempt to pick out $z = 0$ disk analogues by applying stricter sample-selection criteria and so the star-forming galaxies are likely to be representative of the evolving-disk population at the redshifts studied. The broad sample selection criteria and subsequent lack of inferred evolution in the stellar-mass Tully-Fisher relation for these galaxies is consistent with the findings in § 4.3.2, despite the lack of reported velocity dispersions preventing us from plotting datapoints in Figs 4.3 and 4.4 to show this explicitly.

IMAGES ($z \simeq 0.6$)

In Puech et al. (2008) the authors evaluated the stellar-mass Tully-Fisher relation using 63 star-forming galaxies from the IMAGES large programme Yang et al. (2008), which made use of the GIRAFFE integral-field spectrograph. The velocity measurements were made by fitting PSF-convolved thin-disk models with arctangent velocity fields to the observed [O II] velocity fields, and extracting at the flat region of the rotation curve. Velocity dispersion values were not reported in Puech et al. (2008) or in the companion IMAGES survey papers (e.g. Neichel et al., 2008; Yang et al., 2008). The authors

provided a kinematic classification for each galaxy following Flores et al. (2006), and we removed all those with 'complex kinematics' to leave a sample of 28 galaxies. We also constructed a sample containing 14 galaxies that are classed as 'rotation-dominated', plotted in the $V_C/\sigma_{int} > 1$ panels throughout § 4.3 and § 4.4, although there is only a very small difference in the velocity zero-point offsets between these and the sample of 28 galaxies that also contain 'perturbed rotators'. Stellar masses were computed using *K*-band luminosities and a colour dependent mass-to-light ratio following the method described in Bell et al. (2003). This method assumed a diet Salpeter IMF, which we corrected to Chabrier by reducing the stellar masses by a factor 1.19 (Cresci et al., 2009). The median stellar mass value amongst the full sample is $\log(M_\star/M_\odot) = 10.3$. In Puech et al. (2008) the authors studied the stellar-mass Tully-Fisher relation and found an evolution of $+0.13 \pm 0.06$ dex in velocity zero-point in comparison with the local relation described in § 4.6.1. When fitting the same data with the slope fixed to the shallower value found in the Reyes et al. (2011) relation, which also has higher velocity zero-point, we found an evolution of $+0.04 \pm 0.03$ dex. This highlights the importance of the choice of local reference relation in determining the extent of the evolution, which is much less extreme in comparison to the Reyes et al. (2011) relation. The galaxies to which the relation is fitted are the 'diskiest' in the Puech et al. (2008) sample. Observing evolution in the relation when fitting these galaxies is therefore consistent with the discussion throughout § 4.3.2, although we cannot plot the Puech et al. (2008) data point in Figs 4.3 and 4.4 to show this explicitly due to the lack of reported velocity dispersions.

MUSE+KMOS - MKS ($z \simeq 0.65$ and $z \simeq 1.25$)

Swinbank et al. (2017) measured the kinematics of $\simeq 150$ main-sequence star-forming galaxies spanning $0.28 < z < 1.65$ using Multi-Unit Spectroscopic Explorer (MUSE) observations of [O II] emitters and KMOS observations of Hα emitters. In this work we split the sample into two redshift ranges; the lower redshift subsample with $0.28 < z < 1.0$, median $z = 0.65$ and containing 107 galaxies and a higher redshift subsample with $1.0 < z < 1.65$, median $z = 1.25$ and containing 43 galaxies. The velocity was

measured by fitting disk+halo dynamical models to the observed data and extracting at $3.0R_{\rm d}$. These measurements have not had beam-smearing corrections applied and so throughout § 4.3 and § 4.4 the points are plotted with hollow symbols. The velocity dispersions were measured from the observed linewidths and corrected for beam-smearing following the method described in Johnson et al. (2018). We used the combination of the two measurements to construct rotation-dominated and dispersion-dominated subsamples in each redshift range on the basis of $V_{\rm C}/\sigma_{\rm int} > 1$. Stellar masses were computed using the HYPER-Z SED fitting code with a Chabrier IMF, with a median stellar mass of $\log(M_\star/M_\odot) = 9.3$ across the lower redshift subsample and $\log(M_\star/M_\odot) = 9.9$ across the higher redshift subsample. The stellar mass Tully-Fisher relation is not studied in Swinbank et al. (2017).

HR-COSMOS ($z \simeq 0.9$)

Pelliccia et al. (2017) described kinematic measurements for a subsample of 82 galaxies from the HR-COSMOS survey, which made use of slit spectroscopy using the Visible Multi-Object Spectrograph (VIMOS). Various optical emission lines were targeted and velocity measurements were extracted by fitting PSF-convolved exponential disk, flat and arctangent velocity field models to the data. The results from these different models are consistent within the uncertainties and in most cases the rotation velocity was extracted at $2.2R_{\rm d}$ from the exponential disk model. The velocity dispersion was also constrained as a parameter in the model, giving beam-smearing corrected measurements of both velocity and velocity dispersion for the sample. This allowed for classification into rotation-dominated and dispersion-dominated subsamples. Stellar masses were computed from SED fits to 30-band UV-IR photometry in the COSMOS field using the LE PHARE software (Arnouts et al., 2002; Ilbert et al., 2006) with a Chabrier IMF. The rotation-dominated subsample have $\log(M_\star/M_\odot) = 10.2$, whilst the dispersion-dominated subsample have $\log(M_\star/M_\odot) = 9.7$. Throughout Pelliccia et al. (2017) the authors studied the evolution of the stellar-mass Tully-Fisher relation over the range $0 < z < 1.2$ using several datasets from the literature, concluding that there is no significant evolution in their dataset or when studying all datasets together.

This is consistent with the results we find when fitting the HR-COSMOS data, which we conclude are representative of the evolving-disk population at $z \simeq 0.9$ due to the lack of additional sample cuts which aim to isolate the most disky galaxies.

KROSS ($z \simeq 0.9$)

Stott et al. (2016) described the first kinematic measurements from the KMOS Redshift One Spectroscopic Survey, with the full sample and derived values presented in Harrison et al. (2017). Velocity and velocity dispersion measurements were made from IFU observations of the Hα emission line for $\simeq 600$ galaxies as explained below, providing a very large and diverse statistical sample at $z \simeq 1.0$. Exponential disk models were fitted to the observed 2D velocity fields to provide a smoothly varying 1D profile, and measurements were extracted at $3.4R_{\rm d}$. Velocity dispersion measurements were extracted either at the outskirts when the data extend to large enough radii, or using a median of the observed values when they do not. The observed velocity and velocity dispersion measurements were then corrected for the effects of beam-smearing using the methods discussed in Johnson et al. (2018). We only used sources with quality flags 1-3, with no sign of AGN and with inclination angles $\theta_{\rm im} > 25^{\circ}$ from the catalogue presented in Harrison et al. (2017), in order to minimise the uncertainties on the kinematic parameters, which left a total of 475 galaxies. Using the velocity and velocity dispersion measurements we defined rotation-dominated (382/475, 80 per cent) and dispersion-dominated (93/475, 20 per cent) subsamples. Stellar masses were estimated using a fixed mass-to-light ratio applied to the H-band magnitudes, with median value $\log(M_{\star}/M_{\odot}) = 10.1$ for the rotation-dominated subsample and $\log(M_{\star}/M_{\odot}) = 9.7$ for the dispersion-dominated subsample. The analysis presented in Harrison et al. (2017) suggestsed that rotation-dominated galaxies ($V_{\rm C}/\sigma_{\rm int} > 1$) at $z \simeq 1$ lie on the Reyes et al. (2011) stellar-mass Tully-Fisher relation. This is consistent with the results we found when fitting the KROSS sample. In Tiley et al. (2016), an analysis of the stellar mass Tully-Fisher relation for the KROSS sample, it was reported that applying stricter $V_{\rm C}/\sigma_{\rm int}$ cuts led to inferred evolution towards higher velocities at fixed stellar mass in the stellar-mass Tully-Fisher relation. We reproduced this trend

throughout the analysis presented in this chapter, interpreting these cuts as selecting galaxies that are more kinematically evolved and closer to tracing dynamical mass using rotation velocities alone.

KMOS^{3D} ($z \simeq 0.9$ and $z \simeq 1.25$)

The KMOS^{3D} survey presented in Wisnioski et al. (2015) described KMOS Hα observations of $\simeq$ 600 massive SFGs clustered around $z \simeq 0.9$ and $z \simeq 2.3$. We made use of data presented in a recent, thorough study of the evolution of the stellar-mass Tully-Fisher relation over the range $0.9 < z < 2.3$ from Übler et al. (2017), using 316 KMOS^{3D} galaxies with detected and spatially resolved Hα emission. The dynamical modelling of the data was presented in Wuyts et al. (2016b), in which exponential mass models were fitted simultaneously to one-dimensional extractions along the kinematic axis of the velocity and velocity dispersion fields. The rotation velocity was extracted as the maximum of the model rotation curve. Various cuts were made to the parent sample to remove merger candidates and to ensure high signal-to-noise and main-sequence sampling, leaving 240 galaxies. Further cuts were made to remove galaxies where the peak velocity was not constrained, where the velocity dispersion peak did not coincide with the galaxy centre and where $V_C/\sigma_{\rm int} < \sqrt{4.4}$, in order to build a Tully-Fisher sample of 65 galaxies at $z \simeq 0.9$ and 46 at $z \simeq 2.3$. To calculate the parent fractions we assumed that the parent sample of 316 galaxies is divided evenly between the two redshift slices. The extracted stellar masses were computed following the procedure described in Wuyts et al. (2011a), which uses a Chabrier IMF. The median stellar mass in both redshift slices is $\log(M_\star/M_\odot) = 10.5$.

We were provided with the data used throughout Übler et al. (2017) by Hannah Übler *(private communication)* for the analysis in this work. In Übler et al. (2017) the authors found velocity zero-point offsets, in comparison to the Reyes et al. (2011) local relation, of +0.095 dex and +0.073 dex for the $z \simeq 0.9$ and $z \simeq 2.3$ subsamples respectively (errors not quoted). These are in agreement with the values $+0.115 \pm 0.013$ dex and

+0.094 ± 0.017 dex we found when fitting the same samples. The observed evolution from the local relation at both redshift slices is expected following the discussion of § 4.3.2, since the sample selection described in Übler et al. (2017) was designed to pick out the most 'disky' galaxies with high V_C/σ_{int} values.

Throughout Übler et al. (2017) the authors also considered a *circular velocity*, which contains a velocity dispersion term, to account for the non-negligible contribution of pressure to the gravitational support of the systems. The measured offsets from the local relation in the circular velocity versus stellar-mass plane increased to +0.123 dex and +0.118 dex for the low and high redshift samples respectively, slightly lower than the offset values of +0.145 ± 0.012 and +0.140 ± 0.015 we find when using the total velocity discussed in 4.4.2.

MASSIV ($z \simeq 1.2$)

The Mass Assembly Survey with SINFONI in VVDS (MASSIV) (Vergani et al., 2012; Contini et al., 2012; Epinat et al., 2012) utilised the Spectrograph for INtegral-Field Observations in the Near Infrared (SINFONI) to collect Hα emission line observations for 46 star-forming galaxies over the range $0.9 < z < 1.6$. The velocity and velocity dispersion measurements were extracted after fitting a PSF-convolved model arctangent function to the data to counter the effects of beam-smearing. The rotation velocity was extracted at $\simeq 3R_d$ from the intrinsic model and the velocity dispersion is taken as the average of the beam-smearing corrected velocity dispersion map. We defined rotation-dominated and dispersion-dominated subsamples of 30 and 16 galaxies respectively using the ratio $V/\sigma_{int} > 1$. The stellar masses were computed in Contini et al. (2012) using SED fits to the photometry with an assumed Salpeter IMF (Salpeter, 1955), which we converted to a Chabrier IMF by dividing by a factor 1.8. The median stellar mass is $\log(M_\star/M_\odot) = 10.1$ in the rotation-dominated subsample and $\log(M_\star/M_\odot) = 9.8$ in the dispersion-dominated subsample. In Vergani et al. (2012) the authors studied the evolution of the stellar-mass Tully-Fisher relation since $z \simeq 1.2$ using the MASSIV

sample, making comparisons with both the Bell & de Jong (2001) and Pizagno et al. (2007) local relations. For the rotation-dominated MASSIV galaxies, velocity zero-point evolution of +0.11 dex was found in comparison to the Pizagno et al. (2007) local relation, whereas no evolution was found in comparison with the Bell & de Jong (2001) relation, consistent with our findings for the MASSIV sample. This stresses further the importance of choosing a consistent reference relation when making comparisons between different intermediate and high-redshift studies.

SIGMA ($z \simeq 1.5$ and $z \simeq 2.25$)

Simons et al. (2016) presented the Keck/MOSFIRE Survey in the near-Infrared of Galaxies with Multiple position Angles (SIGMA), which was a study of the internal kinematics of star-forming galaxies at $z \simeq 2$. We split the full sample into 27 galaxies with $1.3 < z < 1.8$ and 17 galaxies with $2.0 < z < 2.5$ with measured velocities and velocity dispersions. These come from parent samples of 33 and 25 galaxies at the respective redshift intervals, assuming that 9 galaxies which were cut from the sample on the basis of emission line extent are divided equally between the two ranges. The velocity and velocity dispersion were measured using ROTCURVE to fit the 2D longslit spectra (containing high S/N detections of either the Hα or [O III]λ5007 emission line), which takes into account the effects of beam-smearing. The rotation velocities were extracted at the flat part of the modelled rotation curves. Stellar masses were computed using SED fits with a Chabrier IMF with median values of $\log(M_\star/M_\odot) = 10.1$ and $\log(M_\star/M_\odot) = 10.0$ for the samples at lower and higher redshift respectively.

In Simons et al. (2016) the stellar-mass Tully-Fisher was explored, with the location of galaxies in the velocity versus stellar-mass plane found to depend strongly on the ratio of $V_C/\sigma_{\rm int}$. For 12 massive, rotation-dominated galaxies from the full sample (both redshift ranges) an evolution of -0.44 dex in $\log(M_\star/M_\odot)$ zero-point offset was reported, in comparison to the Reyes et al. (2011) relation, corresponding to +0.12 dex in velocity zero-point offset. After splitting the sample into two redshift ranges we

found velocity zero-point offsets of $+0.09 \pm 0.04$ dex at $z \sim 1.5$ and -0.04 ± 0.05 dex at $z \sim 2.25$, although there is a large degree of scatter in the velocity versus stellar-mass plane amongst the higher redshift galaxies. Given the normalised parent fraction and the median V_C/σ_{int} of the lower redshift sample, there is a discrepancy between the observed and expected stellar mass Tully-Fisher offsets in the right panels of Figs 4.3 and 4.4. This suggests higher observed rotation velocities at fixed stellar mass relative to the other comparison samples.

SINS ($z \simeq 2.0$)

The Spectroscopic Imaging survey in the near-infrared (SINS) was presented in Förster Schreiber et al. (2009), describing SINFONI Hα observations of 80 massive star-forming galaxies. Cresci et al. (2009) described dynamical modelling of a subsample of 18 galaxies from the SINS parent sample, selected due to the prominence of ordered rotational motions. We concentrated solely on this subsample, since the dynamical modelling included steps to correct the velocity and velocity dispersion fields for the effects of beam-smearing. 16 of the 18 galaxies have reliable stellar mass measurements and 11 have intrinsic velocity dispersion measurements provided in Cresci et al. (2009), which we used as comparison samples in the velocity versus stellar-mass and total-velocity versus stellar-mass planes respectively.

The velocities were extracted in Cresci et al. (2009) as the best fit parameter from the IDL code DYSMAL, which derives rotation curves given an input radial mass distribution. This fitting procedure also constrained the intrinsic velocity dispersions of the disks, corrected for beam-smearing and instrumental resolution effects. Stellar masses were computed using SED fitting with a Chabrier IMF, with median value for the 16 galaxies of $\log(M_\star/M_\odot) = 10.6$. In Cresci et al. (2009) the authors constructed the $z \simeq 2$ stellar-mass Tully-Fisher relation and found a $\log(M_\star/M_\odot)$ zero-point offset of +0.09 dex in comparison to the Bell & de Jong (2001) local relation. This is in agreement with the value of $+0.11 \pm 0.01$ dex that we found when fitting the Cresci et al. (2009)

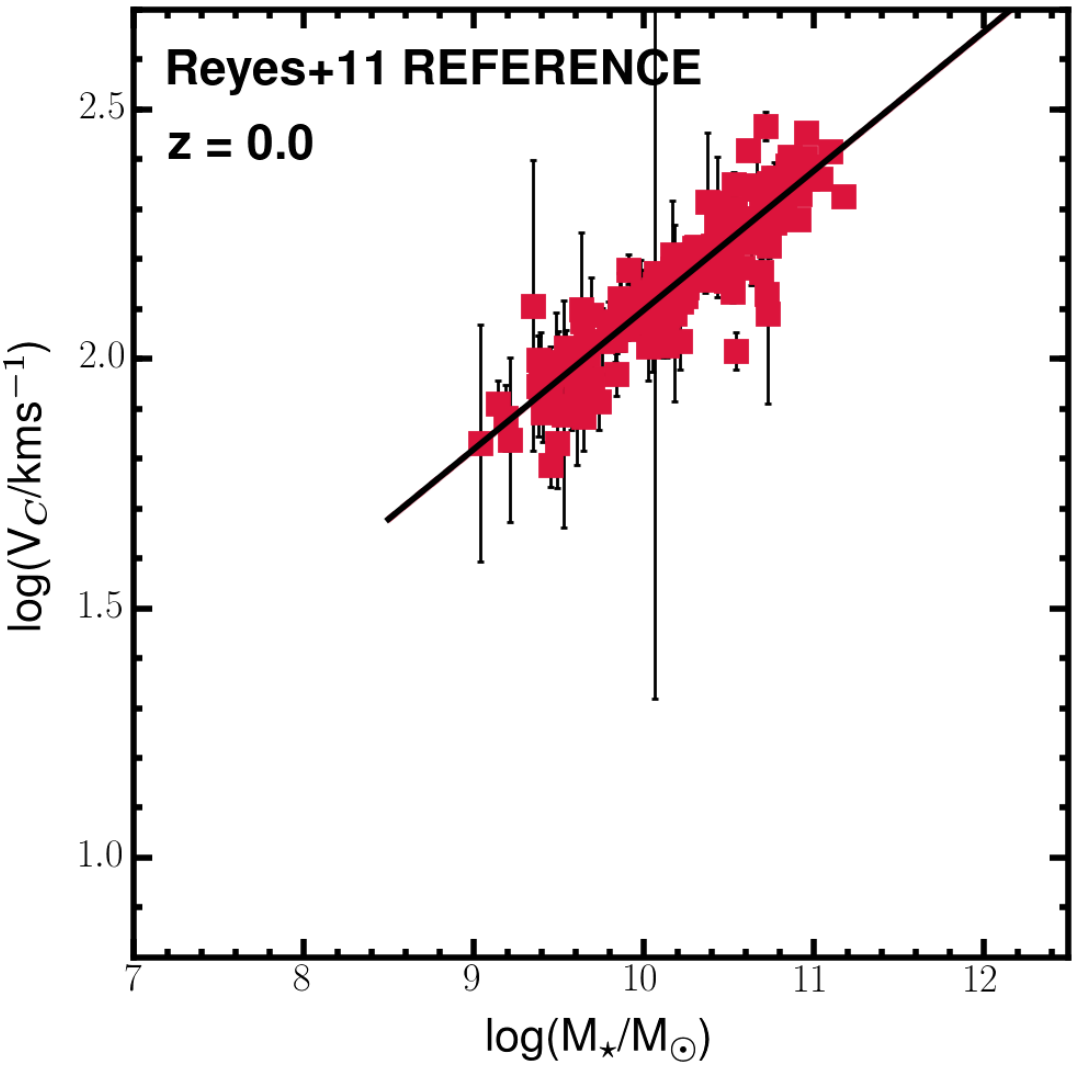

Figure 4.12: As an enlarged example of the subplots shown throughout Figs 4.13 and 4.14, we plot the 189 spiral galaxies from Reyes et al. (2011) with the solid red squares with best-fit relation $\log(V_C) = 2.125 + 0.279[\log(M_\star) - 10.1]$ (solid-black line).

galaxies, consistent with evolution of the stellar-mass Tully-Fisher relation since $z \simeq 2$. In the context of the discussion throughout § 4.3.2, we expected to find evolution for this sample due to the nature of the sample selection criteria, which aimed to isolate the highest V_C/σ_{int} galaxies from the SINS sample.

ZFIRE ($z \simeq 2.15$)

In Straatman et al. (2017), the authors described Keck/MOSFIRE longslit spectroscopic observations of 22 star-forming galaxies over the range $2.0 < z < 2.5$. The initial

sample consisted of 38 galaxies from which the 22 were selected as the best candidates for accurate kinematic modelling on the basis of the S/N of the emission lines. Rotation velocities and velocity dispersions were measured by fitting an arctangent function to the spectra in 2D, assuming an exponential disk profile for the emission line intensity (which is either Hα or [O III]λ5007). The fitting procedure included a beam-smearing correction so that the velocities, extracted at $2.2R_{\rm d}$, and velocity dispersions used in fitting the stellar-mass Tully-Fisher relation were intrinsic properties. Only one galaxy in the sample shows $V_{\rm C}/\sigma_{\rm int} < 1$, which we removed to focus solely on the 21 rotation-dominated galaxies. The stellar masses were computed using the FAST SED fitting code with Chabrier IMF, with median value for the sample $\log(M_\star/M_\odot) = 10.2$. The authors fitted the stellar-mass Tully-Fisher relation to these galaxies and recovered the best-fit relation $\log(V_{\rm C}) = (2.20 \pm 0.05) + (0.193 \pm 0.108)[\log(M_\star) - 10.1]$ when allowing both the slope and zero-point to vary. When fixing the slope to the value described in Reyes et al. (2011) the authors inferred a velocity zero-point evolution of +0.07 dex. This is consistent with the value $+0.08 \pm 0.02$ dex that we find when fitting the same galaxies and consistent with a moderate evolution of the stellar-mass Tully-Fisher relation since $z \simeq 2.15$. Given that no special selection criteria have been applied, the ZFIRE datapoint is an outlier in the right panel of Fig. 4.3, since the normalised parent fraction for the sample is ~ 1. However, the observed Tully-Fisher velocity offset agrees with the expectation in the right panel of Fig. 4.4, as the sample has high median $V_{\rm C}/\sigma_{\rm int}$ in comparison to the model prediction.

AMAZE ($z \simeq 3.0$)

Gnerucci et al. (2011) presented the resolved dynamical properties of the Assessing the Mass-Abundance redshift Evolution (AMAZE) sample, using SINFONI [O III]λ5007 measurements for 33 galaxies. 11 of these galaxies were judged to be rotation-dominated by assessing the deviations from a planar fit to the position-velocity diagram, with the other 22 discarded in the analysis presented in Gnerucci et al. (2011). Rotation velocities and intrinsic velocity dispersions were measured by fitting model rotation curves, derived from exponential mass distributions, to the observed velocity fields,

with the extracted V_C value taken as the large radius limit of the rotation curve and the σ_{int} as the maximum of the difference in quadrature between the σ_{obs} map and the σ_{model} map (which also takes into account instrumental resolution and beam-smearing; see their Equation 8).

As explained in Chapter 3, we constructed a 'clean' sample of 5 galaxies that have constrained velocity measurements, and velocity dispersion measurements consistent with being greater than zero. Stellar masses were derived from SED fitting using a Chabrier IMF, with median value for the clean sample of $\log(M_\star/M_\odot) = 10.0$. Due to the small sample size with large intrinsic scatter, we plot all comparison points for the AMAZE sample with hollow symbols. In Gnerucci et al. (2011) the authors fitted the stellar-mass Tully-Fisher relation at $z \simeq 3$ to the full sample of 11 rotation-dominated galaxies. A velocity zero-point evolution of +0.286 dex is claimed in comparison to the Bell & de Jong (2001) relation, far higher than in any of the other comparison samples and requiring rapid evolution of the relation over the range $2 < z < 3$. In our clean sample, many of the uncertain high-velocity galaxies are omitted and we find a velocity zero-point evolution of −0.01 dex, consistent with a picture in which the large velocity dispersions observed throughout this sample become a significant component of the dynamical mass budget.

Summary of distant comparison samples

We have endeavoured to collect a large number of star-forming galaxy samples with kinematic measurements, covering a wide range in physical properties, redshift and sample-selection criteria. This is to provide an unbiased perspective of the evolution of the stellar mass Tully-Fisher relation over cosmic time. Given the numerous methodologies which have been followed in the different studies to compute and extract physical properties, there are unavoidable systematics associated with making use of published measurements. Keeping this in mind as an important caveat, and to summarise the results of § 4.3 and § 4.4, the normalisation of the Tully-Fisher relation does appear to evolve with cosmic time for the diskiest subsamples of galaxies,

and the range of normalisation shifts quoted in the literature are quantifiable through an understanding of sample-selection criteria. As the sample sizes and data quality continue to increase over the range $0 < z < 4$, it will be possible to further understand the physical processes which are driving this evolution.

4.7 Fits to comparison sample data

We include for reference the fits to the comparison sample data in the V_C vs. $M_\star$ plane (Fig. 4.13) and the V_{tot} vs. $M_\star$ plane (Fig. 4.14). In each subplot the reference sample and redshift are indicated, with solid points indicating rotation-dominated galaxies, hollow points dispersion-dominated (where applicable), the solid colour line the fit to 'All' galaxies, the colour-dashed line the fit to the rotation-dominated galaxies and the colour-dash-dot line the fit to the dispersion-dominated galaxies (where applicable). The shaded regions around these lines indicate the $1-\sigma$ uncertainties on the fits. The solid black line shows the local reference relation from fitting the Reyes et al. (2011) sample, which we show enlarged in Fig. 4.12 (and see 4.9) which is used for comparison when constructing Figs 4.2 and 4.7.

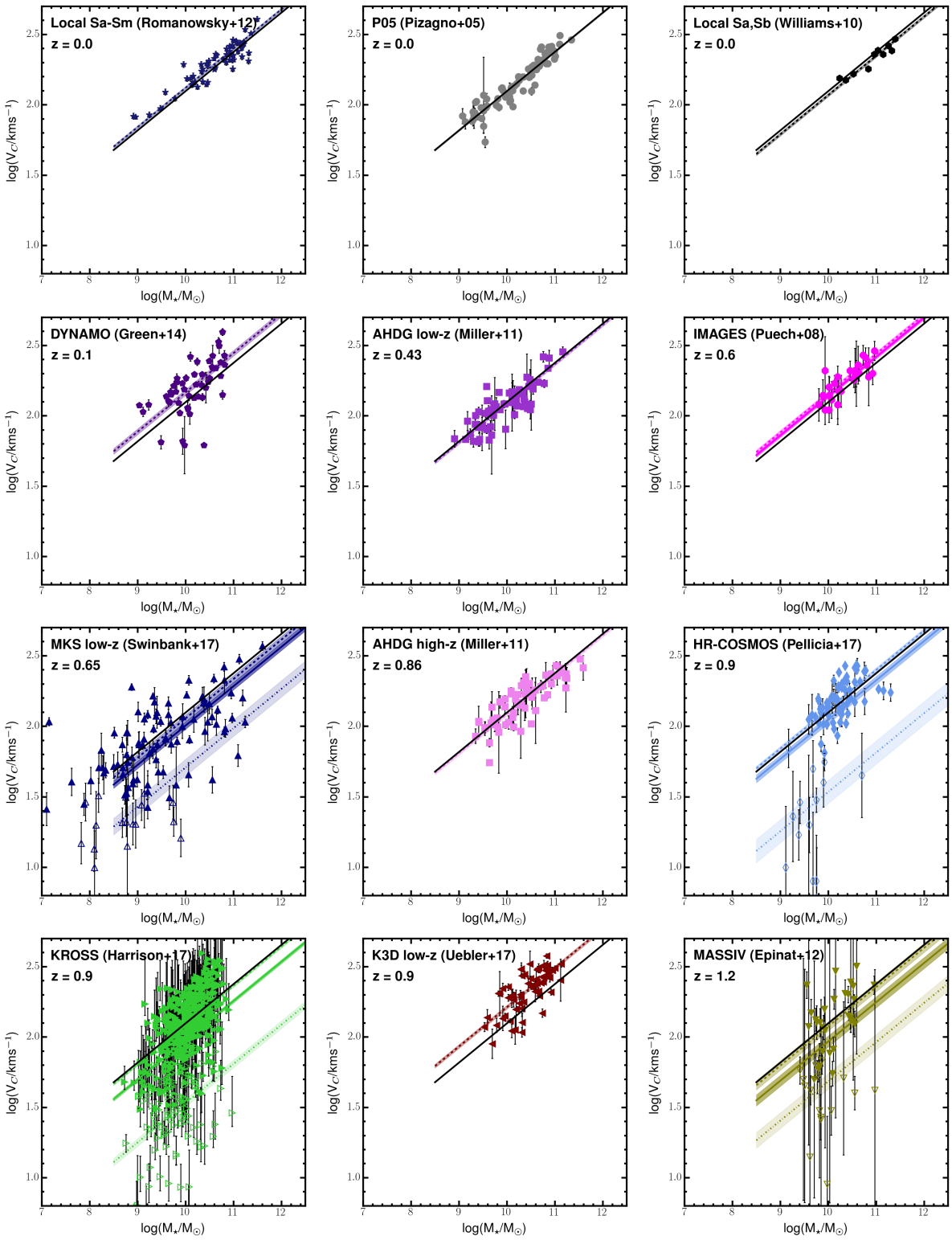

Figure 4.13: Best fits of the relation $\log(V_C) = \beta + \alpha[\log(M_\star) - 10.1]$ to the comparison samples, using fixed slope $\alpha = 0.279$, with the recovered β values used throughout Fig. 4.2. Rotation-dominated and dispersion-dominated galaxies have filled and hollow symbols respectively. The solid line shows the fit to the full samples, the dashed-line the fit to the rotation-dominated galaxies and the dot-dashed line the fit to the dispersion-dominated galaxies. Shaded regions represent the $1-\sigma$ uncertainty on the fits.

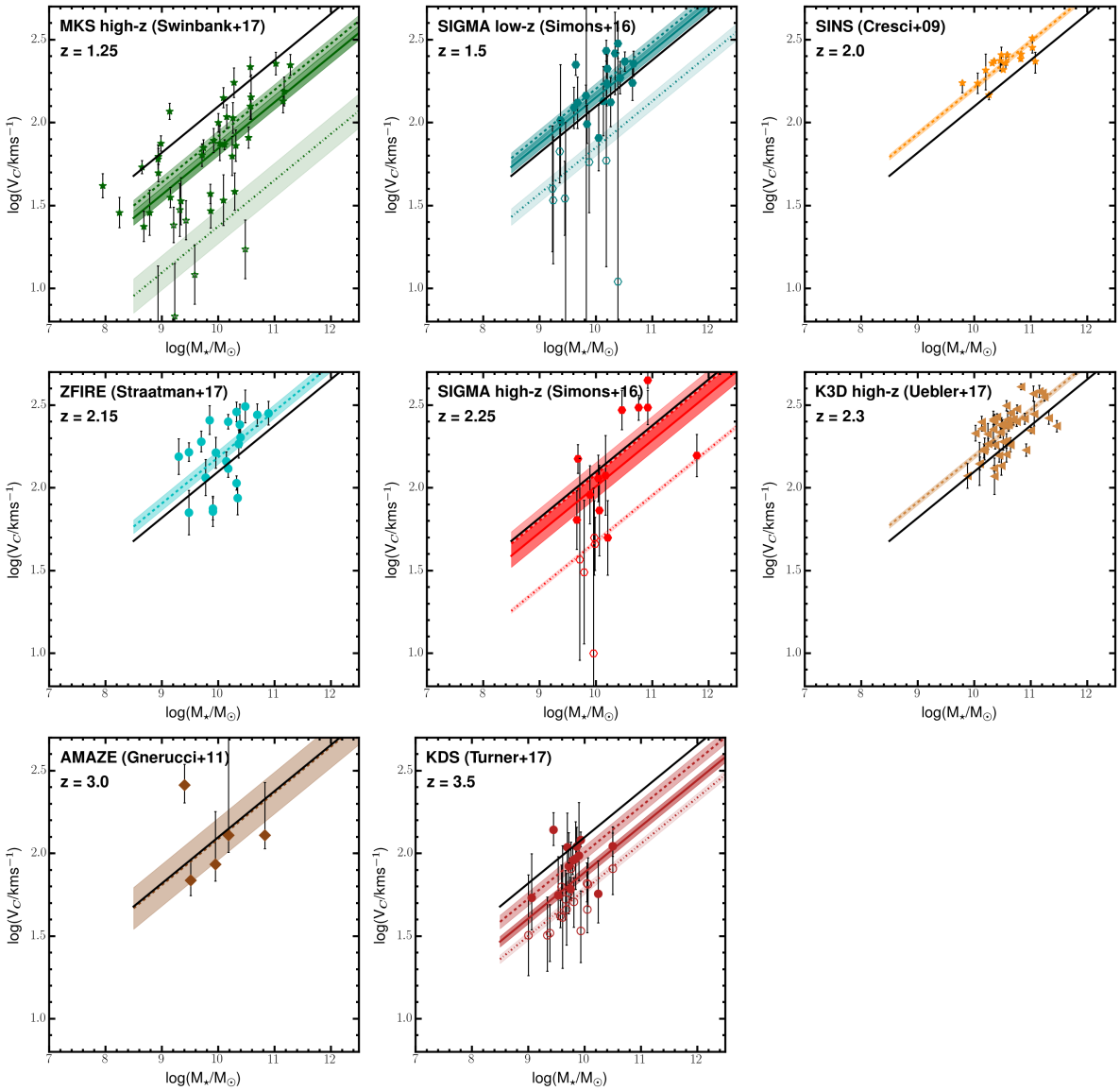

Figure 4.13: Continued.

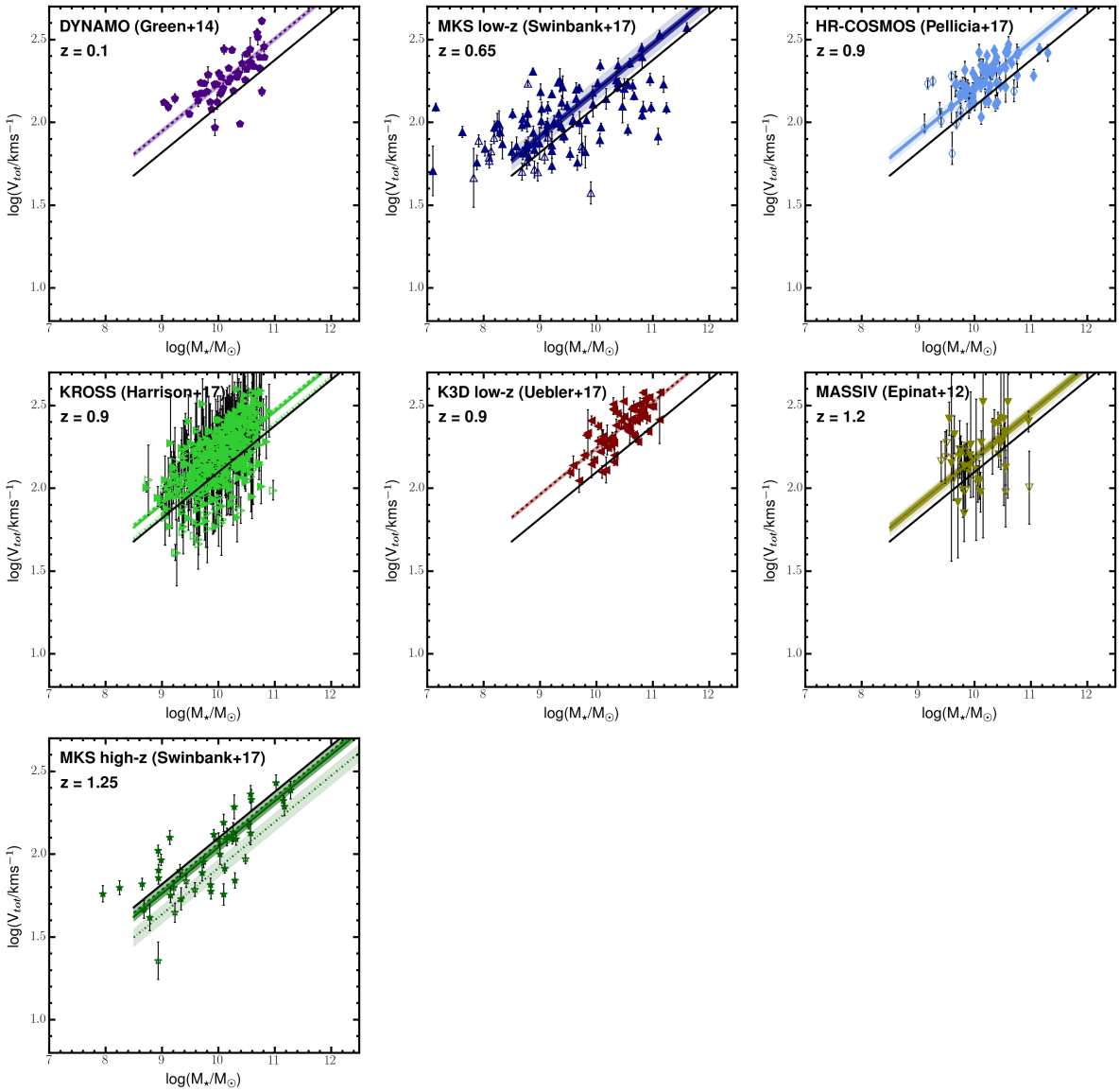

Figure 4.14: Best fits of the relation $\log(V_{\rm tot}) = \beta + \alpha[\log(M_\star) - 10.1]$ to the comparison samples, using fixed slope $\alpha = 0.279$, with the recovered β values used throughout Fig. 4.7. The symbol convention is equivalent to Fig. 4.13.

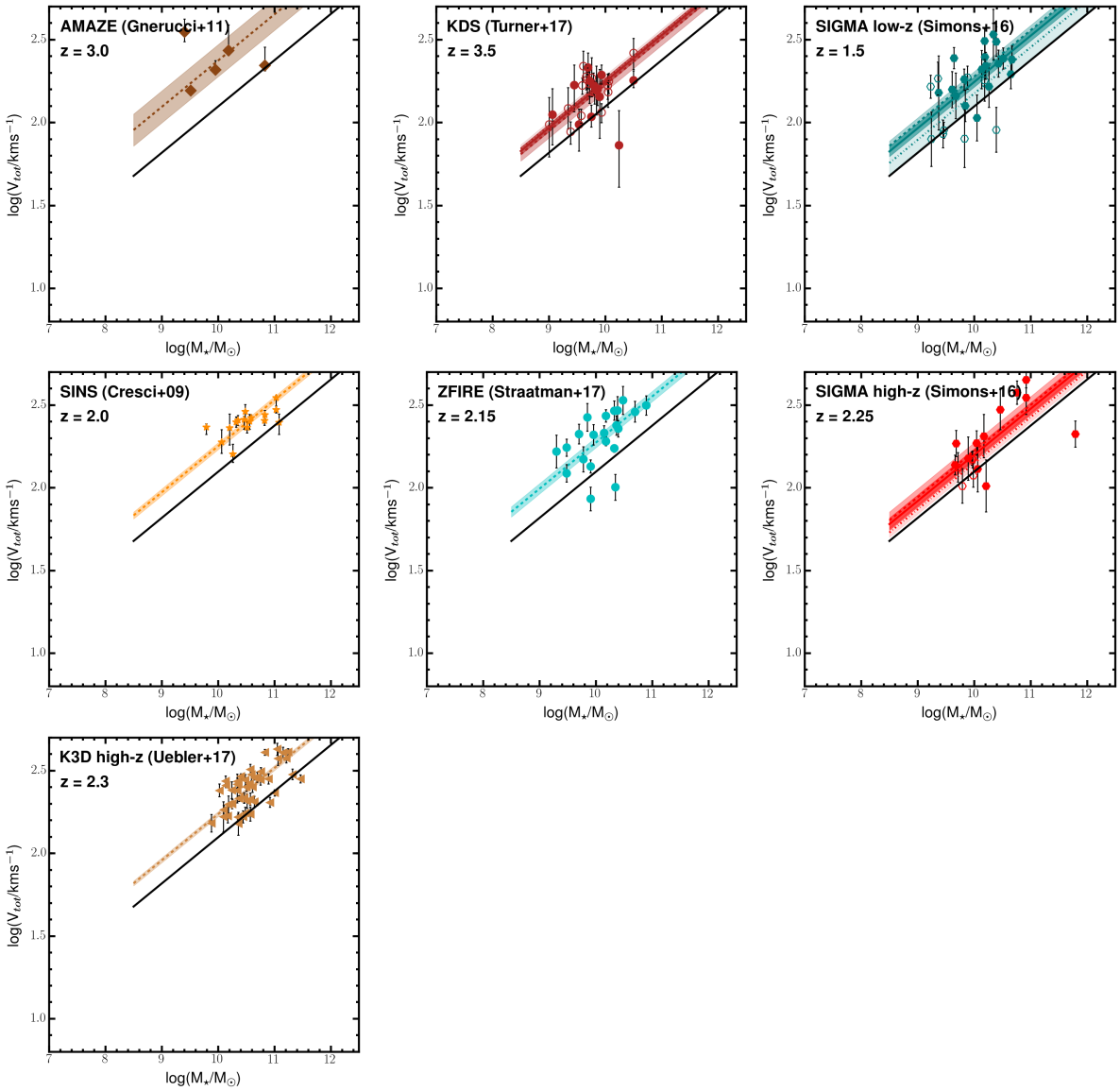

Figure 4.14: Continued.

Chapter 5

Spatially resolved emission-line ratio gradients at $z \simeq 2.3$ from the KLEVER Survey

Abstract

We provide an overview of the KMOS LEnsed galaxies Velocity and Emission line Review (KLEVER) survey, and describe IFS observations of 63 star-forming galaxies at $z \sim 2.2$ from the first 4 KMOS pointings. The KLEVER observations cover the *YJ* and *H*-bands, and the supplementary *K*-band observations from the KMOS^{3D} programme provide access to spatially-resolved observations for a suite of rest-optical strong emission lines. We use information obtained from fitting the integrated spectra to define a high-S/N subsample of 22 galaxies, upon which we concentrate for the remainder of the analysis. The integrated emission-line ratios place the high-S/N galaxies in similar regions of the BPT and O32 vs. R23 diagnostic diagrams to other samples at $z \sim 2.2$, which are offset from the local distributions defined by SDSS star-forming galaxies as a consequence of differing ISM conditions. We carry out a first preliminary analysis of the radial profiles of the Balmer decrement at $z \sim 2.2$ across 18

galaxies from the high-S/N subsample, using both a fixed grid of square segments and a series of annuli defined using the galaxy structural properties. We find that the majority of this sample have negative Balmer decrement gradients (i.e. centrally concentrated dust distributions) and that galaxies with strong, negative gradients have lower velocity dispersions, higher stellar masses and lower Hα luminosities. Using the Balmer decrement values, we apply dust corrections to the O32 radial profiles and find that the majority have positive gradients, with more-positive values generally correlating with lower velocity dispersions, higher stellar masses and lower Hα luminosities. This can qualitatively be interpreted as most of the sample having negative metallicity gradients, although understanding this in more detail requires photoionisation modelling. The galaxy physical properties associated with more-negative Balmer decrement gradients (more-positive O32 gradients) are indicative of more-advanced states in the process of galaxy evolution. Analysis of the full KLEVER sample will provide a more complete understanding of the chemical evolution of star-forming galaxies at $z \sim 2.2$.

5.1 Introduction

Over the last 5 years, the integrated spectra of large samples of high-redshift star-forming galaxies have been observed using Near-Infrared (NIR) Multi-Object Spectrographs (MOSs). These observations typically span the *YJ*, *H* and *K*-bands, which at $z \sim 2$ corresponds roughly to the rest-frame wavelength range 0.3−0.8μm. This range encapsulates many of the strong emission lines required to infer the physical properties of the ISM within galaxies, including the [O II]$\lambda\lambda$3727,3729 doublet, Hβ, the [O III]$\lambda\lambda$4960,5007, Hα and [N II]λ6583. As a result, both the Keck Baryonic Structure Survey (KBSS)−MOSFIRE (Steidel et al., 2014) and the MOSFIRE Deep Evolution Field (MOSDEF; Shapley et al. 2015) survey have used the KECK telescope instrument MOSFIRE to study star-forming galaxy samples at $z \sim 2.3$. The conclusion from both of these surveys is that the galaxy samples occupy different areas of emission-line-ratio diagnostic plots, such as the [N II] Baldwin-Phillips-Terlevich (BPT; Baldwin et al. 1981) diagram, than local galaxies.

Galaxies from the Sloan Digital Sky Survey (e.g. York et al., 2000; Tremonti & Heckman, 2004), are commonly used for comparison, and the high-redshift samples are either offset entirely or else sit at the extreme end of the local distributions, depending on the choice of diagnostic plot. These observations are interpreted as high-redshift galaxies having more extreme ISM conditions, specifically higher electron densities, higher ionisation parameters, harder ionising radiation fields and differing nitrogen-to-oxygen (N/O) abundance ratios. There is debate as to which or which combination of these physical properties drives the observed emission-line ratios at high redshift. In the series of KBSS−MOSFIRE and Keck Lyman Continuum Spectroscopic survey (KLCS) papers (e.g. Steidel et al., 2014, 2016; Strom et al., 2017; Steidel et al., 2018), the authors self-consistently model the input ionising radiation field (constrained with rest-frame UV measurements of the galaxies) and emphasise the increased nebular excitation, and hence higher ionisation parameter, of the high-redshift galaxies. In the MOSDEF paper series (e.g. Shapley et al., 2015; Sanders et al., 2016), higher electron densities are measured explicitly using the [O II]$\lambda\lambda$3727,3729 and [S II]$\lambda\lambda$6716,6731 doublets and the lack of offsets in line-ratio diagrams involving only hydrogen, oxygen and sulphur are interpreted as suggesting redshift evolution of the relationship between N/O and O/H.

Additionally, in Masters et al. (2014) the authors reach similar conclusions using the Magellan Baade telescope Folded-port InfraRed Echellette (FIRE) instrument observations, suggesting that the observed shift in the diagnostic diagrams could be a consequence of an increase in the N/O abundance ratio at fixed metallicity in tandem with higher electron densities. As a final example, the FMOS-COSMOS survey (e.g. Kashino et al., 2016) is a study of the ISM properties of galaxies at $z \sim 1.6$. Kashino et al. (2016) report similar emission-line ratios to those observed in Steidel et al. (2014), and also cite higher electron densities, harder ionising radiation fields and higher ionisation parameters as the cause for this. Ubiquitously, the papers described above highlight the dangers of applying locally-calibrated strong-line abundance indicators to high-redshift galaxies as a consequence of the differences in ISM conditions. To briefly summarise, the major questions arising from these integrated-light studies, and which

remain to be answered, are: **1)** what combination of physical properties determine the excitation state of high-redshift star-forming galaxies? **2)** by what mechanism and over what timescale do these physical properties change to bring the star-forming population in line with the SDSS distributions?

All of the high-redshift studies mentioned above observed integrated spectra, and therefore only consider the average properties of the whole galaxy without any spatial information. However, from studies in the local Universe, we have evidence that physical conditions in the ISM vary significantly as a function of position across the galaxy. Indeed there have been several studies of the spatial distribution of emission-line ratios, and hence excitation conditions, within star-forming galaxies using integral-field spectroscopy. In the local Universe, the largest samples are those compiled by the Sydney-Australian-Astronomical-Observatory Multi-object Integral-Field Spectrograph (SAMI; Croom et al. 2012) and Mapping Nearby Galaxies at Apache point observatory (MaNGA; Bundy et al. 2015) surveys. Overall, the data support an 'inside-out' galaxy formation scenario whereby the central regions of star-forming galaxies have already processed most of their fuel supply, may be dominated by different ionisation sources, have older stellar populations and higher metallicities (e.g. Belfiore et al., 2015, 2016). These properties are also correlated with stellar mass and environment, in that metal abundance and age gradients appear to be more pronounced in higher-mass systems (e.g. Belfiore et al., 2017) and higher metallicities and older stellar populations are preferentially found in high-density environments (Zheng et al. 2017; although the *gradients* do not appear to correlate with environment). The MaNGA data in particular highlight that classifications[1] inferred from integrated spectra may be misleading due to the variety of apparent physical conditions within individual galaxies (Belfiore et al., 2015, 2016). Generally though, in systems dominated by H II

[1]classifications refer to the source of ionising radiation, for example the hot, young stars which characterise H II regions, or the much harder spectra emitted by AGN

region-like ionisation conditions, the abundance gradients traced by both:

$$\mathrm{R23} = \frac{([\mathrm{O\,II}]\lambda\lambda 3727, 3729 + [\mathrm{O\,III}]\lambda\lambda 4960, 5007)}{\mathrm{H}\beta} \tag{5.1}$$

$$\mathrm{O3N2} = \frac{[\mathrm{O\,III}]\lambda 5007/\mathrm{H}\beta}{[\mathrm{N\,II}]\lambda 6583/\mathrm{H}\alpha} \tag{5.2}$$

are flat or weakly negative and ionisation parameter gradients traced by:

$$\mathrm{O32} = \frac{[\mathrm{O\,III}]\lambda\lambda 4960, 5007}{[\mathrm{O\,II}]\lambda\lambda 3727, 3729} \tag{5.3}$$

are flat beyond the very central regions (Belfiore et al., 2016) (i.e. beyond 0.5 half-light radii, $\mathrm{R}_{1/2}$).

To understand how the physical conditions of the ISM evolve with time, similar spatially-resolved studies are needed at high redshift. Large samples of distant star-forming galaxies observed with integral-field spectroscopy at $z \sim 1$ and $z \sim 2$ have been accumulated using KMOS during the KMOS Redshift One Spectroscopic Survey (KROSS) and the KMOS^{3D} survey, although in both cases targetting only the Hα and [N II]$\lambda\lambda$6583 emission lines. This wavelength coverage is insufficient to reliably measure abundance, since the [N II]$\lambda\lambda$6583/Hα (N2) ratio is sensitive to a combination of metallicity, ionisation parameter, electron density, hardness of radiation field, shock and AGN contribution, saturation at high metallicity and variation in N/O. To break the degeneracies it is necessary to observe additional line ratios. However, Wuyts et al. (2016a) use the Pettini & Pagel (2004) linear conversion between metallicity and N2 to demonstrate that, for the vast majority of the KMOS^{3D} sample, the apparent abundance gradients are flat. This is in contrast to the theoretical prediction for an inside-out formation scenario, in which the gradients should become increasingly negative with increasing lookback time (e.g. Gibson et al., 2013). Strong feedback from AGN and supernovae is required to redistribute material across the galaxy disk, leading to flat

abundance gradients. At $z \sim 3.5$ positive abundance gradients have been observed in star-forming galaxies from the AMAZE sample (e.g. Cresci et al., 2010; Troncoso et al., 2014; Stott et al., 2014), which is interpreted as pristine inflowing gas which reaches and dilutes the galaxy central regions.

Small samples of gravitationally lensed galaxies have been observed with integral-field spectroscopy at much higher spatial resolution than can be achieved otherwise (e.g. Yuan et al., 2011; Jones et al., 2013; Leethochawalit et al., 2016). These observations show a wide range of positive, negative and flat abundance gradients at particular redshift slices and so do not support the notion of a single, common enrichment history. Adaptive optics assisted observations with SINFONI Genzel et al. (2011) reveal giant, clumpy star-forming regions embedded within galaxy disks (i.e. the morphologies are neither smooth nor symmetric), which complicates the measurement and interpretation of excitation and abundance gradients.

With these considerations in mind, the KMOS LEnsed galaxies Velocity and Emission line Review (KLEVER) survey is an ESO large programme designed to observe a sample of ~ 100 lensed and ~ 100 unlensed galaxies with wavelength coverage spanning the $YJ-K$-bands in integral-field spectroscopy. The primary science goals of this project are as follows:

- By carrying out a systematic comparison of the lensed and unlensed samples, assess the impact of angular resolution and sensitivity on our ability to discern abundance gradients
- Explore the abundance and excitation gradients in a large sample of galaxies using the full suite of rest-optical strong emission lines (with dust-extinction corrections informed using spatially-resolved Balmer decrements)
- Examine correlations between the galaxy kinematic and chemical properties on spatially-resolved scales

- Explore the possible evolution of the relationship between O/H and N/O using the measured abundance ratios

- Examine the feasibility of applying locally-calibrated abundance indicators on spatially-resolved scales at high redshift

- Determine the physical origins of the offsets of the high-redshift star-forming galaxy locus in emission line diagnostic diagrams

The survey makes use of existing *K*-band observations from the KMOS^{3D} survey, supplementing this with new *YJ* and *H*-band data with $\sim$ 5 hours integration time per-band per-pointing. In this chapter, the preliminary analysis of the first 5 unlensed pointings from the KLEVER survey, spanning the COSMOS and GOODS-S fields, will be described. We have observed 80 star-forming galaxies from the KMOS^{3D} survey at $z \sim 2.3$ in the mass range $9.5 < \log(M_\star/M_\odot) < 11.0$ (see Tables 5.1 - 5.3), detecting emission other than Hα in 54 galaxies and defining a high signal-to-noise sample of 33 galaxies. This work focusses on the sample refinement, emission line flux measurement and the exploration of emission-line ratio gradients from this sample. The chapter is organised as follows. In § 5.2 we present the survey description, sample selection, observations and data reduction. In § 5.3 we present the integrated emission-line flux measurements and contextualise the sample using complimentary $z \sim 2.3$ integrated measurements in common emission-line diagnostic diagrams. In § 5.4 we explore the spatially-resolved emission-line ratios within individual galaxies and search for abundance gradients and excitation condition gradients. We discuss these results in § 5.6 and conclude in § 5.7.

5.2 Survey description, sample selection and observations

5.2.1 The KLEVER survey description and sample selection

As described in the previous section, the key aim of the KLEVER survey is to ensure coverage of a wide-wavelength range, thus encompassing an almost-complete set of rest-optical emission lines. This requires observations in the *YJ*, *H* and *K*-bands of both lensed and unlensed galaxies. Collecting these observations for a large sample of galaxies with sufficient depth to allow for spatially-resolved measurements of the weaker emission lines is very expensive in terms of exposure times, even when making use of the multiplexing capabilities of KMOS. This chapter is focussed exclusively on the unlensed sample; details of the lensed observations will be described in Curti et al. *in prep.*

To reduce the total exposure time required for the unlensed project, we selected archival $z \sim 2.3$ targets from the KMOS^{3D} programme, which were originally selected as bright star-forming galaxies at the appropriate spectroscopic or photometric redshift from the 3D-HST Treasury Survey (details are provided in Wisnioski et al. 2015). These observations cover the Hα and [N II]$\lambda\lambda$6583 emission lines in the *K*-band with a minimum of 8 hours on-source exposure time. We carried out a full re-reduction of this dataset (see § 5.2.2) which allowed us to use the strength of the emission features in the *K*-band to aid the KLEVER sample selection. This ensured a high success rate in the detection of the strong emission lines in the other bands. Where possible (as constrained by our ability to allocate targets within the KMOS field of view), we chose targets with a KMOS^{3D} Hα detection, and use the KARMA observation preparation software (Wegner & Muschielok, 2008) to distribute these across the 7 KMOS pointings, 4 of which are to be described in the following subsection (see table 5.1). The median redshift of the targets is $z = 2.2$ and 90 per cent of these span

the range $4.8 \times 10^{-17} - 3.2 \times 10^{-16}$erg s^{-1} in observed H$\alpha$ flux, with median value of 8.6×10^{-17}erg s^{-1}. At the median target redshift this corresponds to the Hα luminosity log(L$_{\rm H\alpha}$) = 42.6 erg s^{-1}, which is ~ 0.5L$^{\star}_{\rm H\alpha}$ at $z = 2.2$ (Sobral et al., 2013a).

5.2.2 KMOS observations and data reduction

The KLEVER observing strategy follows the same structure as the KDS observations described in Chapter 3 § 3.2.2. We supplemented the KMOS^{3D} *K*-band observations with 7 new *YJ* and *H*-band pointings, 4 of which are complete at the time of writing and we concentrate solely on these in all further discussion. The observations were carried out during ESO observing periods P97-P100 (Programme IDs: 197.A-0717(A,B,C,D)). 4 of the pointings are in GOODS-S and 1 is in the COSMOS field, ensuring excellent ancillary photometric coverage from *HST* as part of the CANDELS project (Grogin et al., 2011). Table 5.1 lists the pointing names, positions, exposures times and average PSFs in both the *YJ* and *H*-bands. In each pointing we allocate 3 KMOS IFUs to control stars in order to monitor both the evolution of the seeing conditions and the shift of the telescope away from the prescribed dither pattern. We adopted the object-sky-object (OSO) nod-to-sky observation pattern, with 300s exposures and alternating 0.2″/0.1″ dither pattern for increased spatial sampling around each of the target galaxies. As well as the $z \sim 2.2$ sample, we also targetted some lower redshift galaxies at $z \sim 1.5$ to supplement the lensed observations at this redshift. The final $z \sim 2.2$ sample thus comprises 63 targetted galaxies, which are refined into 'detected', 'low-S/N' and 'high-S/N' subsamples in § 5.3.

The data reduction is carried out in exactly the same way as described in § 3.2.2, with the important addition of the Zurich Atmosphere Purge (ZAP) principal component analysis sky subtraction described in § 2.2.1. To briefly summarise, we apply the EsoRex recipes to identify bad detector pixels, flatfield, wavelength and flux calibrate (using standard star observations concurrent with the observations), illumination correct, subtract the sky with skytweak (Davies, 2007) and reconstruct the datacubes for each 300s exposure

Table 5.1: The names of the KLEVER pointings referred to throughout this chapter, as well as the pointing positions, exposure times and the full width at half maximum of the two-dimensional gaussian fit to the stacked control stars are listed in the following table.

Pointing[a]	**RA**[deg]	**DEC**[deg]	**Int.**$_{YJ}$[s]	**Int.**$_{H}$[s]	**PSF**$_{YJ}$ [″][b]	**PSF**$_{H}$ [″]
GOODS-S-P1 (GP1)	53.148446	−-27.741697	14100	14400	0.42	0.71
GOODS-S-P2 (GP2)	53.098608	−27.733363	16200	20400	0.50	0.55
GOODS-S-P3 (GP3)	53.146586	−27.728630	9000	7800	0.52	0.58
COSMOS-P1 (COS1)	150.117617	−2.239861	17700	19200	0.64	0.57

[a] Name in brackets links to Table 5.2.
[b] The PSF in each case is taken as the average of the FWHM across the 3 stacked control stars observed as part of the pointing.

in each band. The additional custom processing steps, including bad pixel map growth and readout channel bias correction, are also carried out in this pipeline. At this stage we perform additional sky subtraction using ZAP, which utilises singular value decomposition in discrete spectral regions to identify prominent skytweak residuals across the spaxels in each datacube. The residual spectrum reconstructed from this procedure is then scaled and subtracted from each spaxel in turn. As mentioned above, we also carried out a full reduction of the archival KMOS^{3D} data to ensure that the final, stacked datacubes had been processed in each band following the same procedures. We do not apply the additional ZAP sky subtraction to the *K*-band cubes as the skytweak routine performs very well alone.

Following the additional sky-subtraction step, we stack the individual exposures together using the positions of the control stars to calculate the shifts which must be applied in each case. The end product is a calibrated and stacked datacube for every targetted galaxy across the 3 wavebands. Table 5.2 lists details for each targetted galaxy in the full $z \sim 2.2$ sample, including exposure times across each band, the pointing to which the galaxy belongs and detection information for each of the strongest lines. The 'YES' or 'NO' values beneath the emission lines correspond to whether an integrated detection has been made with a signal-to-noise greater than 2σ for the [O II], Hβ and [N II] lines and greater than 3σ for [O III] and Hα.

Table 5.2: The detection information for the full sample of galaxies observed across the 4 pointings detailed in Table 5.1. Each of the strong emission lines used throughout this survey across the $YJ-K$-bands are classified as 'YES' detected and 'NO' undetected. We stress that the K-band measurements come from a re-reduction of the KMOS^{3D} data and are not part of the KLEVER survey.

Galaxy	**Pointing**[a]	**RA [deg]**	**DEC [deg]**	z	*YJ*-band		*H*-band				*K*-band		
					Int.[s]	**[O II]$\lambda\lambda$3727,3729**	**Int.[s]**	**Hβ**	**[O III]λ5007**	**PSF$_K$**[b] [$''$]	**Int.[s]**	**Hα**	**[N II]λ6583**
COS4_10565	COS1	150.09424	2.28727	-	17700	NO	19200	NO	NO	0.52	33900	NO	NO
COS4_10347	COS1	150.08344	2.28578	2.0641	17700	YES	19200	YES	YES	0.46	30600	YES	YES
COS4_08775	COS1	150.06895	2.26927	2.1634	17700	YES	19200	YES	YES	0.50	41100	YES	NO
COS4_09044	COS1	150.14877	2.27205	2.1996	17700	YES	19200	NO	YES	0.50	41100	YES	NO
COS4_06963	COS1	150.07658	2.24968	2.3033	17700	NO	19200	NO	NO	0.50	41100	NO	NO
COS4_06820	COS1	150.10298	2.24842	-	17700	NO	19200	NO	NO	0.52	33900	NO	NO
COS4_06750	COS1	150.16302	2.24748	2.1273	17700	YES	19200	YES	YES	0.50	41100	YES	YES
COS4_06079	COS1	150.10947	2.24007	2.4392	17700	NO	19200	NO	NO	0.52	33900	YES	NO
COS4_05540	COS1	150.12886	2.23491	-	17700	NO	19200	NO	NO	0.50	41100	NO	NO
COS4_05415	COS1	150.07344	2.23332	2.3053	17700	NO	19200	NO	NO	0.52	33900	YES	NO
COS4_05094	COS1	150.14037	2.23018	2.1721	17700	YES	19200	NO	YES	0.50	41100	YES	NO
COS4_05152	COS1	150.15750	2.23015	-	17700	NO	19200	NO	NO	0.52	33900	NO	NO
COS4_04717	COS1	150.10498	2.22624	2.4404	17700	NO	19200	NO	NO	0.50	41100	YES	NO
COS4_04519	COS1	150.11934	2.22416	2.2298	17700	YES	19200	YES	YES	0.50	41100	YES	YES
COS4_04453	COS1	150.12706	2.22325	2.4383	17700	YES	19200	NO	NO	0.50	41100	YES	YES
COS4_03324	COS1	150.14840	2.21313	2.3073	17700	YES	19200	YES	YES	0.52	33900	YES	YES
v4_COS4_03206	COS1	150.13270	2.21186	2.1050	17700	NO	19200	NO	NO	0.50	41100	YES	YES
COS4_03179	COS1	150.16808	2.21130	2.1709	17700	YES	19200	YES	YES	0.52	33900	YES	NO
COS4_02887	COS1	150.09695	2.20917	-	17700	NO	19200	NO	NO	0.52	33900	NO	NO
COS4_01966	COS1	150.12587	2.19932	2.3053	17700	YES	19200	NO	YES	0.52	33900	YES	NO
GS4_46072	GS1	53.13895	-27.69512	-	14100	NO	14400	NO	NO	0.55	23400	NO	NO
GS4_42363	GS1	53.11840	-27.71290	2.1420	14100	YES	14400	YES	YES	0.44	36600	YES	YES
GS4_40795	GS1	53.18575	-27.72017	-	14100	NO	14400	NO	NO	0.55	23400	NO	NO

Table 5.2: **Continued.**

Galaxy	Pointing[a]	RA [deg]	DEC [deg]	z	*YJ*-band		*H*-band				*K*-band		
					Int.[s]	[O II]$\lambda\lambda$3727,3729	Int.[s]	Hβ	[O III]λ5007	PSF$_K$	Int.[s]	Hα	[N II]λ6583
GS3_26790	GS1	53.17451	-27.72536	2.2283	14100	YES	14400	YES	YES	0.50	29100	YES	YES
GS4_38046	GS1	53.17444	-27.73330	-	14100	NO	14400	NO	NO	0.55	23400	NO	NO
GS3_25445	GS1	53.18284	-27.73491	2.4328	14100	NO	14400	NO	NO	0.50	29100	YES	YES
GS3_24273	GS1	53.19953	-27.74258	2.1873	14100	NO	14400	NO	NO	0.50	29100	YES	NO
GS3_23570	GS1	53.16835	-27.74848	2.2288	14100	NO	14400	NO	NO	0.44	36600	YES	YES
GS4_29773_1	GS1	53.12112	-27.77505	2.2252	14100	YES	14400	YES	YES	0.55	23400	YES	NO
GS4_28844	GS1	53.14614	-27.77987	-	14100	NO	14400	NO	NO	0.55	23400	NO	NO
GS3_28464	GS1,2	53.10081	-27.71599	2.3022	30300	YES	30800	YES	YES	†0.48	80100	YES	YES
GS4_31452	GS1,2	53.13078	-27.76786	-	30300	NO	30800	NO	NO	0.55	23400	NO	NO
GS3_18419	GS1,2	53.11877	-27.78279	2.3093	30300	NO	30800	NO	YES	‡0.47	65700	YES	YES
GS3_17650	GS1,2	53.10660	-27.78730	-	30300	NO	30800	NO	NO	0.58	25800	NO	NO
GS4_40218	GS1,2,3	53.16195	-27.72266	2.4522	39300	YES	38600	YES	YES	0.55	23400	YES	YES
GS3_26192	GS1,3	53.18180	-27.72992	2.3189	23100	YES	22200	NO	YES	0.50	29100	YES	YES
GS4_38116	GS1,3	53.17131	-27.73295	2.1983	23100	YES	22200	YES	YES	0.55	23400	YES	YES
GS4_37124	GS1,3	53.19294	-27.73833	2.4338	23100	NO	22200	NO	YES	0.44	36600	YES	YES
GS4_34568	GS1,3	53.12654	-27.75035	2.5729	23100	YES	22200	YES	YES	0.44	36600	YES	NO
GS4_29606	GS1,3	53.16059	-27.77612	2.5439	23100	YES	22200	YES	YES	0.55	23400	YES	NO
GS3_31118	GS2	53.13757	-27.70010	2.4534	16200	YES	20400	YES	YES	⊕0.50	89100	YES	YES
GS3_28991	GS2	53.05094	-27.71379	2.4428	16200	YES	20400	NO	YES	0.51	26700	YES	NO
GS3_28004	GS2	53.04083	-27.71906	2.3043	16200	YES	20400	YES	YES	0.51	26700	YES	YES
GS3_28008	GS2	53.10701	-27.71823	2.3022	16200	YES	20400	YES	YES	†0.48	80100	YES	YES
GS3_26017	GS2	53.07811	-27.73111	2.4175	16200	NO	20400	NO	YES	0.51	26700	YES	NO
GS3_25595	GS2	53.05197	-27.73412	2.2015	16200	NO	20400	NO	NO	0.51	26700	YES	NO

Table 5.2: **Continued.**

Galaxy	Pointing[a]	RA [deg]	DEC [deg]	z	*YJ*-band		*H*-band				*K*-band		
					Int.[s]	[O II]$\lambda\lambda$3727,3729	Int.[s]	Hβ	[O III]λ5007	PSF$_K$	Int.[s]	Hα	[N II]λ6583
GS3_25028	GS2	53.04254	-27.73794	2.3074	16200	YES	20400	NO	YES	0.51	26700	YES	NO
GS3_22738	GS2	53.06550	-27.75433	-	16200	NO	20400	NO	NO	0.51	26700	NO	NO
GS3_20271	GS2	53.04845	-27.77007	-	16200	NO	20400	NO	NO	0.51	26700	NO	NO
GS3_17716	GS2	53.07210	-27.78575	2.0376	16200	NO	20400	NO	NO	0.51	26700	YES	NO
GS4_46432	GS2,3	53.11245	-27.69263	2.4366	25200	YES	28200	YES	YES	0.55	23400	YES	NO
GS3_28692	GS2,3	53.09768	-27.71525	2.1420	25200	YES	28200	YES	YES	†0.48	80100	YES	YES
GS3_24364	GS2,3	53.15892	-27.74268	2.3303	25200	YES	28200	YES	YES	0.50	29100	YES	YES
GS3_19791	GS2,3	53.13108	-27.77311	2.2254	25200	YES	28200	YES	YES	†0.48	80100	YES	YES
GS4_44133	GS3	53.11041	-27.70371	2.1415	9000	YES	7800	YES	YES	0.55	23400	YES	YES
GS4_46938	GS3	53.13456	-27.69066	2.3336	9000	YES	7800	YES	YES	0.55	23400	YES	YES
GS4_42089	GS3	53.10373	-27.71409	2.2584	9000	NO	7800	NO	NO	0.55	23400	YES	NO
GS4_42235	GS3	53.13485	-27.71333	2.4333	9000	YES	7800	YES	YES	0.44	36600	YES	NO
GS4_42930	GS3	53.16419	-27.70987	2.4523	9000	YES	7800	YES	YES	0.44	36600	YES	NO
GS4_43631	GS3	53.15371	-27.70715	2.1420	9000	YES	7800	YES	YES	0.44	36600	YES	YES
GS3_22466	GS3	53.12133	-27.75588	2.2360	9000	YES	7800	NO	NO	0.50	29100	YES	NO
GS4_30443	GS3	53.15446	-27.77143	2.2278	9000	YES	7800	YES	YES	0.55	23400	YES	NO
GS4_29868	GS3	53.12114	-27.77458	2.2259	9000	YES	7800	YES	YES	0.44	36600	YES	YES

[a] Some galaxies have been observed across multiple KLEVER pointings to fill the KMOS arms or to increase the signal-to-noise. These are highlighted in the 'pointing' column by including each individual pointing name

[b] Some galaxies in KMOS^{3D} were observed in multiple pointings. These are indicated with the following symbols: † corresponds to GP1,GP2 & GP5, ‡ corresponds to GP1 & GP5, ⊕ corresponds to GP1,GP5 & GP6. The KLEVER pointing column designation does not apply to the *K*-band objects from KMOS^{3D}, which follow a separate pointing structure.

5.2.3 Datacube alignment

As a consequence of the observations in the various bands being carried out at different times, the object positions within the datacubes and the datacube sizes vary across the *YJ*, *H* and *K*-bands. For ease of subsequent analysis, we shape the datacubes in the three bands corresponding to a single object so that they have common x and y spatial dimensions and shift the central object locations so that they coincide with the central spatial pixels. This is done by fitting a two-dimensional gaussian to the median-stacked stellar continuum image in each band to recover the continuum centre, recording the difference between this and the central pixel coordinates and using the `kmos_shift` EsoRex recipe to shift the object by the computed difference. The advantage of doing this is to align the physical location of the galaxy across the three bands, which allows for direct comparisons of the emission line strengths across the spaxels. This assumes that the continuum peak in the *YJ* through *K*-bands corresponds to the same physical location in the galaxy. This step has only been applied to the high-S/N galaxies (see § 5.3.3), for which the continuum peak in each case and in each band was unambiguously located.

5.2.4 Stellar masses and SFRs

For the galaxies in the GOODS-S field, we use the stellar masses and star-formation rates from the catalogues reported in Santini et al. (2015), which detail median values from a range of different softwares and input parameters. Specifically, we use the median stellar mass value of the methods which include nebular emission (M_ned_med) as detailed in table 1 of Santini et al. (2015). For the COSMOS galaxies, we use the stellar mass and star-formation rate catalogue described in Laigle et al. (2016). These are computed using the `LePhare` software following the method described in Ilbert et al. (2015); synthetic spectra are generated using the Bruzual & Charlot (2003) synthesis models with a Chabrier (2003) IMF using a combination of exponentially declining and delayed SFHs. Emission lines are added and the models are computed at both solar and half-solar metallicity with both the Calzetti et al. (2000) and Arnouts et al. (2013)

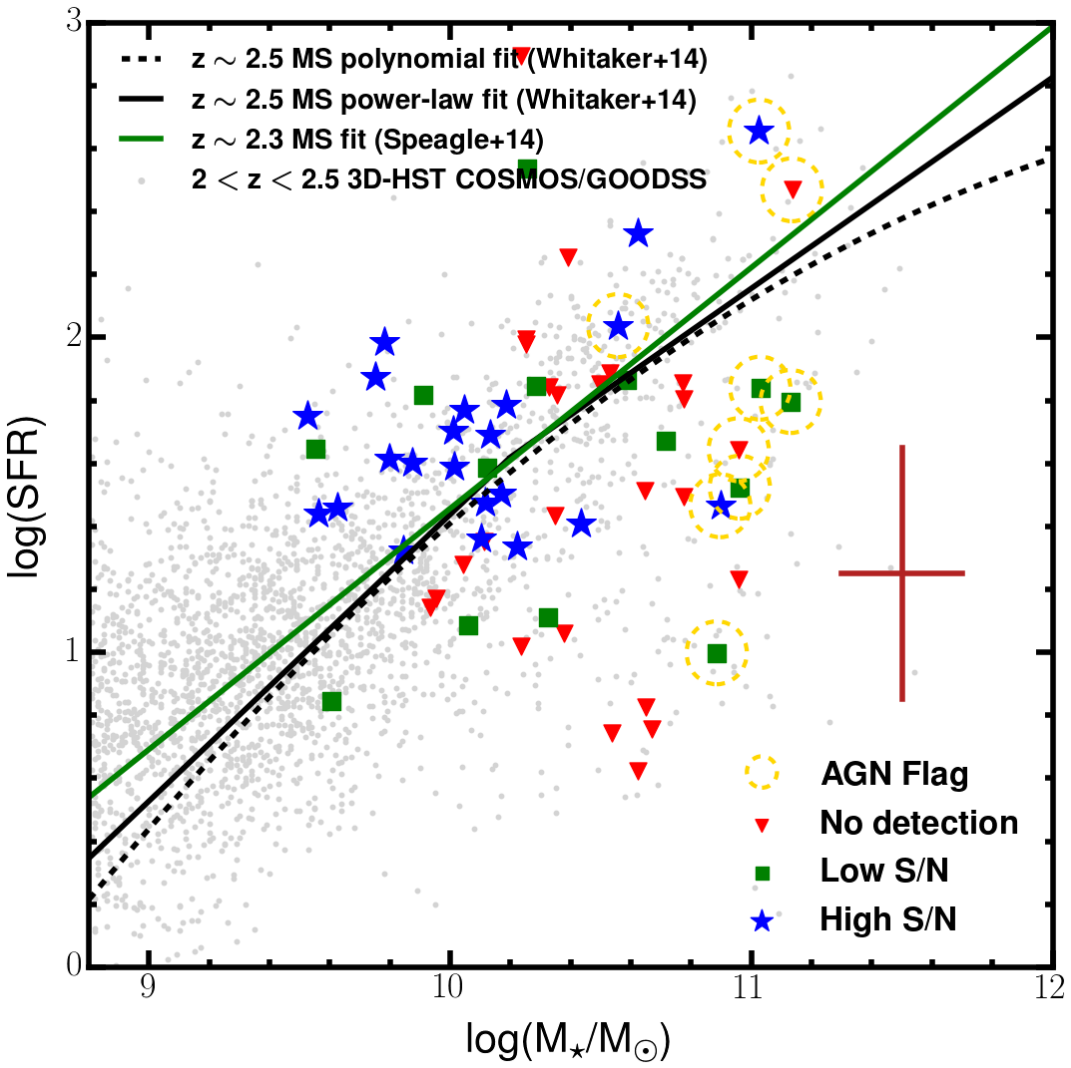

Figure 5.1: Galaxies from the first 4 KLEVER pointings are plotted in the star-formation rate versus stellar-mass plane. Different subsamples are defined in the text and the symbols used for these in the plot are indicated in the lower-right legend. In particular, galaxies classified as AGN on the basis of their emission line properties are highlighted with the dashed-orange circles. The typical errors on the SED fitting-derived properties are indicated with the red cross on the right of the plot. Broadly, the KLEVER galaxies scatter around the $z \sim 2.3$ main sequence defined in previous studies as indicated by the overplotted fits from Whitaker et al. (2014); Speagle et al. (2014). The light-grey points in the background are $2.0 < z < 2.5$ 3D-HST galaxies from the COSMOS and GOODS-S fields, which also fall in roughly the same location in the diagram as the KLEVER galaxies.

Appendix A attenuation curves.

There does not appear to be any systematic difference between the stellar masses and star-formation rates for the GOODS-S and COSMOS galaxies and the median values

across the 63 targetted $z \sim 2.2$ galaxies are $\log(M_\star/M_\odot) = 10.3$ and SFR = $43 M_\odot yr^{-1}$. In Fig. 5.1 we plot the galaxy locations in the star-formation rate versus stellar-mass diagram, along with the main-sequence relations from Whitaker et al. (2014) at $z \sim 2.5$ and Speagle et al. (2014) at $z \sim 2.3$. The small, light-grey points on this plot are galaxies from the 3D-*HST* survey with photometric redshifts in the range $2 < z < 2.5$. Overall there is good agreement between the galaxies from the KLEVER survey, which have been subdivided into different classifications as described in the following section, and both the 3D-*HST* galaxies and main-sequence relations.

5.3 Galaxy integrated emission line diagnostics

5.3.1 Defining apertures using `DS9` regions

To extract integrated spectra from the spatially-aligned datacubes, we made use of the 'regions' feature within `DS9`. The *HST WFC3 F160W* band imaging[2] was used to view the stellar emission from each galaxy. We first convolved the *HST* images using gaussian filters with the FWHM determined by the median seeing of the KMOS observations. For each galaxy, an elliptical aperture which encloses the convolved stellar emission was defined and saved as a 'regions' file. The `pyregions` package interfaces with the `DS9` region files, allowing for datacube masks to be constructed which define the spaxels from which integrated spectra are to be extracted.

Fig. 5.2 shows an example of this process, with the right image showing the elliptical aperture defined against the convolved, 3-band stellar continuum emission and the left panel showing the mapping of this region back onto the KMOS datacubes with `pyregions`, ensuring that the same physical size is enclosed in both cases. The `spectral-cube` package then deciphers which spaxels are enclosed by the elliptical region and uses these to build the integrated spectra for each galaxy. We combined these spaxels using a sum over all individual values, giving us a one-dimensional spectrum

[2]This is longest wavelength imaging band available from *HST*, into which the light emitted from older stellar populations is redshifted.

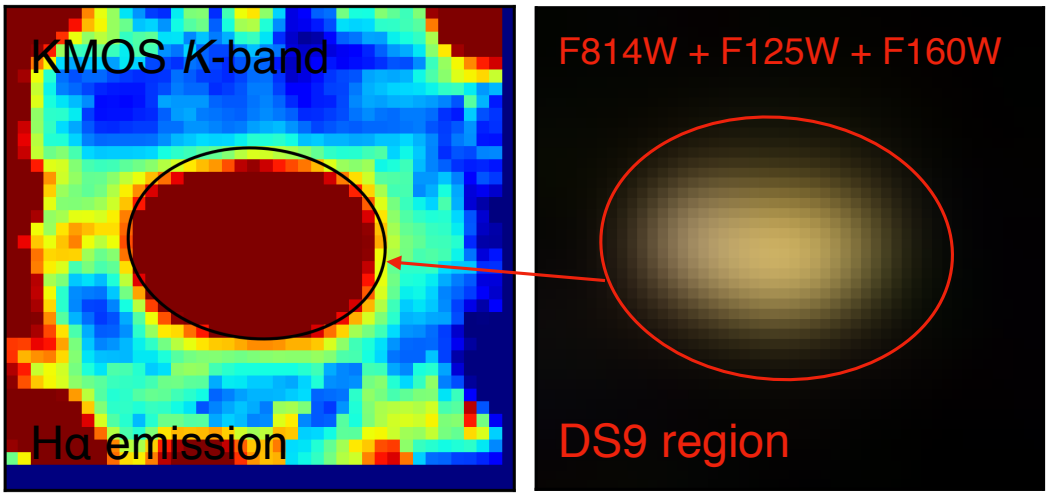

Figure 5.2: We utilise the regions feature within DS9 to draw regions which encapsulate the *WFC3 F160W* band stellar emission for each galaxy. The right panel shows the seeing-convolved *HST* 3-colour image constructed from the *F814W, F125W* and *F160W* bands. The `pyregions` package is then used to read the created regions files and create masks for the astrometrically matched KMOS cubes. This ensures that the regions extracted from the datacube are the same physical size as those defined on the *F160W* band imaging. The left panel shows the Hα narrowband image from the KMOS *K*-band datacube. The spectra are extracted from the KMOS cubes using the `astropy spectral-cube` package.

for each galaxy in each waveband. These are used in the following section to determine the integrated emission-line fluxes and to refine the KLEVER sample into different signal-to-noise classes.

5.3.2 Measuring the integrated line fluxes

The integrated spectra extracted from the DS9 regions are fitted separately in each band. We first constructed an empirical noise spectrum to be used in combination with each summed, integrated spectrum using the following procedure. A one-dimensional weights spectrum, W_i, was produced for each galaxy in each band by masking the pixels containing the object and taking the median absolute deviation of the unmasked spectra at each wavelength pixel. This serves as the basic noise spectrum, but must be scaled to

be used with the integrated spectrum. To find the scaling factor, ξ, we used the spectra from the individual spaxels of the DS9 masks, masked the emission and OH lines, and took the median of the median absolute deviations from each of these spectra to find $\epsilon_{\rm single}$. The same masking was applied and the median absolute deviation found for the summed spectra to give $\epsilon_{\rm summed}$. The scaling factor is then $\xi = \epsilon_{\rm single}/\epsilon_{\rm summed}$. The final weights spectrum for each integrated fit is given by $\Delta_i = \xi \times \mathrm{W}_i$, with these used as the individual errors when computing the best fit model spectra. This method has the advantage of empirically assigning large errors to regions of the spectra dominated by large OH line residuals.

This analysis is concerned with the [O II]$\lambda\lambda$3727,3729 doublet in the *YJ*-band, the Hβ and [O III]$\lambda\lambda$4960,5007 lines in the *H*-band and the Hα and [N II]λ6583 lines in the *K*-band, which we restricted ourselves to during the fitting process. This is due to the very low signal-to-noise of other emission lines falling within the KMOS bands in the vast majority of galaxies (e.g. He Iλ3889, [N II]$\lambda\lambda$6549 and [S II]$\lambda\lambda$6717,6731), which consequently are not useful for galaxy classification. In the *YJ*-band we use the python package LMFIT (Newville et al., 2014) to build a model [O II]$\lambda\lambda$3727,3729 doublet, which is comprised of two blended gaussians with central wavelengths constrained to be separated by the redshifted difference between the doublet vacuum wavelengths, the fluxes of each line left free to vary and the linewidth free to vary but fixed to take the same value for each line. LMFIT makes use of the Levenberg-Marquardt algorithm for figure-of-merit minimisation, the figure of merit being the error weighted (using Δ_i) difference between the summed spectrum and the model. To determine the model parameter values we perform a Monte Carlo process and repeat the fit 500 times, varying the summed-spectra values by a random number drawn from a gaussian of width equal to the corresponding Δ_i. The final parameter values are taken as the median of the resultant distributions and the lower and upper errors as the 16th and 84th percentiles of the distributions respectively.

In the *H*-band, the model spectrum is comprised of three gaussians for respectively

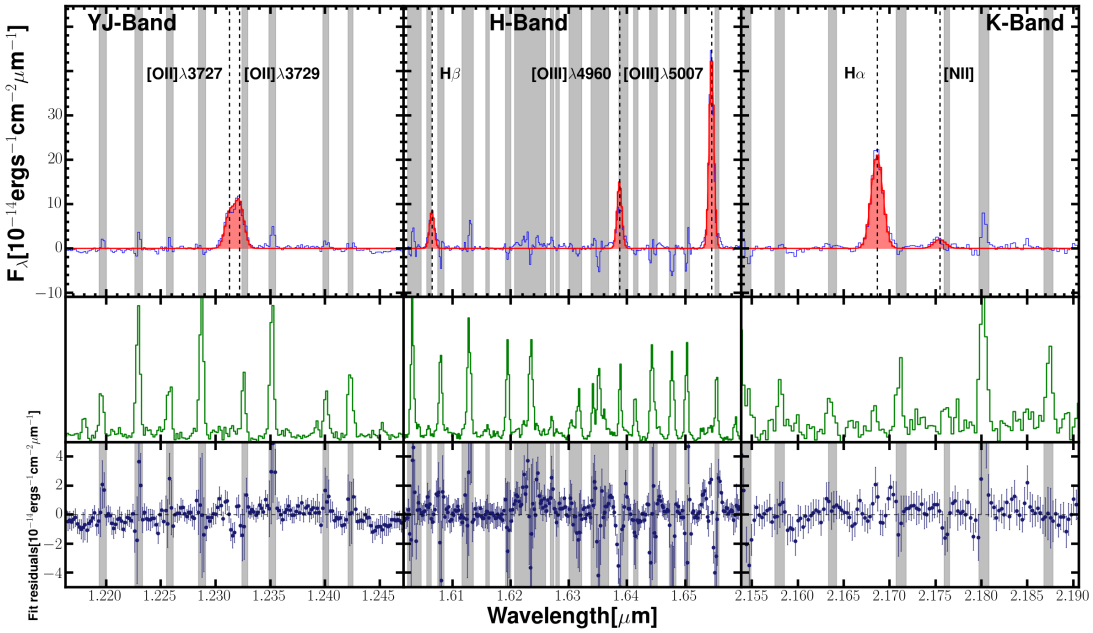

Figure 5.3: The measured and model flux densities, fit following the procedure described in the text, for the high signal-to-noise galaxy GS3_28004 across the three wavebands is shown in the top panels. The middle panels show the sky spectra in arbitrary units and the bottom panels show the fit residuals, with error bars equal to the error spectrum values, Δ_i, also described in the text.

the Hβ, and both the [O III]$\lambda\lambda$4960,5007 lines, with central wavelengths determined by their redshifted vacuum values[3], linewidths free to vary (the two oxygen lines are constrained to have the same width) and fluxes free to vary, except the [O III]$\lambda\lambda$4960 line which is set to the theoretical value of $0.33\times f_{5007}$ (Osterbrock, 1989). In the *K*-band, the model spectrum is built in the same way for the Hα and [N II]λ6583 lines, with linewidths and the fluxes both free to vary. For both these bands, the fitting is carried out in the same way as described above for the *YJ*-band. Fig. 5.3 provides an example of measured and fitted model spectra across the three wavebands for one of the high signal-to-noise galaxies described in § 5.3.3.

We also correct each of the emission lines for dust extinction within the galaxy using the following procedure. We adopt the Calzetti et al. (2000) extinction curve, k_λ, and use the observed Balmer decrement, $(\mathrm{H}\alpha/\mathrm{H}\beta)_{\mathrm{obs}}$, in order to find the value of a_λ at the

[3]A central wavelength tolerance of 2 times the wavelength resolution is used in the fitting process

wavelength of the emission line

$$a_\lambda = 1.97 \times k_\lambda \times \log\left(\frac{[\mathrm{H}\alpha/H\beta]_{\mathrm{obs}}}{2.86}\right) \tag{5.4}$$

where the value 2.86 is the theoretical expectation for the unreddened ratio Hα/Hβ undergoing Case B recombination with $\mathrm{T}_e = 10^4\mathrm{K}$ and $\mathrm{n}_e = 100\mathrm{cm}^{-3}$ (Osterbrock, 1989). This value is then used in the computation

$$f_{\lambda,\mathrm{corr}} = 10^{0.4\times a_\lambda} \times f_\lambda \tag{5.5}$$

where $f_{\lambda,\mathrm{corr}}$ and f_λ are the dust-corrected and observed fluxes of the emission line respectively (see section 3 of Domínguez et al. 2013 for a more thorough derivation of these formulae). We follow Zahid et al. (2014) (and see also Kashino et al. 2016) and correct for the impact of stellar absorption at the wavelength of Hβ using the stellar-mass dependent formula

$$\mathrm{H}\beta_{\mathrm{corr}} = \max\{1, 1.09 + (0.3 \times [\log(\mathrm{M}_\star/\mathrm{M}_\odot) - 10])\} \tag{5.6}$$

and use the absorption corrected, observed Balmer decrement in Equation 5.4.

5.3.3 Sample refinement

In each band, the noise is defined as the width of a gaussian fit to the histogram of individual flux values in the integrated spectra after masking the pixels containing the object's emission lines, as well as the OH sky-lines. This is possible since the stellar continuum for these sources is not detected in the individual spectral pixels. The signal-to-noise of each line is recorded as the ratio of the fitted flux values from the procedure described above to the to the noise in the appropriate waveband. Using this information, we define three subsamples after examining the integrated spectra:

1. **Poor detection** - corresponding either to objects with no significant Hα emission (i.e. $S/N_{H_\alpha} < 3$, also verified by visually inspecting the integrated spectra for the presence of emission lines) or no detected emission from any line other than Hα. From the 63 targetted galaxies detailed in Table 5.2, 13 have no significant Hα emission and 14 are detected in Hα but have no significant detection in any other line.

2. **Low S/N** - either the next strongest line [O III]λ5007 has detected S/N < 3 OR $S/N_{[O\,III]} > 3$, however the combined [O II]λ3727,3729 has S/N < 2. 13/63 galaxies fall into this category.

3. **High-S/N** - objects with at least $S/N_{H_\alpha} > 3$, $S/N_{[O\,III]} > 3$ and $S/N_{[O\,II]} > 2$. 22/63 fall into this category. As can be seen from Table 5.3, the majority of the high-S/N sample greatly exceed the S/N = 3 boundary.

4. **AGN** - The Hα and [N II]λ6583 linewidths are broad towards the galaxy centre, indicating the presence of a broad-line region surrounding a compact nuclear object. 3/22 galaxies in the high-S/N, 4/13 in the low-S/N and 2/27 in the no detection categories are flagged as AGN on the basis of their emission-line properties.

The signal-to-noise values of the [N II]λ6583 and Hβ lines are not used in the classification due to their intrinsic faintness. As mentioned above, Table 5.2 lists the line detections for all objects in the KLEVER $z \sim 2.2$ unlensed sample and the objects are separated into their classifications in Fig. 5.1. In Tables 5.3 we list the integrated-emission-line fluxes and signal-to-noise values and in Table 5.4 we list the morphological[4] and global physical properties for the high-S/N sample.

We also examine the locations of the integrated line ratios from the high-S/N galaxies in both the [N II] BPT diagram (Fig. 5.4) and the O32 versus R23 diagram (Fig. 5.5). The additional requirements for the high-S/N sample that $S/N_{[N\,II]} > 2$ and $S/N_{H_\beta} > 2$ for the [N II] BPT plot leaves 14/22 of the high-S/N galaxies (i.e. the [N II] subsample)

[4]The galaxy morphological properties are taken from the catalogue provided in van der Wel et al. (2012)

Table 5.3: The emission-line fluxes and signal-to-noise values measured from the 3−band KMOS data for the KLEVER high signal-to-noise sample.

Galaxy	$f_{3727}{}^{a,b}$	S/N$_{3727}$	$f_{H\beta}$	S/N$_{H\beta}$	$f_{5007}{}^{c}$	S/N$_{5007}$	$f_{H\alpha}$	S/N$_{H\alpha}$	f_{6583}	S/N$_{6583}$
COS4_03179	$2.45^{+1.39}_{-1.23}$	$2.29^{+0.76}_{-0.69}$	$1.18^{+0.54}_{-0.50}$	$1.58^{+0.76}_{-0.69}$	$6.27^{+0.95}_{-0.93}$	$8.29^{+0.96}_{-0.95}$	$8.08^{+0.48}_{-0.49}$	$9.13^{+0.54}_{-0.54}$	$0.46^{+0.48}_{-0.44}$	$0.51^{+0.52}_{-0.50}$
COS4_04519	$3.23^{+2.11}_{-1.69}$	$3.99^{+1.67}_{-2.83}$	$1.11^{+0.29}_{-0.27}$	$3.86^{+1.3}_{-0.98}$	$3.22^{+0.21}_{-0.23}$	$10.83^{+0.69}_{-0.59}$	$14.01^{+0.39}_{-0.35}$	$24.92^{+0.51}_{-0.56}$	$3.83^{+0.24}_{-0.24}$	$6.77^{+0.43}_{-0.37}$
COS4_06750	$4.99^{+1.52}_{-1.71}$	$8.57^{+1.03}_{-1.4}$	$2.48^{+0.22}_{-0.25}$	$7.72^{+0.74}_{-0.81}$	$6.61^{+0.63}_{-0.59}$	$20.02^{+1.77}_{-1.76}$	$10.65^{+0.55}_{-0.51}$	$21.96^{+0.93}_{-1.12}$	$1.70^{+0.29}_{-0.27}$	$3.49^{+0.62}_{-0.60}$
COS4_09044	$2.07^{+0.48}_{-0.34}$	$4.58^{+0.68}_{-0.67}$	$1.00^{+0.26}_{-0.26}$	$3.64^{+1.03}_{-0.96}$	$2.56^{+0.27}_{-0.25}$	$9.09^{+0.72}_{-0.79}$	$4.97^{+0.25}_{-0.24}$	$13.4^{+0.62}_{-0.60}$	$0.21^{+0.36}_{-0.21}$	$0.58^{+0.97}_{-0.58}$
GS3_19791	$12.67^{+6.83}_{-5.28}$	$4.25^{+2.79}_{-2.58}$	$4.38^{+0.32}_{-0.28}$	$6.01^{+0.45}_{-0.45}$	$37.67^{+0.77}_{-0.77}$	$50.06^{+0.97}_{-0.81}$	$33.64^{+0.83}_{-0.9}$	$19.37^{+0.68}_{-0.63}$	$19.83^{+0.98}_{-0.81}$	$11.50^{+0.53}_{-0.57}$
GS3_24364	$5.26^{+0.72}_{-0.66}$	$4.97^{+0.97}_{-0.97}$	$2.33^{+0.65}_{-0.71}$	$5.66^{+1.6}_{-1.53}$	$4.46^{+0.37}_{-0.4}$	$10.6^{+1.48}_{-1.22}$	$8.28^{+0.89}_{-0.82}$	$12.98^{+1.45}_{-1.2}$	$0.96^{+0.44}_{-0.50}$	$1.50^{+0.69}_{-0.78}$
GS3_25028	$3.69^{+0.68}_{-0.6}$	$5.94^{+1.53}_{-1.45}$	$1.62^{+0.37}_{-0.33}$	$5.10^{+1.3}_{-1.25}$	$3.65^{+0.44}_{-0.4}$	$11.21^{+2.09}_{-1.98}$	$6.25^{+0.96}_{-0.81}$	$7.10^{+0.61}_{-0.62}$	$0.93^{+0.42}_{-0.35}$	$1.06^{+0.52}_{-0.43}$
GS3_26192	$5.07^{+1.48}_{-0.86}$	$5.06^{+1.25}_{-1.34}$	$1.74^{+0.73}_{-0.65}$	$4.50^{+1.64}_{-1.41}$	$4.25^{+0.64}_{-0.77}$	$10.60^{+0.92}_{-0.90}$	$5.97^{+0.52}_{-0.44}$	$10.23^{+0.71}_{-0.76}$	-	-
GS3_26790	$4.21^{+1.43}_{-0.93}$	$7.91^{+1.21}_{-1.15}$	$1.69^{+0.34}_{-0.30}$	$4.78^{+0.91}_{-0.91}$	$3.95^{+0.45}_{-0.43}$	$10.72^{+0.92}_{-0.95}$	$7.27^{+1.35}_{-0.96}$	$11.63^{+1.20}_{-1.09}$	$1.37^{+0.71}_{-0.76}$	$2.06^{+1.24}_{-1.06}$
GS3_28004	$19.01^{+0.82}_{-0.82}$	$22.14^{+1.78}_{-1.46}$	$8.75^{+0.44}_{-0.48}$	$19.04^{+0.93}_{-0.93}$	$46.01^{+1.0}_{-1.0}$	$97.12^{+1.66}_{-1.56}$	$33.78^{+0.88}_{-0.73}$	$26.24^{+0.81}_{-0.79}$	$3.36^{+0.74}_{-0.76}$	$2.62^{+0.57}_{-0.61}$
GS3_28464	$1.58^{+0.78}_{-0.60}$	$3.65^{+1.31}_{-1.18}$	$0.63^{+0.32}_{-0.29}$	$1.81^{+0.68}_{-0.81}$	$1.92^{+0.34}_{-0.36}$	$5.09^{+0.97}_{-0.82}$	$5.56^{+0.49}_{-0.49}$	$6.39^{+0.54}_{-0.59}$	$2.37^{+0.49}_{-0.46}$	$2.72^{+0.55}_{-0.57}$
GS4_30443	$11.74^{+2.15}_{-2.14}$	$7.07^{+1.77}_{-2.10}$	$4.25^{+0.47}_{-0.57}$	$5.03^{+0.50}_{-0.65}$	$19.15^{+0.65}_{-0.66}$	$22.02^{+0.81}_{-0.86}$	$17.71^{+0.85}_{-0.92}$	$20.05^{+0.89}_{-0.82}$	$2.25^{+0.55}_{-0.58}$	$2.57^{+0.64}_{-0.70}$
GS4_34568	$3.84^{+0.62}_{-0.63}$	$2.93^{+0.51}_{-0.61}$	$2.29^{+1.41}_{-0.44}$	$5.19^{+0.87}_{-1.1}$	$1.92^{+0.33}_{-0.34}$	$4.01^{+1.34}_{-1.65}$	$8.98^{+0.97}_{-0.91}$	$20.39^{+3.43}_{-3.24}$	$1.40^{+0.99}_{-0.89}$	$3.22^{+1.91}_{-1.96}$

Table 5.3: **Continued.**

Galaxy	$f_{3727}{}^{a,b}$	S/N$_{3727}$	$f_{H\beta}$	S/N$_{H\beta}$	$f_{5007}{}^{c}$	S/N$_{5007}$	$f_{H\alpha}$	S/N$_{H\alpha}$	f_{6583}	S/N$_{6583}$
GS4_38116	$4.80^{+0.48}_{-0.41}$	$7.13^{+0.91}_{-0.91}$	$2.15^{+0.83}_{-0.71}$	$6.36^{+2.60}_{-2.07}$	$3.56^{+0.32}_{-0.28}$	$10.39^{+0.85}_{-0.87}$	$7.82^{+0.50}_{-0.47}$	$10.83^{+0.63}_{-0.64}$	$2.49^{+0.48}_{-0.51}$	$3.42^{+0.68}_{-0.69}$
GS4_40218	$3.02^{+2.27}_{-2.01}$	$6.83^{+1.99}_{-5.94}$	$1.40^{+0.13}_{-0.15}$	$5.23^{+0.50}_{-0.53}$	$4.18^{+0.34}_{-0.34}$	$15.28^{+1.86}_{-1.80}$	$6.90^{+0.73}_{-0.91}$	$10.47^{+1.3}_{-1.28}$	$0.19^{+0.74}_{-0.19}$	$0.30^{+1.14}_{0.30}$
GS4_42235	$2.53^{+1.00}_{-1.14}$	$2.74^{+1.12}_{-0.72}$	$0.61^{+0.27}_{-0.24}$	$1.80^{+0.86}_{-0.73}$	$4.32^{+0.27}_{-0.24}$	$12.38^{+0.85}_{-0.69}$	$4.54^{+0.78}_{-0.43}$	$23.14^{+1.59}_{-2.20}$	$0.71^{+0.23}_{-0.21}$	$3.54^{+1.04}_{-1.06}$
GS4_42363	$5.15^{+0.90}_{-1.22}$	$7.59^{+3.80}_{-2.23}$	$1.64^{+0.42}_{-0.32}$	$5.86^{+0.99}_{-1.02}$	$3.37^{+0.41}_{-0.37}$	$11.71^{+1.70}_{-1.99}$	$9.16^{+0.50}_{-0.53}$	$19.61^{+1.20}_{-1.21}$	$2.07^{+0.54}_{-0.46}$	$4.43^{+1.13}_{-1.02}$
GS4_42930	$4.61^{+1.04}_{-0.74}$	$3.75^{+1.10}_{-1.17}$	$5.02^{+0.77}_{-0.63}$	$2.15^{+0.22}_{-0.24}$	$8.06^{+0.85}_{-0.86}$	$3.31^{+0.44}_{-0.42}$	$6.91^{+0.84}_{-0.82}$	$11.56^{+1.28}_{-1.08}$	$1.35^{+0.58}_{-0.70}$	$2.27^{+1.03}_{-1.21}$
GS4_43631	$2.23^{+1.08}_{-0.83}$	$4.36^{+1.63}_{-1.64}$	$0.53^{+0.46}_{-0.53}$	$0.92^{+1.32}_{-0.92}$	$1.60^{+2.94}_{-0.60}$	$3.05^{+1.42}_{-1.47}$	$4.96^{+0.25}_{-0.25}$	$11.98^{+0.65}_{-0.53}$	$0.86^{+0.27}_{-0.26}$	$2.08^{+0.67}_{-0.63}$
GS4_44133	$2.24^{+1.17}_{-0.88}$	$3.94^{+3.10}_{-3.14}$	$0.94^{+0.5}_{-0.49}$	$1.31^{+0.81}_{-0.71}$	$3.77^{+0.71}_{-0.65}$	$5.08^{+0.77}_{-0.73}$	$7.70^{+0.38}_{-0.36}$	$9.57^{+0.43}_{-0.43}$	$1.24^{+0.42}_{-0.35}$	$1.52^{+0.51}_{-0.42}$
GS4_46432	$9.29^{+1.69}_{-1.38}$	$12.83^{+1.05}_{-0.93}$	$3.94^{+0.60}_{-0.62}$	$14.34^{+2.24}_{-2.13}$	$17.46^{+0.37}_{-0.36}$	$61.83^{+1.32}_{-1.28}$	$12.35^{+1.02}_{-0.89}$	$19.2^{+1.90}_{-1.63}$	$0.86^{+0.82}_{-0.69}$	$1.37^{+1.21}_{-1.09}$
GS4_46938	$13.04^{+2.21}_{-2.06}$	$12.95^{+3.79}_{-3.34}$	$3.98^{+0.96}_{-0.85}$	$4.32^{+1.09}_{-0.94}$	$14.63^{+1.71}_{-1.59}$	$15.43^{+2.78}_{-2.45}$	$18.24^{+0.75}_{-0.78}$	$21.28^{+0.79}_{-0.73}$	$2.81^{+0.54}_{-0.49}$	$3.30^{+0.60}_{-0.58}$

[a] All fluxes are listed in units of 10^{-17}erg s^{-1}cm^{-2}.

[b] Corresponds to the combined flux of the [O II]$\lambda\lambda$3727,3729 doublet.

[c] Following Osterbrock (1989) the flux of the [O III]λ4960 line is fixed to equal 0.34 times the flux of the [O III]λ5007 line.

Table 5.4: This table lists the physical properties of the high signal-to-noise KLEVER sample measured from ancillary photomerty

Galaxy	$\mathbf{R_e}$ **[kpc]**	**b/a**	n	$\mathbf{PA^{\circ}_{morph}}$	$\log(M_\star/M_\odot)$	**SFR** $[M_\odot yr^{-1}]$
COS4_03179	2.57	0.79	0.57	-18.0	9.84	1.32
COS4_04519	2.56	0.63	1.76	-74.0	10.56	2.04
COS4_06750	3.17	0.51	0.95	46.0	10.01	1.59
COS4_09044	1.54	0.56	0.65	-45.0	9.75	1.87
GS3_19791	3.75	0.44	6.9	-83.0	11.03	2.56
GS3_24364	5.75	0.35	1.57	68.0	10.43	1.41
GS3_25028	1.86	0.62	3.39	-33.0	10.17	1.24
GS3_26192	2.71	0.43	1.62	44.0	10.13	1.77
GS3_26790	4.43	0.83	0.62	-44.0	10.1	1.36
GS3_28004	3.39	0.3	0.2	-84.0	9.8	1.62
GS3_28464	1.78	0.77	3.52	-28.0	10.9	1.47
GS4_30443	2.81	0.46	1.49	19.0	10.22	1.15
GS4_34568	4.48	0.76	1.2	-1.0	10.62	2.33

Table 5.4: **Continued.**

Galaxy	**R_e [kpc]**	**b/a**	n	**PA°_{morph}**	$\log(M_\star/M_\odot)$	**SFR** $[M_\odot yr^{-1}]$
GS4_38116	1.62	0.42	1.31	-73.0	10.01	1.67
GS4_40218	1.59	0.67	0.82	15.0	9.63	1.16
GS4_42235	3.19	0.42	0.81	-72.0	9.78	1.96
GS4_42363	2.14	0.39	1.17	26.0	10.05	1.77
GS4_42930	2.35	0.48	0.23	62.0	10.18	1.73
GS4_43631	2.14	0.59	1.61	-8.0	10.12	1.04
GS4_44133	1.20	0.63	1.08	65.0	9.56	1.45
GS4_46432	2.60	0.61	2.75	-10.0	9.53	1.37
GS4_46938	1.27	0.53	1.63	11.0	9.87	1.27

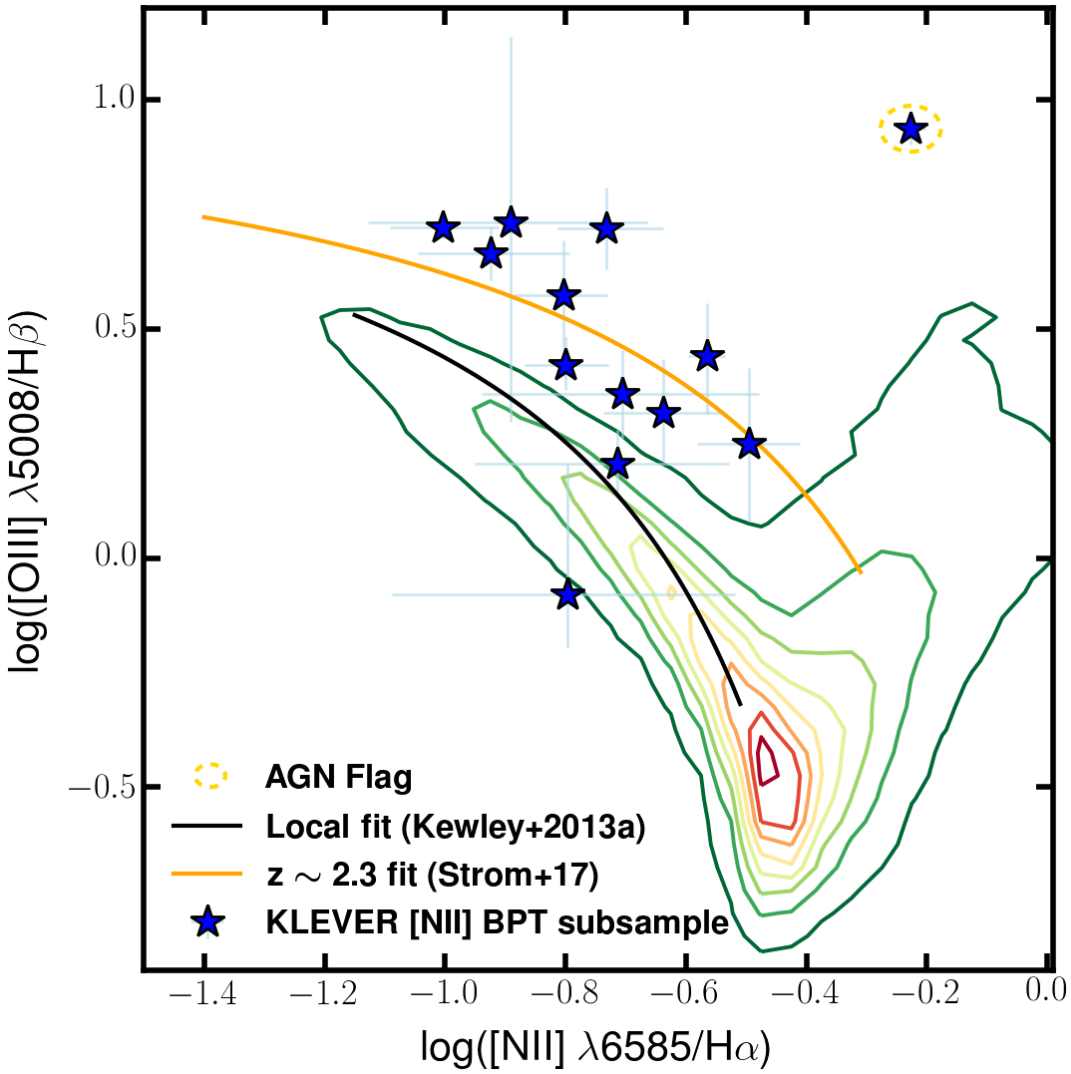

Figure 5.4: Galaxies from the [N II] subsample are plotted in the [O III]/Hβ versus [N II]/Hα diagram with the blue stars, using their integrated emission-line fluxes. Coloured contours indicate the location of local galaxies SDSS galaxies, the primary star-forming locus of which (i.e. the black curve from Kewley et al. (2013a)) is significantly offset from the KLEVER sample. The orange curve shows a fit to the $z \sim 2.3$ galaxies from Strom et al. (2017), the location of which is in good agreement with the position of the KLEVER galaxies.

and that $S/N_{H\beta} > 2$ for the O32 versus R23 plot (i.e. the O32 subsample) leaves 18/22 galaxies.

In both of these diagrams we also plot the distribution of local star-forming galaxies from the SDSS with the coloured contours. The majority of the KLEVER galaxies occupy

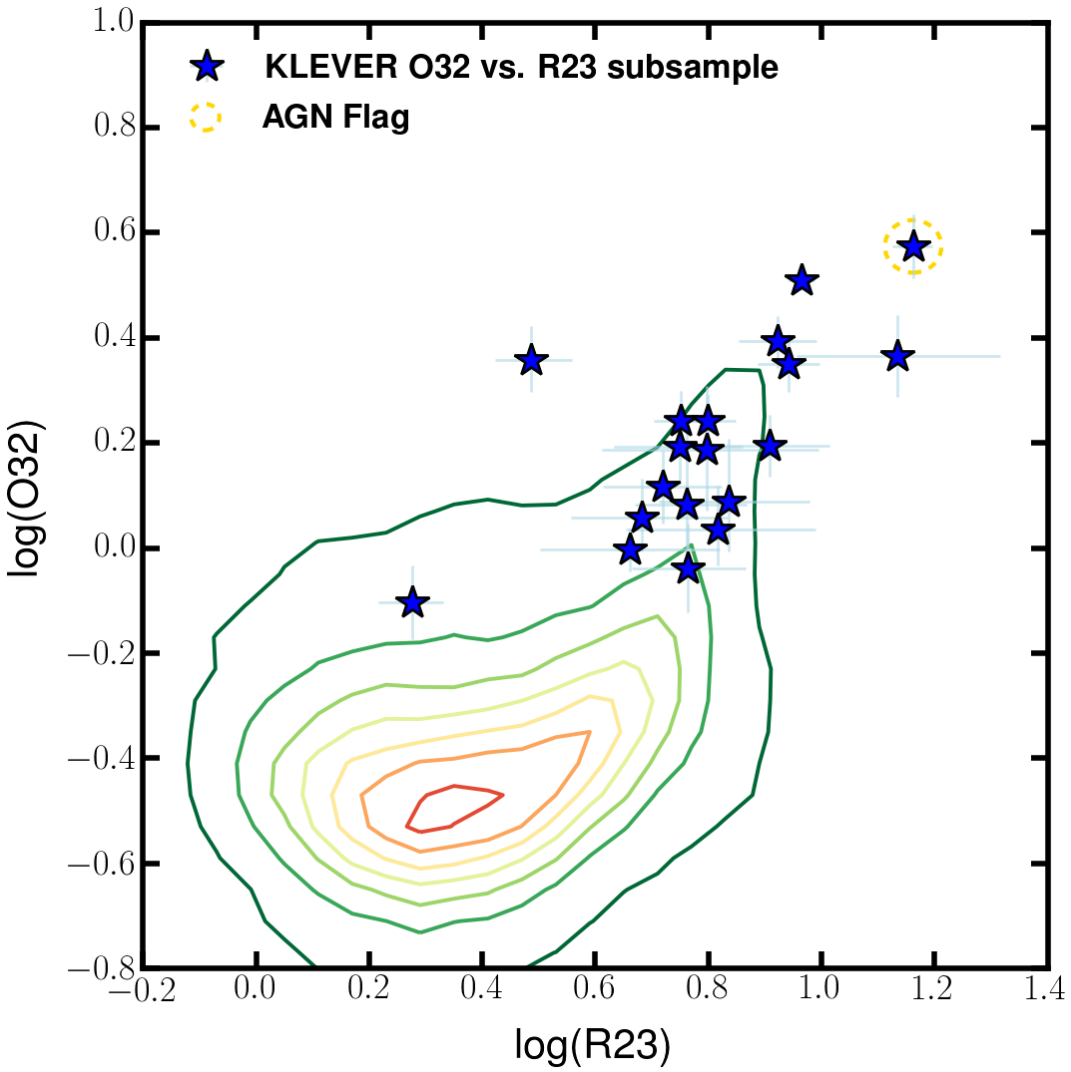

Figure 5.5: The position of the KLEVER galaxies from the O32 subsample are plotted in the O32 vs. R23 diagram with the blue stars, using their integrated emission fluxes. Again, the coloured contours indicate the location of SDSS galaxies, showing, as per previous studies, that the KLEVER galaxies fall at the edge of the local distribution where the galaxies are characterised by lower metallicities and higher ionisation parameters.

the same location in these diagrams as $z \sim 2.3$ galaxies from the KBSS-MOSFIRE survey (Steidel et al., 2014), highlighted explicitly in Fig. 5.4 by overplotting the fit to the high-redshift locus from Strom et al. (2017).

5.4 Spatially resolved emission-line ratios

To utilise their spatial information, we divided the datacubes into smaller segments and made measurements equivalent to those described for the integrated spectra in § 5.3. Generally, at the depth of the KLEVER observations, there is not enough S/N in the weaker lines to make resolved observations across individual spaxels. Also, given the average seeing of the observations is in the range $0.5 - 0.6''$, it is more meaningful to consider binning the spaxels, as described in § 5.4.2. Nonetheless, we attempt to create two-dimensional maps of the emission-line fluxes by fitting the individual spaxels of the high-S/N sample as described in § 5.4.1. These are used only for visual inspection of the trends of the line ratios, velocities and velocity dispersions across the face of the galaxies, and we stress that no quantitative measurements are made from these maps. In § 5.4.2 we describe quantitative measurements made from predefined segments across the galaxies. With these segments there is always a balance to be struck between signal to noise and loss of spatial information, whilst keeping in mind the effects of the PSF on the sizes of spatially-independent regions. We describe a simplistic approach in which the emission-line fluxes are measured within a series of automatically determined rectangular regions, as well as annular regions defined using the galaxy structural information.

5.4.1 Individual spaxel fitting

The process by which two-dimensional kinematic maps are created in the KDS by fitting the [O III]λ5007 emission line within individual spaxels is described in detail in § 3.3.2 and is similar to the procedure described in Stott et al. (2016) for the KROSS galaxies. The salient features of this process are: **1)** fitting a gaussian to the emission line within individual $0.1''$ spaxels and comparing the recovered flux with the sum over the wavelength range covered by the emission line; **2)** comparison of the line signal-to-noise with a chosen limit, nominally 3σ; **3)** expansion of the spaxel size first to $0.3''$ and then to $0.5''$ size to increase the signal-to-noise. The recovered gaussian properties are

then displayed on a two-dimensional grid, representing the galaxy physical properties. We follow the same steps to fit each of the emission lines [O II]$\lambda\lambda$3727,3729, Hβ, [O III]λ5007, Hα and [N II]λ6583 with a few changes to the procedure. Since the maps are used for visual inspection only, we smooth each cube before fitting the chosen emission lines using a gaussian kernel of width $\sigma_{\rm g} = 0.4''$ (roughly equal to the seeing) in order to increase the signal-to-noise at the expense of washing out any features with spatial scales below this value. We also fit the gaussians using the appropriate weights spectrum, W_i, described in § 5.3.2 and use two blended gaussian in order to fit the [O II]$\lambda\lambda$3727,3729 doublet.

Several examples of the maps produced by this fitting process for the highest S/N galaxies, including labelled line-ratio maps, are shown in Fig. 5.6. The plots show the Hα and [O III]λ5007 velocity fields in the top-left and top-right corners and selected emission-line-ratio maps[5] in the bottom-left and bottom-right corners overlaid on a three-colour *HST* image[6]. The three-band integrated spectra and fitted models are also shown for each galaxy. We stress that the limiting factor in the spatial extent of the line-ratio maps is the S/N of the weaker emission lines at the galaxy outskirts. The main virtues of these plots are **1)** to display both the stellar and gaseous emission side-by-side in order to see the correlations between these two components; **2)** to visually inspect the spatial variations in emission-line ratios; **3)** to visually inspect correlations between the velocity fields and the emission-line ratios; **4)** to inform the apportioning of the galaxy into the segments described in § 5.4.2. It is also clear from the emission-line maps, particularly for the maps showing the dust-uncorrected O32 ratio, that the galaxies often do not follow a simple inner−outer radial gradient.

[5]These maps have not been corrected for dust extinction using the observed Balmer decrement, which is discussed for the resolved segments in § 5.4.2.

[6]The *F814W*, *F125W* and *F160W HST* bands are used for the blue, green and red channels of the image respectively, and the image is created using the `astropy make_lupton_rgb` method.

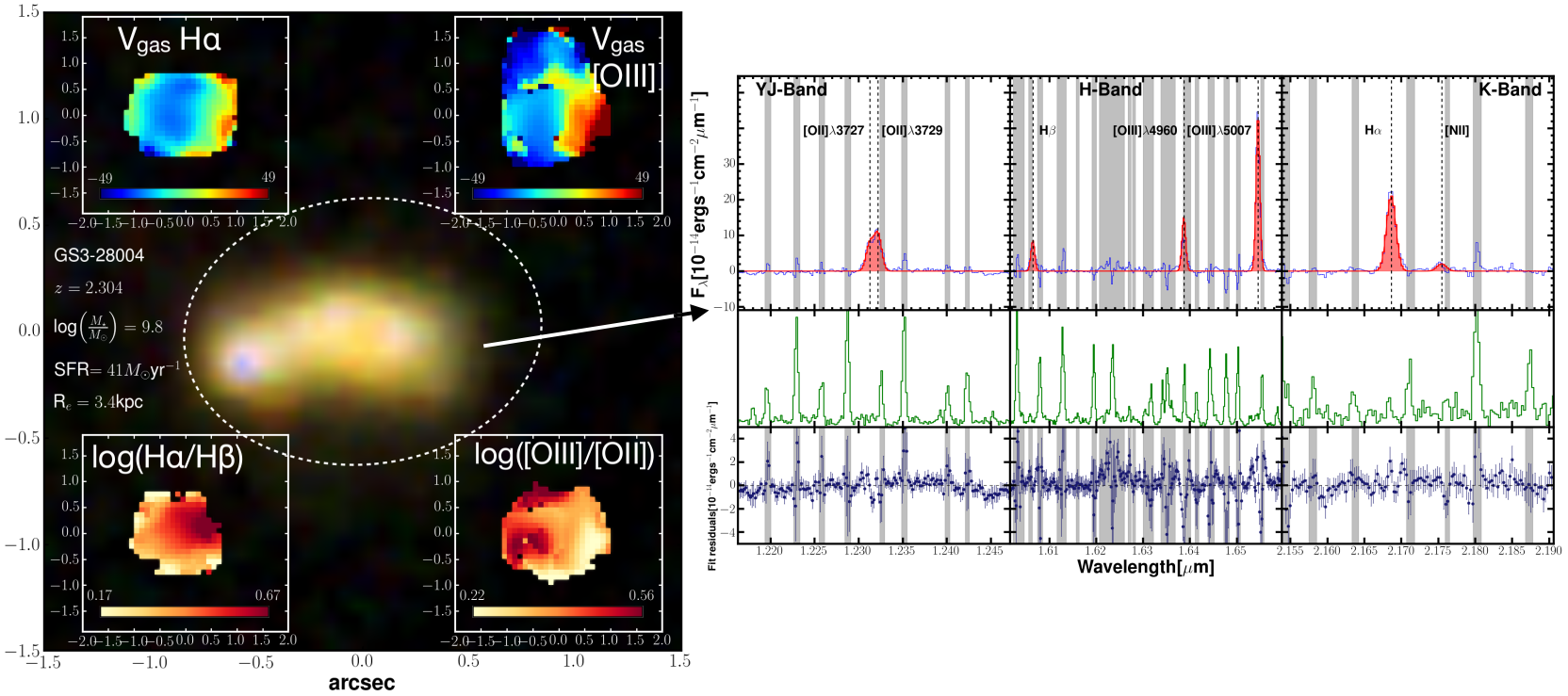

Figure 5.6: Galaxy GS3_28004. The spatially-resolved Hα and [O III]λ5007 velocity fields, generated using the spaxel-fitting procedure described in the text, are overlaid in the top-left and top-right panels of the 3 colour *HST* image. Also shown are the logarithms of the Balmer decrement and O32, to indicate the variation of these ratios across the face of the galaxy. The aperture used to extract the integrated galaxy spectrum is shown with the white-dashed ellipse on the *HST* image and the *YJ*,*H* and *K*-band spectra are shown on the right, as described in Fig. 5.2.

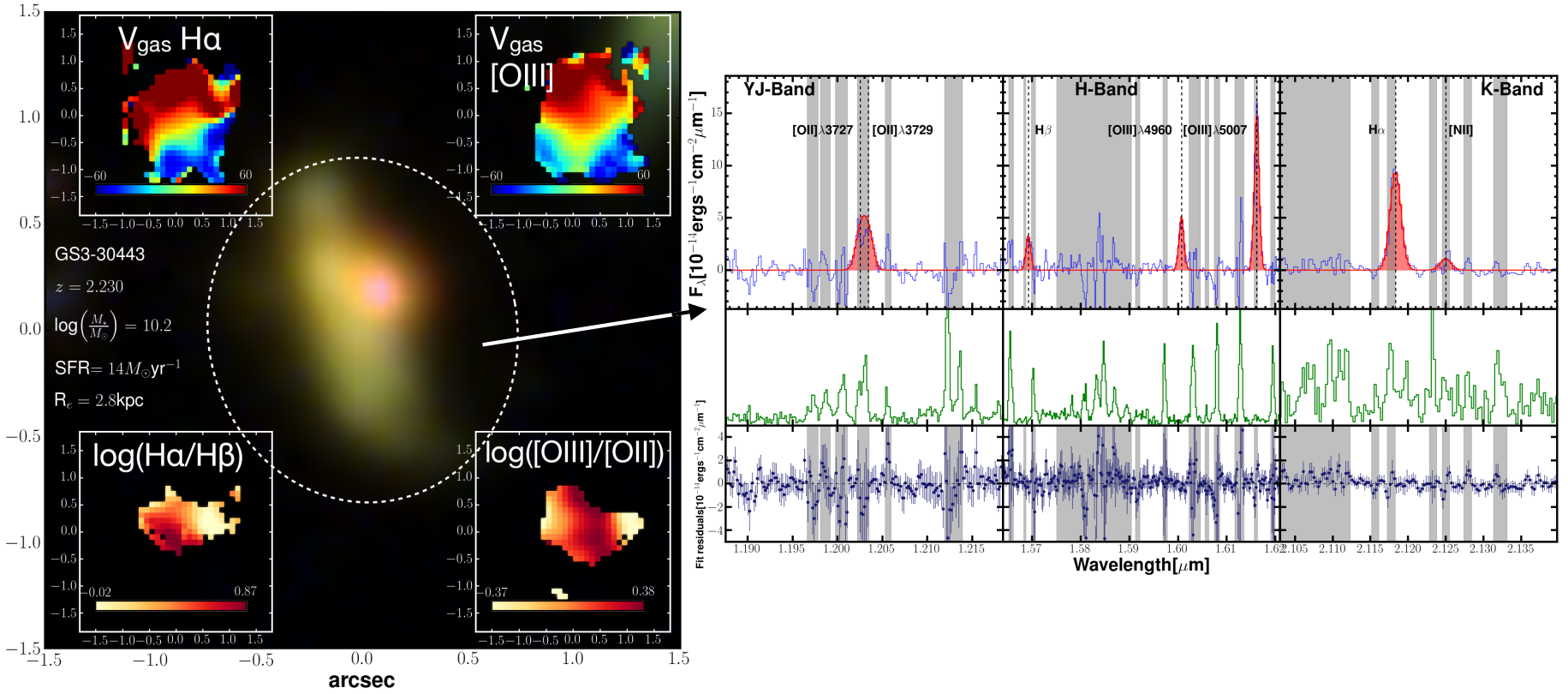

Figure 5.6: **Continued,** galaxy GS4_30443.

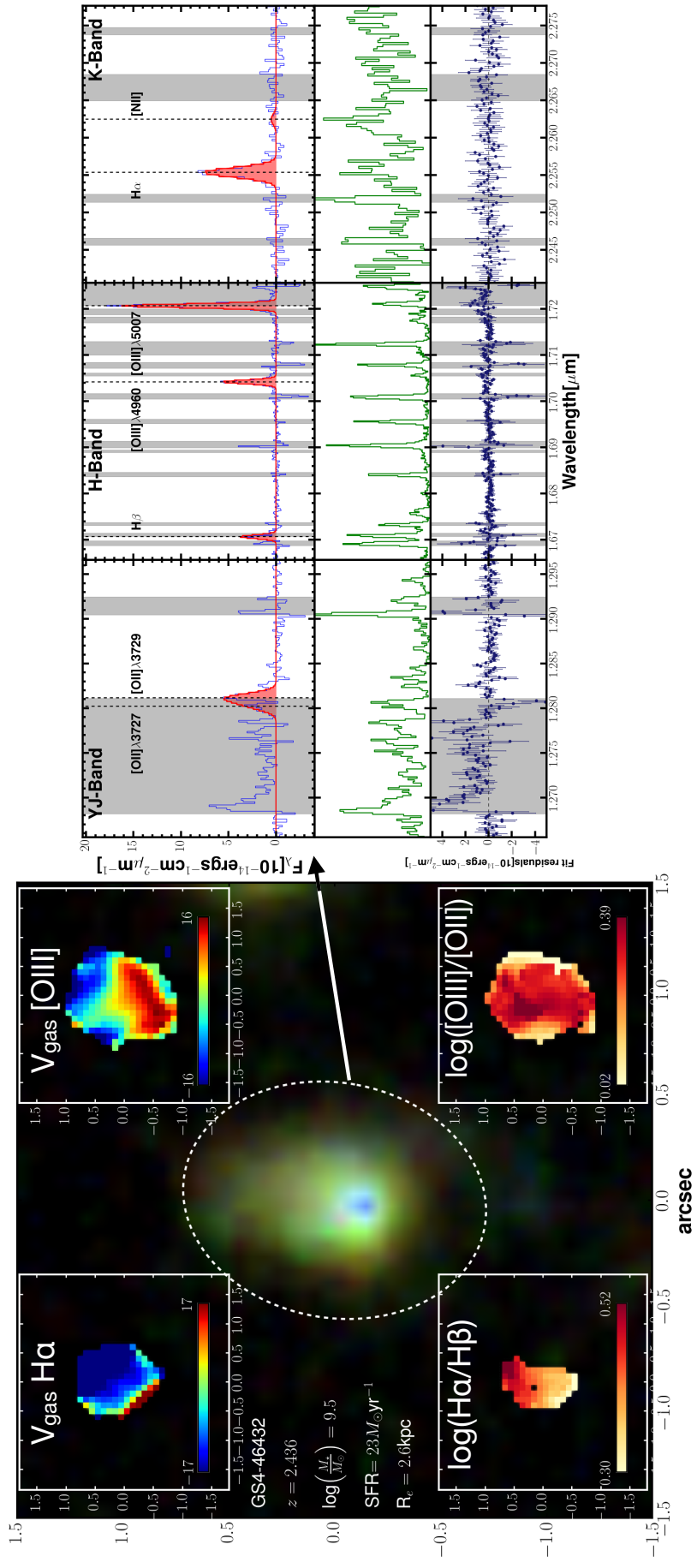

Figure 5.6: **Continued,** galaxy GS4_46432.

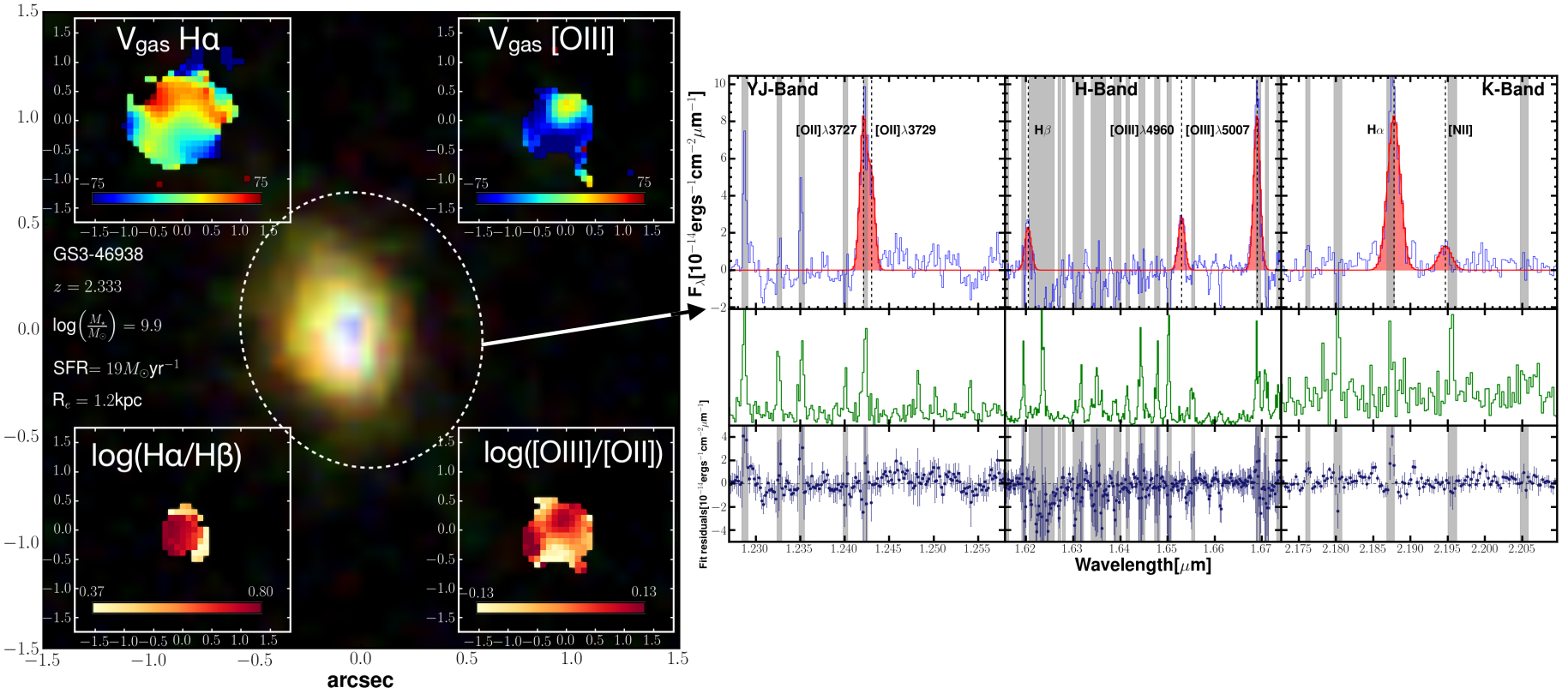

Figure 5.6: **Continued,** galaxy GS4_46938.

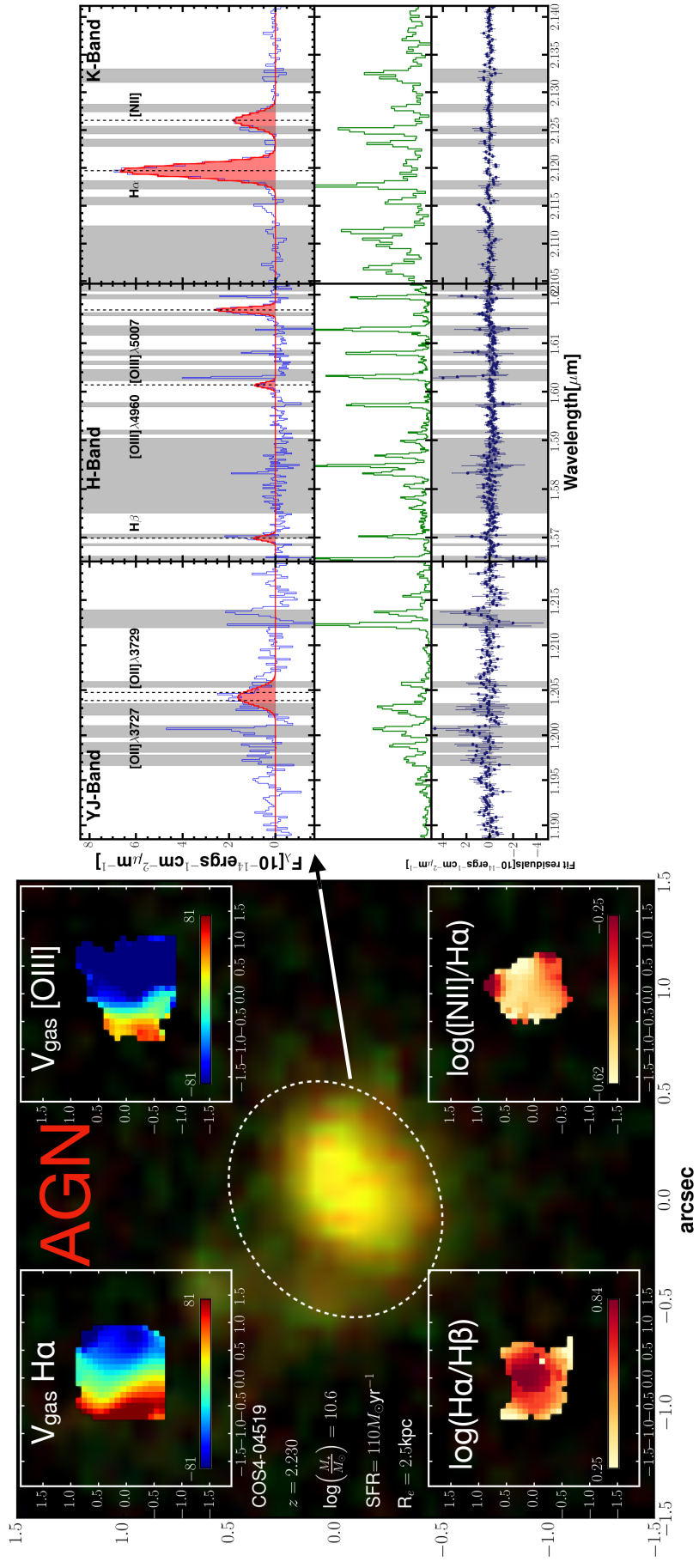

Figure 5.6: **Continued,** galaxy COS4_04519.

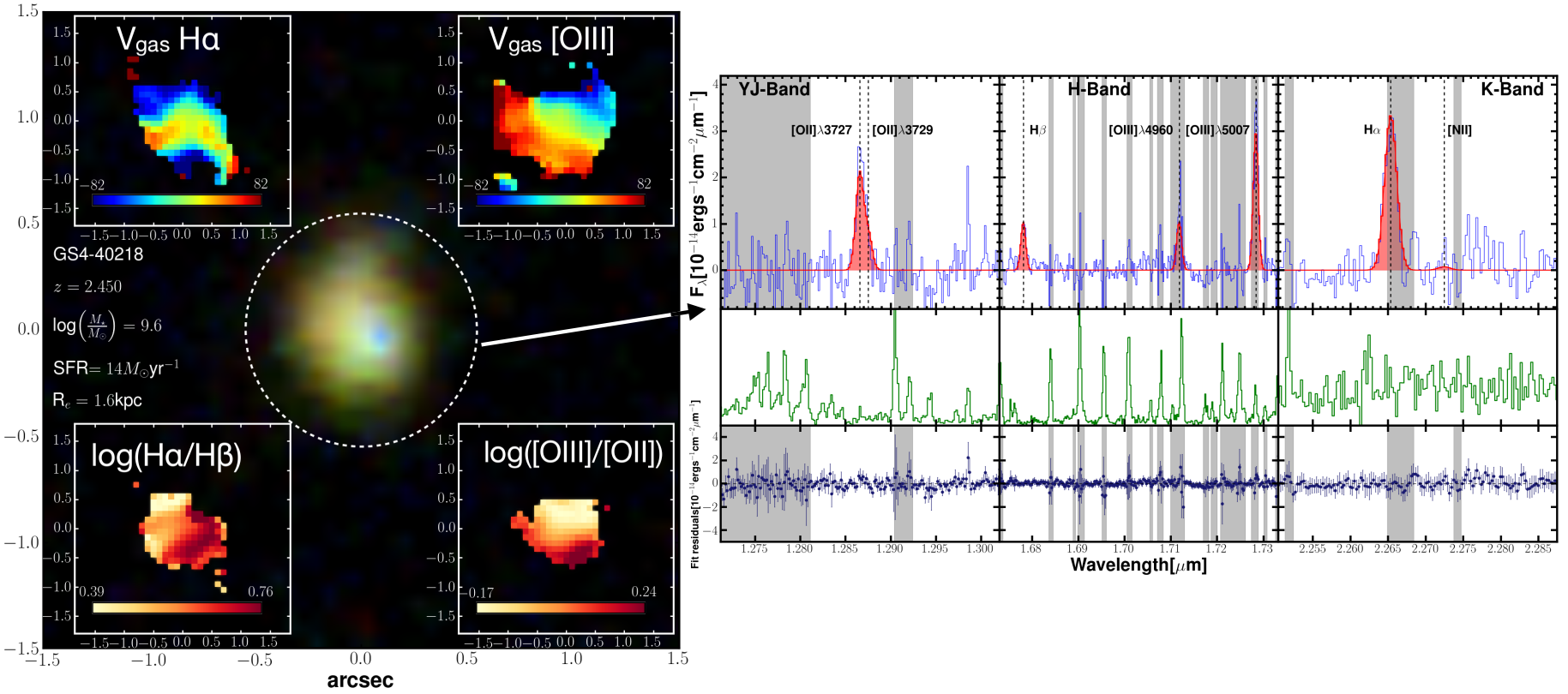

Figure 5.6: **Continued,** galaxy GS4_40218.

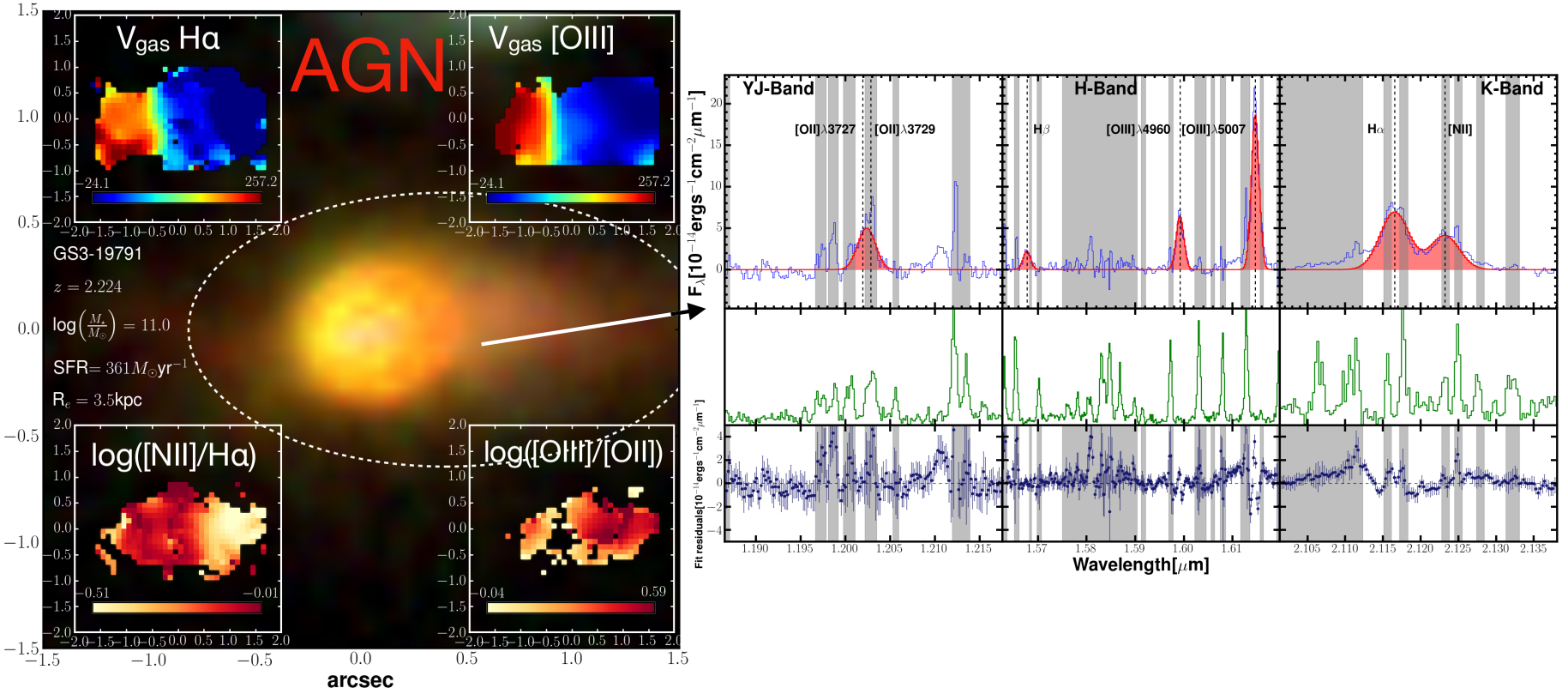

Figure 5.6: **Continued,** galaxy GS3_19791. Demonstrating an AGN candidate with integrated Hα and [N II] emission lines which are not well-described by a single broad gaussian component. The *HST* image shows a distinct, PSF-like central morphology and the emission-line ratios place the galaxy in the AGN region of the [N II] BPT diagram (see Fig. 5.4).

5.4.2 Resolved region fitting

As mentioned in the previous subsection, in order to increase the signal-to-noise and to account for the PSF of the observations, we use 2 methods to spatially bin the datacubes: a fixed grid of square segments and a series of concentric annuli as described below. The fixed grid is defined across the face of the cubes as shown in the right panel of Fig. 5.7, with each region used to construct a series of masks for the galaxies in the high-S/N sample. In each of these segments, the spectra are extracted and fitted following the same procedure described in § 5.3. This provides measurements of the fluxes and signal-to-noise ratios of each of the emission lines, as well as a measurement of the median distance within the segment from the galaxy centre. This distance is defined as the median of the distances from all individual spaxels to the central spaxel within the segment. At this stage, we also apply a dust correction to the emission-line fluxes following the same prescription as described in § 5.3, keeping a record of both the corrected and uncorrected flux values.

We also construct a series of 4 annular masks with inner/outer radii defined by the following sequence of multiples of the half-light radius $R_{1/2}$

1. $r_i = 0, r_o = 0.5R_{1/2}$
2. $r_i = 0.5R_{1/2}, r_o = R_{1/2}$
3. $r_i = R_{1/2}, r_o = 1.6R_{1/2}$
4. $r_i = 1.6R_{1/2}, r_o = 2.2R_{1/2}$

where r_i and r_o are the inner and outer radii of the annuli respectively. The core is defined as all spaxels within an ellipse with major axis direction determined by PA_{morph}, major axis size determined by convolving $R_{1/2}$ with the average PSF across the three wavebands and minor axis size given by the product of the galaxy axis ratio and the major axis size. These core and outskirts regions are shown for the same galaxy in the left panel of Fig. 5.7, from which the line fluxes are also extracted.

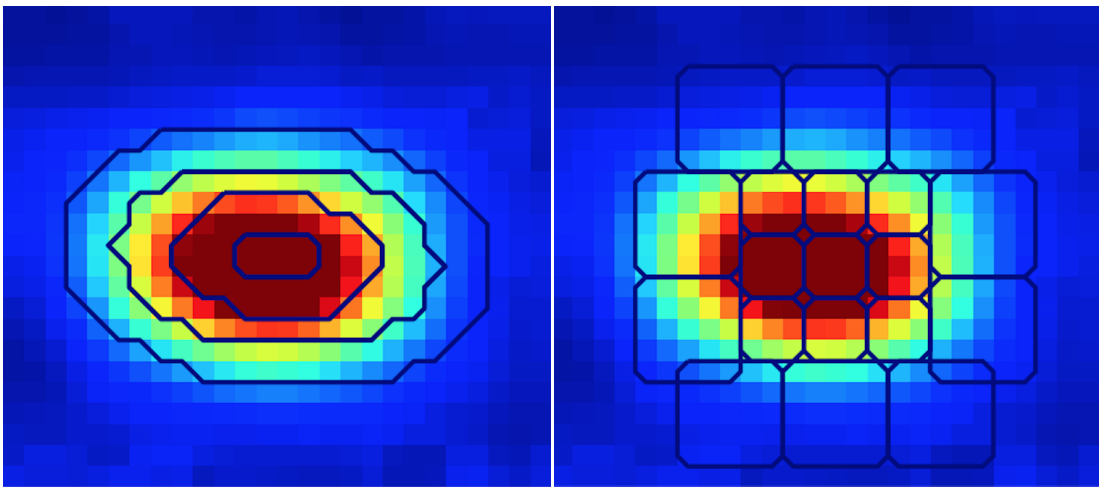

Figure 5.7: To investigate the spatial variation of emission-line ratios we require several measurements which achieve a minimum S/N threshold. The first approach, shown in the right panel, is to blindly segment the galaxies into a series of smaller regions using a fixed grid. This is shown in the right panel, where the spectra are summed and extracted from each square region. A second, complimentary, approach is to divide each galaxy into a series of annuli, constructed using the galaxy structural parameters as shown in the left panel, and to sum the spectra from the spaxels bounded by these. This approach assumes that the galaxies are axisymmetric, so that averaging in rings does not wash out interesting features. Both approaches provide a series of emission-line measurements at different distances from the galaxy centre.

To summarise, we have used the integrated signal-to-noise ratios to build a high-S/N sample which is suitable for resolved analysis. For each of these galaxies, we compute maps of the dynamics, fluxes and emission-line ratios by fitting within the individual spaxels of the datacubes across the *YJ*, *H* and *K*-bands and compare these with the morphologies of the galaxies from *HST* (some examples for the highest S/N galaxies are given in Fig. 5.6). Due to the lack of S/N across the weak lines for individual spaxel fitting, we also extract the emission-line properties across a fixed grid of rectangular segments and in concentric annular regions defined using the galaxy structural properties, recording this information for each of the galaxies in the high-S/N sample. In the following sections we focus on the emission-line ratios extracted within these partially-resolved segments .

5.5 Preliminary Results and Discussion

Throughout the following sections we present the first spatially-resolved results from the KLEVER field sample, using the segmented and annular regions defined in above. It should be stressed that these results are preliminary and require further testing to ensure that they are robust. Throughout this section, we clarify the parts of the analysis which shall be improved in future work.

5.5.1 The observed Balmer decrement radial profiles

In Reddy et al. (2015), the authors studied the integrated Balmer decrement values from the MOSDEF survey, typically finding values in the range $2 < (\mathrm{H}\alpha/\mathrm{H}\beta)_{\mathrm{obs}} < 6$. In this study there is a correlation between the Balmer decrement values and the Hα luminosity, with galaxies that are brighter in Hα, and therefore with larger instantaneous star-formation rates, also having larger Balmer decrement values. In terms of studying these trends as a function of location within the galaxy, the only existing statistical study of Balmer decrement spatial distributions makes use of low-spectral-resolution grism data at $z \simeq 1.4$ from the 3D-HST survey. In this study, Nelson et al. (2015) demonstrated that, on average, galaxies have larger $(\mathrm{H}\alpha/\mathrm{H}\beta)_{\mathrm{obs}}$ and hence larger dust attenuation towards their centres. This is a strong function of galaxy stellar mass, with the galaxies in the highest stellar mass bin of $9.8 < \log(\mathrm{M}_\star/\mathrm{M}_\odot) < 11.0$ showing $2-3$ magnitudes greater extinction towards the Hα emission line than in the lower mass bins of $9.2 < \log(\mathrm{M}_\star/\mathrm{M}_\odot) < 9.8$ and $9.0 < \log(\mathrm{M}_\star/\mathrm{M}_\odot) < 9.2$. This is interpreted as the creation of central bulges in more massive galaxies via central star formation, one of the byproducts of which is strong central dust concentrations. Measuring the Hα and Hβ emission lines simultaneously at intermediate and high redshift requires observations in multiple wavebands. Measuring the ratio of these lines at different spatial locations across a galaxy requires either grism or integral-field spectroscopy, accompanied by long-enough integration times to achieve adequate S/N in the Hβ line. The KLEVER field sample thus offers the first opportunity to study the resolved Balmer decrements

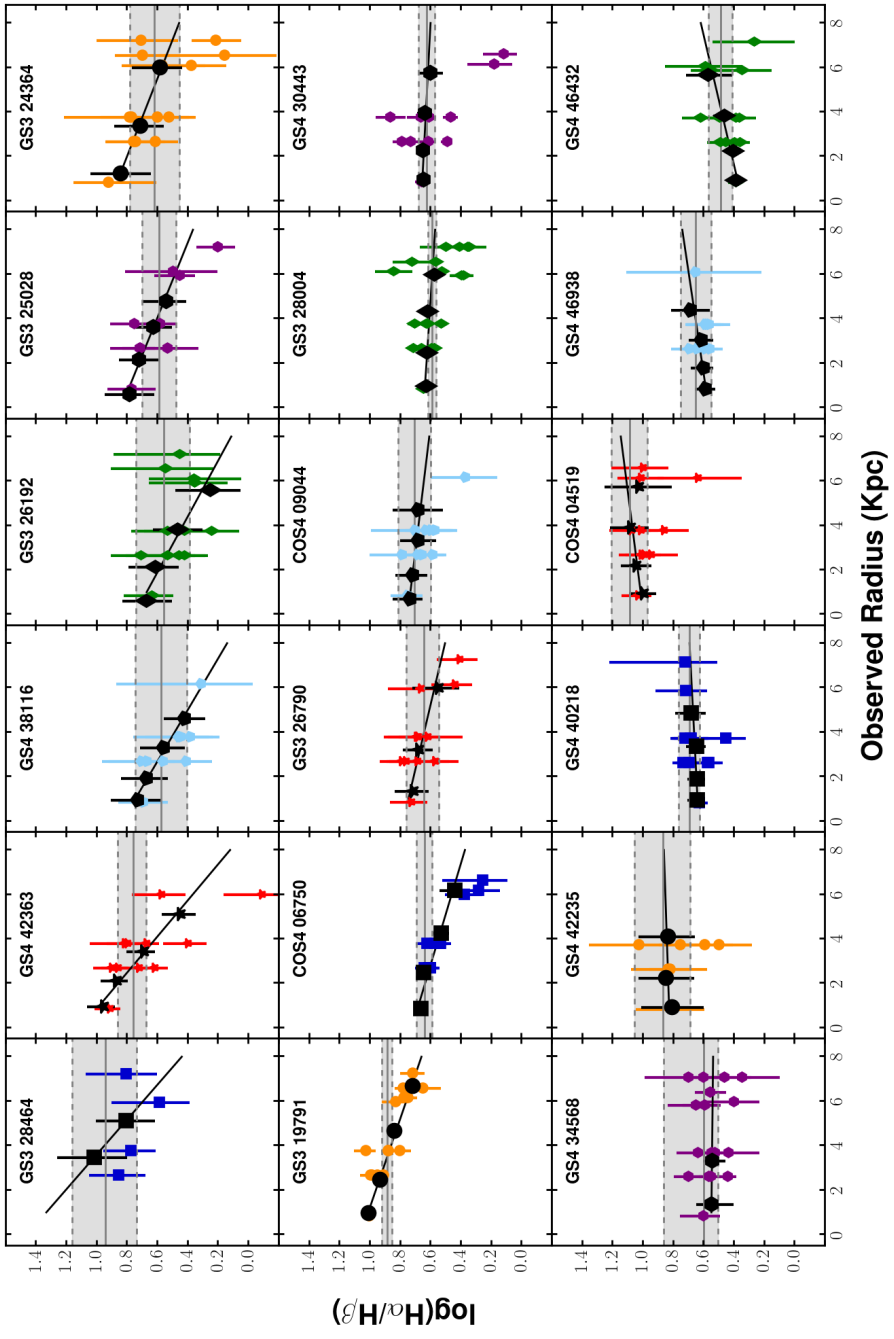

Figure 5.8: Each of the individual panels shows a galaxy from the O32 subsample. As discussed in the text, the Balmer decrement values are extracted in both annular regions (filled, black points) and square segments (filled, colour points) and assigned a radius value using the average distance of the spaxels from the centre of the galaxy. The solid, black lines show fits to the annular regions, as a measure of the strength of the Balmer decrement gradients across the galaxies. The panels are ordered according to the strength of this gradient, and in most cases these gradients suggest that there is relatively more dust towards the galaxy centres than the outskirts. The coloured points tend to scatter around the black lines, suggesting that there is broad agreement between the annular regions and the segments. In each panel the solid, grey line shows the value of the integrated Balmer decrement and the shaded regions indicate the upper and lower 1σ error on this.

at $z \simeq 2.2$, and the correlations between the measured gradients and other physical properties, within a moderate number of galaxies.

Fig. 5.8 shows the measured Balmer decrement values, in units of log(Hα/Hβ), as a function of observed radius (i.e. not corrected for beam smearing) in kpc for the 18 galaxies in the O32 subsample described in § 5.3.3[7]. The solid, black symbols indicate the measurements made within the annular regions, whereas the smaller, colour-filled symbols indicate the measurements from the square regions defined in the right panel of Fig. 5.7. A straight line with slope and intercept free to vary has been fitted to the black points measured from the annuli, to indicate the Balmer decrement gradient, using the python package LMFIT (Newville et al., 2014), with intrinsic scatter taken into account. The best fitting lines are plotted in black and, encouragingly, the measurements from the sqaure regions tend to scatter on either side of these relations. The galaxies have been ordered according to the strength of this gradient, with the most negative gradient in the top-left panel, becoming increasingly flat in the middle row and with several galaxies showing evidence for a positive gradient (i.e. relatively more dust in the galaxy outskirts) in the bottom row. Three of the four galaxies with evidence for positive Balmer decrement gradients (GS4_40218, GS4_46938 and GS4_46432) have clear 'blue' centres in Fig. 5.6.

It is intriguing to investigate the correlations between the measured strength of the Balmer decrement gradient and the global physical properties of the galaxies. As mentioned above, the results presented in Nelson et al. (2015) suggest that galaxies with higher stellar mass have larger values of the Balmer decrement in their centres. Two further properties we will explore here are the Hα integrated emission line width and the Hα luminosity, which is directly related to the star-formation rate of the galaxy. Each of the panels in Fig. 5.9 show the Balmer decrement gradient in units of kpc^{-1} on the y-axis as a function of a given integrated physical property. In these panels we exclude the galaxies GS3_28464 and GS4_34568, where the gradients are

[7]This subsample is used to facilitate the dust correction of the O32 values, as presented in § 5.5.2

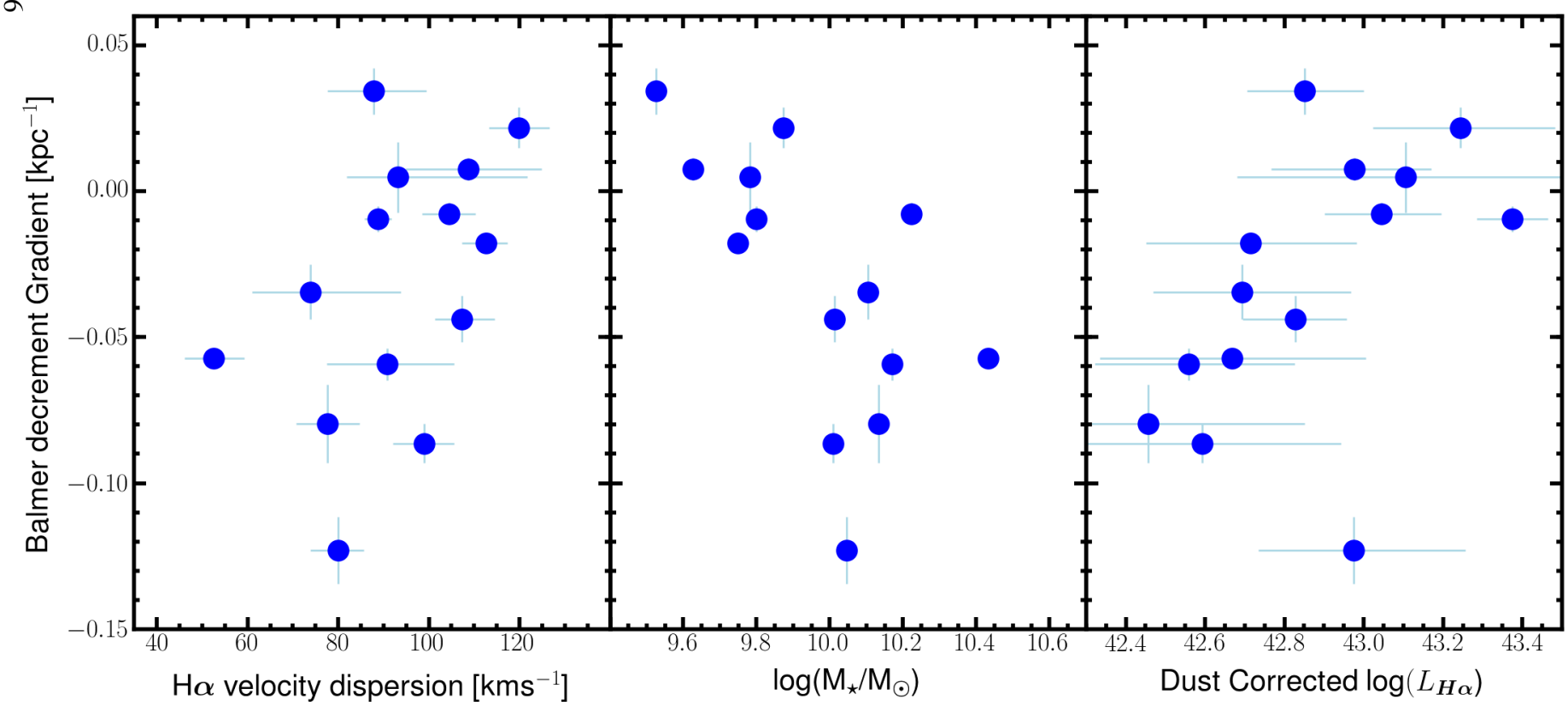

Figure 5.9: The correlations between the strength of the Balmer decrement gradients and several physical properties are shown. The 14 galaxies from the O32 sample which do not show AGN characteristics and have more than 2 annular regions to fit the straight lines to are shown. The left panel shows the relation between Balmer decrement gradients and Hα linewidth, which is a proxy for the prevalence of random motions within the galaxies. The middle panel shows the relationship between Balmer decrement gradient and stellar mass and the right panel between Balmer decrement gradient and Hα luminosity. The interpretation of these relationships is discussed in the text.

measured based on only two annular data points, and also the galaxies GS3_19791 and COS4_04519 which have clear signatures of AGN activity as described in previous sections. Taken together, the panels indicate that galaxies with increasingly-negative Balmer decrement gradients (i.e. a more centrally concentrated dust distribution) have lower Hα velocity dispersions, higher stellar masses and lower Hα luminosities. These results will be discussed further in § 5.6.

Importantly, the Balmer decrement measurements also provide the means to apply a dust correction to other line ratios as described in § 5.3.2. In the following subsections, analogous measurements and plots to those shown above for the Balmer decrements are described for the O32 and R23 radial profiles.

5.5.2 The observed and dust-corrected O32 radial profiles

The O32 ratio has been used to study both the ionisation state (e.g. Shapley et al., 2015) and as a proxy for metallicity (e.g. Bian et al., 2018) in star-forming galaxies. Recently, Bian et al. (2018) used stacks of SDSS galaxies identified as local analogues to z≃2.3 star-forming galaxies in the BPT diagram, to recalibrate the relationship between O32 (as well as several other emission-line ratios) and metallicity, measured using the direct T_e method. For O32 there is a monotonic, negative, linear relationship with metallicity (with a large dispersion) in the sense that an increase in O32 value leads to a decrease in metallicity. There are, however, several complications with applying the derived calibration to the KLEVER sample. Most importantly, the derived calibration is only valid over a certain range of metallicity values ($7.8 < 12 + \log(O/H) < 8.4$) and the integrated and dust-corrected KLEVER line ratios would place the majority of galaxies outside the *upper* metallicity limit. Additionally, there is not a theoretically-simple relationship between only O32 and metallicity, and the form of the relationship is heavily dependent on other factors such as the ionisation parameter and the electron density. Consequently, in this preliminary study, we do not attempt to convert to metallicity and instead defer this to future work which will use photoionisation modelling to properly

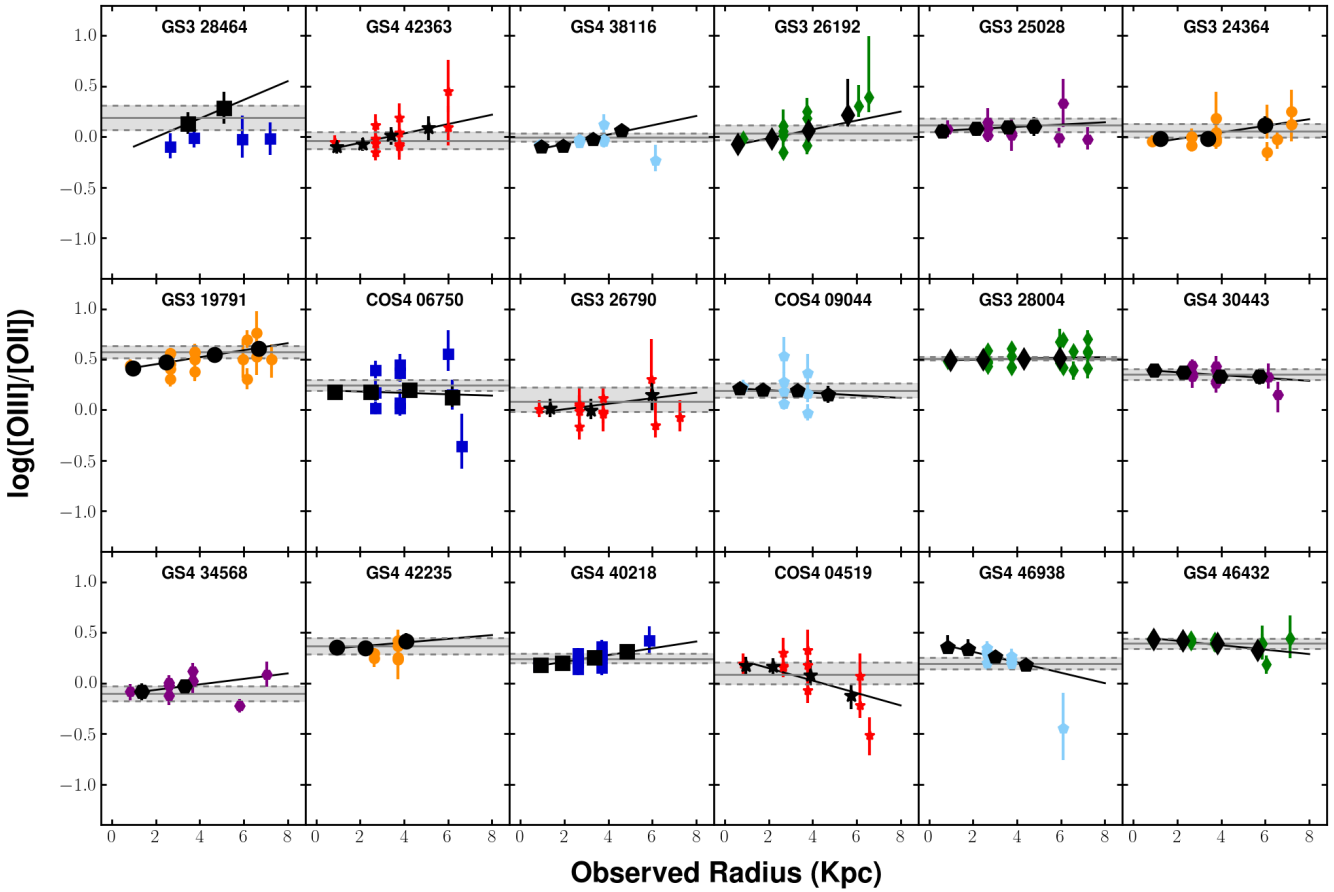

Figure 5.10: Analogous to Fig. 5.8, the O32 values are plotted against radius. The symbols denoting the annular regions, grid segments, linear fits and integrated ratios are identical to Fig. 5.8. In this case the O32 ratio *without* dust correction is plotted, generally showing flat or mildly positive radial gradients.

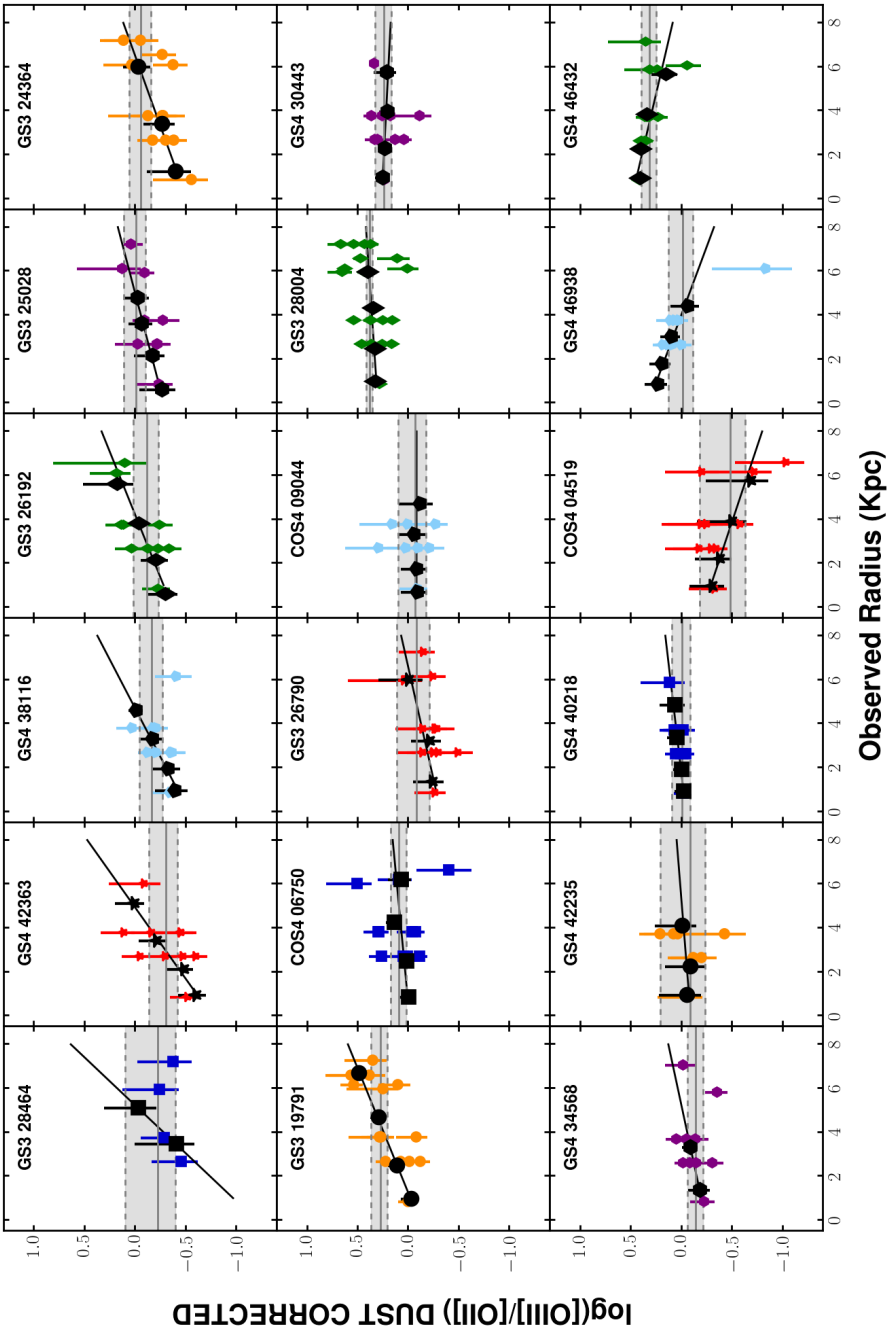

Figure 5.11: The same as per Fig. 5.10 but in these panels the O32 values have been corrected for dust extinction using the Balmer decrement values displayed in Fig. 5.8. The nature of the spatial distribution of the dust leads to the steepening of the O32 gradients, the vast majority of which are positive.

account for the combination of ISM properties which complicate the relationship between line ratios and metallicity. As a compromise, we choose here to broadly, and qualitatively, associate lower O32 values with higher metallicities.

Fig. 5.10 shows the O32 radial profiles from the annuli and the square segments prior to dust correction, for each of the galaxies in the O32 subsample, in the same style as described for Fig. 5.8. Again, the gradients are measured by fitting a straight line to the black data points measured from the annular regions. There is a clear tendency for the galaxies, particularly those in the top rows which are observed to have more-negative Balmer decrement gradients, to have lower O32 values in the centres than in the outskirts. When the dust correction is applied, shown in Fig. 5.11, the O32 gradients become more pronounced as a consequence of the centrally concentrated dust distributions. Using the qualitative interpretation of the O32 ratio mentioned above, this suggests higher metallicities and lower ionisation parameters towards the galaxy centres, and the converse in the galaxy outsirts. Comparing with the distribution of SDSS galaxies in Fig. 5.5, the central regions of the KLEVER galaxies are approaching the integrated ISM conditions observed locally. Three of the four peculiar galaxies which are observed to have positive Balmer decrement gradients also appear to have lower metallicities towards the centres, further supporting the argument that they are currently undergoing a different set of physical processes than the majority of the sample.

Fig. 5.12 shows the correlations between the derived O32 gradients and the global galaxy physical properties. The trends generally suggest that galaxies with more-positive O32 gradients (and hence with larger metallicity discrepancies between core and outskirts in our simplistic interpretation) have lower velocity dispersions, higher stellar masses and lower Hα luminosities. The peculiar galaxies which exhibit negative O32 gradients have high velocity dispersions, low stellar masses and very high Hα luminosities. Again, we shall return to this discussion through § 5.6.

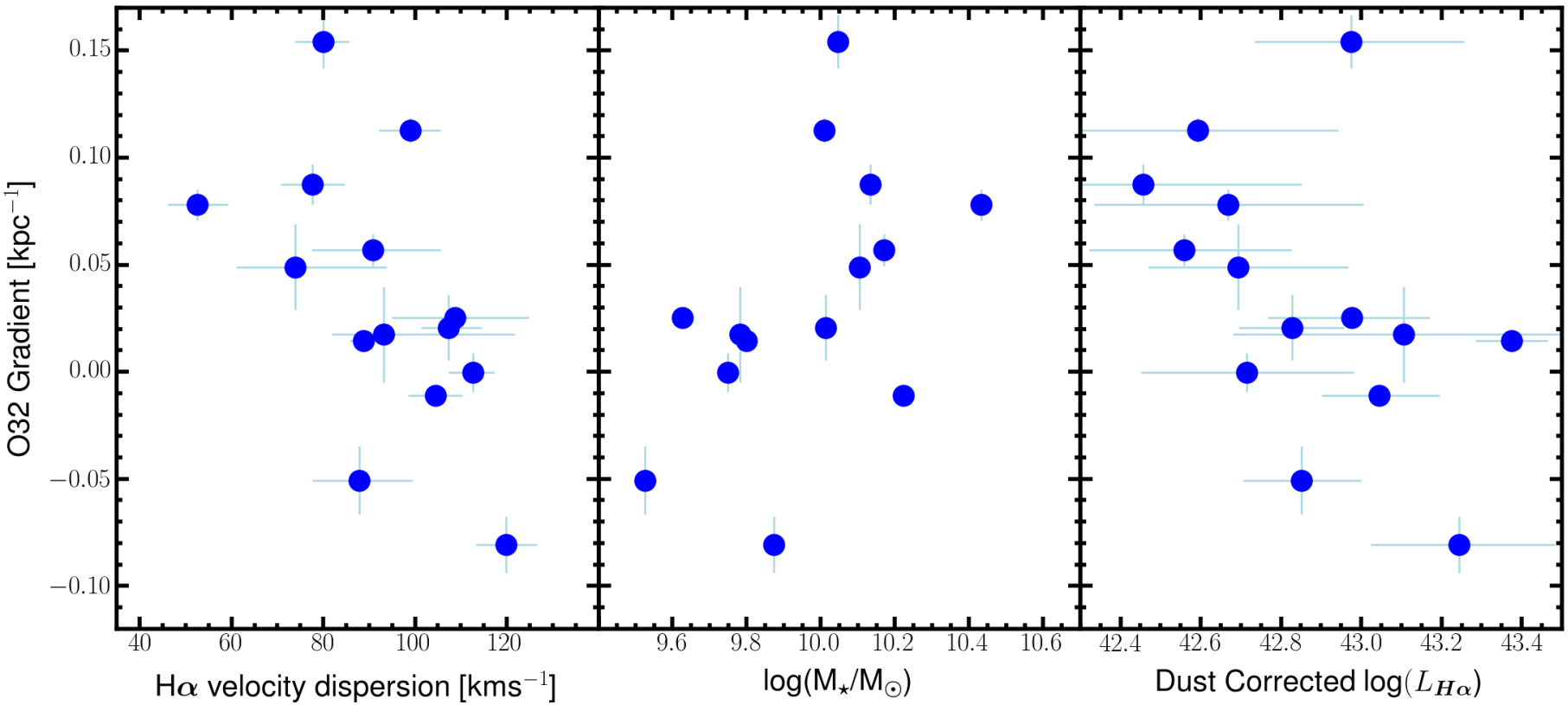

Figure 5.12: Analogous to Fig. 5.9, the O32 dust-corrected gradients are plotted as a function of Hα linewidth, stellar mass and Hα luminosity. Generally, the galaxies with stronger, positive O32 gradients have smaller integrated linewidths, larger stellar masses and are less luminous in Hα.

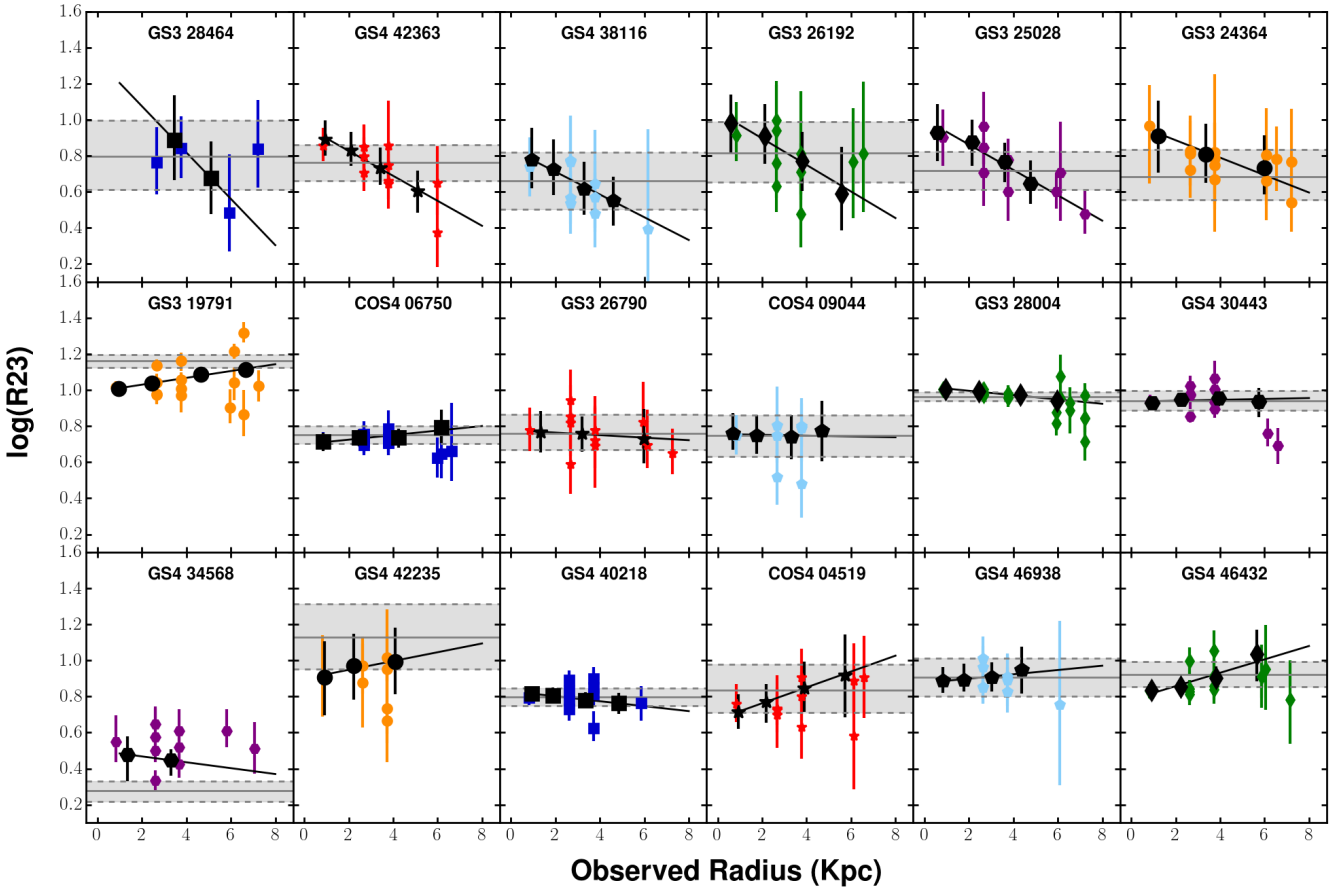

Figure 5.13: The R23 values, not corrected for dust extinction, are plotted against radial distance, using the same symbols as in Fig. 5.8. Generally the R23 values decrease outwards from the centre, which is the same trend as the Balmer decrement gradients and anti-correlated with the O32 gradients.

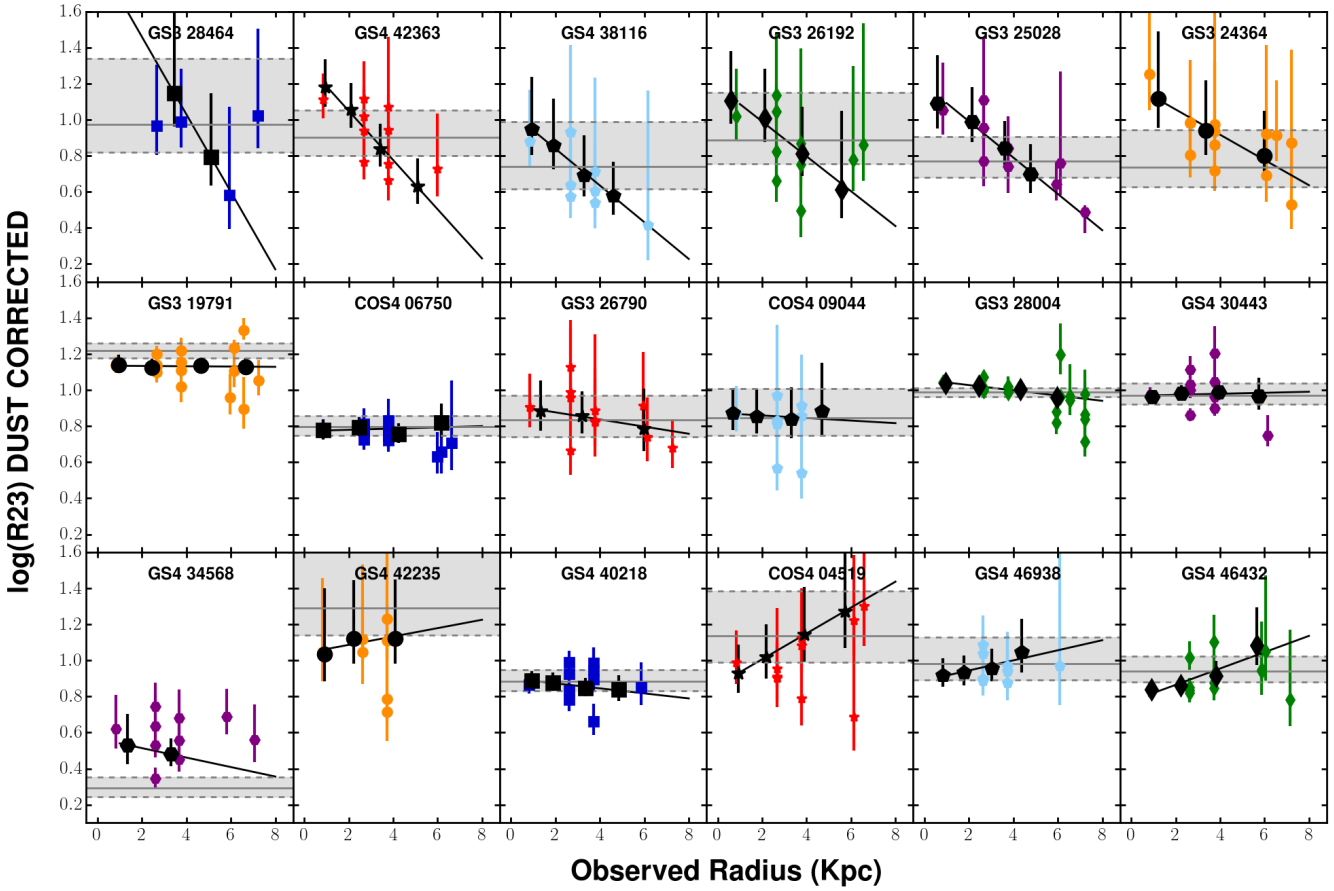

Figure 5.14: The R23 values, corrected for dust extinction, plotted against radial distance. As with the O32 gradients, the application of the dust extinction correction accentuates the strength of the gradient values, which are mostly negative.

5.5.3 The observed and dust-corrected R23 radial profiles

As a final example of line ratios measured in annuli and segments, we consider the radial profiles of R23. This ratio has been utilised as a proxy for metallicity in many previous studies (e.g. Kewley & Ellison, 2008; Maiolino et al., 2008; Moustakas et al., 2010; Troncoso et al., 2014) and recently by Bian et al. (2018) to construct an empirical calibration from local-analogue SDSS stacks as described in the previous subsection. The relationship between R23 is notoriously double-valued, with an upper and lower metallicity branch separated by a region in which R23 is not very sensitive to metallicity. Fig. 5.13 shows the dust-uncorrected R23 radial profiles, which are large positive and hence anti-correlated with the O32 gradients and correlated with the Balmer decrement gradients. This suggests that the galaxies are on the high-metallicity branch, or approaching the turnaround region, of the relationship between R23 and metallicity, which a comparison with the Bian et al. (2018) calibration supports. Typically the errors on the individual data points are large, due to the denominator of the R23 ratio containing the weak Hβ emission line and so the gradients are more uncertain than in the previous cases. Fig. 5.14 shows the R23 profiles after correcting for dust extinction. This correction is less significant than for O32, due to the competing corrections to the the [O II]$\lambda\lambda$3727,3729 doublet on the numerator and the Hβ line on the denominator, which are closer in wavelength than the [O III] and [O II] lines. However the correction again acts to accentuate both the negative and positive gradients due to the nature of the observed dust distributions. If the galaxies are on the high-metallicity branch, the majority of R23 ratios also suggest higher-metallicity centres than outskirts, with the same few galaxies on the bottom row of Fig. 5.14 exhibiting inverted gradients.

Focussing on the correlations between R23 gradients and global galaxy physical properties, Fig. 5.15 demonstrates the same trends, although with more scatter, than observed for the Balmer decrement gradients. In particular the correlation between Hα linewidth and R23 gradient is no longer clear, although it is difficult to tell if this is real or a consequence of the larger errors on the R23 values. In the following section we

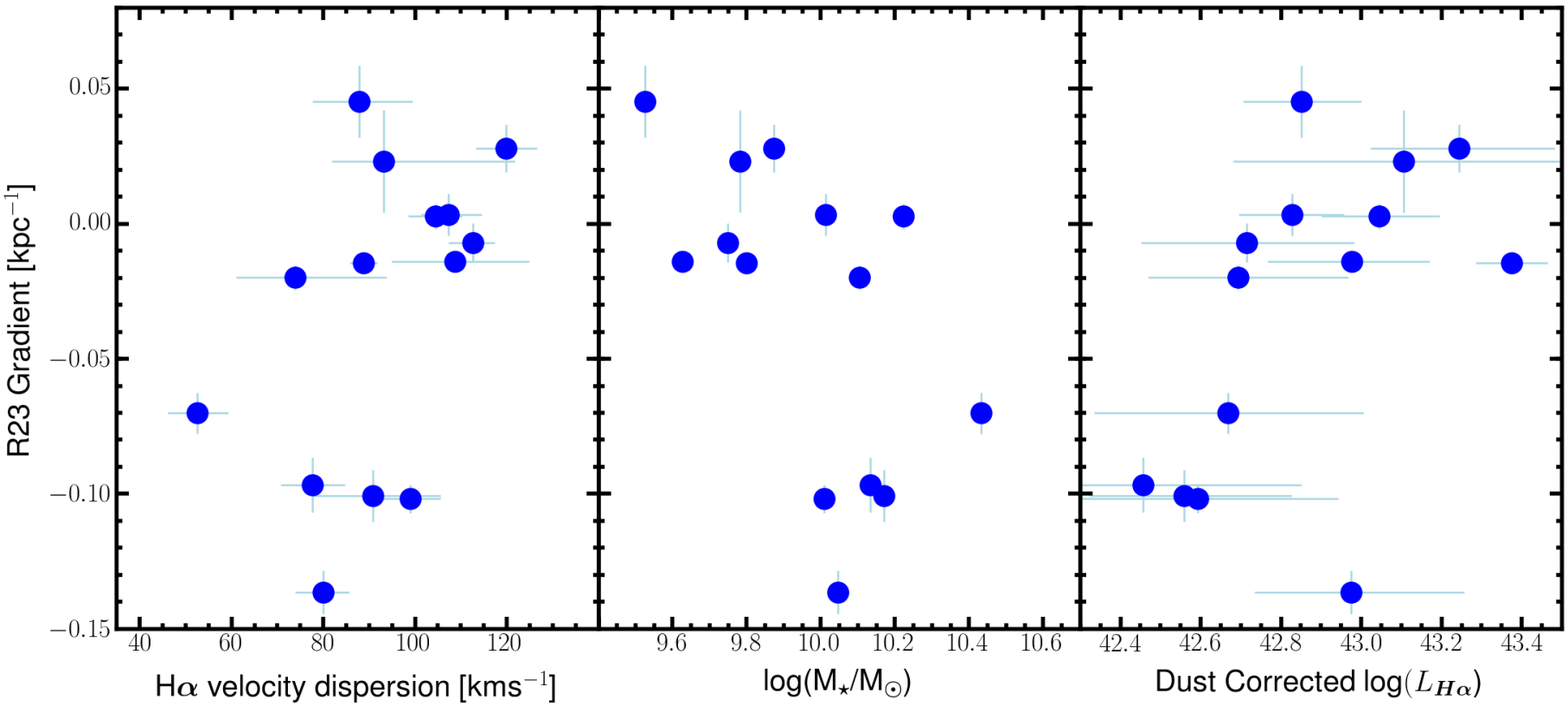

Figure 5.15: The dust-corrected R23 gradient correlations with global galaxy physical properties in the same style as 5.9. The correlation with Hα velocity dispersion is less pronounced, however generally the trends follow that of the Balmer decrements, in that the galaxies with more-negative R23 gradients have larger stellar masses and are less luminous in Hα.

discuss the trends between the emission-line ratios and the distance from galaxy centre, as well as the line-ratio gradients and galaxy physical properties, in more detail.

5.6 Discussion

5.6.1 Balmer decrement gradients

Due to the lack of other literature studies of radial Balmer decrement gradients at high redshift, we attempt to compare with results derived from spatially-resolved measurements of local galaxies. Star-forming galaxies in the local Universe typically have larger extinction values in their centres than in the outskirts (e.g. Boissier et al., 2004; Barrera-Ballesteros et al., 2018) as evidenced by extinction maps derived across individual galaxies from both SED fitting and the Balmer decrement. This is in agreement with the results of this study, in which the majority of galaxies show positive Balmer decrement gradients. Many authors studying low-redshift star-forming galaxies correct emission-line fluxes for extinction using the Balmer decrement derived within individual spaxels, or regions e.g. using MaNGA data (e.g. Belfiore et al., 2016) and SAMI data (e.g. Poetrodjojo et al., 2018). There is, however, a surprising dearth of analysis of the Balmer decrement radial profiles, gradients and correlations between gradients and other physical properties throughout the low-redshift literature. For this reason a detailed comparison of the Balmer decrements of KLEVER survey galaxies with star-forming galaxies in the local Universe will be carried out after the local properties have been studied in more detail. As mentioned previously, our results are consistent with those presented in Nelson et al. (2015), in which more massive galaxies have more central obscuration. Returning to Fig. 5.9, it is the most massive, lowest Hα velocity dispersion and generally the lowest Hα luminosity galaxies that have the most-negative Balmer decrement gradients. This combination of physical properties suggests that the galaxies with more centrally concentrated dust distributions are further through the evolutionary process of settling into stable, rotationally supported disks which have converted most of their gas into stars. The fundamental result of centrally

concentrated dust distributions, which become more extreme with increasing stellar mass, therefore appears consistent in the range $0 < z < 2.3$, although more detailed comparisons, particularly with the local Universe, must be made to explore the evolving dependencies on other physical properties.

5.6.2 Metallicity gradients at high redshift and locally

There is greater scope to compare the results presented in § 5.5.2 and § 5.5.3 with other studies in the literature targetting both local and high-redshift galaxies. The two largest low-redshift IFS surveys, MaNGA and SAMI, both report, using a range of metallicity indicators, that local star-forming galaxies on average exhibit negative metallicity gradients (e.g. Belfiore et al. 2016, 2017 from MaNGA; Poetrodjojo et al. 2018 from SAMI). These studies also demonstrate that the negative metallicity gradients are steepest in the most massive galaxies and flatten in the lowest mass range ($9.0 < \log(M_\star/M_\odot) < 9.5$), but that observing positive metallicity gradients in local galaxies is very rare. Again, it is crucial to note that in this chapter we have not yet converted from line ratios to physical properties, however the qualitative conversions between both O32 and R23 radial profiles and metallicity gradients defined in the previous section suggest that the majority of KLEVER galaxies have negative metallicity gradients. From Fig. 5.12 it also appears broadly true for the KLEVER galaxies that the metallicity gradients become more negative with increasing stellar mass, in agreement with the local results. A detailed comparison of the specific mass range at which gradients begin to flatten at different redshifts, providing an important method to distinguish between galaxy chemical evolution models, is expected to be possible when using the full, completed KLEVER sample. As discussed in the previous section for the Balmer decrement gradients, the physical states of the star-forming galaxies with the most-negative, implied, metallicity gradients suggests that they are further through the typical evolutionary process of converting gas into stars and kinematically settling.

At $z \sim 3$, metallicity gradients from the AMAZE sample have been studied with SINFONI in Troncoso et al. (2014), revealing that the majority of galaxies appear to have positive metallicity gradients, which may be indicative of the prevalence of pristine gas inflow at high redshift (see also Cresci et al. 2010). Although a thorough comparison to this sample will only be possible after the KLEVER metallicities have been computed, the initial results from the high-S/N sample do not appear to be consistent with a majority of positive metallicity gradients. The AMAZE sample does contain lower-mass galaxies on average, which suggests gradients closer to flat, however most of their O32 maps peak in the centre and decrease outwards, in contrast to the profiles shown in Fig. 5.11 (which may partially be a consequence of the application of radial dust corrections informed by the Balmer decrement, which is not possible for the AMAZE sample). Further investigation is required to understand the differences between the measurements from the two samples.

Returning to the peculiar galaxies, in particular GS4_46432 and GS4_46938, which show positive Balmer decrement and R23 gradients and negative O32 gradients as well as blue centres in the *HST* imaging. These galaxies are also characterised by high velocity dispersions, low stellar masses and larger than sample-average Hα luminosities. Further work is required to understand why these objects differ so clearly from the rest of the sample and in which evolutionary stage they reside. It is possible, motivated by the conclusions of Cresci et al. (2010), Troncoso et al. (2014) and Stott et al. (2014) that these galaxies with relatively low stellar mass have recently undergone accretion of pristine gas, which has led to increased turbulence and hence higher velocity dispersions as well as a temporary boost in star-formation rate. It appears that these galaxies are exceptional at $z \simeq 2.3$, however the combined KLEVER lensed and unlensed samples will contribute to our understanding of these possible scenarios, and of the processes involved in chemical evolution generally, using a statistical sample of galaxies.

Common to the analysis of all the line-ratio radial profiles presented above are observational challenges which have not yet been considered in this project. The

ability to infer radial gradients in general will depend on the ratio of the PSF to the intrinsic size, measured using $R_{1/2}$, of the galaxies and also the galaxy inclination angle. We have typically observed in excellent seeing conditions, although part of making this analysis more complete will involve simulating our ability to recover galaxy emission-line ratio gradients observed in different conditions. On top of the above, longer integration times, especially in the *YJ* and *H*−bands would allow for the current results to be extended to greater radii ($> 2R_{1/2}$).

5.6.3 Resolved BPT diagrams

A final view into the variety of ISM conditions probed within individual KLEVER galaxies is provided by the resolved BPT and O32 vs. R23 diagrams shown for 4 high-S/N galaxies in Fig. 5.16. In each of the plots, the square symbols represent the measurements from the square segments, the circular points are the measurements from the annuli and the blue star is the integrated measurement. The point size is determined by distance from the centre of the galaxy, with larger symbols representing greater distances from the centre, and the points are colour coded by the strength of the Balmer decrement as indicated by the colour bars. In the BPT plots, measurements are only included if they have S/N > 2 in Hα, Hβ, [O III]λ5007 and [N II]λ6583 and dust-uncorrected values are used since the ratios are insensitive to dust extinction correction. In the O32 plots, only measurements with S/N > 2 in Hα, Hβ, [O III]λ5007 and [O II]$\lambda\lambda$3727,3729 are used, and we use dust-corrected values.

Clearly the errors on the individual points are large, however it is possible to see the variation in ISM conditions across individual galaxies in these diagrams. The integrated values are averages over a range of conditions and do not provide the full picture, as has been documented at low redshift (e.g. Belfiore et al., 2015, 2016). There has been extensive theoretical investigation, involving photoionisation modelling, into the connection between locations on these diagrams at different redshifts (e.g. Kewley et al., 2013b; Sanders et al., 2016; Strom et al., 2017, 2018) and galaxy ISM properties,

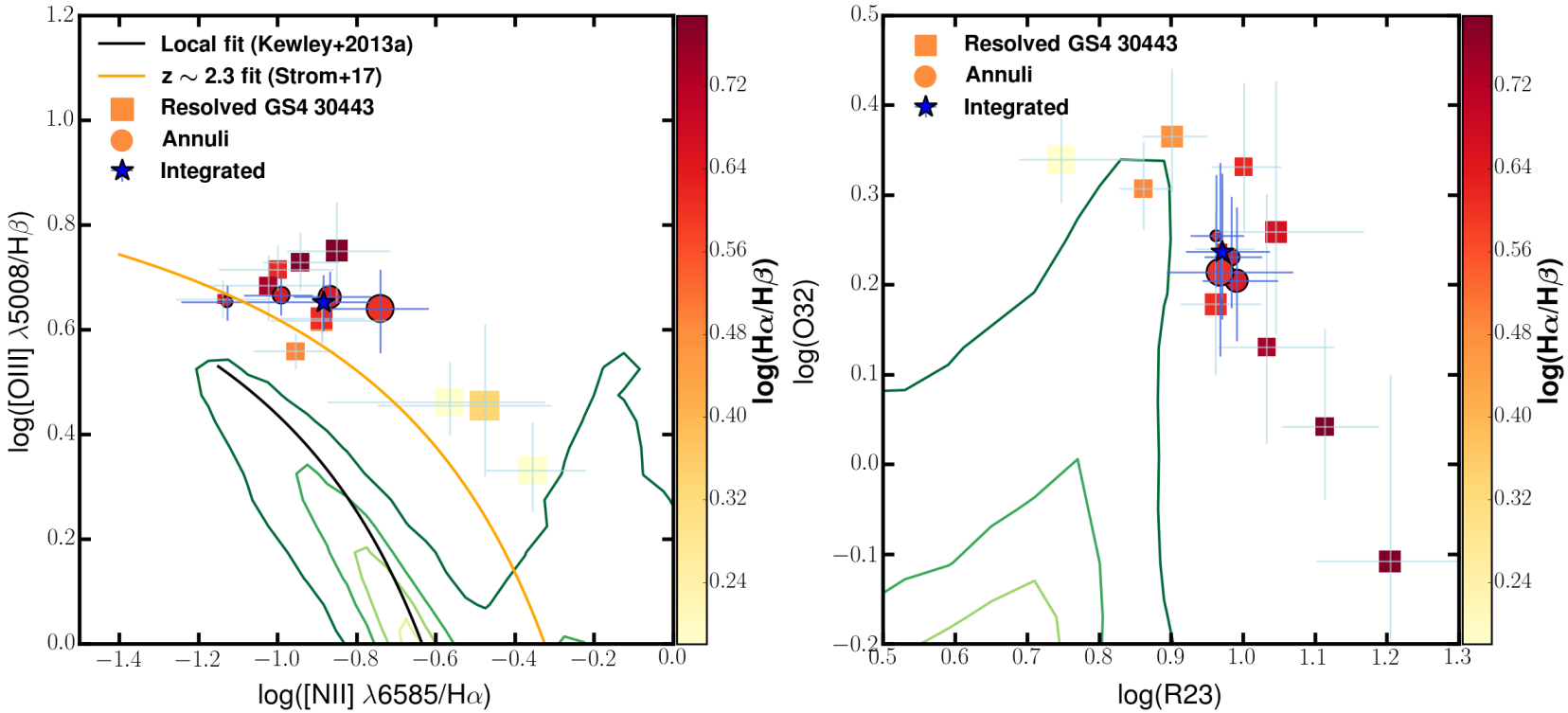

Figure 5.16: *Left:* Galaxy 30443. This and the following plots show the resolved segments (square-symbols), the annuli (circular symbols) and the integrated (blue star) BPT values for individual galaxies in the high-S/N subsample. The green contours show the local relations from SDSS, the black line the fit to local star-forming galaxies from Kewley et al. (2013b) and the orange line the best fit at $z \sim 2.3$ from Strom et al. (2017). The size of the resolved segments and annulus points are dictated by distance from the galaxy centre (larger points further from centre) and are colour coded by the value of the Balmer decrement. Generally the errors on each point are large, however each panel demonstrates the spread of line ratios, and hence of ISM physical conditions, across the spatial extent of the galaxies. *Right:* The same as in the left panel for the O32 vs. R23 diagram.

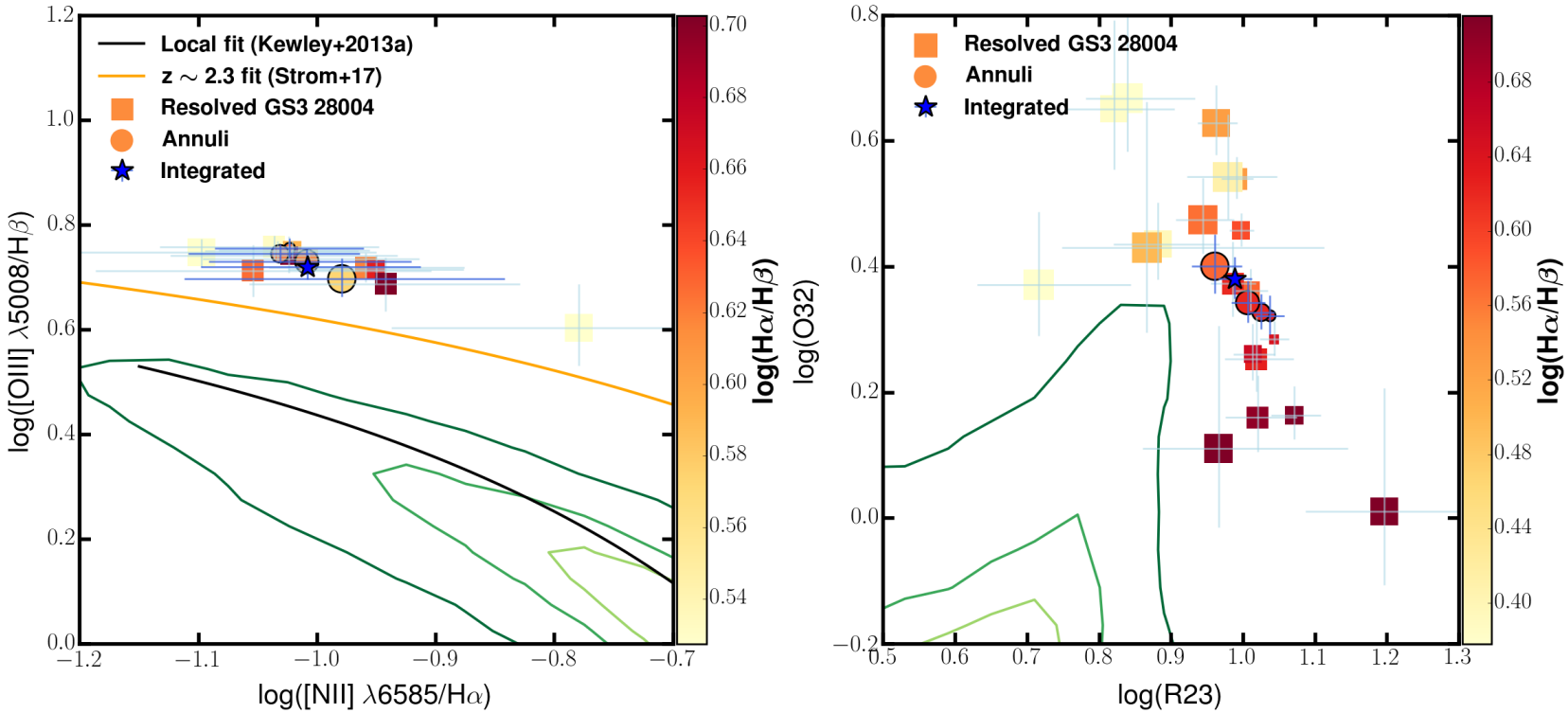

Figure 5.16: Galaxy GS3_28004.

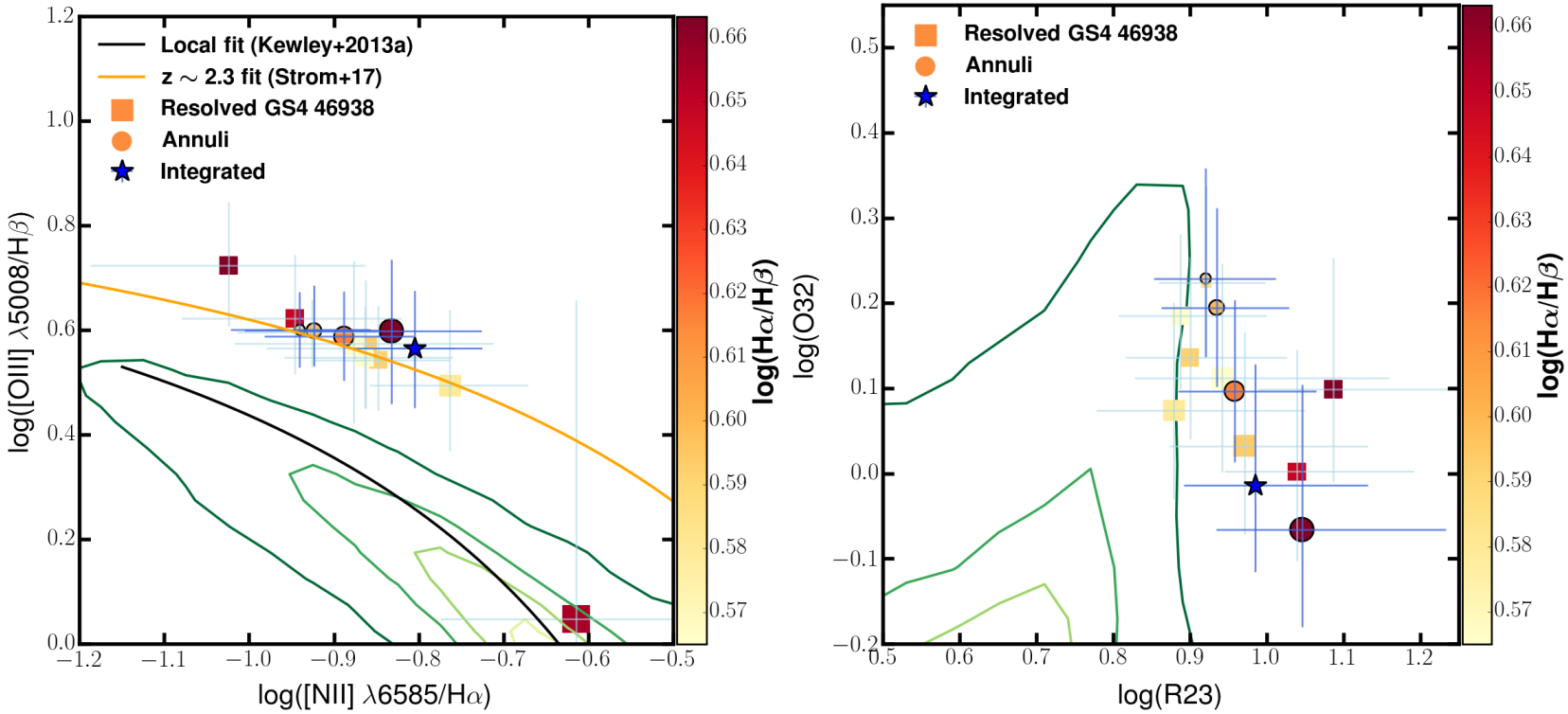

Figure 5.16: Galaxy GS4_46938.

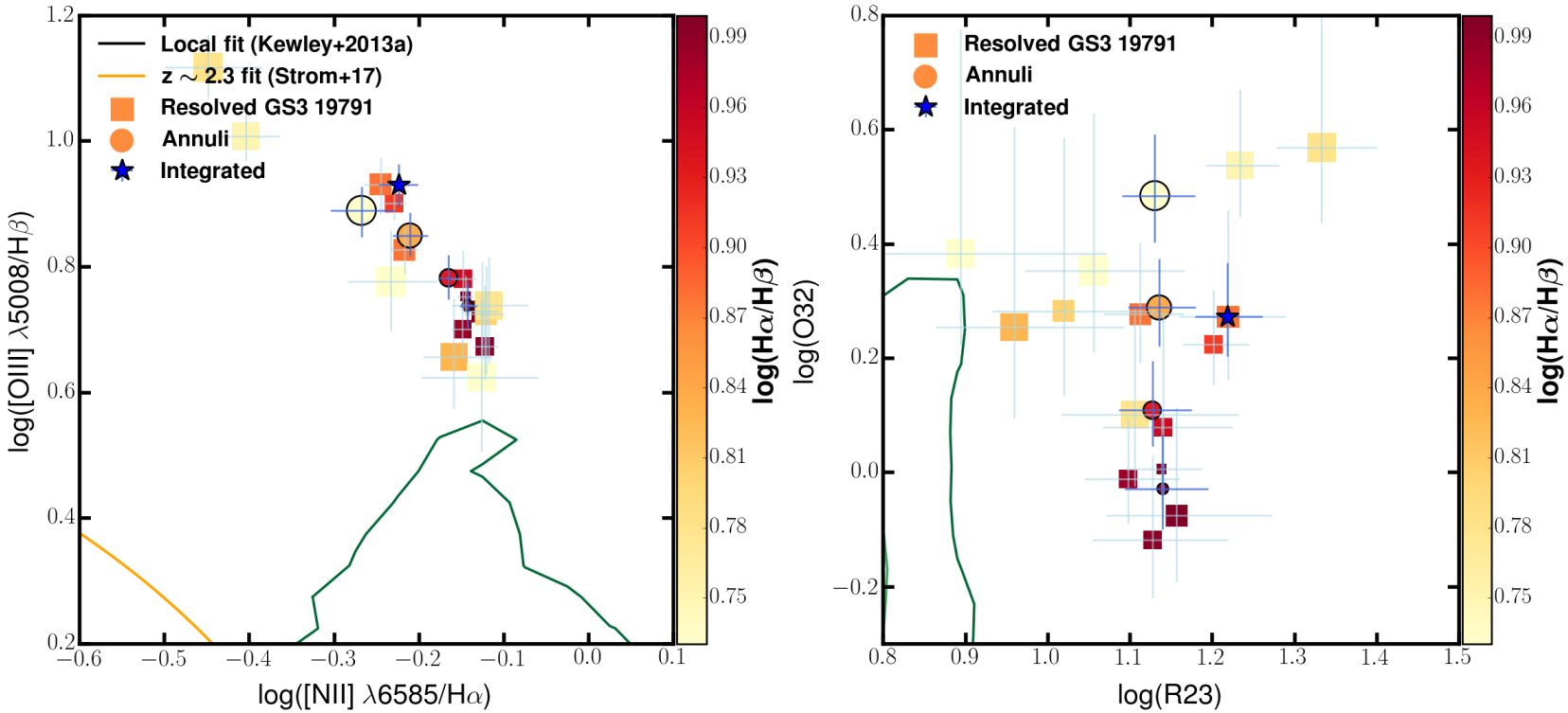

Figure 5.16: AGN candidate galaxy GS3_19791.

which will provide the baseline for making progress with the KLEVER sample. The next step with this project will be to use these photoionisation models to interpret the data. It must be stressed again, however, that these diagrams are currently very challenging to produce at high redshift for individual galaxies, due to the strength of some of the weaker lines. We look forward to a time when it is possible to undertake these types of investigations at $z \sim 2.3$ with the same S/N and angular resolution as is now possible in local galaxies.

5.7 Conclusion

In this chapter, preliminary analysis of emission-line ratio radial gradients in a high-S/N subsample of 18 KLEVER galaxies (the O32 subsample), with median redshift of $z \simeq 2.3$ and median stellar mass of $\log(M_\star/M_\odot) = 10.0$, has been carried out. The findings are summarised in the following points:

- The integrated line ratios of the KLEVER galaxies place them in similar regions of the BPT and O32 vs. R23 diagnostic diagrams to samples at similar redshift from MOSDEF and KBSS-MOSFIRE (see Figures 5.4 and 5.5). The high-redshift distributions are clearly offset from those of SDSS star-forming galaxies, and this has been interpreted throughout the literature as an evolution of average ISM conditions.

- Fitting the strong emission lines within individual spaxels (see Fig. 5.6) reveals that most of the galaxies have clear velocity gradients which are qualitatively similar when traced with both the Hα and [O III]λ5007 emission lines. The spatially-resolved ratios of other emission lines are found to vary across the extents of the galaxies, hinting at the variety of ISM conditions present within individual objects. Combining the emission-line maps with the multiband *HST* images is a powerful tool for diagnosing links between the continuum properties and those of the ionised gas.

- Typically the S/N of the individual spaxels is too low to carry out further

investigation into the radial trends of the emission-line ratios. We instead bin spaxels using annuli constructed from morphological information and a fixed grid of square segments (see Fig. 5.7). The spectra from the spaxels contained within these regions are then summed and fitted following the same procedure as for the integrated spectra.

- Figures 5.8 - 5.15 explore the radial trends of the line ratios and the correlations between the recovered gradients and galaxy physical properties. The majority of Balmer decrement gradients are negative (suggesting centrally concentrated dust distributions), with more-negative gradients observed for galaxies which have lower velocity dispersions, are more massive and have lower dust-corrected Hα luminosities. These physical properties suggest that galaxies with strong, negative Balmer decrement gradients have progressed further through the stages of galaxy evolution. The O32 gradients are generally positive and the R23 gradients are anti-correlated with this and generally negative.

- Some exceptional galaxies emerge from the above analysis, which have positive Balmer decrement gradients and negative O32 gradients. These are likely undergoing different physical processes than the rest of the sample.

- We have qualitatively defined a conversion from O32 to metallicity using the recent Bian et al. (2018) empirical calibration, in which lower O32 values suggest higher metallicities. This implies that the KLEVER galaxies are defined predominantly by negative metallicity gradients, in agreement with IFS studies of local star-forming galaxies but in disagreement with the AMAZE sample at z$\sim$ 3.0.

- The resolved BPT and O32 vs. R23 diagrams (Fig. 5.16) clearly demonstrate the range of ISM properties present within individul galaxies. Utilising the extensive theoretical studies and photoionisation modelling of these diagrams will be the key to converting the line ratios into physical properties.

There is much to learn from studying the spatial variation of emission-line ratios in high-redshift star-forming galaxies, despite the observational challenges associated

with obtaining these measurements. The KLEVER survey has the ambitious goal of extending our understanding of galaxy chemical evolution in the pre-*JWST* and pre-30m class telescope era. The encouraging results described in this chapter will be extended in the future, mainly focussing on confirming that the measurements are robust, converting line ratios to physical properties using photoionisation models and comparing with results at different redshifts in more detail.

Chapter 6

Conclusions and future work

This thesis has presented observational evidence for the spatially-resolved dynamical and chemical compositions of high-redshift galaxies. The findings have been combined with other literature results to examine the evolution of the star-forming galaxy population across cosmic time. The data used were collected using the KMOS instrument operating on UT1 of ESO's Very Large Telescope, and I have invested considereable time exploring and improving my implementation of the data reduction pipeline. Much of the work presented has involved working with faint, distant galaxies and therefore with low-S/N data. Consequently, it has been essential to tease out as much signal from the raw data as possible, whilst minimising the impact of observational factors such as OH skyline emission and beam smearing (as described in Chapter 2). The following sections summarise the primary results of the work I have carried out and outline ongoing and future work stemming from this.

6.1 Summary of the work presented

6.1.1 The KMOS Deep Survey

A large fraction of my thesis is based on the The KMOS Deep Survey, or KDS. This survey was carried out using guaranteed time KMOS observations (for which I contributed as an observer) during ESO observing periods P92-P96 and with PIDs 092.A-0399(A), 093.A-0122(A,B), 094.A-0214(A,B),095.A-0680(A,B),096.A-0315(A,B,C). Over this period, we collected a combination of *H*-band, *K*-band and *HK*-band observations for a sample of 77 typical star-forming galaxies at $3.0 < z < 3.8$. As described throughout Chapter 3, and in Turner et al. (2017), I investigated the internal kinematics of a subsample of 33 isolated field galaxies by modelling the intrinsic rotation velocity fields of the galaxies and fitting to the observed IFS data from KMOS. The results suggest that these galaxies are dynamically hotter than their star-forming counterparts in the local Universe, as evidenced by elevated intrinsic velocity dispersions and low values of $V_C/\sigma_{\rm int}$. One of the key considerations arising from this study, which is to-date the largest sample of star-forming galaxies at $z \simeq 3.5$ with measured kinematics from integral-field-spectroscopy, is the question of what is driving/maintaining the random motions? The elevated velocity dispersions are most likely a relic of the galaxy formation process, and we are observing the galaxies in a pre-disk-settling state, or they are generated by gravitational instabilities across the disk. The low values of $V_C/\sigma_{\rm int}$ also suggest that at high redshift, a larger portion of the dynamical support is provided by random motions rather than the support being dominated by ordered rotation.

Following on from this, I fitted the stellar-mass Tully-Fisher relation, with slope fixed to that of a local comparison sample, to the KDS sample. We focus on the evolution of the *normalisation* of the relation, and find that the KDS rotation-dominated galaxies show evidence for lower rotation velocities at fixed stellar mass than local counterparts. Motivated by the plethora of literature studies at different redshifts which report

discrepant results, I collected 16 distant comparison samples and fit the relation to these following a consistent methodology. In Chapter 4 and Turner et al. (2018), I discuss the relationship between the properties of these comparison samples and the normalisations measured from fitting the Tully-Fisher relationship. This experiment arose from the suspicion that sample selection bias is entirely responsible for the discrepant literature results regarding the evolution of the relationship. Indeed, the results presented in Chapter 4 demonstrate that the median V_C/σ_{int} of a sample dictates the normalisation of the fitted Tully-Fisher relation in a remarkably consistent way. This is apparent when all the samples are considered in a plot of Tully-Fisher offset versus normalised V_C/σ_{int}. Another way of thinking about this is the following. The sample-selection criteria of many high-redshift surveys are geared towards detection success, and so by definition galaxies with bright emission lines (i.e. measured spectroscopic redshifts) are prioritised. This skews the stellar mass distribution of the targets towards higher values. These are also the galaxies which have made further progress towards 'settling', which in this context means that the galaxies are closer to 'pure rotational support' (higher rotation velocities and lower random motions). Sample selection and progress through the stages of galaxy evolution towards forming a thin, rotationally supported disk are thus intertwined at high redshift in a way that they are not in the local Universe. This is why sample selection is so significant in determining the stellar mass Tully-Fisher normalisation (and probably also the slope if the data were there to constrain this) at high redshift.

In Chapter 4, I also explore combining rotation velocity and velocity dispersion into a 'total velocity' for each of the galaxies in the comparison samples, which represents the total kinetic energy. The normalisations of the total-velocity versus stellar-mass relationship fitted to the comparison samples are much more consistent and suggest a gradual decline in normalisation from $z \simeq 3.5$ to $z \simeq 0$. This highlights the importance of accounting for random motions when attempting to trace the potential wells of high-redshift galaxies.

6.1.2 The KLEVER survey

The next step in my thesis has been to expand the study of star-forming galaxies to lower redshift by using a new survey called KLEVER, which has the great advantage of providing access to a complete set of strong-optical emission lines. The KLEVER survey is an ongoing ESO large programme with KMOS, currently comprised of observations collected during ESO observing period P97-P100, with PIDs: 197.A-0717(A,B,C,D). The purpose of the programme is to collect deep KMOS *YJ*-band and *H*-band observations of star-forming galaxies to supplement existing *K*-band measurements from KMOS^{3D}. Together, these observations provide access to the full-suite of rest-optical emission lines which have been calibrated in the local Universe as tracers of the metallicity and ISM conditions in star-forming galaxies. The observations focus partially on strongly-lensed galaxies behind bright galaxy clusters, which are located at both $z \simeq 1.5$ and $z \simeq 2.3$, and on field galaxies which are almost all at $z \simeq 2.3$, aiming to build a sample of 100 lensed and 100 field galaxies. Chapter 5 describes preliminary analysis of the first 4 KMOS pointings dedicated to field galaxies, focussing specifically on measuring the integrated and spatially-resolved emission line ratios of the galaxies.

I have used these observations to initiate the first statistical study of the radial gradients of the observed Balmer decrement values in a high-S/N subset of KLEVER field galaxies. The measurements indicate that the majority of KLEVER galaxies have centrally concentrated dust distributions, evidenced by the negative Balmer decrement gradients, suggesting either that star (and dust) formation has occured preferentially in the galaxy centres and the material has stayed there, or that material has migrated inwards over the course of time. The most-negative Balmer decrement gradients are associated with galaxies that have the lowest velocity dispersions, highest stellar masses and lowest Hα luminosities (i.e. galaxies which carry the hallmarks of being at a later evolutionary stage). These trends are broadly consistent with spatially-resolved results in the local Universe, although there is a surprising paucity of Balmer-

decrement gradient analysis in the literature at both low and high redshift. I then started investigating the radial profiles of metallicity and ISM conditions, as traced by the dust-corrected O32 and R23 ratios. The majority of KLEVER galaxies show positive O32 (negative R23) gradients, which can qualitatively be interpreted as negative metallicity gradients, such as those observed in local star-forming galaxies from the MaNGA and SAMI surveys. The more-negative metallicity gradients are associated with the same physical properties as described above for the negative Balmer decrement gradients. It is important to note that to confirm these results requires photoionisation modelling, in order to translate between line ratios and physical properties whilst properly accounting for degeneracies between ISM properties. This will be carried out in a follow-up study, as described throughout the following subsection.

6.2 Ongoing and future work

6.2.1 Metallicity gradients in the KLEVER high-S/N sample

The analysis described in Chapter 5 has laid the foundations for computing the abundance gradients of galaxies in the KLEVER sample. Nonetheless, several steps must be taken to complete the work. The strength of the KLEVER Survey is that by having the full-line diagnostics, it will be possible to use photoionisation models to properly account for the impact of the gas metallicity, electron density, ionisation parameter and the hardness of the radiation field on the measured line ratios. Following this approach, the metallicity gradients recovered from the lensed and field samples will be compared and aggregated into a statistically signifcant collection spanning a wide range of galaxy physical properties. There are three additional KLEVER field pointings to add to the analysis, with the expected completion date of the observations in ESO observing period P101. As well as the metallicity gradients project, there are several planned ‘next-steps’ for the KLEVER sample which are briefly outlined below.

Connections between spatially-resolved velocities and emission-line ratio gradients

In Chapter 5 I considered the relationship between the integrated velocity dispersions of the KLEVER high-S/N galaxies and the gradients in the radial profiles of the emission-line ratios. The correlation between the O32 gradients and Hα velocity dispersion suggests that there is a connection between the extremity of the ISM conditions and the galaxy kinematics. The integrated velocity dispersions contain a contribution from the bulk-rotation of the galaxy (as a consequence of beam smearing), and so a more rigorous test would use the *intrinsic* velocity dispersions for the comparison. On top of this, it would be interesting to investigate the correlations between $V_C/\sigma_{\rm int}$, a tracer of the dynamical maturity of the galaxies, and the emission-line ratio gradients. The intrinsic rotation velocities and velocity dispersions would be computed as described in Chapter 3, by using the Hα in the *K*-band or [O III]λ5007 in the *H*-band (as shown in Fig. 5.6 of Chapter 5).

Developing new, high-redshift metallicity calibrations

It has been a concern throughout the literature for some time that the metallicity calibrations which have been formulated using very-large samples of local star-forming galaxies may not be applicable to high-redshift star-forming galaxies with different internal ISM conditions. Also, from the results presented in Chapter 5, it is apparent that the ISM conditions vary (sometimes to a large degree) across the face of the galaxies. In these cases it does not make sense to apply a single calibration, tuned to one set of ISM conditions, to the different regions of the galaxies. Indeed, it would have been straightforward to apply a local metallicity calibration to the emission-line ratio values measured in Chapter 5, however the results would not have been accurate. Again, photoionisation modelling may be crucial in formulating new calibrations between line ratios and metallicity based on large statistical samples such as KLEVER.

MUSE and ALMA follow-up

Finally, it will be interesting to expand the wavelength range for which we have resolved measurements of the KLEVER galaxies by considering both MUSE and ALMA data for some of the brightest targets. ALMA continuum measurements provide further constraints on the dust distribution within galaxies, and resolved measurements of the molecular CO line provide important additional constraints on the galaxy kinematics and gas fractions. On the other hand, rest-UV measurements allow for constraints to be placed on the *input* ionising radiation field generated by young stars at the cores of H II regions. On top of this, there are several rest-UV metal emission lines that can help constrain the input parameters of the photoionisation models. Several of the KLEVER targets are already covered serendipitously in the MUSE Deep Field footprints, and so investigating this data is another immediate priority. In recent literature, these types of multi-instrument synergy studies have started to unveil the connections between the output of galaxies in different wavelength regimes *on a spatially-resolved basis*.

6.2.2 KDS ionisation parameter and metallicities

As part of the guaranteed-time observations for the KDS, we also collected deep *H*-band data covering the [O II]$\lambda\lambda$3727,3729 doublet (with excellent seeing conditions) for the target galaxies at $z \simeq 3.5$. At the time of collection (i.e. prior to improving the sky subtraction in the reduction pipeline with ZAP; see § 2.2) the *H*-band datacubes were heavily contaminated with OH residuals. A recent re-reduction greatly improved the data quality and analysis of these data, following the same methodology as described in Chapter 5, is underway. The limitation here is that we do not have access to the Hα line, since it has been redshifted out of the *K*-band, and so cannot study the Balmer decrement gradients or apply differential dust-extinction corrections in the same way as in Chapter 5. However, it may be possible to leverage our understanding of the KLEVER galaxy dust properties to apply a systematic correction to the KDS galaxies as a function of radius. Studying the O32 and R23 ratios for the KDS, and building upon metallicity calibrations derived for the KLEVER sample, will allow for metallicity

gradients to be calculated at $z \simeq 3.5$ for a significant number of galaxies. This, when combined with local results and the KLEVER $z \simeq 1.5$ sample, will provide a coherent picture of spatially-resolved chemical evolution in the interval $0 < z < 3.5$.

6.3 Final remarks

The topics of galaxy formation and evolution are fundamental and dominant components in our understanding of the Universe we inhabit. The considerations involved in these disciplines span backwards in time to the Big Bang and the quantum density fluctuations which seeded the first galaxies, and also forwards to the distant future when we ask what the eventual fate of the 'island Universes' will be. Many open questions remain, of which a short list of those considered in this thesis are listed below:

- How closely do the dynamical structures of very-high redshift star-forming galaxies resemble those at intermediate and low redshift? There is mounting literature evidence for a change in the degree to which galaxies are supported by ordered rotation and random motions over cosmic time, but when and how exactly do galaxies form the thin, rotationally supported disks observed in the local Universe? High-resolution resolved spectroscopy, such as that currently being provided by ALMA, and in the future with ELT, will help to answer these questions.

- To what extent do the stellar and gaseous kinematics of star-forming galaxies match across cosmic time? In principle the stars and gas particles move in the same potential, and so should move in the same way, but different interactions (collisionless versus collisional dynamics) govern the detailed kinematics of these two components. Very deep, resolved observations of the stellar continua, such as those recently reported in the LEGA-C survey, and in the future with MOONS and especially with JWST, will shed light on this issue.

- How can we consistently measure 'metallicity', using a variety of different

tracers, in the extreme and varied ISM conditions of high-redshift galaxies? Large samples of galaxies, observed in a variety of environments and with broad wavelength coverage, such as those we are assembling with the KLEVER programme, are required to answer this question.

- There is now mounting evidence for flat metallicity gradients across the intermediate-redshift regime, mostly determined using an incomplete set of emission-line ratios and with seeing-limited observations. A common explanation for this, which is justified by the results of simulations, is that materials have been redistributed from the inner-regions (i.e. the centre of the potential wells) across the spatial extents of the galaxies by energetic feedback from AGN and evolved stars. To what extent will this prove to be the case, and how does this process depend on other galaxy physical properties such as galaxy stellar/halo mass? More generally, to what extent does energetic feedback contribute to shaping the present day populations of star-forming and passive galaxies?

In order to answer these questions, there has been an explosion of novel data, collected by state-of-the-art instruments, and also computational techniques to analyse this data, over the last decade. Integral-field spectroscopy provides access to the *distribution* of properties within individual galaxies, and so has initiated a new and exciting chapter in the tome of galaxy-evolution studies. Detailed understanding of the dynamical and chemical compositions, as a function of spatial location, of both star-forming and passive galaxies are being developed and pushed to increasingly-high redshifts. The central objective of galaxy evolution now is to use these observational studies in tandem with increasingly-sophisticated simulations to cross-check our theoretical understanding of many of the physical processes for which our knowledge is limited. The next generation of paradigm-shifting facilities, such as *JWST* and the *ELT*, will provide a great leap forwards towards answering the above questions and obtaining the data required to compare with simulations, especially at high redshift. One can imagine, in the not-too-distant future, first-principles simulations operating at very high spatial resolution which reproduce the number counts, morphologies and chemical/dynamical

compositions seen within populations of galaxies from high to low redshifts.

JWST and the *ELT* will also verify much of the work which has been carried out close to signal-to-noise and angular resolution boundaries, such as the results described throughout Chapters 3, 4 and 5. In the meantime, there is much work to be done, and increasingly-so on a spatially-resolved basis, to understand the physical processes which shape the physical properties of galaxies and connect the galaxy populations observed at different stages across the history of the Universe.

Bibliography

Abazajian K., et al., 2009, ApJS, 182, 543

Abramson L. E., Gladders M. D., Dressler A., Oemler A., Poggianti B., Vulcani B., 2016, ApJ, 832, 7

Albrecht A., Steinhardt P. J., 1982, PRL, 48, 1220

Arnouts S., et al., 2002, MNRAS, 329, 355

Arnouts S., et al., 2013, A&A, 558

Bacon R., et al., 2017, A&A, 608

Baldwin J. A., Phillips M. M., Terlevich R., 1981, PASP, 93, 5

Balestra I., et al., 2010, A&A, 512, A12

Balogh M., Pearce F., Bower R., Kay S., 2001, MNRAS, 326, 1228

Barnes J., Efstathiou G., 1987, ApJ, 319, 575

Barrera-Ballesteros J. K., et al., 2014, A&A, 568, A70

Barrera-Ballesteros J. K., et al., 2015, A&A, 582, A21

Barrera-Ballesteros J. K., et al., 2018, ApJ, 852

Behroozi P. S., Wechsler R. H., Conroy C., 2013, ApJ, 770, 57

Belfiore F., et al., 2015, MNRAS, 449, 867

Belfiore F., et al., 2016, MNRAS, 461, 3111

Belfiore F., et al., 2017, MNRAS, 469, 151

Belfiore F., et al., 2018, MNRAS, 477, 3014

Bell E. F., de Jong R. S., 2001, ApJ, 550, 212

Bell E. F., McIntosh D. H., Katz N., Weinberg M. D., 2003, ApJS, 149, 289

Bell E. F., et al., 2004, ApJ, 608, 752

Bertin E., Arnouts S., 1996, A&AS, 117, 393

Bezanson R., et al., 2018

Bian F., Kewley L. J., Dopita M. A., 2018

Bigiel F., Leroy A., Walter F., Brinks E., de Blok W. J. G., Madore B., Thornley M. D., 2008, AJ, 136, 2846

Bluck A. F. L., et al., 2016, MNRAS, 462, 2559

Boissier S., Boselli A., Buat V., Donas J., Milliard B., 2004, A&A, 424, 465

Bouché N., Carfantan H., Schroetter I., Michel-Dansac L., Contini T., 2015, AJ, 150, 92

Bournaud F., Frédéric 2016, Ap&SS, 418, 355

Bournaud F., Elmegreen B. G., Elmegreen D. M., 2007, ApJ, 670, 237

Bournaud F., et al., 2008, A&A, 486, 741

Bouwens R. J., et al., 2015, ApJ, 803

Bower R. G., Benson A. J., Malbon R., Helly J. C., Frenk C. S., Baugh C. M., Cole S., Lacey C. G., 2006, MNRAS, 370, 645

Boyle W. S., Smith G. E., 1970, Bell System Technical Journal, 49, 587

Bradford J. D., Geha M. C., van den Bosch F. C., 2016, ApJ, 832, 11

Brammer G. B., et al., 2011, ApJ, 739, 24

Brammer G. B., et al., 2012, ApJS, 200, 13

Brinchmann J., Charlot S., White S. D. M., Tremonti C., Kauffmann G., Heckman T., Brinkmann J., 2004, Monthly Notices of the Royal Astronomical Society, 351, 1151

Brown M. J. I., Dey A., Jannuzi B. T., Brand K., Benson A. J., Brodwin M., Croton D. J., Eisenhardt P. R., 2007, ApJ, 654, 858

Brown J. S., Martini P., Andrews B. H., 2016, MNRAS, 458, 1529

Bruce V. A., et al., 2012, MNRAS, 427, 1666

Bruzual G., Charlot S., 2003, MNRAS, 344, 1000

Buitrago F., Trujillo I., Conselice C. J., Bouwens R. J., Dickinson M., Yan H., 2008, ApJ, 687, L61

Buitrago F., Trujillo I., Conselice C. J., Haeussler B., 2013, MNRAS, 428, 1460

Bullock J. S., Boylan-Kolchin M., 2017, ARA&A

Bundy K., et al., 2015, ApJ, 798, 7

Burkert A., et al., 2010, ApJ, 725, 2324

Burkert A., et al., 2016, ApJ, 826, 214

Calzetti D., Armus L., Bohlin R., 2000, ApJ, 20, 682

Cappellari M., 2016, ARA&A, p. 67

Cappellari M., et al., 2011, MNRAS, 413, 813

Cassata P., et al., 2015, A&A, 573, A24

Chabrier G., 2003, PASP, 115, 763

Cheng J. Y., et al., 2012, ApJ, 746

Cole S., 1991, ApJ, 367, 45

Cole S., Lacey C., Baugh C., Frenk C., 2000, MNRAS, 319, 168

Colless M., et al., 2001, MNRAS, 328, 1039

Conselice C. J., 2014, ARA&A, 52, 291

Conselice C. J., Bershady M. A., Dickinson M., Papovich C., 2003, AJ, 126, 1183

Conselice C. J., et al., 2011, MNRAS, 413, 80

Contini T., et al., 2012, A&A, 539, A91

Contini T., et al., 2016, A&A, 591, A49

Copernicus N., 1543, De Revolutionibus Orbium Coelestium

Cortese L., et al., 2014, ApJL, 795

Courteau S., 1997, AJ, 114, 2402

Covington M. D., et al., 2010, ApJ, 710, 279

Cowie L. L., Songaila A., Hu E. M., Cohen J. G., 1996, AJ, 112, 839

Cowie L. L., Barger A. J., Songaila A., 2016, ApJ, 817

Crain R. A., et al., 2015, MNRAS, 450, 1937

Cresci G., et al., 2009, ApJ, 697, 115

Cresci G., Mannucci F., Maiolino R., Marconi a., Gnerucci a., Magrini L., 2010, Nature, 467, 811

Croom S. M., et al., 2012, MNRAS, 421, 872

Cullen F., Cirasuolo M., McLure R. J., Dunlop J. S., Bowler R. a. a., 2014, MNRAS, 440, 2300

Cullen F., Cirasuolo M., Kewley L. J., McLure R. J., Dunlop J. S., Bowler R. A. A., 2016, MNRAS, 460, 3002

Curti M., Cresci G., Mannucci F., Marconi A., Maiolino R., Esposito S., 2017, MNRAS, 465, 1384

DES Collaboration D., et al., 2017

Daddi E., et al., 2007, ApJ, 670, 156

Darvish B., Mobasher B., Sobral D., Rettura A., Scoville N., Faisst A., Capak P., 2016, ApJ, 825, 113

Davé R., Oppenheimer B. D., Finlator K., 2011a, MNRAS, 415, 11

Davé R., Finlator K., Oppenheimer B. D., 2011b, MNRAS, 416, 1354

Davé R., Finlator K., Oppenheimer B. D., 2012, MNRAS, 421, 98

Davies R. I., 2007, MNRAS, 375, 1099

Davies R., et al., 2011, ApJ, 741, 69

Davies R. I., et al., 2013, ApJ, 558, A56

Dekel A., Birnboim Y., 2006, MNRAS, 368, 2

Dekel A., et al., 2009, Nature, 457, 451

Di Teodoro E., Fraternali F., 2015, MNRAS, 451, 3021

Di Teodoro E. M., Fraternali F., Miller S. H., 2016, A&A, 594, A77

Domínguez A., et al., 2013, ApJ, 763

Dopita M. A., Kewley L. J., Sutherland R. S., Nicholls D. C., 2016, Ap&SS, 361

Dreyer J. L. E., 1888, Memoirs of the Royal Astronomical Society, Vol. 49, p.1, 49, 1

Dubois Y., et al., 2014, MNRAS, 444, 1453

Dunlop J., 1828, Philosophical Transactions of the Royal Society of London, Volume 118, pp. 113-151, 118, 113

Dutton A. A., van den Bosch F. C., Dekel A., 2010, MNRAS, 405, 1690

Dutton A. A., et al., 2011, MNRAS, 410, 1660

Ebeling H., Barrett E., Donovan D., Ma C. J., Edge A. C., van Speybroeck L., 2007, ApJ, 661, L33

Efstathiou G., Jones B. J. T., 1979, MNRAS, 186, 133

Eggen O. J., Lynden-Bell D., Sandage A. R., 1962, ApJ, 136, 748

Einstein A., 1916, Annalen der Physik, 354, 769

Eisenhauer F., et al., 2003, SPIE, 4841, 1548

Elbaz D., et al., 2007, A&A, 468, 33

Elmegreen D. M., Elmegreen B. G., Sheets C. M., 2004, ApJ, 603, 74

Epinat B., et al., 2008a, MNRAS, 388, 500

Epinat B., Amram P., Marcelin M., 2008b, MNRAS, 390, 466

Epinat B., et al., 2009, A&A, 504, 789

Epinat B., Amram P., Balkowski C., Marcelin M., 2010, MNRAS, 401, 2113

Epinat B., et al., 2012, A&A, 539, A92

Erb D., Shapley A., Pettini M., Steidel C., Reddy N., Adelberger K., 2006, ApJ, 644, 813

Faber S. M., et al., 2007, ApJ, 665, 265

Fall S. M., 1983, IN: Internal kinematics and dynamics of galaxies; Proceedings of the Symposium, Besancon, France, August 9-13, 1982 (A83-49201 24-89). Dordrecht, D. Reidel Publishing Co., 1983, p. 391-398; Discussion, 399., 100, 391

Fall S. M., Romanowsky A. J., 2013, ApJL, 769, L26

Fang J. J., Faber S. M., Koo D. C., Dekel A., 2013, ApJ, 776

Ferland G. J., et al., 2013, Revista Mexicana de Astronomía y Astrofísica Vol. 49, pp. 137-163 (2013), 49, 137

Flores H., Hammer F., Puech M., Amram P., Balkowski C., 2006, A&A, 455, 107

Foreman-Mackey D., Hogg D. W., Lang D., Goodman J., 2013, PASP, 125, 306

Forster Schreiber N. M., et al., 2006, ApJ, 645, 1062

Förster Schreiber N. M., et al., 2009, ApJ, 706, 1364

Förster Schreiber N. M., et al., 2011, ApJ, 739, 45

Förster Schreiber N. M., et al., 2018, preprint, (arxiv:1802.07276)

Fraunhofer J., 1817, Annalen der Physik, 56, 264

Freeman K. C., 1970, ApJ, 160, 811

Freudling W., Romaniello M., Bramich D. M., Ballester P., Forchi V., Garcia-Dablo C. E., Moehler S., Neeser M. J., 2013, A&A, 559, A96

Friel E. D., Janes K. A., Tavarez M., Scott J., Katsanis R., Lotz J., Hong L., Miller N., 2002, AJ, 124, 2693

Gamow G., 1946, Physical Review, 70, 572

Gamow G., 1948, Physical Review, 74, 505

Gamow G., Teller E., 1939, Physical Review, 55, 654

Gao Y., Solomon P. M., 2004, ApJ, 606, 271

Genel S., Fall S. M., Hernquist L., Vogelsberger M., Snyder G. F., Rodriguez-Gomez V., Sijacki D., Springel V., 2015, ApJL, 804

Genzel R., et al., 2006, Nature, 442, 786

Genzel R., et al., 2008, ApJ, 687, 59

Genzel R., et al., 2010, MNRAS, 407, 2091

Genzel R., et al., 2011, ApJ, 733, 101

Genzel R., et al., 2017, Nature, 543, 397

Gibson B. K., Pilkington K., Brook C. B., Stinson G. S., Bailin J., 2013, A&A, 554

Girard M., et al., 2018, A&A, 613

Gladders M. D., Oemler A., Dressler A., Poggianti B., Vulcani B., Abramson L., 2013, ApJ, 770, 64

Glazebrook K., 2013, PASP, 30, e056

Gnerucci A., et al., 2011, A&A, 528, A88

Green A. W., et al., 2014, MNRAS, 437, 1070

Grogin N. A., et al., 2011, ApJS, 197, 35

Guerou A., et al., 2017, A&A, 608

Guo Y., et al., 2013, ApJS, 207, 24

Guth A. H., 1981, Physical Review, 23, 347

Guzzo L., et al., 2014, A&A, 566

Hammer F., Puech M., Chemin L., Flores H., Lehnert M., 2007, ApJ, 662, 322

Harrison C. M., et al., 2017, MNRAS, 467, 1965

Häußler B., et al., 2007, ApJS, 172, 615

Herschel W., 1802, Philosophical Transactions of the Royal Society of London, Volume 92, pp. 477-528, 92, 477

Herschel J. F. W., 1864, Philosophical Transactions of the Royal Society of London, Volume 154, pp. 1-137, 154, 1

Heymans C., et al., 2013, MNRAS, 432, 2433

Hildebrandt H., et al., 2017, MNRAS, 465, 1454

Holmberg E., 1958, Meddelanden fran Lunds Astronomiska Observatorium Serie II, 136, 1

Hopkins P. F., Kere D., Onorbe J., Faucher-Giguere C.-A., Quataert E., Murray N., Bullock J. S., 2014, MNRAS, 445, 581

Hopkins P. F., et al., 2017, eprint arXiv:1702.06148

Hoyle F., 1949, MNRAS, 109, 365

Hubble E. P., 1925, ApJ, 62, 409

Hubble E. P., 1926a, ApJ, 63, 236

Hubble E. P., 1926b, ApJ, 64, 321

Hubble E., 1929a, PNAS, 15, 168

Hubble E. P., 1929b, ApJ, 69, 103

Hung C.-L., et al., 2015, ApJ, 803, 62

Hung C.-L., et al., 2018

Huygens C., 1690, Traité de la lumière

Ilbert O., et al., 2006, A&A, 457, 841

Ilbert O., et al., 2010, ApJ, 709, 644

Ilbert O., et al., 2015, A&A, 579

Jeans J. H., 1902, Philosophical Transactions of the Royal Society A: Mathematical, Physical and Engineering Sciences, 199, 1

Johnson H. L., et al., 2018, MNRAS, 474, 5076

Jones T. A., Swinbank A. M., Ellis R. S., Richard J., Stark D. P., 2010, MNRAS, 404, 1247

Jones T., Ellis R. S., Richard J., Jullo E., 2013, ApJ, 765, 48

Karim A., et al., 2011, ApJ, 730, 61

Kashino D., et al., 2016, ApJ, 835

Kassin S. A., et al., 2007, ApJ, 660, L35

Kassin S. A., et al., 2012, ApJ, 758, 106

Kauffmann G., 2003, MNRAS, 341, 33

Kaviraj S., et al., 2013, MNRASL, 429, L40

Kelson D. D., 2014, preprint, (arxiv:1406.5191)

Kennicutt R. C., 1998, ARA&A, 36, 189

Kennicutt R., Evans N., 2012, ARA&A, 50, 531

Kennicutt R. C., C. R., Jr. 1998, ApJ, 498, 541

Kent S. M., 1986, AJ, 91, 1301

Kent S. M., 1987, AJ, 93, 816

Kent S. M., 1988, AJ, 96, 514

Kepler J., 1619, Harmonices mundi

Kewley L., Dopita M., 2001, ApJ, 20

Kewley L., Dopita M., 2002, ApJS, pp 35–52

Kewley L., Ellison S., 2008, ApJ, 681, 1183

Kewley L. J., Dopita M. A., Leitherer C., Davé R., Yuan T., Allen M., Groves B., Sutherland R., 2013a, ApJ, 774, 100

Kewley L., Maier C., Yabe K., 2013b, ApJ, 1307, 514

Khochfar S., Burkert A., 2001, ApJ, 561, 517

Khochfar S., Silk J., 2006, ApJ, 648, L21

Khostovan A. A., Sobral D., Mobasher B., Best P. N., Smail I., Stott J. P., Hemmati S., Nayyeri H., 2015, MNRAS, 452, 3948

Kimura M., et al., 2010, PASJ, 62, 1135

Kirchhoff G., 1860, Annalen der Physik und Chemie, 185, 275

Kodama T., Tanaka I., Kajisawa M., Kurk J., Venemans B., De Breuck C., Vernet J., Lidman C., 2007, MNRAS, 377, 1717

Koekemoer A. M., et al., 2011, ApJS, 197, 36

Kormendy J., Kennicutt R. C., 2004, ARA&A, 42, 603

Krajnovic D., Cappellari M., De Zeeuw P. T., Copin Y., 2006, MNRAS, 366, 787

Krist J. E., Hook R. N., Stoehr F., 2011, SPIE, 8127, 81270J

Kroupa P., 2002, Science, 295, 82

Krumholz M. R., Burkhart B., Forbes J. C., Crocker R. M., 2017

Lagos C. d. P., Theuns T., Stevens A. R. H., Cortese L., Padilla N. D., Davis T. A., Contreras S., Croton D., 2017, MNRAS, 464, 3850

Laigle C., et al., 2016, ApJS, 224

Lang P., et al., 2017, ApJ, 840, 92

Larson R. B., 1974, MNRAS, 169, 229

Law D. R., Steidel C. C., Erb D. K., Larkin J. E., Pettini M., Shapley A. E., Wright S. A., 2007, ApJ, 669, 929

Law D. R., Steidel C. C., Erb D. K., Larkin J. E., Pettini M., Shapley A. E., Wright S. A., 2009, ApJ, 697, 2057

Law D. R., Steidel C. C., Shapley A. E., Nagy S. R., Reddy N. A., Erb D. K., 2012a, ApJ, 85, 85

Law D. R., Shapley A. E., Steidel C. C., Reddy N. A., Christensen C. R., Erb D. K., 2012b, Nature, 487, 338

Law D. R., Steidel C. C., Shapley A. E., Nagy S. R., Reddy N. A., Erb D. K., 2012c, ApJ, 759, 29

Le Fevre O., et al., 2003, SPIE, 4841, 1670

Leavitt H. S., 1908, Annals of Harvard College Observatory, vol. 60, pp.87-108.3, 60, 87

Leavitt H. S., Pickering E. C., 1912, Harvard College Observatory Circular, vol. 173, pp.1-3, 173, 1

Lee N., et al., 2015, ApJ, 801, 80

Leethochawalit N., Jones T. A., Ellis R. S., Stark D. P., Richard J., Zitrin A., Auger M., 2016, ApJ, 820

Lelli F., McGaugh S. S., Schombert J. M., 2016, AJ, 152

Lemoine-Busserolle M., Bunker A., Lamareille F., Kissler-Patig M., 2010, MNRAS, 401, 1657

Lifshitz E. M., 1946, Zhurnal Eksperimental'noi i Teoreticheskoi Fiziki, 16, 587

Lilly S. J., et al., 2007, ApJS, 172, 70

Lilly S. J., Carollo C. M., Pipino A., Renzini A., Peng Y., 2013, ApJ, 772, 119

Lin L., et al., 2017, ApJ, 851

Linde A., D. A., 1982, Physics Letters B, 108, 389

Livermore R. C., et al., 2015, MNRAS, 450, 1812

Lofthouse E. K., Kaviraj S., Conselice C. J., Mortlock A., Hartley W., 2017, MNRAS, 465, 2895

Longair M. S., 2006, The Cosmic Century. Cambridge University Press, Cambridge, doi:10.1017/CBO9781139878319

Lotz J. M., et al., 2008, ApJ, 672, 177

Lotz J. M., Jonsson P., Cox T. J., Croton D., Primack J. R., Somerville R. S., Stewart K., 2011, ApJ, 742, 103

Maciel W. J., Costa R. D. D., Uchida M. M. M., 2003, A&A, 397, 667

Madau P., Dickinson M., 2014, ARA&A, 52, 415

Maiolino R., et al., 2008, A&A, 488, 463

Maiolino R., Russell H. R., Fabian A. C., Carniani S., Gallagher R., Cazzoli S., 2017, Nature

Mannucci F., Cresci G., Maiolino R., Marconi A., Gnerucci A., 2010, MNRAS, 408, 2115

Marcon-Uchida M. M., Matteucci F., Costa R. D. D., 2010, A&A, 520

Martin D. C., et al., 2007, ApJS, 173, 342

Mason C. A., et al., 2017, ApJ, 838, 14

Masters D., et al., 2014, ApJ, 785

Masters D., Faisst A., Capak P., 2016, ApJ, 828

Matsuda Y., et al., 2004, AJ, 128, 569

McGaugh S. S., 1991, ApJ, 380, 140

McLean I. S., et al., 2012, SPIE, 8446, 84460J

McLeod D. J., McLure R. J., Dunlop J. S., Robertson B. E., Ellis R. S., Targett T. A., 2015, MNRAS, 450, 3032

McLure R. J., et al., 2011, MNRAS, 418, 2074

Messier C., 1781, Connoissance des Temps ou des Mouvements Célestes, for 1784, p. 227-267, pp 227–267

Miller S. H., Bundy K., Sullivan M., Ellis R. S., Treu T., 2011, ApJ, 741, 115

Miller S. H., Ellis R. S., Sullivan M., Bundy K., Newman A. B., Treu T., 2012, ApJ, 753, 74

Miller S. H., Ellis R. S., Newman A. B., Benson A., 2014, ApJ, 782, 115

Mo H. J., Mao S., White S. D. M., 1998, MNRAS, 295, 319

Mo H., van den Bosch F. C., White S., 2010, Galaxy Formation and Evolution. Cambridge University Press

Molina J., Ibar E., Swinbank A. M., Sobral D., Best P. N., Smail I., Escala A., Cirasuolo M., 2017, MNRAS, 466, 892

Momcheva I. G., et al., 2016, ApJS, 225, 27

Moore B., Lake G., Katz N., 1997,] 10.1086/305264

Moster B. P., Naab T., White S. D. M., 2013, MNRAS, 428, 3121

Moustakas J., Kennicutt R. C., Tremonti C. A., Dale D. A., Smith J.-D. T., Calzetti D., 2010, ApJS, 190, 233

Moustakas J., et al., 2011, eprint arXiv:1112.3300

Muzzin A., et al., 2013, ApJ, 777, 18

Naab T., Ostriker J. P., 2017, ARA&A, 55, 59

Nagao T., Maiolino R., Marconi A., 2006, A&A, 459, 85

Neichel B., et al., 2008, A&A, 484, 159

Nelson E. J., et al., 2015

Nelson E. J., et al., 2016, ApJ, 828, 27

Nestor D. B., Shapley A. E., Steidel C. C., Siana B., 2011, ApJ, 736, 18

Nestor D. B., Shapley A. E., Kornei K. A., Steidel C. C., Siana B., 2013, ApJ, 765, 47

Newman S. F., et al., 2013, ApJ, 767, 104

Newton I., 1687, Philosophiae Naturalis Principia Mathematica

Newville M., Ingargiola A., Stensitzki T., Allen D. B., 2014,] 10.5281/ZENODO.11813

Noeske K. G., et al., 2007a, ApJ, 660, L47

Noeske K. G., et al., 2007b, ApJ, 660, L43

Noll S., Kausch W., Kimeswenger S., Barden M., Jones A. M., Modigliani A., Szyszka C., Taylor J., 2014, A&A, 567, A25

Obreschkow D., et al., 2016, ApJ, 815, 97

Osterbrock D., 1989, Astrophysics of gaseous nebulae and active galactic nuclei. University Science Books

Ott T., Thomas 2012, Astrophysics Source Code Library, record ascl:1210.019

Pagel B. E. J., Edmunds M. G., Blackwell D. E., Chun M. S., Smith G., 1979, Monthly Notices of the Royal Astronomical Society, 189

Pannella M., et al., 2014, ApJ, 807, 141

Patricio V., et al., 2018, MNRAS, 477, 18

Patrick L. R., Evans C. J., Davies B., Kudritzki R.-P., Ferguson A. M. N., Bergemann M., Pietrzyński G., Turner O., 2017, MNRAS, 468, 492

Paturel G., Petit C., Prugniel P., Theureau G., Rousseau J., Brouty M., Dubois P., 2003, A&A, 412, 45

Peebles P. J. E., 1969, ApJ, 155, 393

Pelliccia D., Tresse L., Epinat B., Ilbert O., Scoville N., Amram P., Lemaux B. C., Zamorani G., 2017, A&A, 25, 1

Peng C. Y., Ho L. C., Impey C. D., Rix H.-W., 2010a, AJ, 139, 2097

Peng Y.-j., et al., 2010b, ApJ, 721, 193

Peng Y., Maiolino R., Cochrane R., 2015, Nature, 521, 192

Perlmutter S., et al., 1998, ApJ, 517, 565

Pettini M., Pagel B., 2004, MNRAS, 348, L59

Pforr J., Maraston C., Tonini C., 2012, MNRAS, 422, 3285

Pillepich A., et al., 2018, MNRAS, 473, 4077

Pilyugin L. S., 2001, A&A, 369, 594

Pilyugin L. S., Thuan T. X., 2005, ApJ, 631, 231

Pilyugin L. S., Vílchez J. M., Thuan T. X., 2010, ApJ, 720, 1738

Pilyugin L. S., Grebel E. K., Mattsson L., 2012, MNRAS, 424, 2316

Pizagno J., et al., 2005, ApJ, 633, 844

Pizagno J., et al., 2007, AJ, 134, 945

Planck Collaboration P., et al., 2015, A&A, 594

Poetrodjojo H., et al., 2018, MNRAS, 479, 5235

Puech M., et al., 2008, A&A, 484, 173

Puech M., Hammer F., Flores H., Delgado-Serrano R., Rodrigues M., Yang Y., 2010, A&A, 510, A68

Qu Y., et al., 2017, MNRAS, 464, 1659

Queyrel J., et al., 2012, A&A, 539, A93

Reddy N. A., et al., 2015, p. 24

Renzini A., Peng Y., 2015, ApJL, 801, L29

Reyes R., Mandelbaum R., Gunn J. E., Pizagno J., Lackner C. N., 2011, MNRAS, 417, 2347

Rhee G., Valenzuela O., Klypin A., Holtzman J., Moorthy B., 2003, ApJ, 617, 1059

Riess A. G., et al., 1998, AJ, 116, 1009

Robaina A. R., et al., 2009, ApJ, 704, 324

Robotham A. S. G., Obreschkow D., 2015, PASP, 32

Rodighiero G., et al., 2010, A&A, 518

Rodighiero G., et al., 2011, ApJ, 739, L40

Rodighiero G., et al., 2014, MNRAS, 443, 19

Rodrigues M., Hammer F., Flores H., Puech M., Athanassoula E., 2017, MNRAS, 465, 1157

Romanowsky A. J., Fall S. M., 2012, ApJS, 203, 17

Rubin V. C., Thonnard N., Ford, W. K. J., 1978, ApJ, 225, L107

Rubin V. C., Thonnard N., Ford, W. K. J., 1980, ApJ, 238, 471

Rubin V. C., Thonnard N., Ford, W. K. J., Burstein D., 1982, ApJ, 261, 439

Rubin V. C., Burstein D., Ford, W. K. J., Thonnard N., 1985, ApJ, 289, 81

Rupke D. S. N., Kewley L. J., Barnes J. E., 2010a, ApJL, 710, L156

Rupke D. S. N., Kewley L. J., Chien L. H., 2010b, ApJ, 723, 1255

Saintonge A., et al., 2013, ApJ, 778, 2

Salim S., Lee J. C., Davé R., Dickinson M., 2015, ApJ, 808

Salpeter E. E., 1955, ApJ, 121, 161

Sanchez S. F., et al., 2014, A&A, 563

Sanders R. L., et al., 2015, ApJ, 799, 138

Sanders R. L., et al., 2016, ApJ, 816, 23

Sanders R. L., Shapley A. E., Zhang K., Yan R., 2017

Santini P., et al., 2015, ApJ, 801, 97

Sarzi M., et al., 2006, MNRAS, 366, 1151

Schaye J., et al., 2015, MNRAS, 446, 521

Schiminovich D., et al., 2007, ApJS, 173, 315

Schmidt M., Maarten 1959, ApJ, 129, 243

Schreiber C., et al., 2015, A&A, 575, A74

Searle L., 1971, ApJ, 168, 327

Shapiro K. L., et al., 2008, ApJ, 682, 231

Shapley A. E., Steidel C. C., Pettini M., Adelberger K. L., 2003, ApJ, 588, 65

Shapley A. E., et al., 2015, ApJ, 801, 88

Sharples R., et al., 2005, The Messenger, pp 2–5

Sharples R., et al., 2013, The Messenger, 151, 21

Simons R. C., et al., 2016, ApJ, 830, 14

Simons R. C., et al., 2017, ApJ, 843, 46

Slipher V. M., 1917, Proceedings of the American Philosophical Society, vol. 56, p.403-409, 56, 403

Sobral D., Smail I., Best P. N., Geach J. E., Matsuda Y., Stott J. P., Cirasuolo M., Kurk J., 2013a, MNRAS, 428, 1128

Sobral D., et al., 2013b, ApJ, 779, 139

Sobral D., Best P. N., Smail I., Mobasher B., Stott J., Nisbet D., 2014, MNRAS, 437, 3516

Somerville R. S., Davé R., 2015, ARA&A, 53, 51

Soto K. T., Lilly S. J., Bacon R., Richard J., Conseil S., 2016,] 10.1093/mnras/stw474

Sparre M., et al., 2015, MNRAS, 447, 3548

Speagle J. S., Steinhardt C. L., Capak P. L., Silverman J. D., 2014, ApJS, 214, 15

Spergel D. N., et al., 2007, ApJS, 170, 377

Springel V., et al., 2005, Nature, 435, 629

Springel V., et al., 2008, MNRAS, 391, 1685

Stasińska Â., 2002a, eprint arXiv:astro-ph/0207500

Stasińska G., 2002b, Ionized Gaseous Nebulae, 12, 62

Steidel C., Adelberger K., Dickinson M., Giavalisco M., Pettini M., Kellogg M., 1998, ApJ, 492, 428

Steidel C. C., Adelberger K. L., Shapley A. E., Pettini M., Dickinson M., Giavalisco M., 2000, ApJ, 532, 170

Steidel C. C., Adelberger K. L., Shapley A. E., Pettini M., Dickinson M., Giavalisco M., 2003, ApJ, 592, 728

Steidel C. C., et al., 2014, ApJ, 795, 165

Steidel C. C., Strom A. L., Pettini M., Rudie G. C., Reddy N. A., Trainor R. F., 2016, ApJ, 826

Steidel C. C., Bogosavlevic M., Shapley A. E., Reddy N. A., Rudie G. C., Pettini M., Trainor R. F., Strom A. L., 2018

Stott J. P., Sobral D., Smail I., Bower R., Best P. N., Geach J. E., 2013a, MNRAS, 430, 1158

Stott J. P., et al., 2013b, MNRAS, 436, 1130

Stott J. P., et al., 2014, MNRAS, 443, 2695

Stott J. P., et al., 2016, MNRAS, 457, 1888

Straatman C. M. S., et al., 2017, ApJ, 839, 57

Strom A. L., Steidel C. C., Rudie G. C., Trainor R. F., Pettini M., Reddy N. A., 2017, ApJ, 836

Strom A. L., Steidel C. C., Rudie G. C., Trainor R. F., Pettini M., 2018, eprint arXiv:1711.08820

Sutherland R. S., Dopita M. A., 1993, ApJS, 88, 253

Swinbank A. M., Bower R. G., Smith G. P., Wilman R. J., Smail I., Ellis R. S., Morris S. L., Kneib J.-P., 2007, MNRAS, 376, 479

Swinbank A. M., Sobral D., Smail I., Geach J. E., Best P. N., McCarthy I. G., Crain R. A., Theuns T., 2012a, MNRAS, 426, 935

Swinbank M., Smail I., Sobral D., Theuns T., Best P., Geach J., 2012b, ApJ, 760, 130

Swinbank M., et al., 2017, MNRAS, 467, 3140

Tacchella S., Dekel A., Carollo C. M., Ceverino D., DeGraf C., Lapiner S., Mandelker N., Primack J. R., 2015, p. 25

Tacconi L. J., et al., 2010, Nature, 463, 781

Tacconi L. J., et al., 2013, ApJ, 768, 74

Tacconi L. J., et al., 2018, ApJ, 853

Tasca L. A. M., et al., 2016, preprint (arxiv:1602.01842)

Tiley A. L., et al., 2016, MNRAS, 460, 103

Tiley A. L., et al., 2019, MNRAS, 482, 2166

Toft S., et al., 2007, ApJ, 671, 285

Toft S., et al., 2017, Nature, 546, 510

Toomre a., 1964, ApJ, 139, 1217

Toomre A., 1977, Conference Proceedings, p. 401

Toomre A., Toomre J., 1972, ApJ, 178, 623

Tremonti C., Heckman T., 2004, The Astrophysical . . . , pp 898–913

Troncoso P., et al., 2014, A&A, 563, A58

Trujillo I., Conselice C. J., Bundy K., Cooper M. C., Eisenhardt P., Ellis R. S., 2007, MNRAS, 382, 109

Tully R. B., Fisher J. R., 1977, A&A 54, 661

Turner O. J., et al., 2017, MNRAS, 471, 1280

Turner O. J., Harrison C. M., Cirasuolo M., McLure R. J., Dunlop J., Swinbank A. M., Tiley A. L., 2018, eprint arXiv:1711.03604

Übler H., et al., 2017, ApJ, 842, 121

Vanzella E., et al., 2005, A&A, 434, 53

Vanzella E., et al., 2006, A&A, 454, 423

Vanzella E., et al., 2008, A&A, 478, 83

Vergani D., et al., 2012, A&A, 546, A118

Verheijen M. A. W., W. M. A., 1997, PhD thesis, Univ. Groningen, The Netherlands , (1997)

Verheijen M. A. W., W. M. A., 2001, ApJ, 563, 694

Vogelsberger M., et al., 2014, MNRAS, 444, 1518

Wegner M., Muschielok B., 2008, SPIE, 7019, 70190T

Weiner B. J., et al., 2006a, ApJ, 653, 1027

Weiner B. J., et al., 2006b, ApJ, 653, 1049

Westmoquette M. S., Exter K. M., Christensen L., Maier M., Lemoine-Busserolle M., Turner J., Marquart T., 2009, eprint arXiv:0905.3054

Whitaker K. E., Kriek M., van Dokkum P. G., Bezanson R., Brammer G., Franx M., Labbé I., 2012a, ApJ, 745, 179

Whitaker K. E., van Dokkum P. G., Brammer G., Franx M., 2012b, ApJ, 754, L29

Whitaker K. E., et al., 2014, ApJ, 795, 104

White S. D. M., Frenk C. S., 1991, ApJ, 379, 52

White S. D. M., Rees M. J., 1978, MNRAS, 183, 341

White M., Zheng Z., Brown M. J. I., Dey A., Jannuzi B. T., 2007, ApJ, 655, L69

Williams M. J., Bureau M., Cappellari M., 2009a, MNRAS, 400, 1665

Williams R. J., Quadri R. F., Franx M., van Dokkum P., Labbé I., 2009b, ApJ, 691, 1879

Williams M. J., Bureau M., Cappellari M., 2010, MNRAS, 409, 1330

Wisnioski E., et al., 2015, ApJ, 799, 209

Wuyts S., van Dokkum P. G., Franx M., Schreiber N. M. F., Illingworth G. D., Labbe I., Rudnick G., 2009, ApJ, 706, 885

Wuyts S., et al., 2011a, ApJ, 738, 106

Wuyts S., et al., 2011b, ApJ, 742, 96

Wuyts E., et al., 2016a, ApJ, 827, 74

Wuyts S., et al., 2016b, ApJ, 831, 149

Wyder T. K., et al., 2007, ApJS, 173, 293

Yabe K., et al., 2012, PASJ, 64

Yamada T., Nakamura Y., Matsuda Y., Hayashino T., Yamauchi R., Morimoto N., Kousai K., Umemura M., 2012, AJ, 143, 79

Yang Y., et al., 2008, A&A, 477, 789

York D. G., et al., 2000, AJ, 120, 1579

Young T., 1802, Philosophical Transactions of the Royal Society of London, 92, 12

Yuan T.-T., Kewley L. J., Swinbank A. M., Richard J., Livermore R. C., 2011, ApJ, 732, L14

Zahid H. J., Kewley L. J., Bresolin F., 2011, ApJ, 730

Zahid H. J., Geller M. J., Kewley L. J., Hwang H. S., Fabricant D. G., Kurtz M. J., 2013, ApJ, 771, L19

Zahid J., Dima G., Kudritzki R., Kewley L., Geller M., Hwang H. S., Silverman J., Kashino D., 2014, ApJ, 791

Zhang K., et al., 2017, MNRAS, 466, 3217

Zheng Z., Zehavi I., Eisenstein D. J., Weinberg D. H., Jing Y. P., 2009, ApJ, 707, 554

Zheng Z., et al., 2017, MNRAS, 465, 4572

Zwicky F., 1937, ApJ, 86, 217

van Albada T. S., Bahcall J. N., Begeman K., Sancisi R., 1985, ApJ, 295, 305

van Dokkum P. G., 2008, ApJ, 674, 29

van Dokkum P. G., et al., 2001, ApJ, 553, 90

van Dokkum P. G., et al., 2008, ApJ, 677, L5

van der Wel A., et al., 2012, ApJS, 203, 24

van der Wel A., et al., 2014, ApJ, 788, 28